AWARD NUMBER: W81XWH-18-1-0082

TITLE: Design of a 3D Mammography System in the Age of Personalized Medicine

PRINCIPAL INVESTIGATOR: Raymond J. Acciavatti, Ph.D.

CONTRACTING ORGANIZATION: University of Pennsylvania
Philadelphia, PA 19104

REPORT DATE: JULY 2022

TYPE OF REPORT: Final

PREPARED FOR: U.S. Army Medical Research and Development Command
Fort Detrick, Maryland 21702-5012

REPORT DOCUMENTATION PAGE

Form Approved
OMB No. 0704-0188

1. REPORT DATE	**2. REPORT TYPE**	**3. DATES COVERED**
JULY 2022	Final	15 March 2018 – 14 March 2022

4. TITLE AND SUBTITLE

Design of a 3D Mammography System in the Age of Personalized Medicine

5a. CONTRACT NUMBER

5b. GRANT NUMBER
W81XWH-18-1-0082

5c. PROGRAM ELEMENT NUMBER

6. AUTHOR(S)
Raymond J. Acciavatti, Ph.D.

E-Mail: racci@pennmedicine.upenn.edu

5d. PROJECT NUMBER

5e. TASK NUMBER

5f. WORK UNIT NUMBER

7. PERFORMING ORGANIZATION NAME(S) AND ADDRESS(ES)

University of Pennsylvania
Philadelphia, PA 19104

8. PERFORMING ORGANIZATION REPORT NUMBER

9. SPONSORING / MONITORING AGENCY NAME(S) AND ADDRESS(ES)

U.S. Army Medical Research and Development Command
Fort Detrick, Maryland 21702-5012

10. SPONSOR/MONITOR'S ACRONYM(S)

11. SPONSOR/MONITOR'S REPORT NUMBER(S)

12. DISTRIBUTION / AVAILABILITY STATEMENT

Approved for Public Release; Distribution Unlimited

13. SUPPLEMENTARY NOTES

14. ABSTRACT

Digital breast tomosynthesis (DBT) is the latest 3D advancement in breast cancer screening. In conventional systems, the x-ray tube scans in one direction (left-to-right). We modeled a next-generation DBT system with an additional scanning motion in the posteroanterior (PA) direction. Defrise phantoms and anthropomorphic breast models were simulated. In the next-generation design, there was higher area under the receiver-operating-characteristic curve (AUC) in the task of segmenting dense from adipose tissue. Also, in Defrise phantoms, AUC was optimized by personalizing the range of PA motion around the size of the phantom. As a separate task, calcification detection was analyzed. Model-observer performance was improved with the use of "super-resolution" reconstructions. We developed the Fourier Spectral Distortion metric for high-frequency star patterns to quantify anisotropies in super-resolution in the conventional geometry. With theoretical modeling, it was shown that anisotropies can be eliminated by re-arranging the x-ray source locations in clusters with submillimeter spacing. We also analyzed how the principles of 3D imaging could be extended beyond the screening exam to the diagnostic call-back exam, magnification mammography. With theoretical modeling, it was determined that magnification tomosynthesis supports super-resolution. Finally, our 3D breast model was advanced to include Perlin noise [IEEE TMI 2021 40(12): 3436-45].

15. SUBJECT TERMS

Digital breast tomosynthesis (DBT), mammography, super-resolution, personalized medicine, Defrise phantom, image reconstruction, calcification, virtual clinical trial, magnification mammography

16. SECURITY CLASSIFICATION OF:			**17. LIMITATION OF ABSTRACT**	**18. NUMBER OF PAGES**	**19a. NAME OF RESPONSIBLE PERSON**
a. REPORT	**b. ABSTRACT**	**c. THIS PAGE**			**19b. TELEPHONE NUMBER** *(include area code)*
Unclassified	Unclassified	Unclassified	Unclassified	302	USAMRDC

Table of Contents

1. INTRODUCTION

Many medical centers have upgraded their breast cancer screening practices from 2D digital mammography (DM) to 3D digital breast tomosynthesis (DBT), which has improved both the sensitivity and specificity of screening.[1,2] However, current clinical systems represent just the first-generation of DBT. These systems were designed to scan in only one direction (laterally). With theoretical modeling[3-5] and virtual clinical trials (VCTs)[6-8], we have demonstrated the benefits of introducing an additional component of x-ray tube motion in the posteroanterior (PA) direction and customizing the range of x-ray tube motion around the breast's dimension in this direction.[9] Our VCTs with computational phantoms showed that this next-generation tomosynthesis (NGT) system design offers better portrayal of dense tissue (the tissue most susceptible to masking effects).[10] Also, we investigated super-resolution (SR) as a mechanism to improve the visibility of calcifications (small early signs of cancer). VCTs with model observers demonstrated that reconstruction grids prepared with SR resulted in superior calcification detection performance.[11] Our theoretical modeling with high-frequency test objects has also allowed us to identify new ways of arranging the x-ray source locations to optimize SR; specifically, with the use of rapid source pulsing and the arrangement of x-ray source locations in clusters with submillimeter spacing.[4,5] Finally, we have analyzed how magnification mammography, a 2D diagnostic call-back exam for suspicious calcifications, can be re-designed to incorporate 3D imaging with tomosynthesis. We have shown that magnification tomosynthesis is capable of SR.[12] There is superior spatial resolution if a magnification mammogram is acquired with 3D imaging techniques as opposed to the conventional 2D imaging techniques being used clinically.

2. KEYWORDS

Digital breast tomosynthesis (DBT), mammography, super-resolution, personalized medicine, Defrise phantom, image reconstruction, calcification, virtual clinical trial, magnification mammography.

3. ACCOMPLISHMENTS

3.A. What were the major goals of the project?

The Statement of Work is shown below. Milestones are summarized for each of the major tasks. More detail about these milestones is given in Section 3.B.

3.A.1. Specific Aim 1: Design a personalized image acquisition technique for screening mammography.

Specific Aim 1: Design a personalized image acquisition technique for screening mammography.	**Timeline (Months)**
Major Task 1: Optimize super-resolution (SR) with simulations of high-frequency, sinusoidal test objects and calculations of the *r*-factor.	
Subtask 1: Develop a design for optimizing SR. Through our prototype system, we learned that SR can be optimized by introducing detector motion that varies the source-to-image distance (SID) during the scan. However, to minimize the need for a thick detector housing, we will investigate more complex combinations of x-ray tube and detector motion that can be used to optimize SR.	1-12
Subtask 2: Make refinements to the motions of the x-ray tube and detector based on the on-going results of the virtual clinical trial (VCT) in specific aim 3.	13-30
Milestones: Modeling and simulation of acquisition geometries with superior image quality and suppression of anisotropies in SR • See Acciavatti et al. (Proc. of SPIE 2020, Vol. 11312 p. 113125G) Table 1 and Figures 4-7 (document 6 of Section 9).[4] Described in Year 2 progress report. • See Acciavatti et al. (Proc. of SPIE 2020, Vol. 11513 p. 115130V) Figures 1-5 and Figure 8 (document 9 of Section 9).[5] Described in Year 2 progress report.	

• See Vent et al. (Proc. of SPIE 2020, Vol. 11513, 1151317) Figures 1-6 (document 11 of Section 9).[13] Described in Year 3 progress report. • See Acciavatti et al. (Proc. of SPIE 2022, Vol. 12031, 120314B) Table 1 and Figures 1-7 (document 23 of Section 9).[14] Described in Year 4 progress report (final report / NCE). Development of Fourier Spectral Distortion metric[15] for evaluating anisotropies in SR • See Vent et al. (IEEE TMI 2021, Vol. 40 p. 1055-1064) Figures 8, 10-14 (document 17 of Section 9).[15] Described in Year 3 progress report. • See Choi et al. (Proc. of SPIE 2022, Vol. 12031, p. 120314C) Figures 5-7 (document 24 of Section 9).[16] Described in Year 4 progress report (final report / NCE). Analysis of Fourier-space sampling and power spectra to identify acquisition geometries with the highest resolution in all three directions • See Choi et al. (Proc. of SPIE 2021, Vol. 11595 p. 115954W) Figure 1 (document 14 of Section 9).[17] Described in Year 3 progress report. • See Vent et al. (Proc. of SPIE 2022, Vol. 12031, p. 1203142) Figures 2-3 (document 27 of Section 9).[18] Described in Year 4 progress report (final report / NCE).	
Major Task 2: Simulate the reconstruction of glandular and adipose tissue with Defrise phantoms.	
Subtask 1: Prepare Defrise phantoms modeled in the shape of breasts.	1-3
Subtask 2: Simulate the image acquisition. First, a 2D scout image is acquired at low radiation dose. Second, the 3D scan parameters are determined based on estimates of the breast size, shape, and internal composition.	4-9
Subtask 3: Prepare reconstructions, and calculate the relative contrast at the septa between glandular and adipose tissue.	10-15
Subtask 4: Determine the effect of the reconstruction filter on the relative contrast. To optimize the image quality, the filter will be personalized to the phantom.	16-21
Subtask 5: Update the reconstructions and calculations of contrast as new acquisition geometries are identified based on the on-going results of the virtual clinical trial in specific aim 3.	22-30
<u>Milestones:</u> Database of virtual Defrise phantoms and reconstructions, demonstrating that personalized scanning motions yield improvements in breast-density visualization • See Acciavatti et al. (Proc. of SPIE 2019, Vol. 10948, p. 109480B) Table 1 and Figures 3, 5, 6 (document 3 of Section 9).[9] Described in Year 1 progress report. Virtual phantom model consisting of equidistant tubes of dense tissue in a background of adipose tissue for optimization of signal-to-noise ratio (SNR) in next-generation DBT system designs • See Martin et al. (Proc. of SPIE 2021, Vol. 10948, p. 109480B) Figures 6-8 (document 15 of Section 9).[19] Described in Year 3 progress report.	
Major Task 3: Develop a personalized acquisition geometry yielding a more accurate segmentation of the breast outline.	
Subtask 1: Prepare database of binary phantom masks (uniform phantoms with no internal composition). These will be used to calculate the breast outline (convex hull) in the reconstruction.	4-6
Subtask 2: Determine the motions of the x-ray tube and detector that yield the most accurate breast outline segmentation. These motions will be personalized to the breast size and shape based on a 2D scout image.	7-21
<u>Milestone:</u> Database of virtual breast phantoms demonstrating improvements in the accuracy of the breast outline segmentation with the next-generation scanning motion • See Teixeira et al. (Proc. of SPIE 2022, Vol. 12031, p. 120313S) Figures 4-5 (document 26 of Section 9).[20] Described in Year 4 progress report (final report / NCE).	

3.A.2. Specific Aim 2: Design a 3D Magnification Mammography Call-Back Exam.

Specific Aim 2: Design a 3D Magnification Mammography Call-Back Exam.	**Timelines (Months)**
Major Task 4: Optimize super-resolution (SR).	
Subtask 1: Develop designs for the source and detector motion that optimize SR in magnification imaging. This will ensure the highest image quality in imaging calcifications (small, closely-spaced structures).	1-12
Subtask 2: Make refinements to the motion of the x-ray tube and detector based on the on-going results of the virtual clinical trial in specific aim 3.	13-30
Milestones: Theoretical model of anisotropies in SR in magnification tomosynthesis • See Acciavatti et al. (Med. Phys. 2021 Vol. 48) Conference abstract (document 19 of Section 9).[21] Described in Year 4 progress report (final report / NCE). Theoretical model of next-generation system design for suppressing anisotropies in magnification tomosynthesis • See Acciavatti et al. (Proc. of SPIE 2021, Vol. 11595, p. 115951J) Table 1 and Figures 4-6 (document 13 of Section 9).[12] Described in Year 3 progress report.	
Major Task 5: Perform a contrast-detail reader study.	
Subtask 1: Simulate a contrast-detail (C-D) array in a uniform background at different positions. The scan parameters for the 3D acquisition will be customized around the region containing the C-D array.	7-12
Subtask 2: Perform a reader study. Prepare plots of the smallest thickness visible as a function of the cross-sectional area of the lesion. Determine how a personalized 3D acquisition compares against: (1) a non-personalized 3D acquisition, and (2) 2D magnification imaging (the current gold standard).	13-18
Subtask 3: Repeat subtasks 1 and 2 with the C-D array in structured (anatomical) backgrounds. Determine how the breast background (density and texture) impacts the reader performance.	19-24
Subtask 4: Update the results of subtasks 2-3 based on the new reconstruction filters and the new acquisition geometries developed in specific aims 1 and 3.	25-30
Milestones: Database of calcification polycubes with varying size (detail) and varying contrast (percentage of hydroxyapatite, or weighting fraction) with potential applications in both screening and magnification tomosynthesis • See Vu et al. (Student Abstract for Summer SUPERS Program at Penn) Abstract (document 4 of Section 9). Described in Year 2 progress report. • See Acciavatti et al. (Proc. of SPIE 2020, Vol. 11513, p. 115130V) Figure 7 (document 9 of Section 9).[5] Described in Year 3 progress report. • See Barufaldi et al. (Proc. of SPIE 2020, Vol. 11513, p. 1151313) Figure 1 (document 10 of Section 9).[11] Described in Year 3 progress report. • See Barufaldi et al. (Proc. of SPIE 2020, Vol. 11312, p. 113120I) Table 2 (document 7 of Section 9).[22] Described in Year 2 progress report. • See Barufaldi et al. (Radiation Protection Dosimetry 2021, Vol. 195, p. 363-371) Figure 1, Figure 3 (document 18 of Section 9).[23] Described in Year 4 progress report (final report / NCE).	

3.A.3. Specific Aim 3: Evaluate the new designs for screening and call-back imaging with a virtual clinical trial.

Specific Aim 3: Evaluate the new designs for screening and call-back imaging with a virtual clinical trial.	**Timeline (Months)**
Major Task 6: Quantify breast density in anatomical phantoms.	
Subtask 1: Prepare anatomical phantoms with variable size, shape, and internal composition.	1-3
Subtask 2: Simulate x-ray images in personalized and non-personalized acquisition geometries.	4-6
Subtask 3: Calculate reconstructions. Model the differentiation between adipose and glandular tissue as a binary classification task with a receiver operating characteristic (ROC) curve.	7-12

Subtask 4: Optimize the reconstruction filter; it will be personalized to the phantom. The filter should maximize the area under the ROC curve.	13-18
Subtask 5: Repeat subtasks 2-4 as on-going refinements are made to the motion paths of the x-ray tube and detector, as well as the reconstruction filter. We are working to maximize the area under the ROC curve.	19-30
Milestone: Model of classification accuracy of segmenting fibroglandular (dense) and adipose tissue compartments in voxel breast phantoms. • See Peregrino et al. (Proceedings of the 14th International Joint Conference on Biomedical Engineering Systems and Technologies BIOSTEC 2021, Vol. 4, p. 252-259) Figures 3-6 (document 12 of Section 9).[24] Described in Year 4 progress report (final report / NCE). • See Vent et al. (Proc. of SPIE 2021, Vol. 11595, p. 115954V) Figures 4-8 (document 16 of Section 9).[10] Described in Year 3 progress report. • See Dong et al. (Proc. of SPIE 2022, Vol. 12031, p. 120311W) Figure 2 (document 25 of Section 9).[25] Described in Year 4 progress report (final report / NCE).	
Major Task 7: Perform a virtual clinical trial (VCT) with simulated lesions.	
Subtask 1: Prepare computational breast phantoms with lesions (masses and calcifications) of variable size, shape, and contrast.	1-6
Subtask 2: Design the VCT. Numerical observers will be trained on the statistics of images. Channelized Hotelling Observer parameters will be determined to match the performance of the observer on real and breast model images.	7-12
Subtask 3: Conduct the VCT. The sensitivity index (d') and call-back rate will be estimated for the detection and characterization of lesions in different system designs. These calculations will be used to compare new acquisition geometries against conventional acquisition geometries.	13-30
Subtask 4: The results of the VCT will be used to rule out poor design choices and identify the best possible system designs for a human clinical trial. We will perform statistical power calculations to design the future clinical trial.	31-36
Milestones: VCTs of breast phantoms with lesions • See Barufaldi et al. (Proc. of SPIE 2020, Vol. 11312, p. 113120I) Figures 2-3 (document 7 of Section 9).[22] Described in Year 2 progress report. • See Barufaldi et al. (Proc. of SPIE 2020, Vol. 11513, p. 1151313) Figures 2-3 (document 10 of Section 9).[11] Described in Year 3 progress report. • See Barufaldi et al. (Medical Physics 2022, Vol. 49, p. 2220-2232) Figures 3, 6-7 (document 22 of Section 9).[26] Described in Year 4 progress report (final report / NCE). • See Choi et al. (Proc. of SPIE 2022, Vol. 12286, p. 1228618) Figures 3-6, Tables 2-3 (document 28 of Section 9).[27] Described in Year 4 progress report (final report / NCE). • See Nobrega et al. (Proc. of SPIE 2022, Vol. 12286, p. 122860L) Figures 2-6 (document 29 of Section 9).[28] Described in Year 4 progress report (final report / NCE). Publication of advanced detector model for VCTs • See Acciavatti et al. (Medical Physics 2019, Vol. 46, p. 494-504) Figures 4-8 (document 1 of Section 9).[29] Described in Year 1 progress report. • See Acciavatti et al. (Medical Physics 2019, Vol. 46, p. 505-516) Figures 1-12 (document 2 of Section 9).[30] Described in Year 1 progress report. Development of more advanced voxel breast phantom with Perlin noise • See Barufaldi et al. (IEEE TMI 2021, Vol. 40, p. 3436-3445) Figure 5 (document 21 of Section 9).[31] Described in Year 4 progress report (final report / NCE). X-ray technique optimization for breast phantom • See Acciavatti et al. (Proc. of SPIE 2020, Vol. 11314, p. 113140W) Figures 2-4 (document 5 of Section 9).[32] Described in Year 2 progress report. • See Acciavatti et al. (Cancers 2021, Vol. 13, p. 5497) Figures 1, 3, and 4 (document 20 of Section 9).[33] Described in Year 4 progress report (final report / NCE). Validation of breast phantom model. • See Acciavatti et al. (Proc. of SPIE 2020, Vol. 11513, p. 1151309) Figures 3-5, Table 4 (document 8 of Section 9).[34] Described in Year 3 progress report.	

3.B. What was accomplished under these goals?

3.B.1. Specific Aim 1: Design a personalized image acquisition technique for screening mammography.

Aim 1 Overview:

Rafferty *et al*. showed that DBT offers an improvement in mass imaging over conventional 2D DM.[35] However, the benefits of DBT are limited to non-calcification findings. We have investigated SR as a mechanism to improve calcification visibility.[4,5] We developed technical innovations to the acquisition geometry to optimize SR and suppress anisotropies. We have shown that more complex motions for the x-ray tube give rise to SR with even better quality and at more positions in the image. Another benefit of these new scanning motions is improving the visualization of dense tissue.[10] To maximize the image quality, we have also shown that the scanning motion should be personalized to the woman being imaged; specifically, to the size of the breast.[9] A key advantage of computational modeling is that promising system designs can be identified rapidly and in a cost-effective manner without requiring human subject recruitment.

Major Task 1: Optimize super-resolution (SR) with simulations of high-frequency, sinusoidal test objects and calculations of the *r*-factor.

In our previous work, we demonstrated that clinical DBT systems support super-resolution (SR), or subpixel resolution relative to the detector. SR is a mechanism for improving the visibility of calcifications.[3] However, clinical DBT systems are not yet designed to maximize this effect. There are "blind spots" throughout the image at which SR is not achievable.

As part of this DoD grant, we identified new system designs with superior image quality and more isotropic SR. Our design strategy for optimizing SR differs from conventional DBT systems in which the source positions are equally spaced over a circular arc.[36] The x-ray source positions under the new design are re-arranged in "clusters" with submillimeter spacing.[4,5] The new design can be implemented by rapidly pulsing the x-ray source during a continuous sweep of the x-ray tube. In our Year 2 progress report, we detailed the clustering method (**Figure 1 below**), which we analyzed in the work Acciavatti et al.[4] (Proc. of SPIE 2020, Vol. 11312, p. 113125G, Table 1 and Figures 4-7 in document 6 of Section 9). In our Year 2 progress report, we also expanded from one-dimensional source motion to two-dimensional source motion, which we analyzed in the work Acciavatti et al.[5] (Proc. of SPIE 2020, Vol. 11513 p. 115130V, Figures 1-5 and Figure 8 in document 9 of Section 9).

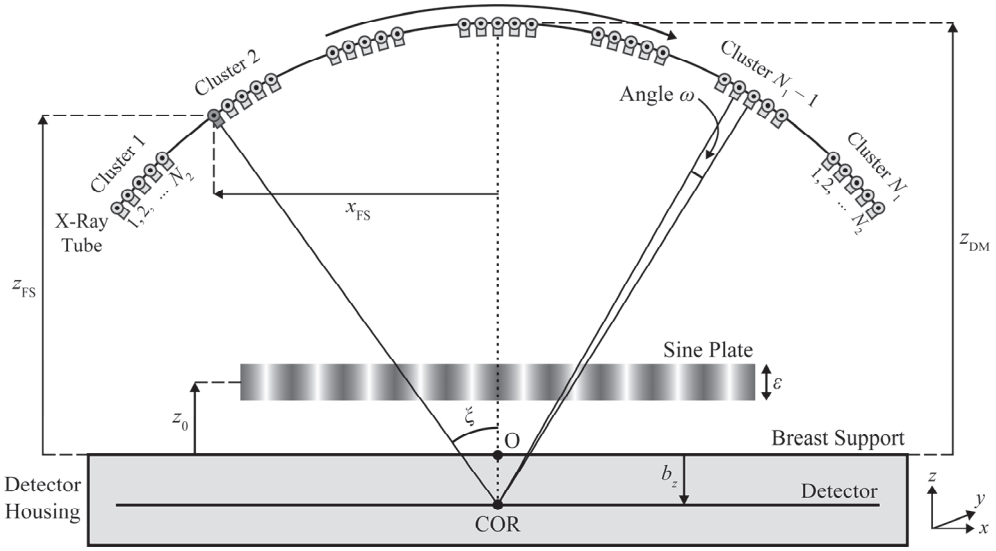

Figure 1. A DBT system design with clustered source positions is modeled. The parameter N_1 controls the number of clusters, while the parameter N_2 controls the number of source positions per cluster. In this example, $N_1 = 7$ and $N_2 = 5$. Figure and caption from Acciavatti et al.[4] (Proc. of SPIE 2020, Vol. 11312 p. 113125G) Figure 3 in document 6 of Section 9.

To illustrate improvements in image quality with new tomosynthesis system designs in the NGT system, we performed "Physics VCTs" with simulated star- and bar-pattern phantoms, as described in our Year 3 progress report through the work Vent et al.[13] (Proc. of SPIE 2020, Vol. 11513, 1151317, Figures 1-6 in document 11 of Section 9). Most recently (new to this Year 4 progress report), we performed an experimental validation of isotropic super-resolution in the NGT system.[14] We analyzed a 360°-star pattern (Type 9/10/360-003, Supertech, Elkhart, IN) in a geometry with 15° of lateral source motion and 0.085 mm detector pixelation (**Figure 2 below**). The NGT scan allows for isotropic SR (i.e., SR in all directions), more reliably allowing for visualization of small features in the image regardless of orientation.

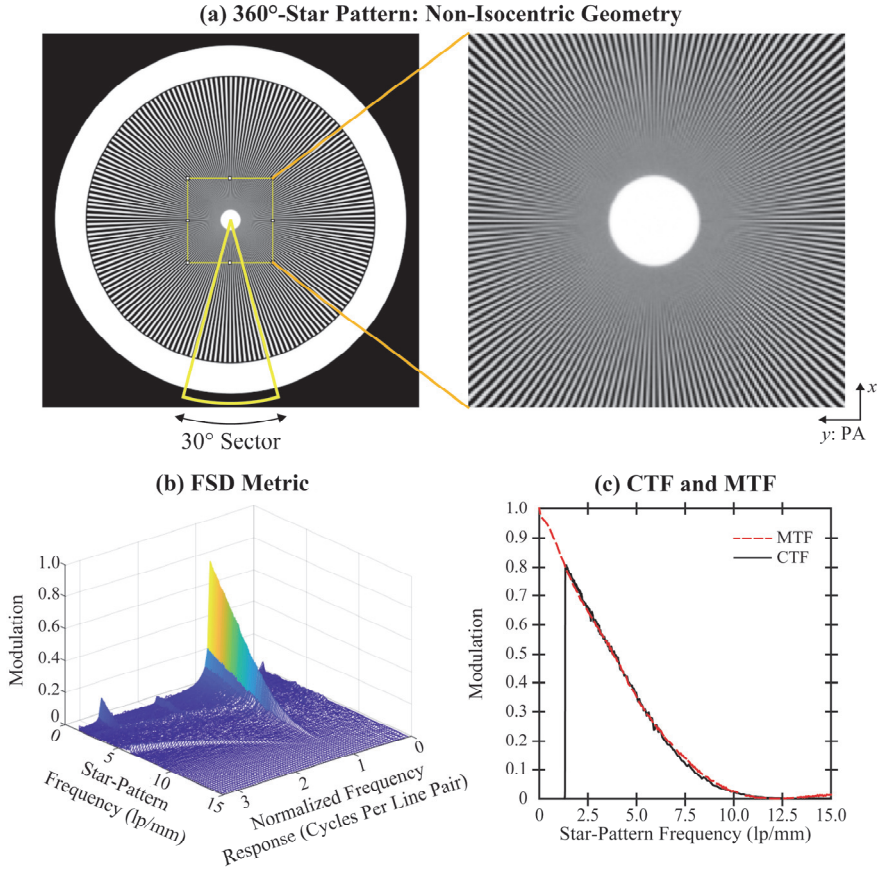

Figure 2. (a) With the use of a non-isocentric geometry, there are no longer Moiré artifacts in the PA direction in the 360°-star pattern. (b) Spectral leakage in the FSD metric is minimized relative to the conventional geometry. (c) The CTF illustrates how aliasing artifacts at frequencies exceeding the detector alias frequency (5.9 mm^{-1}) are suppressed. Figure and caption adapted from Acciavatti et al.[14] (Proc. of SPIE 2022, Vol. 12031 p. 120314B) Figure 9 in document 23 of Section 9.

As described in our Year 3 progress report, we developed the Fourier Spectral Distortion (FSD) metric to evaluate anisotropies in SR. At each frequency in a star-pattern phantom, we calculated the Fourier transform as a function of the frequency response, measured in cycles per line pair (lp). The FSD should ideally peak at a frequency response of 1.0 cycles per lp, corresponding to the input frequency; all other signal reflects spectral leakage. The FSD metric [**Figure 2(b) above**] illustrates how spectral leakage is minimized in the NGT system for frequency signals distal to the spine of the surface plot. Our latest work (new to this progress report) demonstrated that spectral leakage in the FSD is also minimized by increasing the number of projections, and thus this is also a strategy for optimizing image quality; see Choi et al.[16] (Proc. of SPIE 2022, Vol. 12031, p. 120314C) Figure 8 in document 24 of Section 9.

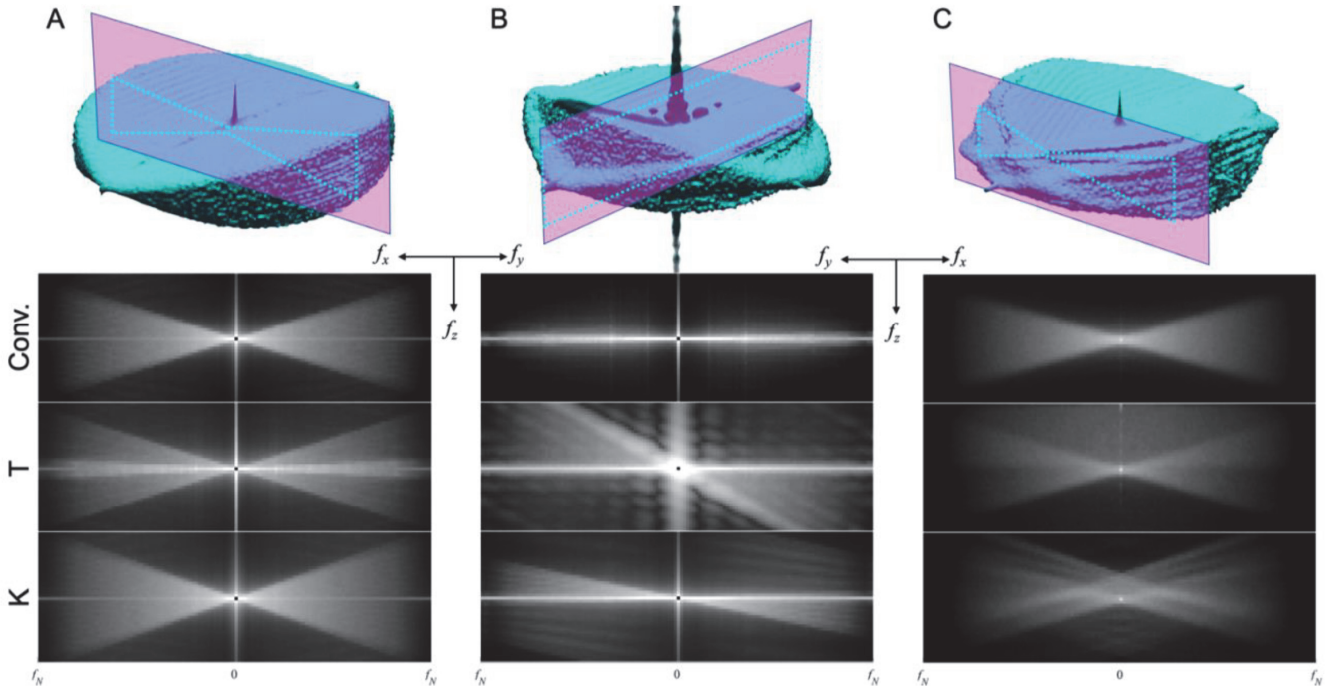

Figure 3. Examples of different slices through the NPS volumes for each geometry. Zero-frequency NPS slice of the f_x-f_z plane (left). NPS slice of the f_y-f_z plane at $f_x = 0$ (middle). High-frequency NPS slice in the f_x-f_z plane at $f_y = 2/3 \cdot f_N$. Figure and caption from Vent et al.[18] (Proc. of SPIE 2022, Vol. 12031 p. 1203142) Figure 3 in document 27 of Section 9.

To illustrate additional improvements in image quality, we calculated the Fourier-sampling planes of various scanning motions, and showed that the NGT scanning motion offers better Fourier-space sampling than the conventional DBT scanning motions, meaning there is better resolution in all three directions, as described in our Year 3 progress report; see Figure 1 of Choi et al.[17] (Proc. of SPIE 2021, Vol. 11595 p. 115954W) in document 14 of Section 9. Additionally, we showed that the noise power spectra (NPS) of the NGT scanning motion is characterized by more extensive *z*-axis resolution than the conventional scanning motion in the work by Vent et al.[18], which is new to this progress report (**Figure 3 above**); see Vent et al.[18] (Proc. of SPIE 2022, Vol. 12031, p. 1203142) Figure 3 in document 27 of Section 9.

<u>Major Task 2:</u> Simulate the reconstruction of glandular and adipose tissue with Defrise phantoms.

As described in our Year 1 progress report, we developed a "personalized" system design offering advantages in breast density visualization in DBT. We used Defrise phantoms with alternating bands of fibroglandular and adipose tissue to illustrate the advantage of PA scanning motions.[9] The reconstruction was analyzed voxel-by-voxel as a binary classification of the two tissue types using area under the receiver-operating-characteristic curve (AUC) as the metric of image quality. Each phantom was simulated in multiple acquisition geometries (441 in total) which varied in terms of the range of x-ray tube motion in two directions (mediolateral and posteroanterior). We demonstrated that AUC for each phantom was optimized by a different scanning motion, and that this motion is dependent on the chest wall-to-nipple distance (CND). In phantoms with a larger CND, it is necessary to translate the source further from the chest-wall plane to optimize the image quality. Based on these results, we successfully met our goal of demonstrating that image quality is improved by <u>personalizing</u> the scanning motion to the woman being imaged; specifically, to the size of the breast; see Acciavatti et al.[9] (Proc. SPIE 2019, Vol. 10948, p. 109480B) Table 1 and Figures 3, 5, 6 (document 3 of Section 9).

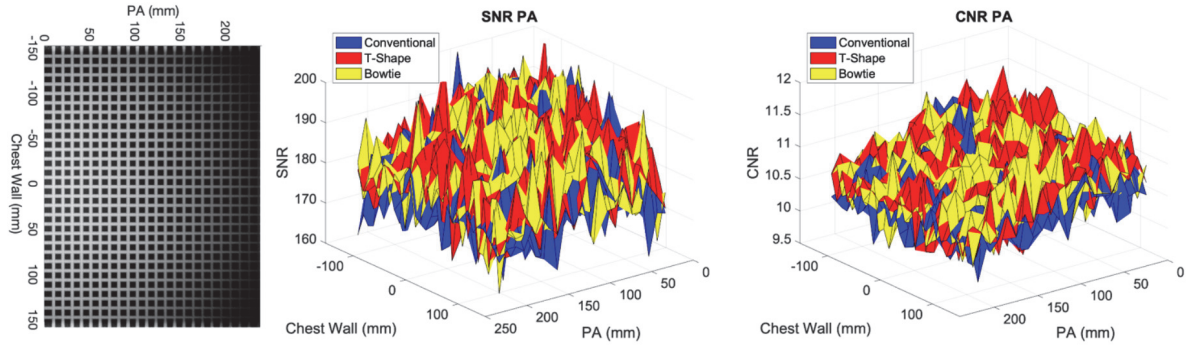

Figure 4. Central reconstruction slice, SNR, and CNR for PA measurements. Figure and caption from Martin et al.[19] (Proc. of SPIE 2021, Vol. 10948 p. 109480B) Figure 6 in document 15 of Section 9.

To expand the work on Defrise phantoms with alternating patterns of fibroglandular and adipose tissue, we also created computational phantoms consisting of equidistant tubes of fibroglandular tissue in a background of adipose tissue, as described in our Year 3 progress report. These phantoms were used to measure the signal-to-noise ratio (SNR) throughout the image. The tubes run in two directions (x and y), forming a lattice. Each tube has dimensions 4.4 × 240 × 4.4 (in mm). We determined SNR in a region-of-interest (15 × 15 pixels) using the ratio μ/σ (mean to standard deviation in signal). The regions-of-interest (ROIs) were shifted in each direction, at intervals halfway between tube intersections, to generate a surface plot of SNR and contrast-to-noise ratio (CNR) at all positions. We demonstrated that the NGT system offers higher SNR and CNR than the conventional system design (**Figure 4 above**);[19] also see Martin et al.[19] (Proc. of SPIE 2021, Vol. 10948, p. 109480B) Figures 6-8 in document 15 of Section 9.

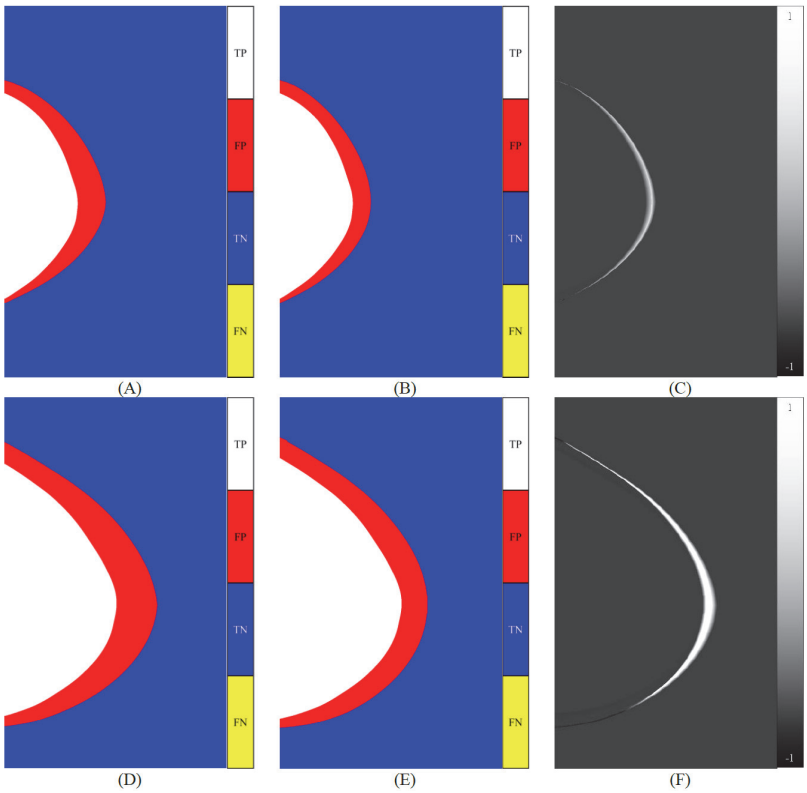

Figure 5. Segmented breast of DBT reconstructions (uppermost slice) of a Perlin phantom with magnified regions of breast skin (accuracy map). The accuracy map of (A, D) conventional and (B, E) t-shape acquisition geometries are shown. (C, F) Sum of differences between reconstructed slices using the conventional and t-shape acquisition geometries are also shown. Figure and caption from Teixeira et al.[20] (Proc. of SPIE 2022, Vol. 12031 p. 120313S) Figure 4 in document 26 of Section 9.

<u>Major Task 3:</u> Develop a personalized acquisition geometry yielding a more accurate segmentation of the breast outline.

An additional drawback of the conventional system design is that the reconstruction of the 3D breast outline is overestimated in the PA direction.[37] We have calculated the reconstructed breast volume for various scanning motions, and showed that the NGT system design offers a more accurate breast outline segmentation than the conventional system design (**Figure 5 above**); see Teixeria et al.[20] (Proc. of SPIE 2022, Vol. 12031, p. 120313S) Figure 4 (document 26 of Section 9). This research is new to this Year 4 progress report.

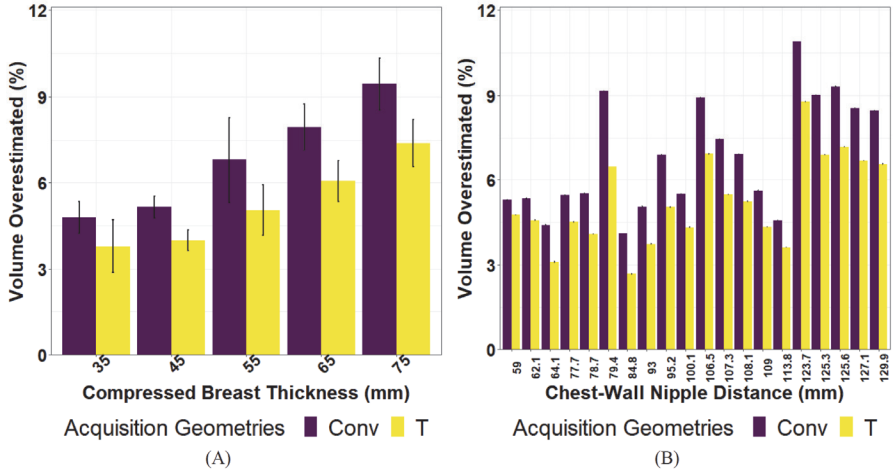

Figure 6. Summary of volume overestimated categorized by (A) compressed breast thickness and (B) chest-wall to nipple distance. Figure and caption from Teixeira et al.[20] (Proc. of SPIE 2022, Vol. 12031 p. 120313S) Figure 5 in document 26 of Section 9.

Also as a new result to this progress report, we successfully met our goal of demonstrating that novel NGT scanning motions are capable of a more accurate breast outline segmentation than the conventional scanning motion. **Figure 6 above** illustrates these results for virtual phantoms created using the 3D breast model developed by Rodríguez-Ruiz *et al*.[38]. The novel NGT scan (yellow) offers less volume overestimation than the conventional scan (purple) for all phantoms analyzed, spanning a range of thicknesses and dimensions in the PA direction; see Teixeira et al.[20] (Proc. of SPIE 2022, Vol. 12031, p. 120313S) Figure 5 (document 26 of Section 9).

3.B.2. Specific Aim 2: Design a 3D Magnification Mammography Call-Back Exam.

<u>Aim 2 Overview:</u>

Calcifications are often less than 1.0 mm in diameter and require additional diagnostic imaging, such as magnification mammography, for more detailed characterization. In magnification mammography, the breast is elevated closer to the x-ray tube and the small focal spot is used. With this setup, small details appear bigger, and the modulation transfer function (MTF) increases at each frequency, making it easier for radiologists to characterize suspicious findings. Clinical magnification mammography exams continue to rely on conventional 2D imaging techniques, even though the technology used for screening has advanced from 2D to 3D imaging. Through this DoD grant, we successfully performed the computational modeling to design a <u>3D</u> magnification exam with SR and thus the highest possible resolution for calcification imaging.[12]

<u>Major Task 4:</u> Optimize super-resolution (SR).

As described in our Year 3 progress report, we presented our work on magnification tomosynthesis at the virtual 2021 SPIE Medical Imaging conference (document 13 of Section 9).[12] In that work, we demonstrated that PA source motion (a technical innovation in the NGT system) is an important tool to suppress anisotropies in SR. We modeled the system with a secondary component of scanning motion in the PA direction. The focal spot (FS) motion is directed along the angle β relative to the chest wall (**Figure 7 below** - Acciavatti et al.[12]

Proc. of SPIE 2021, Vol. 11595 p. 115951J Figure 1 in document 13 of Section 9). Whereas the conventional scan is directed at the angle $\beta = 0°$, the novel scanning motion is directed at the angle $\beta = 0.3°$. Angling the FS positions in this manner results in subpixel sampling gain in the PA direction that is not achievable in the conventional geometry. As shown in **Figure 8 below** (Acciavatti et al.[12] Proc. of SPIE 2021, Vol. 11595 p. 115951J Figure 6 in document 13 of Section 9), the *r*-factor and upper tails of the *r*-factor distribution are all minimized by the secondary scanning motion at the angle $\beta = 0.3°$, resulting in high image quality with super-resolution.

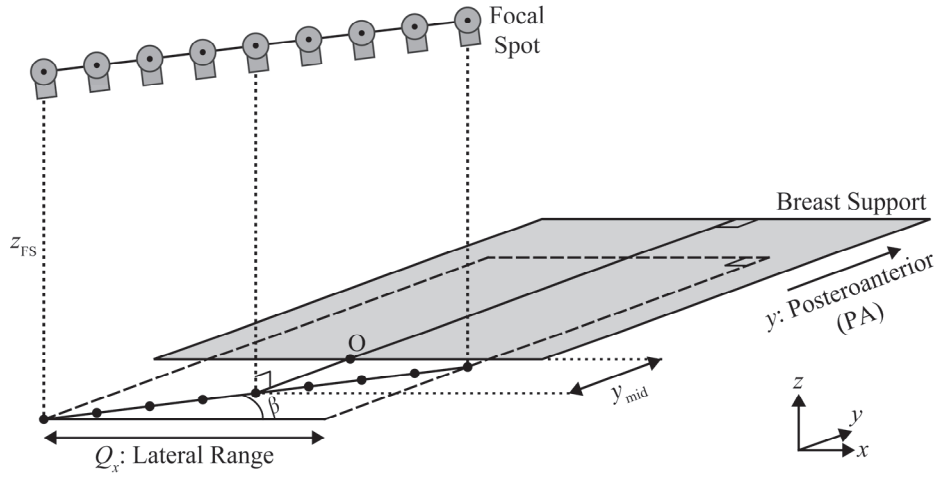

Figure 7. In this acquisition geometry, the focal spot (FS) motion is directed along the angle β. Angling the FS positions in this manner introduces a small secondary component of motion in the PA direction. Figure and caption from Acciavatti et al.[12] (Proc. of SPIE 2021, Vol. 11595 p. 115951J) Figure 1 in document 13 of Section 9.

The PI was the first author of a "work-in-progress" poster at the 16th International Workshop on Breast Imaging (IWBI) titled "Next-Generation 3D Magnification Mammography Offers Super-Resolution" (presenting author: Andrew D. A. Maidment, Ph.D.) held in Leuven, Belgium in May 2022. This work (new to this Year 4 progress report) earned the Best Poster Award at the 2022 IWBI conference.

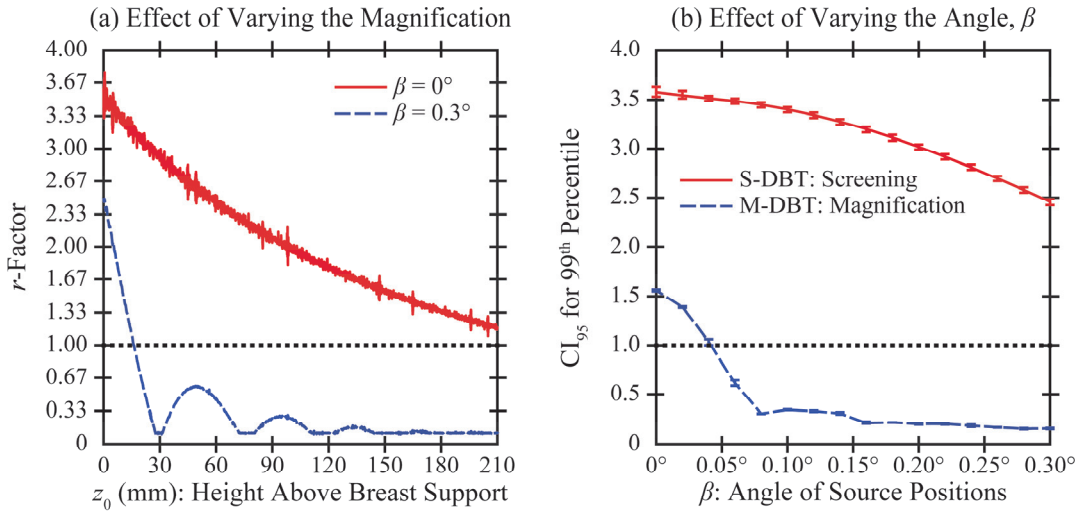

Figure 8. (a) Two acquisition geometries are analyzed in terms of the effect of increasing z_0 (increasing magnification). Higher image quality is achieved in the acquisition geometry with a small secondary component of source motion in the PA direction ($\beta = 0.3°$). (b) The upper tail of the *r*-factor distribution was analyzed in terms of the 99th percentile. In contact mode (S-DBT), the 95% confidence interval (CI_{95}) for this percentile is higher than 1.0, irrespective of the angle β. However, in magnification mode (M-DBT), CI_{95} does not fall below 1.0 as the angle β increases. Figure and caption from Acciavatti et al.[12] (Proc. of SPIE 2021, Vol. 11595 p. 115951J) Figure 6 in document 13 of Section 9.

<u>Major Task 5:</u> Perform a contrast-detail reader study.

We created a database of 3D calcification polycube models of varying size (detail) and contrast (percentage of hydroxyapatite) with potential applications in both screening and magnification tomosynthesis. As shown in **Figure 9 below**, these calcification polycubes were inserted in anthropomorphic voxel phantoms, and reconstructions were generated at 0.085 mm and 0.0425 mm resolution; see Barufaldi et al.[11] (Proc. of SPIE 2020, Vol. 11513 p. 1151313 Figure 1 in document 10 of Section 9) described in our Year 3 progress report. Polycubes varied in size from one to three voxels.

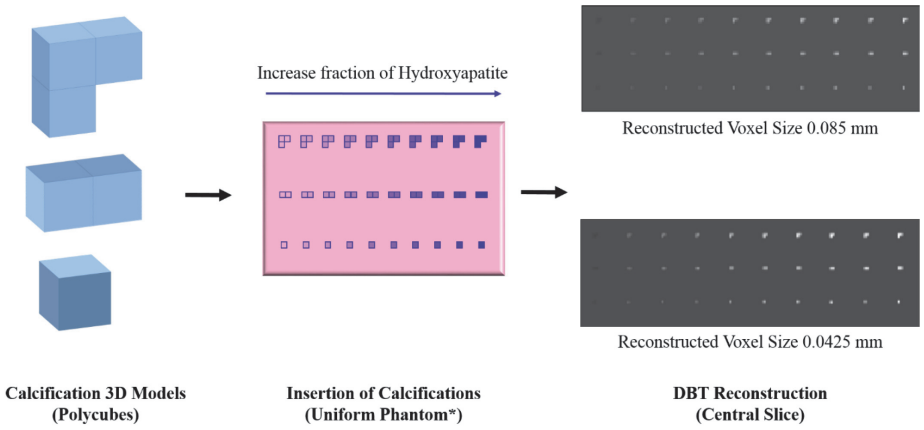

Figure 9. Method used to insert calcifications into the anthropomorphic breast phantoms. *Illustrative phantom used to visualize differences in fraction of hydroxyapatite in the DBT reconstructions. Figure and caption from Barufaldi et al.[11] (Proc. of SPIE 2020, Vol. 11513 p. 1151313) Figure 1 in document 10 of Section 9.

A central purpose of these calcification models was to demonstrate anisotropies in SR. This is illustrated in **Figure 10 below**; see Acciavatti et al.[5] (Proc. of SPIE 2020, Vol. 11513 p. 115130V Figure 7 in document 9 of Section 9) – a paper described in our Year 3 progress report. As shown in that figure, spacings between calcifications are not resolved at the depth z = 30.73 mm in the reconstruction, yet super-resolution is achieved at the depth z = 32.55 mm. This database of calcifications was an important tool to demonstrate anisotropies in SR. We have used VCTs to demonstrate anisotropies in calcification visualization in the conventional geometry depending on position (slice) in the 3D image. VCTs validated the anisotropies in SR predicted with theoretical modeling.[5]

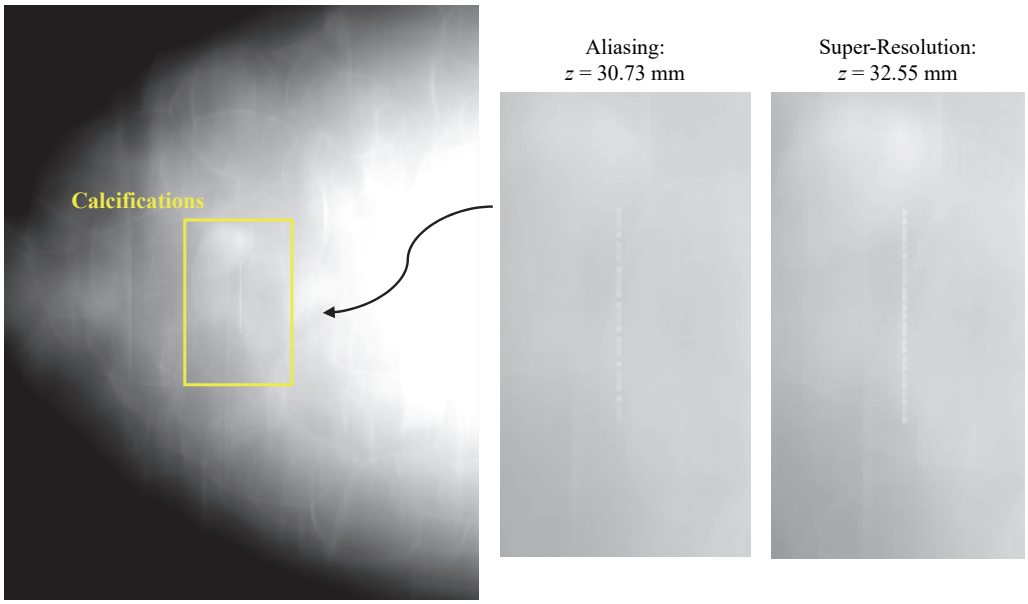

Figure 10. The ability to resolve individual punctate calcifications in a linear array is dependent on the positioning of the cluster. Figure and caption from Acciavatti et al.[5] (Proc. of SPIE 2020, Vol. 11513 p. 115130V) Figure 7 in document 9 of Section 9.

3.B.3. Specific Aim 3: Evaluate the New Designs for Screening and Call-Back Imaging with a Virtual Clinical Trial

Aim 3 Overview:

We have performed VCTs with 3D breast models to analyze lesion detection in DBT. VCTs were conducted with highly-attenuating polycubes used to simulate small calcifications, as well as spherical mass lesions. We also used VCTs to optimize the acquisition geometry for breast-density visualization, using AUC to quantify the separation of dense and adipose tissue as a binary classification task.[10] Finally, we upgraded our breast model to include Perlin noise to ensure that power-law and higher-order texture are as realistic as possible.[31]

Major Task 6: Quantify breast density in anatomical phantoms.

As described in our Year 3 progress report, we used VCTs to demonstrate that breast-density visualization is optimized by the NGT design with PA scanning motion.[10] We used a signal-intensity threshold to classify each voxel in the reconstruction as dense or adipose tissue; the true and false classifications were analyzed with the ROC method described previously.[9] We optimized the selection of the threshold based on the point on the ROC curve closest to the upper-left corner of ROC space or the point (0, 1). We then generated a coronal slice with this classification threshold (**Figure 11 below**) - see the work Vent et al.[10] (Proc. of SPIE 2021, Vol. 11595 p. 115954V Figure 7 in document 16 of Section 9) described in our Year 3 progress report. This coronal slice is useful for visualizing out-of-focus artifacts. In the NGT scan (a T-shaped scan), there are fewer false positive voxels (blue), meaning there are fewer out-of-focus artifacts resembling dense tissue.

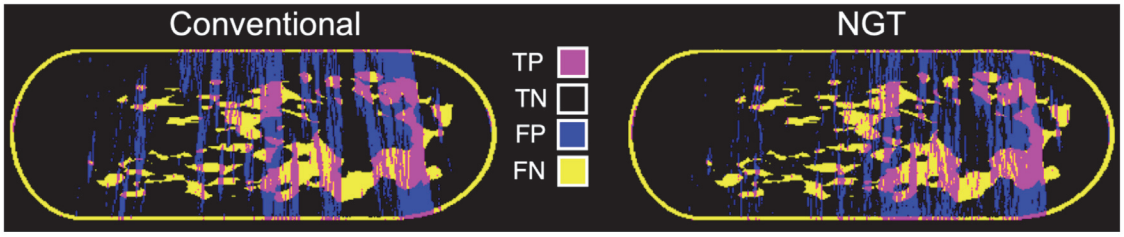

Figure 11. Coronal slice examples of the colormap images. The NGT acquisition geometry shows fewer out-of-plane artifacts (false positives) compared with the conventional geometry. Figure and caption from Vent et al.[10] (Proc. of SPIE 2021, Vol. 11595 p. 115954V) Figure 7 in document 16 of Section 9.

Additionally, we applied U-Net to train a model to segment fibroglandular (dense) tissue in anthropomorphic voxel phantoms.[24] A U-Net was trained with 2,880 images and model performance was evaluated in terms of percent of density. As shown in the example in **Figure 12 (below)**, our results demonstrate that the U-Net can segment dense tissue from adipose tissue with overall loss, accuracy (Acc), and intersection over union (IoU) of 0.18, 0.95, and 0.56; see Peregrino et al.[24] (Proceedings of the 14th International Joint Conference on Biomedical Engineering Systems and Technologies BIOSTEC 2021, Vol. 4, p. 252-259) Figure 4 in document 12 of Section 9. These results illustrate how U-Net can be used to segment dense tissue and automate the calculations of percent density. Complementing the U-Net analysis of phantoms, we also performed research on denoising in phantoms (which is new to this progress report). Our denoising research has applications in dense tissue visualization; see Dong et al.[25] Proc. of SPIE 2022, Vol. 12031, p. 120311W Figure 2 (document 25 of Section 9).

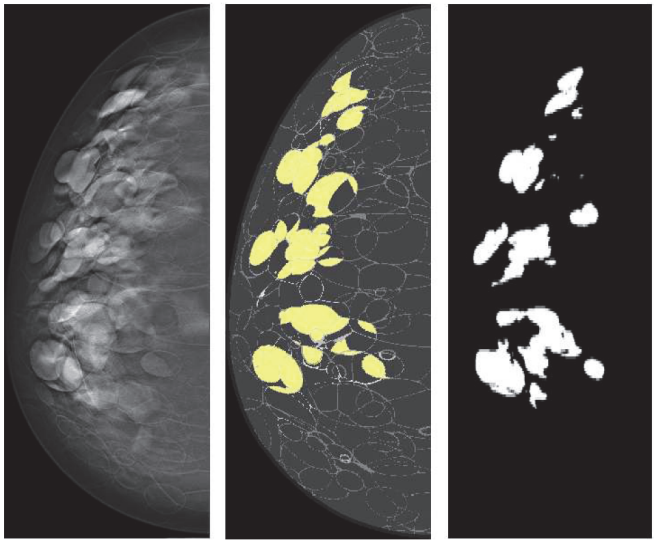

Figure 12. (Left) central slice of reconstructed DBT image, (middle) label map with glandular tissue highlighted in yellow (PD%=12%), and (right) binary segmentation. The segmentation metrics for this input image were 0.18, 0.95, and 0.56 for Loss, Acc, and IoU, respectively. Figure and caption from Peregrino et al.[24] (Proceedings of the 14th International Joint Conference on Biomedical Engineering Systems and Technologies BIOSTEC 2021, Vol. 4, p. 252-259) Figure 4 in document 12 of Section 9.

<u>Major Task 7:</u> Perform a virtual clinical trial (VCT) with simulated lesions.

Conventional detector models presume that the x-ray beam is normally incident on the detector. As described in our Year 1 progress report, we developed a theoretical model of amorphous-selenium (*a*-Se) detectors that quantifies the loss of spatial resolution due to obliquely-incident x rays.[29,30] We showed that the use of a PA scanning motion allows for more isotropic image quality through calculations of detective quantum efficiency (DQE), a measure of relative signal-to-noise. This model has applications in ensuring that VCTs have a realistic detector simulation for arbitrary incidence angles; see Acciavatti et al.[29] (Medical Physics 2019, Vol. 46, p. 494-504) Figures 4-8 (document 1 of Section 9), as well as Acciavatti et al.[30] (Medical Physics 2019, Vol. 46, p. 505-516) Figures 1-12 (document 2 of Section 9). **Figure 13 below** illustrates how the point spread function (PSF) is blurred with increasing obliquity in the incidence angle θ (varying from 0° to 22.5°). This PSF model is illustrated for 20 keV x rays.

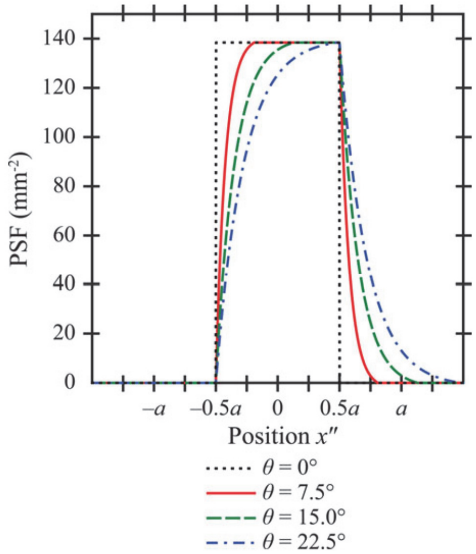

Figure 13. The net PSF is broadened with increasing obliquity. This figure assumes that the x-ray energy is 20 keV, and that the PSF is measured along the polar angle aligned with the ray incidence direction ($\Gamma = \alpha = 90°$). Color figure can be viewed at wileyonlinelibrary.com. Figure and caption from Acciavatti et al.[29] (Medical Physics 2019, Vol. 46 p. 494-504) Figure 8 in document 1 of Section 9.

As described in our Year 3 progress report, we have used VCTs to validate SR as a mechanism for improving calcification detection with model observers. There was an improvement in the receiver-operating-characteristic (ROC) performance of model observers in the task of detecting calcification polycubes.[11] **Figure 14 below** illustrates how area under the ROC curve (AUC) in one-shot multi-reader multi-case (MRMC) analyses increased with the use of 0.0425 mm voxels (SR voxels) as opposed to 0.085 mm voxels (conventional voxels); see Barufaldi et al.[11] (Proc. of SPIE 2020, Vol. 11513 p. 1151313) Figure 3 in document 10 of Section 9. As described in our Year 2 progress report, we have also used VCTs with calcification polycubes to optimize the angular range of the scan for calcification detection; see Barufaldi et al.[22] (Proc. of SPIE 2020, Vol. 11312 p. 113120I) Figure 3 in document 7 of Section 9.

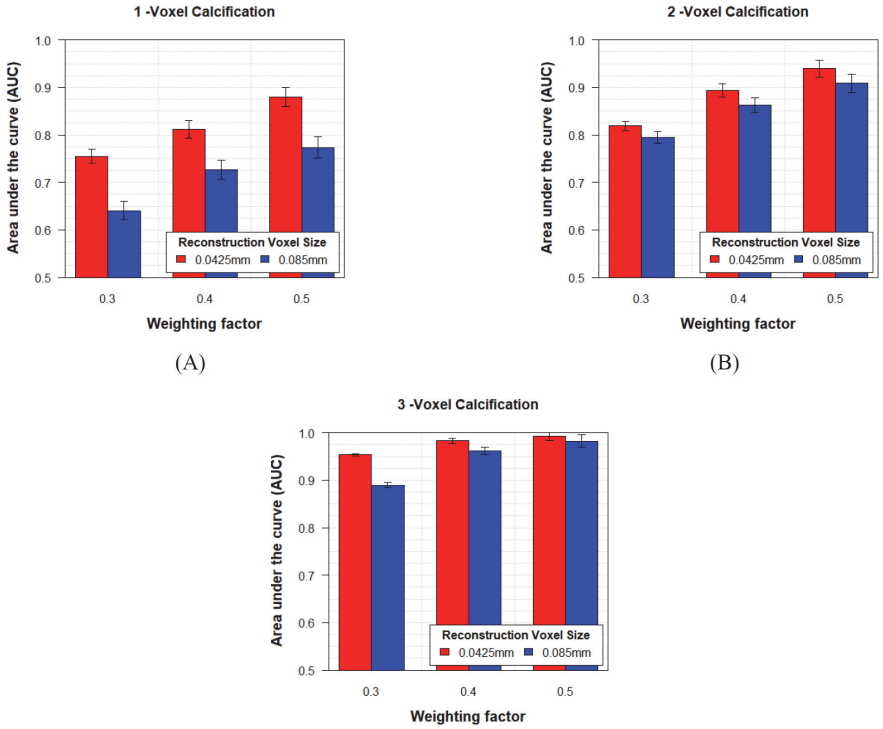

Figure 14. Summary of the AUCs of one-shot MRMC ROC analyses, categorized by weighing factor. Standard deviations between five virtual readers are shown. Figure and caption from Barufaldi et al.[11] (Proc. of SPIE 2020, Vol. 11513 p. 1151313) Figure 3 in document 10 of Section 9.

As described in our Year 2 progress report, VCTs were extensively used by a summer student (Brian Vu, University of Houston) mentored by the PI (Raymond Acciavatti) between 6/3/2019 and 8/9/2019. Brian participated in the AAPM summer undergraduate fellowship program as well as the Summer Undergraduate Program for Educating Radiation Scientists (SUPERS) at the University of Pennsylvania. He prepared an abstract and gave a presentation on 8/7/2019, describing how calcification visibility differs between synthetic 2D mammography, conventional 2D DM, and 3D DBT; see Vu et al. (Student Abstract for Summer SUPERS Program at Penn) Abstract (document 4 of Section 9).

To ensure that our VCTs include the most realistic breast phantoms possible, we have validated that our breast phantom model has realistic parenchymal texture relative to clinical data.[34] We also advanced our 3D anthropomorphic breast phantom model to include Perlin noise, and validated the power-law and higher-order texture (Laplacian Fractional Entropy) of the Perlin-noise model; see Barufaldi et al.[31] (IEEE TMI 2021, Vol. 40, p. 3436-3445) Figure 5 (document 21 of Section 9).[31] This research is new to this Year 4 progress report.

In two works, we acquired images of a breast phantom over many technique settings.[32,33] This research has applications in x-ray technique optimization for VCTs: (1) Acciavatti et al.[32] Proc. of SPIE 2020, Vol. 11314 p. 113140W Figures 2-4 in document 5 of Section 9 as described in Year 2 progress report;

(2) Acciavatti et al.[33] Cancers 2021, Vol. 13, p. 5497 Figures 1, 3, and 4 in document 20 of Section 9 (new to this Year 4 progress report). As described in our Year 3 progress report, we also used the phantom to validate the realism of the breast model used in VCTs in terms of matching radiomic texture features with clinical data; see Acciavatti et al.[34] Proc. of SPIE 2020, Vol. 11513, p. 1151309 Figures 3-5, Table 4 (document 8 of Section 9).

Finally, we used VCTs to demonstrate that the PA scanning motion results in more isotropic AUC for detection of spherical mass lesions. These results are new to this Year 4 progress report. In that work, we simulated breast texture with Perlin noise. An 11 × 14 grid with 154 lesions was inserted in the central slice of the phantom. The detectability index d' was calculated with ROC curves using a channelized Hotelling observer. As shown in **Figure 15 below**, the NGT scan (T Geometry) offers higher mean d' and lower standard deviation in d' across 154 lesion locations, which means that image quality is generally superior and more isotropic (less variable) than the conventional scan (X Geometry); see Choi et al.[27] Proc. of SPIE 2022, Vol. 12286 p. 1228618 Figure 8 in document 28 of Section 9.

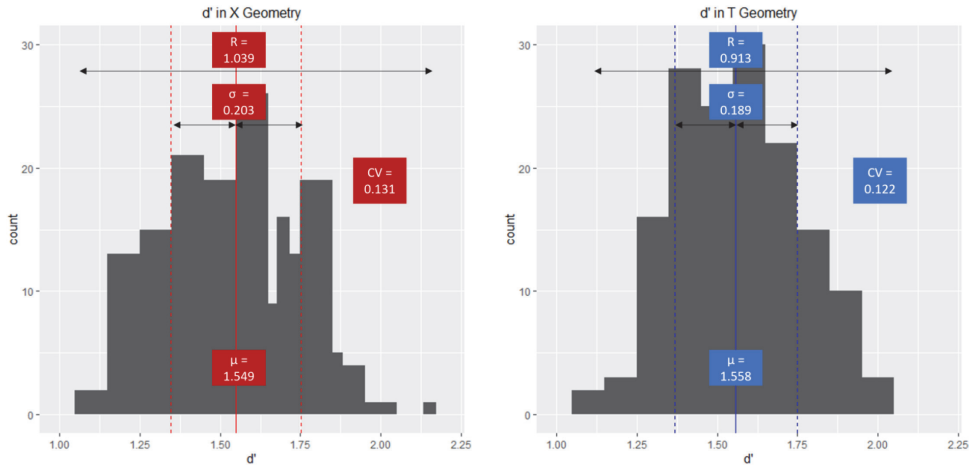

Figure 15. A histogram of d' values for X geometry (left) and T geometry (right) is shown, along with the mean (μ), standard deviation (σ), range I and coefficient of variation (CV). The total count is equal to the number of lesions in a phantom, which is 154. Figure and caption from Choi et al.[27] (Proc. of SPIE 2022, Vol. 12286 p. 1228618) Figure 6 in document 28 of Section 9.

3.C. What opportunities for training and professional development has the project provided?

- In the first year of this grant, the PI (Raymond J. Acciavatti, Ph.D.) gained experience mentoring a student (Matthew Willardson) working toward a Master's Degree in the Bioengineering Department. This student worked on VCT software and lesion simulations.

- At the 2019 SPIE Medical Imaging Conference in San Diego, the PI obtained additional training through the class "SC1239: Virtual Clinical Trials: An In-depth Tutorial".

- The PI (Raymond Acciavatti) was a mentor for the AAPM summer undergraduate fellowship program between 6/3/19 and 8/9/19. The research performed by the summer student is described in document 4 of Section 9 (Vu et al. Student Abstract for Summer SUPERS Program at Penn); it is complementary to the VCTs in Specific Aim 3 (Section 3.B.3.).

- At the 2020 SPIE Medical Imaging Conference in Houston, the PI (Raymond Acciavatti) was a teaching assistant for the class "SC1239: Virtual Clinical Trials: An In-depth Tutorial", which was held on 2/18/2020. The class instructors were Andrew Maidment, Predrag Bakic, and Bruno Barufaldi. At the 2022 SPIE Medical Imaging conference, Andrew Maidment and Bruno Barufaldi were "virtual" instructors for a similar class. This class on VCTs is complementary to research conducted in Specific Aim 3 (Section 3.B.3.).

- The PI (Raymond Acciavatti) became a Research Assistant Professor in the Radiology Department at Penn on 7/1/2020. Previously the PI was a Research Associate in the Radiology Department at Penn.

- The PI (Raymond Acciavatti) gained experience as a Jury Member of a Ph.D. thesis defense on 3/10/22. The Ph.D. student (Liesbeth Vancoillie) presented the thesis "Technical and Task-Based Performance Evaluation of Synthetic Mammograms" (KU Leuven in Belgium). Raymond Acciavatti participated in the thesis defense virtually on-line.

3.D. How were the results disseminated to communities of interest?

- Our work on VCTs received the "Live Demonstration" award at the 2019 SPIE Medical Imaging conference in San Diego, California. The demonstration was titled "OpenVCT – Open Source Simulation Platform for Designing and Performing Virtual Clinical Trials", and it was held on 2/19/2019.

- Our work on VCTs was presented in a "Live Demonstration" session on 2/16/2020 at the SPIE Medical Imaging conference in Houston. Conference attendees were given a demonstration of our VCT software. The PI (Raymond Acciavatti) was a co-author on this demonstration.

- Our work on VCTs was presented in the "Computer-Aided Diagnosis Live Demonstrations" session on 2/17/2021 at the SPIE Medical Imaging conference, which was held virtually due to the COVID-19 Pandemic. The presentation was titled "PhysicsVCTs: A Framework to Evaluate Spectral Distortion in the Fourier Domain" (authors: Trevor Vent, Bruno Barufaldi, Raymond Acciavatti, and Andrew Maidment). The presenting author for this Live Demonstration was Trevor Vent.

- The PI (Raymond J. Acciavatti, Ph.D.) gave the following invited lectures (non-proffered):
    - "Design of a Prototype 3D Mammography System" on 4/29/2021 during the Spring 2021 Medical Image Processing Group (MIPG) Seminar Series of the University of Pennsylvania (virtual on-line presentation organized by the MIPG group of the Radiology Department at the University of Pennsylvania).
    - "Next-Generation Tomosynthesis Modeling and Optimization" on 11/19/2021 during the Malmö and Lund Friday Seminar Series (virtual on-line presentation to audience in Lund University in Sweden).
    - "VCT to Optimize the Technical Settings of New DBT Devices" on 5/22/2022 at the 16th International Workshop on Breast Imaging (the PI gave the presentation virtually on-line to the conference hall in Leuven, Belgium).

3.E. What do you plan to do during the next reporting period to accomplish the goals?

Nothing to report.

4. IMPACT

4.A. What was the impact on the development of the principal discipline(s) of the project?

In this grant, we performed the computational modeling and simulations to justify new designs for future 3D mammography systems – both for screening and diagnostic call-back imaging.

- We justified the importance of PA x-ray source motion with VCTs; this source motion is not being used clinically in DBT. The use of PA motion results in clearer separation between

fibroglandular and adipose tissue (Vent et al.[10] Proc. of SPIE 2021, Vol. 11595 p. 115954V Figures 4-8 in document 16 of Section 9 - Year 3 progress report). Customizing the range of PA motion around the breast size in this direction results in even better breast density visualization (Acciavatti et al.[9] Proc. of SPIE 2019 Vol. 10948 p. 109480B Table 1 and Figures 3, 5, and 6 in document 3 of Section 9 - Year 1 progress report). With PA motion, model-observer performance is also more isotropic in terms of lesion detection at various positions in the image (Choi et al.[27] Proc. of SPIE 2022, Vol. 12286 p. 1228618 Figures 3-6 and Tables 2-3 in document 28 of Section 9 - new to this Year 4 progress report).

- With VCTs (Barufaldi et al.[11] Proc. of SPIE 2020 Vol. 11513 p. 1151313 Figures 2-3 in document 10 of Section 9 - Year 3 progress report), we justified the importance of generating reconstructions with SR grids (finer pixelation than the detector). We have shown that SR can be achieved with better quality at more positions in the image by re-designing the acquisition geometry (Acciavatti et al.[14] Proc. of SPIE 2022 Vol. 12031 p. 120314B Table 1 and Figures 1-7 in document 23 of Section 9 - new to this Year 4 progress report). We project that this new design will improve image quality for calcifications.

- There is far superior spatial resolution with the use of 3D magnification imaging than with the use of 2D magnification imaging, the current standard for clinical diagnostic magnification imaging (Acciavatti et al.[12], Proc. of SPIE 2021, Vol. 11595 p. 115951J Table 1 and Figures 4-6 in document 13 of Section 9 - Year 3 progress report).

- Re-arranging the x-ray source positions in clusters (Acciavatti et al.[4], Proc. of SPIE 2020, Vol. 11312 p. 113125G Table 1 and Figures 4-7 in document 6 of Section 9) allows the anisotropies in SR to be suppressed, so SR can be achieved reliably everywhere in the image. This offers the best possible resolution for calcification imaging.

4.B. What was the impact on other disciplines?
Nothing to report.

4.C. What was the impact on technology transfer?
Nothing to report.

4.D. What was the impact on society beyond science and technology?
Nothing to report.

5. CHANGES / PROBLEMS

5.A. Changes in approach and reasons for change
Nothing to report.

5.B. Actual or anticipated problems or delays and actions or plans to resolve them
Nothing to report.

5.C. Changes that had a significant impact on expenditures
Nothing to report.

5.D. Significant changes in use or care of human subjects, vertebrate animals, biohazards, and/or select agents
Nothing to report.

5.E. Significant changes in use or care of human subjects
Nothing to report.

5.F. Significant changes in use or care of vertebrate animals
Nothing to report.

5.G. Significant changes in use of biohazards and/or select agents
Nothing to report.

6. PRODUCTS.

6.A. Publications, conference papers, and presentations

- **Journal publications**
  - Acciavatti RJ, Maidment ADA. Non-stationary model of oblique x-ray incidence in amorphous selenium detectors: I. Point spread function. Medical Physics. 2019; 46(2):494-504. Document 1 of Section 9.
  - Acciavatti RJ, Maidment ADA. Nonstationary model of oblique x-ray incidence in amorphous selenium detectors: II. Transfer Functions. Medical Physics. 2019; 46(2): 505-16. Document 2 of Section 9.
  - Vent TL, Acciavatti RJ, Maidment ADA. Development and Evaluation of the Fourier Spectral Distortion Metric. IEEE Transactions on Medical Imaging 2021; 40(3): 1055-64. Document 17 of Section 9.
  - Barufaldi B, Maidment ADA, Dustler M, Axelsson R, Tomic H, Zackrisson S, Tingberg A, Bakic PR. Virtual Clinical Trials in Medical Imaging System Evaluation and Optimisation. Radiation Protection Dosimetry 2021; 195(3-4): 363-371. Document 18 of Section 9.
  - Acciavatti RJ, Cohen EA, Maghsoudi OH, Gastounioti A, Pantalone L, Hsieh M-K, Conant EF, Scott CG, Winham SJ, Kerlikowske K, Vachon C, Maidment ADA, Kontos D. Incorporating Robustness to Imaging Physics into Radiomic Feature Selection for Breast Cancer Risk Estimation. Cancers 2021; 13(21): 5497. Document 20 of Section 9.
  - Barufaldi B, Abbey CK, Lago MA, Vent TL, Acciavatti RJ, Bakic PR, Maidment ADA. Computational Breast Anatomy Simulation Using Multi-Scale Perlin Noise. IEEE Transactions on Medical Imaging 2021; 40(12): 3436-45. Document 21 of Section 9.
  - Barufaldi B, Vent TL, Bakic PR, Maidment ADA. Computer simulations of case difficulty in digital breast tomosynthesis using virtual clinical trials. Medical Physics 2022; 49: 2220-2232. Document 22 of Section 9.

- **Books or other non-periodical, one-time publications**
  - Nothing to report.

- **Other publications, conference papers, and presentations**
  - Acciavatti RJ, Barufaldi B, Vent TL, Wileyto EP, Maidment ADA. Personalization of x-ray tube motion in digital breast tomosynthesis using virtual Defrise phantoms. In: Schmidt TG, Chen G-H, Bosmans H, editors; Physics of Medical Imaging; 2019; San Diego, CA: SPIE; 2019. p. 109480B. The PI (Raymond J. Acciavatti, Ph.D.) presented this work at the SPIE Medical Imaging conference on 2/17/19 in San Diego, CA. Document 3 of Section 9.
  - Acciavatti RJ, Cohen EA, Maghsoudi OH, Gastounioti A, Pantalone L, Hsieh M-K, Conant EF, Scott CG, Winham SJ, Kerlikowske K, Vachon C, Maidment ADA, Kontos D. Robust Radiomic Feature Selection in Digital Mammography: Understanding the Effect of Imaging Acquisition Physics Using Phantom and Clinical Data Analysis. In: Hahn HK, Mazurowski MA, editors; Computer-Aided Diagnosis; 2020; Houston, TX: SPIE; 2020. p. 113140W. The PI (Raymond

Acciavatti) gave an oral presentation at the SPIE Medical Imaging conference on 2/17/2020 in Houston, TX. Document 5 of Section 9.

- Acciavatti RJ, Vent TL, Barufaldi B, Wileyto EP, Noël PB, Maidment ADA. Proposing Rapid Source Pulsing for Improved Super-Resolution in Digital Breast Tomosynthesis. In: Chen G-H, Bosmans H, editors; Physics of Medical Imaging; 2020; Houston, TX: SPIE; 2020. p. 113125G. The PI (Raymond Acciavatti) presented this work as a poster at the SPIE Medical Imaging conference on 2/17/2020 in Houston, TX. Document 6 of Section 9.
- Barufaldi B, Vent TL, Acciavatti RJ, Bakic PR, Noël PB, Conant EF, Maidment ADA. Determining the Optimal Angular Range of the X-Ray Source Motion in Tomosynthesis Using Virtual Clinical Trials. In: Chen G-H, Bosmans H, editors; Physics of Medical Imaging; 2020; Houston, TX: SPIE; 2020. p. 113120I. Bruno Barufaldi (first author of this paper) gave an oral presentation at the SPIE Medical Imaging conference on 2/16/2020 in Houston, TX. Document 7 of Section 9.
- Acciavatti RJ, Cohen EA, Maghsoudi OH, Gastounioti A, Pantalone L, Hsieh M-K, Barufaldi B, Bakic PR, Chen J, Conant EF, Kontos D, Maidment ADA. Calculation of Radiomic Features to Validate the Textural Realism of Physical Anthropomorphic Phantoms for Digital Mammography. In: Bosmans H, Marshall N, Van Ongeval C, editors; 15th International Workshop on Breast Imaging; 2020; Virtual Conference (held during COVID-19 Pandemic): SPIE; 2020. p. 1151309. This paper was published in May of 2020. The PI (Raymond Acciavatti) gave a "virtual" presentation at this conference. Document 8 of Section 9.
- Acciavatti RJ, Vent TL, Barufaldi B, Wileyto EP, Noël PB, Maidment ADA. Super-Resolution in Digital Breast Tomosynthesis: Limitations of the Conventional System Design and Strategies for Optimization. In: Bosmans H, Marshall N, Van Ongeval C, editors; 15th International Workshop on Breast Imaging; 2020; Virtual Conference (held during COVID-19 Pandemic): SPIE; 2020. p. 115130V. This paper was published in May of 2020. The PI (Raymond Acciavatti) gave a "virtual" presentation at this conference. Document 9 of Section 9.
- Barufaldi B, Vent TL, Acciavatti RJ, Bakic PR, Noël PB, Maidment ADA. MRMC ROC Analysis of Calcification Detection in Tomosynthesis Using Computed Super Resolution and Virtual Clinical Trials. In: Bosmans H, Marshall N, Van Ongeval C, editors; 15th International Workshop on Breast Imaging; 2020; Virtual Conference (held during COVID-19 Pandemic): SPIE; 2020. p. 1151313. This paper was published in May of 2020. The first author (Bruno Barufaldi) gave a "virtual" presentation at this conference. Document 10 of Section 9.
- Vent TL, Barufaldi B, Acciavatti RJ, Maidment ADA. Simulation of high-resolution test objects using non isocentric acquisition geometries in next-generation digital tomosynthesis. In: Bosmans H, Marshall N, Van Ongeval C, editors; 15th International Workshop on Breast Imaging; 2020; Virtual Conference (held during COVID-19 Pandemic): SPIE; 2020. p. 1151317. This paper was published in May of 2020. The first author (Trevor Vent) gave a "virtual" presentation at this conference. Document 11 of Section 9.
- Peregrino LR, Gomes JV, Rego T, Barbosa Y, Filho T, Maidment ADA, Barufaldi B. Automatic Segmentation of Mammary Tissue using Computer Simulations of Breast Phantoms and Deep-Learning Techniques. Proceedings of the 14th International Joint Conference on Biomedical Engineering Systems and Technologies (BIOSTEC 2021) – Vol. 4: BIOSIGNALS, p. 252-259. Document 12 of Section 9.
- Acciavatti RJ, Vent TL, Choi CJ, Wileyto EP, Noël PB, Maidment ADA. Development of Magnification Tomosynthesis for Superior Resolution in Diagnostic Mammography. In: Bosmans H, Zhao W, Yu L, editors; Physics of Medical Imaging; 2021 (virtual conference held during COVID-19 Pandemic): SPIE; 2021. p. 115951J. This conference paper was published in February 2021. The PI (Raymond Acciavatti) gave a "virtual" presentation. Document 13 of Section 9.
- Choi CJ, Vent TL, Acciavatti RJ, Maidment ADA. Analysis of Digital Breast Tomosynthesis Acquisition Geometries in Sampling Fourier Space. In: Bosmans H, Zhao W, Yu L, editors; Physics of Medical Imaging; 2021 (virtual conference held during COVID-19 Pandemic): SPIE;

2021. p. 115954W. This conference paper was published in February 2021. The first author (Chloe Choi) gave a "virtual" poster presentation. Document 14 of Section 9.

- Martin DA, Vent TL, Choi CJ, Barufaldi B, Acciavatti RJ, Maidment ADA. Signal-to-Noise Ratio and Contrast-to-Noise Ratio Measurements for Next Generation Tomosynthesis. In: Bosmans H, Zhao W, Yu L, editors; Physics of Medical Imaging; 2021 (virtual conference held during COVID-19 Pandemic): SPIE; 2021. p. 115951L. This conference paper was published in February 2021. The first author (David Martin) gave a "virtual" presentation. Document 15 of Section 9.
- Vent TL, Barufaldi B, Acciavatti RJ, Krishnamoorthy S, Surti S, Maidment ADA. Next generation tomosynthesis image acquisition optimization for dedicated PET-DBT attenuation corrections. In: Bosmans H, Zhao W, Yu L, editors; Physics of Medical Imaging; 2021 (virtual conference held during COVID-19 Pandemic): SPIE; 2021. p. 115954V. This conference paper was published in February 2021. The first author (Trevor Vent) gave a "virtual" poster presentation. Document 16 of Section 9.
- Acciavatti R, Vent T, Choi C, Noel P, Maidment A. Anisotropies in Super-Resolution in 3D Magnification Mammography Using a Next-Generation Tomosynthesis System. Medical Physics. 2021; 48(6): 51. This conference abstract was presented by the PI (Raymond Acciavatti) at the Virtual Annual Meeting of the AAPM in 2021. Document 19 of Section 9.
- Acciavatti RJ, Choi CJ, Vent TL, Barufaldi B, Maidment ADA. Achieving Isotropic Super-Resolution with a Non-Isocentric Acquisition Geometry in a Next-Generation Tomosynthesis System. In: Zhao W, Yu L, editors; Physics of Medical Imaging; 2022: SPIE; 2022. p. 120314B. This work was presented as part of the "On Demand" 2022 SPIE Medical Imaging Conference ("virtual" poster presentation). Document 23 of Section 9.
- Choi CJ, Vent TL, Geagan MJ, Noel PB, Maidment ADA. Investigation of optimal angular range and projection density for next generation tomosynthesis. In: Zhao W, Yu L, editors; Physics of Medical Imaging; 2022: SPIE; 2022. p. 120314C. This work was presented as part of the "On Demand" 2022 SPIE Medical Imaging Conference ("virtual" poster presentation). Document 24 of Section 9.
- Dong V, Maidment TD, Borges LR, Barufaldi B, Ng S, Maidment ADA. Assessment of patch-based mammogram denoising methods using virtual clinical trials and deep learning: trade-off between denoising strength and preservation of structural details. In: Zhao W, Yu L, editors; Physics of Medical Imaging; 2022: SPIE; 2022. p. 120311W. This work was presented as part of the "On Demand" 2022 SPIE Medical Imaging Conference ("virtual" poster presentation). Document 25 of Section 9.
- Teixeira JPV, Filho TMS, Rego TG, Malheiros YB, Dustler M, Bakic PR, Vent TL, Acciavatti RJ, Krishnamoorthy S, Surti S, Maidment ADA, Barufaldi B. Novel Perlin-based Phantoms Using 3D Models of Compressed Breast Shape and Fractal Noise. In: Zhao W, Yu L, editors; Physics of Medical Imaging; 2022: SPIE; 2022. p. 120313S. This work was presented as part of the "On Demand" 2022 SPIE Medical Imaging Conference ("virtual" poster presentation). Document 26 of Section 9.
- Vent TL, Acciavatti RJ, Choi C, Barufaldi B, Krishnamoorthy S, Borges L, Kuo J, Ringer PA, Ng S, Surti S, Maidment ADA. Pre-clinical evaluation and optimization of image quality for a Next Generation Tomosynthesis prototype. In: Zhao W, Yu L, editors; Physics of Medical Imaging; 2022: SPIE; 2022. p. 1203142. This work was presented as part of the "On Demand" 2022 SPIE Medical Imaging Conference ("virtual" poster presentation). Document 27 of Section 9.
- Choi CJ, Barufaldi B, Teixeira JPV, Acciavatti RJ, Maidment ADA. Spatial dependency of lesion detectability in digital breast tomosynthesis. Proc. SPIE 2022, Vol. 12286, p. 1228618. The first author (Chloe J. Choi) presented this work in Leuven, Belgium at the 16th International Workshop on Breast Imaging. Document 28 of Section 9.
- Nobrega Y, Carvalhal G, Teixeira JPV, Camargo BP, Rego TG, Malheiros Y, Filho T, Vent TL, Acciavatti RJ, Maidment ADA, Barufaldi B. Multiclass Segmentation of Suspicious Findings in

Simulated Breast Tomosynthesis Images Using a U-Net. Proc. SPIE 2022, Vol. 12286, p. 122860L. One of the authors (Telmo de M. E Silva Filho) presented this work in Leuven, Belgium at the 16th International Workshop on Breast Imaging. Document 29 of Section 9.

6.B. Website(s) or other Internet site(s)

The VCT software developed by the X-Ray Physics Lab at the University of Pennsylvania can be accessed through the website https://sourceforge.net/projects/openvct/.

6.C. Technologies or techniques

Through computational modeling and simulations, this grant developed the knowledge needed to re-design DBT systems for superior lesion and breast-density visualization. A physical DBT system, called the next-generation tomosynthesis (NGT) system[39], has been constructed in the X-Ray Physics Lab at Penn through separate grant funding; namely, through grants NIH R01CA196528 (PI: Surti) and Komen IIR13264610 (PI: Maidment). The knowledge gained from modeling and simulations in this DoD grant will ultimately be incorporated into the scanning motions and acquisition geometry used in the NGT system.

6.D. Inventions, patent applications, and/or licenses

Nothing to report.

6.E. Other products

Nothing to report.

7. PARTICIPANTS AND OTHER COLLABORATING ORGANIZATIONS.

7.A. What individuals have worked on the project?

Person months below pertain to the final year with the No Cost Extension. A complete list of all personnel who worked on this grant in all years is included in document 30 of Section 9.

Name:	Raymond J. Acciavatti, Ph.D.
Project Role:	Principal Investigator (Research Assistant Professor)
Research Identifier:	ORCiD ID: 0000-0003-4822-3353
Nearest person month worked:	4
Contribution to project:	Lead investigator for all specific aims of the project.
Funding Support:	

Name:	David Higginbotham
Project Role:	Software Developer
Research Identifier:	
Nearest person month worked:	1
Contribution to project:	VCT software development for x-ray projection simulation and breast phantom creation.
Funding Support:	

7.B. Has there been a change in the active other support of the PD/PI(s) or senior / key personnel since the last reporting period?

In addition to this DoD grant (W81XWH-18-1-0082), below is a list of grant support for the key personnel during the final year of this grant with the No Cost Extension.

Raymond J. Acciavatti, Ph.D.

Abramson Cancer Center Pilot Grant Program
UPenn Internal
Acciavatti, Raymond (PI) / Maidment, Andrew (Co-PI)
7/1/2021-6/30/2022
Feasibility of Self-Steering 3D Mammography
The grant proposes exploratory research with the raw (unprocessed) clinical DBT projection images. These calculations are geared toward determining the potential feasibility of real-time image analysis during the scan. This UPenn pilot grant is funded by the Abramson Cancer Center's support grant (NCI P30 CA016520).

Translational Biomedical Imaging Center Collaborative Pilot Grant Program
UPenn Internal
Acciavatti, Raymond (PI) / Conant, Emily (Co-PI) /Feldman, Michael (Co-PI)
3/1/2022-2/28/2023
Self-Steering Tomosynthesis Using Mastectomy Specimens
This one-year pilot grant is a preliminary feasibility study of task-directed imaging in DBT using fresh mastectomy specimens. We are proposing exploratory research to generate reconstructions of the same specimen with different combinations of projection images (corresponding to different locations for the x-ray source positions). This one-year pilot grant is supported in part by the Institute for Translational Medicine and Therapeutics of the University of Pennsylvania and also supported by the National Center for Advancing Translational Sciences of the National Institutes of Health under Award Number UL1TR001878.

2022 Young Investigator Grant
Breast Cancer Alliance
Acciavatti, Raymond (PI)
3/1/2022-2/28/2024
Self-Steering 3D Mammography
This grant is a preliminary feasibility study of self-steering 3D mammography using retrospective clinical screening data with findings (masses, calcifications, and architectural distortions). Additionally, virtual clinical trials using anthropomorphic phantoms with lesions are proposed with novel scanning motions. Lesion detection performance is analyzed with model observers using receiver operating-characteristic curves.

R01CA161749
NIH
Kontos, Despina
4/1/2017-3/31/2022
Digital breast tomosynthesis imaging biomarkers for breast cancer risk estimation
The improved clinical performance achieved with digital breast tomosynthesis is currently fueling a broad adaptation of tomosynthesis for general population breast cancer screening. Our study will be the first to evaluate tomosynthesis imaging measures in breast cancer risk assessment and will develop the necessary technology to enable larger multi-center studies. Ultimately, these novel imaging biomarkers may lead to more accurate individualized risk stratification, improving personalized breast cancer screening and prevention.

IRSA 1016451
Burroughs Wellcome Fund
Maidment, Andrew
9/1/2016-8/31/2021
ViCTRE – Virtual Clinical Trials in the Regulatory Environment
We propose ViCTRE as a cost-effective and timely alternative to the current regulatory process. This vision is not fanciful; the elements of our proposed virtual clinical trial (VCT) pipeline are mature. VCTs are already commonly used in the design and development of imaging devices by academia and industry.

OVERLAP: There is no scientific or budgetary overlap between the above research grants and DoD grant W81XWH-18-1-0082.

Emily Conant, M.D.

R01CA259048
NIH
Mello-Thoms, Claudia
3/15/2021-2/28/2026
Satisfaction of Search in Breast Cancer Detection

R01CA161749
NIH
Kontos, Despina, PhD
4/1/2017-3/31/2022
Digital breast tomosynthesis imaging biomarkers for breast cancer risk estimation
The improved clinical performance achieved with digital breast tomosynthesis is currently fueling a broad adaptation of tomosynthesis for general population breast cancer screening. Our study will be the first to evaluate tomosynthesis imaging measures in breast cancer risk assessment and will develop the necessary technology to enable larger multi-center studies. Ultimately, these novel imaging biomarkers may lead to more accurate individualized risk stratification, improving personalized breast cancer screening and prevention.

4/1/2017-3/31/2021
NIH 1R01CA207084 – Mayo Clinic Rochester
Radiomic phenotypes of breast parenchyma and breast cancer risk and detection
The main goals of this study are to characterize 'intrinsic' parenchymal complexity features reflecting the heterogeneity of breast tissue, to examine the association of 'intrinsic' parenchymal complexity features with breast cancer risk and to examine the contribution of parenchymal complexity features to masking cancers.

OM1
Conant, Emily, MD
10/11/2017-6/30/2022
Effectiveness and value of digital breast tomosynthesis: outcomes analysis of breast cancer screening
OM1, on behalf of Hologic, is conducting the Study (entitled: Effectiveness and Value of Digital Breast Tomosynthesis: Outcomes Analysis of Breast Cancer Screening). The Study is designed to establish a learning health system for breast cancer screening that provides longitudinal data on a cohort of women who are referred for screening mammography as well as women who are eligible for but did not receive screening mammography. The Study is a longitudinal, multi-center observational study that will include data on eligible women who receive a screening mammogram and women who were eligible for but did not receive a screening mammogram.

Hologic, Conant, Emily, MD
11/21/2019-06/31/2021
Hologic Case Transfer Agreement
The objective of this protocol is IRB-approved case collection for research, development, user training and support further product performance claims for breast imaging modalities and computer-aided detection. The study set will include mammography, tomosynthesis, and computer-generated images, including image meta-data and corresponding medical reports, relevant associated exams and reports which are all de-identified prior to transfer to the Sponsor.

OVERLAP: There is no scientific or budgetary overlap between the above research grants and DoD grant W81XWH-18-1-0082.

Despina Kontos, Ph.D.

1-U01-CA-242871-01
NIH
09/2019 - 08/2022
Spyridon Bakas
The Federated Tumor Segmentation (FeTS) platform: An intuitive tool facilitating secure multi-institutional collaboration
Successful completion of this project will lead to a clinically translatable, easy-to-use software tool that offers a) pre-trained tumor segmentation models and their fusion, to perform better than experts, and b) a federated learning framework facilitating secure multi-institutional collaborations to improve these pre-trained models without the need to share patient data, thereby overcoming legal, privacy, and data-ownership challenges, towards accelerating research of cancer radio-phenotypes.

R01CA197000
NIH
Kontos, Despina
4/19/2016-3/31/2022
Multi-parametric 4-D Imaging Biomarkers for Neoadjuvant Treatment Response
Pattern analysis and machine learning methods are powerful knowledge discovery tools that can be very effective in identifying complex multi-parametric patterns from a diverse set of imaging and non-imaging biomarkers that can best predict treatment response and outcome. Our method will leverage the richness of available data to point to new imaging biomarkers that are better early predictors of response, enabling personalized treatment decisions for women undergoing neoadjuvant chemotherapy for breast cancer.

R01CA161749
NIH
Kontos, Despina, PhD
4/1/2017-3/31/2022
Digital breast tomosynthesis imaging biomarkers for breast cancer risk estimation
The improved clinical performance achieved with digital breast tomosynthesis is currently fueling a broad adaptation of tomosynthesis for general population breast cancer screening. Our study will be the first to evaluate tomosynthesis imaging measures in breast cancer risk assessment and will develop the necessary technology to enable larger multi-center studies. Ultimately, these novel imaging biomarkers may lead to more accurate individualized risk stratification, improving personalized breast cancer screening and prevention.

4/1/2017-3/31/2022
NIH 1R01CA207084 – Mayo Clinic Rochester
Radiomic phenotypes of breast parenchyma and breast cancer risk and detection
The main goals of this study are to characterize ‘intrinsic’ parenchymal complexity features reflecting the heterogeneity of breast tissue, to examine the association of ‘intrinsic’ parenchymal complexity features with breast cancer risk and to examine the contribution of parenchymal complexity features to masking cancers.

R33CA225310
NIH
Mankoff, David
9/1/17-8/31/21 (NCE)
Area B: Multi-Tracer Volumetric PET (MTV-PET) to Measure Tumor Glutamine and Glucose Metabolic Rates in a Single Imaging Session
We will take advantage of recent developments in volumetric positron emission tomography (PET) scanners, fast reconstruction, and 4D image analysis to develop methods for multi-tracer PET with the goal of generating quantitative, multi-parametric whole-body images of specific aspects of cancer biology, including cancer metabolism as the focus of our proposed technology development projects. Successful completion of our proposed technology development will yield a clinically practical method for multi-tracer PET that would provide multi-valent, whole-body molecular parametric images that would change the landscape for cancer imaging diagnostic biomarkers and precision oncology.

U24CA189523
NIH
Davatzikos/Kontos
9/1/2015-8/31/2021
Cancer imaging phenomics software suite: application to brain and breast cancer
This project will develop advanced computer analysis methodology for interpretation of radiologic images of cancer, emphasizing brain and breast cancer. The functionality of the software will substantially transcend limitations of current analysis of cancer images, and will open the way for more precise and effective surgical planning as well as for more specific diagnosis of cancer based on its imaging characteristics, eventually leading to individualized medicine.

1R01CA223816
NIH
Kontos/Chodosh
4/1/2018-3/31/2023
Radiogenomic Biomarkers of Breast Cancer Recurrence
We propose to analyze imaging features of phenotypic tumor heterogeneity that will provide information to complement histopathologic and molecular markers, enhancing our prognostic ability for breast cancer. Ultimately, integrating imaging with novel molecular tumor markers could enable more informed, precision-medicine, treatment decisions to reduce unnecessary side-effects while improving long-term outcomes for women diagnosed with breast cancer.

UM1CA221939
NIH
Ritzwoller/Doubeni
4/15/2018-3/31/2023
Center for Research to Optimize Precision Lung Cancer Screening in Diverse Populations
The goal of this Center is to build a comprehensive data ecosystem of the entire lung cancer screening process and to assess associated multilevel factors to conduct high impact multilevel studies including interventions to address gaps in care that may lead to lung cancer health disparities in the PROSPR initiative.

R01CA237129
NIH
UNC subcontract / Kontos
9/1/2019-8/31/2024
Understanding the biological basis for the association between parenchymal texture features and breast cancer risk
The goals of this study are to identify parenchymal texture features associated with breast cancer risk in general population of women participating in screening mammography and, for those features associated with breast cancer risk, to evaluate (1) associations with endogenous estrogens and (2) associations with benign breast histologic features.

R01CA236468
NIH
Chen, Jinbo
9/15/2019-6/30/2023
Data and Information Integration for Risk Prediction in the Era of Big Data
Toward precision medicine and precision disease prevention, the over-arching goal of this proposal is to develop innovative statistical methods for accurate risk prediction. We address three challenges that plague studies on the value of new predictors that adds to standard predictors for improving predictive accuracy: lack of independent validation data, lack of statistical methods for developing risk prediction models using individually-matched case-control data, and lack of statistical methods to guide study design beyond standard power calculation for testing predictor-outcome association.

ECOG-ACRIN Medical Research Foundation, Inc. (NCI / NIH)
U10CA180820-06UPA6C
Kontos, Despina
03/2019 - 02/2023
ECOG-ACRIN Operations Center Clinical Trials
As Co-Chair of the Radiomics Working Group, Dr. Despina Kontos is responsible for the following: Setting annual working goals and a brief work plan for the working group; Organizing working group membership; Establishing a topical working group agenda to a) survey the research issues in their areas of expertise and b) support ideas for future ECOG-ACRIN protocols; Reporting to the ECOG-ACRIN Group Co-Chairs regarding the activities of the working group and progress toward established goals; Attending the ECOG-ACRIN meetings at least annually to Chair the Working group meeting and represent the Working group at other meetings; Preparing reports on the activities of the working group for progress reports and grants at the request of the ECOG-ACRIN Group Co-Chairs.

AWD101462-O
08/2020 - 08/2022
Medical Imaging and Data Consortium: Rapid Response to COVID-19 Pandemic
A virtual clinical trial that simulates a randomization assignment for a diagnostic or treatment modality for COVID-19 will be designed and carried out using the available clinical and imaging data. While the exact question to be answered has not yet been selected, it will be selected at the time the study is launched based on what is most important clinically and how many clinical cases are in the data base that can answer the query selected.

UPenn Internal
Anne Marie McCarthy (PI)
07/2020 - 06/2022
Risk stratification among known BRCA1/2 mutation carriers using polygenic risk and imaging biomarkers
To combine polygenic risk scores and BPE to improve breast cancer risk assessment among BRCA1/2 carriers, and help guide precision-based recommendations for risk-reducing interventions.

1-R01-CA-264835-01
NIH
Despina Kontos
06/2021 - 05/2026
Predictive and Diagnostic Radiomic Signatures in Non-Small Cell Lung Cancer (NSCLC) on Immunotherapy
We propose a strategy to develop an integrated-diagnostics tool for eventual clinical translation, which will enable enhanced predictive modeling of clinical outcome and diagnostic precision in 1st line immunotherapy for NSCLC, the choice of which has shown to have a large impact on patient survival during the course of cancer management since subsequent lines of treatment are increasingly less likely to be successful. Our radiomics signatures, combined with clinically established and emerging biomarkers, will result in increased precision for the management of patients selected for anti-PD1/PDL1 therapy by more accurately predicting who will benefit from therapy and detect response with more precision and earlier than currently possible.

UPenn Internal
Anne Marie McCarthy (PI)
03/2022 - 02/2023
Interplay of obesity and volumetric breast density with respect to breast cancer risk
We will leverage our large, racially diverse cohort of women undergoing DBT screening at Penn Medicine linked with germline genetic data from the Penn Medicine Biobank (PMBB) to better understand the nature and mechanisms of the interplay between BMI and quantitative volumetric breast density measures with respect to breast cancer risk.

OVERLAP: There is no scientific or budgetary overlap between the above research grants and DoD grant W81XWH-18-1-0082.

Andrew Maidment, Ph.D.

R01CA227142
NIH
Cormode, David
5/1/2018-4/30/2023
Nanoparticle contrast agents for earlier breast cancer detection
The objective of this project is to develop polyphosphazene nanoparticles containing silver alloy contrast agents to enhance the efficacy of dual energy mammography for tumor detection.

R01CA161749
NIH
Kontos, Despina
4/1/2017-3/31/2022
Digital breast tomosynthesis imaging biomarkers for breast cancer risk estimation
The improved clinical performance achieved with digital breast tomosynthesis is currently fueling a broad adaptation of tomosynthesis for general population breast cancer screening. Our study will be the first to evaluate tomosynthesis imaging measures in breast cancer risk assessment and will develop the necessary technology to enable larger multi-center studies. Ultimately, these novel imaging biomarkers may lead to more accurate individualized risk stratification, improving personalized breast cancer screening and prevention.

IRSA 1016451
Burroughs Wellcome Fund
Maidment, Andrew
9/1/2016-8/31/2021
ViCTRE – Virtual Clinical Trials in the Regulatory Environment
We propose ViCTRE as a cost-effective and timely alternative to the current regulatory process. This vision is not fanciful; the elements of our proposed VCT pipeline are mature. VCTs are already commonly used in the design and development of imaging devices by academia and industry.

R01CA196528
NIH
Surti, Suleman
4/1/2016-3/31/2022
High Performance, Quantitative Breast PET Scanner Integrated with Tomosynthesis
A dedicated breast PET-DBT scanner provides higher resolution and sensitivity compared to a wholebody PET/CT scanner, and hence quantitative images from such a device can play a significant role in providing personalized therapy for patients diagnosed with breast cancer. In this project we develop such a device in an integrated multi-modality design, and subsequently evaluate its clinical performance in patients for ER+ tumor characterization and diagnostic imaging of patients with dense breasts.

4/1/2017-3/31/2022
NIH 1R01CA207084 – Mayo Clinic Rochester
Radiomic phenotypes of breast parenchyma and breast cancer risk and detection
The main goals of this study are to characterize ‘intrinsic’ parenchymal complexity features reflecting the heterogeneity of breast tissue, to examine the association of ‘intrinsic’ parenchymal complexity features with breast cancer risk and to examine the contribution of parenchymal complexity features to masking cancers.

T32EB009384
NIH
Gee, Maidment, Ives
8/1/2009-7/31/2024
Training Program in Biomedical Imaging and Informational Sciences
A PhD training program with a focus on medical imaging.

OVERLAP: There is no scientific or budgetary overlap between the above research grants and DoD grant W81XWH-18-1-0082.

7.C. What other organizations were involved as partners?
Nothing to report.

8. SPECIAL REPORTING REQUIREMENTS.

8.A. Collaborative Awards
Nothing to report.

8.B. Quad Charts
Nothing to report.

REFERENCES

1. Conant EF, Zuckerman SP, McDonald ES, et al. Five Consecutive Years of Screening with Digital Breast Tomosynthesis: Outcomes by Screening Year and Round. Radiology 2020;295:285-93.
2. Friedewald SM, Rafferty EA, Rose SL, et al. Breast Cancer Screening Using Tomosynthesis in Combination With Digital Mammography. JAMA 2014;311:2499-507.
3. Acciavatti RJ, Maidment ADA. Observation of super-resolution in digital breast tomosynthesis. Medical Physics 2012;39:7518-39.
4. Acciavatti RJ, Vent TL, Barufaldi B, Wileyto EP, Noel PB, Maidment ADA. Proposing Rapid Source Pulsing for Improved Super-Resolution in Digital Breast Tomosynthesis. Proc SPIE 2020;11312:113125G.
5. Acciavatti RJ, Vent TL, Barufaldi B, Wileyto EP, Noel PB, Maidment ADA. Super-Resolution in Digital Breast Tomosynthesis: Limitations of the Conventional System Design and Strategies for Optimization. Proc SPIE 2020;11513:115130V.
6. Maidment ADA. Virtual Clinical Trials for the Assessment of Novel Breast Screening Modalities. Lecture Notes in Computer Science 2014;8539:1-8.
7. Barufaldi B, Higginbotham D, Bakic PR, Maidment ADA. OpenVCT: A GPU-Accelerated Virtual Clinical Trial Pipeline for Mammography and Digital Breast Tomosynthesis. In: Lo JY, Schmidt TG, Chen G-H, editors. SPIE Medical Imaging; 2018; Houston, TX: SPIE. p. 1057358.
8. Barufaldi B, Bakic PR, Pokrajac DD, Lago MA, Maidment ADA. Developing Populations of Software Breast Phantoms for Virtual Clinical Trials. In: Krupinski EA, editor. 14th International Workshop on Breast Imaging (IWBI 2018); 2018; Atlanta, GA: Proceedings of SPIE. p. 107181U.
9. Acciavatti RJ, Barufaldi B, Vent TL, Wileyto EP, Maidment ADA. Personalization of X-Ray Tube Motion in Digital Breast Tomosynthesis Using Virtual Defrise Phantoms. In: Schmidt TG, Chen G-H, Bosmans H, editors. SPIE Medical Imaging; 2019; San Diego, CA: SPIE. p. 109480B.
10. Vent TL, Barufaldi B, Acciavatti RJ, Krishnamoorthy S, Surti S, Maidment ADA. Next generation tomosynthesis image acquisition optimization for dedicated PET-DBT attenuation corrections. Proc SPIE 2021;11595:115954V.
11. Barufaldi B, Vent TL, Acciavatti RJ, Bakic PR, Noel PB, Maidment ADA. MRMC ROC Analysis of Calcification Detection in Tomosynthesis Using Computed Super Resolution and Virtual Clinical Trials. Proc SPIE 2020;11513:1151313.
12. Acciavatti RJ, Vent TL, Choi CJ, Wileyto EP, Noël PB, Maidment ADA. Development of Magnification Tomosynthesis for Superior Resolution in Diagnostic Mammography. In: Bosmans H, Zhao W, Yu L, editors. SPIE Medical Imaging; 2021: SPIE. p. 115951J.
13. Vent TL, Barufaldi B, Acciavatti RJ, Maidment ADA. Simulation of high-resolution test objects using non-isocentric acquisition geometries in next-generation digital tomosynthesis. Proc SPIE 2020;11513:1151317.
14. Acciavatti RJ, Choi CJ, Vent TL, Barufaldi B, Maidment ADA. Achieving Isotropic Super-Resolution with a Non-Isocentric Acquisition Geometry in a Next-Generation Tomosynthesis System. Proc SPIE 2022;12031:120314B.
15. Vent TL, Acciavatti RJ, Maidment ADA. Development and Evaluation of the Fourier Spectral Distortion Metric. IEEE Transactions on Medical Imaging 2021;40:1055-64.

16. Choi CJ, Vent TL, Geagan MJ, Noël PB, Maidment ADA. Investigation of optimal angular range and projection density for next generation tomosynthesis. Proc SPIE 2022;12031:120314C.
17. Choi CJ, Vent TL, Acciavatti RJ, Maidment ADA. Analysis of Digital Breast Tomosynthesis Acquisition Geometries in Sampling Fourier Space. In: Bosmans H, Zhao W, Yu L, editors. SPIE Medical Imaging; 2021; Conference Held Virtually Due to COVID-19 Pandemic: SPIE. p. 115954W.
18. Vent TL, Acciavatti RJ, Choi C, et al. Pre-clinical evaluation and optimization of image quality for a next generation tomosynthesis prototype. In: Zhao W, Yu L, editors. SPIE Medical Imaging; 2022: SPIE. p. 1203142.
19. Martin DA, Vent TL, Choi CJ, Barufaldi B, Acciavatti RJ, Maidment ADA. Signal-to-Noise Ratio and Contrast-to-Noise Ratio Measurements for Next Generation Tomosynthesis. In: Bosmans H, Zhao W, Yu L, editors. SPIE Medical Imaging; 2021; Conference Held Virtually Due to COVID-19 Pandemic: SPIE. p. 115951L.
20. Teixeira JPV, Filho TMS, Rêgo TGd, et al. Novel Perlin-based Phantoms Using 3D Models of Compressed Breast Shape and Fractal Noise. In: Zhao W, Yu L, editors. SPIE Medical Imaging; 2022: SPIE. p. 120313S.
21. Acciavatti R, Vent T, Choi C, Noel P, Maidment A. Anisotropies in Super-Resolution in 3D Magnification Mammography Using a Next-Generation Tomosynthesis System. Medical Physics 2021 (AAPM conference abstract);48.
22. Barufaldi B, Vent TL, Acciavatti RJ, et al. Determining the Optimal Angular Range of the X-Ray Source Motion in Tomosynthesis Using Virtual Clinical Trials. Proc SPIE 2020;11312:113120I.
23. Barufaldi B, Maidment ADA, Dustler M, et al. Virtual Clinical Trials in Medical Imaging System Evaluation and Optimisation. Radiation Protection Dosimetry 2021;195:363-71.
24. Peregrino L, Gomes J, Rêgo TGd, et al. Automatic Segmentation of Mammary Tissue using Computer Simulations of Breast Phantoms and Deep-learning Techniques. Proceedings of the 14th International Joint Conference on Biomedical Engineering Systems and Technologies - BIOSIGNALS 2021:252-9.
25. Dong V, Maidment TD, Borges LR, Barufaldi B, Ng S, Maidment ADA. Assessment of patch-based mammogram denoising methods using virtual clinical trials and deep learning: trade-off between denoising strength and preservation of structural details. Proc SPIE 2022;12031:120311W.
26. Barufaldi B, Vent TL, Bakic PR, Maidment ADA. Computer simulations of case difficulty in digital breast tomosynthesis using virtual clinical trials. Medical Physics 2022;49:2220-32.
27. Choi CJ, Barufaldi B, Teixeira JPV, Acciavatti RJ, Maidment ADA. Spatial dependency of lesion detectability in digital breast tomosynthesis. Proc SPIE 2022;12286:1228618.
28. Nobrega YNGd, Carvalhal G, Teixeira JPV, et al. Multiclass Segmentation of Suspicious Findings in Simulated Breast Tomosynthesis Images Using U-Net. Proc SPIE 2022;12286:122860L.
29. Acciavatti RJ, Maidment ADA. Non-stationary model of oblique x-ray incidence in amorphous selenium detectors: I. Point spread function. Medical Physics 2019;46:494-504.
30. Acciavatti RJ, Maidment ADA. Nonstationary model of oblique x-ray incidence in amorphous selenium detectors: II. Transfer functions. Medical Physics 2019;46:505-16.
31. Barufaldi B, Abbey CK, Lago MA, et al. Computational Breast Anatomy Simulation Using Multi-Scale Perlin Noise. IEEE Transactions on Medical Imaging 2021;40:3436-45.
32. Acciavatti RJ, Cohen EA, Maghsoudi OH, et al. Robust Radiomic Feature Selection in Digital Mammography: Understanding the Effect of Imaging Acquisition Physics Using Phantom and Clinical Data Analysis. Proc SPIE 2020;11314:113140W.
33. Acciavatti RJ, Cohen EA, Maghsoudi OH, et al. Incorporating Robustness to Imaging Physics into Radiomic Feature Selection for Breast Cancer Risk Estimation. Cancers 2021;13:5497.
34. Acciavatti RJ, Cohen EA, Maghsoudi OH, et al. Calculation of Radiomic Features to Validate the Textural Realism of Physical Anthropomorphic Phantoms for Digital Mammography. Proc SPIE 2020;11513:1151309.
35. Rafferty EA, Park JM, Philpotts LE, et al. Assessing Radiologist Performance Using Combined Digital Mammography and Breast Tomosynthesis Compared with Digital Mammography Alone: Results of a Multicenter, Multireader Trial. Radiology 2013;266:104-13.

36. Sechopoulos I. A review of breast tomosynthesis. Part I. The image acquisition process. Med Phys 2013;40:014301.
37. Acciavatti RJ, Rodriguez-Ruiz A, Vent TL, et al. Analysis of Volume Overestimation Artifacts in the Breast Outline Segmentation in Tomosynthesis. In: Lo JY, Schmidt TG, Chen G-H, editors. SPIE Medical Imaging; 2018; Houston, TX: SPIE. p. 1057359.
38. Rodriguez-Ruiz A, Agasthya GA, Sechopoulos I. The compressed breast during mammography and breast tomosynthesis: in vivo shape characterization and modeling. Physics in Medicine and Biology 2017;62:6920-37.
39. Eben JE, Vent TL, Choi CJ, et al. Development of a Next Generation Tomosynthesis System. In: Lo JY, Schmidt TG, Chen G-H, editors. SPIE Medical Imaging; 2018; Houston, TX: SPIE. p. 105735Q.

9. APPENDICES

1. Acciavatti RJ, Maidment ADA. Non-stationary model of oblique x-ray incidence in amorphous selenium detectors: I. Point spread function. Medical Physics. 2019; 46(2):494-504.
2. Acciavatti RJ, Maidment ADA. Nonstationary model of oblique x-ray incidence in amorphous selenium detectors: II. Transfer Functions. Medical Physics. 2019; 46(2); 505-16.
3. Acciavatti RJ, Barufaldi B, Vent TL, Wileyto EP, Maidment ADA. Personalization of x-ray tube motion in digital breast tomosynthesis using virtual Defrise phantoms. In: Schmidt TG, Chen G-H, Bosmans H, editors; Physics of Medical Imaging; 2019; San Diego, CA: SPIE; 2019. p. 109480B-1 – 109480B-9. The PI (Raymond Acciavatti) presented this work at the SPIE Medical Imaging conference on 2/17/19 in San Diego, CA.
4. Vu B-T, Barufaldi B, Vent T, Acciavatti R, Maidment A. Automation of Virtual Clinical Trials Used to Evaluate Efficacy of Breast Cancer Screening Modalities. The PI (Raymond Acciavatti) mentored an undergraduate student (Brian Vu, Univ. of Houston) in 2019 through the AAPM summer undergraduate fellowship program. During that summer, Brian also participated in the Summer Undergraduate Program for Educating Radiation Scientists (SUPERS), for which he prepared an abstract and gave a presentation on 8/7/2019.
5. Acciavatti RJ, Cohen EA, Maghsoudi OH, Gastounioti A, Pantalone L, Hsieh M-K, Conant EF, Scott CG, Winham SJ, Kerlikowske K, Vachon C, Maidment ADA, Kontos D. Robust Radiomic Feature Selection in Digital Mammography: Understanding the Effect of Imaging Acquisition Physics Using Phantom and Clinical Data Analysis. In: Hahn HK, Mazurowski MA, editors; Computer-Aided Diagnosis; 2020; Houston, TX: SPIE; 2020. p. 113140W. The PI (Raymond Acciavatti) gave an oral presentation at the SPIE Medical Imaging conference on 2/17/2020 in Houston, TX.
6. Acciavatti RJ, Vent TL, Barufaldi B, Wileyto EP, Noël PB, Maidment ADA. Proposing Rapid Source Pulsing for Improved Super-Resolution in Digital Breast Tomosynthesis. In: Chen G-H, Bosmans H, editors; Physics of Medical Imaging; 2020; Houston, TX: SPIE; 2020. p. 113125G. The PI (Raymond Acciavatti) presented this work as a poster at the SPIE Medical Imaging conference on 2/17/2020 in Houston, TX.
7. Barufaldi B, Vent TL, Acciavatti RJ, Bakic PR, Noël PB, Conant EF, Maidment ADA. Determining the Optimal Angular Range of the X-Ray Source Motion in Tomosynthesis Using Virtual Clinical Trials. In: Chen G-H, Bosmans H, editors; Physics of Medical Imaging; 2020; Houston, TX: SPIE; 2020. p. 113120I.
8. Acciavatti RJ, Cohen EA, Maghsoudi OH, Gastounioti A, Pantalone L, Hsieh M-K, Barufaldi B, Bakic PR, Chen J, Conant EF, Kontos D, Maidment ADA. Calculation of Radiomic Features to Validate the Textural Realism of Physical Anthropomorphic Phantoms for Digital Mammography. In: Bosmans H, Marshall N, Van Ongeval C, editors; 15th International Workshop on Breast Imaging; 2020; Virtual Conference (held during COVID-19 Pandemic): SPIE; 2020. p. 1151309-1 - 1151309-7. *This paper was published in May of 2020. The PI (Raymond Acciavatti) gave a "virtual" presentation at this conference.*
9. Acciavatti RJ, Vent TL, Barufaldi B, Wileyto EP, Noël PB, Maidment ADA. Super-Resolution in Digital Breast Tomosynthesis: Limitations of the Conventional System Design and Strategies for Optimization. In: Bosmans H, Marshall N, Van Ongeval C, editors; 15th International Workshop on Breast Imaging; 2020; Virtual Conference (held during COVID-19 Pandemic): SPIE; 2020. p. 115130V-1 - 115130V-9. *This paper was published in May of 2020. The PI (Raymond Acciavatti) gave a "virtual" presentation at this conference.*
10. Barufaldi B, Vent TL, Acciavatti RJ, Bakic PR, Noël PB, Maidment ADA. MRMC ROC Analysis of Calcification Detection in Tomosynthesis Using Computed Super Resolution and Virtual Clinical Trials.

In: Bosmans H, Marshall N, Van Ongeval C, editors; 15th International Workshop on Breast Imaging; 2020; Virtual Conference (held during COVID-19 Pandemic): SPIE; 2020. p. 1151313-1 - 1151313-7. *This paper was published in May of 2020. The first author (Bruno Barufaldi) gave a "virtual" presentation at this conference.*

11. Vent TL, Barufaldi B, Acciavatti RJ, Maidment ADA. Simulation of high-resolution test objects using non isocentric acquisition geometries in next-generation digital tomosynthesis. In: Bosmans H, Marshall N, Van Ongeval C, editors; 15th International Workshop on Breast Imaging; 2020; Virtual Conference (held during COVID-19 Pandemic): SPIE; 2020. p. 1151317-1 - 1151317-8. *This paper was published in May of 2020. The first author (Trevor Vent) gave a "virtual" presentation at this conference.*
12. Peregrino LR, Gomes JV, do Rêgo TG, Barbosa Y, Filho T, Maidment ADA, Barufaldi B. Automatic Segmentation of Mammary Tissue using Computer Simulations of Breast Phantoms and Deep-learning Techniques. Proceedings of the 14th International Joint Conference on Biomedical Engineering Systems and Technologies (BIOSTEC 2021), vol. 4: BIOSIGNALS, p. 252-259.
13. Acciavatti RJ, Vent TL, Choi CJ, Wileyto EP, Noël PB, Maidment ADA. Development of Magnification Tomosynthesis for Superior Resolution in Diagnostic Mammography. In: Bosmans H, Zhao W, Yu L, editors; Physics of Medical Imaging; 2021 (virtual conference held during COVID-19 Pandemic): SPIE; 2021. p. 115951J 1 - 115951J-7. *This conference paper was published in February 2021. The PI (Raymond Acciavatti) gave a "virtual" presentation.*
14. Choi CJ, Vent TL, Acciavatti RJ, Maidment ADA. Analysis of Digital Breast Tomosynthesis Acquisition Geometries in Sampling Fourier Space. In: Bosmans H, Zhao W, Yu L, editors; Physics of Medical Imaging; 2021 (virtual conference held during COVID-19 Pandemic): SPIE; 2021. p. 115954W-1 - 115954W-10. *This conference paper was published in February 2021. The first author (Chloe Choi) gave a "virtual" poster presentation.*
15. Martin DA, Vent TL, Choi CJ, Barufaldi B, Acciavatti RJ, Maidment ADA. Signal-to-Noise Ratio and Contrast-to-Noise Ratio Measurements for Next Generation Tomosynthesis. In: Bosmans H, Zhao W, Yu L, editors; Physics of Medical Imaging; 2021 (virtual conference held during COVID-19 Pandemic): SPIE; 2021. p. 115951L-1 - 115951L-9. *This conference paper was published in February 2021. The first author (David Martin) gave a "virtual" presentation.*
16. Vent TL, Barufaldi B, Acciavatti RJ, Krishnamoorthy S, Surti S, Maidment ADA. Next generation tomosynthesis image acquisition optimization for dedicated PET-DBT attenuation corrections. In: Bosmans H, Zhao W, Yu L, editors; Physics of Medical Imaging; 2021 (virtual conference held during COVID-19 Pandemic): SPIE; 2021. p. 115954V-1 - 115954V-7. *This conference paper was published in February 2021. The first author (Trevor Vent) gave a "virtual" poster presentation.*
17. Vent TL, Acciavatti RJ, Maidment ADA. Development and Evaluation of the Fourier Spectral Distortion Metric. IEEE Transactions on Medical Imaging, vol. 40, no. 3, pp. 1055-1064. *This paper was published in March of 2021.*
18. Barufaldi B, Maidment ADA, Dustler M, Axelsson R, Tomic H, Zackrisson S, Tingberg A, Bakic PR. Virtual Clinical Trials in Medical Imaging System Evaluation and Optimisation. Radiation Protection Dosimetry, vol. 195, no. 3-4, p. 363-371. *This paper was published in April of 2021.*
19. Acciavatti R, Vent T, Choi C, Noel P, Maidment A. Anisotropies in Super-Resolution in 3D Magnification Mammography Using a Next-Generation Tomosynthesis System. Medical Physics. 2021; 48(6):51. *This conference abstract was published in June 2021. The PI (Raymond Acciavatti) gave a "virtual" presentation at the 2021 virtual Annual Meeting of the American Association of Physicists in Medicine (AAPM).*
20. Acciavatti RJ, Cohen EA, Maghsoudi OH, Gastounioti A, Pantalone L, Hsieh M-K, Conant EF, Scott CG, Winham SJ, Kerlikowske K, Vachon C, Maidment ADA, Kontos D. Incorporating Robustness to

Imaging Physics into Radiomic Feature Selection for Breast Cancer Risk Estimation. Cancers, vol. 13, no. 21, p. 5497. *This paper was published in November of 2021.*

21. Barufaldi B, Abbey CK, Lago MA, Vent TL, Acciavatt RJ, Bakic PR, Maidment ADA. Computational Breast Anatomy Simulation Using Multi-Scale Perlin Noise. IEEE Transactions on Medical Imaging, vol. 40, no. 12, pp. 3436-3445. *This paper was published in December of 2021.*
22. Barufaldi B, Vent TL, Bakic PR, Maidment ADA. Computer simulations of case difficulty in digital breast tomosynthesis using virtual clinical trials. Medical Physics, vol. 49, no. 4, p. 2220-2232. *This paper was published in April 2022.*
23. Acciavatti RJ, Choi CJ, Vent TL, Barufaldi B, Maidment ADA. Achieving isotropic super-resolution with a non-isocentric acquisition geometry in a next-generation tomosynthesis system. In: Zhao W, Yu L, editors; Physics of Medical Imaging; 2022: SPIE; 2022. p. 120314B-1 - 120314B-10. *This conference paper was published in April 2022. The PI (Raymond Acciavatti) gave a "virtual" poster presentation.*
24. Choi CJ, Vent TL, Geagan MJ, Noël PB, Maidment ADA. Investigation of optimal angular range and projection density for next generation tomosynthesis. In: Zhao W, Yu L, editors; Physics of Medical Imaging; 2022: SPIE; 2022. p. 120314C-1 – 120314C-15. *This conference paper was published in April 2022. Chloe J. Choi gave a "virtual" poster presentation.*
25. Dong V, Maidment TD, Borges LR, Barufaldi B, Ng S, Maidment ADA. Assessment of patch-based mammogram denoising methods using virtual clinical trials and deep learning: trade-off between denoising strength and preservation of structural details. In: Zhao W, Yu L, editors; Physics of Medical Imaging; 2022: SPIE; 2022. p. 120311W-1 – 120311W-10. *This conference paper was published in April 2022. Vincent Dong gave a "virtual" poster presentation.*
26. Teixeira JPV, Filho TMS, do Rêgo TG, Malheiros YB, Dustler M, Bakic PR, Vent TL, Acciavatti RJ, Krishnamoorthy S, Surti S, Maidment ADA, Barufaldi B. Novel Perlin-based Phantoms Using 3D Models of Compressed Breast Shape and Fractal Noise. In: Zhao W, Yu L, editors; Physics of Medical Imaging; 2022: SPIE; 2022. p. 120313S-1 – 120313S-10. *This conference paper was published in April 2022. João P.V. Teixeira gave a "virtual" poster presentation.*
27. Vent TL, Acciavatti RJ, Choi C, Barufaldi B, Krishnamoorthy S, Borges L, Kuo J, Ringer PA, Ng S, Surti S, Maidment ADA. Pre-clinical evaluation and optimization of image quality for a Next Generation Tomosynthesis prototype. In: Zhao W, Yu L, editors; Physics of Medical Imaging; 2022: SPIE; 2022. p. 1203142-1 – 1203142-7. *This conference paper was published in April 2022. Trevor L. Vent gave a "virtual" poster presentation.*
28. Choi CJ, Barufaldi B, Teixeira JPV, Acciavatti RJ, Maidment ADA. Spatial dependency of lesion detectability in digital breast tomosynthesis. In: Bosmans H, Marshall N, Van Ongeval C, editors; 16th International Workshop on Breast Imaging; Proc. SPIE 2022. p. 1228618-1 – 1228618-8. *The first author (Chloe J. Choi) presented this work in Leuven, Belgium at the 16th International Workshop on Breast Imaging.*
29. Nobrega Y, Carvalhal G, Teixeira JPV, Camargo BP, Rego TG, Malheiros Y, Filho T, Vent TL, Acciavatti RJ, Maidment ADA, Barufaldi B. Multiclass Segmentation of Suspicious Findings in Simulated Breast Tomosynthesis Images Using a U-Net. In: Bosmans H, Marshall N, Van Ongeval C, editors; 16th International Workshop on Breast Imaging; Proc. SPIE 2022. p. 122860L-1 – 122860L-10. *One of the authors (Telmo de M. E Silva Filho) presented this work in Leuven, Belgium at the 16th International Workshop on Breast Imaging.*
30. Complete Personnel List (all years of grant).
31. Award Expiration Transition Plan.
32. Award Chart.

Non-stationary model of oblique x-ray incidence in amorphous selenium detectors: I. Point spread function

Raymond J. Acciavatti[a] and Andrew D. A. Maidment
Department of Radiology, Perelman School of Medicine at the University of Pennsylvania, Philadelphia, PA 19104-4206, USA

(Received 23 April 2018; revised 2 October 2018; accepted for publication 16 November 2018; published 16 January 2019)

Purpose: In previous work, a theoretical model of the point spread function (PSF) for oblique x-ray incidence in amorphous selenium (*a*-Se) detectors was proposed. The purpose of this paper is to develop a complementary model that includes two additional features. First, the incidence angle and the directionality of ray incidence are calculated at each position, assuming a divergent x-ray beam geometry. This approach allows the non-stationarity of the PSF to be modeled. Second, this paper develops a framework that is applicable to a digital system, unlike previous work which did not model the presence of a thin-film transistor (TFT) array.
Methods: At each point on the detector, the incidence angle and the ray incidence direction are determined using ray tracing. Based on these calculations, an existing model for the PSF of the x-ray converter (*Med Phys*. 1995;**22**:365-374) is generalized to a non-stationary model. The PSF is convolved with the product of two rectangle functions, which model the sampling of the TFT array. The rectangle functions match the detector element (del) size in two dimensions.
Results: It is shown that the PSF can be calculated in closed form. This solution is used to simulate a digital mammography (DM) system at two x-ray energies (20 and 40 keV). Based on the divergence of the x-ray beam, the direction of ray incidence varies with position. Along this direction, the PSF is broader than the reference rect function matching the del size. The broadening is more pronounced with increasing obliquity. At high energy, the PSF deviates more strongly from the reference rect function, indicating that there is more blurring. In addition, the PSF is calculated along the polar angle perpendicular to the ray incidence direction. For this polar angle, the shape of the PSF is dependent upon whether the ray incidence direction is parallel with the sides of the detector. If the ray incidence direction is parallel with either dimension, the PSF is a perfect rectangle function, matching the del size. However, if the ray incidence direction is at an oblique angle relative to the sides of the detector, the PSF is not rectangular. These results illustrate the non-stationarity of the PSF.
Conclusions: This paper demonstrates that an existing model of the PSF of *a*-Se detectors can be generalized to include the effects of non-stationarity and digitization. The PSF is determined in closed form. This solution offers the advantage of shorter computation time relative to approaches that use numerical methods. This model is a tool for simulating *a*-Se detectors in future work, such as in virtual clinical trials with computational phantoms. [https://doi.org/10.1002/mp.13313]

Key words: amorphous selenium, digital x-ray detectors, obliquity effect, point spread function (PSF), theoretical modeling

1. INTRODUCTION

The detectors commonly used in breast x-ray imaging are either indirect- or direct-converting. In an indirect-conversion detector such as cesium iodide (CsI), x rays are first converted to visible light, which spreads laterally.[1–4] The visible light is then converted to charged particles by photodiodes. This signal is digitized by a thin-film transistor (TFT) array. By contrast, there is no intermediate conversion of x rays to visible light in a direct-conversion detector such as amorphous-selenium (*a*-Se).[5–7] In these detectors, selenium atoms are ionized by x rays, creating electron-hole pairs. Based on an applied electric field, the electrons and holes migrate to opposite surfaces of the detector, and an image is formed. Badano et al. demonstrated that, for a fixed detector thickness and energy, *a*-Se is characterized by a narrower point response function than CsI at normal incidence[8]; in this paper, we use the term point spread function (PSF).

Due to the low atomic number of selenium ($Z = 34$), *a*-Se detectors have low x-ray absorption at high energies, and hence are more commonly used in low-energy applications, such as DM and digital breast tomosynthesis (DBT). At 20 keV, the quantum detection efficiency of 0.200 mm thick selenium is 98.3% at normal incidence, assuming a mass attenuation coefficient[9] of 4.82×10^3 mm^2/g and a density[10] of 4.20×10^{-3} g/mm^3.

Badano et al. developed a model of the obliquity effect in *a*-Se detectors.[8] They demonstrated that the PSF is broadened due to oblique incidence. In their work, the lateral spread of signal at each depth of *a*-Se was modeled with a Lorentzian function. The parameters were fit to the results of Monte Carlo simulations with MANTIS. Que and Rowlands offered a

different approach for calculating the PSF.[11] Rather than calculate a single PSF that models all possible sources of blurring, Que and Rowlands identified multiple x-ray interactions that could introduce blurring, and modeled the PSF for each interaction separately. In their model of the obliquity effect, the PSF is blurred along the ray incidence direction, and is a delta function along the perpendicular direction.

One limitation of these previous works is that the presence of the TFT array was not included in the modeling assumptions, and hence the PSF models a non-pixelated system. The purpose of this paper is to develop a complementary model for a digital system, in which the signal in the x-ray converter is binned into detector elements (dels). For the purpose of this paper, we expand upon the model of the PSF developed by Que and Rowlands.[11] The PSF of the digital system is derived by convolving the PSF of the x-ray converter with the product of two rectangle functions, which match the del size in each direction.[12–14] It is shown that this convolution can be calculated in closed form. The advantage of deriving an analytical formula is that computation time is minimized relative to numerical integration methods.

In x-ray imaging, the shape of the PSF varies with position based on the angle of incidence and the directionality of the incident ray. An additional aim of this paper is to demonstrate how the PSF varies with position. We use this formulation to quantify non-stationarity in *a*-Se detectors.

2. MATERIALS AND METHODS

2.A. Coordinate system

A model of the PSF was previously developed by Que and Rowlands for an arbitrary incidence angle[11]; however, they did not model the non-stationarity of the PSF and did not consider the impact of digitization. These effects are now modeled from first principles for a breast imaging system.

Figure 1 shows a diagram of the acquisition geometry. The exit surface of the detector is defined to be the plane $z = 0$. The origin (O) is the point in this plane at which the ray is normally incident. The x-ray source is treated as a point source at the coordinate $(0, 0, d)$. Figure 1 also allows for the possibility of transforming to a coordinate system with a different reference point (M); in a breast imaging system, point M is the midpoint of the chest wall side of the detector. This transformation is considered in Section 2.D.

At each point along the ray, there are x-ray interactions with selenium atoms (Fig. 2). The electrons and holes that are produced migrate to opposite sides of the x-ray converter due to the applied electric field. We assume that signal is recorded at the exit surface as opposed to the entrance

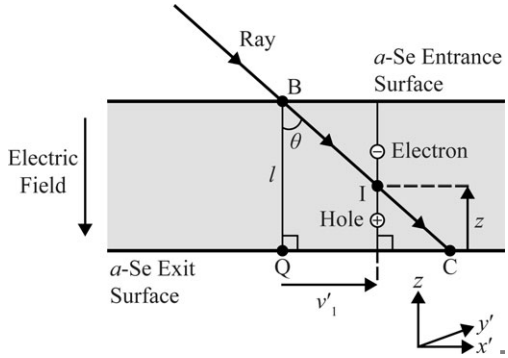

FIG. 2. Electron-hole pairs are produced by the ionization of selenium atoms along the path length of the ray. Due to the applied electric field, the electron and hole migrate to opposite ends of the detector. Signal is formed along the line segment $\overline{QC}$, which lies along the ray incidence direction (x'). For the purpose of this paper, it is presumed that there is no blurring along the perpendicular direction (y').

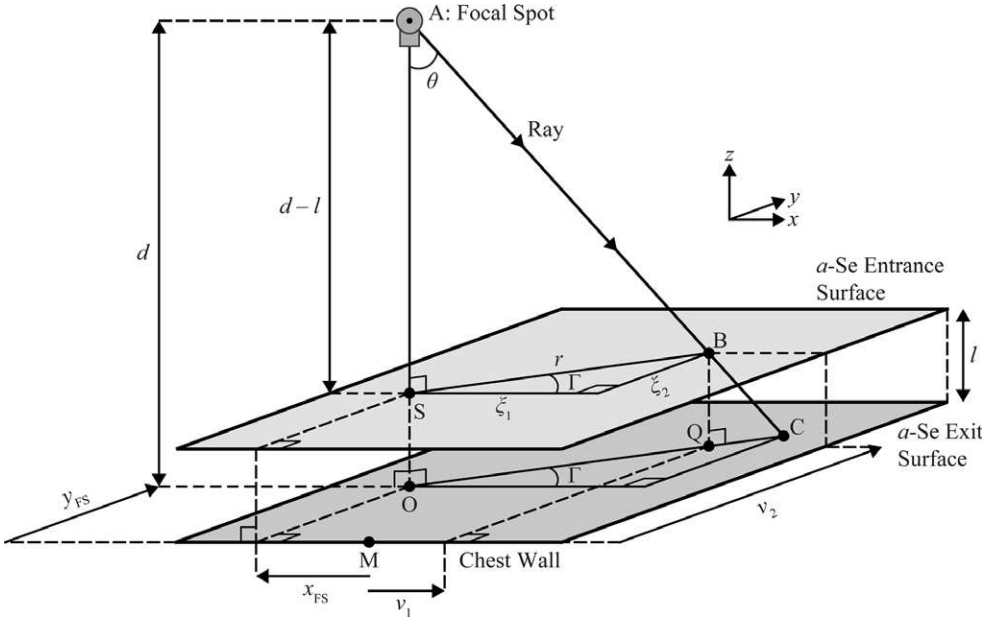

FIG. 1. A diagram of the acquisition geometry is shown. The direction of ray incidence is parallel with vector $\overrightarrow{SB}$ (or equivalently, vector $\overrightarrow{OC}$). Also, θ is the incidence angle, and Γ is the azimuthal angle of the ray. The path length of the ray through *a*-Se (thickness l) begins at point B and ends at point C. This figure is not to scale.

surface. For this reason, the directionality of the electric field determines whether the signal is produced by electrons or holes. The theoretical model can be applied to either. However, in this paper, the signal is taken to be produced by holes, like the AXS-2430 detector (Analogic Canada Corporation, Montreal, Quebec, Canada) modeled in Section 3.

Figure 2 shows how signal is produced along the x' direction in the exit surface of the x-ray converter; this is called the ray incidence direction throughout this paper. This direction lies along the angle Γ relative to the x direction (Fig. 1). To derive the PSF, the signal needs to be calculated in this rotated frame using the transformation

$$\begin{pmatrix} x \\ y \end{pmatrix} = \begin{pmatrix} \xi_1 \\ \xi_2 \end{pmatrix} + \begin{pmatrix} \cos\Gamma & -\sin\Gamma \\ \sin\Gamma & \cos\Gamma \end{pmatrix} \begin{pmatrix} v_1' \\ v_2' \end{pmatrix} \tag{1}$$

where v_1' is position along the ray incidence direction, v_2' is position in the perpendicular direction, and ξ_1 and ξ_2 are the x and y coordinates of the entrance point (B), respectively. Two trigonometric substitutions can be made based on Fig. 1

$$\cos\Gamma = \frac{\xi_1}{r} \tag{2}$$

$$\sin\Gamma = \frac{\xi_2}{r} \tag{3}$$

where

$$r = \sqrt{\xi_1^2 + \xi_2^2} \tag{4}$$

giving

$$v_1' = \frac{\xi_1}{r}x + \frac{\xi_2}{r}y - r \tag{5}$$

$$v_2' = \frac{-\xi_2}{r}x + \frac{\xi_1}{r}y \tag{6}$$

as the inverse transformation. The derivation that follows presumes that $r > 0$. There is normal incidence at the position for which $r = 0$; the PSF at this position is simply the TFT sampling function described in Section 2.B.

2.B. Depth-dependent PSF

The PSF associated with an arbitrary ionization point is now calculated. From Fig. 2, the v_1-coordinate of the ionization point (I) is $(l - z)\tan\theta$, where θ is the incidence angle. The PSF is

$$P_{\mathrm{I}} = \delta\left[v_1' - (l - z)\tan\theta\right]\delta(v_2'), \tag{7}$$

where the subscript "I" is an abbreviation for "Ionization". The angle θ can be determined from Fig. 1.

$$\tan\theta = \frac{r}{d - l} \tag{8}$$

Combining Eqs. (5)–(8) yields

$$P_{\mathrm{I}} = \delta\left(\frac{\xi_1}{r}x + \frac{\xi_2}{r}y + \frac{r}{d-l}z - \frac{dr}{d-l}\right)\delta\left(\frac{-\xi_2}{r}x + \frac{\xi_1}{r}y\right). \tag{9}$$

In a digital system, a TFT array bins the signal produced by the x-ray converter into dels. We model the PSF of the TFT array using

$$P_{\mathrm{TFT}} = \frac{1}{a_x a_y}\mathrm{rect}\left(\frac{x}{a_x}\right)\cdot\mathrm{rect}\left(\frac{y}{a_y}\right), \tag{10}$$

where a_x and a_y denote the del size in the x and y directions, respectively, and P_{TFT} denotes the PSF of the TFT array. If the x and y subscripts are removed, it is assumed that the del is square ($a_x = a_y = a$). Combining the effects of ionization and TFT sampling, the PSF can be written as the two-dimensional (2D) convolution

$$P_z = P_{\mathrm{I}} *_2 P_{\mathrm{TFT}}, \tag{11}$$

where the subscript z emphasizes that this PSF is associated with a specific depth.

2.C. Net PSF

One can integrate P_z over the thickness (l) to determine the net PSF of the system. This function is denoted P_{Net}.

$$P_{\mathrm{Net}} = \int_0^l N \cdot P_z \cdot dz \tag{12}$$

To convert Eq. (12) into a form with infinite integration limits, one can introduce a rectangle function to match the interval of integration, so that

$$P_{\mathrm{Net}} = \int_{-\infty}^{\infty} N \cdot P_z \cdot \mathrm{rect}\left(\frac{z - l/2}{l}\right)dz, \tag{13}$$

where

$$\mathrm{rect}(v) \equiv \begin{cases} 1, & |v| \le 1/2 \\ 0, & |v| > 1/2 \end{cases}. \tag{14}$$

In Eq. (12), the integrand is weighted by N, the relative number of x-ray quanta at each depth z. The function N is determined from the linear attenuation coefficient (μ) of selenium

$$N = C_{\mathrm{I}} e^{-\mu(l-z)\sec\theta}, \tag{15}$$

where

$$\sec\theta = \sqrt{1 + \left(\frac{r}{d-l}\right)^2}. \tag{16}$$

In Eq. (15), C_{I} is a normalization term, which can be determined from the normalization convention used by Swank[15]

$$\int_0^l N \cdot dz = 1 \tag{17}$$

giving

$$C_{\mathrm{I}} = \frac{\mu\sqrt{1 + \left(\frac{r}{d-l}\right)^2}}{1 - e^{-\mu l\sqrt{1+\left(\frac{r}{d-l}\right)^2}}}. \tag{18}$$

Combining Eqs. (9)–(11), (13), (15), (16) yields

$$P_{\text{Net}} = \int_{-\infty}^{\infty} C_{\text{I}} e^{-\mu\sqrt{1+\left(\frac{r}{d-l}\right)^2}(l-z)} \cdot \left[\int_{-\infty}^{\infty}\int_{-\infty}^{\infty}\begin{pmatrix} \delta\left(\frac{\xi_1}{r}\omega_1 + \frac{\xi_2}{r}\omega_2 + \frac{r}{d-l}z - \frac{dr}{d-l}\right) \\ \cdot\delta\left(\frac{-\xi_2}{r}\omega_1 + \frac{\xi_1}{r}\omega_2\right)\frac{1}{a_x a_y}\text{rect}\left(\frac{x-\omega_1}{a_x}\right)\text{rect}\left(\frac{y-\omega_2}{a_y}\right)\end{pmatrix} d\omega_1 d\omega_2\right] \text{rect}\left(\frac{z-l/2}{l}\right) dz. \tag{19}$$

We can re-order the integration so that the integral over z is calculated first.

$$P_{\text{Net}} = \frac{C_{\text{I}}}{a_x a_y}\int_{-\infty}^{\infty}\int_{-\infty}^{\infty}\delta\left(\frac{-\xi_2}{r}\omega_1 + \frac{\xi_1}{r}\omega_2\right) \cdot \text{rect}\left(\frac{x-\omega_1}{a_x}\right)\text{rect}\left(\frac{y-\omega_2}{a_y}\right) \cdot \int_{-\infty}^{\infty}\begin{pmatrix} e^{-\mu\sqrt{1+\left(\frac{r}{d-l}\right)^2}(l-z)}\text{rect}\left(\frac{z-l/2}{l}\right) \\ \cdot\delta\left(\frac{\xi_1}{r}\omega_1 + \frac{\xi_2}{r}\omega_2 + \frac{r}{d-l}z - \frac{dr}{d-l}\right)\end{pmatrix} dz d\omega_1 d\omega_2 \tag{20}$$

where

$$C_{\text{Net}} = \frac{C_{\text{I}}(d-l)}{a_x a_y r}. \tag{24}$$

The integral can be evaluated using the definition of the delta function

$$\int_{-\infty}^{\infty}\phi(z)\cdot\delta(z-\beta)\cdot dz \equiv \phi(\beta), \tag{25}$$

where ϕ is an arbitrary function of z and $\beta \in \mathbb{R}$. This gives

$$P_{\text{Net}} = C_{\text{Net}}\int_{-\infty}^{\infty}\int_{-\infty}^{\infty}\begin{pmatrix} e^{\frac{-\mu}{r}\sqrt{1+\left(\frac{d-l}{r}\right)^2}\left(\xi_1\omega_1+\xi_2\omega_2-r^2\right)}\text{rect}\left(\frac{-\xi_1(d-l)}{lr^2}\omega_1 - \frac{\xi_2(d-l)}{lr^2}\omega_2 + \frac{2d-l}{2l}\right) \\ \cdot\delta\left(\frac{-\xi_2}{r}\omega_1 + \frac{\xi_1}{r}\omega_2\right)\text{rect}\left(\frac{x-\omega_1}{a_x}\right)\text{rect}\left(\frac{y-\omega_2}{a_y}\right)\end{pmatrix} d\omega_1 d\omega_2. \tag{26}$$

The integral over z can be evaluated using the identity for the delta function of a composition.[16,17] The identity presumes that the argument of the delta function has a finite number of zeros and that there are no repeated zeros.

$$\delta[g(z)] = \sum_k \frac{\delta(z-z_k)}{|g'(z_k)|} \tag{21}$$

Each term z_k denotes the kth zero of the function $g(z)$. In Eq. (20), the argument of the delta function has only one zero; namely,

$$z = \frac{-\xi_1(d-l)}{r^2}\omega_1 - \frac{\xi_2(d-l)}{r^2}\omega_2 + d \tag{22}$$

Thus

$$P_{\text{Net}} = C_{\text{Net}}\int_{-\infty}^{\infty}\int_{-\infty}^{\infty}\delta\left(\frac{-\xi_2}{r}\omega_1 + \frac{\xi_1}{r}\omega_2\right) \cdot \text{rect}\left(\frac{x-\omega_1}{a_x}\right)\text{rect}\left(\frac{y-\omega_2}{a_y}\right) \cdot \int_{-\infty}^{\infty}\begin{pmatrix} e^{-\mu\sqrt{1+\left(\frac{r}{d-l}\right)^2}(l-z)}\text{rect}\left(\frac{z-l/2}{l}\right) \\ \cdot\delta\left[z - \left(\frac{-\xi_1(d-l)}{r^2}\omega_1 - \frac{\xi_2(d-l)}{r^2}\omega_2 + d\right)\right]\end{pmatrix} dz d\omega_1 d\omega_2 \tag{23}$$

Eq. (26) can be evaluated in closed form. There are three cases for the values of ξ_1 and ξ_2 that are now considered separately.

2.C.1. Case 1: ray incidence in ±x direction

First, ray incidence in the $\pm x$ direction is considered; that is, $\xi_1 \neq 0$ and $\xi_2 = 0$. From Eq. (4), it follows that $r = |\xi_1|$.

$$P_{\text{Net},1} = C_{\text{Net}}\int_{-\infty}^{\infty}\delta\left(\frac{\xi_1}{|\xi_1|}\omega_2\right)\text{rect}\left(\frac{y-\omega_2}{a_y}\right)d\omega_2 \cdot \int_{-\infty}^{\infty} e^{\frac{-\xi_1}{|\xi_1|}\mu(\omega_1-\xi_1)\sqrt{1+\left(\frac{d-l}{\xi_1}\right)^2}} \cdot \text{rect}\left(\frac{-(d-l)}{l\xi_1}\omega_1 + \frac{2d-l}{2l}\right)\text{rect}\left(\frac{x-\omega_1}{a_x}\right)d\omega_1 \tag{27}$$

The delta function can be simplified using the sign function ("sgn")

$$\delta\left(\frac{\xi_1}{|\xi_1|}\omega_2\right) = \delta[\text{sgn}(\xi_1)\cdot\omega_2] \tag{28}$$

$$= \delta(\omega_2), \tag{29}$$

where

$$\mathrm{sgn}(v) \equiv \begin{cases} -1, v<0 \\ 0, v=0 \\ 1, v>0. \end{cases} \tag{30}$$

The exponential in Eq. (27) can also be simplified with the sign function. Additionally, it is useful to flip the signs of the arguments of the two rect functions in Eq. (27); this is justified since the rect function [Eq. (14)] is an even function.

$$P_{\mathrm{Net},1} = C_{\mathrm{Net}} \cdot \mathrm{rect}\left(\frac{y}{a_y}\right) \cdot \int_{-\infty}^{\infty} e^{-\mathrm{sgn}(\xi_1)\cdot\mu(\omega_1-\xi_1)\sqrt{1+\left(\frac{d-l}{\xi_1}\right)^2}} \cdot \mathrm{rect}\left(\frac{d-l}{l\xi_1}\omega_1 + \frac{l-2d}{2l}\right)\mathrm{rect}\left(\frac{\omega_1 - x}{a_x}\right)d\omega_1 \tag{31}$$

To determine the interval of overlap for the rect functions in Eq. (31), the integrand needs to be rewritten in a form that shows the centroid and width of each rect function.

$$P_{\mathrm{Net},1} = C_{\mathrm{Net}} \cdot \mathrm{rect}\left(\frac{y}{a_y}\right) \cdot \int_{-\infty}^{\infty} e^{-\mathrm{sgn}(\xi_1)\cdot\mu(\omega_1-\xi_1)\sqrt{1+\left(\frac{d-l}{\xi_1}\right)^2}} \cdot \mathrm{rect}\left(\frac{\omega_1 - \frac{(2d-l)\xi_1}{2(d-l)}}{\frac{\xi_1 l}{d-l}}\right)\mathrm{rect}\left(\frac{\omega_1 - x}{a_x}\right)d\omega_1 \tag{32}$$

For each rect function, the centroid is given by the offset term in the numerator, while the width is given by the denominator. The left-hand endpoints of the two rect functions are thus

$$h_{1,1} = \min\left\{\xi_1, \frac{d\xi_1}{d-l}\right\} \tag{33}$$

$$h_{1,2} = x - \frac{a_x}{2}. \tag{34}$$

The first subscript identifies the case number, while the second subscript identifies the order of the rect function when reading Eq. (32) from left-to-right. Similarly, the right-hand endpoints are

$$j_{1,1} = \max\left\{\xi_1, \frac{d\xi_1}{d-l}\right\} \tag{35}$$

$$j_{1,2} = x + \frac{a_x}{2}. \tag{36}$$

It is useful to re-number the rect functions based on the positioning of the left-hand endpoints.

$$h'_{1,1} = \min\{h_{1,1}, h_{1,2}\} \tag{37}$$

$$h'_{1,2} = \max\{h_{1,1}, h_{1,2}\} \tag{38}$$

The primed superscript emphasizes that the ordering is now based on position in space. Under this ordering of the rect functions, the right-hand endpoints are as follows.

$$j'_{1,1} = \begin{cases} j_{1,1}, & h_{1,1} \le h_{1,2} \\ j_{1,2}, & h_{1,1} > h_{1,2} \end{cases} \tag{39}$$

$$j'_{1,2} = \begin{cases} j_{1,2}, & h_{1,1} \le h_{1,2} \\ j_{1,1}, & h_{1,1} > h_{1,2} \end{cases} \tag{40}$$

Two mutually exclusive possibilities for the positioning of the two rect functions are now considered.

If the two rect functions do not overlap, as would occur if the right-hand endpoint of one rect function is less than or equal to the left-hand endpoint of the other rect function, then $j'_{1,1} \le h'_{1,2}$, and the integral in Eq. (32) is zero.

If the two rect functions overlap, the lower limit of overlap is the larger of the two left-hand endpoints.

$$t_{1,1} = h'_{1,2} \tag{41}$$

Similarly, the upper limit of overlap is the smaller of the two right-hand endpoints.

$$t_{1,2} = \min\{j'_{1,1}, j'_{1,2}\} \tag{42}$$

The limits of overlap ($t_{1,1}$ and $t_{1,2}$) are arranged by position based on the second subscript. The integral in Eq. (32) can now be evaluated

$$P_{\mathrm{Net},1} = \begin{cases} 0, & j'_{1,1} \le h'_{1,2} \\ C_{\mathrm{Net}}\cdot\mathrm{rect}\left(\frac{y}{a_y}\right) \cdot \int_{t_{1,1}}^{t_{1,2}} e^{-\mathrm{sgn}(\xi_1)\cdot\mu(\omega_1-\xi_1)\sqrt{1+\left(\frac{d-l}{\xi_1}\right)^2}} d\omega_1, & \text{otherwise} \end{cases} \tag{43}$$

$$= \begin{cases} 0, & j'_{1,1} \le h'_{1,2} \\ \frac{-\mathrm{sgn}(\xi_1)\cdot\mathrm{rect}\left(\frac{y}{a_y}\right)}{a_x a_y\left(1-e^{-\mu l\sqrt{1+\left(\frac{\xi_1}{d-l}\right)^2}}\right)}\left[e^{-\mathrm{sgn}(\xi_1)\cdot\mu(t_{1,2}-\xi_1)\sqrt{1+\left(\frac{d-l}{\xi_1}\right)^2}} - e^{-\mathrm{sgn}(\xi_1)\cdot\mu(t_{1,1}-\xi_1)\sqrt{1+\left(\frac{d-l}{\xi_1}\right)^2}}\right], & \text{otherwise} \end{cases} \tag{44}$$

which is a closed-form solution for the PSF.

2.C.2. Case 2: ray incidence in ±y direction

In the case of ray incidence in the $\pm y$ direction. Equation (26) can be evaluated with the substitutions: $\xi_1 = 0$ and $\xi_2 \neq 0$. Following the reasoning used in the transition between Eqs. (27) and (32), it can be shown that

$$P_{\text{Net},2} = C_{\text{Net}} \cdot \text{rect}\left(\frac{x}{a_x}\right) \cdot \int_{-\infty}^{\infty} e^{-\text{sgn}(\xi_2)\cdot\mu(\omega_2-\xi_2)\sqrt{1+\left(\frac{d-l}{\xi_2}\right)^2}} \cdot \text{rect}\left(\frac{\omega_2 - \frac{(2d-l)\xi_2}{2(d-l)}}{\frac{\xi_2 l}{d-l}}\right)\text{rect}\left(\frac{\omega_2 - y}{a_y}\right)d\omega_2 \tag{45}$$

Equation (45) is in a form analogous to Eq. (32). This integral can be evaluated with the approach described in Eqs. (33)–(44). This solution is given explicitly in the Data S1.

2.C.3. Case 3: ray incidence in an oblique direction

In the case of ray incidence in an oblique direction, Eq. (26) can be evaluated with the substitutions: $\xi_1 \neq 0$ and $\xi_2 \neq 0$. Rewriting the delta function in Eq. (26)

$$\delta\left(\frac{-\xi_2}{r}\omega_1 + \frac{\xi_1}{r}\omega_2\right) = \frac{r}{|\xi_1|}\delta\left(\omega_2 - \frac{\xi_2}{\xi_1}\omega_1\right), \tag{46}$$

the ω_2-integral can be evaluated.

$$P_{\text{Net},3} = \frac{C_{\text{Net}} r}{|\xi_1|}\int_{-\infty}^{\infty} e^{\frac{-\mu r\left(\omega_1-\xi_1\right)}{\xi_1}\sqrt{1+\left(\frac{d-l}{r}\right)^2}} \cdot \text{rect}\left(\frac{\omega_1 - \frac{(2d-l)\xi_1}{2(d-l)}}{\frac{\xi_1 l}{d-l}}\right)\text{rect}\left(\frac{\omega_1 - x}{a_x}\right) \cdot \text{rect}\left(\frac{\omega_1 - \frac{y\xi_1}{\xi_2}}{\frac{a_y\xi_1}{\xi_2}}\right)d\omega_1 \tag{47}$$

To evaluate Eq. (47) in closed form, it is necessary to determine the interval of overlap for the three rect functions in the integrand. This solution is detailed in the Data S1.

2.D. Coordinate transformation

Figure 1 shows how these equations can be applied to a breast imaging system by transforming the coordinate system. In Fig. 1, point M is a reference point in the plane $z = 0$; that is, the midpoint of the chest wall side of the detector. In our previous work, the focal spot coordinates (x_{FS} and y_{FS}) were measured relative to this point.[18,19] In DM, x_{FS} and y_{FS} should be roughly aligned with point M. The exact positioning in a physical system is sensitive to geometric imprecisions.

The equations for transforming the coordinate system between reference points O and M are as follows:

$$\xi_1 = v_1 - x_{\text{FS}} \tag{48}$$

$$\xi_2 = v_2 - y_{\text{FS}}, \tag{49}$$

where v_1 and v_2 are the coordinates of point B (the entrance point of the ray) relative to point M as shown in Fig. 1.

3. RESULTS

3.A. Modeling parameters

We model a next-generation tomosynthesis (NGT) system that was constructed at the University of Pennsylvania for research use.[20–25] This system, which is discussed in more detail in Part 2, is capable of source motion in two directions (x and y). For the purpose of Part 1, only a 2D DM image is simulated with the acquisition parameters given in Table I.

Similar to previous work[18,19], the focal spot is treated as a point in the plane of the chest wall ($y_{\text{FS}} = 0$), as shown in Fig. 3 by the positioning of the origin (O) along this side of the detector. This differs from the positioning of the origin in Fig. 1, which is more generalized for an arbitrary coordinate for the focal spot.

The NGT system was built with the AXS-2430 detector described previously. The del dimensions are 0.085 mm × 0.085 mm, and the active area is 304.64 mm × 239.36 mm. Each del is labeled with integer indices m_x and m_y. The coordinates of the centroid of an arbitrary del are

$$v_1 = (m_x - 1792 - 1/2)a_x \tag{50}$$

$$v_2 = \left(m_y - 1/2\right)a_y, \tag{51}$$

where m_x varies from 1 to 3584 and m_y varies from 1 to 2816.

Since there is an even number of dels along the chest wall, point M is at the interface between two dels. For the purpose of this simulation, we assume that x_{FS} is aligned with the centroid of the del with an x index of 1793; that is, x_{FS} is displaced from point M by half of a pixel (Table I). This positioning is chosen for convenience so that the centroids of the dels with this x index are aligned with the azimuthal angle $\Gamma = 90°$ (Fig. 3), which is considered in Section 3.B.1.

TABLE I. The acquisition parameters for the simulation of a DM system are summarized.

Acquisition parameter	Value (mm)
Del size (a)	0.085
d	650.0
Se thickness (l)	0.200
x_{FS}	0.5a (0.0425)
y_{FS}	0

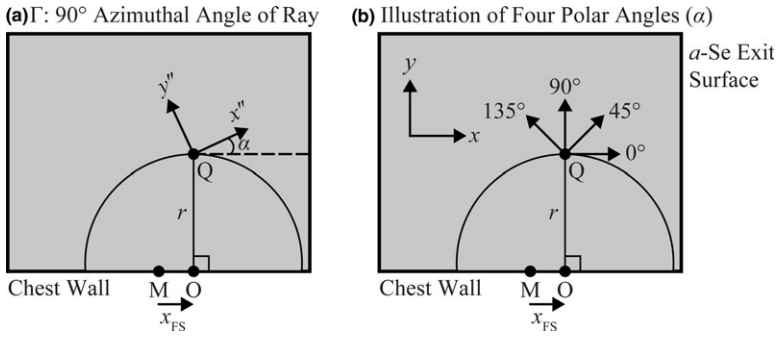

FIG. 3. (a) For simulation of a DM system, the focal spot is treated as a point in the plane of the chest wall, and hence the origin (O) is positioned along this side of the detector. Each point on the circle centered on point O is characterized by the same incidence angle (θ), but by a different azimuthal angle (Γ) for the ray; here, $\Gamma = 90°$. (b) Four examples are given (0°, 45°, 90°, and 135°) to illustrate the polar angle, α.

3.B. Calculation of the net PSF

3.B.1. Ray Incidence along 90° azimuthal angle

In Fig. 4(b), the net PSF is calculated at 20 keV at a position with 15° incidence; that is, at the coordinates $m_x = 1793$ and $m_y = 2049$. This position is aligned with the azimuthal angle $\Gamma = 90°$ (Fig. 3). The origin of the surface plot is matched to this position. Due to the obliquity effect, the surface is not a perfect 2D rect function [Fig. 4(a)], like the PSF for detector sampling (P_{TFT}).

In Fig. 5, cross sections through this surface plot are calculated along various polar angles (α) using the transformation

$$\begin{pmatrix} x \\ y \end{pmatrix} = \begin{pmatrix} \xi_1 \\ \xi_2 \end{pmatrix} + \begin{pmatrix} \cos\alpha & -\sin\alpha \\ \sin\alpha & \cos\alpha \end{pmatrix} \begin{pmatrix} x'' \\ y'' \end{pmatrix}. \tag{52}$$

Figure 3(a) illustrates the rotated coordinates x'' and y''. Also, Fig. 3(b) shows four polar angles ($\alpha = 0°$, 45°, 90°, and 135°), which are used as examples throughout this paper. In Fig. 5, the cross sections align with the centroid of the del; thus, $y'' = 0$.

If the polar angle is perpendicular to the ray incidence direction ($\alpha = 0°$), Fig. 5(a) shows that the cross section is a 2D rect function with 0.085 mm width. This width matches the del size. Conversely, if the polar angle is aligned with the ray incidence direction ($\alpha = 90°$), the width of the net PSF is broadened by 63.2% [Fig. 5(c)]. This broadening is an illustration of the obliquity effect.

Measurements can also be made along 45° or 135° polar angles, which lie along the diagonal of the del. These two cross sections are equivalent, as shown in Fig. 5(b). The width of this cross section is 0.120 mm; that is, $\sqrt{2}$ times larger than 0.085 mm.

3.B.2. Ray incidence along 45° azimuthal angle

In Fig. 3, a circle centered on point O can be used to identify positions with the same incidence angle but different azimuthal angles for the ray incidence direction. The position corresponding to a 45° azimuthal angle (Γ) is illustrated in Fig. 6 (point C). At 15° incidence, the del that is most closely aligned with this azimuthal angle has the coordinates $m_x = 3241$ and $m_y = 1449$. Figure 7 shows cross sections of the net PSF along various polar angles, similar to Fig. 5.

In Section 3.B.1., we found that the net PSF is a rect function along the polar angle perpendicular to the ray incidence

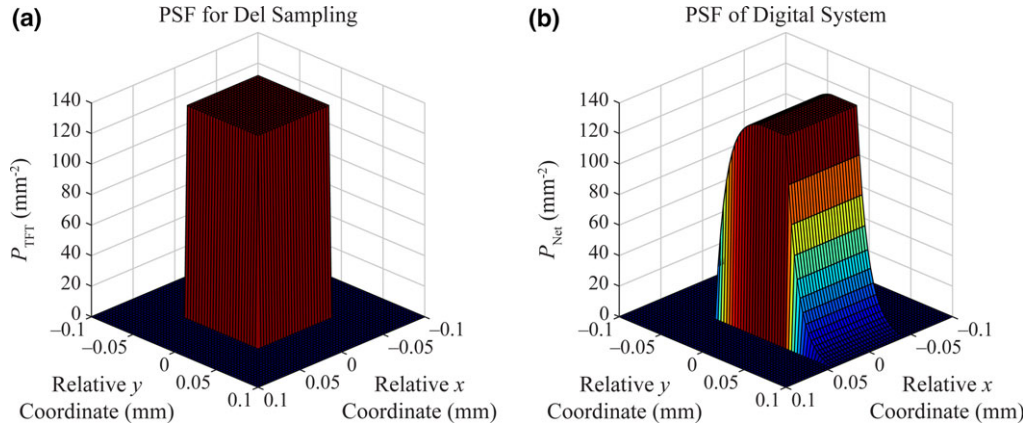

FIG. 4. The PSF is illustrated by surface plots at 20 keV. (a) The PSF for del sampling (P_{TFT}) is a 2D rect function with dimensions 0.085 mm × 0.085 mm. (b) The net PSF is shown at a position with 15° incidence and a 90° azimuthal angle. The cross sections are rect functions along the x direction (perpendicular to the ray incidence direction), but are blurred along the y direction (parallel with the ray incidence direction). [Color figure can be viewed at wileyonlinelibrary.com]

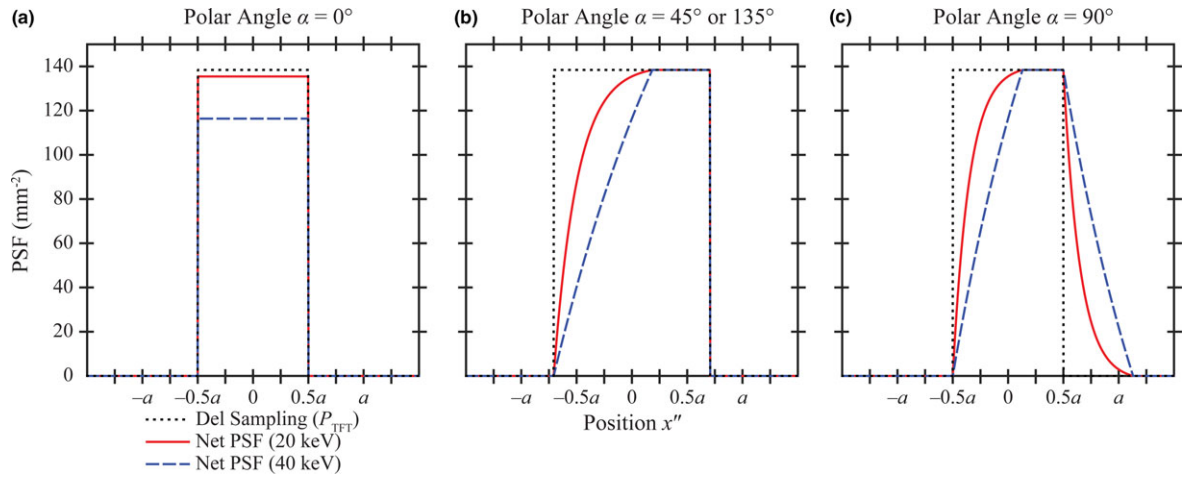

FIG. 5. Cross sections of the net PSF are shown at a position with 15° incidence and a 90° azimuthal angle. (a) The signal is a rect function along the 0° polar angle (perpendicular to the ray incidence direction). (b) Along the 45° or 135° polar angle, the net PSF is blurred over a 0.120 mm length, matching the diagonal of the del. (c) The net PSF is broader than the width of the del (0.085 mm) along a 90° polar angle (the ray incidence direction). [Color figure can be viewed at wileyonlinelibrary.com]

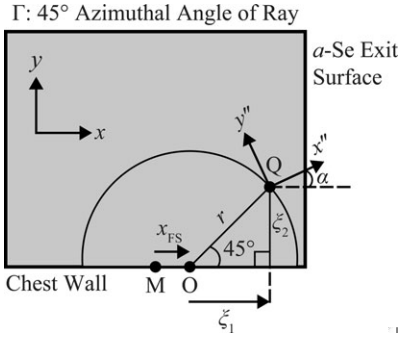

FIG. 6. Varying the position around the circle centered on point O changes the azimuthal angle (Γ); here, Γ = 45°.

direction. This result is no longer the case, as shown in Fig. 7(c) at a 135° polar angle. This finding illustrates the non-stationarity of the net PSF.

Figure 7 indicates that the net PSF is 0.174 mm wide along the ray incidence direction [α = 45°, Fig. 7(b)], and is 0.123 mm wide along a 45° angle relative to the ray incidence direction [α = 0° or 90°, Fig. 7(a)]. These cross sections are broader than the reference rect functions. Also, they do not match the cross sections in Section 3.B.1. at similar polar angles, further demonstrating the non-stationarity of the net PSF.

3.B.3. Effect of x-ray energy

Although low energies are typically used in breast imaging to maximize subject contrast,[26,27] there are applications that require higher energy; for example, contrast-enhanced digital mammography (CE-DM) and contrast-enhanced digital breast tomosynthesis (CE-DBT).[28–37] In CE-DM and CE-DBT, an iodinated contrast agent is used to quantify blood flow to a tumor. X-ray images are acquired at energies above

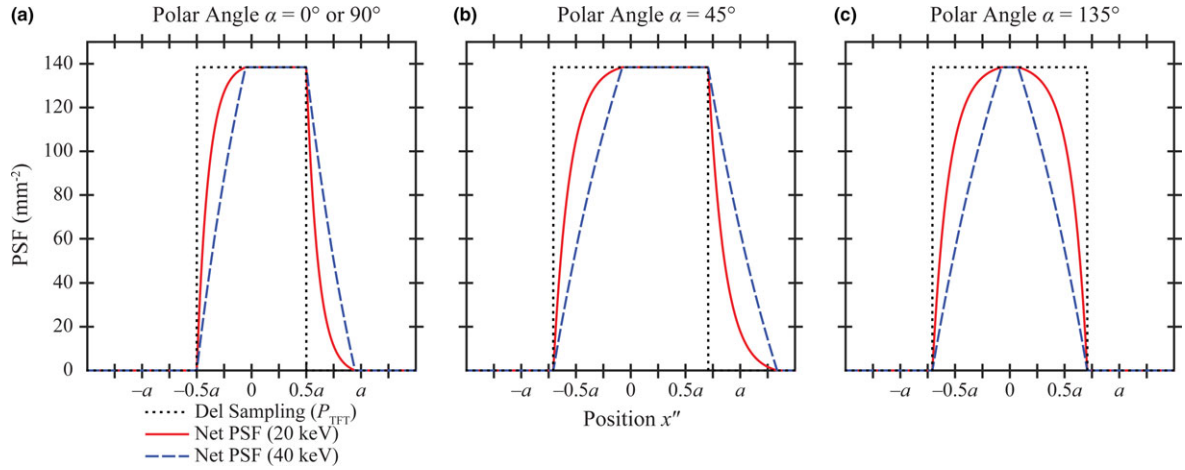

FIG. 7. Cross sections of the net PSF are shown at a position with the same incidence angle as Fig. 5 but a different azimuthal angle (Γ = 45°). The cross sections differ from those in Fig. 5 at similar polar angles; this illustrates the non-stationarity of the net PSF. [Color figure can be viewed at wileyonlinelibrary.com]

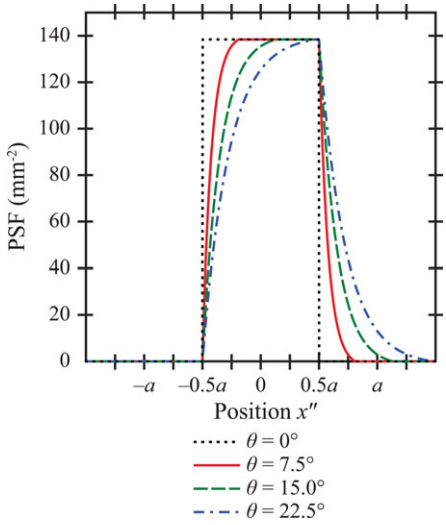

FIG. 8. The net PSF is broadened with increasing obliquity. This figure assumes that the x-ray energy is 20 keV, and that the PSF is measured along the polar angle aligned with the ray incidence direction ($\Gamma = \alpha = 90°$). [Color figure can be viewed at wileyonlinelibrary.com]

and below the K edge of iodine (33.2 keV), and a weighted logarithmic subtraction is used to measure perfusion.

For simulation of CE-DM, the PSF at 40 keV is also shown in Figs. 5 and 7. The PSF deviates more strongly from the reference rect function at 40 keV (μ = 3.02 mm^{-1}) than at 20 keV (μ = 20.2 mm^{-1}). These results illustrate that there is loss of resolution at high energy; this is expected, since the x-ray beam is attenuated less quickly as it passes through the x-ray converter.

3.B.4. Effect of incidence angle

Figure 8 considers four incidence angles ($\theta = 0°$, 7.5°, 15.0°, and 22.5°) to illustrate the effect on the PSF. For the purpose of this figure, the 90° azimuthal angle (Γ) is considered (Fig. 3), and the polar angle (α) is aligned with this direction ($\Gamma = \alpha = 90°$). The x-ray energy is taken to be 20 keV.

Figure 8 demonstrates that increasing the incidence angle gives rise to a broader PSF. This result is expected; the x-ray beam projects onto the exit surface with the length $l \tan\theta$ (line segment $\overline{QC}$ in Fig. 2). Since $\tan\theta$ is an increasing function, the signal is spread across a broader length at higher obliquity.

4. DISCUSSION

In previous work, the PSF of an *a*-Se detector was calculated from first principles, assuming that the incidence angle (θ) was given and that the ray incidence direction was the x direction.[11] By contrast, this paper determines how the incidence angle and the ray incidence direction vary with position based on the divergence of the x-ray beam. This allows the non-stationarity of the PSF to be demonstrated. In addition, this paper includes digitization in the model, unlike previous work.

We analyze cross sections through the PSF at various polar angles. Oblique incidence blurs the shape of the PSF relative to a reference rect function matching the del size. The resolution loss is more pronounced at high energy, since there is less attenuation in the x-ray converter. In addition, the PSF is blurred more strongly at positions with higher obliquity; for example, at positions with increasing distance (y) from the chest wall in DM. Although these results were illustrated with the AXS-2430 detector, similar results are expected in other *a*-Se detectors.

This paper has applications in simulating *a*-Se detectors in virtual clinical trials (VCTs), which can be used to evaluate new imaging technologies at low cost without requiring human subjects.[38] Since P_{Net} was evaluated with a closed-form solution, this paper ensures that the detector signal calculation in a VCT is computationally efficient.

Some of the limitations of this paper and directions for future modeling are now discussed. In future work, the three-dimensional (3D) PSF of a DBT reconstruction should be calculated from the 2D PSFs of the projection images. In some DBT systems, the detector rotates during the scan.[18,19,39–41] Detector rotation can be modeled with a different coordinate transformation for point M (Section 2.D.). In addition, the 3D PSF should model the reconstruction filter.[42]

In this paper, it is assumed that the electron and hole migrate in perfect orthogonal paths to opposite sides of the *a*-Se x-ray converter (Fig. 2). However, future work should consider additional x-ray interactions such as K fluorescence and Compton scatter, which can act as sources of blurring according to the work of Que and Rowlands.[11] Also, the focal spot can introduce blurring[43] that was not modeled in this paper, since the x-ray source was assumed to be point-like.

This paper presumes that the collection efficiency of selenium is 100%. However, future work should model how the collection efficiency is dependent on the depth (z) of the interaction.[8] Also, while this paper presumes that the entire area of each del is sensitive to x-rays, future work should model the fill factor.

5. CONCLUSION

This paper is an extension of previous work modeling the PSF for oblique x-ray incidence in *a*-Se detectors.[11] There are two differences between this paper and previous work. First, this paper develops a model of the non-stationarity of the PSF based on the divergent x-ray beam geometry. Second, while previous work calculated the PSF for the x-ray converter, this paper provides a complementary derivation for a digital system.

In this paper, the solution for the PSF is determined in closed form. This formula is a tool that can be used in future simulations of *a*-Se detectors (e.g., in VCTs). One advantage of a closed-form solution is that computation time is minimized relative to numerical methods.

ACKNOWLEDGMENTS

We thank Denny L. Y. Lee for many useful discussions on the physics of *a*-Se detectors. In addition, we are grateful to David Higginbotham for providing constructive feedback. Support was provided by the following grants: PDF14302589 and IIR13264610 from Susan G. Komen®; 1R01CA154444 and 1R01CA196528 from the National Institute of Health; IRSA 1016451 from the Burroughs Wellcome Fund; and W81XWH-18-1-0082 from the Department of Defense Breast Cancer Research Program. In addition, equipment support was provided by Analogic Inc., Barco NV, and Real Time Tomography (RTT), LLC (Villanova, PA). The content is solely the responsibility of the authors and does not necessarily represent the official views of the funding agencies.

CONFLICTS OF INTEREST

Andrew D. A. Maidment is a scientific advisor to RTT, and his spouse is an employee and shareholder of RTT.

APPENDIX: NOMENCLATURE

Symbol	Meaning
$*_2$	Two-dimensional convolution operator
α	Polar angle (defined in Figs. 3 and 6)
Γ	Azimuthal angle of ray (Fig. 1)
δ	Delta function
θ	Incidence angle (Figs. 1, 2).
μ	Linear attenuation coefficient of selenium
ξ_1, ξ_2	Coordinates of point B relative to point S (Fig. 1)
ω_1, ω_2	Dummy variables in the evaluation of a convolution [Eq. (19)].
a_x, a_y	Del dimensions; if $a_x = a_y$, the dimension is abbreviated a
C_I	Normalization term for P_I [Eq. (18)]
C_Net	Normalization term for P_Net [Eq. (24)]
CE-DBT	Contrast-enhanced digital breast tomosynthesis
CE-DM	Contrast-enhanced digital mammography.
d	Distance between focal spot and origin in Fig. 1
DBT	Digital breast tomosynthesis
Del	Detector element
DM	Digital mammography
FS	Focal spot
$h_{i,k}$	Left-hand endpoint of rect function [i = case number, k = ordering based on Eq. (32)]
$h'_{i,k}$	Left-hand endpoint of rect function [i = case number, k = ordering by positioning of left-hand endpoints]
$j_{i,k}$	Right-hand endpoint of rect function [i = case number, k = ordering based on Eq. (32)]
$j'_{i,k}$	Right-hand endpoint of rect function [i = case number, k = ordering by positioning of left-hand endpoints]
l	Selenium thickness
m_x, m_y	Del indices [Eqs. (50), (51)]
MTF	Modulation transfer function
N	Relative number of x-ray quanta at depth z [Eq. (15)]
P_I	PSF associated with arbitrary ionization point in x-ray converter
P_Net	Net PSF (additional subscripts denote case number)
P_TFT	PSF of TFT array
P_z	Depth-dependent PSF (combined effect of P_I and P_TFT)
PSF	Point spread function
r	Distance between points B and S in Fig. 1
$t_{i,k}$	Lower (k = 1) or upper (k = 2) limit of overlap of rect functions (i = case number)
TFT	Thin-film transistor
v_1, v_2	Coordinate transformation for point B [Eqs. (48), (49)]
v'_1	Position (relative to point Q) measured along x' direction in Fig. 2
v'_2	Position (relative to point Q) measured along y' direction
VCT	Virtual clinical trial
x'	Position along ray incidence direction
x''	Position measured along polar angle α in Figs. 3 and 6
x_FS, y_FS	Focal spot coordinates (Fig. 1)
y'	Position perpendicular to ray incidence direction
y''	Position measured perpendicular to polar angle α in Figs. 3 and 6
Z	Atomic number

[a]Author to whom correspondence should be addressed. Electronic mail: raymond.acciavatti@uphs.upenn.edu; Telephone: +1 215 746 8759; Fax: +1 215 746 8764.

REFERENCES

1. Zhao W, Ristic G, Rowlands JA. X-ray imaging performance of structured cesium iodide scintillators. *Med Phys*. 2004;31:2594–605.
2. Badano A, Kyprianou IS, Jennings RJ. Anisotropic imaging performance in breast tomosynthesis. *Med Phys*. 2007;34:4076–4091.
3. Freed M, Park S, Badano A. A fast, angle-dependent, analytical model of CsI detector response for optimization of 3D x-ray breast imaging systems. *Med Phys*. 2010;37:2593–2605.
4. Freed M, Park S, Badano A. Erratum: a fast, angle-dependent, analytical model of CsI detector response for optimization of 3D x-ray breast imaging systems [Med. Phys. 37, 2593-2605 (2010)]. *Med Phys*. 2011;38:2307.
5. Zhao W, Ji WG, Debrie A, Rowlands JA. Imaging performance of amorphous selenium based flat-panel detectors for digital mammography: characterization of a small area prototype detector. *Med Phys*. 2003;30:254–263.
6. Zhao B, Zhao W. Imaging performance of an amorphous selenium digital mammography detector in a breast tomosynthesis system. *Med Phys*. 2008;35:1978–1987.
7. Hajdok G, Battista JJ, Cunningham IA. Fundamental x-ray interaction limits in diagnostic imaging detectors: spatial resolution. *Med Phys*. 2008;35:3180–3193.
8. Badano A, Freed M, Fang Y. Oblique incidence effects in direct x-ray detectors: a first-order approximation using a physics-based analytical model. *Med Phys*. 2011;38:2095–2098.
9. Hubbell JH, Seltzer SM. X-Ray Mass Attenuation Coefficients [cited 2018 March 12]. Available from: https://www.nist.gov/pml/x-ray-mass-attenuation-coefficients.
10. Hajdok G, Cunningham IA. Penalty on the detective quantum efficiency from off-axis incident x rays. In: Yaffe MJ, Flynn MJ, eds. *Physics of Medical Imaging*. San Diego, CA: SPIE; 2004:109–118.

11. Que W, Rowlands JA. X-ray imaging using amorphous selenium: inherent spatial resolution. *Med Phys*. 1995;22:365–374.
12. Acciavatti RJ, Maidment ADA. An analytical model of NPS and DQE comparing photon counting and energy integrating detectors. In: Samei E, Pelc NJ, eds. *Physics of Medical Imaging*. San Diego, CA: SPIE; 2010:76220I-1–76220I-12.
13. Acciavatti RJ, Maidment ADA. A comparative analysis of OTF, NPS, and DQE in energy integrating and photon counting digital x-ray detectors. *Med Phys*. 2010;37:6480–6495.
14. Acciavatti R, Maidment A. TU-FG-209-01: a model of noise anisotropy in amorphous selenium digital detectors. *Med Phys*. 2016;43:3760.
15. Swank RK. Calculation of modulation transfer functions of x-ray fluorescent screens. *Appl Opt*. 1973;12:1865–1870.
16. Barrett HH, Myers KJ. Chapter 2: dirac delta and other generalized functions. In: Saleh BEA, ed. *Foundations of Image Science*. New York, NY: John Wiley & Sons; 2004:63–94.
17. Lea SM. Chapter 6: generalized functions in physics. In: *Mathematics for Physicists*. Belmont, CA: Brooks/Cole - Thomson Learning; 2004:287–322.
18. Acciavatti RJ, Maidment ADA. Observation of super-resolution in digital breast tomosynthesis. *Med Phys*. 2012;39:7518–7539.
19. Acciavatti RJ, Maidment ADA. Oblique reconstructions in tomosynthesis: II. Super-resolution. *Med Phys*. 2013;40:111912-1–111912-19.
20. Maidment AD, Acciavatti R, Vent T, et al. *SSC14-03: Construction of a Prototype Digital Breast Tomosynthesis System with Superior Spatial Resolution*. Radiological Society of North America (RSNA) Conference, Chicago, IL; 2016.
21. Ferris WS, Vent TL, Maidment TD, Acciavatti RJ, Wurtele DE, Maidment ADA. Geometric Calibration for a Next-Generation Digital Breast Tomosynthesis System. In: Flohr TG, Lo JY, Schmidt TG, eds. *Physics of Medical Imaging*. Orlando, FL: SPIE; 2017:101324C-1–101324C-10.
22. Maidment TD, Vent TL, Ferris WS, Wurtele DE, Acciavatti RJ, Maidment ADA. Comparing the Imaging Performance of Computed Super Resolution and Magnification Tomosynthesis. In: Flohr TG, Lo JY, Schmidt TG, eds. *Physics of Medical Imaging*. Orlando, FL: SPIE; 2017:1013222-1–1013222-10.
23. Acciavatti RJ, Rodríguez-Ruiz A, Vent TL, et al. Analysis of Volume Overestimation Artifacts in the Breast Outline Segmentation in Tomosynthesis. In: Lo JY, Schmidt TG, Chen G-H, eds. *Physics of Medical Imaging*. Houston, TX: SPIE; 2018:1057359-1–1057359-8.
24. Choi CJ, Vent TL, Acciavatti RJ, Maidment ADA. Geometric Calibration for a Next-Generation Digital Breast Tomosynthesis System Using Virtual Line Segments. In: Lo JY, Schmidt TG, Chen G-H, eds. *Physics of Medical Imaging*. Houston, TX: SPIE; 2018:105730D-1–105730D-10.
25. Eben JE, Vent TL, Choi CJ, et al. Development of a Next Generation Tomosynthesis System. In: Lo JY, Schmidt TG, Chen G-H, eds. *Physics of Medical Imaging*. Houston, TX: SPIE; 2018:105735Q-1–105735Q-8.
26. Johns PC, Yaffe MJ. X-ray characterization of normal and neoplastic breast tissues. *Phys Med Biol*. 1987;32:675–695.
27. Yaffe MJ. Chapter 5: digital mammography. In: Beutel J, Kundel HL, Metter RLV, eds. *Handbook of Medical Imaging Volume 1 Physics and Psychophysics*. Bellingham, WA: SPIE - The International Society for Optical Engineering; 2000. 329–372.
28. Carton A-K, Li J, Chen SC, Conant EF, Maidment ADA. Optimization of contrast-enhanced digital breast tomosynthesis. In: Astley SM, Brady M, Rose C, Zwiggelaar R, eds. *Digital Mamography.* Vol. 4046. Lecture Notes in Computer Science. Berlin: Springer; 2006:183–189.
29. Chen SC, Carton AK, Albert M, Conant EF, Schnall MD, Maidment ADA. Initial clinical experience with contrast-enhanced digital breast tomosynthesis. *Acad Radiol*. 2007;14:229–238.
30. Fredenberg E, Hemmendorff M, Cederstrom B, Aslund M, Danielsson M. Contrast-enhanced spectral mammography with a photon-counting detector. *Med Phys*. 2010;37:2017–2029.
31. Carton AK, Gavenonis SC, Currivan JA, Conant EF, Schnall MD, Maidment ADA. Dual-energy contrast-enhanced digital breast tomosynthesis - a feasibility study. *Br J Radiol*. 2010;83:344–350.
32. Carton A-K, Ullberg C, Lindman K, Acciavatti R, Francke T, Maidment ADA. Optimization of a dual-energy contrast-enhanced technique for a photon-counting digital breast tomosynthesis system: I. A theoretical model. *Med Phys*. 2010;37:5896–5907.
33. Carton A-K, Ullberg C, Maidment ADA. Optimization of a dual-energy contrast-enhanced technique for a photon-counting digital breast tomosynthesis system: II. An experimental validation. *Med Phys*. 2010;37:5908–5913.
34. Lau KC, Acciavatti RJ, Maidment ADA. Estimating breast thickness for dual-energy subtraction in contrast-enhanced digital mammography: a theoretical model. In: Tingberg A, Lång K, Timberg P, eds. *Breast Imaging*. Vol. 9699. Lecture Notes in Computer Science. Berlin: Springer; 2016:593–600.
35. Lau KC, Kwon YJ, Aziz MK, Acciavatti RJ, Maidment ADA. Estimating breast thickness for dual-energy subtraction in contrast-enhanced digital mammography using calibration phantoms. In: Kontos D, Flohr TG, Lo JY, eds. *Physics of Medical Imaging*. San Diego, CA: SPIE; 2016:978307-1–978307-12.
36. Puong S, Patoureaux F, Iordache R, Bouchevreau X, Muller S. Dual-energy contrast enhanced digital breast tomosynthesis: concept, method and evaluation on phantoms. In: Hsieh J, Flynn MJ, eds. *Physics of Medical Imaging*. San Diego, CA: SPIE; 2007:65100U-1–65100U-12.
37. Puong S, Bouchevreau X, Duchateau N, Iordache R, Muller S. Optimization of beam parameters and iodine quantification in Dual-Energy Contrast Enhanced Digital Breast Tomosynthesis. In: Hsieh J, Samei E, eds. *Physics of Medical Imaging*. San Diego, CA: SPIE; 2008:69130Z-1–69130Z-11.
38. Maidment ADA. Virtual clinical trials for the assessment of novel breast screening modalities. In: Fujita H, Hara T, Muramatsu C, eds. *Breast Imaging*. Lecture Notes in Computer Science. Vol. 8539. Berlin: Springer;2014:1–8.
39. Sechopoulos I. A review of breast tomosynthesis. Part I. The image acquisition process. *Med Phys*. 2013;40:014301-1–014301-12.
40. Acciavatti RJ, Maidment ADA. Investigating the Potential for Super-Resolution in Digital Breast Tomosynthesis. In: Pelc NJ, Samei E, Nishikawa RM, eds. *Physics of Medical Imaging*. Lake Buena Vista, FL: SPIE; 2011:79615K-1–79615K-12.
41. Acciavatti RJ, Maidment ADA. Optimization of Continuous Tube Motion and Step-and-Shoot Motion in Digital Breast Tomosynthesis Systems with Patient Motion. In: Pelc NJ, Nishikawa RM, Whiting BR, eds. *Physics of Medical Imaging*. San Diego, CA: SPIE; 2012:831306-1–831306-12.
42. Zhao B, Zhao W. Three-dimensional linear system analysis for breast tomosynthesis. *Med Phys*. 2008;35:5219–5232.
43. Johns HE, Cunningham JR. *The Physics of Radiology.* Chapter 16: Diagnostic Radiology, 4th ed. Springfield, IL: Charles C Thomas; 1983:557–669.

SUPPORTING INFORMATION

Additional supporting information may be found online in the Supporting Information section at the end of the article.

Data S1. Closed-form solutions for the net PSF in Case 2 (Section 2.C.2.) and Case 3 (Section 2.C.3.) are derived.

Nonstationary model of oblique x-ray incidence in amorphous selenium detectors: II. Transfer functions

Raymond J. Acciavatti[a)] and Andrew D. A. Maidment
Department of Radiology, Perelman School of Medicine at the University of Pennsylvania, Philadelphia, PA 19104-4206, USA

(Received 23 April 2018; revised 2 October 2018; accepted for publication 16 November 2018; published 11 January 2019)

Purpose: One limitation of experimental techniques for quantifying resolution and noise in detectors is that the measurement is made in a region-of-interest (ROI). With theoretical modeling, these properties can be measured at a point, allowing for quantification of spatial anisotropy. This paper calculates nonstationary transfer functions for amorphous selenium (*a*-Se) detectors in breast imaging. We use this model to demonstrate the performance advantage of a "next-generation" tomosynthesis (NGT) system, which is capable of x-ray source motion with more degrees of freedom than a clinical tomosynthesis system.

Methods: Using Swank's formulation, the optical transfer function (OTF) and presampled noise power spectra (NPS) are determined based on the point spread function derived in Part 1. The modulation transfer function (MTF) is found from the normalized modulus of the OTF. To take into account the presence of digitization, the presampled NPS is convolved with a two-dimensional comb function, for which the period along each direction is the reciprocal of the detector element size. The detective quantum efficiency (DQE) is then determined from combined knowledge of the OTF and NPS.

Results: First, the model is used to demonstrate the loss of image quality due to oblique x-ray incidence. The MTF is calculated along various polar angles, corresponding to different orientations of the input frequency. The MTF is independent of the incidence angle if the polar angle is perpendicular to the ray incidence direction. However, along other polar angles, oblique incidence results in MTF degradation at high frequencies. The MTF degradation is most substantial along the ray incidence direction. Unlike the MTF, the normalized NPS (NNPS) is independent of the incidence angle. To measure the relative signal-to-noise, the DQE is also calculated. Oblique incidence yields high-frequency DQE degradation, which is more pronounced than the MTF degradation. This arises because the DQE is proportionate with the square of the MTF. Ultimately, this model is used to evaluate how the image quality varies over the detector area. For various projection images, we calculate the variation in the incidence angle over this area. With the NGT system, the source can be positioned in such a way that this variation is minimized, and hence the DQE exhibits less anisotropy. To achieve this improvement in the image quality, the source needs to have a component of motion in the posteroanterior (PA) direction, which is perpendicular to the conventional direction of source motion in tomosynthesis.

Conclusions: In *a*-Se detectors, the DQE at high frequencies is degraded due to oblique incidence. The DQE degradation is more pronounced than the MTF degradation. This model is used to quantify the spatial variation in DQE over the detector area. The use of PA source motion is a strategy for minimizing this variation and thus improving the image quality. [https://doi.org/10.1002/mp.13312]

Key words: amorphous selenium, detective quantum efficiency (DQE), digital x-ray detectors, modulation transfer function (MTF), obliquity effect

1. INTRODUCTION

Oblique x-ray incidence is a source of resolution loss in amorphous selenium (*a*-Se) detectors. The loss of resolution can be quantified with the modulation transfer function (MTF). Que and Rowlands used theoretical modeling to derive a closed-form solution for the MTF in *a*-Se detectors.[1] This model was later validated by Hajdok and Cunningham with Monte Carlo simulations.[2] These simulations show that the MTF degradation is pronounced at high energy, since the incident ray is less attenuated as it passes through the x-ray converter.

X-ray experiments in previous works have validated the MTF degradation due to oblique incidence. The MTF was calculated with a digital breast tomosynthesis (DBT) system using a tungsten edge.[3,4] Previous works have also shown that increasing the thickness of selenium results in more substantial MTF degradation.[3,5] This arises because the incident ray traverses a broader path length through the x-ray converter, yielding more blurring.

The purpose of this paper is to develop a nonstationary model of the MTF in *a*-Se detectors. This model is used to quantify the spatial variation in the image quality across the detector area. One limitation of experimental methods[6–9] used to measure MTF is that spatial anisotropy cannot be quantified, since it is presumed that the MTF is stationary within a region-of-interest (ROI). We calculate the MTF using the model of the point spread function (PSF) developed in Part 1.[10] This model includes the effects of the divergent-beam geometry and digitization.

Unlike the MTF, the NPS is effectively independent of the incidence angle in *a*-Se detectors. This result was demonstrated by Hajdok and Cunningham with Monte Carlo simulations.[2] Hu et al. reached a similar conclusion in an experimental study.[3] Based on the MTF and NPS results, it has been shown that the detective quantum efficiency (DQE) is degraded by oblique incidence. The DQE is proportionate with the square of the MTF, and hence, the DQE degradation is more pronounced than the MTF degradation.[2]

Ultimately, this model is used to demonstrate the performance advantage of a prototype "next-generation" tomosynthesis (NGT) system, which we are developing at the University of Pennsylvania.[11–16] This system is capable of x-ray source motion with more degrees of freedom than a clinical DBT system. Our previous work showed that the NGT system offers an improvement in image quality using the Defrise phantom.[13,16] This paper analyzes how the DQE varies over the detector area in different projection views supported by the NGT system. We demonstrate that the source can be positioned in such a way that there is less pronounced variation in DQE, and hence, the image quality is more isotropic.

2. MATERIALS AND METHODS

2.A. Modulation transfer function (MTF)

2.A.1 X-ray converter

To determine the MTF of the x-ray converter, it is first necessary to calculate the two-dimensional (2D) Fourier transform of P_{I}; that is, the PSF associated with the interaction point at the height z above the exit surface of the x-ray converter

$$\mathcal{F}_2P_{\mathrm{I}} = \int_{-\infty}^{\infty}\int_{-\infty}^{\infty} P_{\mathrm{I}} \cdot e^{-2\pi i\left(f_x x + f_y y\right)} dxdy \tag{1}$$

where $i = \sqrt{-1}$ and where f_x and f_y measure the frequency along the x and y directions, respectively. This integral can be transformed from the (x, y) coordinate system into the (v'_1, v'_2) coordinate system using the equations of Part 1.[10]

$$\mathcal{F}_2P_{\mathrm{I}} = \int_{-\infty}^{\infty}\int_{-\infty}^{\infty} \delta[v'_1 - (l-z)\tan\theta]\delta(v'_2) \cdot e^{-2\pi i\left[f_x\left(\xi_1 + v'_1\cos\Gamma - v'_2\sin\Gamma\right) + f_y\left(\xi_2 + v'_1\sin\Gamma + v'_2\cos\Gamma\right)\right]} dv'_1 dv'_2 \tag{2}$$

$$\mathcal{F}_2P_{\mathrm{I}} = \int_{-\infty}^{\infty}\int_{-\infty}^{\infty} \delta\left[v'_1 - \frac{r(l-z)}{d-l}\right]\delta(v'_2) \cdot e^{-2\pi i\left[f_x\left(\xi_1 + v'_1\frac{\xi_1}{r} - v'_2\frac{\xi_2}{r}\right) + f_y\left(\xi_2 + v'_1\frac{\xi_2}{r} + v'_2\frac{\xi_1}{r}\right)\right]} dv'_1 dv'_2 \tag{3}$$

$$= e^{-2\pi i\left(\frac{\xi_1 f_x + \xi_2 f_y}{d-l}\right)(d-z)} \tag{4}$$

These equations presume that $r > 0$, as was the case in Part 1.[10] Following Swank,[17] the optical transfer function (OTF) of the x-ray converter is determined by integrating $\mathcal{F}_2P_{\mathrm{I}}$ over the thickness (l) of selenium, and weighting the integrand by the relative number of x-ray quanta at each depth z.

$$G_{\mathrm{Se}} = \int_0^l N \cdot \mathcal{F}_2P_{\mathrm{I}} \cdot dz \tag{5}$$

$$= C_{\mathrm{I}} e^{\frac{-2\pi i d\left(\xi_1 f_x + \xi_2 f_y\right)}{d-l}} \int_0^l e^{-\mu(l-z)\sqrt{1+\left(\frac{r}{d-l}\right)^2} + \frac{2\pi i\left(\xi_1 f_x + \xi_2 f_y\right)}{d-l} z} dz \tag{6}$$

$$= \frac{e^{-2\pi i\left(\xi_1 f_x + \xi_2 f_y\right)}}{1 - e^{-\mu l\sqrt{1+\left(\frac{r}{d-l}\right)^2}}} \left[\frac{1 - e^{-\mu l\sqrt{1+\left(\frac{r}{d-l}\right)^2} + \frac{-2\pi i\left(\xi_1 f_x + \xi_2 f_y\right) l}{d-l}}}{1 + \frac{2\pi i\left(\xi_1 f_x + \xi_2 f_y\right)}{\mu r\sqrt{1+\left(\frac{d-l}{r}\right)^2}}}\right] \tag{7}$$

The MTF of the x-ray converter can be determined from the normalized modulus of the OTF

$$\mathrm{MTF}_{\mathrm{Se}} = \frac{|G_{\mathrm{Se}}|}{G_{\mathrm{Se}}|_{\mathbf{f}=\mathbf{0}}} \tag{8}$$

where $\mathbf{f}$ denotes the doublet with components f_x and f_y.

2.A.2. Digital system

Analogous to Eq. (5), the net OTF of the digital system can be calculated by replacing P_{I} with P_z.

$$G_{\mathrm{Net}} = \int_0^l N \cdot \mathcal{F}_2P_z \cdot dz \tag{9}$$

Since P_z is a convolution of two functions [Eq. (11), Acciavatti and Maidment[10]], the 2D Fourier transform can be evaluated using the convolution theorem

$$\mathcal{F}_2P_z = \mathcal{F}_2P_{\mathrm{I}} \cdot \mathcal{F}_2P_{\mathrm{TFT}} \tag{10}$$

where

$$\mathcal{F}_2P_{\mathrm{TFT}} = \mathrm{sinc}(a_x f_x) \cdot \mathrm{sinc}(a_y f_y) \tag{11}$$

and where

$$\mathrm{sinc}(v) \equiv \frac{\sin(\pi v)}{\pi v} \tag{12}$$

Hence,

$$G_{\text{Net}} = \mathcal{F}_2 P_{\text{TFT}} \cdot \int_0^l N \cdot \mathcal{F}_2 P_{\text{I}} \cdot dz \tag{13}$$

$$= \mathcal{F}_2 P_{\text{TFT}} \cdot G_{\text{Se}} \tag{14}$$

The MTF of the digital system can be determined with a normalization formula similar to the one described by Eq. (8) for the x-ray converter. In the special case of normal incidence ($r = 0$), G_{Se} is unity since there is no loss of image quality; hence, G_{Net} is given by 2D Fourier transform of P_{TFT} [Eq. (11)].

2.B. Normalized noise power spectra (NNPS)

2.B.1. X-ray converter

The NPS of the x-ray converter can be calculated from P_{I}, the PSF associated with each interaction point in selenium. Since the Fourier transform of P_{I} has a modulus of unity, the NPS is white (i.e., frequency-independent) at all incidence angles.

$$W_{\text{Se}} = \int_0^l N \cdot |\mathcal{F}_2 P_{\text{I}}|^2 \cdot dz \tag{15}$$

$$= \int_0^l N \cdot 1^2 \cdot dz \tag{16}$$

$$= 1 \tag{17}$$

The notation "W" comes from the alternate NPS term "Wiener spectra."[18] Eqs. (15)–(17) represent the normalized NPS (NNPS), as there is no weighting based on the x-ray fluence.[19,20]

2.B.2. Digital system

In the digital system, the presampled NPS is calculated with the same approach, but P_{I} is replaced with P_z to take into account the presence of the TFT array.

$$W_{\text{Pre}} = \int_0^l N \cdot |\mathcal{F}_2 P_z|^2 \cdot dz \tag{18}$$

$$= \int_0^l N \cdot |\mathcal{F}_2 P_{\text{I}}|^2 \cdot |\mathcal{F}_2 P_{\text{TFT}}|^2 \cdot dz \tag{19}$$

$$= |\mathcal{F}_2 P_{\text{TFT}}|^2 \cdot \int_0^l N \cdot 1^2 \cdot dz \tag{20}$$

$$= |\mathcal{F}_2 P_{\text{TFT}}|^2 \tag{21}$$

Previous work demonstrated that the digital NPS is found by convolving W_{Pre} with a 2D comb function. The period of the comb function is a_x^{-1} in the x direction and a_y^{-1} in the y direction, where a_x and a_y are the del dimensions in the two respective directions.

$$W_{\text{Net}}(f_x, f_y) = \sum_{k_y=-\infty}^{\infty} \sum_{k_x=-\infty}^{\infty} W_{\text{Pre}} *_2 \delta\left(f_x - \frac{k_x}{a_x}\right) \delta\left(f_y - \frac{k_y}{a_y}\right) \tag{22}$$

$$= \sum_{k_y=-\infty}^{\infty} \sum_{k_x=-\infty}^{\infty} \operatorname{sinc}^2(a_x f_x) \cdot \operatorname{sinc}^2(a_y f_y) *_2 \delta\left(f_x - \frac{k_x}{a_x}\right) \delta\left(f_y - \frac{k_y}{a_y}\right) \tag{23}$$

$$= \sum_{k_x=-\infty}^{\infty} \operatorname{sinc}^2\left[a_x\left(f_x - \frac{k_x}{a_x}\right)\right] \cdot \sum_{k_y=-\infty}^{\infty} \operatorname{sinc}^2\left[a_y\left(f_y - \frac{k_y}{a_y}\right)\right] \tag{24}$$

$$= 1 \tag{25}$$

The transition from Eq. (24) to Eq. (25) follows from an identity described in our previous work.[20] Eq. (25) indicates that the NNPS of the digital system is white, just as the NNPS of the x-ray converter is white.

2.C. Detective quantum efficiency (DQE)

Following Nishikawa and Yaffe,[21] the DQE is calculated from the product of four terms

$$\text{DQE} = A_{\text{Q}} A_{\text{S}} R_{\text{C}} R_{\text{N}}, \tag{26}$$

where A_{Q} is the quantum detection efficiency (QDE).

$$A_{\text{Q}} = \left(1 - e^{-\mu l \sec\theta}\right) \cos\theta \tag{27}$$

$$= \frac{1 - e^{-\mu l \sqrt{1 + \left(\frac{r}{d-l}\right)^2}}}{\sqrt{1 + \left(\frac{r}{d-l}\right)^2}} \tag{28}$$

In Eq. (27), the quantity in parentheses is the percentage of x rays that are absorbed based on the attenuation coefficient (μ) of selenium. The term $\cos\theta$ models the degradation in x-ray fluence with increasing obliquity, which approaches zero at shearing incidence ($\theta = 90°$).

Second, A_{S} is the Swank factor[17,22]; it measures the relative signal-to-noise at zero frequency.

$$A_{\text{S}} = \frac{G^2|_{\mathbf{f}=\mathbf{0}}}{W|_{\mathbf{f}=\mathbf{0}}} \tag{29}$$

Since this formula applies to both the x-ray converter and the digital system, the subscripts "Se" and "Net" are being removed from the terms G and W.

Third, the term R_{C} is the Lubberts fraction; it quantifies the frequency dependence of the DQE.

$$R_{\text{C}} = \frac{1}{A_{\text{S}}} \cdot \frac{|G|^2}{W} \tag{30}$$

Finally, the term R_N is a relative measure of quantum noise power to total noise power. For the purpose of this paper, it is assumed that R_N is unity at all frequencies.

3. RESULTS

3.A. Calculation of MTF

3.A.1. Low x-ray energy

We model the NGT system[11–16] with the same acquisition parameters as those described in Part 1[10] for a digital mammography (DM) image (analogous to the central projection in DBT). To calculate the MTF along any polar angle (α), a coordinate transformation can be introduced

$$f_x = f_r \cos\alpha \tag{31}$$

$$f_y = f_r \sin\alpha, \tag{32}$$

where f_r denotes radial frequency. Figures 1(a) and 2(a) illustrate how the MTF at 15° incidence varies with radial frequency at an energy of 20 keV. The two plots differ in terms of the azimuthal angle (Γ) of the ray; that is, 90° in Fig. 1(a) and 45° in Fig. 2(a). The detector positions corresponding to these angles were illustrated in Part 1 (Acciavatti and Maidment,[10] Figs. 3 and 6).

In a non-pixelated system, the MTF is perfect (1.0 at all frequencies) if the polar angle is perpendicular to the ray incidence direction; that is, 0° in Fig. 1(a) and 135° in Fig. 2(a). However, there is loss of resolution along the other polar angles, as one would expect.

It is also shown that the digital system has lower MTF than the x-ray converter. At a 0° or 90° polar angle, MTF_{Net} is zero at the frequency a^{-1} (11.8 mm^{-1}). By contrast, along 45° or 135° polar angles, the zero increases by a factor of $\sqrt{2}$, giving 16.6 mm^{-1}. These zeros are not dependent on the parameter Γ, which controls the direction of ray incidence.

3.A.2. High x-ray energy

At high energy, the x-ray beam is attenuated less quickly as it passes through the x-ray converter. As a result, the MTF degradation due to the obliquity effect is more pronounced [Figs. 1(b) and 2(b)]. This finding is consistent with previous work.[2]

The plots at high energy show Gibbs ringing,[23] unlike the plots at low energy. This result is concordant with the work of Que and Rowlands,[1] who demonstrated that the frequency span of the MTF can be determined from the equation

$$f_g = \max\left\{(l\tan\theta)^{-1}, \mu\csc\theta\right\} \tag{33}$$

At 20 keV, f_g is so large (78.2 mm^{-1}) that it exceeds the frequency range of the plot. However, at 40 keV, f_g is 18.7 mm^{-1}. This frequency is a perfect match to the local minimum if the polar angle (α) is aligned with the ray incidence direction; that is, 90° in Fig. 1(b) and 45° in Fig. 2(b). If the polar angle is at a 45° angle relative to the ray incidence direction, this frequency is scaled up by a factor of $\sqrt{2}$, giving 26.4 mm^{-1}.

3.A.3. Dependency on incidence angle

Figure 3 illustrates how the MTF is degraded as a function of the incidence angle, assuming that f_r = 5.0 mm^{-1} and Γ = 90°. The incidence angle is varied by increasing the distance from the chest wall along the +y direction. This plot presumes that the x-ray energy is 20 keV, as is the case in all subsequent plots unless explicitly stated. The MTFs are shown for both a digital and a non-pixelated system. The MTFs of these two systems differ by a constant factor, which is given by the MTF of the detector sampling function [Eq. (11)].

If frequency is perpendicular to the ray incidence direction (α = 0°), the MTF is independent of the incidence angle. However, there is MTF degradation along the other polar angles. The most pronounced resolution loss is seen along the 90° polar angle (parallel to the ray incidence direction).

To generalize Fig. 3 to more than one frequency, Fig. 4 shows the MTF at 20 keV as a function of both incidence angle and frequency. This figure presumes that $\Gamma = \alpha$ = 90°, so the polar angle is aligned with the ray incidence direction. Frequencies up to the alias frequency $0.5a^{-1}$ (5.88 mm^{-1})

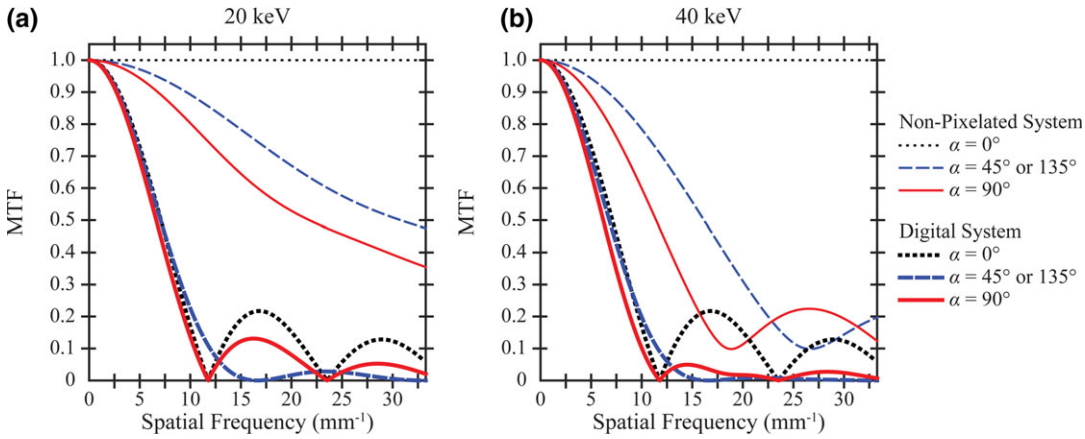

FIG. 1. The MTF at 15° incidence is plotted as a function of frequency. The ray incidence direction is at a 90° azimuthal angle (Γ), so the most MTF degradation is seen along this direction. The MTF degradation is more pronounced at high energy. [Color figure can be viewed at wileyonlinelibrary.com]

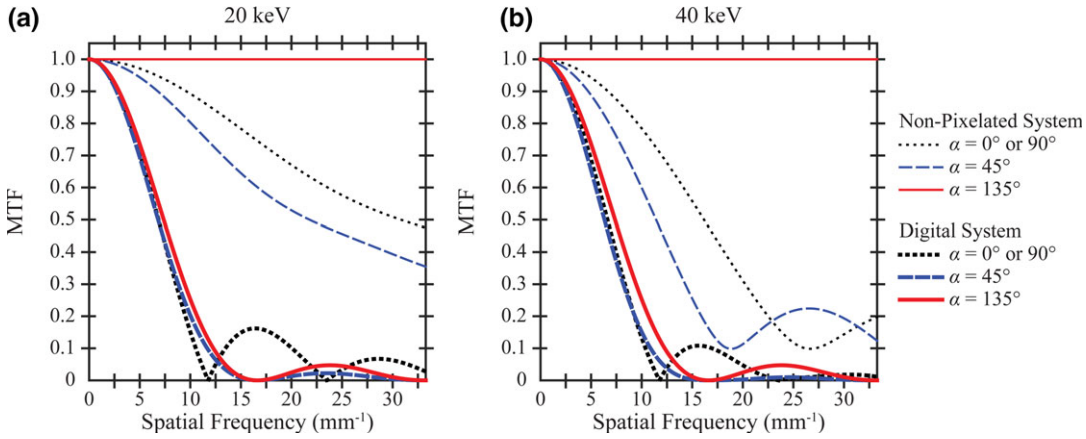

FIG. 2. The MTF is calculated under assumptions similar to Fig. 1, but the azimuthal angle (Γ) is 45°. Along the perpendicular direction (α = 135°), there is no MTF degradation due to oblique incidence. [Color figure can be viewed at wileyonlinelibrary.com]

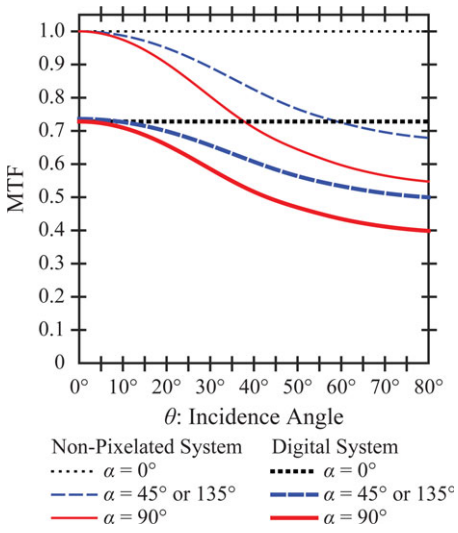

FIG. 3. For a 20 keV x-ray beam, the MTF at 5.0 mm^{-1} is plotted as a function of the incidence angle, assuming Γ = 90°. The MTF is unaffected by oblique incidence if frequency is measured along the polar angle perpendicular to the ray incidence direction (α = 0°). However, the MTF is degraded by oblique incidence along the other polar angles shown. [Color figure can be viewed at wileyonlinelibrary.com]

are considered. At low obliquity ($\theta \sim 0°$), the MTF of a non-pixelated system [Fig. 4(a)] is effectively constant, yet the MTF of a digital system [Fig. 4(b)] is degraded at high frequencies. As the incidence angle increases, both the non-pixelated and digital systems show MTF degradation at high frequencies.

3.B. Calculation of DQE

3.B.1. Effect of x-ray energy and polar angle

Under assumptions similar to Figs. 1 and 2, the DQE is plotted as a function of frequency in Figs. 5 and 6. Following the approach used in previous work, the DQE is plotted up to the alias frequency.[20,24] Along the 0° and 90° polar angles, the alias frequency is $0.5a^{-1}$ (5.88 mm^{-1}). By contrast, along the 45° and 135° polar angles, the alias frequency increases by a factor of $\sqrt{2}$, giving 8.32 mm^{-1}.

Using Eq. (29) and the equations for OTF and NPS, it can be shown that the Swank factor (A_S) is unity for both the non-pixelated and digital systems. Therefore, the DQE at zero-frequency is equivalent to A_Q (the QDE); namely, 0.951 at 20 keV and 0.449 at 40 keV. There is lower DQE at high energy, since fewer x rays are absorbed by the detector. These results hold for both the non-pixelated and digital systems.

The DQE degradation is most pronounced along the polar angle aligned with the ray incidence direction; that is, 90° in Fig. 5 and 45° in Fig. 6. These are consistent with the polar angles corresponding to the most pronounced MTF degradation.

In a non-pixelated system, the DQE is not degraded along the polar angle perpendicular to the ray incidence direction. This arises because the MTF and NNPS of the x-ray converter are independent of frequency along this direction. By contrast, in the digital system, the DQE is frequency-dependent along all polar angles.

It should be noted that digitization introduces electronic noise not modeled in this paper. Based on our previous work,[20] including this noise source in the model would rescale the curves in Figs. 5 and 6 by a constant factor, reducing the DQE.

3.B.2. Obliquity effect

Figure 7 shows the dependency of DQE on incidence angle (under similar assumptions as Fig. 3). Oblique incidence results in DQE degradation along all polar angles. This includes the polar angle perpendicular to the ray incidence direction (α = 0°), even though there is no MTF degradation along this direction. To understand why there is DQE degradation along this direction, it is important to recall the QDE formula [Eq. (27)]. The formula consists of two terms. The term $\left(1 - e^{-\mu l \sec\theta}\right)$ is an increasing function of the incidence

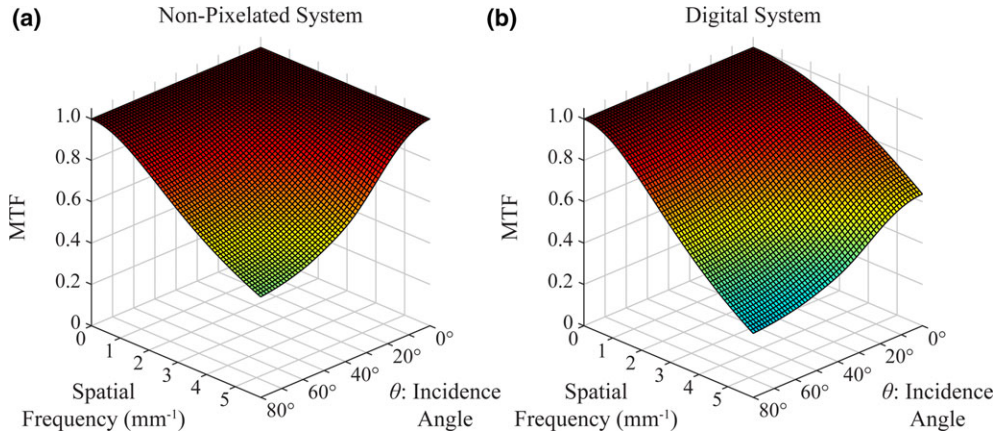

FIG. 4. The MTF at 20 keV is plotted as a function of both the incidence angle and frequency, assuming that $\Gamma = \alpha = 90°$. At low frequency, the MTF is effectively independent of the incidence angle. However, at high frequency, the MTF is more strongly dependent on the incidence angle. [Color figure can be viewed at wileyonlinelibrary.com]

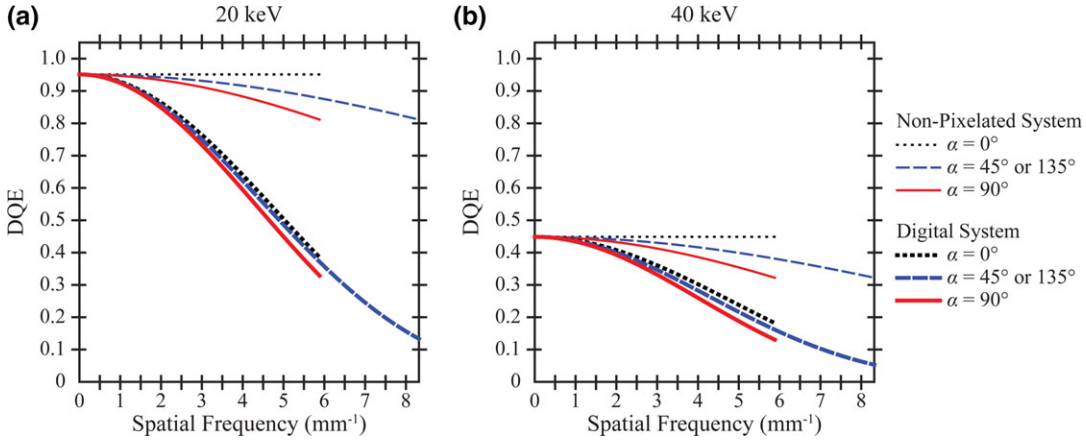

FIG. 5. The DQE is calculated under assumptions similar to Fig. 1; that is, $\Gamma = 90°$. Unlike the DQE of the x-ray converter, the DQE of the digital system is frequency-dependent along all polar angles, including the polar angle perpendicular to the ray incidence direction ($\alpha = 0°$). Increasing the energy results in less x-ray absorption and hence lower DQE. [Color figure can be viewed at wileyonlinelibrary.com]

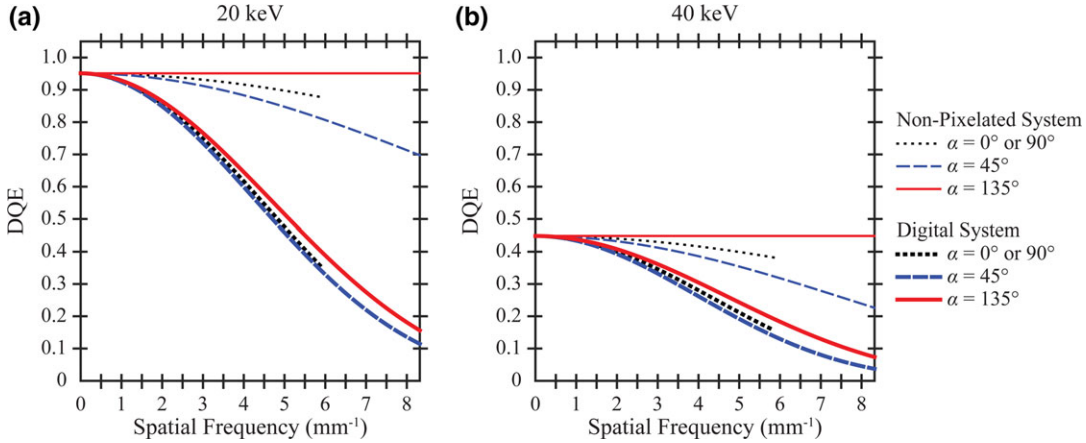

FIG. 6. The DQE is calculated under assumptions similar to Fig. 2. Hence, the direction corresponding to the most DQE degradation is aligned with the 45° polar angle (α). [Color figure can be viewed at wileyonlinelibrary.com]

angle; yet, the term $\cos\theta$ is a decreasing function. The latter term has a more dominant effect on QDE.

Figure 7 also illustrates that the DQE is degraded by oblique incidence more strongly than the MTF. The DQE degradation is most pronounced along the ray incidence direction ($\alpha = 90°$); for example, at 15° incidence, the percent change in MTF relative to normal incidence is 5.6%, yet the percent change in DQE is 13.7%. These percent differences are the same for both the x-ray converter and the digital system.

Figure 8 is an extension of Fig. 7 to a broader range of frequencies, assuming that frequency is measured along the ray incidence direction. At low frequency ($f \sim 0$ mm^{-1}), the DQE is given by the QDE and thus is degraded by oblique incidence. This differs from the MTF (Fig. 4), which is unaffected by oblique incidence at low frequency. At high frequencies, the MTF and DQE are both degraded by oblique incidence, although the DQE degradation is greater.

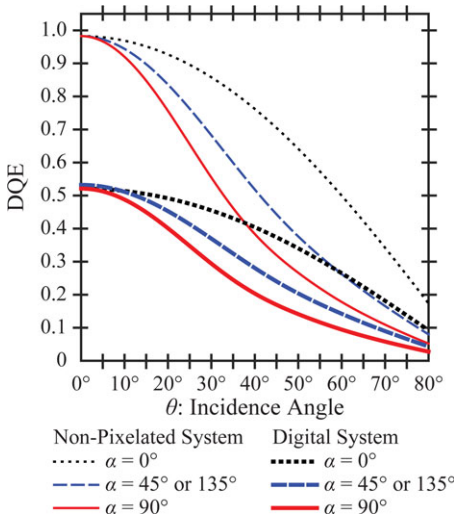

FIG. 7. The DQE is degraded by oblique incidence. Similar to the MTF, the degradation is most pronounced along the ray incidence direction ($\alpha = 90°$). There is also DQE degradation along the perpendicular direction ($\alpha = 0°$); this is due to degradation in QDE. The assumptions made in this figure are similar to Fig. 3. [Color figure can be viewed at wileyonlinelibrary.com]

3.C. An application in tomosynthesis system design

3.C.1. Acquisition geometry

We now explore how the obliquity effect gives rise to spatial variation in image quality. This calculation is used to demonstrate an advantage of the NGT design; namely, that the image quality shows less spatial anisotropy.

In the NGT system, the source is capable of arbitrary motions in a plane parallel to the breast support; for example, T-shaped motion (Fig. 9). This motion includes a component in the conventional scan direction (x). There is also a component of motion in the perpendicular direction (y); that is, the posteroanterior (PA) direction. To demonstrate the advantage of this design, the image quality can be quantified in different projection views.

3.C.2. Spatial anisotropy in the incidence angle

For image quality to be high, the incidence angle should be as close to 0° as possible. Figure 10 illustrates how the incidence angle varies over the active area of the detector (304.64 mm × 239.36 mm) in the central and oblique projection images of a conventional system design. The central projection [Fig. 10(a)] uses the same acquisition geometry considered previously for DM imaging. By contrast, in the oblique projection [Fig. 10(b)], the source is shifted by −100.0 mm in the x direction. The incidence angle increases at positions distal to the (x, y) coordinate of the source. It should be noted that, in the NGT system, the z-coordinate of the source is the same in all projections; this differs from a clinical system, in which there is circular motion in the xz plane.

Figure 11 shows the benefit of introducing source motion in the PA direction. For the purpose of this figure, it is

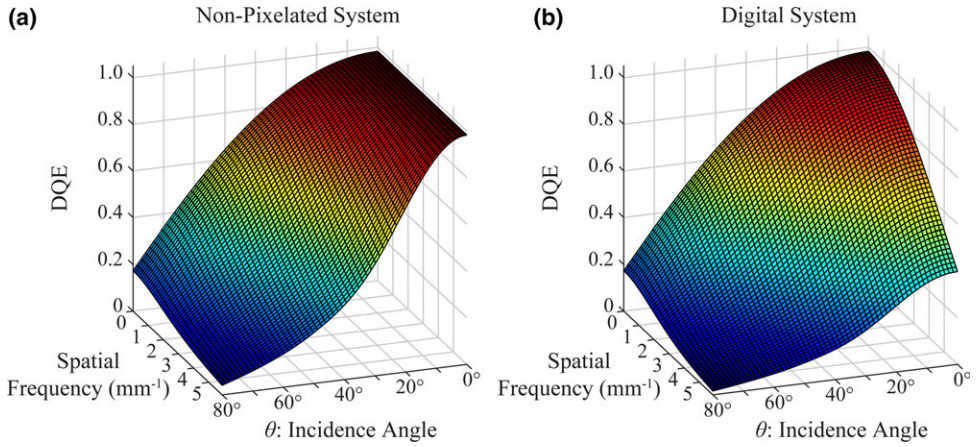

FIG. 8. Figure 7 is generalized to a range of frequencies under assumptions similar to Fig. 4. Increasing the incidence angle results in DQE degradation at all frequencies (including zero-frequency due to loss of QDE). [Color figure can be viewed at wileyonlinelibrary.com]

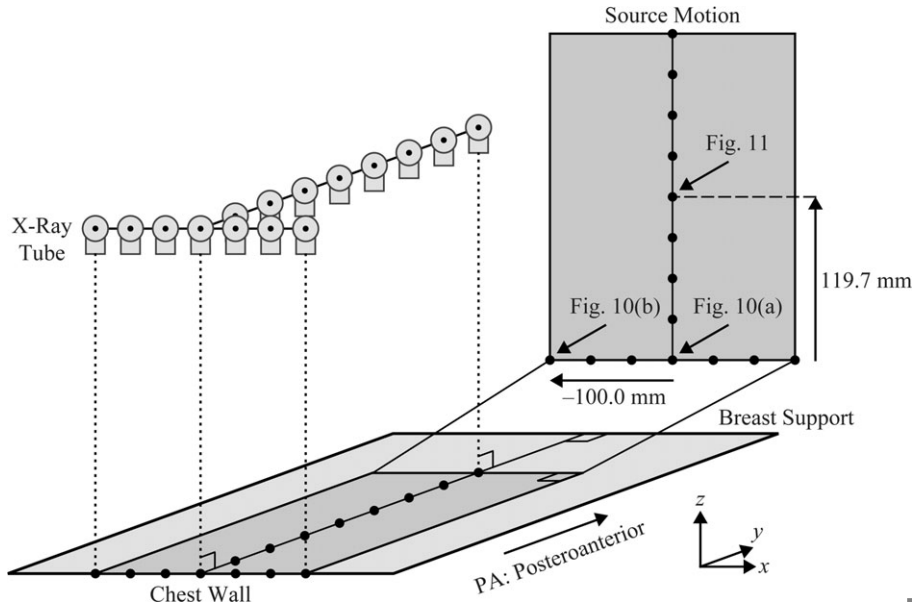

FIG. 9. In the NGT system, there are two degrees of freedom in the motion of the source (x and y). This differs from a clinical DBT system in which there is no source motion in the y direction; that is, posteroanteriorly. An example of a motion supported by the NGT system is T-shaped. This figure is not to scale.

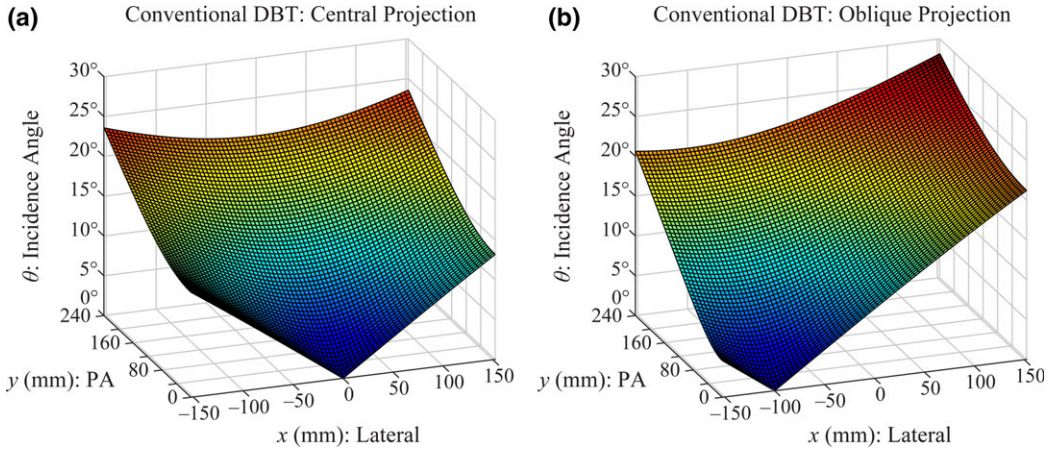

FIG. 10. The incidence angle varies over the detector area. (a) In the central projection of a conventional DBT system, the angle increases up to 23.6°. (b) In the oblique projection, the angle increases up to 28.2°. [Color figure can be viewed at wileyonlinelibrary.com]

assumed that the x-coordinate of the source is the same as the central projection of the conventional design [Fig. 10(a)] but the y-coordinate is displaced halfway between the chest wall and the opposite end of the detector (i.e., 119.7 mm anterior to the chest wall). Compared against the projections in the conventional design, the incidence angle varies over a smaller range of values, and hence one would expect more isotropic image quality across the detector area.

3.C.3. Spatial anisotropy in DQE

Figure 12 illustrates how the net DQE at 5.0 mm^{-1} varies over the detector area for these three projections, assuming 20 keV x rays. For better visualization of the surface, the plots are prepared with a different orientation than Figs. 10 and 11. The benefit of PA source motion (bottom row) is that there is less spatial variation in DQE. This can be illustrated with the results along a 90° polar angle (α). The DQE range (difference between max and min) is 0.13 for the central projection and 0.14 for the oblique projection in the conventional design. Yet, the DQE range is only 0.047 for the projection obtained with PA source motion.

Figure 12 also illustrates how the DQE is sensitive to the polar angle (α) of the input frequency. In the conventional design, the spatial anisotropy is more pronounced along a 45° polar angle (DQE ranges of 0.16 and 0.21 for the central and oblique projections, respectively) than along a 90° polar angle. The use of PA source motion minimizes the anisotropy (DQE range of 0.087).

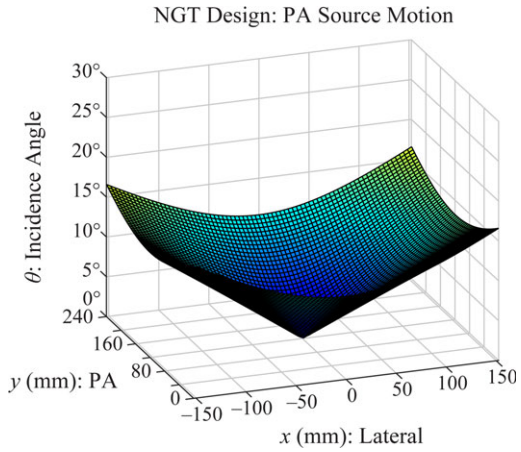

FIG. 11. The NGT system supports PA source motion. There is a smaller range of incidence angles (up to 16.6°) compared against projections obtained with the conventional design (Fig. 10). [Color figure can be viewed at wileyonlinelibrary.com]

4. DISCUSSION

This paper develops a nonstationary model of the obliquity effect in *a*-Se detectors. We show that the MTF is degraded by oblique incidence. This result is consistent with previous works on both direct- and indirect-converting detectors.[1–5,9,25,26] The MTF degradation is most pronounced along the ray incidence direction. There is no MTF degradation along the perpendicular direction. Although these results were illustrated with the AXS-2430 detector, similar results are expected in other detector applications.

We follow the approach used by Que and Rowlands[1] to model the obliquity effect; namely, we consider this effect separate from other x-ray interactions in selenium. With this approach, we find that the NPS is white. Previous work has demonstrated that, at low energy, the NPS is effectively white.[4] However, in high-energy applications, it has been shown that the NPS exhibits more pronounced dependency on frequency.[2–4] This arises from x-ray interactions not included in our model; for example, Compton scattering.[2]

This paper shows that the DQE is degraded by oblique incidence, similar to the MTF. The DQE degradation is most pronounced along the ray incidence direction. The DQE is more strongly dependent on the incidence angle than the MTF, since the DQE is proportionate with the square of the MTF. There is additional DQE degradation due to the dependency of QDE on $\cos\theta$ [Eq. (27)].

In breast imaging, calcifications are high-frequency structures that can act as an early sign of cancer. Based on Monte Carlo simulations of DQE, Hajdok and Cunningham concluded that oblique incidence gives rise to poorer calcification visibility.[2] However, their work is limited in that they did not calculate how the DQE varies over the detector area. Furthermore, they did not model the presence of detector pixelation (i.e., digitization). Our results suggest that calcification visibility does indeed fluctuate over the detector area, and that the image quality at a given detector position differs between projection views (Fig. 12). Exploring the anisotropies in calcification imaging should be the subject of future work.

In the work by Hajdok and Cunningham, the DQE was calculated assuming that frequency is oriented along the ray incidence direction.[2] By contrast, in this paper, the input frequency is modeled along an arbitrary polar angle (α). In studying the spatial variation in DQE, we show that the net DQE variation over the detector area is dependent on the polar angle.

This model is a tool for evaluating the image quality in a prototype NGT system. This system is capable of source motion in the PA direction, unlike a clinical system. In various projection images supported by this system, we analyze how the incidence angle varies over the detector area. The use of PA source motion minimizes the range of angles over this area, and hence anisotropies in the DQE are minimized. This results in an improvement in image quality.

While this paper proposes a model of image quality in an individual projection image, future work should perform these calculations in the reconstruction. In addition, the three-dimensional transfer functions should simulate the reconstruction filter.[27,28]

This paper shows that the Swank factor (A_S) is unity for all incidence angles, and thus the DQE at zero-frequency is determined by the QDE [Eq. (26)]. This result differs from our previous work modeling indirect-converting detectors.[25,26] We demonstrated that A_S does show angular dependence if an optical dye is added to a scintillator. The purpose of the optical dye is to absorb some of the visible light produced by the scintillator, and thus minimize the lateral spread of light due to optical scatter.

As was discussed in Section 3.B.1., electronic noise has not been included in the modeling assumptions of this paper. This noise source re-scales the DQE in Figs. 5 and 6 by a constant factor,[20] resulting in a loss of image quality. While this paper presumes that the x-ray system is quantum-limited, future work should explore additional sources of noise[29] affecting the term R_N in the DQE formula [Eq. (26)].

5. CONCLUSION

In Part 1, the consequences of oblique incidence in *a*-Se detectors were analyzed in the spatial domain.[10] By contrast, this paper focuses on the Fourier domain. We show that there is MTF and DQE degradation resulting from oblique incidence.

This model is ultimately used to quantify spatial variation in image quality over the detector area. We calculate the DQE in projection images supported by the NGT system. The benefit of PA source motion is that it minimizes the spatial variation in DQE, and hence the image quality is more isotropic.

ACKNOWLEDGMENTS

We thank Denny L. Y. Lee for many useful discussions on the physics of *a*-Se detectors. In addition, we

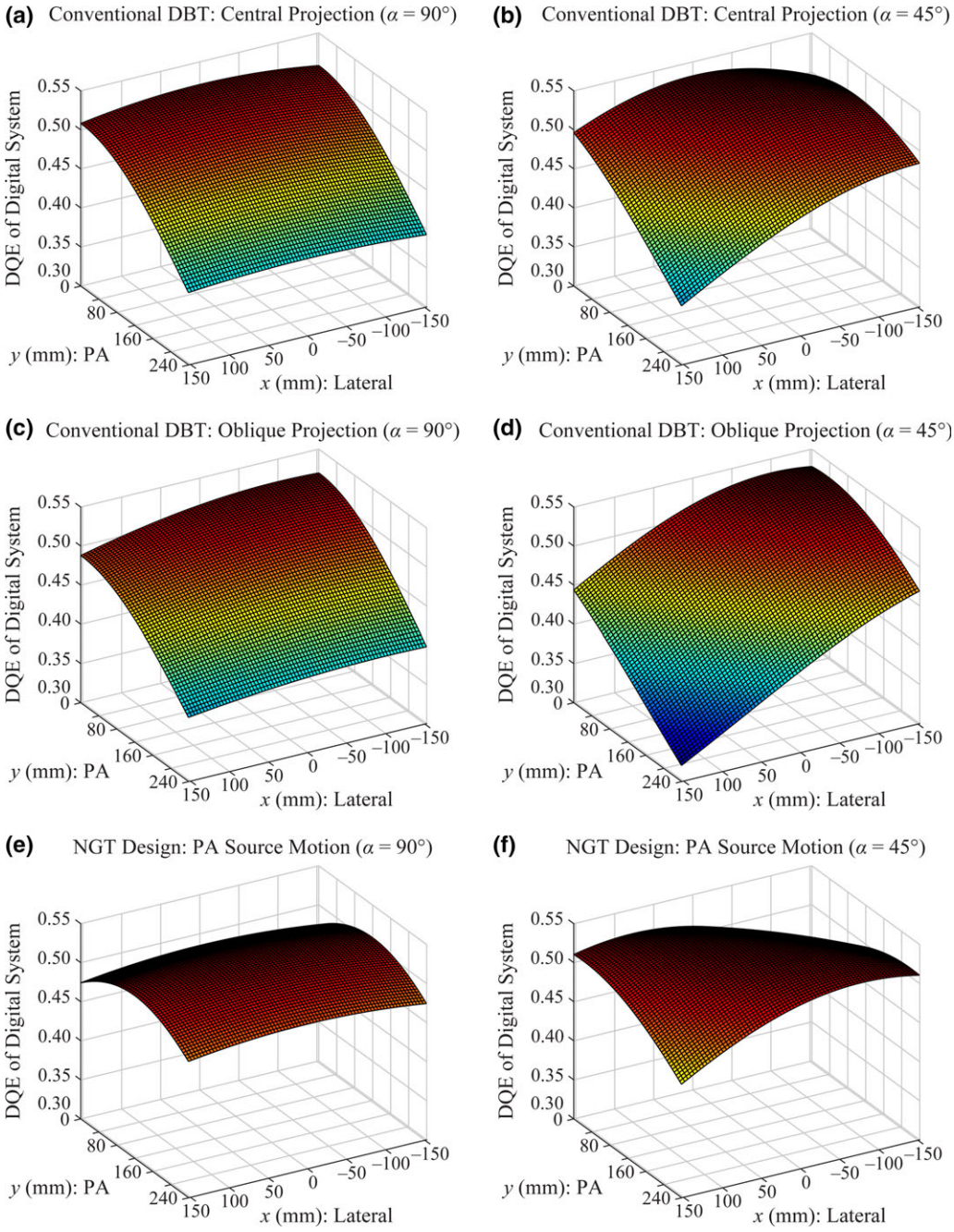

FIG. 12. The net DQE varies over the detector area. With PA source motion (bottom row), there is less pronounced variation and hence more isotropic image quality. The shape of these surface plots is dependent on the polar angle (α) of the input frequency. These calculations presume an input frequency of 5.0 mm^{-1} and an energy of 20 keV. [Color figure can be viewed at wileyonlinelibrary.com]

are grateful to David Higginbotham for providing constructive feedback. Support was provided by the following grants: PDF14302589 and IIR13264610 from Susan G. Komen®; 1R01CA154444 and 1R01CA196528 from the National Institute of Health; IRSA 1016451 from the Burroughs Wellcome Fund; and W81XWH-18-1-0082 from the Department of Defense Breast Cancer Research Program. In addition, equipment support was provided by Analogic Inc., Barco NV, and Real Time Tomography (RTT), LLC (Villanova, PA). The content is solely the responsibility of the authors and does not necessarily represent the official views of the funding agencies.

CONFLICTS OF INTEREST

Andrew D. A. Maidment is a scientific advisor to RTT, and his spouse is an employee and shareholder of RTT.

APPENDIX: NOMENCLATURE

Symbol	Meaning
$*_2$	2D convolution operator
$\mathcal{F}_2$	2D Fourier operator
α	Polar angle (defined in Part 1[10])
Γ	Azimuthal angle of ray (defined in Part 1[10])
δ	Delta function
θ	Incidence angle (defined in Part 1[10])
μ	Linear attenuation coefficient of selenium
ξ_1, ξ_2	Coordinates of entrance point of ray in x-ray converter (defined in Part 1[10])
A_Q	Abbreviation for QDE
A_S	Swank factor
a_x, a_y	Del dimensions; if $a_x = a_y$, the dimension is abbreviated a
C_I	Normalization term for P_I (defined in Part 1[10])
d	Distance between source and exit surface of x-ray converter (defined in Part 1[10])
DBT	Digital breast tomosynthesis
Del	Detector element
DM	Digital mammography
DQE	Detective quantum efficiency
DQE_{Net}	DQE of digital system
DQE_{Se}	DQE of x-ray converter
f_g	Frequency span of MTF [Eq. (33)], as shown by Que and Rowlands[1]
f_r	Radial frequency
f_x, f_y	Frequency along x and y directions
FS	Focal spot
G_{Net}	OTF of digital system
G_{Se}	OTF of x-ray converter
l	Selenium thickness
MTF	Modulation transfer function
MTF_{Net}	MTF of digital system
MTF_{Se}	MTF of x-ray converter
N	Relative number of x-ray quanta (defined in Part 1[10])
NNPS	Normalized NPS
NPS	Noise power spectra
OTF	Optical transfer function
P_I	PSF associated with arbitrary ionization point in x-ray converter
P_{TFT}	PSF of TFT array
P_z	Depth-dependent PSF (combined effect of P_I and P_{TFT})
PA	Posteroanterior
PSF	Point spread function
QDE	Quantum detection efficiency
r	$\sqrt{\xi_1^2 + \xi_2^2}$ as defined in Part 1[10]
R_C	Lubberts fraction
R_N	Ratio of quantum noise power to total noise power
TFT	Thin-film transistor
v_1'	Position along ray incidence direction (defined in Part 1[10])
v_2'	Position perpendicular to ray incidence direction (defined in Part 1[10])
W_{Net}	NNPS of digital system
W_{Pre}	Presampled NNPS
W_{Se}	NNPS of x-ray converter

[a]Author to whom correspondence should be addressed. Electronic mail: raymond.acciavatti@uphs.upenn.edu; Telephone: +1-215-746-8759; Fax: +1-215-746-8764.

REFERENCES

1. Que W, Rowlands JA. X-ray imaging using amorphous selenium: inherent spatial resolution. *Med Phys*. 1995;22:365–374.
2. Hajdok G, Cunningham IA. Penalty on the detective quantum efficiency from off-axis incident x rays. In: Yaffe MJ, Flynn MJ, eds. *Physics of Medical Imaging*. San Diego, CA: SPIE; 2004:109–118.
3. Hu Y-H, Scaduto DA, Zhao W. The effect of amorphous selenium thickness on imaging performance of contrast enhanced digital breast tomosynthesis. *Lect Notes Comput Sci*. 2012;7361:9–16.
4. Scaduto DA, Tousignant O, Zhao W. Experimental characterization of a direct conversion amorphous selenium detector with thicker conversion layer for dual-energy contrast-enhanced breast imaging. *Med Phys*. 2017;44:3965–3977.
5. Hu Y-H, Zhao W. The effect of amorphous selenium detector thickness on dual-energy digital breast imaging. *Med Phys*. 2014;41:111904-1–111904-10.
6. Fujita H, Tsai D-Y, Itoh T, et al. A simple method for determining the modulation transfer function in digital radiography. *IEEE Trans Med Imaging*. 1992;11:34–39.
7. Maidment ADA, Albert M. Conditioning data for calculation of the modulation transfer function. *Med Phys*. 2003;30:248–253.
8. Carton A-K, Vandenbroucke D, Struye L, et al. Validation of MTF measurement for digital mammography quality control. *Med Phys*. 2005;32:1684–1695.
9. Mainprize JG, Bloomquist AK, Kempston MP, Yaffe MJ. Resolution at oblique incidence angles of a flat panel imager for breast tomosynthesis. *Med Phys*. 2006;33:3159–3164.
10. Acciavatti RJ, Maidment ADA. Non-stationary model of oblique X-ray incidence in amorphous-selenium detectors: I. point spread function. *Med Phys*. (in press).
11. Maidment AD, Acciavatti R, Vent T, et al. SSC14-03: Construction of a prototype digital breast tomosynthesis system with superior spatial resolution. Radiological Society of North America (RSNA) Conference, 2016; Chicago, IL.
12. Ferris WS, Vent TL, Maidment TD, Acciavatti RJ, Wurtele DE, Maidment ADA. Geometric calibration for a next-generation digital breast tomosynthesis system. In: Flohr TG, Lo JY, Schmidt TG, eds. *Physics of Medical Imaging*. Orlando, FL: SPIE; 2017:101324C-1–101324C-10.
13. Maidment TD, Vent TL, Ferris WS, Wurtele DE, Acciavatti RJ, Maidment ADA. Comparing the imaging performance of computed super resolution and magnification tomosynthesis. In: Flohr TG, Lo JY, Schmidt TG, eds. *Physics of Medical Imaging*. Orlando, FL: SPIE; 2017:1013222-1–1013222-10.
14. Acciavatti RJ, Rodríguez-Ruiz A, Vent TL, et al. Analysis of volume overestimation artifacts in the breast outline segmentation in tomosynthesis. In: Lo JY, Schmidt TG, Chen G-H, eds. *Physics of Medical Imaging*. Houston, TX: SPIE; 2018:1057359-1–1057359-8.
15. Choi CJ, Vent TL, Acciavatti RJ, Maidment ADA. Geometric calibration for a next-generation digital breast tomosynthesis system using virtual line segments. In: Lo JY, Schmidt TG, Chen G-H, eds. *Physics of Medical Imaging*. Houston, TX: SPIE; 2018:105730D-1–105730D-10.
16. Eben JE, Vent TL, Choi CJ, et al. Development of a next generation tomosynthesis system. In: Lo JY, Schmidt TG, Chen G-H, eds. *Physics of Medical Imaging*. Houston, TX: SPIE; 2018:105735Q-1–105735Q-8.
17. Swank RK. Calculation of modulation transfer functions of x-ray fluorescent screens. *Appl Opt*. 1973;12:1865–1870.
18. Giger ML, Doi K, Metz CE. Investigation of basic imaging properties in digital radiography. 2. Noise Wiener spectrum. *Med Phys*. 1984;11:797–805.
19. Albert M, Maidment ADA. Linear response theory for detectors consisting of discrete arrays. *Med Phys*. 2000;27:2417–2434.

20. Acciavatti RJ, Maidment ADA. A comparative analysis of OTF, NPS, and DQE in energy integrating and photon counting digital x-ray detectors. *Med Phys*. 2010;37:6480–6495.
21. Nishikawa RM, Yaffe MJ. Model of the spatial-frequency-dependent detective quantum efficiency of phosphor screens. *Med Phys*. 1990;17:894–904.
22. Swank RK. Absorption and noise in x-ray phosphors. *J Appl Phys*. 1973;44:4199–4203.
23. Barrett HH, Myers KJ. Chapter 3: fourier analysis. In: Saleh BEA, ed. *Foundations of Image Science*. New York, NY: John Wiley & Sons; 2004:95–174.
24. Acciavatti RJ, Maidment ADA. An analytical model of NPS and DQE comparing photon counting and energy integrating detectors. In: Samei E, Pelc NJ, eds. *Physics of Medical Imaging*. San Diego, CA: SPIE; 2010:76220I-1–76220I-12.
25. Acciavatti RJ, Maidment ADA. Calculation of OTF, NPS, and DQE for oblique x-ray incidence on turbid granular phosphors. *Lect Notes Comput Sci*. 2010;6136:436–443.
26. Acciavatti RJ, Maidment ADA. Optimization of phosphor-based detector design for oblique x-ray incidence in digital breast tomosynthesis. *Med Phys*. 2011;38:6188–6202.
27. Zhao B, Zhao W. Three-dimensional linear system analysis for breast tomosynthesis. *Med Phys*. 2008;35:5219–5232.
28. Zhao B, Zhou J, Hu Y-H, Mertelmeier T, Ludwig J, Zhao W. Experimental validation of a three-dimensional linear system model for breast tomosynthesis. *Med Phys*. 2009;36:240–251.
29. Barrett HH, Myers KJ. Chapter 12: noise in detectors. In: Saleh BEA, ed. *Foundations of Image Science*. New York, NY: John Wiley & Sons; 2004:701–800.

Personalization of X-Ray Tube Motion in Digital Breast Tomosynthesis Using Virtual Defrise Phantoms

Raymond J. Acciavatti[1], Bruno Barufaldi[1], Trevor L. Vent[1],
E. Paul Wileyto[2], Andrew D. A. Maidment[1]
[1]University of Pennsylvania, Department of Radiology, 3400 Spruce Street, Philadelphia PA 19104
[2]University of Pennsylvania, Department of Epidemiology, Biostatistics, & Informatics,
423 Guardian Drive, Philadelphia PA 19104
E-mail: {Raymond.Acciavatti@uphs | Bruno.Barufaldi@uphs | tvent@seas |
epw@pennmedicine | Andrew.Maidment@uphs}.upenn.edu

ABSTRACT

In digital breast tomosynthesis (DBT), projection images are acquired as the x-ray tube rotates in the plane of the chest wall. We constructed a prototype next-generation tomosynthesis (NGT) system that has an additional component of tube motion in the perpendicular direction (*i.e.*, posteroanterior motion). Our previous work demonstrated the advantages of the NGT system using the Defrise phantom. The reconstruction shows higher contrast and fewer blurring artifacts. To expand upon that work, this paper analyzes how image quality can be further improved by customizing the motion path of the x-ray tube based on the object being imaged. In simulations, phantoms are created with realistic 3D breast outlines based on an established model of the breast under compression. The phantoms are given an internal structure similar to a Defrise phantom. Two tissue types (fibroglandular and adipose) are arranged in a square-wave pattern. The reconstruction is analyzed as a binary classification task using thresholding to segment the two tissue types. At various thresholds, the classification of each voxel in the reconstruction is compared against the phantom, and receiver operating characteristic (ROC) curves are calculated. It is shown that the area under the ROC curve (AUC) is dependent on the x-ray tube trajectory. The trajectory that maximizes AUC differs between phantoms. In conclusion, this paper demonstrates that the acquisition geometry in DBT should be personalized to the object being imaged in order to optimize the image quality.

Keywords: Digital Breast Tomosynthesis, Mammography, X-Ray Imaging, Digital Imaging, Defrise Phantom, Image Quality, Image Reconstruction, Receiver Operating Characteristic Curve.

1. INTRODUCTION

The Defrise phantom is a test object for evaluating image quality in cone-beam computed tomography (CT). The phantom consists of multiple disks, which are spaced along the direction perpendicular to the plane of source motion. In the reconstruction, there is a cone-beam artifact along this direction; the spacings between the disks are not properly visualized at positions distal to the plane of source motion.[1]

One application of the Defrise phantom is to demonstrate the advantage of new acquisition geometries for CT. For example, in the work of Becker *et al*., a multisource system for dedicated breast CT was evaluated.[2] The system was built with five sources, which were spaced in 2.0 cm increments along the direction of the cone-beam artifact. The contrast between disks was used to quantify image quality. With multisource scanning, there is a broader range of positions over which contrast is within detectable limits, yielding an improvement in image quality over single-source scanning.

Our previous work showed that the Defrise phantom can also be used to evaluate image quality in digital breast tomosynthesis (DBT).[3,4] We demonstrated the existence of a cone-beam artifact along the posteroanterior (PA) direction, which is perpendicular to the motion of the source. To show that image quality can be improved, we later constructed a prototype next-generation tomosynthesis (NGT) system, which is capable of source motion with an additional degree of freedom in the PA direction.[5,6] Although a single source is used in the NGT system, our strategy for

Medical Imaging 2019: Physics of Medical Imaging, edited by Taly Gilat Schmidt, Guang-Hong Chen, Hilde Bosmans,
Proc. of SPIE Vol. 10948, 109480B · © 2019 SPIE · CCC code: 1605-7422/19/$18 · doi: 10.1117/12.2511780

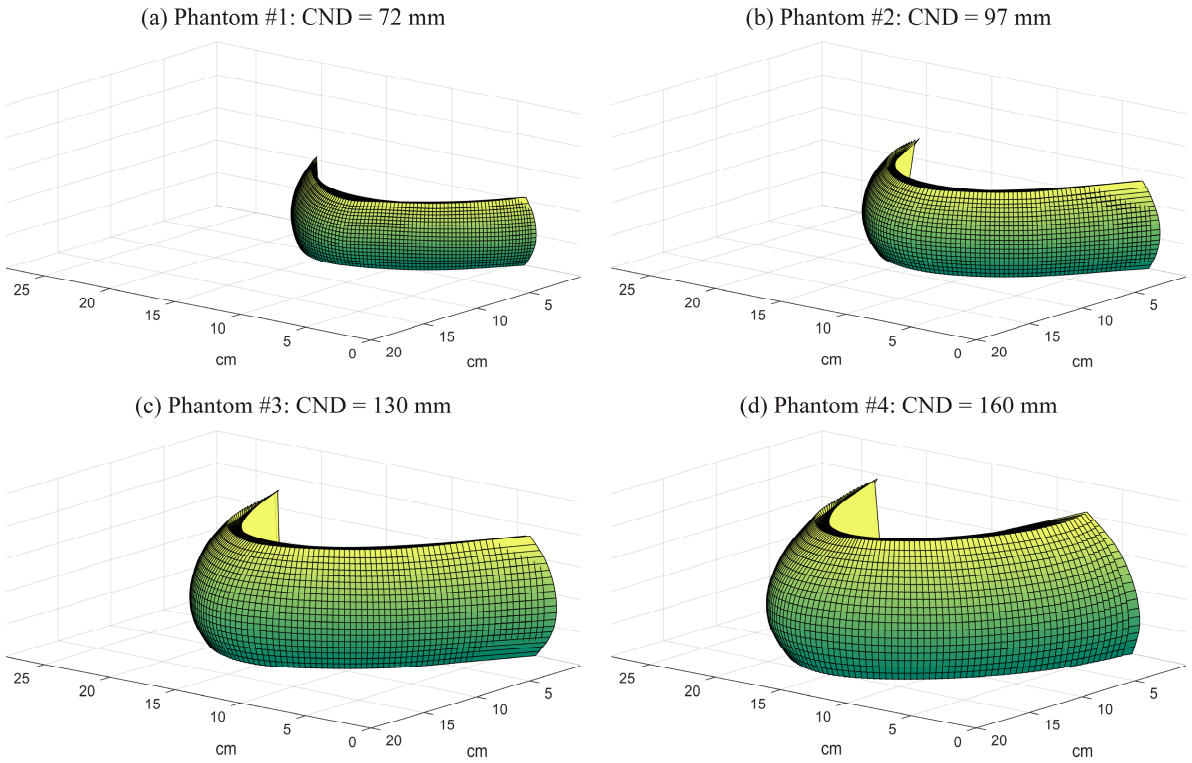

Figure 1. Breast outlines under compression are shown for four phantoms using the model of Rodríguez-Ruiz *et al*.[7]

improving the image quality is similar to the one used by Becker *et al*.[2] in that source positions are introduced along the direction of the cone-beam artifact.

The latest CT scanners incorporate the newest trends in personalized medicine. In point-of-care CT, the scan orbit is customized to the clinical task and body habitus.[8-14] The purpose of this paper is to demonstrate that the acquisition settings in DBT also need to be personalized to each patient. We model virtual Defrise phantoms that are created in the shape of the 3D breast outline under compression.[7] Various acquisition geometries are simulated for each phantom. This paper shows that a given scan motion will not benefit all phantoms the same way. The best image quality is achieved by customizing the motion of the source to the dimensions of the phantom.

2. METHODS

2.1 Phantom Model

Four phantoms were considered for the purpose of this study. The 3D phantom outlines were created based on previous work modeling the breast under compression.[7] Figure 1 shows the output of the MATLAB® software developed by that work. Random phantoms with "advanced 3D curvature" were generated by specifying thicknesses of 45, 55, 75, and 85 mm in this software. Table 1 shows the chest-wall to nipple distance (CND) for each phantom. We truncated some slices at the superior surface of each phantom, as we did in our previous work[15], since the shape of the breast outline was not representative of a breast under compression in these slices. More specifically, three slices in phantom #1, four slices in phantom #2, five slices in phantom #3, and six slices in phantom #4 were truncated. The resultant thicknesses of each phantom are summarized in Table 1.

The 3D breast outline was initially created with 1.0 mm^3 voxels, and then up-sampled to 0.50 mm^3 voxels. Each phantom was given internal structure consisting of two tissue types (fibroglandular and adipose) arranged in a square-wave pattern with a frequency of 0.17 mm^{-1} oriented in the PA direction. This frequency is chosen based on our previous work on the Defrise phantom.[3,4]

Table 1. Four phantoms with different sizes and shapes were analyzed in this simulation study.

Phantom	CND: Chest-Wall to Nipple Distance (mm)	Thickness (mm)	kV	mAs
#1	72	40	29	45
#2	97	50	31	52
#3	130	69	35	72
#4	160	77	37	70

2.2 X-Ray Projection Images

X-ray projection images were simulated with ray-tracing software developed for virtual clinical trials.[16] For the purpose of this study, there were no sources of noise or blurring. Also, the AXS-2430 detector (Analogic Canada Corporation, Montreal, Quebec, Canada) was simulated, since this is the detector used in the NGT system. This detector has 0.085 mm pixels and an active area of 304.64 mm × 239.36 mm.

The kV and mAs for each projection image were determined from a table developed by Feng and Sechopoulos for the automatic exposure control (AEC) settings in DBT for a W/Al target filter combination.[17] According to that table, the kV is dependent on the compressed breast thickness. The kV for each phantom was determined by linear interpolation. This result was rounded to the nearest integer. Next, the mAs was determined based on the kV using linear interpolation, assuming a glandular fraction of 50%.

Figure 2 illustrates an example of a source motion supported by the NGT system. There are components of motion in both the conventional tube travel direction (x) and the PA direction (y). The source can be positioned at arbitrary points in these two directions; for example, along the outline of an ellipse. The trajectory shown in Figure 2 consists of two concentric half-ellipses. The semi-axis lengths for the outer ellipse are a and b in the x and y directions, respectively. These parameters control the range of source motion in each direction. The lengths of the axes of the inner ellipse are modeled to be half of these values.

For the purpose of this paper, we assume that the source positions are displaced around each half-ellipse in 30° increments and that there is an additional source position at the centroid of the ellipses. Hence there are 15 projection images. We define the centroid at the midpoint of the chest wall; this matches the central source position in a conventional DBT scan. The x- and y-coordinates of the focal spot (FS) can be described in terms of the projection number (n) based on the equations

$$x_{\mathrm{FS}} = \begin{cases} 0, & n = 1 \\ \dfrac{a}{2} \cdot \cos\left[(n-2)\dfrac{\pi}{6} \right], & 2 \le n \le 8 \\ a \cdot \cos\left[(15-n)\dfrac{\pi}{6} \right], & 9 \le n \le 15 \end{cases} \tag{1}$$

$$y_{\mathrm{FS}} = \begin{cases} 0, & n = 1 \\ \dfrac{b}{2} \cdot \sin\left[(n-2)\dfrac{\pi}{6} \right], & 2 \le n \le 8 \\ b \cdot \sin\left[(15-n)\dfrac{\pi}{6} \right], & 9 \le n \le 15 \end{cases}, \tag{2}$$

where n varies between 1 and 15 in integer steps. Figure 2 illustrates the ordering of the FS positions, as shown by the arrows. In all projections, the source-to-support distance is 621.0 mm and the source-to-image distance (SID) is 652.0 mm.

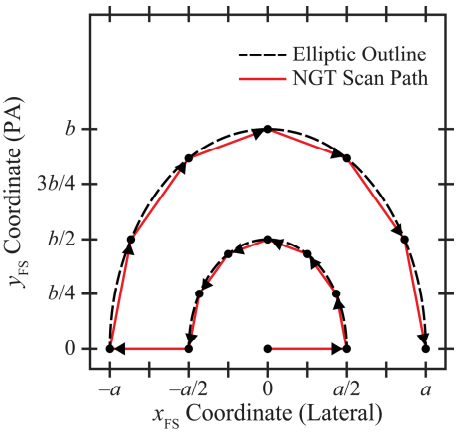

Figure 2. In this trajectory, there are five source positions along the chest wall and 10 additional source positions in the PA direction. The parameters a and b control the range of source motion in each direction.

If Eqs. (1)-(2) were used in the special case $b = 0$, there would be three overlapping FS coordinates at the point (0, 0); *i.e.*, the midpoint of the chest wall. For this reason, a different motion needs to be considered to simulate the conventional acquisition geometry. In this paper, this motion is simulated with equal spacing between source positions; namely, $x_{FS} = a \cdot (n - 8) / 7$. The range of source motion is thus $2a$ in the x direction, similar to Eq. (1). It should be noted that the SID is held constant in the NGT system for all acquisition geometries. Therefore, the simulation of the conventional motion differs from a clinical system in which the source rotates in a circular arc in the plane of the chest wall.

For these simulations, a is varied between 50.0 and 150.0 mm in 5.0 mm increments (or 21 steps), and b is varied between 0 and 200.0 mm in 10.0 mm increments (also 21 steps). This results in 441 acquisition geometries that are simulated. We determine the optimum acquisition geometry for each phantom using the approach described in Section 2.3.

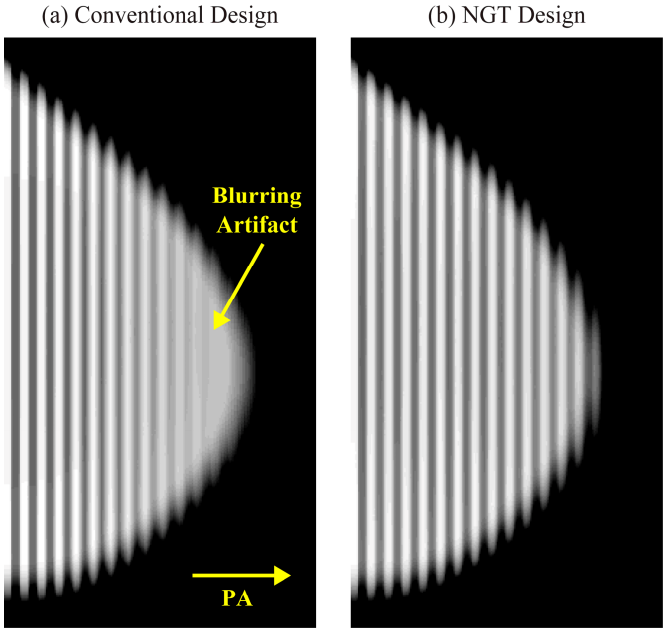

Figure 3. (a) In the central slice of the reconstruction for phantom #2, there is loss of image quality in the PA direction in the conventional design, as shown by the blurring artifact. (b) The NGT design offers better image quality in the PA direction ($b = 90$ mm).

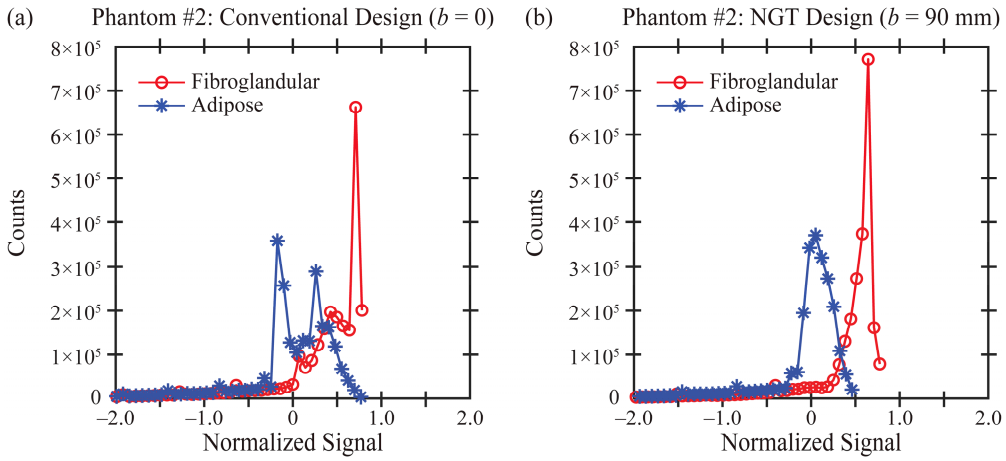

Figure 4. Using the reconstruction obtained with phantom #2, the histograms for the signal in each tissue type (fibroglandular and adipose) are calculated. The separation between the two tissue types is more pronounced in the NGT design (b) than in the conventional design (a).

2.3 Image Analysis

Reconstructions were calculated with Briona™ (Real Time Tomography, LLC, Villanova, PA) with an in-plane pixelation of 0.085 mm × 0.085 mm and a slice spacing of 0.50 mm. Subsequently, the reconstructions were re-scaled to the voxel size of the phantom with bicubic interpolation.

Receiver operating characteristic (ROC) curves were then calculated by using thresholding to segment the two tissue types.[18] Each voxel was classified as fibroglandular tissue (FGT) if the signal exceeds a user-specified threshold. All other voxels were classified as adipose tissue (AT). We define the true positive rate (TPR) as the ratio of the number of voxels classified correctly as FGT to the total number of fibroglandular voxels in the input phantom. The false positive rate (FPR) is the ratio of the number of voxels classified incorrectly as FGT to the total number of adipose voxels in the input phantom. ROC curves were generated by calculating TPR and FPR at all possible thresholds. The area under the ROC curve (AUC) was calculated as a figure-of-merit to identify the acquisition geometry that maximizes the image quality for each phantom.

3. RESULTS

3.1 Results for Conventional and NGT Designs

Figure 3 illustrates the central slice in the reconstruction for the conventional and NGT designs for one phantom (#2). Both figures presume that the range of source motion in the x direction is 200.0 mm; *i.e.*, a = 100.0 mm. As one would expect from previous work[3-6], there is a blurring artifact at positions distal to the chest wall in the conventional design [Figure 3(a)]. It is difficult to discern the spacings between the two tissue types at these positions. By contrast, in the NGT design with PA source motion (b = 90 mm), the relative contrast is improved [Figure 3(b)].

To analyze these results more quantitatively, the signal in each tissue type is visualized with a histogram in Figure 4. These histograms are created using all slices in the reconstruction, not just the central slice shown in Figure 3. The signal (I) has been re-scaled with Z-score normalization based on the mean (μ) and standard deviation (σ) for each tissue type. Eq. (3) describes this transformation. The origin is shifted halfway between the means of each distribution. Also, the signal is normalized by the pooled standard deviation.

$$Z = \frac{I - \frac{\mu_{\mathrm{FGT}} + \mu_{\mathrm{AT}}}{2}}{\sqrt{\frac{\sigma_{\mathrm{FGT}}^2 + \sigma_{\mathrm{AT}}^2}{2}}} \tag{3}$$

In Figure 4, the distributions are plotted to within ± two units of the pooled standard deviation. As can be seen from this figure, the histograms are highly skewed to the left, and therefore, the tails in the extreme left have been truncated.

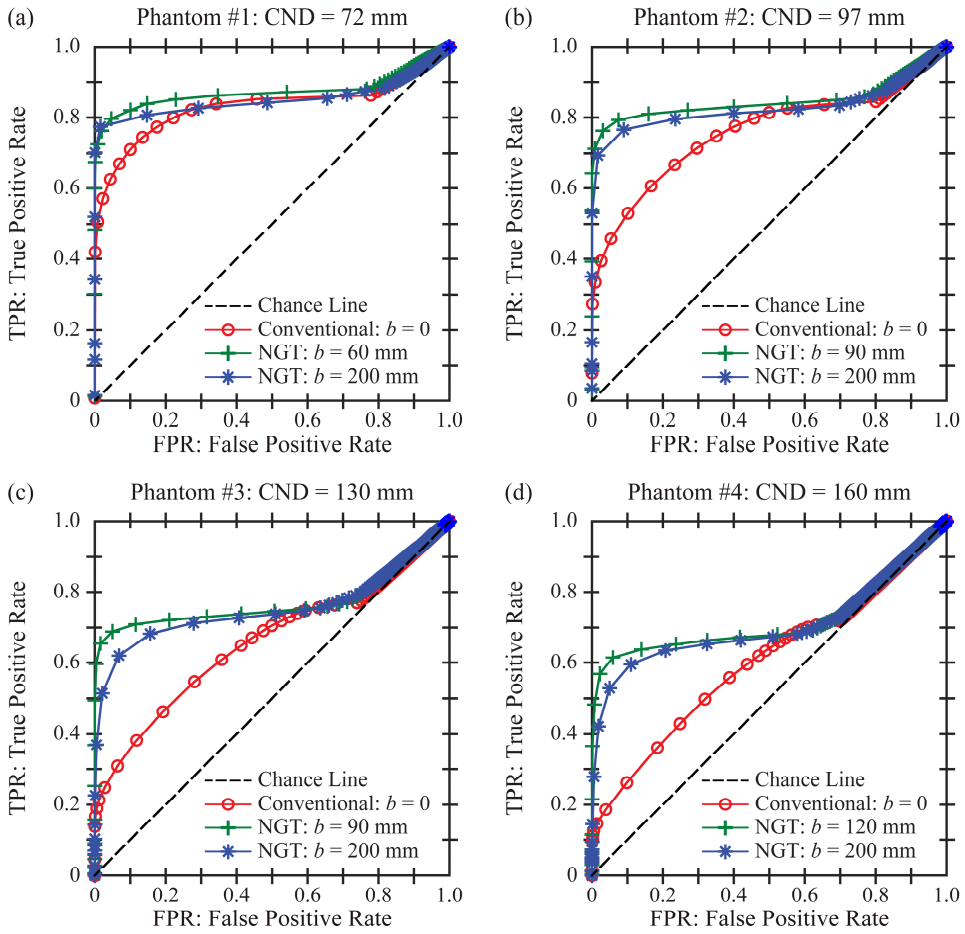

Figure 5. The reconstruction is analyzed as a binary classification task. A threshold is used to segment the two tissue types (fibroglandular and adipose). For each phantom, ROC curves are calculated for three acquisition geometries by varying the threshold, assuming $a = 100.0$ mm. The three acquisition geometries differ in terms of the range of PA source motion; *i.e.*, the conventional design, the NGT design with the highest AUC, and the NGT design with the broadest range of PA source motion.

For image quality to be high, there needs to be a clear separation between the FGT and AT histograms. This separation can be quantified in terms of a ROC curve [Figure 5(b)]. Each point on the ROC curve is calculated using a different threshold to segment the two tissue types. The NGT design for which $b = 90$ mm offers an improvement in image quality (AUC = 0.85) relative to the conventional design (AUC = 0.76). In Section 3.2, AUC is analyzed in all 441 acquisition geometries in order to identify the optimum scan parameters for each phantom.

3.2 Optimization of the Acquisition Geometry

Figure 6 shows a surface plot of AUC as a function of the scan parameters (a and b) for each phantom. These plots first illustrate that the image quality is effectively independent of the parameter a; *i.e.*, the range of source motion perpendicular to the input frequency. The parameter b, which controls the range of motion in the PA direction, has a more pronounced effect on AUC.

Figure 6 can be used to calculate the value of b that maximizes AUC. Assuming that $a = 100.0$ mm, the optimum values of b are 60, 90, 90, and 120 mm for phantoms #1 to #4, respectively. These optimum values are correlated with CND; Pearson's correlation coefficient is 94%. These results illustrate the benefit of personalizing the source motion based on the dimensions of the phantom.

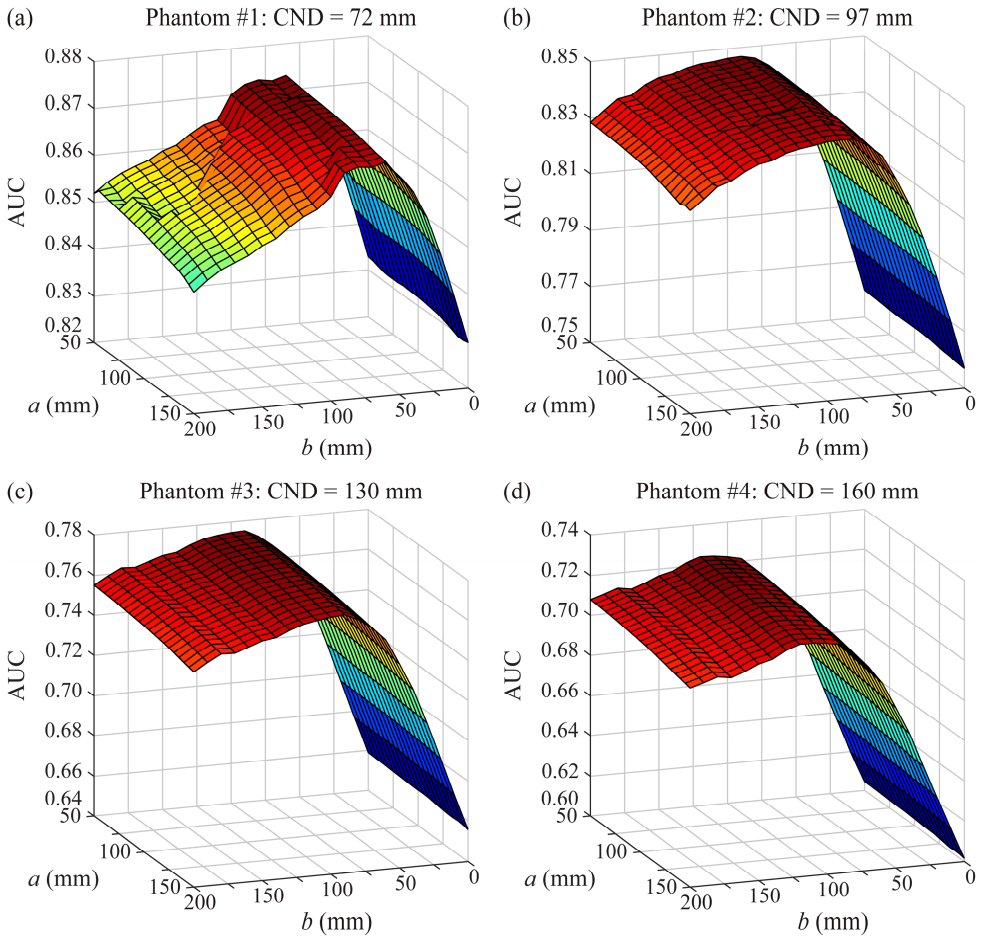

Figure 6. For each phantom, the AUC is plotted as a function of the scan parameters. These results are used to identify the optimum acquisition geometry for each phantom. In these simulations, the input frequency is oriented in the PA direction. The parameter *a* controls the range of source motion in the perpendicular direction; this parameter has only a small effect on AUC. By contrast, the parameter *b* needs to be customized to each phantom to optimize the image quality. It should be noted that the range of values in the vertical axis differs between subplots.

For each phantom, the ROC curve for the optimum geometry is compared against the conventional geometry in Figure 5. We continue to make the assumption that a = 100.0 mm. As shown, there is an improvement in AUC; namely, ΔAUC = 0.040, 0.088, 0.115, and 0.118 for phantoms #1 to #4, respectively. Figures 5-6 demonstrate that the phantoms with larger dimensions have inherently lower AUC. This result is expected from previous work, which showed that increasing the thickness of the phantom results in less relative contrast in the reconstruction.[4]

In addition, the ROC curves for the broadest range of PA motion (b = 200.0 mm) are shown in Figure 5. This motion is also characterized by an improvement over the conventional geometry; namely, ΔAUC = 0.019, 0.068, 0.095, and 0.101 for the four respective phantoms.

4. DISCUSSION AND CONCLUSION

In this paper, virtual Defrise phantoms are created in the shape of breasts under compression. There are two tissue types in the phantom (FGT and AT). Consequently, the reconstruction can be analyzed voxel-by-voxel as a binary classification task with a ROC curve. We find that the source motion needs to be customized to the dimensions of the phantom to maximize the AUC. Specifically, as the CND increases, the source needs to traverse a broader range of motion in the PA direction. Since the scan time is proportionate with the path length of the source motion, these results suggest that the phantoms with the broadest CND will require the longest scan time.

Figures 5-6 show that the improvement over the conventional geometry is preserved as the range of PA motion increases beyond the optimum value. However, this comes with the trade-off of increasing the scan time, and therefore, increasing the potential for blurring due to patient motion.[19] Another disadvantage of a longer scan time is prolonging the discomfort associated with breast compression.

One limitation of this paper is that, based on the orientation of the input frequency, image quality is investigated in only one direction (PA). There was no analysis of image quality in the conventional tube travel direction (x). Previous work has demonstrated that image quality is indeed dependent on the range of source motion in this direction. For example, a narrow range of source motion has been shown to be beneficial in calcification imaging.[20] Future work needs to investigate how the source motion can be optimized based on the imaging task.

The results of this paper were determined using a limited number of phantoms. In future work, additional phantoms with different sizes, shapes, and internal compositions should be analyzed, including anthropomorphic phantoms[21-23] with more complex fibroglandular distributions. Future work also needs to investigate whether the CND could be estimated from a low-dose scout image; in a clinical exam, the CND is not known *a priori* as is the case with a phantom. The source motion could be customized around the dimensions obtained from the scout image.

5. ACKNOWLEDGEMENT

The authors acknowledge the early work of Margaret Nolan, Elizabeth Kobe, Sushmitha Yarrabothula, and Lucy Chai at the University of Pennsylvania on this topic. We also thank Johnny Kuo, Susan Ng, and Peter Ringer of Real Time Tomography for technical assistance with Briona™. Andrew D. A. Maidment is a shareholder of Real Time Tomography, and is a member of the scientific advisory board.

Support was provided by the following grants: W81XWH-18-1-0082 from the Department of Defense Breast Cancer Research Program, IRSA 1016451 from the Burroughs Wellcome Fund, 1R01CA196528 from the National Institute of Health, and IIR13264610 from Susan G. Komen®. In addition, equipment support was provided by Analogic Inc., Barco NV, and Real Time Tomography. The content is solely the responsibility of the authors and does not necessarily represent the official views of the funding agencies.

6. REFERENCES

1. Hsieh J. Chapter 10: Multislice and Cone-beam CT. *Computed Tomography: Principles, Design, Artifacts, and Recent Advances*. Third ed. Bellingham, WA: SPIE Press; 2015:423-486.
2. Becker AE, Hernandez AM, Schwoebel P, Boone JM. Multisource x-ray system for artifact reduction in dedicated breast CT. Paper presented at: 14th International Workshop on Breast Imaging (IWBI 2018)2018; Atlanta, GA.
3. Acciavatti RJ, Chang A, Woodbridge L, Maidment ADA. Optimizing the Acquisition Geometry for Digital Breast Tomosynthesis Using the Defrise Phantom. Paper presented at: SPIE Medical Imaging2014; San Diego, CA.
4. Acciavatti RJ, Mannherz W, Nolan M, Maidment ADA. An Alternate Design for the Defrise Phantom To Quantify Resolution in Digital Breast Tomosynthesis. Paper presented at: SPIE Medical Imaging2017; Orlando, FL.
5. Maidment TD, Vent TL, Ferris WS, Wurtele DE, Acciavatti RJ, Maidment ADA. Comparing the Imaging Performance of Computed Super Resolution and Magnification Tomosynthesis. Paper presented at: SPIE Medical Imaging2017; Orlando, FL.
6. Eben JE, Vent TL, Choi CJ, et al. Development of a Next Generation Tomosynthesis System. Paper presented at: SPIE Medical Imaging2018; Houston, TX.
7. Rodriguez-Ruiz A, Agasthya GA, Sechopoulos I. The compressed breast during mammography and breast tomosynthesis: in vivo shape characterization and modeling. *Physics in Medicine and Biology.* 2017;62:6920-6937.
8. Siewerdsen JH, Moseley DJ, Burch S, et al. Volume CT with a flat-panel detector on a mobile, isocentric C-arm: Pre-clinical investigation in guidance of minimally invasive surgery. *Medical Physics.* 2005;32(1):241-254.
9. Schafer S, Nithiananthan S, Mirota DJ, et al. Mobile C-arm cone-beam CT for guidance of spine surgery: Image quality, radiation dose, and integration with interventional guidance. *Medical Physics.* 2011;38(8):4563-4574.
10. Dang H, Stayman JW, Sisniega A, et al. Statistical reconstruction for cone-beam CT with a post-artifact-correction noise model: application to high-quality head imaging. *Physics in Medicine and Biology.* 2015;60:6153-6175.

11. Sisniega A, Zbijewski W, Xu J, et al. High-fidelity artifact correction for cone-beam CT imaging of the brain. *Physics in Medicine and Biology*. 2015;60:1415-1439.

12. Xu J, Sisniega A, Zbijewski W, et al. Modeling and design of a cone-beam CT head scanner using task-based imaging performance optimization. *Physics in Medicine and Biology*. 2016;61:3180-3207.

13. Ouadah S, Jacobson M, Stayman JW, Ehtiati T, Weiss C, Siewerdsen JH. Task-Driven Orbit Design and Implementation on a Robotic C-Arm System for Cone-Beam CT. Paper presented at: SPIE Medical Imaging2017; Orlando, FL.

14. Gang GJ, Stayman JW, Ehtiati T, Siewerdsen JH. Task-driven image acquisition and reconstruction in cone-beam CT. *Physics in Medicine and Biology*. 2015;60:3129-3150.

15. Acciavatti RJ, Rodriguez-Ruiz A, Vent TL, et al. Analysis of Volume Overestimation Artifacts in the Breast Outline Segmentation in Tomosynthesis. Paper presented at: SPIE Medical Imaging2018; Houston, TX.

16. Barufaldi B, Higginbotham D, Bakic PR, Maidment ADA. OpenVCT: A GPU-Accelerated Virtual Clinical Trial Pipeline for Mammography and Digital Breast Tomosynthesis. Paper presented at: SPIE Medical Imaging2018; Houston, TX.

17. Feng SSJ, Sechopoulos I. Clinical Digital Breast Tomosynthesis System: Dosimetric Characterization. *Radiology*. 2012;263(1):35-42.

18. Bakic PR, Ng S, Ringer P, Carton A-K, Conant EF, Maidment ADA. Validation and Optimization of Digital Breast Tomosynthesis Reconstruction using an Anthropomorphic Software Breast Phantom. Paper presented at: SPIE Medical Imaging2010; San Diego, CA.

19. Acciavatti RJ, Maidment ADA. Optimization of Continuous Tube Motion and Step-and-Shoot Motion in Digital Breast Tomosynthesis Systems with Patient Motion. Paper presented at: SPIE Medical Imaging2012; San Diego, CA.

20. Chan H-P, Goodsitt MM, Helvie MA, et al. Digital Breast Tomosynthesis: Observer Performance of Clustered Microcalcification Detection on Breast Phantom Images Acquired with an Experimental System Using Variable Scan Angles, Angular Increments, and Number of Projections Views. *Radiology*. 2014;273(3):675-685.

21. Pokrajac DD, Maidment ADA, Bakic PR. Optimized generation of high resolution breast anthropomorphic software phantoms. *Medical Physics*. 2012;39(4):2290-2302.

22. Chui JH, Pokrajac DD, Maidment ADA, Bakic PR. Towards Breast Anatomy Simulation Using GPUs. *Lecture Notes in Computer Science*. 2012;7361:506-513.

23. Bakic PR, Pokrajac DD, Caro RD, Maidment ADA. Realistic Simulation of Breast Tissue Microstructure in Software Anthropomorphic Phantoms. *Lecture Notes in Computer Science*. 2014;8539:348-355.

4A.

Automation of Virtual Clinical Trials Used to Evaluate Efficacy of Breast Cancer Screening Modalities

Brian-Tinh Vu[1, 2], Bruno Barufaldi[1], Trevor Vent[1], Raymond Acciavatti[1], Andrew Maidment[1].

[1] Department of Radiology, Perelman School of Medicine, University of Pennsylvania, Philadelphia, PA 19104, [2] Department of Physics, University of Houston, Houston, TX 77004

Clinical trials aimed at evaluating the relative efficacies of breast cancer screening modalities are often delayed by the need to recruit patients. Virtual clinical trials (VCTs) save time and cost by circumventing the need for patient recruitment while providing researchers the ability to finely control parameters of a virtual breast. *OpenVCT* has shown it can accurately simulate 2D and 3D breast screening modalities. In this study, the following steps of the *OpenVCT* pipeline were automated: lesion insertion, x-ray projection, 3D reconstruction, and isolation of regions of interest (ROIs) containing lesions. Automation of the pipeline removes the need for human presence during the experiments altogether. Digital mammography (DM), digital breast tomosynthesis (DBT), and synthetic 2D mammography (a 2D alternative to DM by processing 3D images from DBT) experiments were conducted with 36 phantoms; each phantom had differing tissue structure and was presented to the pipeline. From these, 1296 additional phantoms were generated, each with 42 equally-spaced calcifications (milk-like secretions) varying in lesion size (0.1-0.5 mm) and weighting fraction (how subtle the lesion appears) inserted in the breast's midplane. At the end of the automated pipeline 42 regions of interest containing calcifications were isolated from each phantom in preparation for model observers to generate the receiver operating characteristic curve, used for measuring true positive and false positive rates. This process took 4.28 days, or approximately 2.86 hours per phantom. The implementation and automation of *OpenVCT* in Python will further solidify its use as a cost- and time-saving tool in the evaluation of breast cancer x-ray imaging modality efficacy. The implementation of the pipeline's functions in Python, a high-level and open-source programming language, make them accessible to scientists without an extensive programming background. The automated pipeline currently is being used in the evaluation of efficacies of conventional DM, DBT, and synthetic 2D mammography.

5A.

High Resolution Profiling of EGFR Mutations in Glioblastoma Patients using an Ultrasensitive Digital PCR Approach

Sujay Ratna[1,2], Deeksha Saxena[1], Jay Dorsey[1]. [1]Department of Radiation Oncology, Smilow Center for Translational Research, Perelman School of Medicine, University of Pennsylvania, Philadelphia, PA 19104; [2]Rutgers University

Glioblastoma Multiforme (GBM) is the most aggressive adult brain cancer. The average survival time after GBM diagnosis is 14.6 months even with current trimodality therapy. In 57% of gliomas, the Epidermal Growth Factor Receptor, a tyrosine kinase gene, is amplified. Mutations such as EGFR variant III, A289V, and R108K lead to more aggressive & malignant tumors, and a lower survival time. We are in need of an assay that detects these mutations as soon as possible since other assays currently available in clinical workflows, like Next Generation Sequencing, may take up to 3-4 weeks. Our lab has established a very sensitive and novel digital Polymerase Chain

Robust Radiomic Feature Selection in Digital Mammography: Understanding the Effect of Imaging Acquisition Physics Using Phantom and Clinical Data Analysis

Raymond J. Acciavatti[1], Eric A. Cohen[1], Omid Haji Maghsoudi[1], Aimilia Gastounioti[1], Lauren Pantalone[1], Meng-Kang Hsieh[1], Emily F. Conant[1], Christopher G. Scott[2], Stacey J. Winham[2], Karla Kerlikowske[3], Celine Vachon[2], Andrew D. A. Maidment[1], Despina Kontos[1]
[1]University of Pennsylvania, Department of Radiology, 3400 Spruce Street, Philadelphia PA 19104
[2]Mayo Clinic, 200 First Street SW, Rochester MN 55905
[3]UCSF Women's Health Clinical Research Center, 550 16th Street, San Francisco CA 94143
E-mail: {Raymond.Acciavatti | Andrew.Maidment | Despina.Kontos}@pennmedicine.upenn.edu

ABSTRACT

Studies have shown that combining calculations of radiomic features with estimates of mammographic density results in an even better assessment of breast cancer risk than density alone. However, to ensure that risk assessment calculations are consistent across different imaging acquisition settings, it is important to identify features that are not overly sensitive to changes in these settings. In this study, digital mammography (DM) images of an anthropomorphic phantom ("Rachel", Gammex 169, Madison, WI) were acquired at various technique settings. We varied kV and mAs, which control contrast and noise, respectively. DM images in women with negative screening exams were also analyzed. Radiomic features were calculated in the raw ("FOR PROCESSING") DM images; i.e., grey-level histogram, co-occurrence, run length, fractal dimension, Gabor Wavelet, local binary pattern, Laws, and co-occurrence Laws features. For each feature, the range of variation across technique settings in phantom images was calculated. This range was scaled against the range of variation in the clinical distribution (specifically, the range corresponding to the middle 90% of the distribution). In order for a radiomic feature to be considered robust, this metric of imaging acquisition variation (IAV) should be as small as possible (approaching zero). An IAV threshold of 0.25 was proposed for the purpose of this study. Out of 341 features, 284 features (83%) met the threshold IAV $\leq$ 0.25. In conclusion, we have developed a method to identify robust radiomic features in DM.

Keywords: Radiomics, Digital Mammography, Robustness, Anthropomorphic Phantom, Risk Assessment, Breast Cancer.

1. INTRODUCTION

In digital mammography (DM), estimates of breast density can be complemented with radiomic feature calculations to provide an even better assessment of breast cancer risk than density alone.[1] The number of features used in these calculations is constantly growing, as new features continue to be introduced. However, having more features is not necessarily beneficial if many of the features are highly correlated with each other. Two examples of techniques that can be used to identify the uncorrelated features include cluster analysis and principal component analysis.[2-10]

In addition to these two techniques, previous works have also shown that features can be selected based on their robustness to imaging acquisition parameters. The goal is to identify features that are not overly sensitive to small variations in contrast, noise, and image sharpness. Instead, it is important to select features that capture underlying breast parenchymal patterns, which could be suggestive of breast cancer risk. One way to identify robust features is to consider their variation across vendors. In the work by Keller *et al*., robust features were identified by acquiring images of an anthropomorphic phantom with three DM systems.[11] Each image was *Z*-score normalized, and feature distributions across vendors were analyzed with equivalence tests. Keller *et al*. showed that histogram and structural features, such as fractal dimension, tended to be robust across vendors.

Medical Imaging 2020: Computer-Aided Diagnosis, edited by Horst K. Hahn, Maciej A. Mazurowski, Proc. of SPIE Vol. 11314, 113140W · © 2020 SPIE
CCC code: 1605-7422/20/$21 · doi: 10.1117/12.2549163

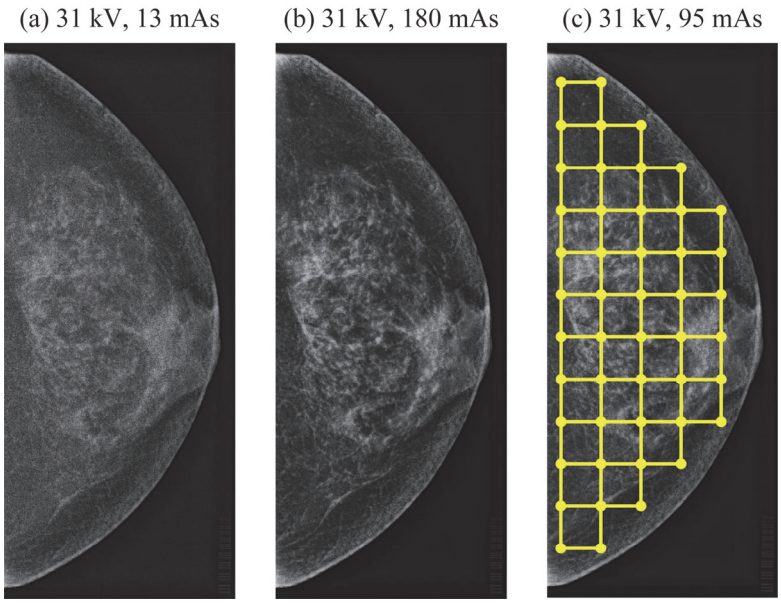

Figure 1. Increasing mAs reduces noise. The auto-time image in (c) illustrates the lattice used for radiomic feature calculations.

Alternatively, robust features can be identified based on clinical data; for example, more recently Mendel *et al*. analyzed data obtained from women imaged at different time points with different DM vendors.[12] Based on calculations of correlations across vendors, features describing spatial patterns were found to be robust; in accord with the work of Keller *et al*.[11], fractal dimension was included among the robust features. In a follow-up study, this analysis was applied in combination with hierarchical clustering to identify features that were both robust and non-redundant.[10]

In this paper, DM images of an anthropomorphic phantom are calculated at various technique settings (kV and mAs), and 341 radiomic features are analyzed in terms of their sensitivity to these settings. These two settings control the contrast and noise, respectively. Our method for identifying robust features is unique in that we analyze phantom data in combination with clinical data. Specifically, we measure how much the variation across technique settings scales against the variation seen in a negative screening population. In order for a feature to be considered robust, the variation across technique settings should be small. We propose a criterion for selecting robust features based on an analysis of sensitivity to changes in the technique settings.

2. METHODS

2.1 Phantom Image Acquisitions

DM images of an anthropomorphic phantom[13] ("Rachel", Gammex 169, Madison, WI) were acquired using a Selenia Dimensions system (Hologic Inc., Bedford, MA) with a W/Rh target-filter combination and cranial-caudal (CC) views (Figure 1). Multiple images were acquired at different technique settings. First, kV was varied (27 to 35 in increments of 1 kV) with mAs at each kV determined by auto-timing (Figure 2). Second, kV was fixed at 31 and mAs was varied from 13 to 180 mAs. The mAs increments were all varied approximately by a factor of $2^{1/2}$ based on the closest mAs setting supported by the system. Two images were acquired at each technique setting. The phantom was in the same position for all acquisitions.

2.2 Overview of Clinical Data Set

In addition, raw ("FOR PROCESSING") DM images of 1,000 women with negative screening exams between 9/1/14 and 12/31/14 were analyzed. These included 46% African American and 44% Caucasian women (in the remaining 10% of patients, ethnicity was unknown). The images were acquired at the Hospital of the University of Pennsylvania using Selenia Dimensions systems. This research was approved by the Institutional Review Board at the University of Pennsylvania and was compliant with the Health Insurance Portability and Accountability Act (HIPAA). Because the phantom is representative of a CC view, the clinical image analysis was restricted to CC views.

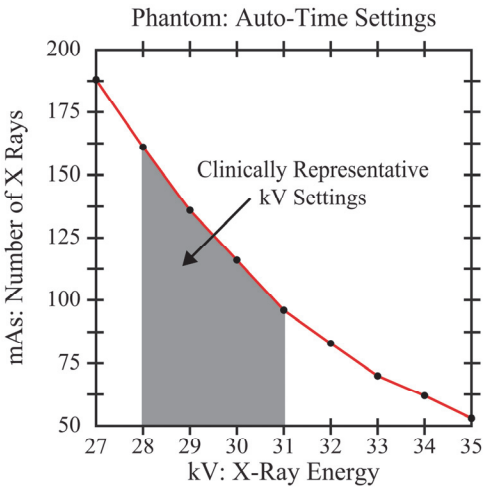

Figure 2. The mAs controls the number of x-ray photons. At high kV, there is greater x-ray penetration and hence mAs is reduced.

2.3 Radiomic Feature Extraction

The first step in radiomic feature extraction was to segment the breast area from background with LIBRA (Laboratory for Breast Radiodensity Assessment), an automated software tool.[14] From the raw ("FOR PROCESSING") DM images, 341 radiomic features were calculated. This included eight families of features: grey-level histogram, *i.e.*, 12 statistics derived from the histogram of the image; co-occurrence, *i.e.*, 7 measures of spatial relationships among grey levels; run length, *i.e.*, 7 measures of texture coarseness; fractal dimension, *i.e.*, 2 measures of self-similarity; local binary pattern (LBP), *i.e.*, 36 measures of intensity variation comparing a central pixel against its neighbors; Laws, *i.e.*, 125 grey-level histogram features derived from the convolution of the image with a 5 × 5 kernel; Co-occurrence Laws, *i.e.*, 120 co-occurrence features derived from the convolution of the image with a 5 × 5 kernel; and Gabor Wavelet, *i.e.*, 32 features measuring image details at different scales and orientations.[15-19]

From the raw ("FOR PROCESSING") DM images, these 341 features were calculated by partitioning the segmented breast area into a regular grid (lattice) of square windows [Figure 1(c)]. For a given feature, the feature value was calculated within every window, and then these values were averaged over all windows to provide a single image-wise value for that feature. The use of a lattice for calculating texture features is motivated by previous work which demonstrated that that this approach yields higher area under the curve (AUC) in receiver-operating-characteristic (ROC) experiments in case-control classification than the use of a single region-of-interest (ROI), such as a central or retroareolar ROI.[1]

All radiomic feature calculations were done with a 6.3 mm window size. This value was chosen based on previous work, which analyzed the effect of varying the window size (between 6.3 and 25.5 mm). Zheng *et al*. showed that ROC performance in case-control classification is optimized by the use of a 6.3 mm window size.[1]

2.4 Robustness Analysis

Previous work has shown that radiomic features are dependent on breast thickness under compression.[20] For this reason, we focused specifically on the subset of clinical data with comparable thickness (± 10 mm) to the phantom (50.0 mm thick). For a given feature, the range of values obtained in this subset of the clinical data was *Z*-score normalized, and the same normalization was applied to the phantom.

Table 1. In the phantom acquisitions, there were six settings within the range seen clinically in women with 40-60 mm thickness.

kV	Clinical mAs Range	Phantom mAs Settings
28	[56, 228]	160
29	[63, 277]	140
30	[81, 386]	120
31	[102, 311]	120, 140, 180

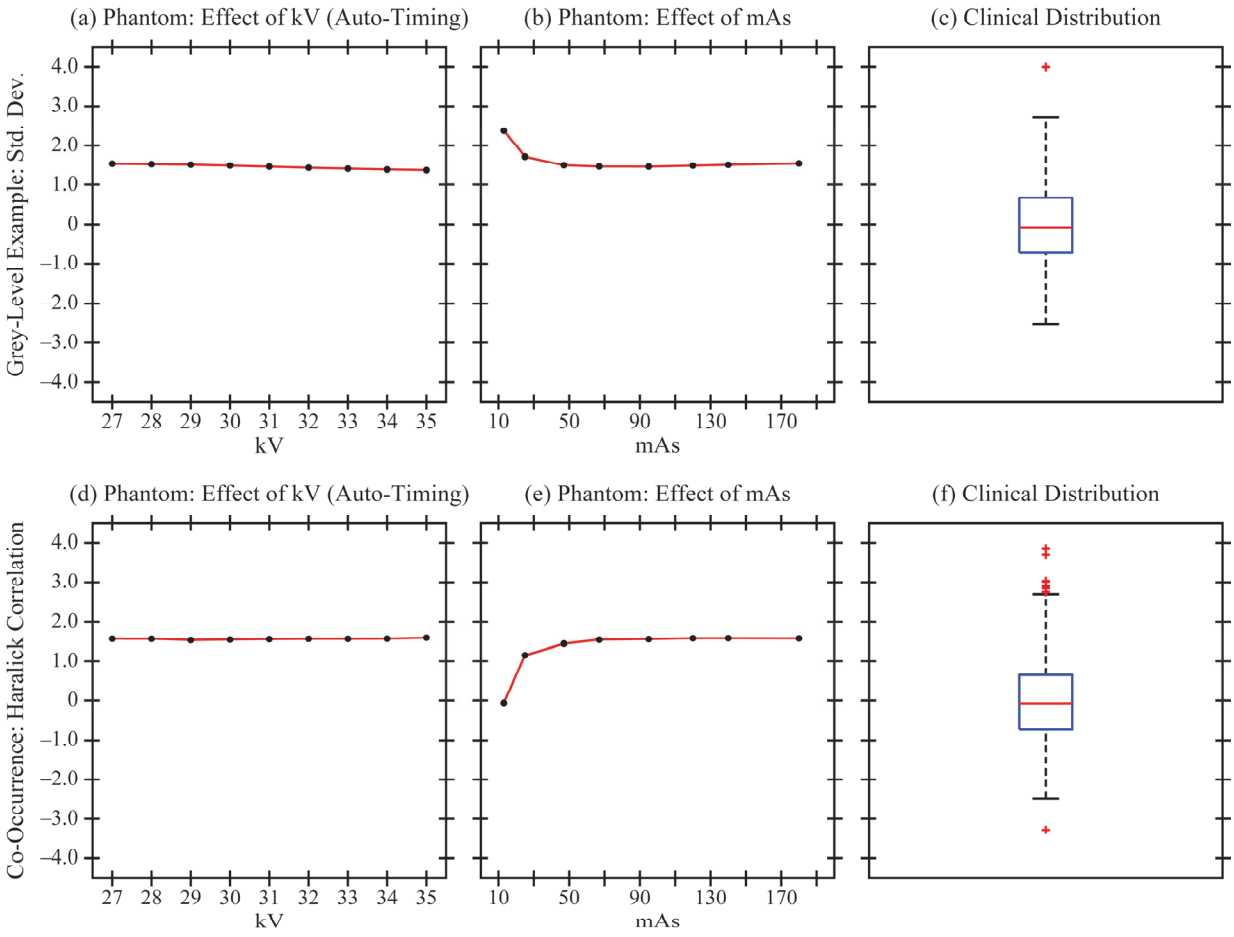

Figure 3. In robust features, the variation across kV and mAs settings is small compared against the range of the clinical distribution.

We initially analyzed how each feature varied as a function of kV and mAs in the phantom acquisitions (Figures 3-4). However, to develop a robustness metric for feature selection, we subsequently restricted the technique settings in the phantom acquisitions to those consistent with women with 40-60 mm thickness (± 10 mm relative to the phantom). This included six combinations of kV and mAs (Table 1). Since each technique setting was repeated twice, there were 12 acquisitions in this analysis. Restricting the technique settings in this manner ensured that measures of robustness did not include extreme settings which would not be representative of those used clinically.

Denoting $P_j = \{p_{ij}\}_{i=1}^{12}$ as the set of feature values in 12 phantom acquisitions for the j^{th} feature, the imaging acquisition variation (IAV) was then defined as

$$\text{IAV} = \frac{\max P_j - \min P_j}{c_{95,j} - c_{5,j}}, \qquad j \in [1,341], \tag{1}$$

where $c_{95,j}$ and $c_{5,j}$ denote the 95th and 5th percentile of the clinical distribution for the j^{th} feature, respectively. In Eq. (1), the range of variation across technique settings is scaled against the spread in the clinical distribution. Since the tails of the clinical distribution could be sensitive to outliers, we measure the spread in terms of the middle 90% of this distribution. In a robust feature, the range of values across technique settings, in a single phantom, should be small compared to the range of values in a population having broadly varying parenchymal patterns.

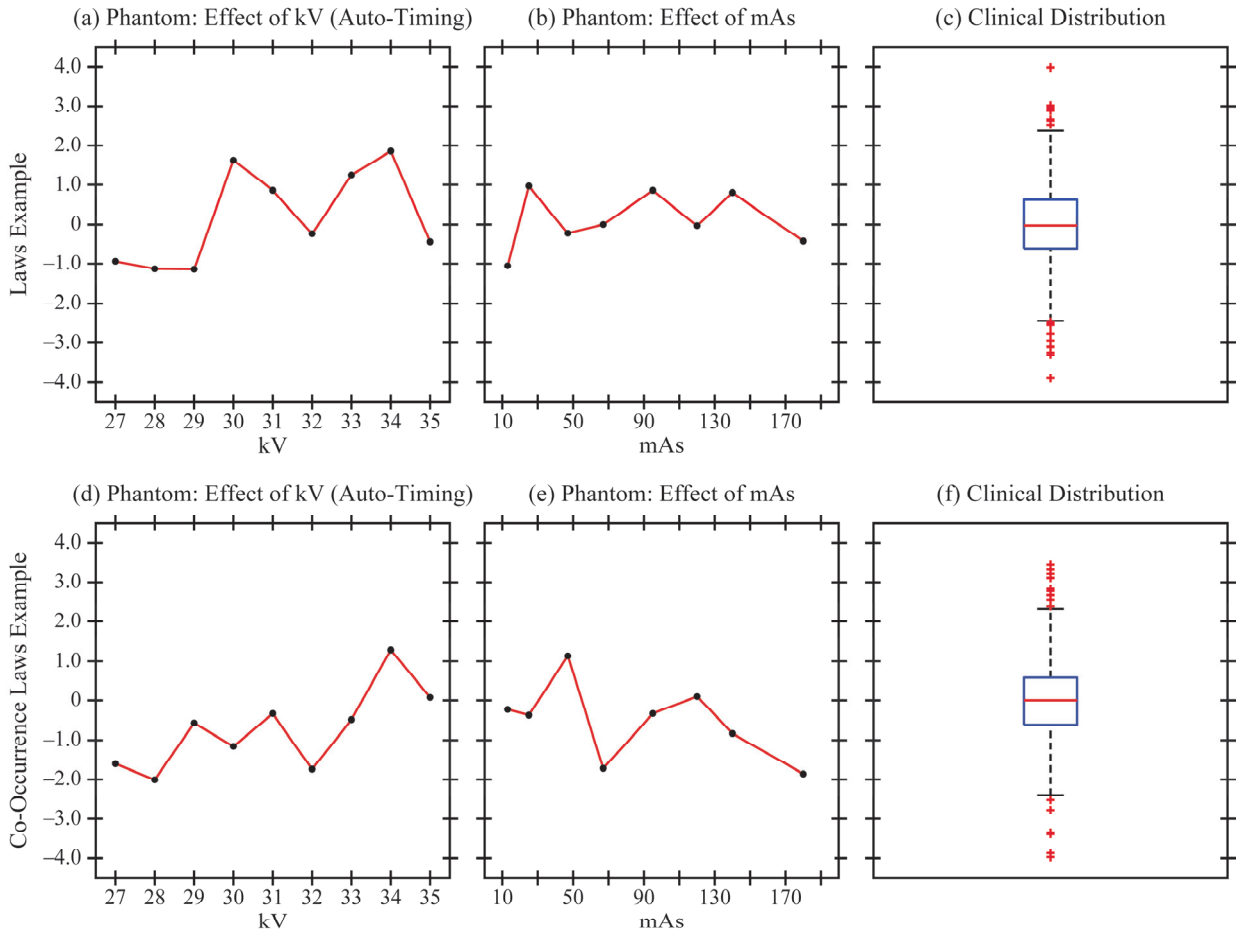

Figure 4. Unlike the robust features shown in Figure 3, the variation across kV and mAs settings is much larger in these Laws and co-occurrence Laws features. Also, the trends versus kV and mAs are not monotonic. For these reasons, the two features shown here are examples of nonrobust features.

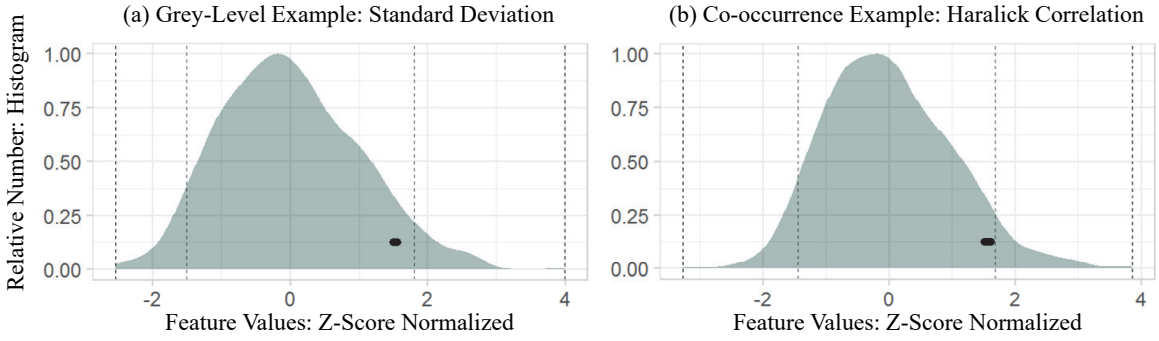

Figure 5. For each feature, the data points obtained from the phantom at different technique settings were compared against the clinical distribution, yielding a measure of imaging acquisition variation (IAV). The data points show little variation relative to the clinical distribution, and hence these are two examples of robust features. The 5th and 95th percentiles of the clinical distribution are denoted by the thin dashed vertical lines.

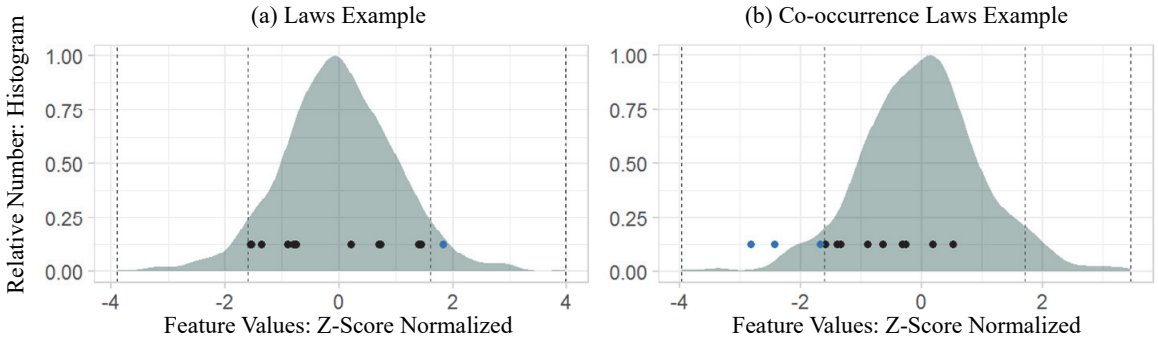

Figure 6. The 12 data points, corresponding to various phantom acquisitions, vary much more broadly than Figure 5. Also, some data points (in blue) extend beyond the 5th or 95th percentile of the clinical distribution (thin dashed vertical lines).

3. RESULTS

3.1 Effect of Varying kV and mAs in Phantom Acquisitions

First, we analyzed the full range of kV and mAs settings in the phantom acquisitions (Figures 3-4). Since the phantom was imaged twice at each setting, we averaged the results at each setting for the purpose of these plots. Two examples of features that are robust to changes in technique settings are shown in Figure 3: a grey-level feature (standard deviation) and a co-occurrence feature (Haralick correlation). The range of variation is small compared against the clinical distribution. By contrast, two examples of features that are sensitive to changes in acquisition settings are shown in Figure 4: Laws and co-occurrence Laws features. In Figure 4, the trends versus kV and mAs are not monotonic.

3.2 Calculation of Robustness Scores for Each Feature

To calculate IAV for each feature, the 12 values derived from phantom acquisitions were analyzed in conjunction with the clinical distribution. In robust features, the 12 data points are clustered within a small range of values compared against the clinical distribution (Figure 5). For the grey-level and co-occurrence features described previously as examples of robust features, the IAV scores are 0.0183 and 0.0309, respectively (approaching zero).

By contrast, some features vary much more broadly with kV and mAs, and thus are much more sensitive to small changes in noise and contrast. These features have higher IAV scores, specifically 1.05 and 1.01 for the Laws and co-occurrence Laws features described previously as examples of nonrobust features (Figure 6).

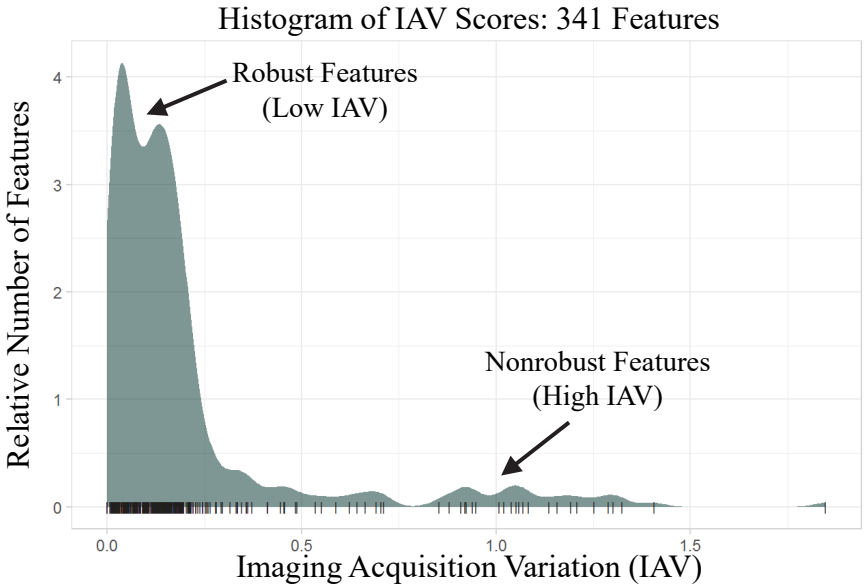

Figure 7. Imaging acquisition variation (IAV) scores determined by Eq. (1) can be used to identify robust features.

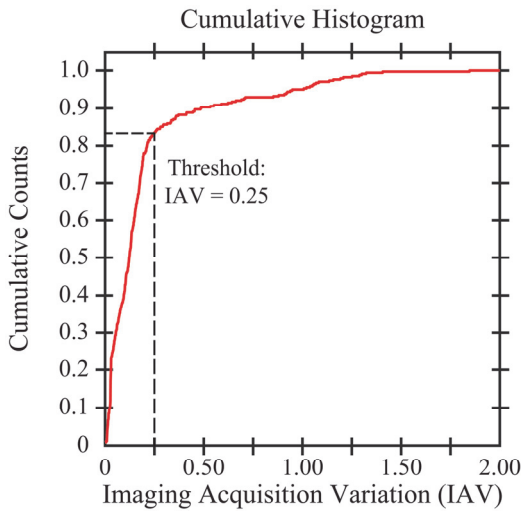

Figure 8. In the cumulative histogram of IAV scores, the curve rises sharply up to an IAV of 0.25. At this threshold, 284 features out of 341 (83%) are considered robust (IAV ≤ 0.25).

Results for all 341 features can be summarized in terms of the histogram of IAV scores (Figure 7). Most IAV scores are clustered around zero, corresponding to robust features. There is an extended tail corresponding to features with high IAV scores. The maximum IAV score is 1.85.

A threshold for identifying robust features can be introduced based on the cumulative histogram of IAV scores (Figure 8). The cumulative histogram peaks sharply up to an IAV of 0.25. Above this value, the curvature starts to change. This curvature suggests that an IAV score of 0.25 can be used as a threshold for identifying robust features. Out of 341 features, 284 features (83%) meet the threshold IAV ≤ 0.25.

3.3 Analysis of Eight Feature Families

Next, the IAV scores were analyzed separately in each of the eight feature families (Figure 9). In five families out of eight, all features met the threshold IAV ≤ 0.25; namely, grey-level histogram, co-occurrence, run length, Gabor Wavelet, and fractal dimension. The three remaining feature families included a combination of robust and nonrobust features. Specifically, 81% of LBP features (29 out of 36), 73% of Laws features (91 out of 125), and 87% of co-occurrence Laws features (104 out of 120) can be considered robust.

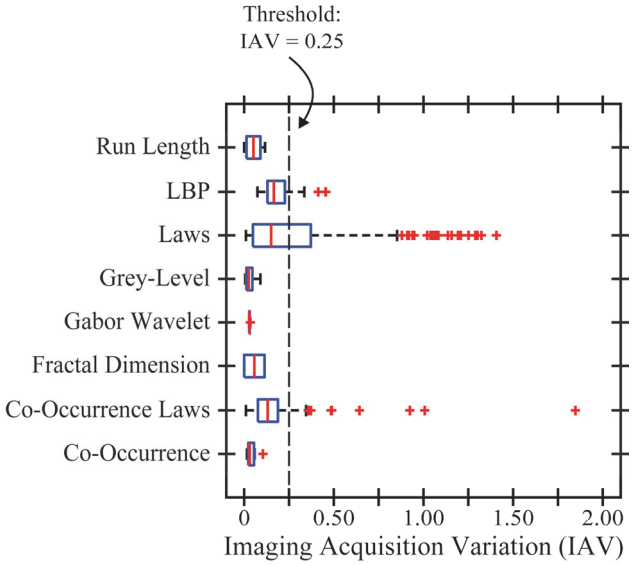

Figure 9. The features that fail to meet the threshold for robustness (IAV ≤ 0.25) come from three families: LBP, Laws, and co-occurrence Laws.

4. DISCUSSION AND CONCLUSION

Although it is not possible to acquire x-ray images of a patient with numerous technique settings, it is indeed possible to perform these experiments with an anthropomorphic phantom. The phantom used in this study was based off an actual woman's mammogram[13], and hence these x-ray experiments were equivalent to imaging the same woman under various technique settings. Since the underlying texture of the phantom was fixed, robust features were identified under the assumption that variation across technique settings should be small.

In a previous study, Mendel *et al*. identified robust features based on a data set of women imaged separately with two DM vendors.[12] They showed, for example, that measures of fractal dimension are robust. The results of this study are consistent with that finding (Figure 9). Our approach for identifying robust features is unique in that we analyze phantom and clinical data in combination; this allows the effect of imaging acquisition physics to be measured relative to the spread of values in a clinical population.

In our future work, we will investigate whether features selected based on a robustness criterion offer better ROC performance in case-control classification with an independent data set. Another point of future investigation is to study the effect of image processing on the robustness of the features. For the purpose of this study, only raw ("FOR PROCESSING") DM images were analyzed.

5. ACKNOWLEDGEMENT

Support was provided by the following grants: R01CA207084 and U54CA163313 from the National Institute of Health, W81XWH-18-1-0082 from the Department of Defense Breast Cancer Research Program, and PDF17479714 from Susan G. Komen®. The content is solely the responsibility of the authors and does not necessarily represent the official views of the funding agencies.

ADAM receives research support from Hologic Inc., Barco NV, and Analogic Corporation. Also, ADAM is a shareholder and member of the scientific advisory board of Real Time Tomography, LLC. EFC receives grant support and is part of the advisory panel of Hologic Inc. EFC also receives grant support and is part of the advisory panel of iCAD Inc.

6. REFERENCES

1. Zheng Y, Keller BM, Ray S, et al. Parenchymal texture analysis in digital mammography: A fully automated pipeline for breast cancer risk assessment. *Medical Physics.* 2015;42(7):4149-4160.
2. Balagurunathan Y, Kumar V, Gu Y, et al. Test–Retest Reproducibility Analysis of Lung CT Image Features. *Journal of Digital Imaging.* 2014;27:805-823.
3. Zhang Y, Oikonomou A, Wong A, Haider MA, Khalvati F. Radiomics-based Prognosis Analysis for Non-Small Cell Lung Cancer. *Scientific Reports.* 2017;7:46349.
4. Parmar C, Grossmann P, Bussink J, Lambin P, Aerts HJWL. Machine Learning methods for Quantitative Radiomic Biomarkers. *Scientific Reports.* 2015;5:13087.
5. Rizzo S, Botta F, Raimondi S, et al. Radiomics of high-grade serous ovarian cancer: association between quantitative CT features, residual tumour and disease progression within 12 months. *European Radiology.* 2018;28(11):4849-4859.
6. Huynh E, Coroller TP, Narayan V, et al. Associations of Radiomic Data Extracted from Static and Respiratory-Gated CT Scans with Disease Recurrence in Lung Cancer Patients Treated with SBRT. *PLoS One.* 2017;12(1):e0169172.
7. Wilkinson L, Friendly M. The History of the Cluster Heat Map. *The American Statistician.* 2009;63(2):179-184.
8. Rizzo S, Botta F, Raimondi S, et al. Radiomics: the facts and the challenges of image analysis. *European Radiology Experimental.* 2018;2:36.
9. Yousefi B, Jahani N, LaRiviere MJ, et al. Correlative Hierarchical Clustering-based Low-Rank dimensionality reduction of radiomics-driven phenotype in Non-Small Cell Lung Cancer. Paper presented at: SPIE Medical Imaging2019; San Diego, CA.

10. Robinson K, Li H, Lan L, Schacht D, Giger M. Radiomics robustness assessment and classification evaluation: A two-stage method demonstrated on multivendor FFDM. *Medical Physics.* 2019;46(5):2145-2156.

11. Keller BM, Oustimov A, Wang Y, et al. Parenchymal texture analysis in digital mammography: robust texture feature identification and equivalence across devices. *Journal of Medical Imaging.* 2015;2(2):024501-024501 - 024501-024513.

12. Mendel KR, Li H, Lan L, et al. Quantitative texture analysis: robustness of radiomics across two digital mammography manufacturers' systems. *Journal of Medical Imaging.* 2018;5(1):011002-011001 - 011002-011009.

13. Yaffe MJ, Johns PC, Nishikawa RM, Mawdsley GE, Caldwell CB. Anthropomorphic radiologic phantoms. *Radiology.* 1986;158(2):550-552.

14. Keller BM, Nathan DL, Wang Y, et al. Estimation of breast percent density in raw and processed full field digital mammography images via adaptive fuzzy c-means clustering and support vector machine segmentation. *Medical Physics.* 2012;39(8):4903-4917.

15. Haralick RM, Shanmugam K, Dinstein IH. Textural Features for Image Classification. *IEEE Transactions on Systems, Man, and Cybernetics.* 1973;SMC-3(6):610-621.

16. Galloway MM. Texture analysis using gray level run lengths. *Computer Graphics and Image Processing.* 1975;4(2):172-179.

17. Chu A, Sehgal CM, Greenleaf JF. Use of gray value distribution of run lengths for texture analysis. *Pattern Recognition Letters.* 1990;11(6):415-419.

18. Ojala T, Pietikäinen M, Mäenpää T. Multiresolution Gray-Scale and Rotation Invariant Texture Classification with Local Binary Patterns. *IEEE Transactions on Pattern Analysis and Machine Intelligence.* 2002;24(7):971-987.

19. Manduca A, Carston MJ, Heine JJ, et al. Texture Features from Mammographic Images and Risk of Breast Cancer. *Cancer Epidemiology, Biomarkers & Prevention.* 2009;18(3):837-845.

20. Acciavatti RJ, Hsieh M-K, Gastounioti A, et al. Validation of the Textural Realism of a 3D Anthropomorphic Phantom for Digital Breast Tomosynthesis. Paper presented at: 14th International Workshop on Breast Imaging (IWBI 2018)2018; Atlanta, GA.

Proposing Rapid Source Pulsing for Improved Super-Resolution in Digital Breast Tomosynthesis

Raymond J. Acciavatti[1], Trevor L. Vent[1], Bruno Barufaldi[1], E. Paul Wileyto[2],
Peter B. Noël[1], Andrew D. A. Maidment[1]
[1]University of Pennsylvania, Department of Radiology, 3400 Spruce Street, Philadelphia PA 19104
[2]University of Pennsylvania, Department of Epidemiology, Biostatistics, & Informatics,
423 Guardian Drive, Philadelphia, PA 19104
E-mail: {Raymond.Acciavatti | Trevor.Vent | Bruno.Barufaldi | epw |
Peter.Noel | Andrew.Maidment}@pennmedicine.upenn.edu

ABSTRACT

Our previous work showed that digital breast tomosynthesis (DBT) systems are capable of super-resolution, or subpixel resolution relative to the detector. Using a bar pattern phantom, it is possible to demonstrate that there are anisotropies in super-resolution throughout the reconstruction. These anisotropies are lessened in acquisition geometries with narrow spacing between source positions. This paper demonstrates that by re-arranging the source positions in the scan, the anisotropies can be minimized even further. To this end, a theoretical model of the reconstruction of a high-frequency sinusoidal test object was developed from first principles. We modeled the effect of clustering additional source positions around each conventional source position in fine increments (submillimeter). This design can be implemented by rapidly pulsing the source during a continuous sweep of the x-ray tube. It is shown that it is not possible to eliminate the anisotropies in a conventional DBT system with uniformly-spaced source positions, even if the increments of spacing are narrower than those used clinically. However, super-resolution can be achieved everywhere if the source positions are re-arranged in clusters with submillimeter spacing. Our previous work investigated a different approach for optimizing super-resolution through the use of detector motion perpendicular to the breast support. The advantage of introducing rapid source pulsing is that detector motion is no longer required; this mitigates the need for a thick detector housing, which may be cumbersome for patient positioning.

Keywords: Digital Breast Tomosynthesis, Mammography, Super-Resolution, Aliasing, Fourier Transform, Digital Imaging, Image Quality, Image Reconstruction.

1. INTRODUCTION

1.1 Review of Previous Work

Our previous work showed that it is possible to improve the visualization of subtle findings in digital breast tomosynthesis (DBT), such as calcifications, based on the principle of super-resolution.[1,2] This can be demonstrated with a bar pattern phantom. By preparing a DBT reconstruction with finer pixelation than the detector, we found that test frequencies exceeding the alias frequency of the detector can be resolved.

We have also shown that super-resolution in DBT is not achieved uniformly throughout the image.[2,3] There are anisotropies in regularly-spaced increments (z), corresponding to various slices in the reconstruction. These anisotropies can be visualized with a clinical DBT system by using a goniometry stand to angle a bar pattern phantom in an oblique plane. In our previous work, the reconstruction plane was tilted to match this angle.[3] This setup allowed for assessment of image resolution over a continuous range of z-coordinates (distance perpendicular to the breast support).

With theoretical modeling, we also analyzed how the number of anisotropies is dependent on the angular range of the scan. In a wide-range DBT scan, there are more anisotropies in a given volume.[3] This idea can be illustrated with an oblique reconstruction of the bar pattern phantom described previously (Figures 1-2). For these experiments, we used the Selenia Dimensions system (Hologic Inc., Bedford, MA, USA) with 15 projections, and we considered a test frequency of 5.0 mm^{-1}, since this exceeds the alias frequency (3.6 mm^{-1}) of the Hologic detector with 0.140 mm pixelation. Reconstructions were created with different subsets of projections, varying in terms of the spacing between

Medical Imaging 2020: Physics of Medical Imaging, edited by Guang-Hong Chen, Hilde Bosmans, Proc. of SPIE
Vol. 11312, 113125G · © 2020 SPIE · CCC code: 1605-7422/20/$21 · doi: 10.1117/12.2542551

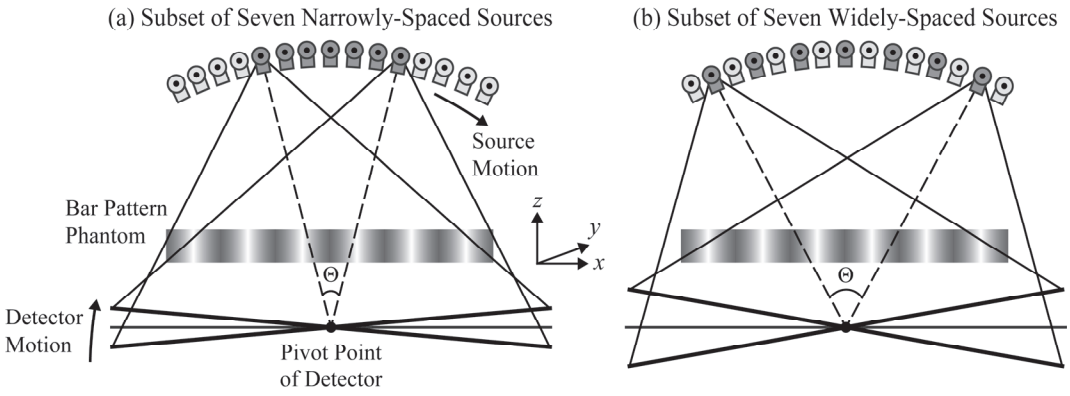

Figure 1. Shown are two different subsets of seven projections (dark grey), varying in terms of spacing between source positions.

source positions. The subset of seven projections with 1.07° spacing was analyzed as a surrogate for a narrow-range DBT scan [Figure 1(a)], while the subset of seven projections with 2.14° spacing was analyzed as a surrogate for a wide-range DBT scan [Figure 1(b)].

The reconstructions were prepared with Piccolo™ (Real Time Tomography, LLC, Villanova, PA), a software that allows the user to tilt the reconstruction plane to match the plane of the bar pattern phantom.[4] Super-resolution is not achieved everywhere; the aliasing artifacts are denoted by the arrows (Figure 2). There are more anisotropies in the acquisition with the wider angular range. More specifically, in the *z* direction, there is 6 mm spacing between anisotropies in the scan with 1.07° spacing between projections [Figure 2(a)], and there is 3 mm spacing between anisotropies in the scan with 2.14° spacing between projections [Figure 2(b)].

1.2 Overview of Anti-Aliasing Strategies

This paper explores how many of the anti-aliasing strategies that guided the evolution of computed tomography (CT) scanners can be applied to the design of DBT systems. One such strategy is focal spot wobble.[5] This strategy has been used in some third-generation CT scanners. After the gantry has rotated by half of a pixel, the x-ray source position is translated back half of a pixel, so that pairs of rays are created with the same source position but where the detector location differs by half the detector's width. This effectively doubles the sampling rate and provides anti-aliasing. This paper demonstrates that a similar strategy can be applied to DBT; however, here the detector position is stationary and the x-ray source is moved by approximately half a detector element referenced to the mid-plane of the breast. Specifically, we show that introducing fine (submillimeter) motions of the source between projections results in an improvement in resolution, and aliasing artifacts are eliminated. Anisotropies are no longer present throughout the reconstruction.

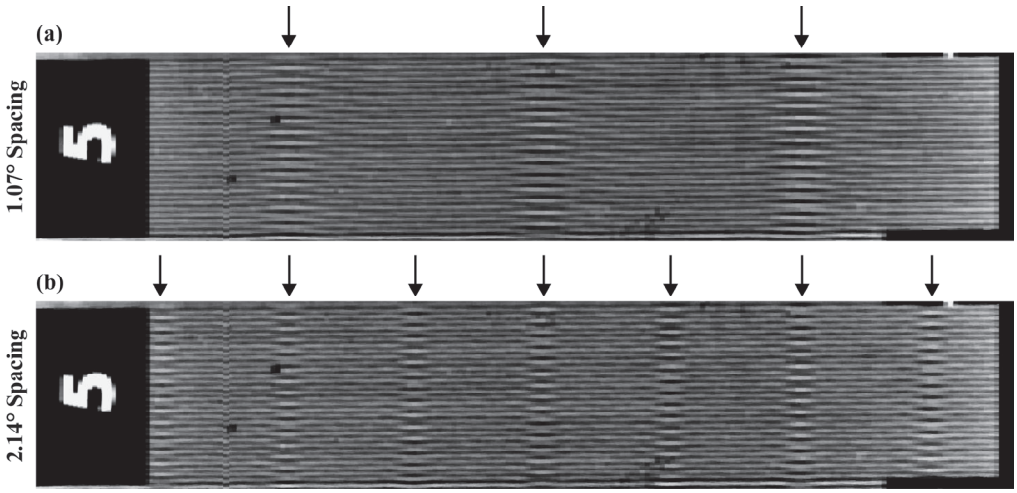

Figure 2. There are fewer aliasing artifacts (denoted by the arrows) in the scan with narrowly-spaced source positions.

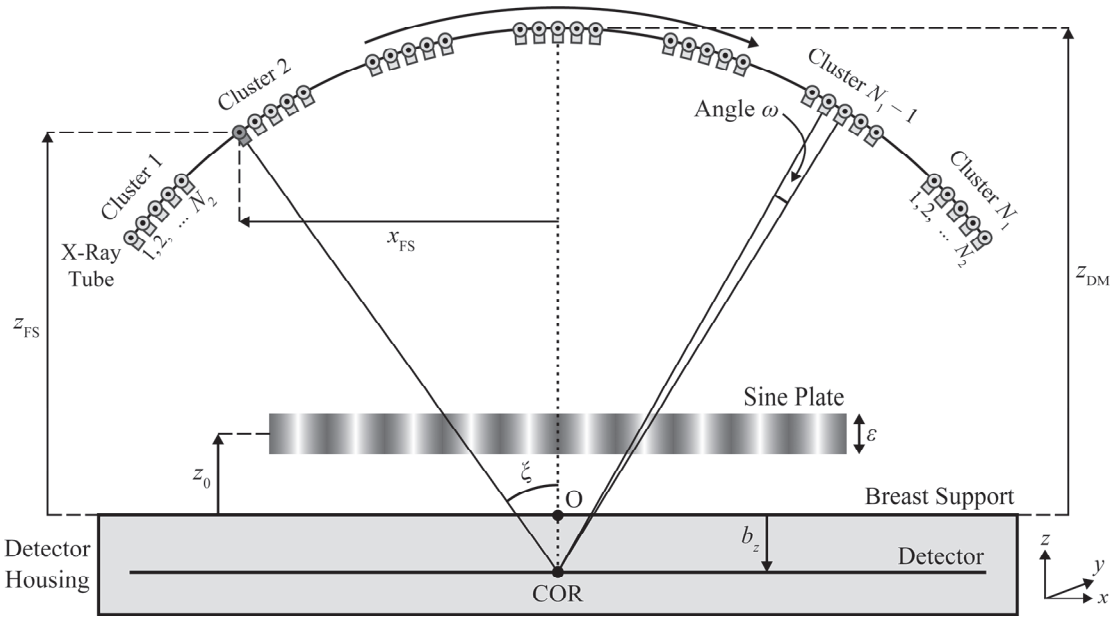

Figure 3. A DBT system design with clustered source positions is modeled. The parameter N_1 controls the number of clusters, while the parameter N_2 controls the number of source positions per cluster. In this example, $N_1 = 7$ and $N_2 = 5$.

Another strategy for improving resolution and hence reducing aliasing in CT is to increase the number of projections. The minimum number of projections needed to avoid aliasing can be understood from the formula

$$N_{\min} = \frac{4\pi R \nu_M}{1 - \sin(\psi / 2)}, \tag{1}$$

where ν_M is frequency, ψ is fan angle, and R is the radius over which the frequency ν_M can be resolved without aliasing, assuming source rotation over a 360° arc.[6] This paper demonstrates that in DBT, there is also a resolution gain achieved by increasing the number of projections. Although the DBT system is modeled with a larger number of projections than those used clinically, the radiation dose per projection can be reduced so that the total dose of the scan is unchanged.

2. METHODS

2.1 Simulated Acquisition Geometry

In clinical DBT systems, the source rotates in a circular arc in the chest-wall plane, and the projection images are acquired at a constant angular spacing.[7,8] In this paper, we re-arrange the source positions in clusters (Figure 3). Within each cluster, there is very fine (submillimeter) spacing between source positions; this spacing is denoted by the angle ω. We assume that there are N_1 clusters and N_2 positions per cluster. Hence the total number of projections (N_t) is given by the product

$$N_t = N_1 \times N_2 . \tag{2}$$

The center-of-rotation (COR) of the source motion is treated as the midpoint of the detector. The detector is taken to be stationary during the scan, unlike the Selenia Dimensions system (Figure 1). The source coordinate (x_{FS}, y_{FS}, z_{FS}) at an arbitrary point in the arc can be written in terms of the projection angle ξ.

$$x_{FS} = (z_{DM} - b_z)\sin\xi , \quad y_{FS} = 0 , \quad z_{FS} = (z_{DM} - b_z)\cos\xi + b_z \tag{3}$$

The origin of this coordinate system (point O) is the midpoint of the breast support directly above the COR (at distance b_z). Also, z_{DM} denotes the z-coordinate of the central source position; the subscript "DM" emphasizes that this source position is the same as the one used in digital mammography, the conventional 2D modality for breast cancer screening. The y-coordinate of the source (not shown in Figure 3) is zero for all projections, since there is no source motion perpendicular to the chest-wall plane (into the plane of the page).

Table 1. The simulation parameters for the test object and acquisition geometry are summarized below.

Parameter	Value
Distance z_{DM}: Breast Support to Source	625.0 mm
Distance b_z: Breast Support to Detector	–25.0 mm
N_t: Total Number of Projections	60
Increment ω: Angular Spacing	0.05°
Detector Pixel Size	0.085 mm × 0.085 mm
Thickness (ε) of Test Object	0.50 mm
Frequency of Test Object	8.0 mm^{-1}
Fourier Sampling: J_{FT}	1,000
x''_{min}: Lower Endpoint of Fourier Transform	–3.125 mm
x''_{max}: Upper Endpoint of Fourier Transform	3.125 mm

Going from left to right in Figure 3, each source position can be numbered with an integer (n) between 1 and N_t. Assuming that there is equal spacing between clusters, it can be shown that

$$\xi = \frac{\left(2n' - N_1 - 1\right)\left[\Theta - \omega\left(N_2 - 1\right)\right]}{2\left(N_1 - 1\right)} + \left(n'' - \frac{N_2 + 1}{2}\right)\omega\,, \tag{4}$$

where Θ denotes the total angular range of the scan (Figure 1) and where

$$n' = 1 + \left\lfloor \frac{n-1}{N_2} \right\rfloor, \quad n'' = n - N_2 \left\lfloor \frac{n-1}{N_2} \right\rfloor, \quad \lfloor v_1 \rfloor \equiv \max\left\{v_2 \in \mathbb{Z} : v_2 \le v_1\right\}. \tag{5}$$

In Eq. (5), the symbol $\lfloor\ \rfloor$ denotes the floor function.

2.2 Theoretical Model of Super-Resolution

In our previous work, we modeled the reconstruction of a sine plate to analyze super-resolution (Figure 3).[3] This object is a thin rectangular prism (thickness ε) with a sinusoidal attenuation coefficient, μ. In this paper, the simple backprojection (SBP) reconstruction of this object is analyzed in an acquisition geometry based off the "next-generation" tomosynthesis (NGT) system, a DBT system constructed for research use at the University of Pennsylvania (Table 1).[9]

For analysis of super-resolution, a test frequency of 8.0 mm^{-1} is chosen, since this frequency is higher than the alias frequency of the detector (5.9 mm^{-1}) used in the NGT system. To determine how well the input frequency is resolved, the Fourier transform of the reconstruction (μ_{SBP}) is calculated with the midpoint formula for integration

$$\mathcal{F}_1\mu_{SBP} \approx \left(\frac{x''_{max} - x''_{min}}{J_{FT}}\right)\sum_{j_{FT}=1}^{J_{FT}} \mu_{SBP} e^{-2\pi i f_x'' x''}\Big|_{x''=x''_{min}+(x''_{max}-x''_{min})\left(\frac{j_{FT}-1/2}{J_{FT}}\right)}, \tag{6}$$

where x'' is position measured in the x direction relative to the point of interest, x''_{min} and x''_{max} are the integration limits, and J_{FT} is the number of samples.

The r-factor, a metric proposed in our previous work, is calculated to summarize the results in Fourier space.[2,3] To illustrate this metric in the conventional acquisition geometry ($\Theta = 20°$, $N_t = 15$), reconstructions at two z-coordinates in the chest-wall plane are shown (Figure 4). At the coordinate demonstrating super-resolution [Figure 4(a)-(b)], the Fourier transform has a major peak at the input frequency, 8.0 mm^{-1}. By contrast, at the coordinate exhibiting aliasing [Figure 4(c)-(d)], the major peak is at a lower frequency (4.3 mm^{-1}). The r-factor is the ratio of the amplitude of the highest peak less than the alias frequency (5.9 mm^{-1}) to the amplitude at the input frequency (8.0 mm^{-1}); *i.e.*, the ratio of the amplitudes A_1 to A_2.

$$r\text{-Factor} = \frac{A_1}{A_2} \tag{7}$$

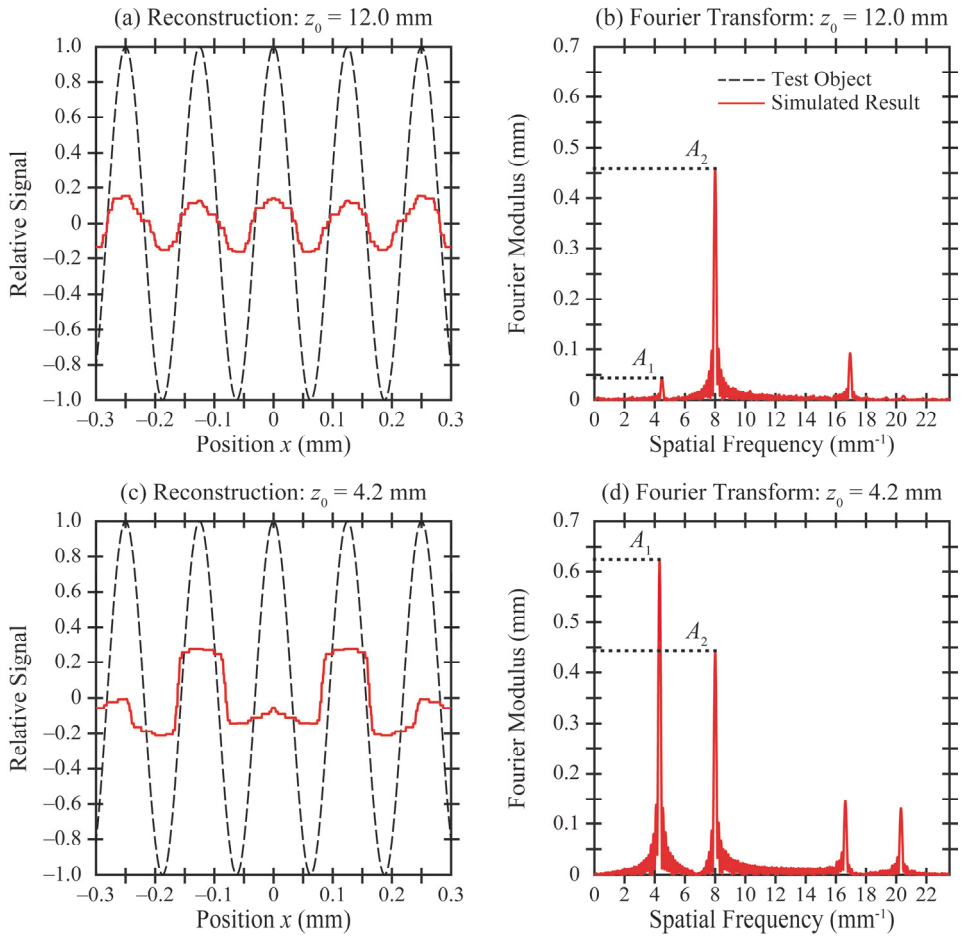

Figure 4. In the conventional acquisition geometry ($\Theta = 20°$, $N_t = 15$), the ability to achieve super-resolution is dependent on the z_0-coordinate of the object. Two z_0-coordinates are shown here as examples. In order for super-resolution to be achieved with high quality, the ratio of amplitudes A_1 to A_2 (r-factor) in Fourier space should be as small as possible.

In these two examples, the r-factor is 0.096 at the position demonstrating super-resolution [Figure 4(b)], and is 1.4 at the position exhibiting aliasing [Figure 4(d)]. In order for super-resolution to be achieved with high quality, the r-factor should be as small as possible (approaching zero). For the purpose of this paper, we set this threshold as: r-factor < 1/3. That is, the amplitude A_2 should be at least three times higher than the amplitude A_1.

2.3 Statistical Calculations

To quantify the variation in the r-factor throughout the reconstruction volume, 1,000 randomly-sampled points are analyzed in a volume-of-interest (VOI). The VOI is a rectangular prism with dimensions 200.0 × 100.0 × 50.0 (in mm) and 0.020 mm spacing between points in each direction; the VOI is taken to be centered on the point (0, 50.0, 25.0) (in mm). From the histogram obtained from 1,000 points [Figure 5(a)], the proportion of points for which r-factor < 1/3 is calculated.

Next, the VOI is analyzed with bootstrapping. From the histogram of 200 re-samplings of the proportion of points with high-quality super-resolution, the middle 95% is used to calculate a 95% confidence interval. For example, in the acquisition geometry described previously, the 95% confidence interval for this proportion ranges between 0.607 and 0.665 [Figure 5(b)].

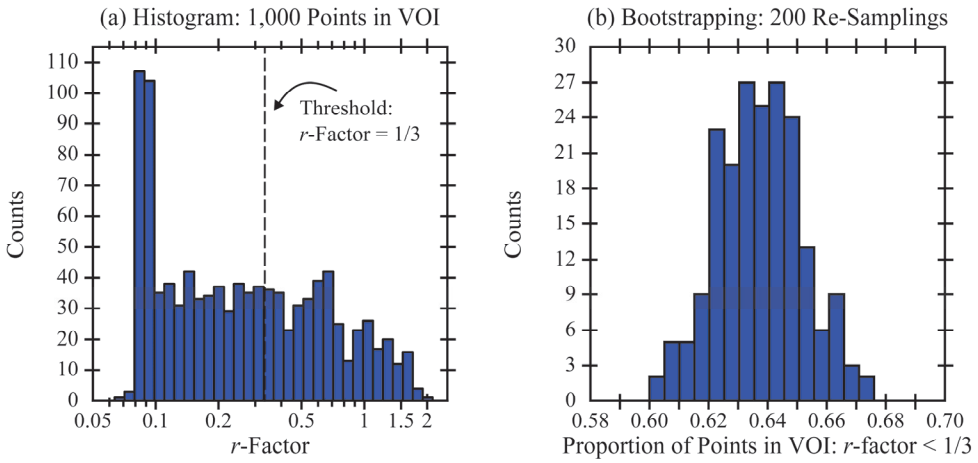

Figure 5. (a) In the conventional acquisition geometry ($\Theta = 20°$, $N_t = 15$), the *r*-factor varies between 0.067 and 1.92 in the histogram of 1,000 randomly-sampled points in the VOI. (b) The proportion of points in the VOI with high-quality super-resolution is calculated by introducing a threshold (*r*-factor < 1/3). Based on 200 bootstrapped re-samplings of this proportion, the 95% confidence interval varies between 0.607 and 0.665.

3. RESULTS

3.1 Super-Resolution in the Next-Generation System Design

First, an acquisition geometry with a 30° scanning range and 60 projections is simulated (Figure 6). In a conventional system with uniformly-spaced source positions ($N_2 = 1$), there are sharp peaks in the *r*-factor in the range $z = 0$ to 50.0 mm [Figure 6(a)]. These peaks correspond to the positions at which super-resolution is not achievable. In our previous work, we showed that increasing the number of projections is beneficial in terms of minimizing the number of anisotropies.[3] Even with the use of 60 projections (well above the number used clinically), the anisotropies are unavoidable in the conventional acquisition geometry.

The anisotropies can be suppressed by re-designing the acquisition geometry with clustered source positions [Figures 6(b)-(f)]. It is beneficial to cluster as many source positions together as possible; *i.e.*, to increase the value of N_2. This decreases the maximum amplitude of the *r*-factor; it ensures that the *r*-factor is well below unity at every position.

3.2 Statistical Calculations

Next, the VOI is analyzed in terms of the proportion of points with high-quality super-resolution (Figure 7). In the case of the conventional acquisition geometry ($N_2 = 1$), the proportion is highest in a narrow-range DBT scan ($\Theta = 10°$). As the angular range increases to 30°, the proportion is degraded. This illustrates the drawback of wide-range DBT; fewer points in the VOI achieve super-resolution with high quality.

As the value of N_2 increases, the proportion of points with high-quality super-resolution approaches unity, and there is effectively no difference between the three scanning ranges (10°, 20°, and 30°). This demonstrates that a wide-range DBT scan can indeed be optimized for super-resolution.

4. DISCUSSION AND CONCLUSION

In DBT, there are benefits and drawbacks to the use of a wide angular range. For example, we previously considered the task of segmenting the 3D breast outline in the reconstruction; this is determined based on the detector pixels that fall outside the shadow of the breast in each projection.[10] This task is optimized with a wide-range DBT scan. Additionally, previous work has shown that there are improvements in resolving the spacing between objects in the *z* direction, which can benefit masses.[11,12]

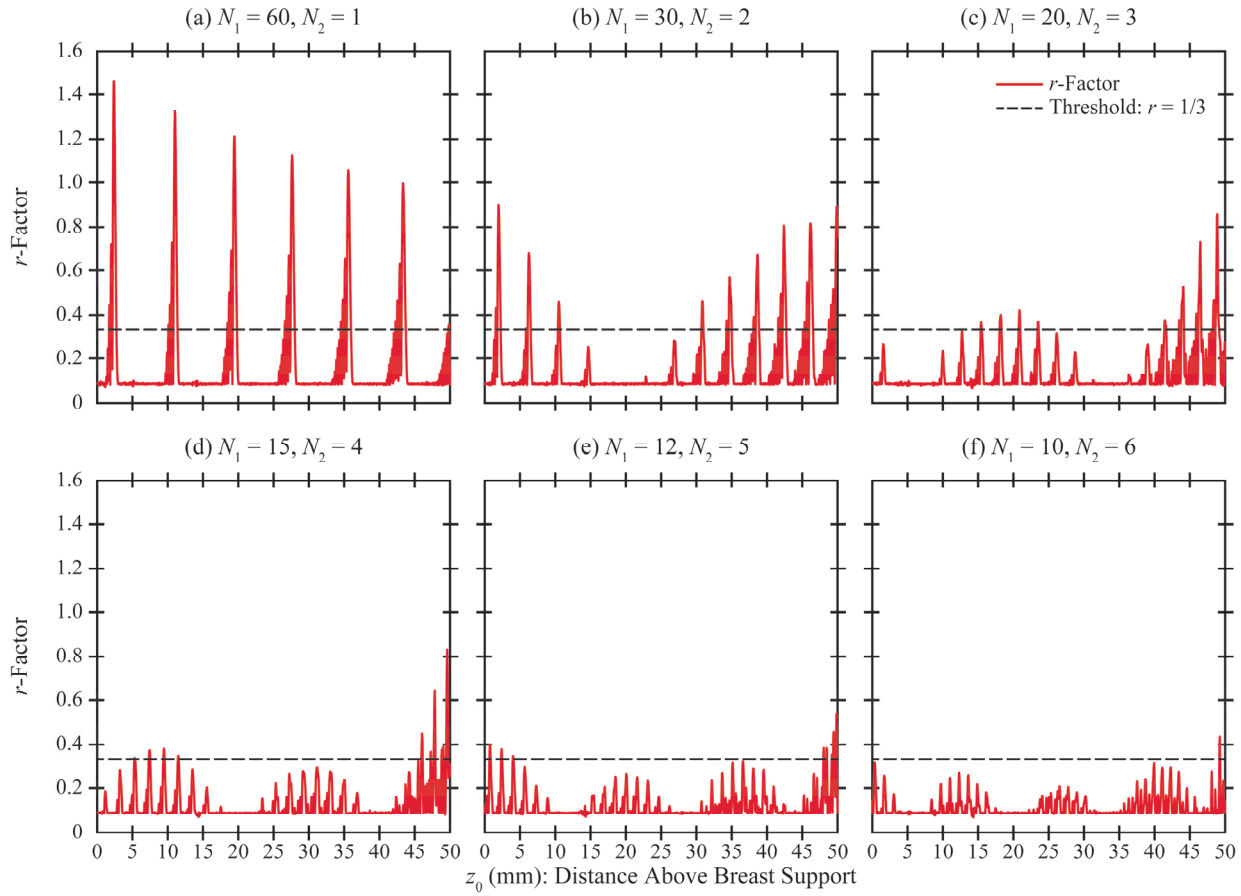

Figure 6. As N_2 increases, the maximum amplitude of the *r*-factor decreases. Therefore, in order for super-resolution to be achieved uniformly throughout the image with high quality, the source positions should be clustered together as much as possible (in this example, with 0.05° spacing).

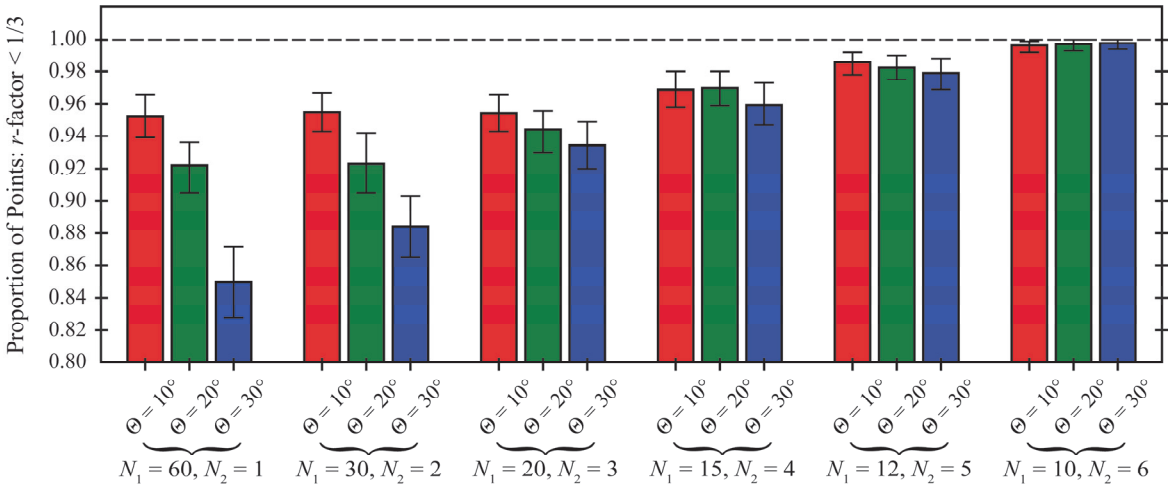

Figure 7. As N_2 increases, there are more points in the VOI at which super-resolution is achieved with high quality (*r*-factor < 1/3). The error bars denote 95% confidence intervals for the proportion.

Despite these benefits, there are other tasks, such as imaging calcifications, for which a narrow angular range is advantageous. For example, according to the study by Chan *et al*., the detectability and conspicuity of calcifications are poorer at large scan angles.[13] In this paper, we consider the task of achieving super-resolution; this task is complementary to imaging calcifications, which are high-frequency structures. In a wide-range DBT scan, we show that there is closer spacing between anisotropies, and hence there are more positions at which super-resolution is not feasible (Figures 1-2).

By increasing the number of projections, there are fewer anisotropies in a given volume.[3] However, even with the use of 60 projections (well above the number that would typically be used clinically), it is not possible to eliminate the anisotropies entirely [Figure 6(a)]. With theoretical modeling, we demonstrate the advantage of re-arranging the source positions in clusters in submillimeter increments ($\omega = 0.05°$), as could be achieved by rapidly pulsing the source during a continuous sweep of the x-ray tube. With this design, the anisotropies are eliminated. In order for this design to be implemented in practice, the detector would need to be capable of a high frame rate, and the radiation dose per projection would need to be reduced so that the total dose of the scan is unchanged.

Our previous work considered a different design for eliminating these anisotropies; specifically, the use of detector motion in the *z* direction (perpendicular to the breast support).[3] However, the trade-off of detector motion is that it may require a thicker detector housing, which is potentially cumbersome for patient positioning. By re-designing the source motion in the manner described in this paper, detector motion is no longer necessary to optimize super-resolution.

In future work, there are areas in which this theoretical model can be expanded. This paper presumes that there are no sources of detector blurring. However, previous works have shown that, in a divergent x-ray beam geometry, there is resolution loss due to non-normal x-ray incidence, and that this effect is pronounced at broad projection angles.[14-22] Future work should also analyze the effect of focal spot blurring during a continuous sweep of the x-ray tube[23,24]; this could potentially reduce the modulation of the sinusoidal waveform (Figure 4).

5. ACKNOWLEDGEMENT

We thank Johnny Kuo, Susan Ng, and Peter Ringer of Real Time Tomography (RTT) for technical assistance with Piccolo™. Andrew D. A. Maidment is a shareholder of RTT, and is a member of the scientific advisory board. Support was provided by the following grants: W81XWH-18-1-0082 from the Department of Defense Breast Cancer Research Program, IRSA 1016451 from the Burroughs Wellcome Fund, 1R01CA196528 from the National Institute of Health, and IIR13264610 from Susan G. Komen®. In addition, equipment support was provided by Analogic Inc., Barco NV, and RTT. The content is solely the responsibility of the authors and does not necessarily represent the official views of the funding agencies.

6. REFERENCES

1. Acciavatti RJ, Maidment ADA. Investigating the Potential for Super-Resolution in Digital Breast Tomosynthesis. Paper presented at: SPIE Medical Imaging2011; Lake Buena Vista, FL.
2. Acciavatti RJ, Maidment ADA. Observation of super-resolution in digital breast tomosynthesis. *Medical Physics.* 2012;39(12):7518-7539.
3. Acciavatti RJ, Wileyto EP, Maidment ADA. Modeling Acquisition Geometries with Improved Super-Resolution in Digital Breast Tomosynthesis. Paper presented at: SPIE Medical Imaging2016; San Diego, CA.
4. Kuo J, Ringer PA, Fallows SG, Bakic PR, Maidment ADA, Ng S. Dynamic Reconstruction and Rendering of 3D Tomosynthesis Images. Paper presented at: SPIE Medical Imaging2011; Lake Buena Vista, FL.
5. Hsieh J, Gard MA, Gravelle S. A Reconstruction Technique for Focal Spot Wobbling. Paper presented at: SPIE Medical Imaging1992; Newport Beach, CA.
6. Joseph PM, Schulz RA. View sampling requirements in fan beam computed tomography. *Medical Physics.* 1980;7(6):692-702.
7. Sechopoulos I. A review of breast tomosynthesis. Part I. The image acquisition process. *Medical Physics.* 2013;40(1):014301-014301 to 014301-014312.
8. Sechopoulos I. A review of breast tomosynthesis. Part II. Image reconstruction, processing and analysis, and advanced applications. *Medical Physics.* 2013;40(1):014302-014301 to 014302-014317.

9. Eben JE, Vent TL, Choi CJ, et al. Development of a Next Generation Tomosynthesis System. Paper presented at: SPIE Medical Imaging2018; Houston, TX.

10. Acciavatti RJ, Rodriguez-Ruiz A, Vent TL, et al. Analysis of Volume Overestimation Artifacts in the Breast Outline Segmentation in Tomosynthesis. Paper presented at: SPIE Medical Imaging2018; Houston, TX.

11. Mertelmeier T, Ludwig J, Zhao B, Zhao W. Optimization of Tomosynthesis Acquisition Parameters: Angular Range and Number of Projections. *Lecture Notes in Computer Science.* 2008;5116:220-227.

12. Zhao B, Zhao W. Three-dimensional linear system analysis for breast tomosynthesis. *Medical Physics.* 2008;35(12):5219-5232.

13. Chan H-P, Goodsitt MM, Helvie MA, et al. Digital Breast Tomosynthesis: Observer Performance of Clustered Microcalcification Detection on Breast Phantom Images Acquired with an Experimental System Using Variable Scan Angles, Angular Increments, and Number of Projections Views. *Radiology.* 2014;273(3):675-685.

14. Que W, Rowlands JA. X-ray imaging using amorphous selenium: Inherent spatial resolution. *Medical Physics.* 1995;22(4):365-374.

15. Hajdok G, Cunningham IA. Penalty on the detective quantum efficiency from off-axis incident x rays. Paper presented at: Medical Imaging 2004: Physics of Medical Imaging2004; San Diego, CA.

16. Mainprize JG, Bloomquist AK, Kempston MP, Yaffe MJ. Resolution at oblique incidence angles of a flat panel imager for breast tomosynthesis. *Medical Physics.* 2006;33(9):3159-3164.

17. Acciavatti RJ, Maidment ADA. Calculation of OTF, NPS, and DQE for Oblique X-Ray Incidence on Turbid Granular Phosphors. *Lecture Notes in Computer Science.* 2010;6136:436-443.

18. Hu Y-H, Scaduto DA, Zhao W. The Effect of Amorphous Selenium Thickness on Imaging Performance of Contrast Enhanced Digital Breast Tomosynthesis. *Lecture Notes in Computer Science.* 2012;7361:9-16.

19. Hu Y-H, Zhao W. The effect of amorphous selenium detector thickness on dual-energy digital breast imaging. *Medical Physics.* 2014;41(11):111904-111901 - 111904-111910.

20. Scaduto DA, Tousignant O, Zhao W. Experimental characterization of a direct conversion amorphous selenium detector with thicker conversion layer for dual-energy contrast-enhanced breast imaging. *Medical Physics.* 2017;44(8):3965-3977.

21. Acciavatti RJ, Maidment ADA. Non-stationary model of oblique x-ray incidence in amorphous selenium detectors: I. Point spread function. *Medical Physics.* 2019;46(2):494-504.

22. Acciavatti RJ, Maidment ADA. Nonstationary model of oblique x-ray incidence in amorphous selenium detectors: II. Transfer functions. *Medical Physics.* 2019;46(2):505-516.

23. Acciavatti RJ, Maidment ADA. Optimization of Continuous Tube Motion and Step-and-Shoot Motion in Digital Breast Tomosynthesis Systems with Patient Motion. Paper presented at: SPIE Medical Imaging2012; San Diego, CA.

24. Shaheen E, Marshall N, Bosmans H. Investigation of the effect of tube motion in breast tomosynthesis: continuous or step and shoot? Paper presented at: SPIE Medical Imaging2011; Lake Buena Vista, FL.

Determining the Optimal Angular Range of the X-Ray Source Motion in Tomosynthesis Using Virtual Clinical Trials

Bruno Barufaldi*, Trevor L. Vent, Raymond J. Acciavatti, Predrag R. Bakic, Peter B. Noël, Emily F. Conant, and Andrew D. A. Maidment

Department of Radiology, University of Pennsylvania, Philadelphia, United States.
*Bruno.Barufaldi@uphs.upenn.edu

ABSTRACT

The limited angle and limited number of projections in digital breast tomosynthesis (DBT) produce under-sampled datasets that may compromise calcification detection. Small breast lesions, such as microcalcifications, may not be discernible without sufficient sampling in the reconstructed DBT images. We propose a virtual clinical trial (VCT) method to evaluate the calcification detection in DBT using computer simulations of breast phantoms, images, and virtual readers. We used multiple-reader multiple-case (MRMC) receiver operating characteristic (ROC) analyses to evaluate the performance of channelized Hotelling observers (CHOs) in calcification detection. The angular motion path of the x-ray source was varied to simulate different DBT acquisition geometries. We simulated continuous and step-and-shoot x-ray source motion and three angular motion paths: ±7.5°, ±15°, and ±25°. The detection of calcifications is affected by the angular motion path, particularly for the ±25° angular range, combined with continuous tube motion, larger detector element sizes (0.14 mm) and larger reconstructed voxel sizes (0.10 mm). When an angular range of ±25° is compared to ±7.5°, the difference in the area under the curve (AUC) is -0.030 (*d'* ratio=0.633) and -0.067 (*d'* ratio=0.584), for one- and two- voxel calcifications (0.1 mm³ and 0.2 mm³), respectively. There is no significant difference in calcification detection using images acquired with ±7.5° and ±15°. The results provide insight on the impact of angular range for calcification detection, an ongoing limitation of tomosynthesis.

Keywords: virtual clinical trial; multiple-reader, multiple-case; digital breast tomosynthesis.

1. INTRODUCTION

Digital breast tomosynthesis (DBT) is a limited-angle tomographic technique that provides high-resolution 3D image reconstructions of the breast. DBT has shown substantial improvements in the detectability and characterization of subtle, soft-tissue lesions.[1–3] Conversely however, previous studies have shown that DBT is not superior to full-field digital mammography (FFDM) for calcification detection.[4–6]

The detectability of calcifications is dependent on the DBT acquisition parameters (e.g., scan angle, x-ray source motion, number of projections, detector element size, and reconstructed pixel size).[7–9] The optimal combination of the acquisition parameters in DBT is still the subject of further investigation.[7]

Virtual clinical trials (VCT) can be used for the evaluation and optimization of imaging systems by performing simulations of the human anatomy, image acquisition, and image interpretation.[10–12] We have conducted VCTs to investigate the limit of breast lesion detection and to evaluate promising imaging designs, avoiding the pursuit of inefficient DBT acquisition parameters.[8,13] Bakic *et al.* have shown that VCT simulations exhibit a mean area under the curve (AUC) improvement of 0.10 for masses and only 0.03 for calcifications when comparing the performance of DBT with FFDM for breast lesion detection.[14] We also showed that the limit of calcification detection is affected by reconstructed voxel size, x-ray source motion, and detector element size, especially for small calcifications.[8]

In this work, we present a simulation method for determining the most suitable angular range of x-ray source motion for calcification detection in DBT. Voxelized calcifications of 100, 200, and 300 µm³ were inserted into software breast phantoms. Fifteen DBT projections (i.e., equal filtration, kV, and mAs) of the breast phantoms with and without lesions were synthesized assuming a clinical acquisition geometry. We simulated the angular range of the x-ray source in DBT using projections of the breast phantoms over a ±7.5°, ±15°, and ±25° angles. We also simulated the detector element size (0.140 mm and 0.085 mm) and reconstructed voxel size (0.100 mm and 0.085 mm). Virtual readers were used to evaluate the calcification detection using one-shot multiple-reader, multiple-case (MRMC) receiver operator curve (ROC) analyses.

Medical Imaging 2020: Physics of Medical Imaging, edited by Guang-Hong Chen, Hilde Bosmans, Proc. of SPIE
Vol. 11312, 113120I · © 2020 SPIE · CCC code: 1605-7422/20/$21 · doi: 10.1117/12.2549600

2. MATERIALS & METHODS

2.1. Virtual Patient Accrual

An open-source VCT framework (OpenVCT) was developed to simulate the accrual of virtual patients.[10] Anthropomorphic breast phantoms were simulated using a recursive partitioning algorithm optimized to reduce computational complexity.[15,16] The recursive partitioning algorithm was implemented using GPU programming to support a large number of breast simulations in reasonable time. In total, 80 uncompressed breast phantoms (volume=700 mL and thickness=126.6 mm) were simulated by combining coarse- and fine-breast tissue models into phantoms,[16] with volumetric breast densities that varied from 10% to 50%.

Medio-lateral (ML) breast compression was simulated using customized finite element (FE) meshes.[17] We simulated the mechanical properties of breast tissue compression using neo-Hookean models, with Poisson ratio of 0.49, and Young's modulus of 12.750 kPa. These compression parameters reduce the phantom thickness by 50% (thickness=63.3 mm).[11]

Single calcifications were simulated as polycubes containing one to three cubes with a voxel size of 100 μm^3.[16] The contrast of the simulated calcifications was controlled by varying the voxel composition, defined by a weighting factor (WF). The WF represents the fraction of hydroxyapatite (i.e., material composition) of the calcifications. In total, 42 calcifications were embedded into each compressed breast phantom. The method for inserting lesions was published previously.[8] The calcifications were positioned 20 mm apart in the plane parallel to detector at the level of the nipple.

2.2. Acquisition Geometry Simulation

DBT projections of phantoms with and without lesions were synthesized assuming different DBT acquisition geometries (Table 1). The DBT projections are simulated using the Siddon algorithm for x-ray tracing.[18] This algorithm describes a 3D dataset, arranged as three sets of orthogonal planes that facilitate the tracing of a ray from the source, through a volume, onto each detector element. The radiological path length is determined by the sum of the length traveled by this ray in each voxel, multiplied by the relative electron density of the voxel. This process is repeated for each ray trajectory, and the intensity of the rays in a detector element determine the pixel value for the projection image.

The x-ray acquisitions were simulated using continuous tube motion, and the angular range of the x-ray source was simulated using ±7.5°, ±15°, and ±25° (Figure 1). Reconstructed DBT slices were produced using a commercially available software library.[19,20]

Table 1. Summary of DBT acquisition geometries simulated.

DBT System	(A)	(B)
X-Ray Imaging		
Anode Material (a.u)	Tungsten	
Filter Material (a.u)	Aluminum	
Filter Thickness (mm)	0.7	
Angular Range (°)	[±7.5, ±15, ±25]	
Number of Projections (#)	15	
Tube Motion (a.u)	Continuous	Step-and-Shoot
Detector		
Detection Material (a.u.)	a-Se	
Detector Element Size (mm)	0.140 × 0.140	0.085 × 0.085
Number of Elements (#)	2048 × 1664	3584 × 2816
Detector Size (mm)	286.72 × 232.96	304.64 × 239.36
Source-to-Image Distance (mm)	700.0	652.0
Reconstruction		
Voxel Size (mm)	0.100	0.085

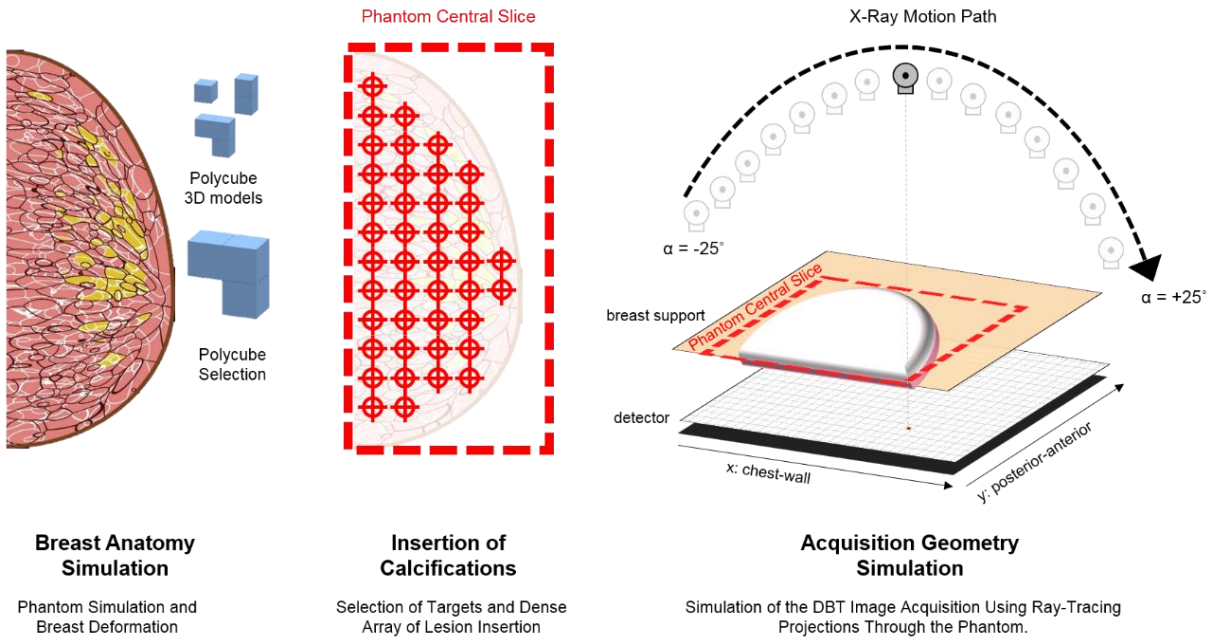

Figure 1. Method used for inserting dense grid of calcifications in the breast phantoms and for simulating the DBT acquisition geometry using angular motion path of the x-ray source.

2.3. Virtual Reader Simulation

We used channelized Hotelling observers (CHOs) to simulate virtual readers.[21,22] The CHOs were designed using 15 Laguerre-Gauss channels and, spread of 22 and 26, for images simulated using the DBT acquisition geometries (A) and (B), respectively. For each image reconstructed at the central phantom slice, we cropped ROIs centered about each calcification. The ROIs were cropped using 150×150 and 175×175 pixels for images simulated using the DBT acquisition geometries (A) and (B), respectively. For each CHO, training and testing image sets for each acquisition geometry included 252 ROIs with simulated calcifications and 252 calcification-free ROIs.

The ROIs were divided into "calcification-free" and "calcification" cohorts. The ROIs were also divided into independent training and testing ROI sets. Each reader was trained with an independent training set, but tested with a common ROI set. The ROIs used for training and testing were selected randomly for each reader.

2.4. Statistical Analyses

We measured the performance of calcification detection using ROC analyses provided by the MeVIC software (Barco NV, Kortrijk, Belgium).[23] The MeVIC software includes a module that estimates one-shot MRMC statistics.[24,25] We calculated the area under the curve (AUC) and *d'* statistics for every DBT acquisition geometry.

The non-parametric Kruskal-Wallis (K-W) test by rank and Mann-Whitney-Wilcoxon (MWW) test were used to estimate differences in mean AUCs of five readers. We analyzed significant differences in the pairwise comparison of continuous variables for every DBT acquisition geometries. The scores of each reader was pooled to calculate empirical ROC curves that represent a cumulative ROC analysis of five readers.

3. RESULTS & DISCUSSION

The AUCs of the pooled ROC improve with greater number of calcification voxels and reduce with lower fraction of hydroxyapatite (Table 2). The acquisition geometry and tube motion also affect the AUCs. For acquisition geometry A (continuous tube motion), images acquired with ±7.5° and ±25° show a significant difference in the detection of one- and two-voxel calcifications (P<0.001 and P<0.05). There is no significant difference in the detection of these calcifications (P=0.86 and P=0.22) using images acquired with ±7.5° and ±25° for DBT acquisition geometry B (step-and-shoot) suggesting that tube motion is an important contributor to calcification detection. Similarly, there is no significant

difference in three-voxel calcifications for any condition, nor for any calcification size using images acquired with ±7.5° and ±15° for both DBT acquisition geometries A and B.

AUC varies from 0.5 (i.e., random guessing) to 1.0 (i.e., relationship between disease and normal found with 100% certainty). Using the AUC values, we calculated *d'* that represents the effective signal-to-noise ratio perceived by the observer. Note that *d'* also improves with greater number of calcification voxels and reduces with lower fraction of hydroxyapatite (Table 3).

Table 2. Summary of AUC stratified by number of voxels, x-ray source angle and weight factor (WF).

(A)									
	1-Voxel Polycube			**2-Voxel Polycube**			**3-Voxel Polycube**		
	X-ray Source Angle			**X-ray Source Angle**			**X-ray Source Angle**		
WF	**7.5**	**15**	**25**	**7.5**	**15**	**25**	**7.5**	**15**	**25**
1.0	0.832	0.808	0.800	-	-	-	-	-	-
0.9	0.800	0.778	0.739	0.950	0.945	0.887	0.981	0.984	0.963
0.8	0.736	0.700	0.696	0.910	0.912	0.832	0.973	0.970	0.933
0.7	0.688	0.696	0.629	0.852	0.855	0.754	0.934	0.930	0.908
0.6	0.626	0.604	0.586	0.730	0.751	0.692	0.863	0.836	0.841
0.5	0.568	0.567	0.553	0.673	0.655	0.620	0.742	0.761	0.754
0.4	-	-	-	0.565	0.545	0.535	0.669	0.637	0.618
0.3	-	-	-	-	-	-	0.519	0.546	0.536
(B)									
1.0	0.932	0.948	0.938	-	-	-	-	-	-
0.9	0.917	0.912	0.906	0.984	0.978	0.973	0.997	0.998	0.998
0.8	0.901	0.894	0.877	0.978	0.962	0.966	0.998	0.996	0.996
0.7	0.857	0.873	0.857	0.961	0.955	0.950	0.999	0.994	0.989
0.6	0.827	0.843	0.819	0.942	0.943	0.921	0.992	0.982	0.986
0.5	0.774	0.793	0.789	0.908	0.898	0.866	0.983	0.975	0.960
0.4	0.727	0.718	0.703	0.862	0.846	0.837	0.962	0.945	0.945
0.3	0.640	0.661	0.646	0.794	0.780	0.768	0.890	0.873	0.895
0.2	0.570	0.586	0.593	0.699	0.680	0.669	0.750	0.775	0.789
0.1	-	-	-	0.538	0.539	0.516	0.579	0.594	0.611

Table 3. Summary of *d'* stratified by number of voxels, x-ray source angle and weight factor (WF).

(A)									
	1-Voxel Polycube			**2-Voxel Polycube**			**3-Voxel Polycube**		
	X-ray Source Angle			**X-ray Source Angle**			**X-ray Source Angle**		
WF	**7.5**	**15**	**25**	**7.5**	**15**	**25**	**7.5**	**15**	**25**
1.0	1.36	1.23	1.19	-	-	-	-	-	-
0.9	1.19	1.08	0.90	2.32	2.25	1.71	2.95	3.03	2.54
0.8	0.89	0.74	0.73	1.90	1.91	1.36	2.73	2.65	2.12
0.7	0.69	0.73	0.47	1.48	1.50	0.97	2.13	2.09	1.88
0.6	0.45	0.37	0.31	0.87	0.96	0.71	1.55	1.38	1.41
0.5	0.24	0.24	0.19	0.63	0.57	0.43	0.92	1.00	0.97
0.4	-	-	-	0.23	0.16	0.12	0.62	0.50	0.43
0.3	-	-	-	-	-	-	0.07	0.16	0.13
(B)									
1.0	2.11	2.30	2.17	-	-	-	-	-	-
0.9	1.96	1.91	1.86	3.03	2.84	2.73	3.94	4.08	4.10
0.8	1.82	1.76	1.64	2.85	2.51	2.58	4.17	3.75	3.71
0.7	1.51	1.61	1.51	2.48	2.39	2.33	4.27	3.58	3.24
0.6	1.33	1.43	1.29	2.23	2.24	2.00	3.38	2.98	3.10
0.5	1.06	1.15	1.13	1.88	1.80	1.57	2.98	2.78	2.48
0.4	0.85	0.81	0.75	1.54	1.44	1.39	2.51	2.26	2.26
0.3	0.51	0.59	0.53	1.16	1.09	1.03	1.73	1.62	1.77
0.2	0.25	0.31	0.33	0.74	0.66	0.62	0.95	1.07	1.14
0.1	-	-	-	0.13	0.14	0.06	0.28	0.34	0.40

Overall, for DBT acquisition geometry A there is a significant difference in calcification detection for images acquired with ±7.5° and ±25° (P<0.048), but no difference in calcification detection for images acquired with ±7.5° and 15° (P=0.70). There is no significant difference in calcification detection for images acquired using DBT acquisition geometry B with ±7.5° and ±15° (P=0.77), and ±7.5° and ±25° (P=0.43). The pooled AUC of 5 readers and *d'* of stratified calcification size and angular motion path of the x-ray source is shown in Figure 2 and Figure 3, respectively.

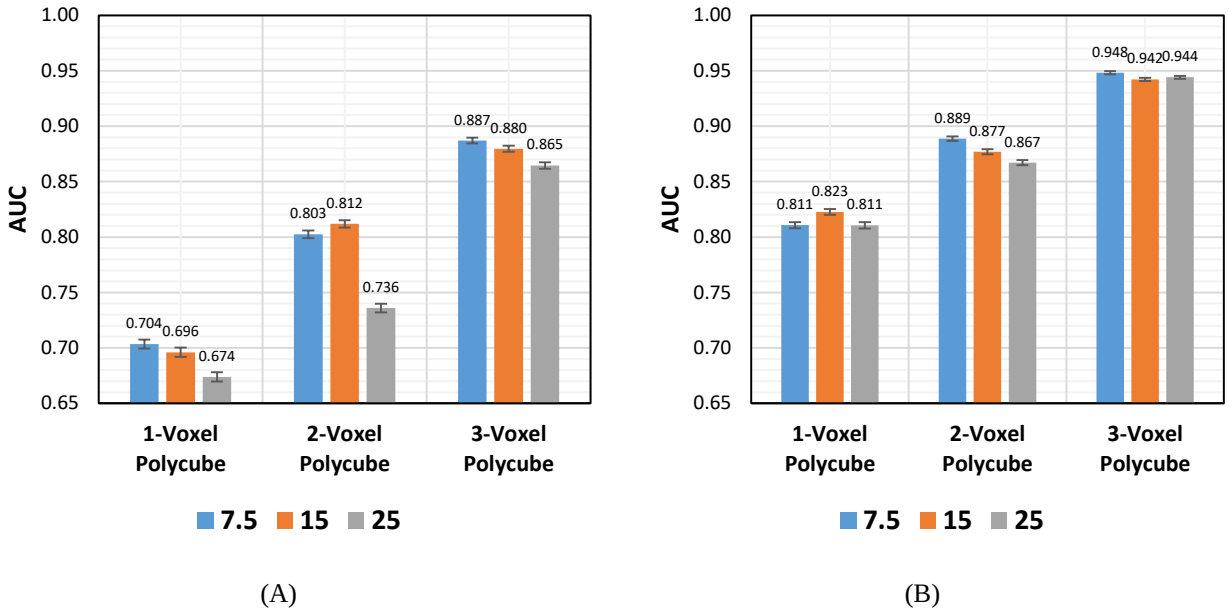

(A) (B)

Figure 2. AUC analyses of five readers for calcification detection (from 1- to 3-voxel polycube), stratified by angular range of the x-ray source.

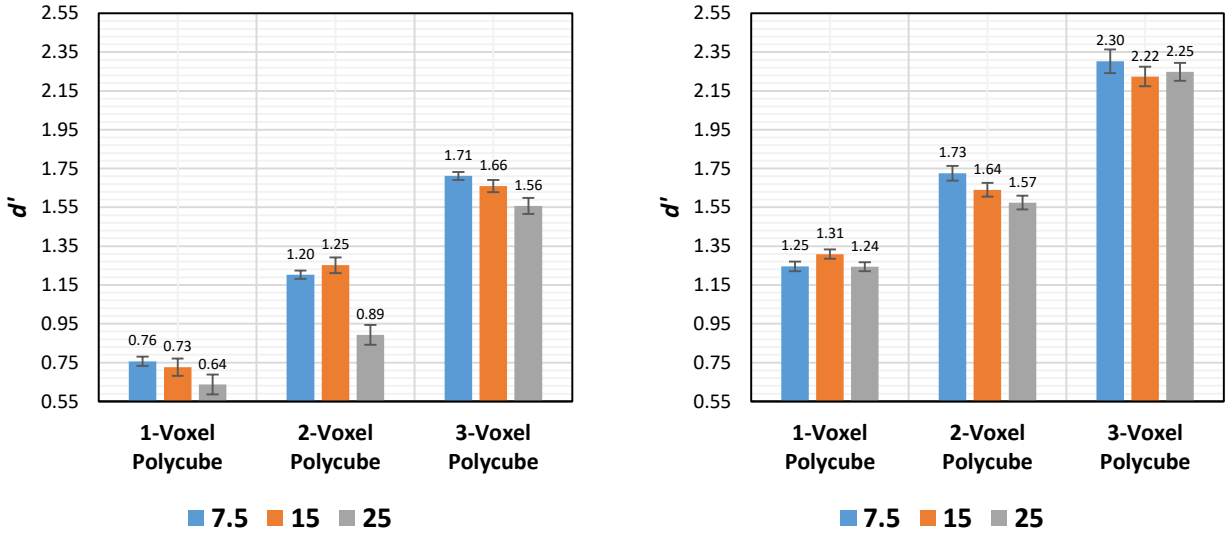

(A) (B)

Figure 3. *d'* analyses of five readers for calcification detection (from 1- to 3-voxel polycube), stratified by angular range of the x-ray source.

The detection of calcifications is affected by angular motion path of the x-ray source, in particular for wide angle. Our results indicate that ±25° source motion reduces substantially the calcification detection when the DBT acquisition geometry is combined with larger detector element sizes (0.140 mm) and continuous x-ray source motion. The impact in calcification detection is greater for two-voxel calcifications (0.200 mm^3). The detection of calcifications is not significantly affected by angular motion path when the DBT acquisition geometry is combined with step-and-shoot source motion and smaller detector element sizes (0.085 mm).

4. CONCLUSION

We simulated the detectability of calcifications in DBT using two DBT imaging geometries (A and B) and three angular ranges of the x-ray source motion: ±7.5°, ±15°, and ±25°. The impact on calcification detection is more prominent for small calcifications and/or lower fraction of hydroxyapatite in composition. The performance in calcification detection is degraded when the DBT acquisition geometry is combined with wide-angle path (±25°), continuous source motion, and larger detector element size (0.14 mm).

These results are preliminary; however, we believe they provide guidance on how to improve the detectability of calcifications, which is an ongoing problem in tomosynthesis. We are also investigating the experimental validation of this study using a DBT prototype fabricated in our laboratory[26], which is capable of customizable acquisition geometries for DBT.

ACKNOWLEDGEMENTS

Funding for the research is supported by the following grants: NIH R01 CA154444, NIH R01 EB018958, Komen IIR-13262248, BWF IRSA 1016451, and DoD W81XWH-18-1-0082.

REFERENCES

[1] Kopans, D. B., "Basic Physics and Doubts about Relationship between Mammographically Determined Tissue Density and Breast Cancer Risk," Radiology **246**(2), 1–6 (2008).

[2] Conant, E. F., "Clinical Implementation of Digital Breast Tomosynthesis," Radiol. Clin. North Am. **52**(3), 499–518 (2014).

[3] Vedantham, S., Karellas, A., Vijayaraghavan, G. R. and Kopans, D. B., "Digital Breast Tomosynthesis: State of the Art," Radiology **277**(3), 663–684 (2015).

[4] Rafferty, E. A., Park, J. M., Philpotts, L. E., Poplack, S. P. and Sumkin, J. H., "Digital Mammography and Breast Tomosynthesis Compared with Digital Mammography Alone: Results of a Multicenter, multireader trial," Radiology **266**(1), 104–113 (2013).

[5] Rafferty, E. A., Park, J. M., Philpotts, L. E., Poplack, S. P., Sumkin, J. H., Halpern, E. F. and Niklason, L. T., "Diagnostic accuracy and recall rates for digital mammography and digital mammography combined with one-view and two-view tomosynthesis: Results of an enriched reader study," Am. J. Roentgenol. **202**(2), 273–281 (2014).

[6] Zuckerman, S. P., Conant, E. F., Keller, B. M., Maidment, A. D. A., Barufaldi, B., Weinstein, S. P., Synnestvedt, M. and Mcdonald, E., "Implementation of Synthesized Two-dimensional Mammography in a Population-based Digital Breast Tomosynthesis Screening," Radiol. J. **000**(0), 1–7 (2016).

[7] Elangovan, P., Mackenzie, A., Dance, D. R., Young, K. C., Cooke, V., Wilkinson, L., Given-Wilson, R. M., Wallis, M. G. and Wells, K., "Design and validation of realistic breast models for use in multiple alternative forced choice virtual clinical trials," Phys. Med. Biol. (2017).

[8] Barufaldi, B., Bakic, P. R. and Maidment, A. D. A., "Multiple-reader, multiple-case ROC analysis for determining the limit of calcification detection in tomosynthesis," SPIE Med. Imaging 2019 Phys. od Med. Imaging **10948**(March), 22 (2019).

[9] Chan, H.-P., Goodsitt, M. M., Helvie, M. A., Zelakiewicz, S., Schmitz, A., Noroozian, M., Paramagul, C., Roubidoux, M. A., Nees, A. V., Neal, C. H., Carson, P., Lu, Y., Hadjiiski, L. and Wei, J., "Digital Breast Tomosynthesis: Observer Performance of Clustered Microcalcification Detection on Breast Phantom Images Acquired with an Experimental System Using Variable Scan Angles, Angular Increments, and Number of Projection Views," Radiology **273**(3), 675–685 (2014).

[10] Barufaldi, B., Bakic, P. R., Higginbotham, D. and Maidment, A. D. A., "OpenVCT: a GPU-accelerated virtual clinical trial pipeline for mammography and digital breast tomosynthesis," SPIE Med. Imaging 2018 **1057358**(March), 1–8, Houston, TX (2018).

[11] Barufaldi, B., Bakic, P. R., Pokrajac, D. D., Lago, M. A. and Maidment, A. D. A., "Developing populations of software breast phantoms for virtual clinical trials," 14th Int. Work. Breast Imaging (IWBI 2018)(July), 73 (2018).
[12] Badano, A., Graff, C. G., Badal, A., Sharma, D., Zeng, R., Samuelson, F. W., Glick, S. J. and Myers, K. J., "Evaluation of Digital Breast Tomosynthesis as Replacement of Full-Field Digital Mammography Using an In Silico Imaging Trial," JAMA Netw. Open **1**(7), 1–12 (2018).
[13] Vent, T. L., Barufaldi, B. and Maidment, A. D. A., "Simulation and experimental validation of high-resolution test objects for evaluating a next-generation digital breast tomosynthesis prototype," SPIE Med. Imaging 2019(March), 21 (2019).
[14] Bakic, P. R., Barufaldi, B., Higginbotham, D., Weinstein, S. P., Avanaki, A., Espig, K., Xthona, A., Kimpe, T. and Maidment, A. D. A., "Virtual clinical trial of lesion detection in digital mammography and digital breast tomosynthesis," SPIE Med. Imaging 2018 **1057306**(March), 1–13 (2018).
[15] Pokrajac, D. D., Maidment, A. D. A. and Bakic, P. R., "Optimized generation of high resolution breast anthropomorphic software phantoms," Med. Phys. **39**(4), 2290 (2012).
[16] Bakic, P. R., Barufaldi, B., Pokrajac, D., Weinstein, S. P. and Maidment, A. D., "Optimized simulation of breast anatomy for virtual clinical trials," 14th Int. Work. Breast Imaging (IWBI 2018)(July), 73 (2018).
[17] Lago, M. A., Maidment, A. D. A. and Bakic, P. R., "Modelling of mammographic compression of anthropomorphic software breast phantom using FEBio," Int'l Symp. Comput. Methods Biomech. Biomed. Eng., Salt Lake City, UT (2013).
[18] Siddon, R. L., "Fast calculation of the exact radiological path for a three dimensional CT array," Med. Phys. **12**(2), 252–255 (1985).
[19] Kuo, J., Ringer, P. A., Fallows, S. G., Bakic, P. R., Maidment, A. D. A. and Ng, S., "Dynamic reconstruction and rendering of 3D tomosynthesis images," SPIE Med. Imaging **796116**(March 2011), 796116-796116–11, Orlando, FL (2011).
[20] Chui, J. H., Pokrajac, D. D., Maidment, A. A. D. A. and Bakic, P. R., "Roadmap for efficient parallelization of breast anatomy simulation," SPIE Med. Imaging **8313**, 83134T (2012).
[21] Abbey, C. K. and Barrett, H. H., "Human- and model-observer performance in ramp-spectrum noise: effects of regularization and object variability," J. Opt. Soc. Am. A (2001).
[22] Park, S., Zhang, G. and Myers, K. J., "Comparison of Channel Methods and Observer Models for the Task-Based Assessment of Multi-Projection Imaging in the Presence of Structured Anatomical Noise," IEEE Trans. Med. Imaging **35**(6), 1431–1442 (2016).
[23] Marchessoux, C., Kimpe, T. and Bert, T., "A virtual image chain for perceived and clinical image quality of medical display," IEEE/OSA J. Disp. Technol. **4**(4), 356–368 (2008).
[24] Gallas, B. D. and Barrett, H. H., "Validating the use of channels to estimate the ideal linear observer.," J. Opt. Soc. Am. A. Opt. Image Sci. Vis. **20**(9), 1725–1738 (2003).
[25] Gallas, B. D., "One-shot estimate of MRMC variance: AUC," Acad. Radiol. **13**(3), 353–362 (2006).
[26] Acciavatti, R. J., Barufaldi, B., Vent, T. L., Wileyto, E. P. and Maidment, A. D. A., "Personalization of x-ray tube motion in digital breast tomosynthesis using virtual Defrise phantoms," Med. Imaging 2019 Phys. Med. Imaging(March), 10 (2019).

Calculation of Radiomic Features to Validate the Textural Realism of Physical Anthropomorphic Phantoms for Digital Mammography

Raymond J. Acciavatti[1], Eric A. Cohen[1], Omid Haji Maghsoudi[1], Aimilia Gastounioti[1], Lauren Pantalone[1], Meng-Kang Hsieh[1], Bruno Barufaldi[1], Predrag R. Bakic[1], Jinbo Chen[2], Emily F. Conant[1], Despina Kontos[1], Andrew D. A. Maidment[1]
[1]University of Pennsylvania, Department of Radiology, 3400 Spruce Street, Philadelphia PA 19104
[2]University of Pennsylvania, Department of Epidemiology, Biostatistics, & Informatics, 423 Guardian Drive, Philadelphia, PA 19104
E-mail: {Raymond.Acciavatti | Andrew.Maidment}@pennmedicine.upenn.edu

ABSTRACT

In this paper, radiomic features are used to validate the textural realism of two anthropomorphic phantoms for digital mammography. One phantom was based off a computational breast model; it was 3D printed by CIRS (Computerized Imaging Reference Systems, Inc., Norfolk, VA) under license from the University of Pennsylvania. We investigate how the textural realism of this phantom compares against a phantom derived from an actual patient's mammogram ("Rachel", Gammex 169, Madison, WI). Images of each phantom were acquired at three kV in 1 kV increments using auto-time technique settings. Acquisitions at each technique setting were repeated twice, resulting in six images per phantom. In the raw ("FOR PROCESSING") images, 341 features were calculated; *i.e.*, gray-level histogram, co-occurrence, run length, fractal dimension, Gabor Wavelet, local binary pattern, Laws, and co-occurrence Laws features. Features were also calculated in a negative screening population. For each feature, the middle 95% of the clinical distribution was used to evaluate the textural realism of each phantom. A feature was considered realistic if all six measurements in the phantom were within the middle 95% of the clinical distribution. Otherwise, a feature was considered unrealistic. More features were actually found to be realistic by this definition in the CIRS phantom (305 out of 341 features or 89.44%) than in the phantom derived from a specific patient's mammogram (261 out of 341 features or 76.54%). We conclude that the texture is realistic overall in both phantoms.

Keywords: Radiomics, digital mammography, anthropomorphic phantom, x-ray imaging, image acquisition.

1. INTRODUCTION

Breast density has consistently been shown to be an independent predictor of breast cancer risk.[1,2] Recent studies have demonstrated that combining radiomic texture features with mammographic density results in an even better assessment of breast cancer risk.[3,4] This paper explores a different application for radiomic texture feature calculations; namely, evaluating how closely the breast parenchymal patterns in an anthropomorphic phantom match a clinical population.

In our previous work, we developed a computational model of the breast in which multiple compartments of dense tissue are grown from seed points in voxel phantoms.[5,6] The user can vary parameters controlling the size and shape of the phantom, as well as the percent density and spatial arrangement of dense tissue.[7] A key advantage of this model is that a population of virtual phantoms[8] can be simulated quickly on a graphics processing unit (GPU).

A physical phantom based off this model was 3D printed by CIRS (Computerized Imaging Reference Systems, Inc., Norfolk, VA) under license from the University of Pennsylvania. The CIRS phantom models a 50 mm thick breast under compression (450 mL by volume) with a volumetric density of 17%.[9] The phantom can be used in both 2D digital mammography (DM) and 3D digital breast tomosynthesis (DBT). The phantom was 3D printed in sections (slabs), allowing clusters of calcium oxalate to be inserted within the thickness of the phantom; these are surrogates for calcification clusters.[10]

15th International Workshop on Breast Imaging (IWBI2020), edited by Hilde Bosmans, Nicholas Marshall, Chantal Van Ongeval, Proc. of SPIE Vol. 11513, 1151309
© 2020 SPIE · CCC code: 0277-786X/20/$21 · doi: 10.1117/12.2564363

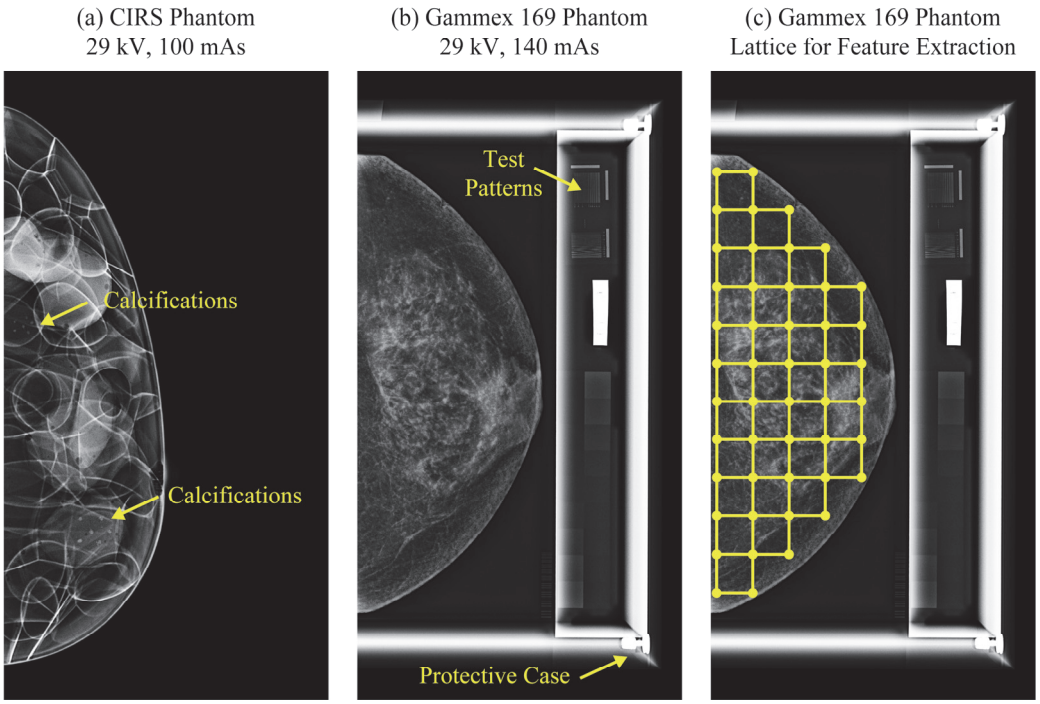

Figure 1. (a) The CIRS phantom was 3D printed from a computational breast model. (b) The Gammex 169 phantom was derived from an actual patient's mammogram. There are test patterns adjacent to the phantom; these were not analyzed for the purpose of this study. (c) The breast area was partitioned into a lattice of square windows (6.3 mm × 6.3 mm) for calculation of radiomic features. Although these calculations were done in raw DM images, processed DM images are shown.

In a previous study, Cockmartin *et al*. calculated power spectra in 2D and 3D images of the CIRS phantom, and showed that the power-law coefficients were in agreement with the values derived from a clinical population.[9] In radiomics, there are a multitude of additional features that can be used to validate the texture of a phantom. In this paper, 341 radiomic features are calculated in the CIRS phantom and compared against a clinical population. We also investigate how the texture of the CIRS phantom compares against a phantom derived from an actual patient's mammogram[11] ("Rachel, Gammex 169, Madison, WI), which by nature is expected to be highly realistic. For the purpose of this paper, all radiomics calculations are done exclusively for DM, since the Gammex 169 phantom was developed specifically for DM and not DBT.

2. METHODS

2.1 X-Ray Acquisitions of Phantoms

DM images of the two phantoms (CIRS and Gammex 169) were acquired with a Selenia Dimensions system (Hologic Inc., Bedford, MA) with a W/Rh target-filter combination (Figure 1). Images were acquired over a number of different kV and mAs combinations; the auto-timing curves illustrating the effect of kV are shown in Figure 2. A subset of these technique settings was chosen for the purpose of validating the texture of the phantoms. We based the choice of acquisition settings off of data tables for the automatic exposure control settings for a breast with comparable thickness (50 mm) to the phantoms; the appropriate kV is 29 kV for a W/Rh target-filter combination. Additional kV settings in ± 1 kV increments relative to 29 kV were also analyzed. These images were acquired in "Manual" mode at mAs settings designed to match the auto-timing curves. Since the system supports a discrete set of mAs values in "Manual" mode, the closest mAs settings were chosen (Table 1). Two cranial-caudal (CC) images were acquired at each technique setting; these were used for reproducibility analysis. Hence there were six acquisitions per phantom.

Table 1. DM technique settings for each phantom are summarized below. The target-filter combination was W/Rh.

	mAs Setting (28 kV)	mAs Setting (29 kV)	mAs Setting (30 kV)
CIRS Phantom	120 mAs	100 mAs	95 mAs
Gammex 169 Phantom	160 mAs	140 mAs	120 mAs

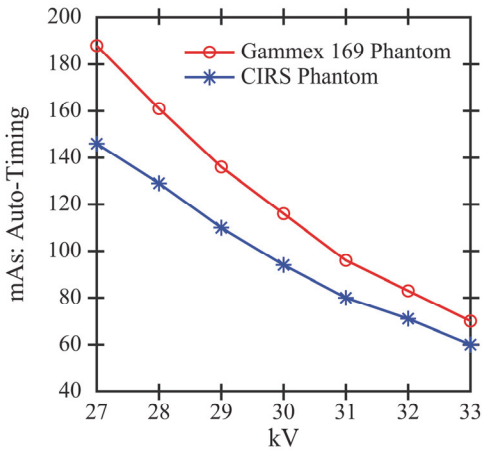

Figure 2. DM images of the two phantoms were acquired at auto-timed technique settings. As the kV increases, there is greater x-ray penetration and hence the mAs (relative number of x-ray photons) is reduced.

2.2 Overview of Clinical Data Set

DM images (CC views) were also analyzed from 1,000 women with negative screening exams at the University of Pennsylvania (Table 2). The images were acquired with Selenia Dimensions systems between 9/1/2014 and 12/31/2014. This research was approved by the Institutional Review Board at the University of Pennsylvania and was compliant with the Health Insurance Portability and Accountability Act. Since previous work demonstrated that radiomic features are dependent on breast thickness under compression[12], we compared the phantom data against the subset of clinical data with comparable thickness (±10 mm relative to a 50 mm thick phantom).

2.3 Calculation of Radiomic Texture Features

Radiomic features were calculated in raw ("FOR PROCESSING") DM images. As the first step in these calculations, the breast outline was segmented with LIBRA (Laboratory for Individualized Breast Radiodensity Assessment), a software tool.[13] Next, the breast area was partitioned into a regular lattice of square windows [Figure 1(c)]. Each feature was calculated separately in each window. These values were in turn averaged across all windows, resulting in a single image-wise value for each feature. A total of 341 features were calculated; *i.e.*, 12 gray-level histogram, 7 co-occurrence, 7 run length, 2 fractal dimension, 32 Gabor Wavelet, 36 local binary pattern, 125 Laws, and 120 co-occurrence Laws features.[14-18]

The window size used in the lattice for these feature calculations was 6.3 mm. A previous work by Zheng *et al*. considered the effect of varying the window size between 6.3 mm and 25.5 mm.[3] They found that the smallest window size (6.3 mm) yields the highest area under the receiver-operating-characteristic curve in case-control classification calculations.

Table 2. Demographic information derived from the data set of 1,000 women with negative screening exams is summarized below.

Age	< 40 y	29 (2.9 %)
	40-49 y	255 (25.5%)
	50-59 y	292 (29.2%)
	60-69 y	279 (27.9 %)
	≥ 70 y	145 (14.5%)
BI-RADS® Density	Type a	114 (11.4%)
	Type b	553 (55.3%)
	Type c	311 (31.1%)
	Type d	22 (2.2%)
Ethnicity	African American	463 (46.3%)
	Caucasian	441 (44.1%)
	Other/Unknown	96 (9.6%)

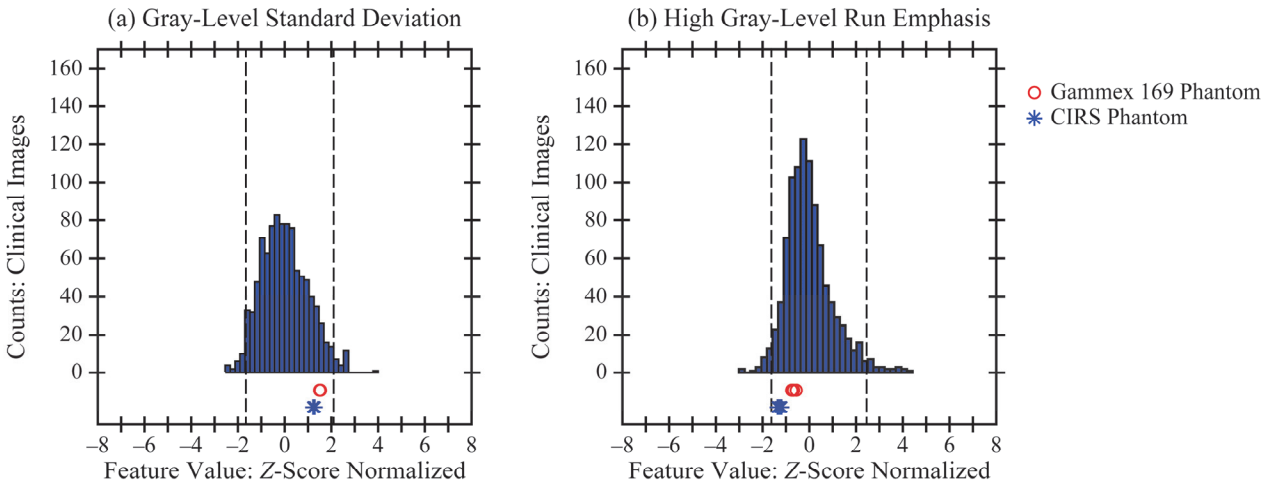

Figure 3. Each phantom was found to have realistic texture in terms of these two features. The phantom data points derived from six images are all within the middle 95% of the clinical distribution. Dashed lines denote the 2.5th and 97.5th percentiles of the clinical distribution.

2.4 Analysis of Textural Realism of Phantoms

For the two phantoms, the textural realism of each feature was defined based on the middle 95% of the clinical distribution; this was considered to be a realistic range of values for a feature. More specifically, a feature was considered realistic if all six data points derived from phantom images were between the 2.5th and 97.5th percentiles of the clinical distribution. By contrast, a feature was considered unrealistic if the percentile ranks of at least one of the six phantom data points was below 2.5% or above 97.5% (dashed vertical lines in Figures 3-5). Note that other definitions of realism exist, and that different conclusions may result from the use of alternate definitions of realism. For example, in Figure 3, both phantoms are deemed realistic by our metric, but if we defined textural realism in terms of closeness to the 50th percentile of the clinical distribution, then the CIRS phantom is more realistic in terms of the gray-level standard deviation and the Gammex 169 phantom is more realistic in terms of high gray-level run emphasis.

3. RESULTS

3.1 Calculations of Textural Realism

For each feature, the distribution of values in the clinical data set was *Z*-score normalized and plotted as a histogram (Figures 3-5). This normalization was also applied to the six phantom data points. To illustrate examples of realistic texture in both phantoms, standard deviation (a gray-level feature) and high gray-level run emphasis (a run length feature) are shown in Figure 3. In these examples, the six data points derived from the phantom acquisitions are clustered over a narrow range of values within the middle 95% of the clinical distribution.

Table 3. Summary statistics for each phantom were calculated separately by feature family.

Feature Family (Number of Features)	Realistic Features in CIRS Phantom	Realistic Features in Gammex 169 Phantom
Co-occurrence (7)	7 (100%)	3 (42.86%)
Co-occurrence Laws (120)	106 (88.33%)	87 (72.50%)
Fractal Dimension (2)	1 (50%)	0 (0%)
Gabor Wavelet (32)	32 (100%)	32 (100%)
Gray Level (12)	12 (100%)	12 (100%)
Laws (125)	111 (88.80%)	93 (74.40%)
LBP (36)	29 (80.56%)	29 (80.56%)
Run Length (7)	7 (100%)	5 (71.43%)

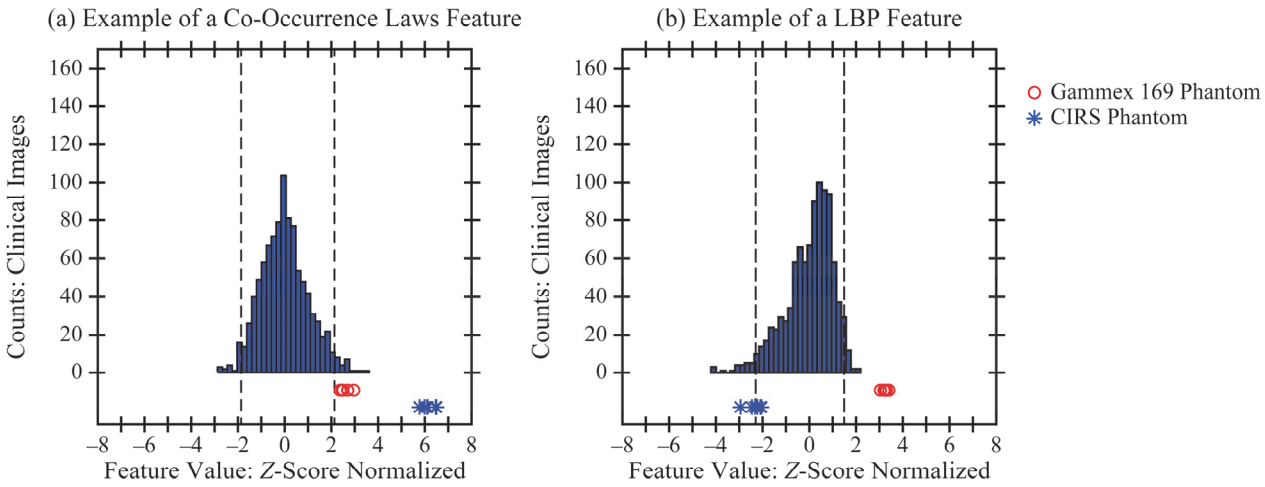

Figure 4. The phantoms were found to have unrealistic texture in terms of these two features. At least one of the six phantom data points is outside the middle 95% of the clinical distribution.

To illustrate the opposite result (unrealistic texture in both phantoms), two additional examples are shown in Figure 4. In some features, all six phantom data points were outside the middle 95% of the clinical distribution, as can be seen in one of the co-occurrence Laws features [Figure 4(a)]. The texture was also considered unrealistic if any subset of phantom data points was outside the middle 95% of the clinical distribution [Figure 4(b)].

3.2 Summary Statistics

The CIRS phantom was found to have realistic texture in terms of 305 features out of 341 (89.44%). By contrast, the Gammex 169 phantom was found to have realistic texture in terms of 261 features out of 341 (76.54%). These results can be analyzed in more detail on the basis of individual feature families (Table 3). The phantoms showed realistic texture in terms of all the gray-level and Gabor Wavelet features. The phantoms showed unrealistic texture in terms of some measures of fine structural detail.

It is also useful to create a confusion matrix (a 2 × 2 table) summarizing the results for each phantom (Table 4). Both phantoms were shown to have realistic texture in terms of 239 features (70.09%) and unrealistic texture in terms of 14 features (4.11%). In addition, there are 88 features (25.81%) for which the texture is realistic in one phantom but not the other; Figure 5 shows examples of these features.

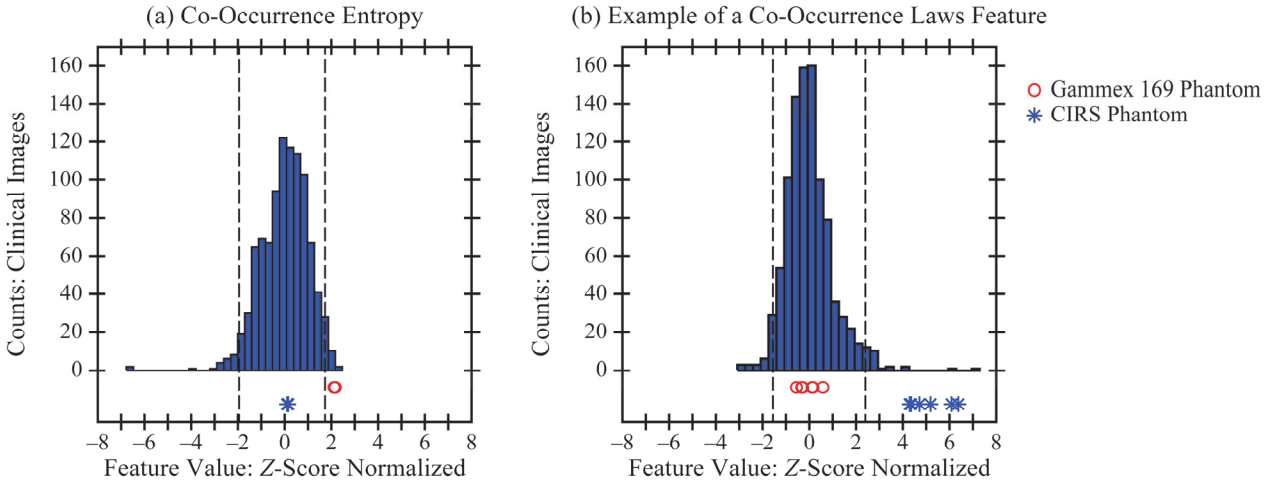

Figure 5. In some features, only one of the two phantoms was shown to have realistic texture; for example, the CIRS phantom in terms of co-occurrence entropy and the Gammex 169 phantom in terms of a Co-Occurrence Laws features.

Table 4. Summary statistics for each phantom can be analyzed with a confusion matrix.

Gammex 169 Phantom

CIRS Phantom	Realistic	Unrealistic	
Realistic	239 (70.09%)	66 (19.35%)	305 (89.44%)
Unrealistic	22 (6.45%)	14 (4.11%)	36 (10.56%)
	261 (76.54%)	80 (23.46%)	341 (100%)

4. DISCUSSION AND CONCLUSION

This paper evaluates the textural realism of two phantoms for DM. One would expect the Gammex 169 phantom to have realistic texture by its very nature, since it was created from an actual patient's mammogram. In this paper, we offer a validation of the textural realism of this phantom, and show that the CIRS phantom also has realistic texture. We conclude that phantoms based off a computational model can indeed have realistic texture.

In the years since the CIRS phantom was 3D printed, there have been advancements in the voxel phantom. The phantom now includes a model of tissue microstructure, which is simulated with the use of subcompartments of breast tissue designed to match the appearance of histological images.[19] Future work should investigate how the texture of the phantom changes based on the addition of these finer details.

5. ACKNOWLEDGEMENT

Support was provided by the following grants: R01CA207084 and U54CA163313 from the National Institute of Health, W81XWH-18-1-0082 from the Department of Defense Breast Cancer Research Program, and PDF17479714 from Susan G. Komen®. The content is solely the responsibility of the authors and does not necessarily represent the official views of the funding agencies.

ADAM receives research support from Hologic Inc., Barco NV, and Analogic Corporation. Also, ADAM is a shareholder and member of the scientific advisory board of Real Time Tomography, LLC. EFC receives grant support and is part of the advisory panel of Hologic Inc. EFC also receives grant support and is part of the advisory panel of iCAD Inc.

6. REFERENCES

1. Boyd NF, Rommens JM, Vogt K, et al. Mammographic breast density as an intermediate phenotype for breast cancer. *The Lancet Oncology.* 2005;6(10):798-808.
2. Boyd NF, Guo H, Martin LJ, et al. Mammographic Density and the Risk and Detection of Breast Cancer. *The New England Journal of Medicine.* 2007;356(3):227-236.
3. Zheng Y, Keller BM, Ray S, et al. Parenchymal texture analysis in digital mammography: A fully automated pipeline for breast cancer risk assessment. *Medical Physics.* 2015;42(7):4149-4160.
4. Gastounioti A, Conant EF, Kontos D. Beyond breast density: a review on the advancing role of parenchymal texture analysis in breast cancer risk assessment. *Breast Cancer Research.* 2016;18:91.
5. Chui JH, Pokrajac DD, Maidment ADA, Bakic PR. Towards Breast Anatomy Simulation Using GPUs. *Lecture Notes in Computer Science.* 2012;7361:506-513.
6. Pokrajac DD, Maidment ADA, Bakic PR. Optimized generation of high resolution breast anthropomorphic software phantoms. *Medical Physics.* 2012;39(4):2290-2302.

7. Chui JH, Zeng R, Pokrajac DD, et al. Two Methods for Simulation of Dense Tissue Distribution in Software Breast Phantoms. Paper presented at: SPIE Medical Imaging2013; Orlando, FL.

8. Barufaldi B, Bakic PR, Pokrajac DD, Lago MA, Maidment ADA. Developing Populations of Software Breast Phantoms for Virtual Clinical Trials. Paper presented at: 14th International Workshop on Breast Imaging (IWBI 2018)2018; Atlanta, GA.

9. Cockmartin L, Bakic PR, Bosmans H, et al. Power Spectrum Analysis of an Anthropomorphic Breast Phantom Compared to Patient Data in 2D Digital Mammography and Breast Tomosynthesis. *Lecture Notes in Computer Science.* 2014;8539:423-429.

10. Vieira MAC, Oliveira HCRd, Nunes PF, et al. Feasibility Study of Dose Reduction in Digital Breast Tomosynthesis Using Non-Local Denoising Algorithms. Paper presented at: SPIE Medical Imaging2015; Orlando, FL.

11. Yaffe MJ, Johns PC, Nishikawa RM, Mawdsley GE, Caldwell CB. Anthropomorphic radiologic phantoms. *Radiology.* 1986;158(2):550-552.

12. Acciavatti RJ, Hsieh M-K, Gastounioti A, et al. Validation of the Textural Realism of a 3D Anthropomorphic Phantom for Digital Breast Tomosynthesis. Paper presented at: 14th International Workshop on Breast Imaging (IWBI 2018)2018; Atlanta, GA.

13. Keller BM, Nathan DL, Wang Y, et al. Estimation of breast percent density in raw and processed full field digital mammography images via adaptive fuzzy c-means clustering and support vector machine segmentation. *Medical Physics.* 2012;39(8):4903-4917.

14. Haralick RM, Shanmugam K, Dinstein IH. Textural Features for Image Classification. *IEEE Transactions on Systems, Man, and Cybernetics.* 1973;SMC-3(6):610-621.

15. Galloway MM. Texture analysis using gray level run lengths. *Computer Graphics and Image Processing.* 1975;4(2):172-179.

16. Chu A, Sehgal CM, Greenleaf JF. Use of gray value distribution of run lengths for texture analysis. *Pattern Recognition Letters.* 1990;11(6):415-419.

17. Ojala T, Pietikäinen M, Mäenpää T. Multiresolution Gray-Scale and Rotation Invariant Texture Classification with Local Binary Patterns. *IEEE Transactions on Pattern Analysis and Machine Intelligence.* 2002;24(7):971-987.

18. Manduca A, Carston MJ, Heine JJ, et al. Texture Features from Mammographic Images and Risk of Breast Cancer. *Cancer Epidemiology, Biomarkers & Prevention.* 2009;18(3):837-845.

19. Bakic PR, Pokrajac DD, Caro RD, Maidment ADA. Realistic Simulation of Breast Tissue Microstructure in Software Anthropomorphic Phantoms. *Lecture Notes in Computer Science.* 2014;8539:348-355.

Super-Resolution in Digital Breast Tomosynthesis: Limitations of the Conventional System Design and Strategies for Optimization

Raymond J. Acciavatti[1], Trevor L. Vent[1], Bruno Barufaldi[1], E. Paul Wileyto[2],
Peter B. Noël[1], Andrew D. A. Maidment[1]
[1]University of Pennsylvania, Department of Radiology, 3400 Spruce Street, Philadelphia PA 19104
[2]University of Pennsylvania, Department of Epidemiology, Biostatistics, & Informatics,
423 Guardian Drive, Philadelphia, PA 19104
E-mail: {Raymond.Acciavatti | Trevor.Vent | Bruno.Barufaldi | epw |
Peter.Noel | Andrew.Maidment}@pennmedicine.upenn.edu

ABSTRACT

Our previous work explored the use of super-resolution as a way to improve the visibility of calcifications in digital breast tomosynthesis. This paper demonstrates that there are anisotropies in super-resolution throughout the reconstruction, and investigates new motion paths for the x-ray tube to suppress these anisotropies. We used a theoretical model of a sinusoidal test object to demonstrate the existence of the anisotropies. In addition, high-frequency test objects were simulated with virtual clinical trial (VCT) software developed for breast imaging. The simulated objects include a lead bar pattern phantom as well as punctate calcifications in a breast-like background. In a conventional acquisition geometry in which the source motion is directed laterally, we found that super-resolution is not achievable if the frequency is oriented in the perpendicular direction (posteroanteriorly). Also, there are positions, corresponding to various slices above the breast support, at which super-resolution is inherently not achievable. The existence of these anisotropies was validated with VCT simulations. At locations predicted by theoretical modeling, the bar pattern phantom showed aliasing, and the spacing between individual calcifications was not properly resolved. To show that super-resolution can be optimized by re-designing the acquisition geometry, we applied our theoretical model to the analysis of new motion paths for the x-ray tube; specifically, motions with more degrees of freedom and with more rapid pulsing (submillimeter spacing) between source positions. These two strategies can be used in combination to suppress the anisotropies in super-resolution.

Keywords: Digital Breast Tomosynthesis, Virtual Clinical Trials, Super-Resolution, Calcifications, Anthropomorphic Phantom, Fourier Transform, Image Quality, Image Reconstruction.

1. INTRODUCTION

1.1 Overview of Super-Resolution in Tomosynthesis

Many medical centers now use digital breast tomosynthesis (DBT) for breast cancer screening.[1-3] In DBT, the x-ray tube rotates in the plane of the chest wall, and a reconstruction is created from a small number of projection views (Figure 1). Since the image of an object is translated in subpixel increments between each projection, a reconstruction created with smaller pixelation than the detector is capable of super-resolution, or resolution of frequencies exceeding the alias frequency of the detector.[4,5] Super-resolution allows fine details to be visualized more clearly, including calcifications. These benefits can be achieved with either backprojection filtering[4] or iterative reconstructions[6].

With theoretical modeling, we have shown that there are some z-coordinates at which super-resolution cannot be achieved, corresponding to regularly-spaced slices in the reconstruction.[7] One of the aims of this paper is to understand how these anisotropies could impact virtual clinical trials (VCTs). A VCT is a software tool that allows for simulation of anatomical phantoms under different imaging conditions using model observers to quantify the detection of lesions (*e.g.*, calcifications) with receiver operating characteristic curves.[8] Our recent work showed that a VCT of DBT and 2D digital mammography (DM) performed extremely well in comparison with clinical data.[9] In this paper, we demonstrate that the visualization of calcifications in a VCT is impacted by the presence of the anisotropies in super-resolution. We use theoretical modeling to guide the positioning of these lesions based on the known locations of the anisotropies.

15th International Workshop on Breast Imaging (IWBI2020), edited by Hilde Bosmans,
Nicholas Marshall, Chantal Van Ongeval, Proc. of SPIE Vol. 11513, 115130V
 · doi: 10.1117/12.2563839

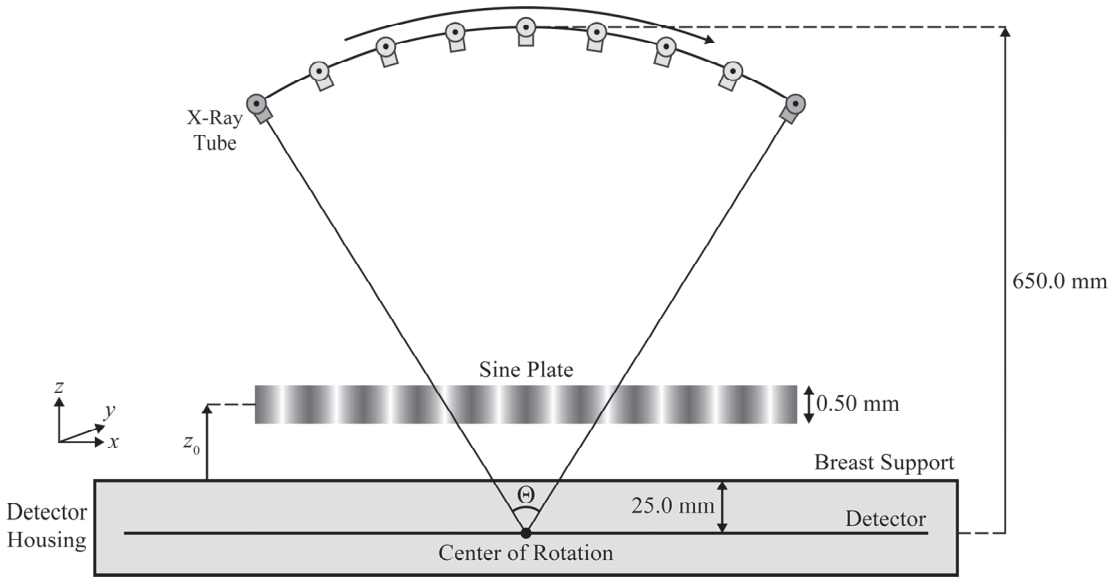

Figure 1. The sine plate is a test object for investigating the existence of super-resolution with theoretical modeling. In a conventional DBT scan, there is source motion in a circular arc in the *xz* plane; *i.e.*, the plane of the chest wall.

1.2 Design of a Next-Generation Tomosynthesis System

In our previous work, we showed that there are fewer anisotropies in a DBT system with narrowly-spaced source positions, but that it is not possible to eliminate the anisotropies entirely. Recently, we proposed a "next-generation" DBT system design in which additional source positions are clustered around the conventional positions in submillimeter increments.[10] This design can be implemented by rapidly pulsing the source during continuous motion of the x-ray tube. For frequencies oriented in the *x* direction (laterally or left-to-right in Figure 1), the anisotropies can be eliminated with the use of rapid source pulsing.

A limitation of our previous work[10] on rapid source pulsing is that the perpendicular orientation of the test frequency was not considered; *i.e.*, the posteroanterior (PA) orientation (into the plane of the page in Figure 1). In a conventional DBT system, super-resolution is not achievable in the PA direction. This idea can be illustrated with projection images of a point-like object (Figure 2). Because there is x-ray tube motion in the *x* direction (laterally), there are noticeable shifts in the image of the object between projections, and hence super-resolution is achieved in this direction. However, the shifts in the *y* direction are too small to achieve super-resolution; there is no x-ray tube motion in this direction. In this paper, we show that super-resolution can indeed be achieved in the PA direction with the use of source motion in this direction. This motion can be applied in combination with the use of rapid source pulsing to ensure that super-resolution is achieved with high quality, regardless of the orientation of the input frequency.

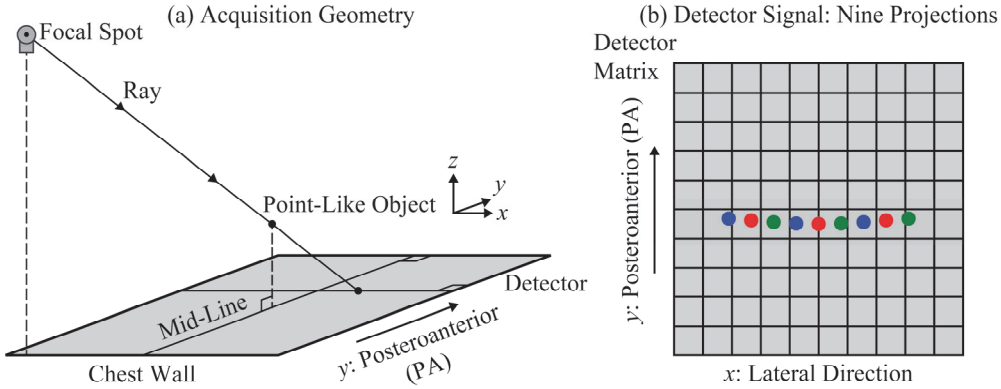

Figure 2. In clinical DBT systems, super-resolution is achieved in the *x* direction, since there is x-ray tube motion in this direction. However, super-resolution is not achieved in the *y* direction; the shifts in the object positions in this direction are minimal.

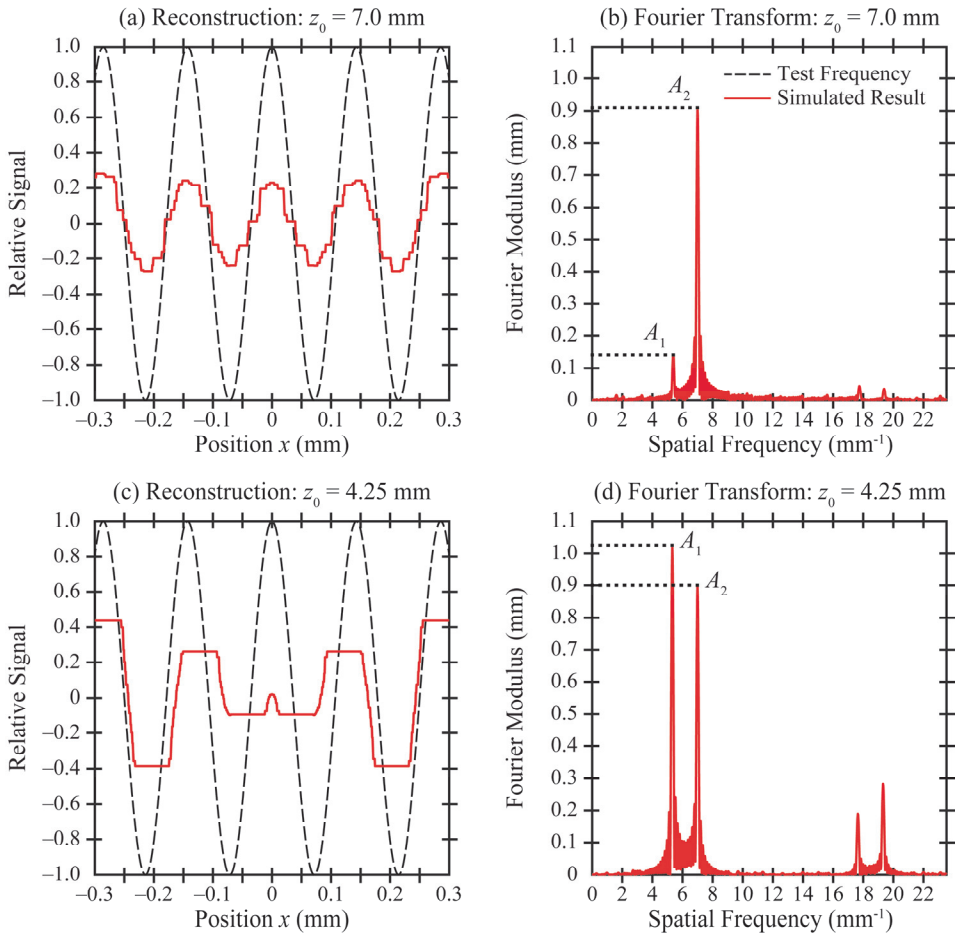

Figure 3. The Fourier transform of the reconstruction is analyzed in terms of two peaks: one at the input frequency (A_2) and one at a lower frequency (A_1). In order for super-resolution to be achieved with high quality, the ratio A_1/A_2 should be as small as possible.

2. METHODS

2.1 Identification of Anisotropies in the Conventional Design

As the first aim of this paper, we demonstrate the existence of anisotropies in the conventional system design. We apply the theoretical model of super-resolution developed in our previous work.[7] In that work, the reconstruction of a sinusoidal test object was calculated from first principles.

The input frequency is modeled separately in two directions: lateral and PA. Anisotropies are identified using the Fourier transform of the reconstruction; this is calculated over 50 cycles with 20 points sampled per cycle. To illustrate how the Fourier transform can be used to assess super-resolution, a 7.0 mm^{-1} test frequency is considered with sampling by a detector with 0.085 mm × 0.085 mm detector elements (Figure 3). The Fourier transform has a major peak at the input frequency if the object is resolved [Figure 3(b)], but has a major peak at a lower frequency if the object is aliased [Figure 3(d)]. Our previous work defined the *r*-factor as a metric to summarize the results in Fourier space.[4,7]

$$r\text{-Factor} = \frac{A_1}{A_2} \tag{1}$$

In order for super-resolution to be achieved with high quality, the *r*-factor should be as small as possible. That is, the amplitude of the low-frequency peak (A_1) should be smaller than the amplitude at the input frequency (A_2). For the purpose of this paper, the threshold for high-quality super-resolution is: *r*-factor < 1/3.

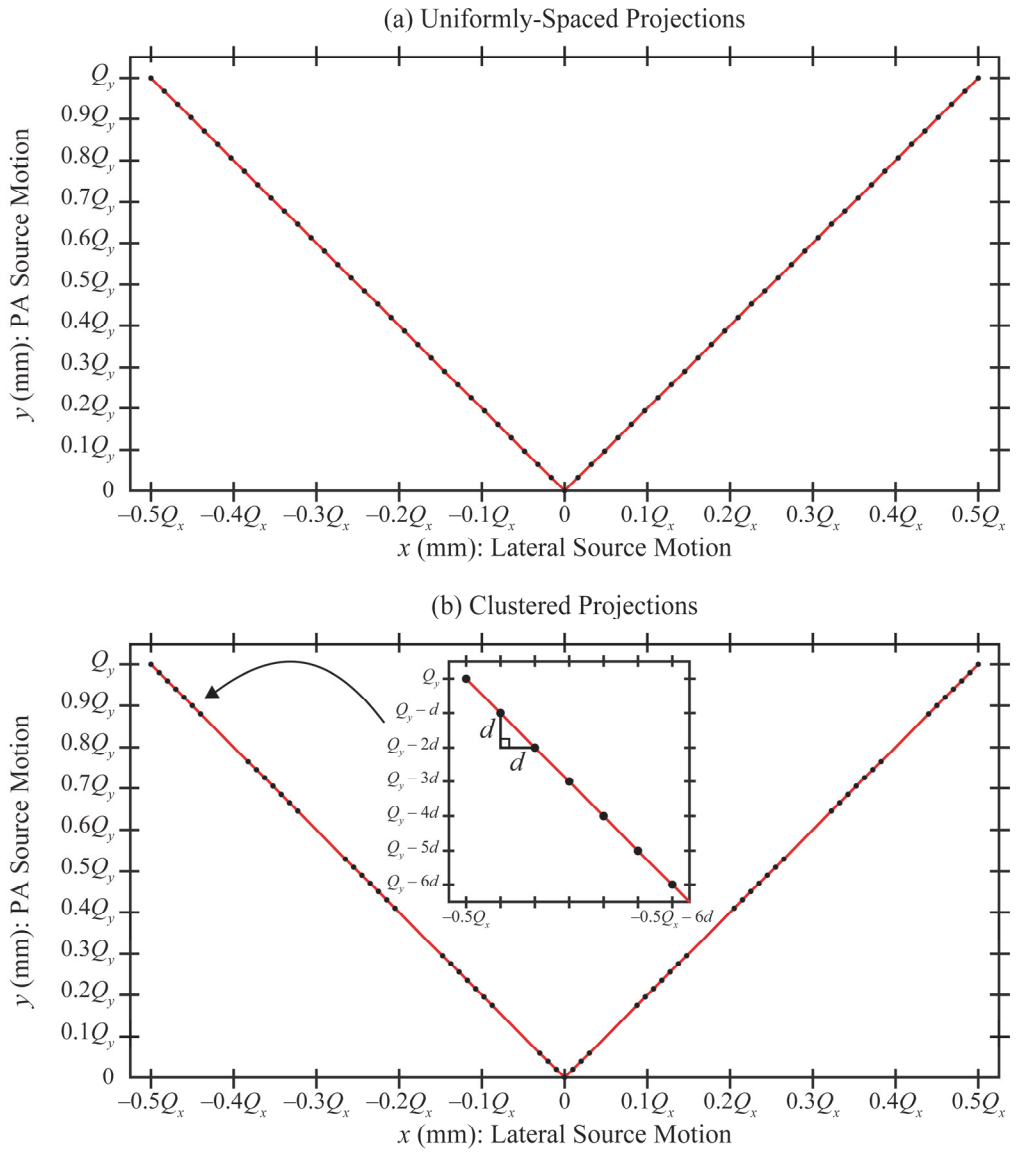

Figure 4. (a) There are 63 source positions spaced uniformly along a V-shaped trajectory. (b) The source positions are re-arranged in nine clusters in the same V-shaped trajectory. There is submillimeter spacing between the seven source positions in each cluster (d = 0.5 mm).

To identify all the coordinates of the anisotropies in the range between z_0 = 0 and z_0 = 50.0 mm, we generated a plot of r-factor as a function of z_0. For this simulation, the sine wave was centered at the position 25.0 mm anterior to the chest wall along the mid-line defined in Figure 2. The acquisition parameters for this simulation are summarized in Table 1.

2.2 VCT Simulations of Bar Pattern Phantom and Calcifications

VCT software was then used to validate the position of the anisotropies expected from theoretical modeling. The acquisition parameters in this simulation are detailed in Table 1. First, we simulated a bar pattern phantom with 0.070 mm cubic voxels, a thickness of 0.070 mm, and a frequency of 7.0 mm^{-1} oriented laterally (parallel with the source motion); *i.e.*, the same orientation as Figure 1. Since the input frequency is higher than the alias frequency of the detector (5.9 mm^{-1} in a 0.085 mm detector), this object can be used to investigate super-resolution.

Table 1. The acquisition parameters for theoretical modeling and VCT simulations are summarized below.

Acquisition Parameter	Theoretical Modeling: Conventional DBT	VCT Simulation: Conventional DBT	Theoretical Modeling: Next-Generation DBT
Source Motion	Circular Arc (*xz* Plane)	Linear (*x*): Constant *z*	V-Shaped: Constant *z*
Source-to-Image Distance	650.0 mm (Central Projection)	621.0 mm	650.0 mm
Number of Projections	15	15	63
Range of Source Motion	$\Theta = 17.7°$ (200.0 mm in *x*)	182.7 mm (in *x*)	200.0 mm (*x*), 100.0 mm (*y*)

Secondly, punctate calcifications[11] were simulated in an anthropomorphic voxel phantom.[12] The phantom was positioned in such a way that the inferior surface was in contact with the detector. Each calcification was modeled by a single voxel with dimensions of 0.070 mm in each direction. There were 25 calcifications arranged linearly in the direction of the source motion. Reconstructions for both the bar pattern and calcifications were prepared with Piccolo™ (Real Time Tomography, LLC, Villanova, PA).[13]

The calcification size and composition were chosen with care. The linear dimension (0.070 mm) was chosen to ensure that the frequency of the array of calcifications was greater than the alias frequency of the detector (5.9 mm^{-1}). This linear dimension is smaller than the smallest calcification (0.16 mm) within the Gammex 156 American College of Radiology (ACR) Mammography Accreditation Phantom; however, the shape of the calcifications in the ACR phantom is unspecified and the volume is less than a cube of that size. In our other work[14], we typically use cubic calcifications with dimensions 0.001 mm^3, 0.002 mm^3, and 0.003 mm^3, with weighting factors (fraction by mass) between 10% and 100% hydroxyapatite. These calcifications are equivalent in volume to spherical calcifications of diameters 0.124, 0.156, and 0.180 mm. In this paper, we use a $(0.070\ mm)^3$ calcification with a weighting factor of 100%, which has the same attenuation as a 0.124 mm diameter calcification with a weighting factor of 0.34, consistent with our other VCTs.

2.3 Modeling A New System Design

Next, we investigated a "next-generation" system design. The number of projections (63) is well above the number used clinically (Table 1); this is known from our previous work to improve the quality of super-resolution.[10] The design modeled in this paper differs from our previous work in that we model PA source motion; *i.e.*, an additional degree of freedom in the *y* direction. The motion follows a V-shape (Figure 4). The ranges of source motion in the lateral and PA directions (Q_x and Q_y) are 200.0 mm and 100.0 mm, respectively. The range of 200.0 mm in the *x* direction is similar to the conventional system described in Section 2.1.

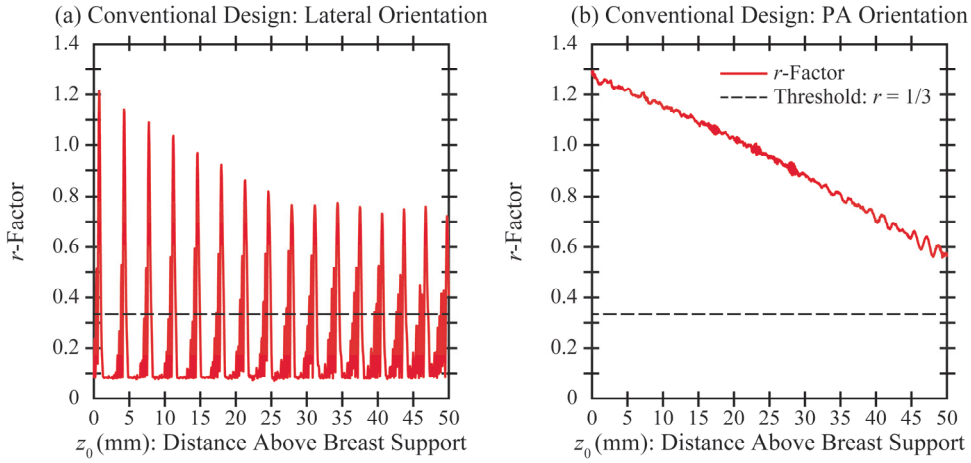

Figure 5. To achieve super-resolution with high quality, the *r*-factor should be as small as possible (below the threshold of 1/3 for the purpose of this paper). The coordinates of the anisotropies differ based on the orientation of the input frequency.

Figure 6. VCT simulations of a 7.0 mm^{-1} bar pattern phantom illustrate the z-dependency of super-resolution in the reconstruction.

For the same V-shaped motion, we investigated two acquisition geometries, each differing in terms of the choice of source positions. In one scan, we applied the principle of rapid source pulsing [Figure 4(b)], which was proposed in our previous work.[10] The source positions were arranged in nine sets of clusters with seven source positions per cluster (63 source positions in total). Within each cluster, the spacing (d) between the source positions was 0.50 mm in each direction. By contrast, in a second scan, there was equal spacing between all 63 source positions [Figure 4(a)]. We investigated whether the use of clustering offers a benefit over the use of uniform spacing. Like the simulations described in Section 2.1, we calculated the r-factor to determine which of these two acquisition geometries offers the best image quality over the broadest range of positions (z_0).

3. RESULTS

3.1 Modeling the Conventional System Design

First, image quality in a conventional DBT system was modeled by the r-factor (Figure 5). Anisotropies are present in both orientations of the input frequency. In the lateral orientation, super-resolution is not achieved at the z-coordinates at which the r-factor peaks sharply. In the PA orientation, super-resolution is not achieved with high quality anywhere; the r-factor is above the threshold of 1/3. In summary, these results illustrate the limitations of current clinical systems.

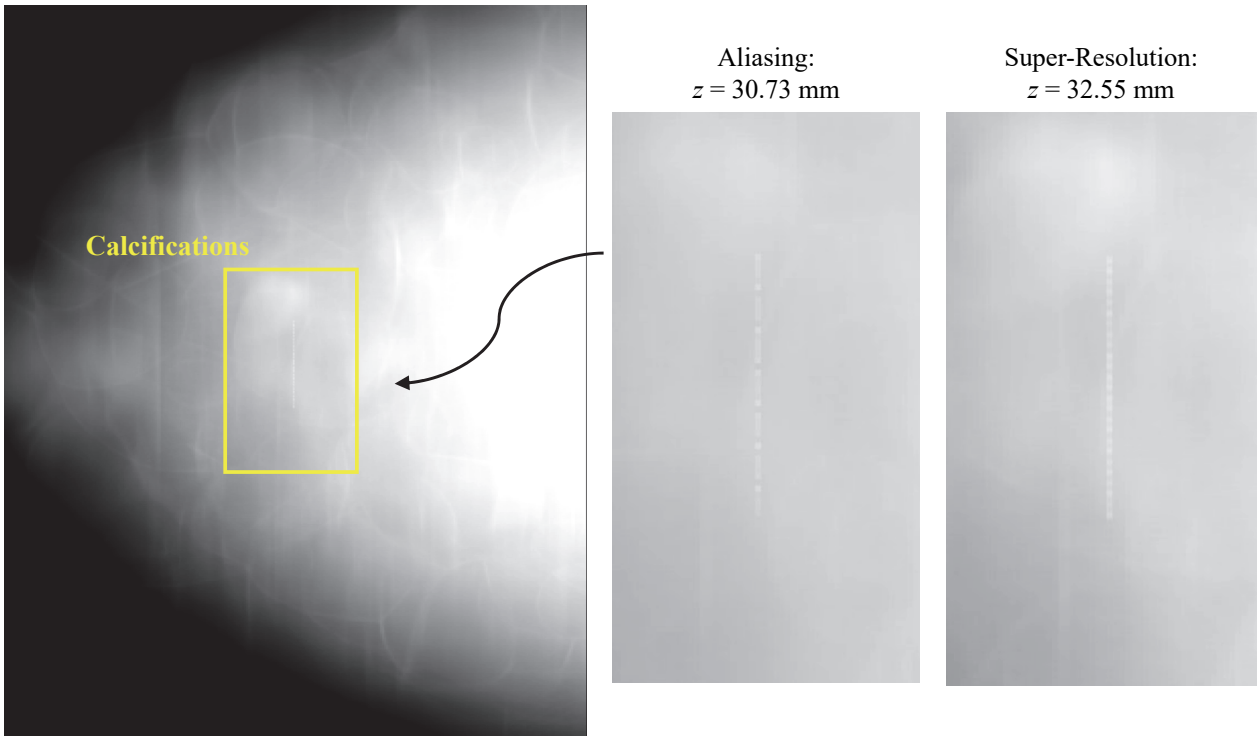

Figure 7. The ability to resolve individual punctate calcifications in a linear array is dependent on the positioning of the cluster.

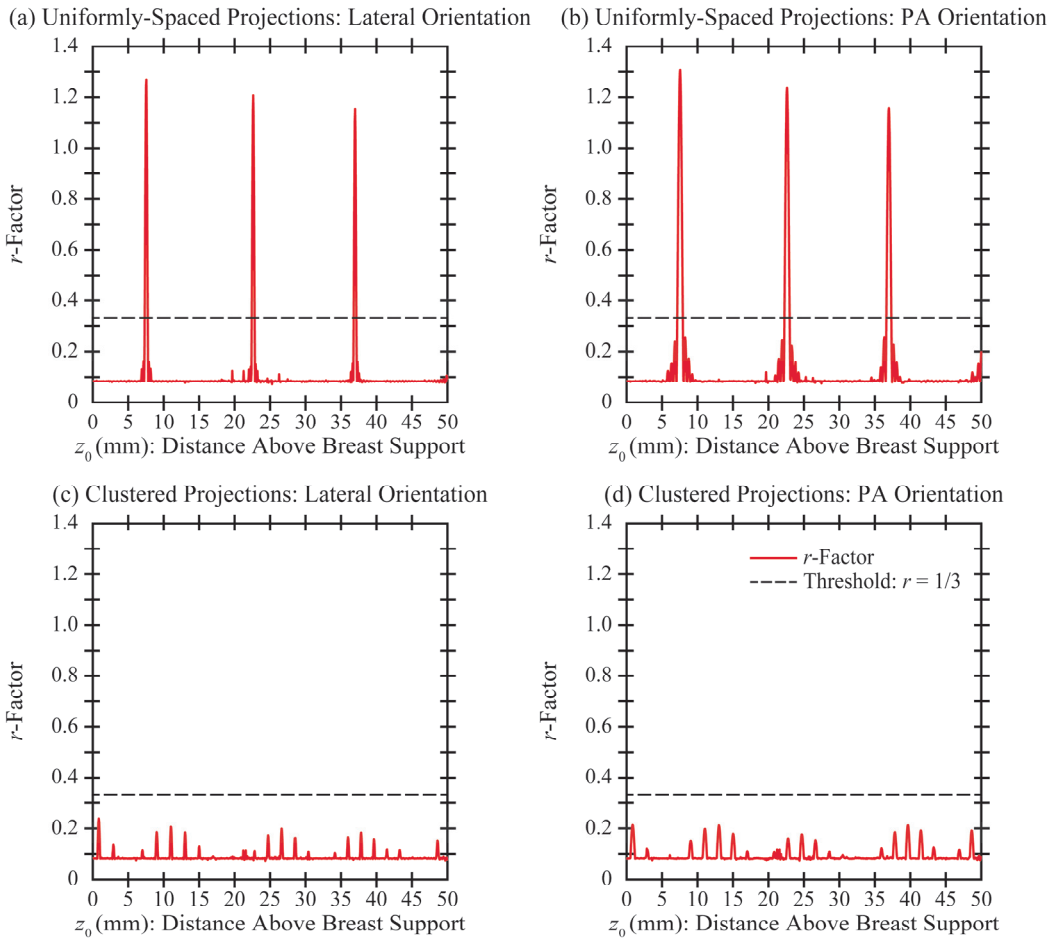

Figure 8. A DBT system is modeled with V-shaped source motion and 63 projections (well above the number of projections used clinically). To eliminate the anisotropies, the source positions should be arranged in clusters; this ensures that the *r*-factor is below 1/3 (the threshold for high-quality super-resolution).

3.2 VCT Simulations of Bar Pattern Phantom and Calcifications

Next, the bar pattern phantom and calcifications were simulated with VCT software in a conventional acquisition geometry (Table 1). This geometry differs slightly from the one analyzed with theoretical modeling (Section 3.1) in that the orbit of the x-ray tube does not follow an arc in the *xz* plane. Instead, the source is translated in only one direction (*x*) at constant *z*. This motion is consistent with the next-generation tomosynthesis (NGT) system, which we built for research use to investigate different acquisitions geometries for DBT.[15]

With theoretical modeling of the *r*-factor, a plot similar to Figure 5(a) can be created to identify anisotropies in this acquisition geometry. It can be shown, for example, that there is an anisotropy at the position 30.73 mm above the detector. At this position, the bar pattern phantom shows aliasing (Figure 6), and it is not possible to resolve each individual calcification in the reconstruction (Figure 7). However, super-resolution is supported at other positions in the reconstruction; for example, at the coordinate 32.55 mm above the detector. Here, the bar pattern phantom is resolved and each individual calcification is discernable.

3.3 Modeling A New System Design

Finally, the two V-shaped acquisition geometries were analyzed with theoretical modeling (Figure 8). Unlike the conventional acquisition geometry, super-resolution can indeed be achieved in the PA orientation; this is due to the use of PA source motion, which introduces subpixel sampling gain in that direction. The disadvantage of having uniform spacing between projections is that there are anisotropies; *i.e.*, three peaks in the *r*-factor [Figure 8(a)-(b)]. In order for the anisotropies to be eliminated, the source positions should be re-arranged in clusters [Figure 8(c)-(d)]; this design ensures that the *r*-factor is below 1/3 at all positions in the reconstruction.

4. DISCUSSION AND CONCLUSION

In our previous work, we showed that DBT is capable of super-resolution, but that clinical systems are not yet designed to optimize this effect.[4,7] There are regularly-spaced positions in the *z* direction at which super-resolution is not achievable. This paper validates the VCT software as a tool to simulate the anisotropies. We also show that the appearance of calcifications can be distorted by the presence of anisotropies; this could potentially impact the way calcifications are characterized by a radiologist.

A design for optimizing super-resolution was proposed in our previous work.[10] We modeled a system with additional source positions clustered around the conventional positions in submillimeter increments, and found that super-resolution is achieved everywhere in the reconstruction. A limitation of our previous work is that we only considered frequencies oriented laterally (Figure 1). In this paper, the PA orientation is also analyzed. Anisotropies in both orientations can be eliminated by applying the use of clustering in combination with PA motion; *i.e.*, an additional degree of freedom in the source motion.

Our previous work demonstrated that the use of PA source motion is also beneficial in other imaging tasks. In clinical DBT systems, there is a cone-beam artifact in the PA direction.[16] With Defrise phantoms, we showed that this artifact can be suppressed with the use of PA source motion.[15,17] Another advantage of PA source motion is that the accuracy of the breast outline segmentation in the reconstruction is improved.[18] The air gap between the breast support and the anterior aspect of the breast is visualized more clearly with the PA projection views.

In our previous work, we investigated a new design for the detector (motion in the *z* direction) as an alternative strategy for optimizing super-resolution.[7] In order for this strategy to be implemented clinically, it may be necessary to increase the thickness of the detector housing, which could be cumbersome for patient positioning. The advantage of the design proposed in this paper is that the detector can remain stationary during the scan. This design will require a detector capable of a high frame rate, since the number of projection views (63) exceeds the number that is typically used clinically. Also, the radiation dose per projection will need to be reduced so that the total dose of the scan is unchanged.

5. ACKNOWLEDGEMENT

We thank Johnny Kuo, Susan Ng, and Peter Ringer of Real Time Tomography (RTT) for technical assistance with Piccolo™. Andrew D. A. Maidment is a shareholder of RTT, and is a member of the scientific advisory board. Support was provided by the following grants: W81XWH-18-1-0082 from the Department of Defense Breast Cancer Research Program, IRSA 1016451 from the Burroughs Wellcome Fund, 1R01CA196528 from the National Institute of Health, and IIR13264610 from Susan G. Komen®. In addition, equipment support was provided by Analogic Inc., Barco NV, and RTT. The content is solely the responsibility of the authors and does not necessarily represent the official views of the funding agencies.

6. REFERENCES

1. Friedewald SM, Rafferty EA, Rose SL, et al. Breast Cancer Screening Using Tomosynthesis in Combination With Digital Mammography. *Journal of the American Medical Association.* 2014;311(24):2499-2507.
2. Sechopoulos I. A review of breast tomosynthesis. Part I. The image acquisition process. *Medical Physics.* 2013;40(1):014301-014301 to 014301-014312.
3. Sechopoulos I. A review of breast tomosynthesis. Part II. Image reconstruction, processing and analysis, and advanced applications. *Medical Physics.* 2013;40(1):014302-014301 to 014302-014317.
4. Acciavatti RJ, Maidment ADA. Observation of super-resolution in digital breast tomosynthesis. *Medical Physics.* 2012;39(12):7518-7539.
5. Acciavatti RJ, Maidment ADA. Investigating the Potential for Super-Resolution in Digital Breast Tomosynthesis. Paper presented at: SPIE Medical Imaging2011; Lake Buena Vista, FL.
6. Lu Y, Chan H-P, Wei J, Hadjiiski L, Samala R. Study of Image Quality in Digital Breast Tomosynthesis by Subpixel Reconstruction. Paper presented at: SPIE Medical Imaging2013; Lake Buena Vista, FL.
7. Acciavatti RJ, Wileyto EP, Maidment ADA. Modeling Acquisition Geometries with Improved Super-Resolution in Digital Breast Tomosynthesis. Paper presented at: SPIE Medical Imaging2016; San Diego, CA.

8. Barufaldi B, Higginbotham D, Bakic PR, Maidment ADA. OpenVCT: A GPU-Accelerated Virtual Clinical Trial Pipeline for Mammography and Digital Breast Tomosynthesis. Paper presented at: SPIE Medical Imaging2018; Houston, TX.

9. Bakic PR, Barufaldi B, Higginbotham D, et al. Virtual Clinical Trial of Lesion Detection in Digital Mammography and Digital Breast Tomosynthesis. Paper presented at: SPIE Medical Imaging2018; Houston, TX.

10. Acciavatti RJ, Noël PB, Maidment ADA. Proposing Rapid Source Pulsing for Improved Super-Resolution in Digital Breast Tomosynthesis. Paper presented at: SPIE Medical Imaging2020 (accepted); Houston, TX.

11. Lanyi M. Chapter 4: Calcifications Within the Lobular and Ductal System of the Breast. *Diagnosis and Differential Diagnosis of Breast Calcifications*. Berlin: Springer-Verlag; 1988:29-143.

12. Pokrajac DD, Maidment ADA, Bakic PR. Optimized generation of high resolution breast anthropomorphic software phantoms. *Medical Physics*. 2012;39(4):2290-2302.

13. Kuo J, Ringer PA, Fallows SG, Bakic PR, Maidment ADA, Ng S. Dynamic Reconstruction and Rendering of 3D Tomosynthesis Images. Paper presented at: SPIE Medical Imaging2011; Lake Buena Vista, FL.

14. Barufaldi B, Vent TL, Acciavatti RJ, et al. Determining the Optimal Angular Range of the X-Ray Source Motion in Tomosynthesis Using Virtual Clinical Trials. Paper presented at: SPIE Medical Imaging2020 (accepted); Houston, TX.

15. Eben JE, Vent TL, Choi CJ, et al. Development of a Next Generation Tomosynthesis System. Paper presented at: SPIE Medical Imaging2018; Houston, TX.

16. Acciavatti RJ, Mannherz W, Nolan M, Maidment ADA. An Alternate Design for the Defrise Phantom To Quantify Resolution in Digital Breast Tomosynthesis. Paper presented at: SPIE Medical Imaging2017; Orlando, FL.

17. Acciavatti RJ, Barufaldi B, Vent TL, Wileyto EP, Maidment ADA. Personalization of X-Ray Tube Motion in Digital Breast Tomosynthesis Using Virtual Defrise Phantoms. Paper presented at: SPIE Medical Imaging2019; San Diego, CA.

18. Acciavatti RJ, Rodriguez-Ruiz A, Vent TL, et al. Analysis of Volume Overestimation Artifacts in the Breast Outline Segmentation in Tomosynthesis. Paper presented at: SPIE Medical Imaging2018; Houston, TX.

MRMC ROC Analysis of Calcification Detection in Tomosynthesis Using Computed Super Resolution and Virtual Clinical Trials

Bruno Barufaldi*, Trevor L. Vent, Raymond J. Acciavatti, Predrag R. Bakic, Peter B. Noël and Andrew D. A. Maidment

Department of Radiology, University of Pennsylvania, Philadelphia, United States.
*Bruno.Barufaldi@pennmedicine.upenn.edu

ABSTRACT

Digital breast tomosynthesis (DBT) reduces breast tissue overlap, which is a major limitation of digital mammography. However, DBT does not show significant improvement in calcification detection, because of the limited angle and small number of projections used to reconstruct the 3D breast volume. Virtual clinical trials (VCTs) were used to evaluate the benefits of computed super resolution (SR) and the optimal combination of the acquisition parameters to improve calcification detection in DBT. We simulated calcifications that were embedded into software breast phantoms. DBT projections of the breast phantoms with and without calcifications were synthesized. We simulated detector elements of 0.085 mm and reconstructed DBT images using 0.0425 mm and 0.085 mm voxels. Channelized Hotelling observers (CHOs) were trained and tested to simulate five virtual readers. Differences in area under the curve (AUC) between SR images and images synthesized with 0.085 mm voxels were calculated using the one-shot multiple-reader multiple-case receiver operator curve (MRMC ROC) methods. Our results show that the differences in AUC is approximately 0.10, 0.03 and 0.03 for DBT images simulated using calcifications sizes 0.001 mm^3, 0.002 mm^3, and 0.003 mm^3, respectively. SR shows a substantial improvement for calcification detection in DBT. The impact of SR on calcification detection is more prominent for small calcifications.

Keywords: virtual clinical trial; multiple-reader, multiple-case; digital breast tomosynthesis; super resolution.

1. INTRODUCTION

Digital breast tomosynthesis (DBT) has been shown to reduce recall rates by resolving overlapped breast structures seen on digital mammography.[1] However, there is some concern that DBT may not depict small breast structures such as calcifications,[2,3] due to the limited angle and small number of tomographic projections. Alternative imaging methods are required to improve calcification detection and to maximize the benefits of mammography screening with DBT.

Computed super-resolution (SR) is a reconstruction method with pixels that are smaller than the detector element size; superior spatial resolution is achieved through the elimination of aliasing and alteration of the sampling function imposed by the reconstructed pixel aperture.[4] However, this reconstruction method is not well explored by others because it can increase the image size and time to reconstruct tomographic projections.

We have developed an open-source Virtual Clinical Trial (Open VCT) framework that allows the projection and reconstruction of DBT images in real-time. Our VCT framework has been used to evaluate and to optimize imaging systems by performing simulations of the human breast anatomy, DBT image acquisition, and image interpretation.[5–7]

We have shown in a previous study that calcification detection in DBT is substantially affected by reconstructed voxel size, detector element size, and tube motion.[8] However, the optimal combination of acquisition parameters in DBT is still under investigation.[9] VCTs can be used to investigate the limit of calcification detection and to evaluate promising imaging designs, avoiding the pursuit of inefficient DBT acquisition parameters.[8,10]

In this work, we present a VCT method for determining the most suitable reconstructed voxel size for calcification detection in DBT. Voxelized single calcifications 0.001 mm^3, 0.002 mm^3, and 0.003 mm^3 were inserted into software breast phantoms. Fifteen DBT projections of the breast phantoms with and without lesions were synthesized simulating the imaging geometry of the next generation of tomosynthesis (NGT) system. We simulated and varied the reconstructed voxel size using 0.0425 mm and 0.085 mm, with 0.085 mm detector elements (del). We also simulate five virtual readers to evaluate the calcification detection using multiple-reader, multiple-case (MRMC) receiver operator curve (ROC) analyses.[11]

15th International Workshop on Breast Imaging (IWBI2020), edited by Hilde Bosmans, Nicholas Marshall, Chantal Van Ongeval, Proc. of SPIE Vol. 11513, 1151313
© 2020 SPIE · CCC code: 0277-786X/20/$21 · doi: 10.1117/12.2564118

2. MATERIALS & METHODS

2.1 DBT Image Simulations

Virtual anthropomorphic breast phantoms were developed to simulate healthy breast anatomy using an efficient recursive partitioning method.[12,13] The recursive partitioning method supports a large number of breast simulations in terms of simulations per GPU-hour.[5] In this work, we simulated 80 breast phantoms with 700mL and uncompressed breast thickness of 126.6 mm. We combined coarse- and fine-breast phantoms,[13] with volumetric breast densities that varied from 5% to 60% to improve the realism of the anthropomorphic breast phantoms.

The simulation of medio-lateral (ML) breast compression uses a GPU accelerated 3D mesh software.[14] The breast tissue compression was simulated using neo-Hookean models, with Poisson ratio of 0.49 and Young's modulus of 12.75 kPa, to reduce the phantom thickness by 50% (thickness=63.3 mm).[6]

Single calcifications were simulated using one-, two- and three- voxel polycubes,[13] with individual cubic voxels of size 0.1 mm. The calcification composition was varied by a weighting factor, which controls the calcification attenuation in the synthesized x-ray image. This factor represents the fraction of hydroxyapatite in the calcifications (Figure 1). The weighting factor was varied as a fraction of 0.30, 0.40, and 0.50 hydroxyapatite. The specific range of weighting factors was selected based upon results presented in a previous study. We inserted a dense array of 42 calcifications, arranged 20 mm apart, into each compressed breast phantoms. The array was positioned in the central plane parallel to detector at the level of the nipple (ML phantom view). The method used for inserting calcifications into the breast phantoms was described in previous studies.[8,15]

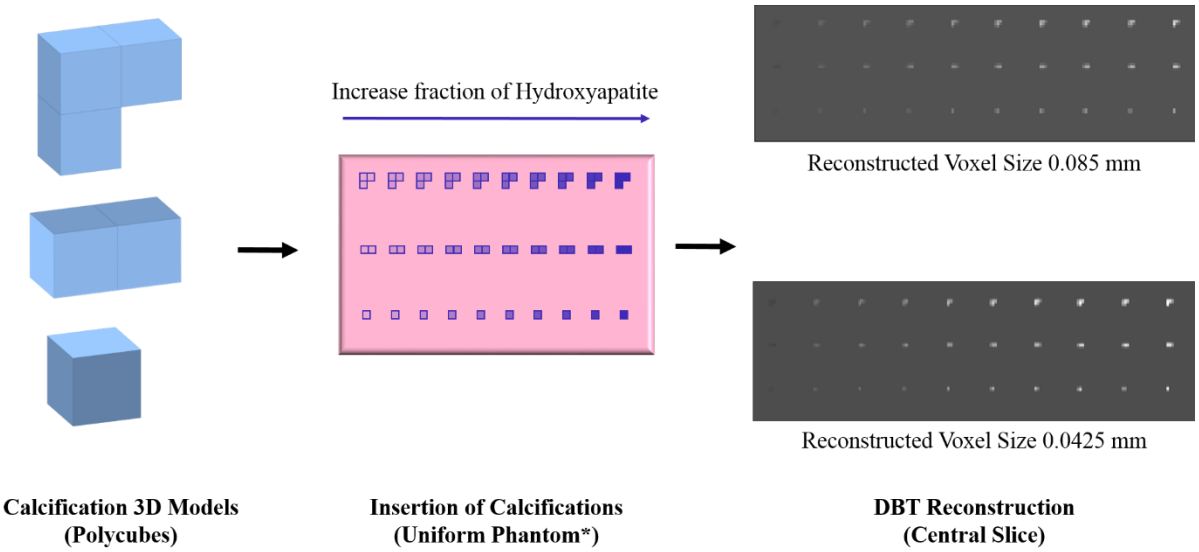

Figure 1. Method used to insert calcifications into the anthropomorphic breast phantoms. *Illustrative phantom used to visualize differences in fraction of hydroxyapatite in the DBT reconstructions.

In this study, we simulated the NGT acquisition geometry to synthesize DBT projections of the breast phantoms with and without calcifications. The image acquisition was simulated using step-and-shoot tube motion, and the angular range of the x-ray source was simulated using ±7.5°. In total, 15 equally-spaced DBT projections were simulated using the Siddon algorithm for x-ray tracing.[16] The DBT projections were generated using 0.085 mm^2 del, with a detector contained a total of 3584×2816 dels. The DBT images were reconstructed using 0.085 mm and 0.0425 mm reconstructed voxel sizes. DBT images reconstructed with 0.0425 mm voxel size represent the SR images. The images were reconstructed only at the central ML phantom view to accelerate the image simulations. The reconstructed DBT images were synthesized using the Briona software (Real-Time Tomography, Villanova, PA).[17]

We cropped regions of interest (ROIs) with and without calcifications, with sizes of 175×175 and 350×350 pixels for each image reconstructed using 0.085 mm and 0.0425 mm reconstructed voxel size, respectively. The ROIs with lesions were selected with the calcifications centered at the ROI.

2.2 Virtual Readers and ROC analyses

Channelized Hotelling observers (CHOs) were trained and tested to simulate five virtual readers.[18,19] The CHOs were simulated using 15 Laguerre-Gauss (LG) channels. We used LG spread sizes of 26 and 52, for each image reconstructed with reconstructed voxel size of 0.085 mm and 0.0425 mm, respectively. For each reader, independent training and testing image sets included 252 ROIs with simulated calcifications and 252 calcification-free ROIs. The readers were tested with a common image set that also included 252 ROIs. The ROIs used for training and testing were selected randomly.

We measured the readers' performance in calcification detection using MRMC ROC analyses provided by the MeVIC software (Barco NV, Kortrijk, Belgium).[20] The MeVIC software provides a module that estimates one-shot MRMC statistics.[11,21] We calculated the ROCs of each individual reader using the readers' scores. We analyzed the difference in area under the curve (AUC) and SE AUC between readers. We also evaluated differences in AUC between SR images and images reconstructed with 0.085 mm voxel size. Finally, we calculated the one-shot MRMC, which summarizes the ROC statistics of five readers.

3. RESULTS & DISCUSSION

The following parameters were varied and evaluated in our DBT simulations: number of calcification voxels (1, 2, and 3), weighting factor (0.30, 0.40, and 0.50), and reconstructed voxel size (0.0425 mm and 0.085 mm). The detector element did not vary (0.085 mm), so we can evaluate the performance of each individual reader in calcification detection using smaller reconstructed voxel sizes (i.e., SR images). The pooled ROC curves of mixed calcifications using the three weighting factors are shown in Figure 2. Note that there is a small variation between readers for each analyzed condition because of the large number of ROIs used for training and testing. There is a significant improvement in the calcification detection using smaller reconstructed voxels; this is more prominent for 1-voxel calcifications.

The AUC results of each reader are summarized in Table 1. Note that SR images (Table 1B, Table 1D, and Table 1F) have an AUC improvement in calcification detection. The improvement in detection of SR images results in a difference in AUC of approximately 0.10, 0.03, and 0.03 for 1-, 2-, and 3- voxel calcifications. For DBT projections simulated using 0.085 mm del, the calcification detection is substantially affected using SR images. Again, the SR impact is more prominent for images synthesized using 1- voxel calcification.

For calcification detection, the difference in AUC between SR images and images synthesized with 0.085 mm reconstructed voxel size were calculated using the one-shot MRMC ROC analysis (Figure 3). For 1-voxel calcifications, the difference in AUC of SR and images reconstructed using 0.085 mm del was 0.11, 0.08 and 0.11 for DBT images simulated using weighting factors 0.3, 0.4, and 0.5, respectively. For 2-voxel calcifications, the difference in AUC of SR and images reconstructed using 0.085 mm del was 0.02, 0.03 and 0.03 for DBT images simulated using weighting factors 0.3, 0.4, and 0.5, respectively. Finally, for 3-voxel calcifications, the difference in AUC of SR and images reconstructed using 0.085 mm del was 0.06, 0.02 and 0.01 for DBT images simulated using weighting factors 0.3, 0.4, and 0.5, respectively. Although the AUC difference is higher for 1-voxel calcifications, the standard deviation is also higher.

To predict readers' performance in calcification detection, synthetic calcifications should be calibrated based upon the size and composition of calcifications found in breast carcinomas. In this study, we simulated single calcifications as polycubes (i.e., cubic calcifications) of sizes 0.001 mm^3, 0.002 mm^3, and 0.003 mm^3 to predict and to evaluate the *limit in calcification detection* of DBT. Previous stereoscopic studies have shown clusters of punctuated calcifications of variable sizes from 0.1 to 0.3 mm, [23,24] which represent spherical calcifications of diameters 0.124, 0.156, and 0.180 mm in the DBT image. In addition, calcifications should be simulated using admixtures of different material compositions [e.g., $Ca_3(PO_4)_2$, $CaCo_3$, $Mg_3(PO_4)_2 \cdot H_2O$, Protein, etc.].[23,24] Thus, we varied the weighting factors of hydroxyapatite to simulate more realistic calcifications.

Ultimately, we will evaluate calcification detection in DBT using SR images synthesized with larger detector element sizes, and a range of weighting factors. We will also calculate the *d'* statistics and validate results acquired using the one-shot MRMC ROC analyses. The *d'* represents the *effective signal-to-noise ratio perceived by the observer*, while the AUC represents values that vary non-linearly from 0.5 (i.e., random guessing) to 1.0 (i.e., relationship between disease and normal found with 100% certainty). Based upon results in previous studies,[8,15] we can better discriminate improvement in the performance of calcification detection in DBT by calculating the ratio of *d'* between the new and the predicate DBT acquisition geometry instead of difference in AUCs.

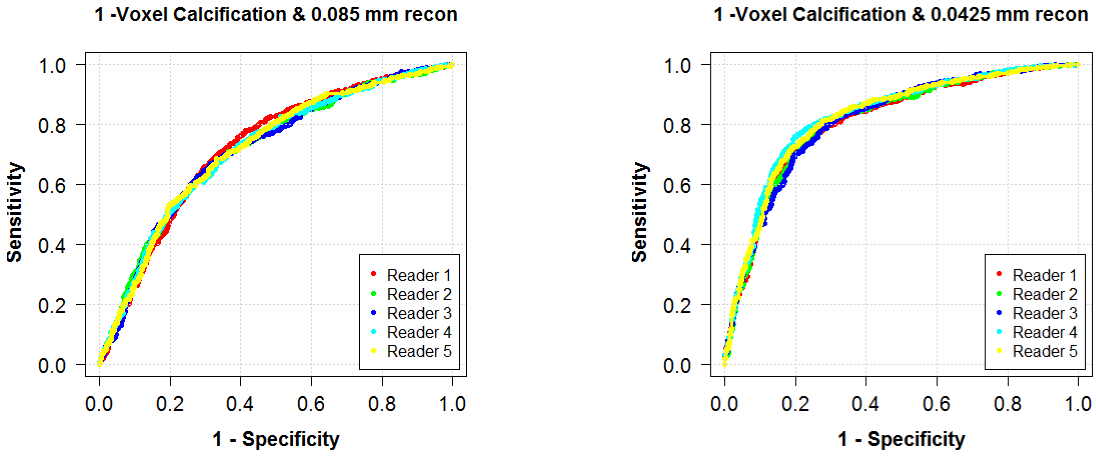

(A)

(B)

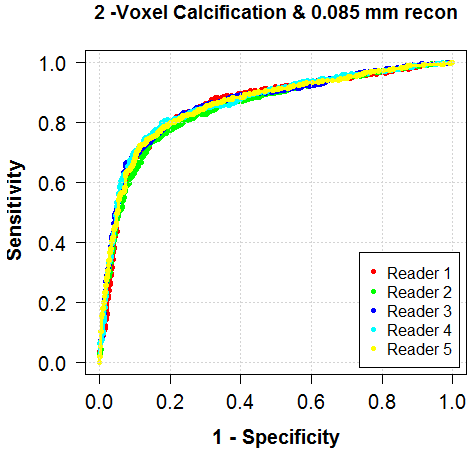

(C)

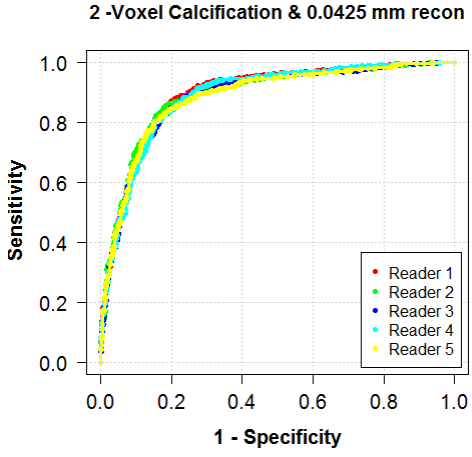

(D)

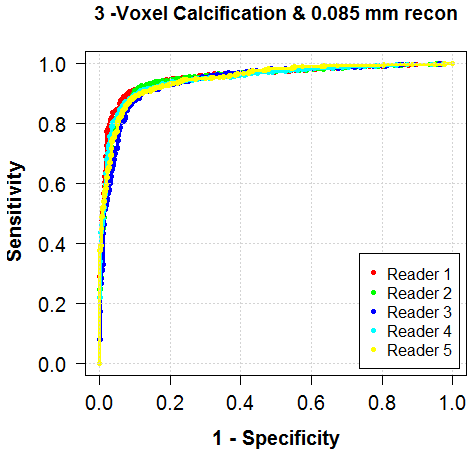

(E)

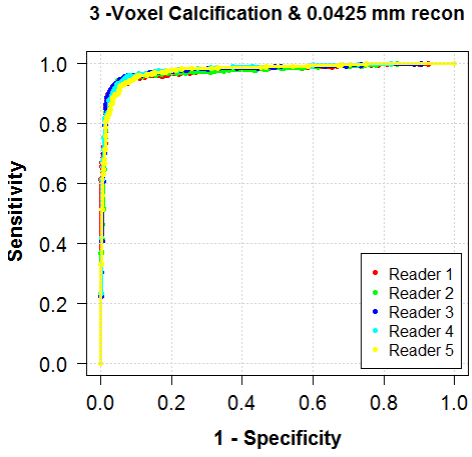

(F)

Figure 2. ROC curves of each individual reader using the image set: (left) 0.085 mm reconstructed voxel size and (right) 0.0425 mm reconstructed voxel size.

Table 1. Summary of the AUCs of each individual reader: (left) 0.085 mm reconstructed voxel size and (right) 0.0425 mm reconstructed voxel size. Standard error (SE) AUC, and 95% CI upper and lower are also shown.

	(A) 1-Voxel Calcification & 0.085 mm recon					(B) 1-Voxel Calcification & 0.0425 mm recon				
	Reader 1	**Reader 2**	**Reader 3**	**Reader 4**	**Reader 5**	**Reader 1**	**Reader 2**	**Reader 3**	**Reader 4**	**Reader 5**
AUC	0.724	0.716	0.715	0.717	0.719	0.812	0.814	0.814	0.830	0.824
SE AUC	0.013	0.013	0.013	0.013	0.013	0.011	0.011	0.011	0.011	0.011
95% CI upper	0.749	0.742	0.741	0.742	0.744	0.834	0.835	0.836	0.850	0.845
95% CI lower	0.698	0.690	0.689	0.691	0.693	0.790	0.792	0.793	0.809	0.803
	(C) 2-Voxel Calcification & 0.085 mm recon					**(D) 2-Voxel Calcification & 0.0425 mm recon**				
	Reader 1	**Reader 2**	**Reader 3**	**Reader 4**	**Reader 5**	**Reader 1**	**Reader 2**	**Reader 3**	**Reader 4**	**Reader 5**
AUC	0.858	0.849	0.863	0.863	0.861	0.895	0.891	0.885	0.890	0.885
SE AUC	0.010	0.010	0.010	0.010	0.010	0.008	0.008	0.009	0.008	0.009
95% CI upper	0.878	0.869	0.882	0.882	0.880	0.911	0.907	0.902	0.906	0.902
95% CI lower	0.839	0.829	0.844	0.844	0.842	0.878	0.874	0.868	0.873	0.868
	(E) 3-Voxel Calcification & 0.085 mm recon					**(F) 3-Voxel Calcification & 0.0425 mm recon**				
	Reader 1	**Reader 2**	**Reader 3**	**Reader 4**	**Reader 5**	**Reader 1**	**Reader 2**	**Reader 3**	**Reader 4**	**Reader 5**
AUC	0.956	0.951	0.944	0.950	0.950	0.975	0.973	0.978	0.981	0.977
SE AUC	0.005	0.006	0.006	0.006	0.005	0.004	0.004	0.004	0.003	0.004
95% CI upper	0.967	0.962	0.955	0.961	0.961	0.983	0.982	0.986	0.987	0.984
95% CI lower	0.946	0.941	0.932	0.939	0.940	0.968	0.965	0.971	0.975	0.971

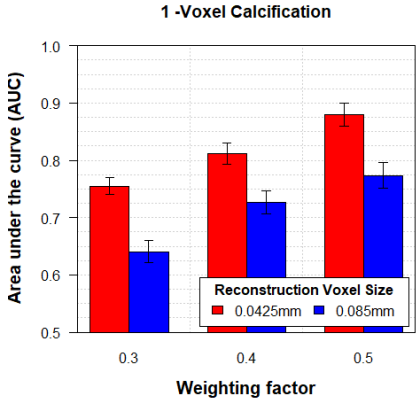

(A)

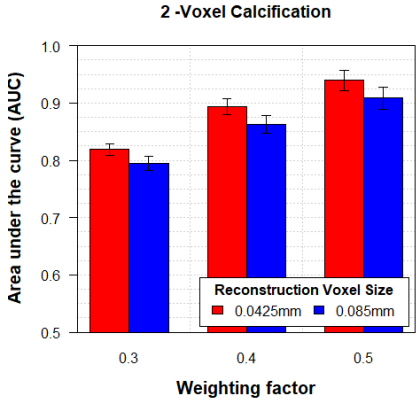

(B)

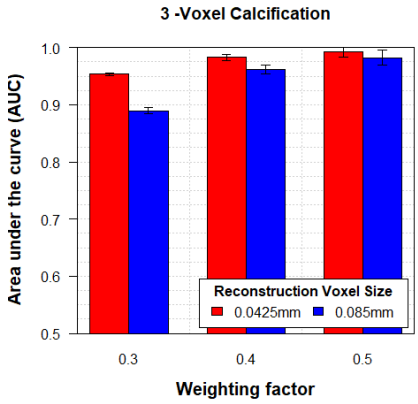

(C)

Figure 3. Summary of the AUCs of one-shot MRMC ROC analyses, categorized by weighing factor. Standard deviations between five virtual readers are shown.

4. CONCLUSION

In this study, we sought to determine the most suitable reconstructed voxel size for calcification detection in DBT, as well as to analyze the impact of computed-SR in calcification detection. Computed-SR is superior to conventional reconstruction methods for calcification detection in DBT. In this study, the impact of SR on calcification detection is more prominent for small calcifications. These results are still preliminary; however, we believe they provide guidance on how to improve the detectability of calcifications, which is an ongoing problem in tomosynthesis. Analysis of how additional conditions may affect calcification detection are forthcoming.

ACKNOWLEDGEMENTS

Funding for the research is supported by the following grants: NIH R01 CA154444, NIH R01 EB018958, Komen IIR-13262248, BWF IRSA 1016451, and DoD W81XWH-18-1-0082.

REFERENCES

[1] Gur, D., Abrams, G. S., Chough, D. M., Ganott, M. a., Hakim, C. M., Perrin, R. L., Rathfon, G. Y., Sumkin, J. H., Zuley, M. L. and Bandos, A. I., "Digital breast tomosynthesis: Observer performance study," Am. J. Roentgenol. **193**(2), 586–591 (2009).

[2] Poplack, S. P., Tosteson, T. D., Kogel, C. A. and Nagy, H. M., "Digital breast tomosynthesis: Initial experience in 98 women with abnormal digital screening mammography," Am. J. Roentgenol. **189**(3), 616–623 (2007).

[3] Rafferty, E. A., Park, J. M., Philpotts, L. E., Poplack, S. P., Sumkin, J. H., Halpern, E. F. and Niklason, L. T., "Diagnostic accuracy and recall rates for digital mammography and digital mammography combined with one-view and two-view tomosynthesis: Results of an enriched reader study," Am. J. Roentgenol. **202**(2), 273–281 (2014).

[4] Maidment, T. D., Vent, T. L., Ferris, W. S., Wurtele, D. E., Acciavatti, R. J. and Maidment, A. D. A., "Comparing the imaging performance of computed super resolution and magnification tomosynthesis," Med. Imaging 2017 Phys. Med. Imaging **10132**, 1013222 (2017).

[5] Barufaldi, B., Bakic, P. R., Higginbotham, D. and Maidment, A. D. A., "OpenVCT: a GPU-accelerated virtual clinical trial pipeline for mammography and digital breast tomosynthesis," SPIE Med. Imaging 2018 **1057358**(March), 1–8, Houston, TX (2018).

[6] Barufaldi, B., Bakic, P. R., Pokrajac, D. D., Lago, M. A. and Maidment, A. D. A., "Developing populations of software breast phantoms for virtual clinical trials," 14th Int. Work. Breast Imaging (IWBI 2018)(July), 73 (2018).

[7] Badano, A., Graff, C. G., Badal, A., Sharma, D., Zeng, R., Samuelson, F. W., Glick, S. J. and Myers, K. J., "Evaluation of Digital Breast Tomosynthesis as Replacement of Full-Field Digital Mammography Using an In Silico Imaging Trial," JAMA Netw. Open **1**(7), 1–12 (2018).

[8] Barufaldi, B., Bakic, P. R. and Maidment, A. D. A., "Multiple-reader, multiple-case ROC analysis for determining the limit of calcification detection in tomosynthesis," SPIE Med. Imaging 2019 Phys. od Med. Imaging **10948**(March), 22 (2019).

[9] Elangovan, P., Mackenzie, A., Dance, D. R., Young, K. C., Cooke, V., Wilkinson, L., Given-Wilson, R. M., Wallis, M. G. and Wells, K., "Design and validation of realistic breast models for use in multiple alternative forced choice virtual clinical trials," Phys. Med. Biol. (2017).

[10] Vent, T. L., Barufaldi, B. and Maidment, A. D. A., "Simulation and experimental validation of high-resolution test objects for evaluating a next-generation digital breast tomosynthesis prototype," SPIE Med. Imaging 2019(March), 21 (2019).

[11] Gallas, B. D., "One-shot estimate of MRMC variance: AUC," Acad. Radiol. **13**(3), 353–362 (2006).

[12] Pokrajac, D. D., Maidment, A. D. A. and Bakic, P. R., "Optimized generation of high resolution breast anthropomorphic software phantoms," Med. Phys. **39**(4), 2290 (2012).

[13] Bakic, P. R., Barufaldi, B., Pokrajac, D., Weinstein, S. P. and Maidment, A. D., "Optimized simulation of breast anatomy for virtual clinical trials," 14th Int. Work. Breast Imaging (IWBI 2018)(July), 73 (2018).

[14] Lago, M. A., Maidment, A. D. A. and Bakic, P. R., "Modelling of mammographic compression of anthropomorphic software breast phantom using FEBio," Int'l Symp. Comput. Methods Biomech. Biomed. Eng., Salt Lake City, UT (2013).
[15] Bakic, P. R., Barufaldi, B., Higginbotham, D., Weinstein, S. P., Avanaki, A., Espig, K., Xthona, A., Kimpe, T. and Maidment, A. D. A., "Virtual clinical trial of lesion detection in digital mammography and digital breast tomosynthesis," SPIE Med. Imaging 2018 **1057306**(March), 1–13 (2018).
[16] Siddon, R. L., "Fast calculation of the exact radiological path for a three dimensional CT array," Med. Phys. **12**(2), 252–255 (1985).
[17] Kuo, J., Ringer, P. A., Fallows, S. G., Bakic, P. R., Maidment, A. D. A. and Ng, S., "Dynamic reconstruction and rendering of 3D tomosynthesis images," SPIE Med. Imaging **796116**(March 2011), 796116-796116–11, Orlando, FL (2011).
[18] Abbey, C. K. and Barrett, H. H., "Human- and model-observer performance in ramp-spectrum noise: effects of regularization and object variability," J. Opt. Soc. Am. A (2001).
[19] Park, S., Zhang, G. and Myers, K. J., "Comparison of Channel Methods and Observer Models for the Task-Based Assessment of Multi-Projection Imaging in the Presence of Structured Anatomical Noise," IEEE Trans. Med. Imaging **35**(6), 1431–1442 (2016).
[20] Marchessoux, C., Kimpe, T. and Bert, T., "A virtual image chain for perceived and clinical image quality of medical display," IEEE/OSA J. Disp. Technol. **4**(4), 356–368 (2008).
[21] Gallas, B. D. and Barrett, H. H., "Validating the use of channels to estimate the ideal linear observer.," J. Opt. Soc. Am. A. Opt. Image Sci. Vis. **20**(9), 1725–1738 (2003).
[22] Vedantham, S., Karellas, A., Vijayaraghavan, G. R. and Kopans, D. B., "Digital Breast Tomosynthesis: State of the Art," Radiology **277**(3), 663–684 (2015).
[23] Lanyi, M. and Lanyi, M., "Clinically Occult, Mammographically Suspicious Microcalcification Clusters: Pre Intra-, and Postoperative Measures," [Diagnosis and Differential Diagnosis of Breast Calcifications] (1986).
[24] Lanyi, M., [Diagnosis and Differential Diagnosis of Breast Calcifications] (1988).

Simulation of high-resolution test objects using non-isocentric acquisition geometries in next-generation digital tomosynthesis

Trevor L. Vent*, Bruno Barufaldi, Raymond J. Acciavatti, Andrew D.A. Maidment
Department of Radiology, University of Pennsylvania, Philadelphia, United States.
*Trevor.Vent@pennmedicine.upenn.edu

ABSTRACT

Digital breast tomosynthesis (DBT) systems utilize an isocentric acquisition geometry which introduces imaging artifacts that are deleterious to image reconstructions. The next-generation tomosynthesis (NGT) prototype was designed to incorporate various x-ray source and detector motions for the purpose of investigating alternative acquisition geometries for DBT. Non-isocentric acquisition geometries, acquisitions that vary the image magnification between projection images, are capable of ameliorating aliasing and other artifacts that are intrinsic to conventional DBT. We used virtual clinical trials (VCTs) to develop custom acquisition geometries for the NGT prototype. A high-resolution (5μm voxel size) star pattern test object was simulated to compare the high-frequency performance of isocentric with non-isocentric image reconstructions. A tilted bar pattern test object was also simulated to compare multiplanar reconstructions (MPR) of isocentric and non-isocentric acquisition geometries. Two source- and detector-motion paths were simulated to obtain super-sampled image reconstructions of the test objects. An aliasing-sensitive metric was used to evaluate spatial resolution performance for two orthogonal frequency orientations. Pairwise comparisons were made for the two frequency orientations between the isocentric and non-isocentric acquisition geometries. Non-isocentric acquisition geometries show an improvement over isocentric acquisition geometries. The greatest improvement was 75.2% for frequencies aligned perpendicular to x-ray source motion, which is the direction of frequencies for which DBT is prone to aliasing. Both frequency orientations exhibit super resolution for non-isocentric geometries. MPR of the tilted bar pattern show z-dependent degeneracies for the isocentric acquisition only, whereas MPR of the non-isocentric acquisition entirely exhibits super resolution.

Keywords: digital breast tomosynthesis, non-isocentric tomosynthesis, physics virtual clinical trial; ray tracing, radial fast Fourier transform, super-resolution, multiplanar reconstruction

1. INTRODUCTION

Digital breast tomosynthesis (DBT) acquires a three-dimensional (3D) image of a patient's breast by acquiring multiple, two-dimensional x-ray images from serial source positions. For a conventional DBT acquisition, the x-ray projections are acquired by translating the x-ray source along an arc in the mediolateral (ML) direction. The projections are spaced equidistantly in the chest-wall plane of the patient. This acquisition geometry is isocentric, because the arc rotates about a single fulcrum in space. Such DBT systems benefit the detection of masses and low-frequency objects in the breast. That said, the detection of high-frequency objects like microcalcifications, is not benefited by DBT when compared with full-field digital mammography (FFDM)[1].

Resolution for conventional DBT is anisotropic, favoring the frequencies that are aligned parallel to x-ray source motion ($\boldsymbol{\nu}_{\parallel}$) with super resolution. Using super-sampled image reconstructions, resolution for $\boldsymbol{\nu}_{\parallel}$ can be increased twofold, whereas the frequencies aligned perpendicular to source motion ($\boldsymbol{\nu}_{\perp}$) are limited to the alias frequency of the detector. Super resolution improves the resolution of periodic objects and the overall appearance and texture of breast tissue and lesions in image reconstructions.

The next-generation tomosynthesis (NGT) system is a DBT prototype that has been developed to improve the detection of microcalcifications in the breast. This prototype system investigates alternative acquisition geometries by introducing novel x-ray source and detector motions. The introduction of posteroanterior (PA) x-ray source motion has been shown to improve the spatial resolution[2–5] and volume estimation of anthropomorphic breast phantoms in image reconstructions[6,7]. Non-isocentric acquisition geometries, acquisitions that increment the detector $\mathbf{z}$-position between each projection, can further improve spatial sampling. Non-isocentric acquisitions can also lessen the impact of imaging artifacts like masking[8,9], spatial resolution anisotropies[10–12], and aliasing[11,13] in image reconstructions.

15th International Workshop on Breast Imaging (IWBI2020), edited by Hilde Bosmans, Nicholas Marshall, Chantal Van Ongeval, Proc. of SPIE Vol. 11513, 1151317
 · doi: 10.1117/12.2561098

The primary method for validating the performance of these prototypes is through clinical trials. Clinical trials of medical imaging systems require a large number of patients, who are imaged repeatedly to compare the performance of different systems. The associated cost, duration, and radiation risk represent a significant impediment to the efficient introduction of novel imaging technologies. Virtual clinical trials (VCTs) represent an approach, based upon computer simulation of human anatomy and imaging modalities, which can help develop, optimize, and validate new and existing medical imaging methods. Fast and detailed simulations of device performance are also instrumental in prototyping clinical trials and augmenting them with simulated data, and may also assist with regulatory approval[4,14,15].

Physics VCTs, in contrast to traditional VCTs, are intended to evaluate the implementation of the novel designs using simulated image acquisitions of virtual test objects and objective metrics to evaluate device performance. We have used physics VCTs to investigate novel acquisition geometries for the NGT prototype[4]. We have shown that physics VCTs can be used to investigate novel acquisition geometries for the NGT system without exhausting resources. In this work, we use physics VCTs and high-resolution test objects to compare the performance of isocentric with non-isocentric acquisition geometries for DBT using configurations of the NGT prototype.

2. MATERIALS & METHOD

Virtual Clinical Trial pipeline

Physics VCTs are implemented using the X-ray Physics Lab's (XPL) physics VCT pipeline. The physics VCT pipeline has been modified from the original VCT pipeline. Physics VCTs simulate the image acquisition of physical test objects and phantoms. However, rather than using a virtual reader phase of the original VCT pipeline, objective measures of physics are used to evaluate the performance of an imaging device. A tomosynthesis acquisition is simulated, in the same manner as the original pipeline, using ray-tracing methods with a dedicated graphics processing unit (GPU). The mechanical configuration of the NGT prototype is modeled using the physics VCT pipeline, where various acquisition geometries can be simulated.

Next-generation tomosynthesis prototype

Alternative acquisition geometries of the NGT prototype are achieved by creating custom x-ray source and detector motion paths for a series of x-ray projection images. The collection of projection images obtained from each custom acquisition geometry are used for tomographic reconstructions. Details of this prototype have been described in previous work[3,4,16,17]. The origin of the NGT system is defined at the center of the chest-wall edge of the breast support (Figure 1). The **x**-**y** plane of the NGT system serves as an address space for the x-ray focal spot to determine an acquisition geometry. The range of the source is $\pm$150mm in **x** and +180mm in **y**. The NGT achieves non-isocentric acquisition geometries by translating the

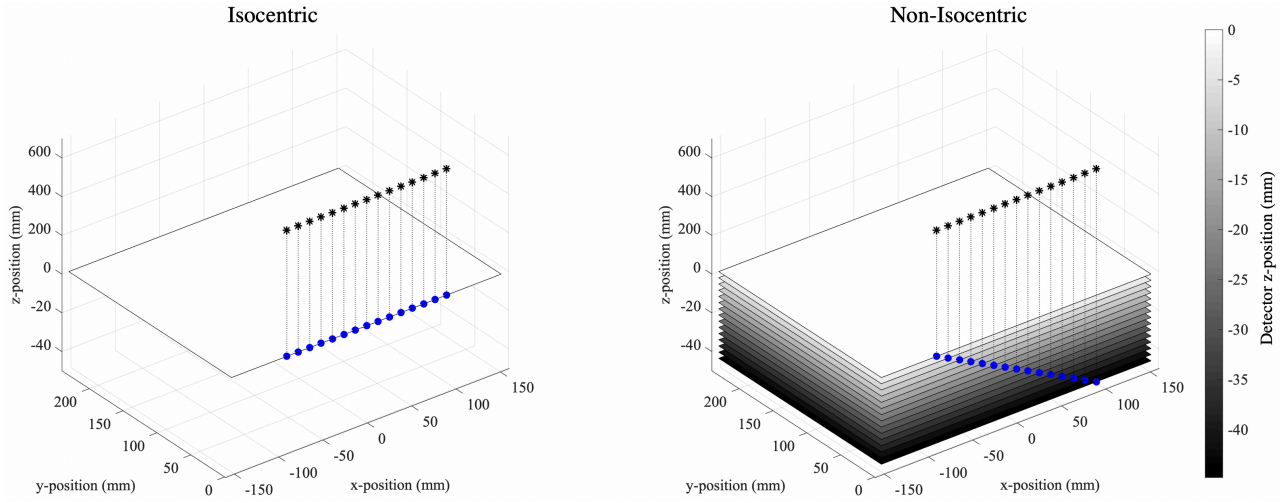

Figure 1: The two acquisition geometries that are used to simulate the NGT prototype. The black stars and blue dots indicate the position of the focal spot in the focal spot plane and the corresponding position of the focal spot relative to the detector position, respectively. **NB:** the positive and negative **z**-axes are scaled differently.

detector in **z** between x-ray projections with a 44.8mm range, translating 3.2 mm between projection over 15 projections. The configuration of the NGT prototype and the two acquisition geometries that are used for the physics VCT simulations in this study are shown in Figure 1. This study is constrained to the conventional x-ray source motion only and does not include acquisition geometries with PA source motion.

The geometric configuration and constraints of the NGT prototype dictate the image acquisition simulation of the physics VCTs. Physics VCTs simulate the radiographic technique for x-ray projection images that are used to render image reconstructions. Tomographic image reconstructions are created by filtered back-projection using commercial reconstruction software (Piccolo version 4.0.5, Real Time Tomography, Villanova, PA).

High-resolution test objects

A voxelized model of a star pattern test object (Model 07-542-1000, Supertech, Elkhart, IN) was created using Matlab (MathWorks, Natick, Massachusetts, version 2018a). This virtual star pattern (Figure 2) consists of 5μm isotropic voxels with three material indices: lead, acrylic, and air. The diameter of the star pattern is 45mm with a total thickness of 30μm. The range of resolution for this star pattern, from the outer edge to the innermost circle, is 1.3–20.0 line pairs per millimeter (lp/mm). The star pattern contains four quadrants, giving two possible frequency orientations for both **x** and **y** ($\boldsymbol{\nu}_{\parallel}$ and $\boldsymbol{\nu}_{\perp}$, respectively).

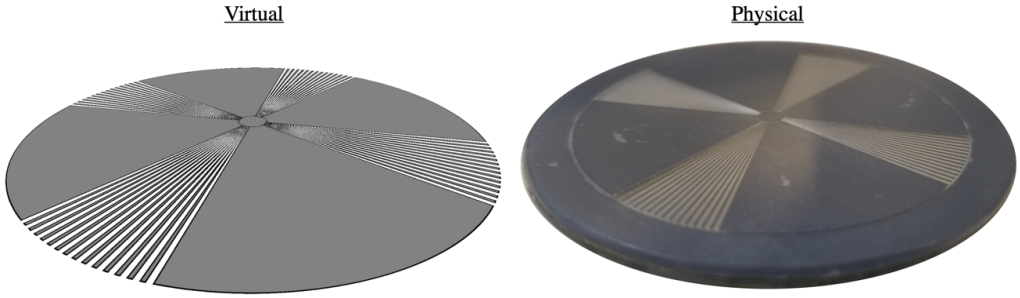

Figure 2: The virtual star pattern test object that was created to simulate the physical star pattern.

In addition to the star pattern, a bar pattern test object was created at a constant spatial resolution of 70 μm with a frequency orientation, $\boldsymbol{\nu}_{\parallel}$. The bar pattern is indexed with lead and air and was created at a 45° tilt relative to the breast support (Figure 3). The tilt of the bar pattern was used to compare the spatial resolution at various depths of the image reconstruction using multiplanar reconstructions (MPR). Using the commercial reconstruction software, MPR can be achieved at arbitrary angles[18]. This allowed us to visualize the plane of the bar pattern test object at a plane that is oriented 45° relative to the detector plane. Conventional DBT is anisotropic in the **z** dimension, which degenerate periodic signals like a bar pattern or punctate calcifications in the breast, at various intervals of **z**. Non-isocentric acquisition geometries can reduce these degeneracies.

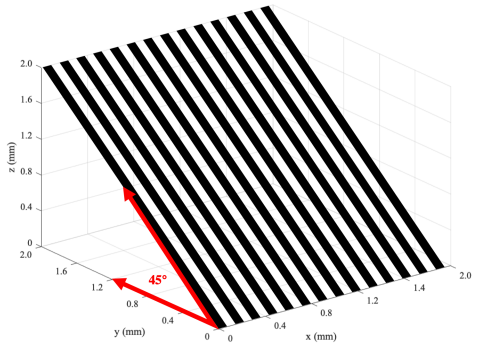

Figure 3: A diagram that illustrates a portion of the tilted bar pattern phantom. The spatial resolution of the phantom is 70μm (7.14 lp/mm).

Physics VCTs were used to simulate image acquisition of the virtual star pattern and tilted bar pattern using isocentric and non-isocentric configurations of the NGT prototype. The conventional x-ray source motion path (Figure 1) was simulated with and without **z**-direction detector motion (the **z**-detector position is 0 over all projections), to simulate non-isocentric and isocentric acquisition geometries, respectively. Repositioning and reproducibility of the image acquisition was simulated by perturbing the position of the phantom within 2 mm of the detector origin over 10 tomosynthesis acquisitions for each geometry. Poisson noise was also simulated for each projection image. Super-sampled image reconstructions of the star pattern test object were obtained using the simulated 2D projection images of each tomosynthesis acquisition simulation. The images were reconstructed at a 2.0x super-sampling rate (42.5 µm for the 85 µm detector element size).

The slice of the image reconstruction that contained the plane of the star pattern was used to evaluate the in-plane spatial resolution properties of the 20 image reconstructions. The radial fast Fourier transform (RFFT)[19] was used to evaluate the in-plane performance of both acquisition geometries. This metric used the star pattern image as an input to produce the contrast transfer function (CTF) and RFFT graphs (e.g. Figure 4), averaged over the 10 reconstruction slices for each geometry. The CTF is analogous to the modulation transfer function (MTF) but is not normalized to unity at zero spatial frequency. The RFFT graph shows modulation of all frequencies contained in a quadrant of a star pattern image reconstruction alongside the modulation of aliased signals. The CTF was used to determine the limit of spatial resolution (LSR). Conventional DBT is spatially anisotropic[11]; therefore, each image reconstruction is evaluated for $\boldsymbol{\nu}_{\parallel}$ and $\boldsymbol{\nu}_{\perp}$.

The same acquisition geometries were used to generate an MPR of the tilted bar pattern. Images of the tilted bar pattern were reconstructed at a 2x sampling rate. The reconstruction plane was oriented at the tilt of the bar pattern. Plot profiles of a degenerate region in the image reconstruction of the isocentric acquisition geometry was produced and compared with the plot profile of the same region for the non-isocentric acquisition geometry.

3. RESULTS AND DISCUSSION

Star pattern RFFT

An example of a Radial FFT and CTF calculation is shown for a single reconstruction slice in Figure 4. The RFFT and CTF graphs of the non-isocentric acquisition geometries show a reduction of spectral leakage compared with the isocentric acquisition geometries. The Radial FFT was computed for both frequency orientations, $\boldsymbol{\nu}_{\parallel}$ and $\boldsymbol{\nu}_{\perp}$, and averaged over the 10 reconstruction slices for each acquisition geometry.

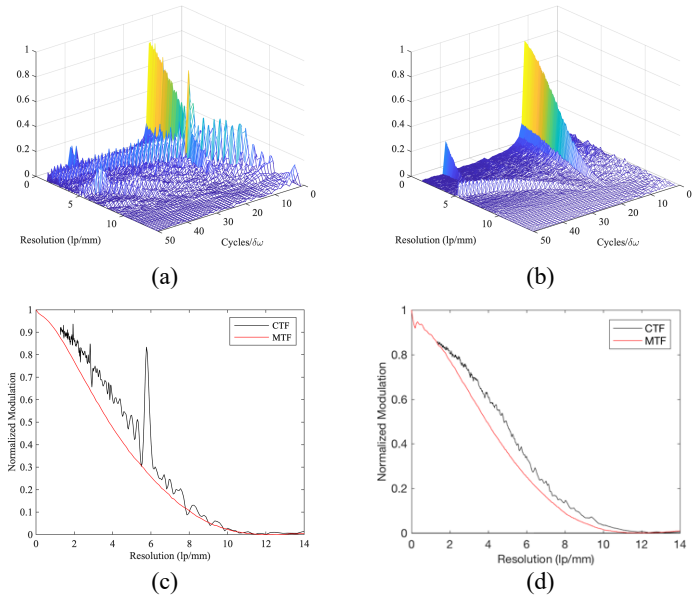

Figure 4: One sample of the Radial FFT for $\boldsymbol{\nu}_{\parallel}$ of the conventional, isocentric geometry (a), and $\boldsymbol{\nu}_{\parallel}$ of the conventional, non-isocentric geometry (b), and the corresponding MTF vs. CTF graphs (c-d).

The non-isocentric acquisition geometry exhibits isotropic super-resolution (Figure 5), achieving a limiting spatial resolution (LSR) above the alias frequency in both $\boldsymbol{\nu}_{\parallel}$ and $\boldsymbol{\nu}_{\perp}$, whereas the isocentric acquisition geometry achieves super resolution for $\boldsymbol{\nu}_{\parallel}$; however, resolution is limited to the alias frequency for $\boldsymbol{\nu}_{\perp}$. The isocentric acquisition geometry shows more significant aliasing in the form of Moiré patterns compared with the non-isocentric acquisition geometry. The modulation contrast is higher for the isocentric acquisition geometries at the lowest spatial frequencies of the star pattern, regardless of frequency orientation.

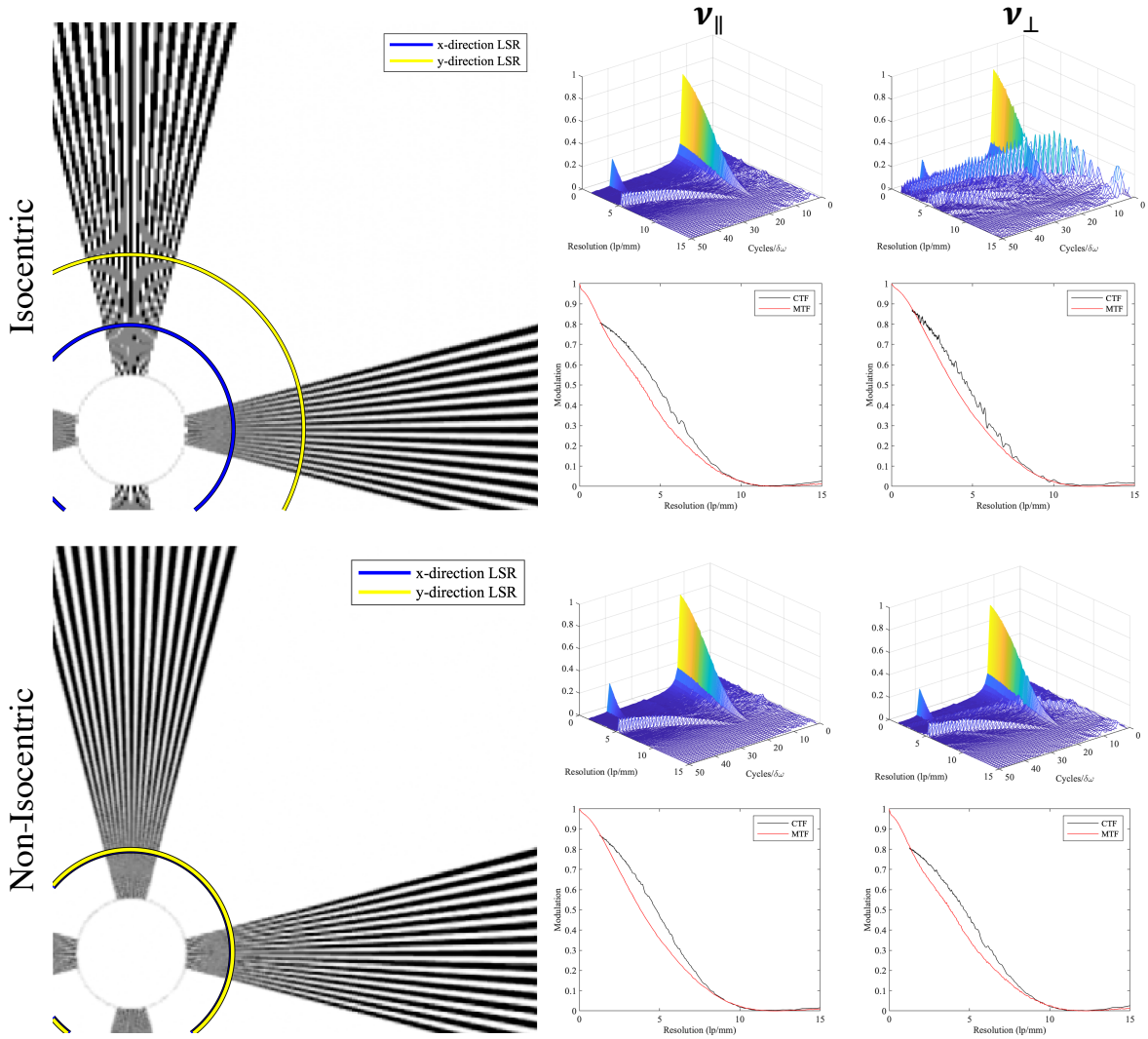

Figure 5: Simulated image reconstruction slices of the isocentric and non-isocentric acquisition geometry (left) and the results of the RFFT metric (right).

The LSR of the four conditions was measured using images of the star pattern and the CTF. All isocentric image reconstructions exhibited significant aliasing for $\boldsymbol{\nu}_{\perp}$, and the LSR was limited to near the alias frequency of the detector (5.88 lp/mm). For reconstruction slices where super resolution was achieved, the LSR was measured at a 5% modulation of the CTF. The improvement of the LSR for the non-isocentric over the isocentric geometry was 75.2% for $\boldsymbol{\nu}_{\perp}$. Both the image of the star pattern and the RFFT graph for the non-isocentric case exhibit residual aliasing artifact, but this artifact does not overcome the modulation of the input frequency.

Tilted bar pattern MPR

The tilted bar pattern was reconstructed with a roll of 45° about the **x**-axis for each acquisition geometry. The MPR of the isocentric acquisition geometry shows four distinct degenerate regions (e.g. the region bounded by the red box in Figure

6). Super resolution cannot be achieved at the corresponding **z**-locations in the image reconstruction. The MPR of the non-isocentric acquisition geometry shows multiple regions of decreased modulation, but no fully degenerate regions of the bar-pattern are seen. Super resolution is observed over the entire MPR.

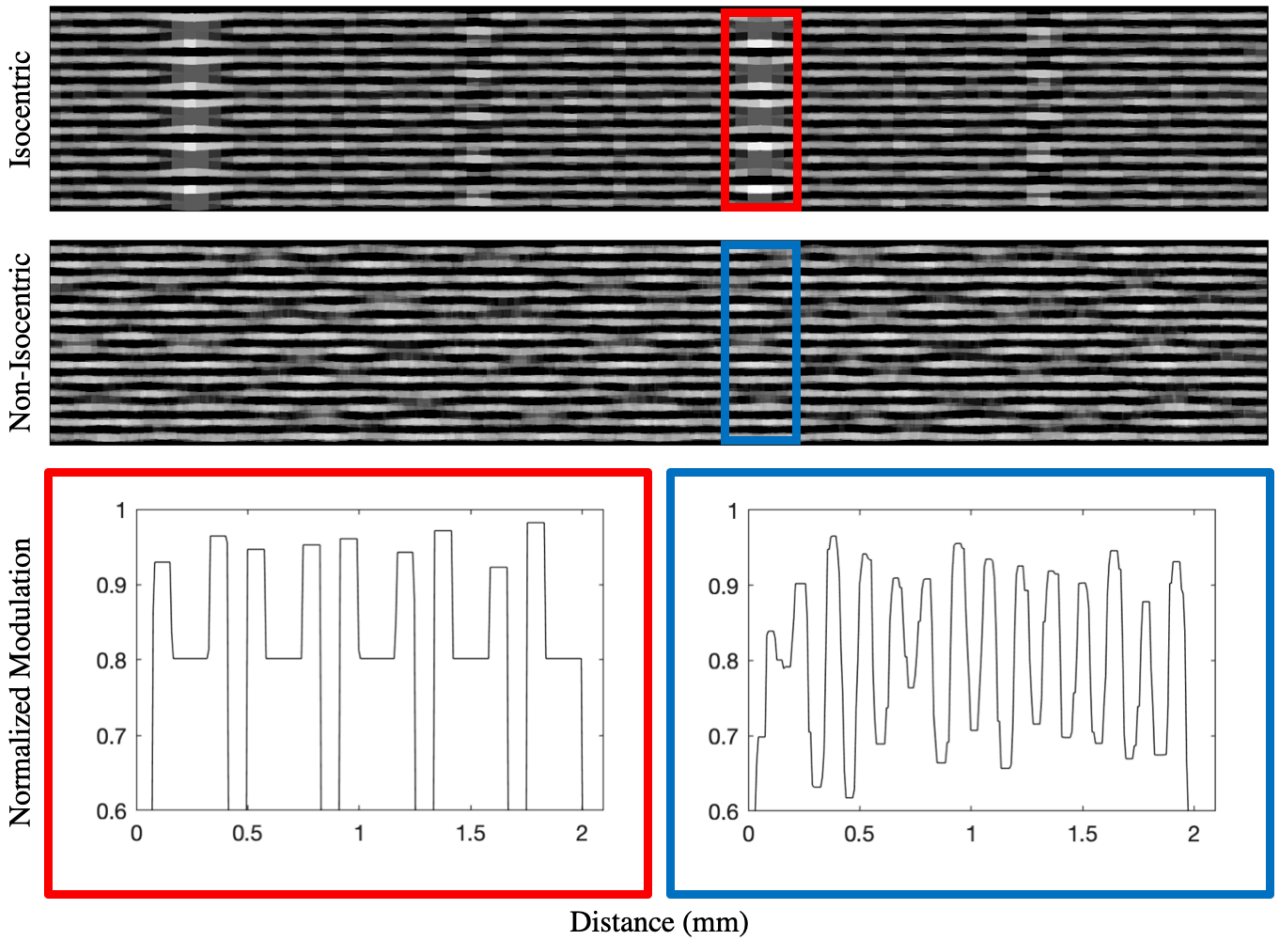

Figure 6: MPR of the tilted bar pattern for the isocentric and non-isocentric acquisition geometries with corresponding plot profiles.

4. CONCLUSION

We have shown that non-isocentric acquisition geometries can be simulated with high accuracy using physics VCTs. With 10 simulated tomosynthesis image reconstructions, we were able to measure the RFFT and LSR accurately and achieve results that are commensurate with physical experiments[4]. The LSR improved for every frequency orientation with the introduction of **z**-detector motion. The highest overall improvement in LSR for the non-isocentric over isocentric acquisition geometry is 75.2% for $\boldsymbol{\nu}_{\perp}$. All frequency orientations of the non-isocentric reconstructions exhibit super resolution, whereas the isocentric geometry was prone to aliasing. These results suggest that non-isocentric acquisition geometries can improve the detection of high-frequency objects like microcalcifications for DBT. In the future, we will simulate additional non-isocentric acquisition geometries that include PA source motion to optimize super resolution further.

5. ACKNOWLEDGEMENTS

The authors would like to thank Johnny Kuo, Susan Ng, and Peter Ringer of Real Time Tomography for technical assistance with Piccolo. Andrew D. A. Maidment is a shareholder of Real Time Tomography and is a member of the scientific advisory board.

Support was provided by the following grants: W81XWH-18-1-0082 from the Department of Defense Breast Cancer Research Program, IRSA 1016451 from the Burroughs Welcome Fund, 1R01CA196528 from the National Institute of Health, and IIR13264610 from Susan G. Komen. In addition, equipment support was provided by Analogic Inc., Barco NV, and Real Time Tomography. The content is solely the responsibility of the authors and does not necessarily represent the official views of the funding agencies.

REFERENCES

[1] Rafferty, E. a, Park, J. M., Philpotts, L. E., Poplack, S. P. and Sumkin, J. H., "Digital Mammography and Breast Tomosynthesis Compared with Digital Mammography Alone : Results of a Multicenter, multireader trial," Radiology **266**(1), 104–113 (2013).

[2] Eben, J. E., Vent, T. L., Choi, C. J., Yarrabothula, S., Chai, L., Nolan, M., Kobe, E., Acciavatti, R. J. and Maidment, A. D. A., "Development of a next generation tomosynthesis system," Prog. Biomed. Opt. Imaging - Proc. SPIE **10573** (2018).

[3] Maidment, T. D., Vent, T. L., Ferris, W. S., Wurtele, D. E., Acciavatti, R. J. and Maidment, A. D. A., "Comparing the imaging performance of computed super resolution and magnification tomosynthesis," Med. Imaging 2017 Phys. Med. Imaging **10132**, 1013222 (2017).

[4] Vent, T. L., Barufaldi, B. and Maidment, A. D. A., "Simulation and experimental validation of high-resolution test objects for evaluating a next-generation digital breast tomosynthesis prototype," 21 (2019).

[5] Vent, T. L., Lepore, B. L. and Maidment, A. D. A., "Evaluating the imaging performance of a next-generation digital breast tomosynthesis prototype," Med. Imaging 2019 Phys. Med. Imaging(March), 19 (2019).

[6] Acciavatti, Raymond; Rodriguez-Ruiz, Alejandro; Vent, Trevor L.; Bakic, Predrag R.; Reiser, Ingrid; Sechopoulos, Ioannis; Maidment, A. D. A., "Analysis of volume overestimation artifacts in the breast outline segmentation in tomosynthesis," Med. Imaging 2018 Phys. Med. Imaging, 10573 (2018).

[7] Acciavatti, R. J., Barufaldi, B., Vent, T. L., Wileyto, E. P. and Maidment, A. D. A., "Personalization of x-ray tube motion in digital breast tomosynthesis using virtual Defrise phantoms," Med. Imaging 2019 Phys. Med. Imaging(March), 10 (2019).

[8] Friedewald, S. M., Rafferty, E. A., Rose, S. L., Durand, M. A., Plecha, D. M., Greenberg, J. S., Hayes, M. K., Copit, D. S., Carlson, K. L., Cink, T. M., Barke, L. D., Greer, L. N., Miller, D. P. and Conant, E. F., "Breast cancer screening using tomosynthesis in combination with digital mammography," JAMA - J. Am. Med. Assoc. **311**(24), 2499–2507 (2014).

[9] Roth, R. G., Maidment, A. D. A., Weinstein, S. P., Roth, S. O. and Conant, E. F., "Digital Breast Tomosynthesis: Lessons Learned from Early Clinical Implementation," RadioGraphics **34**(4), E89–E102 (2014).

[10] Hu, Y.-H., Zhao, B. and Zhao, W., "Image artifacts in digital breast tomosynthesis: Investigation of the effects of system geometry and reconstruction parameters using a linear system approach," Med. Phys. **35**(12), 5242–5252 (2008).

[11] Acciavatti, R. J. and Maidment, A. D. A., "Observation of super-resolution in digital breast tomosynthesis," Med. Phys. **39**(12), 7518–7539 (2012).

[12] Hatt, C. R., Tomkowiak, M. T., Dunkerley, D. A. P., Slagowski, J. M., Funk, T., Raval, A. N. and Speidel, M. A., "Depth-resolved registration of transesophageal echo to x-ray fluoroscopy using an inverse geometry fluoroscopy system," Med. Phys. **42**(12), 7022–7033 (2015).

[13] Vent, T. L., Acciavatti, R. J., Kwon, Y. J. and Maidment, A. D. A., "Quantification of resolution in multiplanar reconstructions for digital breast tomosynthesis," Med. Imaging 2016 Phys. Med. Imaging **9783**(March 2016), 978303 (2016).

[14] Bakic, P. R., Barufaldi, B., Pokrajac, D., Lago, M. A. and Maidment, A. D., "Developing populations of software breast phantoms for virtual clinical trials," 14th Int. Work. Breast Imaging (IWBI 2018)(July 2018), 73 (2018).

[15] Barufaldi, B., Bakic, P. R., Higginbotham, D. and Maidment, A. D. A., "OpenVCT: a GPU-accelerated virtual clinical trial pipeline for mammography and digital breast tomosynthesis," Med. Imaging 2018 Phys. Med. Imaging **1057358**(March), 194 (2018).

[16] Eben, J. E., Vent, T. L., Choi, C. J., Yarrabothula, S., Chai, L., Nolan, M., Kobe, E., Acciavatti, R. J. and Maidment, A. D. A., "Development of a Next Generation Tomosynthesis System," Med. Imaging 2018 Phys. Med. Imaging, 10573 (2018).

[17] Maidment, Andrew D. A.; Acciavatti, Raymond J.; Vent, Trevor L.; Conant, Emily F.; Kwon, Young Joon; NG, Susan; Kuo, Jhonny; Ringer, Peter A.; Maidment, Tristan; Wurtele, David; Licata, Joseph; Narayan, Tejas; Zhang, David; Higginbotham, D., "Construction of a Prototype Digital Breast Tomosynthesis System with Superior Spatial Resolution," RSNA Phys. Basic Sci., RSNA (2016).
[18] Vent, T. L., Acciavatti, R. J., Kwon, Y. J. and Maidment, A. D. A., "Quantification of resolution in multiplanar reconstructions for digital breast tomosynthesis," Med. Imaging 2016 Phys. Med. Imaging **9783**, 978303 (2016).
[19] Vent, T., Acciavatti, R. and Maidment, A., "Development and Evaluation of a Spatial Resolution Metric for Tomosynthesis: we-g-601-02," Med. Phys. **44**(6), 3261 (2017).

Automatic Segmentation of Mammary Tissue using Computer Simulations of Breast Phantoms and Deep-learning Techniques

Lucca R. Peregrino[1], Jordy V. Gomes[1], Thaís G. do Rêgo[1], Yuri de A. M. Barbosa[1][a], Telmo de M. e Silva Filho[2][b], Andrew D. A. Maidment[3] and Bruno Barufaldi[3,*][c]

[1]*Center of Informatics, Federal University of Paraíba, João Pessoa, Brazil*

[2]*Department of Statistics, Federal University of Paraíba, João Pessoa, Brazil*

[3]*Department of Radiology, University of Pennsylvania, 3640 Hamilton Walk, Philadelphia PA, U.S.A.*

Keywords: Phantoms, Tomosynthesis, Deep Learning, U-Net, Segmentation.

Abstract: Digital breast tomosynthesis (DBT) has rapidly emerged for screening mammography to improve cancer detection. Segmentation of dense tissue plays an important role in breast imaging applications to estimate cancer risk. However, the current segmentation methods do not guarantee an ideal ground-truth in clinical practice. Computer simulations provide ground-truth that enables the development of convolutional neural network (CNN) applications designed for image segmentation. This study aims to train a CNN model to segment dense tissue in DBT images simulated using anthropomorphic phantoms. The phantom images were simulated based on clinical settings of a DBT system. A U-Net, a CNN model, was trained with 2,880 images using a slice-wise approach. The U-Net performance was evaluated in terms of percent of density in the central slice and volumetric breast density in the medio-lateral slices. Our results show that the U-Net can segment dense tissue from DBT images with overall loss, accuracy, and intersection over union of 0.27, 0.93, and 0.62 in the central slices, and 0.32, 0.92, and 0.54 in the medio-lateral slices, respectively. These preliminary results allow us to explore the use of CNN architectures to segment dense tissue in clinical images, which is a highly complex task in screening with DBT.

1 INTRODUCTION

Digital mammography (DM) and digital breast tomosynthesis (DBT) are considered the "gold standard" of care for breast cancer screening (Tice and Feldman, 2008; Vedantham et al., 2015; Azar and El-Said, 2013). These imaging modalities increase the sensitivity in cancer detection and reduce the number of recall rates when compared to the traditional screening with screen-film (Vedantham et al., 2015).

Complementary tools such as computer-aided diagnosis systems and convolution neural network (CNN) applications can facilitate the early cancer location by enhancing and detecting lesions (Cheng et al., 2006; Azar and El-Said, 2013), which potentially improve the diagnosis on mammography exams.

Anthropomorphic breast phantoms have been widely used for research and development of mammography imaging systems (Caldwell and Yaffe, 1990; Carton et al., 2011). These phantoms simulate the mammary tissue accurately in terms of size, volume, and composition. Simulations of breast phantoms can be used as data augmentation to support CNN architectures (Lashgari et al., 2020), assisting the lack of data from specific populations (Barufaldi et al., 2018a). In addition, these simulations provide ground-truth images (i.e., ideal reference), which is not provided in clinical practice (Tunçay and Akduman, 2014).

Manual or semi-automatic methods have been developed to obtain ground-truth from images by segmenting and thresholding different findings (Rui et al., 2018; Chatfield et al., 2014; Valverde et al., 2017). In medical imaging, these segmentation methods are commonly performed by experts in radiology. Because of the subjectivity of inter-and/or intra-readers, the output resulting from these methods may include variability and inaccuracy (Oliveira, 2017), while computer simulations provide the *actual ground-truth* for the segmented image.

[a] https://orcid.org/0000-0002-7779-0288
[b] https://orcid.org/0000-0003-0826-6885
[c] https://orcid.org/0000-0003-3954-3611

Peregrino, L., Gomes, J., G. do Rêgo, T., Barbosa, Y., Filho, T., Maidment, A. and Barufaldi, B.
Automatic Segmentation of Mammary Tissue using Computer Simulations of Breast Phantoms and Deep-learning Techniques.
DOI: 10.5220/0010310402520259
In *Proceedings of the 14th International Joint Conference on Biomedical Engineering Systems and Technologies (BIOSTEC 2021) - Volume 4: BIOSIGNALS*, pages 252-259
ISBN: 978-989-758-490-9

The large variability of data with ground-truth provided by computer simulations can improve the performance of image segmentation with CNNs (Hamarneh and Jassi, 2010; Li et al., 2009). The ground-truth identifies each breast tissue, structures, and findings to be used as labels for the input images required in CNNs (Hamarneh and Jassi, 2010).

This study aims to develop a CNN model for tissue segmentation using computer simulations of breast phantoms. The CNN model is trained and tested using an U-Net architecture (Ronneberger et al., 2015). Projections are simulated using the acquisition geometry of a clinical DBT system. DBT phantom images are reconstructed using a customized increment between reconstructed slices (0.1 mm). The U-Net architecture is trained using a slice-wise approach to segment glandular tissue from 2,880 DBT reconstructed images.

2 BACKGROUND

2.1 Antropomorphic Breast Phantoms

Anthropomorphic breast phantoms have been widely used to conduct *in-silico* trials (Bakic et al., 2018; Maidment, 2014; Abadi et al., 2020). Breast characteristics such as shape, size, volume, and tissue composition should be accurately simulated in accordance with the human anatomy (Tunçay and Akduman, 2014). In addition, breast anatomical features (e.g., glandular segments, Cooper's ligaments and blood vessels) should be realistically simulated (Elangovan et al., 2017).

To ensure that images simulated using anthropomorphic breast phantoms are comparable to clinical mammograms, validation methods that rely on human visual inspection and/or computer analyses are required. For example, Elangovan *et al.* (2017) propose a method that can rapidly produce a multiplicity of different breast appearance models using 4-alternative forced choice (4-AFC). Using 4-AFCs, they have shown that simulated and real images were statistically indistinguishable by expert breast readers.

However, the recruitment of breast experts needed to validate anthropomorphic phantoms can be a challenging task, and *in-silico* trials have been designed as attempt to simulate human readings. Badano *et al.* (2018) and Bakic *et al.* have reproduced reading interpretations reported on large scale clinical trials designed for pre-market approval of novel imaging technologies (Badano et al., 2018; Bakic et al., 2018). These previous publications reported a successful use of mathematical models to simulate virtual readers and design virtual anthropomorphic phantoms.

In breast imaging, computer simulations usually require the use of breast phantoms (Bakic et al., 2018; Maidment, 2014; Abadi et al., 2020). In this study, computer simulations of breast phantoms were used to design a novel CNN application for image segmentation using an U-Net architecture.

2.2 U-Net Architecture

CNNs are often used for image classification and segmentation (Rui et al., 2018; Chatfield et al., 2014; Valverde et al., 2017). The U-Net architecture is a CNN that was developed for biomedical image segmentation (Ronneberger et al., 2015). The ultimate goal of the U-Net architecture (Figure 1) is the segmentation and localization of desired objects/structures highlighted in the input images (Paul, 2018). The major benefit of the U-Net is that there is no need to use a large number of images for training and testing (Ronneberger et al., 2015). Thus, U-Net can be useful for segmentation of medical images, due to the fact that the segmented ground-truth is not available in clinical practice. Besides that, U-Net uses a reduced amount of training parameters compared to other CNN's, such as SegNet (Badrinarayanan et al., 2017).

The U-Net architecture consists of contraction (encoder) and expansion (decoder) paths. A set of two convolutions (3×3 kernel) and one maxpooling (2×2 kernel) with ReLU activation are performed in each encoder layer. Similarly, each decoder layer starts with an upsampling and a 2×2 convolution, followed by two 3×3 convolutions with ReLU activation. The encoder provides filtered information (feature maps) acquired during the contraction path to be interpreted by the decoder. The decoder concatenates the output of transposed convolution layers with the feature maps acquired from the encoder at each layer. Finally, an activation function is used to predict classes of the input images based on previous knowledge (training phase) obtained from ground-truth images (Academy, 2019).

The U-Net architecture has been used in several medical applications (Norman et al., 2018; Sevastopolsky, 2017). For example, Tong *et al.* (2018) developed an improved U-Net architecture to segment pulmonary nodules from CT images. The authors concluded that the accuracy of nodule segmentation is comparable or superior to the manual segmentation. A different U-Net application, developed by Norman *et al.* (2018), has shown an improved segmentation of cartilage and meniscus from knees using clinical MRI

images. Similarly, the precision of the automatic segmentation demonstrated to be comparable to the manual segmentation of experts.

In breast imaging, Zhang *et al.* (2020) developed a transfer learning application that uses U-Net and SegNet architectures to segment whole-breasts from MRI scans. The authors modified and adapted both architectures using slice-wise approaches and obtained average dice coefficient results of 0.87 (independent test data set). Although the authors presented compelling results, they emphasized that recruiting experts was challenging because of the limited and expensive time from radiologists to manually segment breasts from MRI scans. In addition, the authors could not obtain the manual segmentation (ground-truth) of the entire image dataset.

Several software have been developed to segment breast glandular tissue and estimate volumetric breast density or breast dense area, such as Volpara *et al.* (2014) and LIBRA *et al.* (2012). These software use image processing techniques (e.g., edge detection, support-vector machine, etc.) to segment breast tissue in clinical images, unlike the methods proposed in the current study.

Our proposed method is based on computer simulations that do not require manual segmentation of breast tissue.

3 MATERIALS AND METHODS

3.1 Computer Simulations

The OpenVCT framework (Barufaldi et al., 2018b) was used to simulate anthropomorphic breast phantoms (Zhang et al., 2008; Pokrajac et al., 2012). The breast phantoms are composed by voxel-materials (labels) that represent various tissue types and air (Barufaldi et al., 2018a). The tissue types are simulated using an octree-based recursive partitioning method (Pokrajac et al., 2012). In this method, seed points are randomly selected within the phantom interior and used to simulate glandular and adipose tissue bounded by fibrous Cooper's ligaments (Figure 2). These tissue types are simulated to mimic the breast anatomy.

We combined and simulated all phantom parameters described in Table 1 (n=96). These parameters were selected based on previous publications (Bakic et al., 2018; Barufaldi et al., 2019). Finally, a breast tissue compression was simulated using a GPU-accelerated mesh software (Barufaldi et al., 2018a). The compression was performed using a medio-lateral (ML) view.

Table 1: Summary of the breast phantom parameters.

Anthropomorphic Breast Phantoms	Parameters
Number of Phantoms (#)	96
Distribution of dense compartments (%)	{1.0; 15.0; 25.0; 50.0}
Breast volume (mL)	700
Breast thickness (mm)	63.3
Voxel size (mm)	{0.1; 0.2}
Number of compartments (#)	{425; 850; 1275; 1700}
Compartment shape	{(0.1; 1.0; 1.0; 2.0), (0.01; 1.0; 1.0; 4.0)}
Ligament thickness (mm)	[0.1;0.18]

The 3D breast phantoms were "sliced" through the entire volume in the sagittal orientation (Figure 2, left). In total, 633 2D slices (784×2053 pixels) were acquired per phantom (ML view). The phantom slices contain label maps at each 0.1 mm thick of compressed breast (Figure 2, right). Each label represents a different x-ray mass attenuation (Hubbell and Seltzer, 1995) used to simulate DBT projections (Feng and Sechopoulos, 2012). For each phantom, a set of 15 x-ray projections was simulated using the acquisition geometry of a clinical DBT system (Table 2). The x-ray projections were simulated using a GPU-enabled x-ray tracing algorithm (Siddon, 1985). The exposure acquisition settings follow the automatic exposure control from the DBT system (Feng and Sechopoulos, 2012).

Table 2: Summary of the DBT acquisition parameters.

DBT System (model)	Selenia Dimensions
X-Ray Imaging	
Anode Material	Tungsten
Filter Material	Aluminum
Filter Thickness (mm)	0.7
Angular Range (°)	[±7.5,±15,±25]
Number of Projections (#)	15
Tube Motion	Continuous
Detector	
Detection Material	a-Se
Detector Element Size(mm)	0.140×0.140
Number of Elements (#)	2048×1664
Detector Size (mm)	286.72×232.96
Source-Image Dis.(mm)	700.0
Rec. Voxel Size (mm)	0.1

A commercial reconstruction software (Briona Std., Real-Time Tomography, Vilanova PA) was used to reconstruct and to process each set of DBT projections (Chui et al., 2012). This software allows us to reconstruct DBT images using customized reconstruction voxel size. In this study, the DBT images

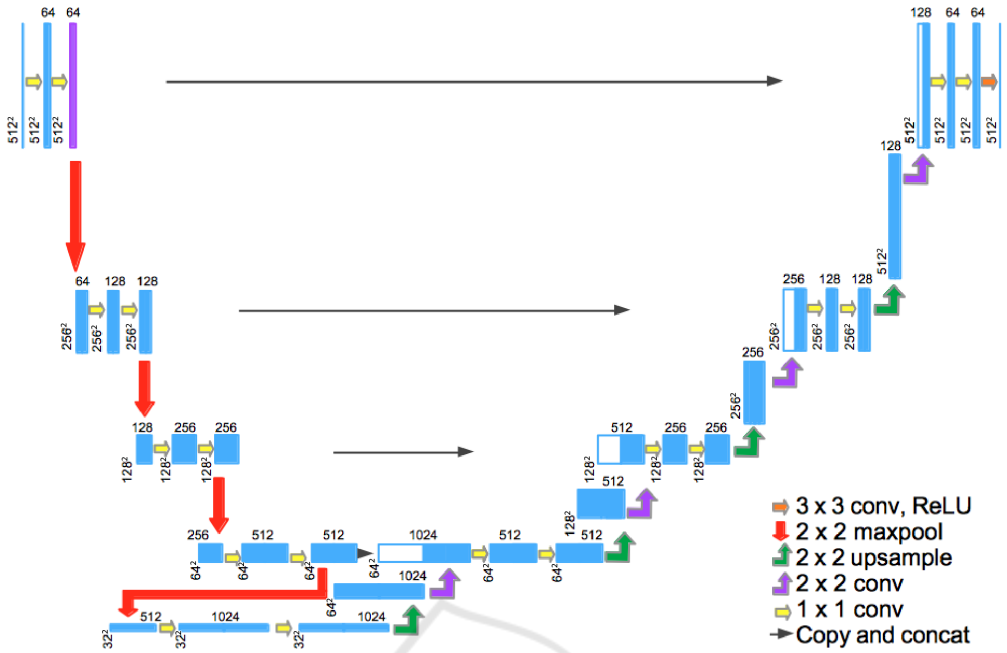

Figure 1: U-Net architecture used in this study. This architecture shows the "u" structure resulting from the encoder and decoder paths.

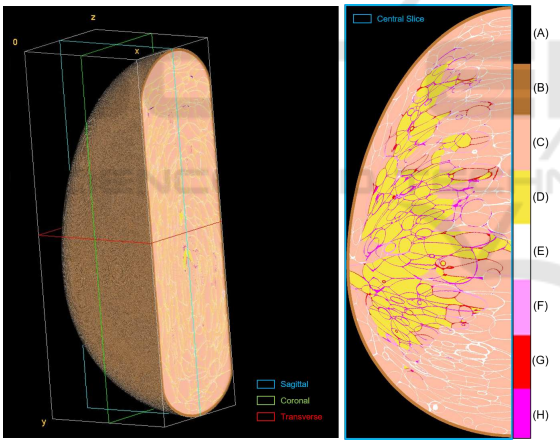

Figure 2: (Left) Volume view of compressed anthropomorphic breast phantom and (right) central slice (ML breast view). The colormap represents the labels used to identify each voxel-material: (A) air, (B) skin, (C) adipose, (D) glandular, (E-H) Cooper's ligaments.

were reconstructed using 0.1 mm increments in depth. In total, 633 reconstructed DBT images (1664×2048 pixels) were acquired per phantom.

3.2 Pre-processing Images

The reconstructed DBT images and correspondent label maps (ground-truth) were used as input for the training and test stages of the U-Net architecture. However, differences between the dimensions of the input images will result in an ineffective CNN model. Pre-processing techniques were required to match the ground-truth to the respective reconstructed DBT image.

The acquisition geometry (Table 2) was used to locate each label on the ground-truth and the respective pixel value in the DBT image. Next, a cropping operation was applied to each DBT image to eliminate excessive background information from the DBT images (Figure 3, left and middle). Finally, the glandular tissue label was thresholded and segmented from the ground-truth to obtain binary masks used for training the CNN model (Figure 3, right). After these pre-processing steps, the reconstructed DBT image, label map, and binary mask are matched (778×2,036 pixels). Finally, both input images, DBT reconstructed image and binary mask, were normalized using the maximum value in bits (2^{14} and 2^{8}, respectively), resulting in images with pixel values in a [0, 1] interval. The input images were resized to 512×512 pixels to optimize the CNN model and reduce computational burden.

3.3 Training the Model

To train the segmentation model, we modified the original U-Net parameters (Zhixuhao, 2016; Ronneberger et al., 2015) using the programming language Python. The optimization of the U-Net parameters, as well as training and testing were performed

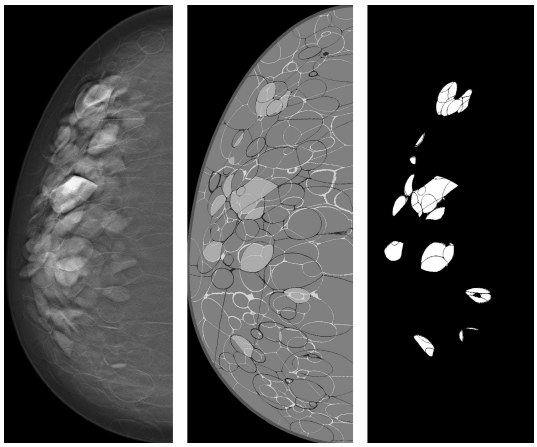

Figure 3: (Left) central slice of reconstructed DBT image, (middle) label map, and (right) binary mask after matching and cropping operations.

using a workstation equipped with Intel(R) Xeon(R) CPU, 16GB RAM, and single graphics card NVIDIA Quadro P5000.

In total, 45 pairs of images (reconstructed DBT image and mask) acquired from 64 phantoms (n=2,880 pairs) were used to train the U-Net model. The image pairs were selected using 45 pairs of phantom central slices, which contain regions with the most amount of glandular tissue.

Our U-Net model (Figure 1) was trained using 120 epochs, batch size 4, and image size 512×512. The weights of the training model were updated after each iteration (n=720). These parameters were selected and constrained based on memory used to train the architecture models. The number of epochs was optimized based on loss and accuracy. It is important to mention that the training models are saved every epoch. The training model did not improve significantly after 120 epoch.

3.4 Evaluation Metrics

The binary crossentropy, accuracy, and intersection over union were used to evaluate the performance of the segmentation models. These metrics are defined as:

Binary Crossentropy (*Loss*) is a loss function that calculates the difference between predicted labels ($\hat{y}$) and true labels (y). The loss is computed following Equation (1):

$$Loss(y,\hat{y}) = -(y \cdot log(\hat{y}) + (1-y) \cdot log(1-\hat{y})) \quad (1)$$

Accuracy (*Acc*) is a metric commonly used for predictive models, calculating the proportion of correct predictions (*CP*) over the total instances. In our approach, each pixel is an instance (*Total*). The formalism of accuracy is defined in accordance with Equation (2):

$$Acc = \frac{CP}{Total} \quad (2)$$

Intersection over Union (*IoU*) is a metric that computes the segmented area ($\hat{y}$) that corresponds to the area of the mask (y), dividing what is in common between them (intersection) by the whole (union). Equation (3) shows the IoU calculation:

$$IoU = \frac{area(\hat{y}) \cap area(y)}{area(\hat{y}) \cup area(y)} \quad (3)$$

Pearson's correlation coefficient (ρ) was calculated to evaluate the linear correlation between the evaluated metrics and the percentage of glandular tissue (PD%) in the phantom images. PD% is calculated by using the ratio of glandular labels and non-air labels (e.g., Figure 2).

The observed values were categorized by slice position through the phantom volume and volumetric breast density (VBD).

4 EXPERIMENTAL ANALYSES

Two experiments were performed to test our segmentation model. For both experiments, we used 32 unique breast phantoms. For each experiment, we varied the slice location as input images. Similarly to the training stage, only the central slice images were used as input for the first experiment. For the second experiment, the entire phantom volume divided in slices was used as input images. The phantom slices and DBT reconstructed images close to the phantom skin (about 1 cm in each extremity) were excluded from the experimental analyses due to the lack of glandular tissue for segmentation.

4.1 Using Central Slices

The experiment using only the central slices resulted in a mean Loss, Acc and IoU of 0.27, 0.93, and 0.62, respectively. Figures 4-6 show three examples from our model segmentation using input images that contain regions with different amounts of glandular tissue (i.e., PD%). Note that the accuracy of the U-Net segmentation varies with PD%.

The correlations between PD% and Loss, Acc, and IoU were ρ=0.77, ρ=-0.85, and ρ=0.60, respectively. This correlation analysis shows moderate to high positive correlation between PD%, IoU and Loss, and high negative correlation with Acc. That

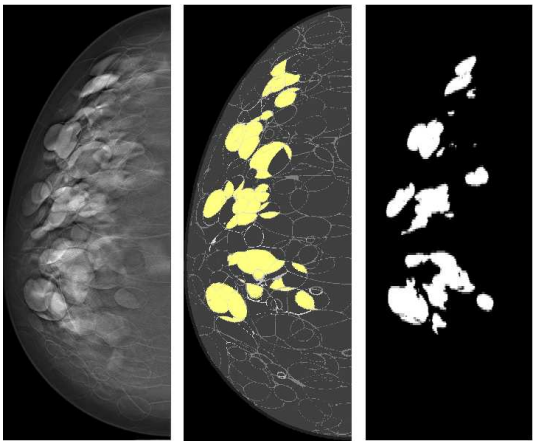

Figure 4: (Left) central slice of reconstructed DBT image, (middle) label map with glandular tissue highlighted in yellow (PD%=12%), and (right) binary segmentation. The segmentation metrics for this input image were 0.18, 0.95, and 0.56 for Loss, Acc, and IoU, respectively.

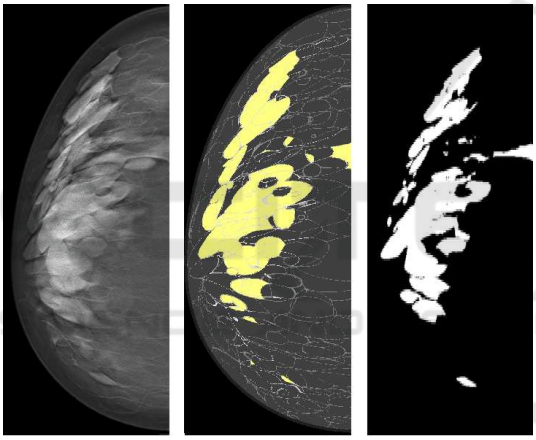

Figure 5: (Left) central slice of reconstructed DBT image, (middle) label map with glandular tissue highlighted in yellow (PD%=20%), and (right) binary segmentation. The segmentation metrics for this input image were 0.19, 0.94, and 0.63 for Loss, Acc, and IoU, respectively.

said, these preliminary results indicate that the accuracy of the U-Net segmentation reduces significantly with PD% (p-value$<$0.001).

4.2 Using Medio-lateral Slices

We also evaluated the U-Net segmentation using all phantom slices that contain glandular labels (ML slices). In total, over 480 ML slices per phantom were selected for this experiment. The U-Net segmentation resulted in overall performance with mean Loss, Acc, and IoU of 0.32, 0.92, and 0.54, respectively (Figure 7a). Note that there was a slight reduction in the Acc and IoU metrics compared to the previous experiment.

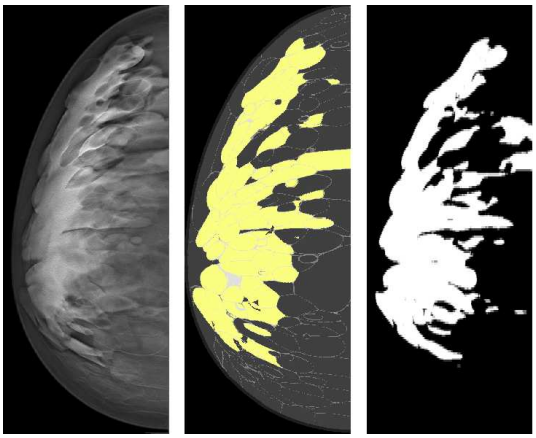

Figure 6: (Left) central slice of reconstructed DBT image, (middle) label map with glandular tissue highlighted in yellow (PD%=34%), and (right) binary segmentation. The segmentation metrics for this input image were 0.31, 0.91, and 0.70 for Loss, Acc, and IoU, respectively.

Figure 7b shows the results of the metrics categorized by slice position through the entire phantom volume. The slice position also affects the U-Net performance, since our CNN was trained using only central slices. The relative difference in IoU between slice positions can reach up to 20%. These differences can also be seen in the Loss. However, these are preliminary results and a more detailed statistical analysis is required to evaluate the U-Net performance in depth.

Finally, Figure 7c shows the Acc results categorized by VBD. These boxplots show changes in U-Net performance throughout the glandular volume of breast phantoms. Note that the overall U-Net performance tends to reduce with denser phantoms (i.e., higher VBD). Again, these are preliminary results and a more detailed statistical analysis is required to support this observation.

5 CONCLUSIONS

These preliminary results show that our U-Net implementation can segment glandular tissue from DBT images with high accuracy. The computer simulations are supervised, thus a known ground-truth is available as input images for the U-Net training. Although our results were based on simulations, our U-Net implementation can be potentially extended to clinical applications if a reasonable ground-truth data set is provided.

This U-Net application allows us to evaluate the impact of 2D breast parameters (PD%) using particular slices and 3D breast parameters (VBD) using sets of slices as input images. For future work, we will provide a more complete statistical analysis of our

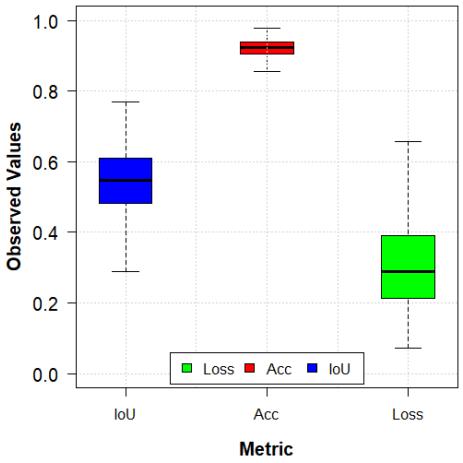

(a)

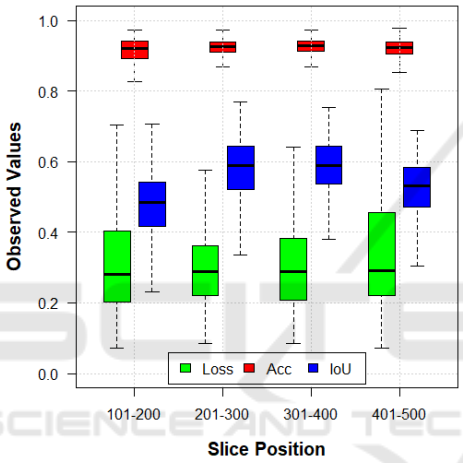

(b)

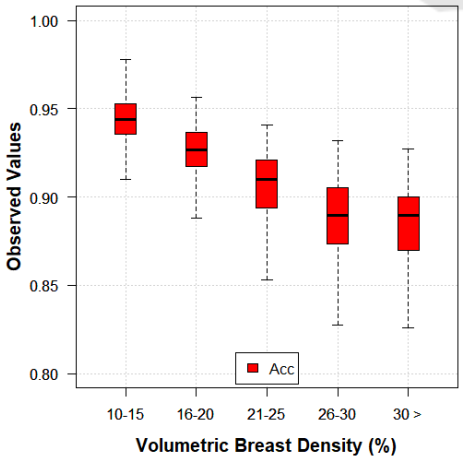

(c)

Figure 7: Boxplots of metrics evaluated using reconstructed slices obtained from 10.1-50.0 mm of phantom thickness (0.1 mm increment). (a) Observed values categorized by metrics, (b) as a function of slice position, and (c) as a function of VBD. Note that there is a difference in y-scale in (c), compared to (a) and (b).

dataset and further explore the use of 3D CNNs for volume segmentation.

ACKNOWLEDGEMENTS

Funding for the research is provided by the following grants: BWF IRSA 1016451, DoD W81XWH-18-1-0082, and AAPM 2020 Research Seed Grant.

REFERENCES

Abadi, E., Segars, W. P., Tsui, B. M., Kinahan, P. E., Bottenus, N., Frangi, A. F., Maidment, A., Lo, J., and Samei, E. (2020). Virtual clinical trials in medical imaging: a review. *Journal of Medical Imaging*, 7(4):042805.

Academy, D. S. (2019). Deep learning book.

Azar, A. T. and El-Said, S. A. (2013). Probabilistic neural network for breast cancer classification. *Neural Computing and Applications*, 23(6):1737–1751.

Badano, A., Graff, C. G., Badal, A., Sharma, D., Zeng, R., Samuelson, F. W., Glick, S. J., and Myers, K. J. (2018). Evaluation of digital breast tomosynthesis as replacement of full-field digital mammography using an in silico imaging trial. *JAMA network open*, 1(7):e185474–e185474.

Badrinarayanan, V., Kendall, A., and Cipolla, R. (2017). Segnet: A deep convolutional encoder-decoder architecture for image segmentation. *IEEE transactions on pattern analysis and machine intelligence*, 39(12):2481–2495.

Bakic, P. R., Barufaldi, B., Higginbotham, D., Weinstein, S. P., Avanaki, A. N., Espig, K. S., Xthona, A., Kimpe, T. R. L., and Maidment, A. D. A. (2018). Virtual clinical trial of lesion detection in digital mammography and digital breast tomosynthesis. In Lo, J. Y., Schmidt, T. G., and Chen, G.-H., editors, *Medical Imaging 2018: Physics of Medical Imaging*, volume 10573, pages 30 – 42. International Society for Optics and Photonics, SPIE.

Barufaldi, B., Bakic, P., and Maidment, A. (2019). Multiple-reader, multiple-case ROC analysis for determining the limit of calcification detection in tomosynthesis . In Schmidt, T. G., Chen, G.-H., and Bosmans, H., editors, *Medical Imaging 2019: Physics of Medical Imaging*, volume 10948, pages 157 – 163. International Society for Optics and Photonics, SPIE.

Barufaldi, B., Bakic, P. R., Pokrajac, D. D., Lago, M. A., and Maidment, A. D. (2018a). Developing populations of software breast phantoms for virtual clinical trials. In *14th International Workshop on Breast Imaging (IWBI 2018)*, volume 10718, page 107181U. International Society for Optics and Photonics.

Barufaldi, B., Higginbotham, D., Bakic, P. R., and Maidment, A. D. A. (2018b). OpenVCT: a GPU-accelerated virtual clinical trial pipeline for mammography and digital breast tomosynthesis. In Lo, J. Y.,

Schmidt, T. G., and Chen, G.-H., editors, *Medical Imaging 2018: Physics of Medical Imaging*, volume 10573, pages 1333 – 1340. International Society for Optics and Photonics, SPIE.

Caldwell, C. B. and Yaffe, M. J. (1990). Development of an anthropomorphic breast phantom. *Medical physics*, 17(2):273–280.

Carton, A.-K., Bakic, P., Ullberg, C., Derand, H., and Maidment, A. D. (2011). Development of a physical 3d anthropomorphic breast phantom. *Medical physics*, 38(2):891–896.

Chatfield, K., Simonyan, K., Vedaldi, A., and Zisserman, A. (2014). Return of the devil in the details: Delving deep into convolutional nets. *CoRR*, abs/1405.3531.

Cheng, H.-D., Shi, X., Min, R., Hu, L., Cai, X., and Du, H. (2006). Approaches for automated detection and classification of masses in mammograms. *Pattern recognition*, 39(4):646–668.

Chui, J. H., Pokrajac, D. D., Maidment, A. D. A., and Bakic, P. R. (2012). Roadmap for efficient parallelization of breast anatomy simulation. In Pelc, N. J., Nishikawa, R. M., and Whiting, B. R., editors, *Medical Imaging 2012: Physics of Medical Imaging*, volume 8313, pages 1369 – 1378. International Society for Optics and Photonics, SPIE.

Elangovan, P., Mackenzie, A., Dance, D. R., Young, K. C., Cooke, V., Wilkinson, L., Given-Wilson, R. M., Wallis, M. G., and Wells, K. (2017). Design and validation of realistic breast models for use in multiple alternative forced choice virtual clinical trials. *Physics in Medicine & Biology*, 62(7):2778.

Feng, S. S. J. and Sechopoulos, I. (2012). Clinical digital breast tomosynthesis system: dosimetric characterization. *Radiology*, 263(1):35–42.

Hamarneh, G. and Jassi, P. (2010). Vascusynth: Simulating vascular trees for generating volumetric image data with ground-truth segmentation and tree analysis. *Computerized medical imaging and graphics*, 34(8):605–616.

Hubbell, J. H. and Seltzer, S. M. (1995). Tables of x-ray mass attenuation coefficients and mass energy-absorption coefficients 1 kev to 20 mev for elements z= 1 to 92 and 48 additional substances of dosimetric interest. Technical report, National Inst. of Standards and Technology-PL, Gaithersburg, MD (United ....

Lashgari, E., Liang, D., and Maoz, U. (2020). Data augmentation for deep-learning-based electroencephalography. *Journal of Neuroscience Methods*, page 108885.

Li, C. M., Segars, W. P., Tourassi, G. D., Boone, J. M., and Dobbins III, J. T. (2009). Methodology for generating a 3d computerized breast phantom from empirical data. *Medical physics*, 36(7):3122–3131.

Maidment, A. D. (2014). Virtual clinical trials for the assessment of novel breast screening modalities. In *International Workshop on Digital Mammography*, pages 1–8. Springer.

Norman, B., Pedoia, V., and Majumdar, S. (2018). Use of 2d u-net convolutional neural networks for automated cartilage and meniscus segmentation of knee mr imaging data to determine relaxometry and morphometry. *Radiology*, 288(1):177–185.

Oliveira, W. d. S. (2017). *Consenso de segmentações de imagens usando classificação de padrões*. PhD thesis, Universidade Federal de Pernambuco.

Paul, S. (2018). Learn how to train u-net on your dataset. https://medium.com/coinmonks/learn-how-to-train-u-net-on-your-dataset-8e3f89fbd623.

Pokrajac, D. D., Maidment, A. D., and Bakic, P. R. (2012). Optimized generation of high resolution breast anthropomorphic software phantoms. *Medical physics*, 39(4):2290–2302.

Ronneberger, O., Fischer, P., and Brox, T. (2015). U-net: Convolutional networks for biomedical image segmentation. In *International Conference on Medical image computing and computer-assisted intervention*, pages 234–241. Springer.

Rui, T., Zou, J., Zhou, Y., Fei, J., and Yang, C. (2018). Convolutional neural network feature maps selection based on lda. *Multimedia Tools and Applications*, 77(9):10635–10649.

Sevastopolsky, A. (2017). Optic disc and cup segmentation methods for glaucoma detection with modification of u-net convolutional neural network. *Pattern Recognition and Image Analysis*, 27(3):618–624.

Siddon, R. L. (1985). Fast calculation of the exact radiological path for a three-dimensional ct array. *Medical physics*, 12(2):252–255.

Tice, J. and Feldman, M. (2008). Full-field digital mammography compared with screen-film mammography in the detection of breast cancer: Rays of light through dmist or more fog? *Breast cancer research and treatment*, 107:157–65.

Tunçay, A. H. and Akduman, I. (2014). Realistic microwave breast models through t1-weighted 3-d mri data. *IEEE Transactions on Biomedical Engineering*, 62(2):688–698.

Valverde, S., Cabezas, M., Roura, E., González-Villà, S., Pareto, D., Vilanova, J. C., Ramió-Torrentà, L., Rovira, A., Oliver, A., and Lladó, X. (2017). Improving automated multiple sclerosis lesion segmentation with a cascaded 3d convolutional neural network approach. *CoRR*, abs/1702.04869.

Vedantham, S., Karellas, A., Vijayaraghavan, G. R., and Kopans, D. B. (2015). Digital breast tomosynthesis: State of the art. *Radiology*, 277(3):663–684. PMID: 26599926.

Zhang, C., Bakic, P., and Maidment, A. (2008). Development of an anthropomorphic breast software phantom based on region growing algorithm - art. no. 69180v. *Proc SPIE*, 6918.

Zhixuhao (2016). Implementation of deep learning framework – unet, using keras. https://github.com/zhixuhao/unet.

Development of Magnification Tomosynthesis for Superior Resolution in Diagnostic Mammography

Raymond J. Acciavatti, Trevor L. Vent, Chloe J. Choi, E. Paul Wileyto,
Peter B. Noël, Andrew D. A. Maidment
University of Pennsylvania, Department of Radiology, 3400 Spruce Street, Philadelphia PA 19104
E-mail: {Raymond.Acciavatti | Trevor.Vent | Jeongin.Choi | epw | Peter.Noel |
Andrew.Maidment}@pennmedicine.upenn.edu

ABSTRACT

Our previous work showed that digital breast tomosynthesis (DBT) supports super-resolution (SR). Clinical systems are not yet designed to optimize SR; this can be demonstrated with a high-frequency line-resolution pattern. SR is achieved if frequencies are oriented laterally, but not if frequencies are oriented in the perpendicular direction; *i.e.*, the posteroanterior (PA) direction. We are developing a next-generation tomosynthesis (NGT) prototype with new trajectories for the x-ray source. This system is being designed to optimize SR not just for screening, but also for diagnostic mammography; specifically, for magnification DBT (M-DBT). SR is not achieved clinically in magnification mammography, since the acquisition is 2D. The aim of this study is to investigate SR in M-DBT, and analyze how anisotropies differ from screening DBT (S-DBT). We have a theoretical model of a high-frequency sinusoidal test object. First, a conventional scanning motion (directed laterally) was simulated. In the PA direction, SR was not achieved in either S-DBT or M-DBT. Next, the scanning motion was angled relative to the lateral direction. This motion introduces submillimeter offsets in source positions in the PA direction. Theoretical modeling demonstrated that SR was achieved in M-DBT, but not in S-DBT, in the PA direction. This work shows that, with the use of magnification, anisotropies in SR are more sensitive to small offsets in the source motion, leading to insights into how to design M-DBT systems.

Keywords: Digital breast tomosynthesis, magnification mammography, super-resolution, aliasing, Fourier transform, digital imaging, image quality, image reconstruction.

1. INTRODUCTION

Magnification mammography is a diagnostic study that uses the principle of geometric magnification to increase the spatial resolution.[1-2] The breast is elevated closer to the x-ray source, allowing subtle structures to appear larger. Current clinical systems support only 2D magnification mammography for diagnostic exams, even though screening exams are increasingly being performed with digital breast tomosynthesis (DBT) or "3D mammography".[3-6]

We have built a prototype next-generation tomosynthesis (NGT) system that supports new acquisition geometries for DBT.[7] Unlike clinical systems, the use of magnification DBT (M-DBT) is unique to the NGT system.[8] The NGT system also supports reconstructions with super-resolution (SR)[9]; the reconstruction grid is prepared with smaller pixelation than the detector. With a high-frequency star-pattern phantom, our previous work showed that the spatial resolution in both screening DBT (S-DBT) and M-DBT is improved with the use of SR. Additionally, a M-DBT image prepared with SR supports even higher resolution than a S-DBT image prepared with SR; hence the use of geometric magnification allows for a gain in resolution that cannot be achieved with SR alone.[8]

Our previous work showed that, in contact mode (S-DBT), there are anisotropies in SR if the input frequency is oriented perpendicular to the direction of the x-ray source motion; *i.e.*, the posteroanterior (PA) direction.[9] While clinical systems are not designed to include x-ray source motion in the PA direction, this paper demonstrates the potential benefit of introducing a secondary component of motion in this direction (Figure 1). The advantage of this design can be understood from the projection images of a point-like object (Figure 2). Angling the x-ray source positions gives rise to subpixel shifts in the image in the PA direction. These shifts are more pronounced in magnification mode (M-DBT), allowing for subpixel sampling gain in the PA direction and hence SR in this direction. In this paper, this design is investigated as a strategy to optimize SR in M-DBT.

Medical Imaging 2021: Physics of Medical Imaging, edited by Hilde Bosmans, Wei Zhao,
Lifeng Yu, Proceedings of SPIE Vol. 11595, 115951J · © 2021 SPIE
CCC code: 1605-7422/21/$21 · doi: 10.1117/12.2580280

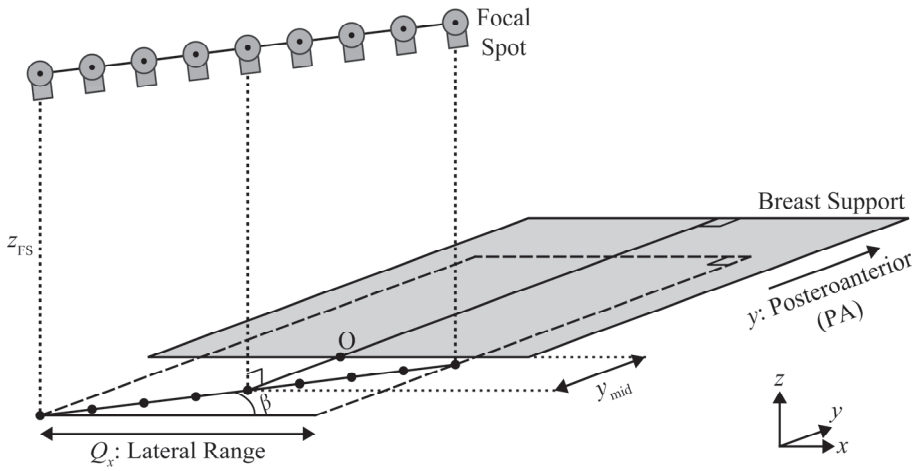

Figure 1. In this acquisition geometry, the focal spot (FS) motion is directed along the angle β. Angling the FS positions in this manner introduces a small secondary component of motion in the PA direction.

Our previous work analyzed SR in contact mode (S-DBT) using a theoretical model of a high-frequency sinusoidal test object.[10] This paper extends the theoretical model to magnification mode (M-DBT). We model the acquisition geometry with a secondary component of scanning motion in the PA direction; specifically, by simulating a range of different angles (β) in this direction. This paper identifies a range of angles, β, that support SR in the PA direction in M-DBT.

2. METHODS

2.1 Acquisition Geometry

We model an acquisition geometry with a small secondary component of motion in the PA direction (Figure 1). In this geometry, the focal spot (FS) positions lie along a line at the angle β relative to the primary direction of motion (lateral or x direction). The FS coordinates x_{FS} and y_{FS} for the n^{th} projection image are thus

$$x_{FS} = \frac{(2n - N - 1)Q_x}{2(N-1)} \tag{1}$$

$$y_{FS} = y_{mid} + x_{FS} \tan\beta \tag{2}$$

where n varies from 1 to N and Q_x is the range of source motion in the x direction (the primary direction of motion). These coordinates are measured relative to point O (the origin in Figure 1); *i.e.*, the midpoint of the chest-wall side of the breast support. The distance y_{mid} is the PA coordinate of the central source position relative to point O.

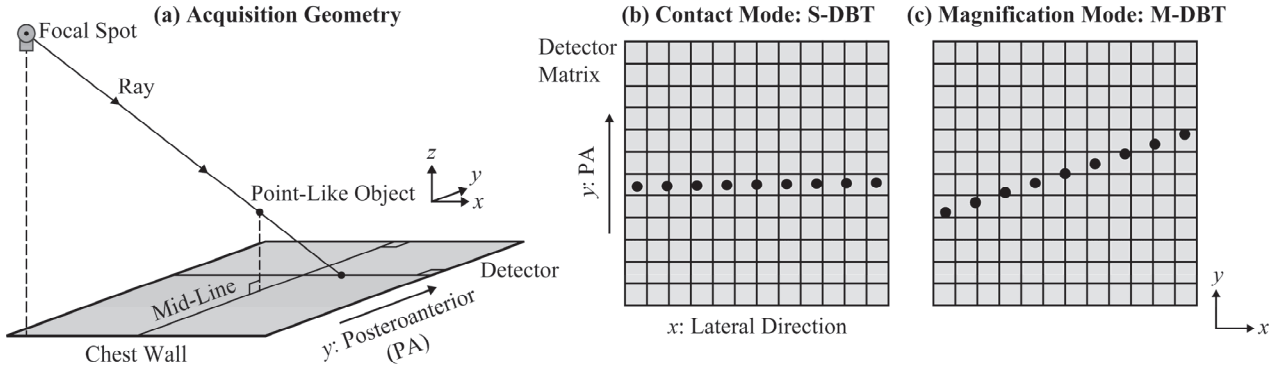

Figure 2. Projection images of a point-like object are shown for the acquisition geometry in Figure 1. In contact mode (S-DBT), the shifts in the image of the object are minimal in the PA direction. In magnification mode (M-DBT), the shifts are more pronounced, allowing for subpixel sampling gain in the PA direction.

Table 1. The simulation parameters for this study are summarized below.

Parameter	Value
Q_x: Lateral Range of X-Ray Source Motion	182.0 mm
y_{mid}: PA Displacement of Central Source Position	–2.0 mm
Distance z_{FS}: Breast Support to Source	685.0 mm
Distance b_z: Breast Support to Detector	–25.0 mm
N: Number of Projections	15
Thickness (ε) of Test Object	0.030 mm
Frequency of Test Object	9.5 mm^{-1}
Fourier Sampling: J_{FT}	1,000
x''_{min}: Lower Endpoint of Fourier Transform	–2.63 mm
x''_{max}: Upper Endpoint of Fourier Transform	2.63 mm

In the NGT system, the z-coordinate of the FS (z_{FS}) is constant in all projection images. The detector is stationary (displaced 25.0 mm below the breast support). The NGT detector (AXS-2430, Analogic Canada Corporation, Montreal, Quebec) has 0.085 mm pixelation and hence an alias frequency of 5.9 mm^{-1}. All other acquisition parameters are shown in Table 1.

2.2 Quantifying the Spatial Resolution

Our previous work developed a theoretical model of a high-frequency test object in DBT.[10] This object is a thin rectangular prism (thickness ε) with a sinusoidal attenuation coefficient (Figure 3). The mid-thickness of the object was modeled at an arbitrary position ($z = z_0$) in our previous work; therefore, magnification mode (M-DBT) can be simulated by varying z_0.

Our previous work calculated the simple backprojection (SBP) reconstruction of this object from first principles.[10] The Fourier transform of the reconstruction (μ_{SBP}) is analyzed to determine if the input frequency (9.5 mm^{-1}, Table 1) is resolved. This transform can be calculated with the midpoint formula for integration

$$\mathcal{F}\mu_{SBP} \approx \left(\frac{x''_{max} - x''_{min}}{J_{FT}} \right) \sum_{j_{FT}=1}^{J_{FT}} \mu_{SBP} e^{-2\pi i f_x'' x''} \Big|_{x''=x''_{min}+(x''_{max}-x''_{min})\left(\frac{j_{FT}-1/2}{J_{FT}}\right)}, \tag{3}$$

where x'' is position in the direction of the input frequency measured relative to a point of interest, x''_{min} and x''_{max} are the endpoints of the interval over which the reconstruction is calculated, and J_{FT} is the number of samples. From this transform, we calculate the r-factor, a metric introduced in our previous work on SR.[9,10] This metric is now illustrated for a conventional acquisition geometry ($\beta = 0°$), assuming $z_0 = 50.0$ mm (Figure 4), under two orientations for the input frequency: lateral (parallel with the direction of source motion) and PA (perpendicular to the direction of source motion).

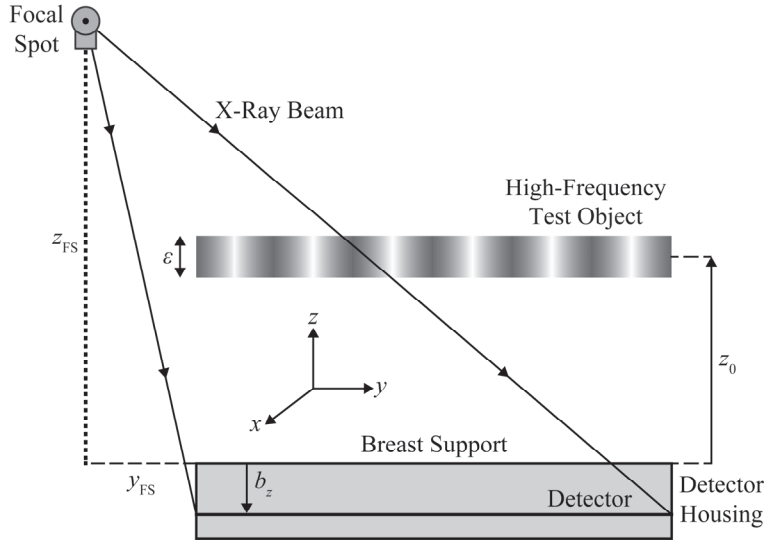

Figure 3. To investigate whether super-resolution is achievable in the PA direction in both contact mode (S-DBT) and magnification mode (M-DBT), the z_0-coordinate can be varied. This coordinate controls the height of the test object above the breast support.

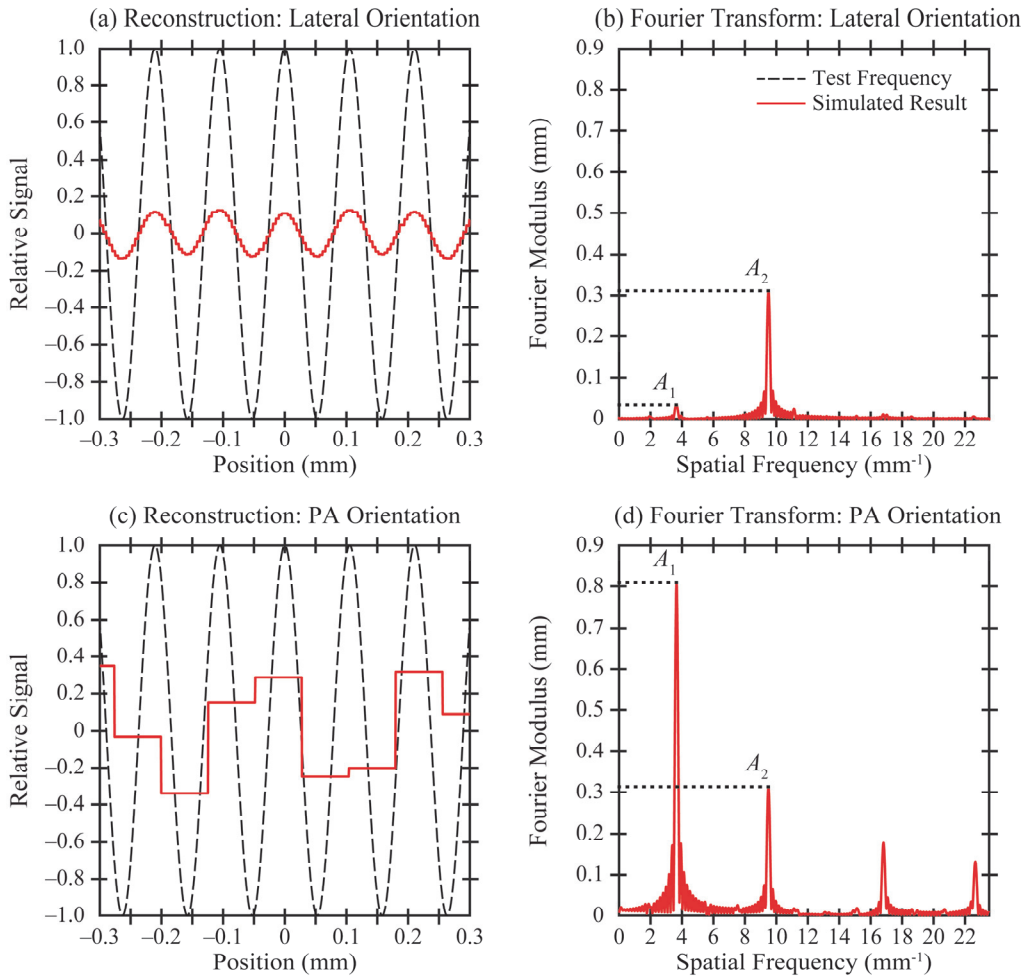

Figure 4. (a) A conventional acquisition geometry, for which $\beta = 0°$, is simulated. The sinusoidal test object is resolved perfectly if frequency is oriented parallel with the direction of x-ray source motion. (b) The Fourier transform has a major peak at the input frequency, 9.5 mm^{-1}, under this orientation. (c) If the input frequency is rotated to the direction perpendicular to the source motion, the same object is not resolved properly. (d) The Fourier transform has a major peak at 3.7 mm^{-1} under this orientation.

Reconstructions of the object clearly differ based on the orientation of the input frequency. For the lateral orientation [Figure 4(b)], the Fourier transform has a major peak at the input frequency (9.5 mm^{-1}). By contrast, for the PA orientation [Figure 4(d)], the Fourier transform has a major peak at a lower frequency (3.7 mm^{-1}). The *r*-factor is defined to be the ratio of the amplitude at the low-frequency peak (A_1) to the amplitude at the input frequency (A_2).

$$r\text{-Factor} = \frac{A_1}{A_2} \tag{4}$$

SR is achieved if *r*-factor ≤ 1. The *r*-factor should be as close to zero as possible to achieve SR with high quality. In the example shown in Figure 4, the *r*-factor is 0.11 for the lateral orientation [Figure 4(b)] and is 2.6 for the PA orientation [Figure 4(d)].

2.3 Statistical Analysis

We used the *r*-factor to measure variation in image quality throughout the breast volume. For the purpose of these simulations, the volume-of-interest (VOI) was a rectangular prism with dimensions 200.0 × 100.0 × 50.0 (in mm) and 0.020 mm spacing between points in each direction. The *r*-factor was calculated at 1,000 random points in the VOI. These simulations focused on the PA orientation of the input frequency (the orientation corresponding to the anisotropy in SR in the conventional geometry). The VOI was displaced anterior to the chest-wall plane by +4.0 mm; this was done to ensure that the interval over which the Fourier transform is calculated [Eq. (3)] is included fully within the detector field-of-view.

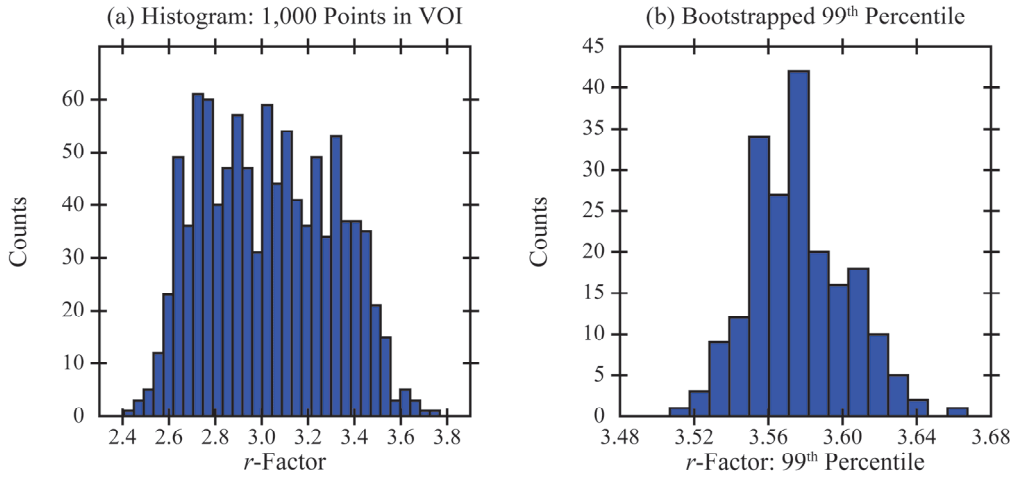

Figure 5. (a) First, the *r*-factor was calculated at 1,000 random points, yielding a histogram of values modeling the variation in image quality throughout the VOI. (b) The 99th percentile of the histogram in (a) was calculated 200 times with bootstrapping, resulting in the histogram shown. The bootstrapped 95% confidence interval (CI_{95}) for the 99th percentile ranges between 3.5 and 3.6.

We calculated the histogram of *r*-factor values at 1,000 random points; an example is shown in Figure 5(a) for the conventional acquisition geometry ($\beta = 0°$) in contact mode (S-DBT). To identify acquisition geometries that eliminate the anisotropy in SR in the PA direction, it is necessary for the upper tail of this histogram (*e.g.*, the 99th percentile) to be minimized below 1.0; this ensures that SR is achieved in at least 99% of points in the VOI. Figure 5(b) is a histogram representing 200 bootstrappings of the 99th percentile; from this histogram, a 95% confidence interval (CI_{95}) can be calculated for the 99th percentile. The middle 95% of the histogram yields CI_{95}. In this example, CI_{95} ranges between 3.5 and 3.6.

2.4 Comparing Contact Mode and Magnification Mode

In addition to contact mode, the same calculations were performed in magnification mode by elevating the VOI by 150.0 mm above the breast support. The z_0-coordinates in the VOI thus ranged between 150.0 and 200.0 mm. These coordinates correspond to magnifications of 1.3 and 1.5, respectively, where magnification (M) is given by

$$M = \frac{z_{FS} - b_z}{z_{FS} - z_0} \tag{5}$$

where b_z is the distance between the breast support and detector (Table 1). The alias frequency, which scales proportionate with the magnification, varies between 7.8 and 8.6 mm^{-1} in the VOI. For the purpose of the simulations, the frequency of the test object was fixed (specifically, at 9.5 mm^{-1}). We chose to hold the input frequency constant since the visualization task was specified relative to the patient anatomy, and hence independent of the positioning of the patient.

For both S-DBT and M-DBT, we simulated 16 acquisition geometries, differing in terms of the angle β (the angle of the secondary scanning motion in Figure 1). The angle β varied between 0° and 0.3° in 0.02° steps. The purpose of these simulations was to investigate whether increasing the angle β allows for SR in the PA direction, as determined by minimizing CI_{95} below 1.0.

3. RESULTS

3.1 Dependency of Super-Resolution on Magnification

First, a single (x, y) coordinate was analyzed; specifically, the coordinate (0, 25.0) (in mm). At this coordinate, the *r*-factor was calculated as a function of z_0, corresponding to an increase in the magnification, M [Figure 6(a)]. In the conventional acquisition geometry for which $\beta = 0°$ (solid red curve), the *r*-factor shows a downward trend as a function of magnification, indicating that there is an improvement in image quality. However, the *r*-factor does not fall below 1.0. Therefore, according to this model, SR is not achievable in the PA direction in either S-DBT or M-DBT.

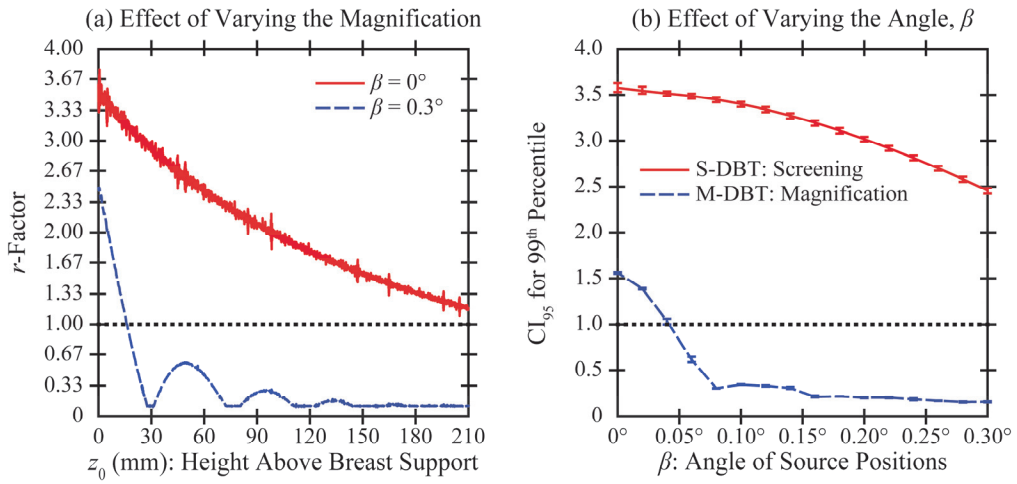

Figure 6. (a) Two acquisition geometries are analyzed in terms of the effect of increasing z_0 (increasing magnification). Higher image quality is achieved in the acquisition geometry with a small secondary component of source motion in the PA direction ($\beta = 0.3°$). (b) The upper tail of the *r*-factor distribution was analyzed in terms of the 99th percentile. In contact mode (S-DBT), the 95% confidence interval (CI_{95}) for this percentile is higher than 1.0, irrespective of the angle β. However, in magnification mode (M-DBT), CI_{95} does fall below 1.0 as the angle β increases.

Next, we simulated a scanning motion oriented at an angle relative to the direction of primary motion; specifically, at a 0.3° angle (dashed blue curve). This geometry is characterized by a secondary component of motion in the PA direction. With theoretical modeling, it can be seen that the *r*-factor exceeds 1.0 in contact mode ($z_0 = 0$, magnification of 1.04), and hence SR is not achieved in the PA direction. However, at magnifications exceeding 1.06 ($z_0 \geq 16.2$ mm), the *r*-factor does fall below 1.0. At magnifications that would be characteristic of M-DBT, the *r*-factor is well below 1.0, which indicates that there is high image quality. For example, at a z_0 coordinate of 200.0 mm (corresponding to a magnification of 1.5), the *r*-factor is 0.12. This indicates that, by angling the source motion in the manner shown by Figure 1, it is possible to achieve SR in the PA direction in M-DBT.

3.2 Statistical Analysis

The next focus of this study was on quantifying image quality as a function of the angle (β) of the source motion [Figure 6(b)]; specifically, through the analysis of CI_{95} as described in Sections 2.3 and 2.4. It can be seen that SR is not achievable in contact mode (S-DBT) at any of the angles considered (ranging between 0° and 0.3°). However, in magnification mode (M-DBT), it is possible to angle the source positions in such a way that CI_{95} does fall below 1.0; specifically, at angles of 0.06° or greater. At the highest angle considered ($\beta = 0.3°$), CI_{95} ranges between 0.15 and 0.16. Since this confidence interval is well below 1.0, SR is achieved with high image quality.

4. DISCUSSION AND CONCLUSION

In our previous work on magnification tomosynthesis, we showed that SR is achievable in experimental images of a star-pattern phantom.[8] This paper expands that work by demonstrating that there are anisotropies in SR in M-DBT depending on the orientation of the input frequency. Specifically, in a conventional acquisition geometry with source motion directed laterally ($\beta = 0°$), SR is not achievable in the PA direction; *i.e.*, the direction perpendicular to the scanning motion.

To achieve SR in the PA direction, it is necessary to re-design the acquisition geometry to include source motion in this direction. We model source motion with submillimeter offsets in the PA direction along the angle β (Figure 1). For example, if $\beta = 0.3°$, the source is translated in 0.068 mm steps in the PA direction per projection (corresponding to a total motion of 0.95 mm in the PA direction over 15 projection views). To validate this design as a strategy for suppressing the anisotropy in M-DBT, a scanning motion similar to the one described in this paper will be the subject of future experiments with the NGT prototype system and a star-pattern phantom.

Although scanning along the angle β is beneficial for magnification mode, the same motion does not suppress the anisotropy in screening mode (S-DBT); the *r*-factor continues to exceed 1.0 over the range of angles considered in this

paper (0° to 0.3°). Our previous work proposed the use of detector motion in the PA direction to optimize SR in S-DBT.[11] The detector motion presented in our previous work is perfectly analogous to the source motion described in this paper in that the offsets are in submillimeter increments in the PA direction.

5. ACKNOWLEDGEMENT

ADAM has received research support from Hologic Inc., Barco NV, and Analogic Corporation; is a spouse to an employee and stockholder of Real Time Tomography (RTT), LLC; is a member of the scientific advisory board of RTT; and is an owner of Daimroc Imaging, LLC. PBN is a consultant to Stryker, and is a member of the computed tomography advisory board of Philips Healthcare. PBN also receives research support, travel award, speaker fees, and paid honorarium from Philips Healthcare.

Support was provided by the following grants: W81XWH-18-1-0082 from the Department of Defense Breast Cancer Research Program, IRSA 1016451 from the Burroughs Wellcome Fund, 1R01CA196528 from the National Institute of Health, and IIR13264610 from Susan G. Komen®. In addition, equipment support was provided by Analogic Inc., Barco NV, and RTT. The content is solely the responsibility of the authors and does not necessarily represent the official views of the funding agencies.

6. REFERENCES

[1] Muntz EP. On the comparison of actual and calculated improvements in the imaging of calcifications using magnification mammography. Medical Physics. 1981;8(4):496-501.
[2] Boyce SJ, Samei E. Imaging properties of digital magnification radiography. Medical Physics. 2006;33(4):984-996.
[3] Sechopoulos I. A review of breast tomosynthesis. Part I. The image acquisition process. Medical Physics. 2013;40(1):014301.
[4] Sechopoulos I. A review of breast tomosynthesis. Part II. Image reconstruction, processing and analysis, and advanced applications. Medical Physics. 2013:40(1):014302.
[5] Friedewald SM, Rafferty EA, Rose SL, Durand MA, Plecha DM, Greenberg JS, et al. Breast cancer screening using tomosynthesis in combination with digital mammography. Journal of the American Medical Association. 2014;311(24):2499-2507.
[6] Conant EF, Zuckerman SP, McDonald ES, Weinstein SP, Korhonen KE, Birnbaum JA, et al. Five consecutive years of screening with digital breast tomosynthesis: outcomes by screening year and round. Radiology. 2020;295(2):285-293.
[7] Eben JE, Vent TL, Choi CJ, Yarrabothula S, Chai L, Nolan M, Kobe E, Acciavatti RJ, Maidment ADA. Development of a Next Generation Tomosynthesis System. In: Lo JY, Schmidt TG, Chen G-H, editors; Physics of Medical Imaging; 2018; Houston, TX: SPIE; 2018. p. 105735Q-1 – 105735Q-8.
[8] Maidment TD, Vent TL, Ferris WS, Wurtele DE, Acciavatti RJ, Maidment ADA. Comparing the Imaging Performance of Computed Super Resolution and Magnification Tomosynthesis. In: Flohr TG, Lo JY, Schmidt TG, editors; Physics of Medical Imaging; 2017; Orlando, FL: SPIE; 2017. p. 1013222-1 – 1013222-10.
[9] Acciavatti RJ, Maidment ADA. Observation of super-resolution in digital breast tomosynthesis. Medical Physics. 2012;39(12):7518-39.
[10] Acciavatti RJ, Wileyto EP, Maidment ADA. Modeling acquisition geometries with improved super-resolution in digital breast tomosynthesis. In: Kontos D, Flohr TG, Lo JY, editors; Physics of Medical Imaging; 2016; San Diego, CA: SPIE; 2016. p. 978363-1 – 978363-12.
[11] Acciavatti RJ, Maidment ADA. Proposing an Acquisition Geometry That Optimizes Super-Resolution in Digital Breast Tomosynthesis. Lecture Notes in Computer Science. 2012;7361:386-93.

Analysis of Digital Breast Tomosynthesis Acquisition Geometries in Sampling Fourier space

Chloe J. Choi, Trevor L. Vent, Raymond J. Acciavatti, Andrew D. A. Maidment
University of Pennsylvania, Department of Radiology, 3400 Spruce Street, Philadelphia, PA 19104
Email: {Jeongin.Choi, Trevor.Vent, Raymond.Acciavatti,
Andrew.Maidment}@pennmedicine.upenn.edu

ABSTRACT

Tomosynthesis acquires projections over a limited angular range and thus samples an incomplete projection set of the object. For a given acquisition geometry, the extent of tomosynthesis sampling can be measured in the frequency domain based on the Fourier Slice Theorem (FST). In this paper we propose a term, "sampling comprehensiveness", to describe how comprehensively an acquisition geometry samples the Fourier domain, and we propose two measurements to assess the sampling comprehensiveness: the volume of the null space and the nearest sampled plane. Four acquisition geometries, conventional (linear), T-shape, bowtie, and circular geometries, were compared on their comprehensiveness. The volume of the null space was estimated as the percentage of voxels subtended by zero slices in the sampled Fourier space. For each voxel in the frequency space, the nearest sampled plane and the distance to that plane were recorded. Among the four, the circular geometry was determined to be the most comprehensive based on the two measurements. We review tomosynthesis sampling with a finite number of projections and discuss how the sampling comprehensiveness should be interpreted. We further suggest that the decision on a system geometry should consider multiple factors including the sampling comprehensiveness, the task to be performed, the thickness of the imaged object, system specifications, and reconstruction algorithm.

Keywords: Fourier space, tomosynthesis sampling, Fourier slice theorem

1. INTRODUCTION

In tomography, the extent to which an object is tomographically sampled can be estimated through analysis of the projections in the Fourier domain. Tomosynthesis acquires projections over a limited angular range, sampling only a subset of the Fourier domain. Due to incomplete sampling, tomosynthesis suffers from more extensive artifacts and poorer in-depth resolution compared to computed tomography.[1-3] To overcome this inevitable limitation of tomosynthesis, researchers have investigated the effects of various acquisition geometries on image quality and hence data sampling.

Multiple acquisition geometries have been investigated since the introduction of tomosynthesis. The conventional geometry is the linear, or arced, geometry, in which the source and the detector move linearly around the patient.[3,5] Although this geometry is well-studied in clinical settings and easy to implement mechanically, out-of-plane objects are blurred into lines and their appearance is highly dependent on orientation[4]. In addition, super-resolution (i.e., subpixel resolution) is absent or poor in the perpendicular direction to the system motion[5]. More advanced geometries including two-dimensional linear source motion, circular source motion, and others have been studied, many of which were shown to have distinct benefits over the linear geometry, although at the expense of other qualities.[4,6-11,13].

A next generation tomosynthesis (NGT) system has been constructed at the University of Pennsylvania to investigate various acquisition geometries.[12] Multiple geometries have been proposed for different tasks and tested with the NGT system including a T-shape source trajectory, a bowtie source trajectory, and a circular source trajectory, with and without detector motion[10,11,13,15,16]. They have been analyzed quantitatively in terms of the modulation transfer function (MTF), noise power spectra (NPS), reconstructed breast volume estimation, and feasibility of super-resolution (SR) in our previous works[10,11,15,22]. However, we have not previously assessed how comprehensively these acquisition geometries sample the imaged object.

The extent of tomosynthesis sampling in the frequency domain can be approximated based on the Fourier Slice Theorem (FST). The Fourier Slice Theorem, also known as the Central Projection Theorem or the Projection Slice Theorem, relates the two-dimensional Fourier transform (2D-FT) of the projection of a three-dimensional object to the three-dimensional Fourier transform (3D-FT) of the same object. Specifically, it states[14] that the 2D-FT of the projection at an angle θ is equal to a slice of the 3D-FT of the object at the same angle θ. One can apply the FST to visualize how various acquisition geometries sample data in the frequency domain as shown in Figure 1.

Medical Imaging 2021: Physics of Medical Imaging, edited by Hilde Bosmans, Wei Zhao,
Lifeng Yu, Proceedings of SPIE Vol. 11595, 115954W · © 2021 SPIE
CCC code: 1605-7422/21/$21 · doi: 10.1117/12.2582229

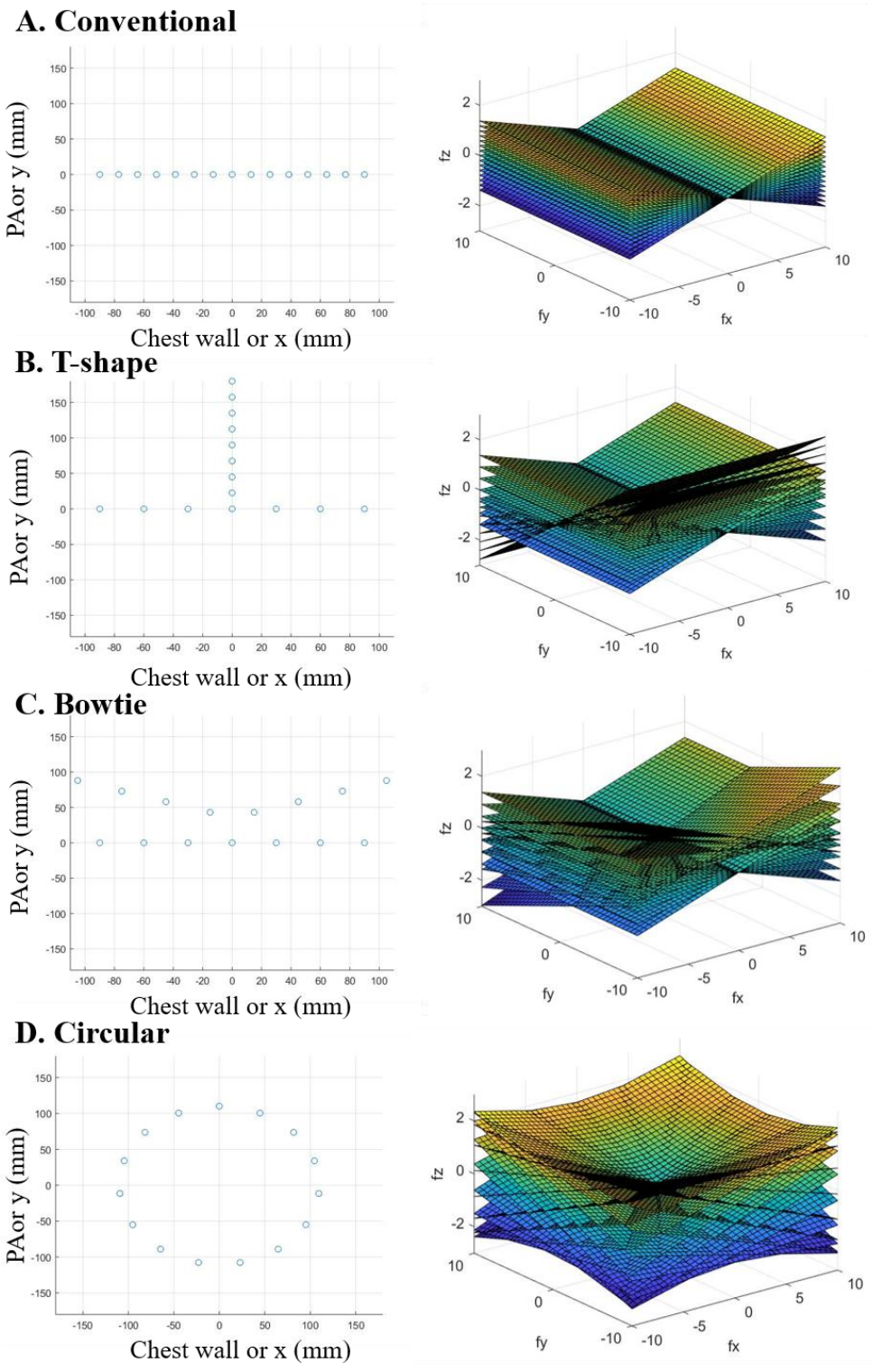

Figure 1. X-ray source acquisition geometries (left) and how each geometry samples the reconstructed images in Fourier space based on the Fourier slice theorem (right). One x-ray projection samples a slice through the origin in Fourier space. f_x, f_y, and f_z are in cycles per millimeters (mm^{-1}).

Each acquisition geometry shown in Figure 1 includes 15 x-ray projections. The axes in the Fourier space figures (Figure 1, right) are frequency domains in x, y, and z (f_x, f_y, f_z) as noted and they are in scale with one another and across all figures. The figures are shown with f_x, $f_y \in [-10,10]$ and $f_z \in [-3,3]$ in mm^{-1}.

Note, the figures are created under the following assumptions:

(1) The object being imaged is located at the origin (0,0,0) of the spatial domain.
(2) A parallel x-ray beam projects onto the detector, which moves isocentrically with the x-ray source.
(3) No imaging parameters (e.g., detector element size, shape and orientation) are considered. This means that the limits of sampling frequency (i.e., Nyquist frequency) in any direction are not illustrated.

In this paper, we propose a term "sampling comprehensiveness" to describe the extent of Fourier data sampling by a particular tomosynthesis scan geometry. An acquisition geometry which spans the greatest volume in Fourier space will be said to have the highest sampling comprehensiveness. The concept of sampling comprehensiveness will be further expanded throughout the paper as we suggest two measurements to assess it. The four acquisition geometries shown in Figure 1 will be compared. We review frequency sampling in tomosynthesis with a finite number of projections and discuss how to interpret the sampling comprehensiveness. We further suggest that the decision on choosing an acquisition geometry for an imaging system should consider multiple factors including the sampling comprehensiveness, the task to be performed, the thickness of the imaged object, system specifications, and reconstruction algorithm.

2. METHODS

Two measurements will be introduced to assess the sampling comprehensiveness of each geometry. Both measurements will be computed in the sampled Fourier space illustrated in Figure 1 (right).

2.1 Volume of the null space

Based on the FST, each slice in the sampled Fourier space (Figure 1) is infinitesimally thin, hence the volume of the sampled space is zero for all acquisition geometries. This assumption is not true for most imaging tasks, as we will discuss below. However, to estimate the volume of the null space, Fourier space was divided into n x n x n voxels with n ranging from 2 to 20. For each voxel, the number of slices going through the voxel was measured. This number indicates the number of x-ray projections which sampled the particular voxel in Fourier space. The volume of the null space is then defined as the percentage of the voxels that were not subtended by any projection.

Because this measurement is dependent on the value of n, it would not be used to evaluate one specific geometry; rather, it will be used to compare two or more geometries as a function of n. For the analysis, the domain of the space was f_x, $f_y \in [-4,4]$ and $f_z \in [-1.2,1.2]$ in mm^{-1}.

As alluded to above, the projection plane is not infinitesimally thin for any real object, because all x-rayed objects have limited thickness (measured in the direction of the projection). As a result, modulation outside the plane arises; the smaller the object the greater the modulation. Knowledge of the imaging task would allow us to calculate the Fourier transform more precisely; however, this is beyond the scope of the current work.

2.2 Distance to the nearest sampled plane

Stevens *et al* has shown that the sampling density in Fourier space can be directly calculated as the inverse of the distance from a sampled point in one view to the nearest sampled point from another view given a large number of projections.[6] As we have attempted to assess and compare the sampling comprehensiveness of acquisition geometries with only a small number of projections, we computed the distance from every point in the space to its nearest sampled plane, rather than its inverse.

For each geometry, the sampled Fourier space within f_x, f_y, $f_z \in [-4,4]$ mm^{-1} was divided into 200 x 200 x 200 cubic voxels. For every voxel, the nearest plane was recorded in terms of its projection number (1 to 15) and the minimum distance to that plane was computed. The distribution of voxels in terms of their nearest projection was then compared.

3. RESULTS

3.1 Volume of the null space

In Figure 2, the percentage of frequency voxels (20 x 20 x 20) subtended by various numbers of projections is shown for each acquisition geometry. In this figure, the percentage of voxels at zero projections represents the percentage of the volume that is never sampled by any x-ray projections in the described acquisition geometry. In this analysis, we define the volume of the null space as this percentage for a given *n* as summarized in Table 1.

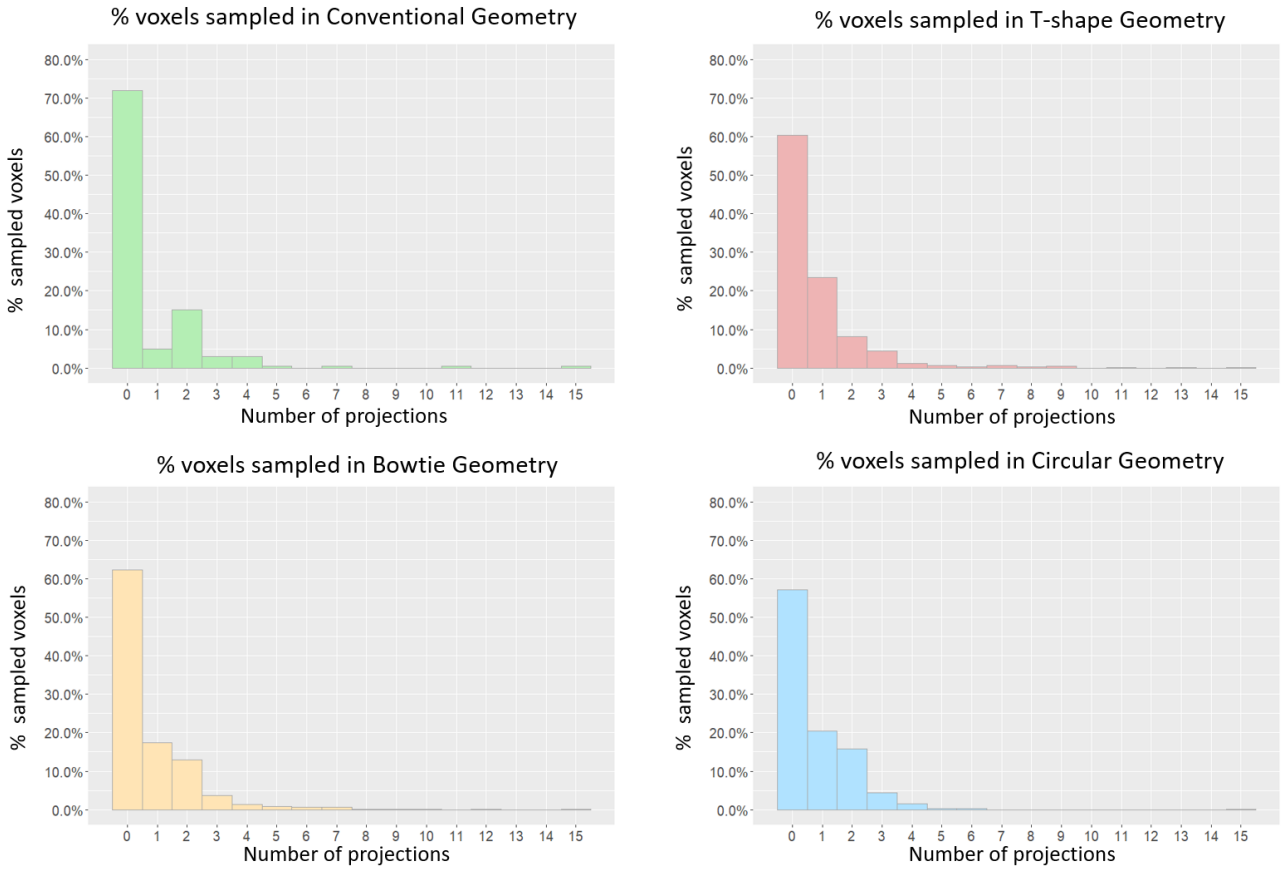

Figure 2. Percentage of voxels sampled by projections in each acquisition geometry. The space is voxelized into 20x20x20 cuboids.

Table 1. The volume of the null space measured for each acquisition geometry. The percentage of voxels sampled by zero projections is defined as the volume of the null space. For each measurement, the space was voxelized into *n* x *n* x *n* cuboids.

n	Conventional	T-shape	Bowtie	Circular
2	50.00 %	50.00 %	50.00 %	50.00 %
4	50.00 %	43.75 %	43.75 %	37.50 %
8	62.50 %	52.34 %	51.56 %	46.88 %
16	70.31 %	57.61 %	58.98 %	53.61 %
20	72.00 %	60.40 %	62.35 %	57.25 %

The distribution of the histograms in Figure 2 varies with acquisition geometries. These differences may portray and compare the sampling comprehensiveness of the listed acquisition geometries. For example, if more voxels are sampled by exactly one projection, the reconstructed space becomes more comprehensively sampled. By the same logic, as more voxels are repeatedly sampled by more than one projection, space becomes less and less comprehensively sampled.

As the volume of the null space is dependent on the total number of voxels (n x n x n), it was computed as a function of n as shown in Table 1. Although the exact values vary with n, the comparison between acquisition geometries mostly holds across the value of n; the volume of null space decreases in the order of Conventional, Bowtie, T-shape, and Circular acquisition geometry.

3.2 Distance to the nearest sampled plane

The distribution of frequency voxels in terms of their nearest projection in the reconstructed Fourier space is illustrated in Figure 3. Most voxels are nearest to either two, three or four specific projection slices in conventional, T-shaped, and bowtie geometries, respectively. On the other hand, the histogram of the circular geometry shows that the voxels are evenly distributed throughout the projections, all with percentages between 5.5% and 8.5%. This indicates that the circular acquisition geometry more comprehensively samples the space and the sampling density within the space does not vary significantly, compared to the others.

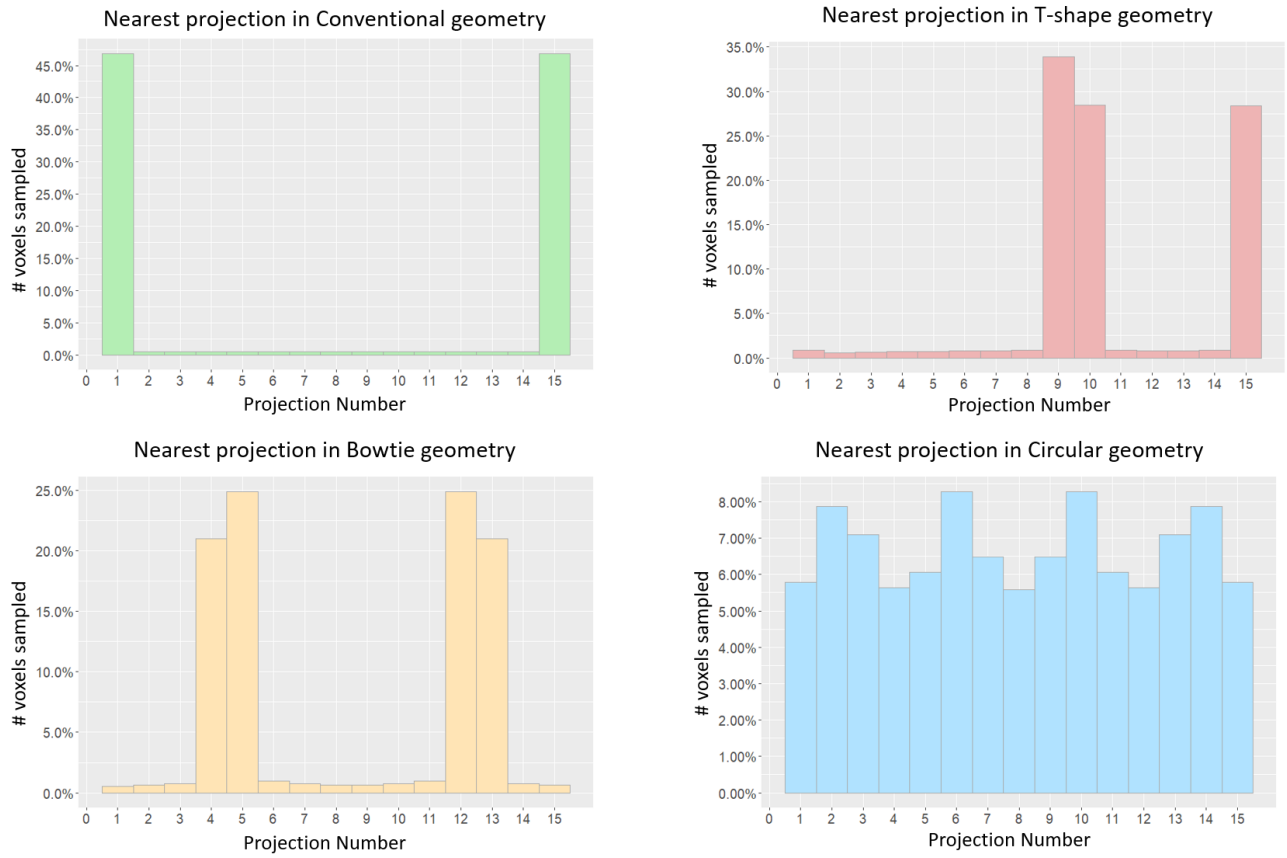

Figure 3. For each voxel (200 x 200 x 200) in the sampled Fourier space (f_x, f_y, $f_z \in$ [-4,4]) for each acquisition geometry, its nearest slice was recorded as projection number from projection 1 to projection 15. Note that the scale of the y-axis differs between the subplots.

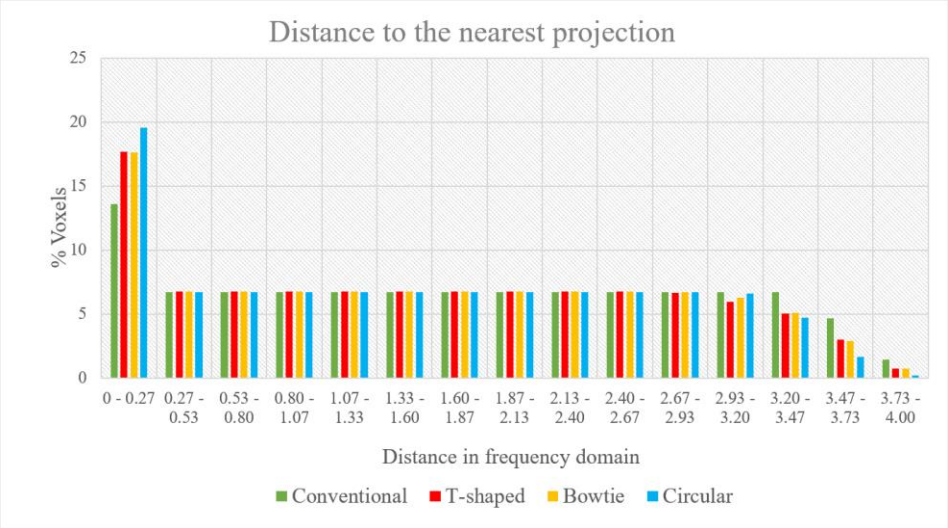

Figure 4. For each voxel (200 x 200 x 200) in the sampled Fourier space for each acquisition geometry, the distance to its nearest projection was measured.

The distance from each voxel to its nearest projection is plotted for each acquisition geometry in Figure 4. As expected from Figure 3 and Table 1, the circular geometry has the highest value in the shortest distance bin and its tail decreases rapidly. This suggests that for a given voxel in the Fourier domain, there is a higher probability that it is adjacent to a measurement point in the circular geometry than in other geometries; that is, the circular geometry is more comprehensive. The conventional, T-shaped, and bowtie acquisition geometries have distinct shapes in the figure as well.

4. DISCUSSION

4.1 Tomosynthesis sampling with a finite number of projections

Assuming an infinite number of projections along the source motion path, the acquisition geometry filling the greatest volume in Fourier space will produce the most comprehensive image reconstruction. In practice, the number of projections in tomosynthesis scans is finite. Assuming a parallel beam, as we did to visualize the Fourier space sampling, projections produce infinitesimally thin planes, comprising zero volume, in the Fourier domain.

Here, we revisit and extend the work by Acciavatti and Maidment to interpret the sampling comprehensiveness for acquisition geometries with a finite number of projections.[17] In their work, they mathematically prove that the Fourier transform of a pitched sine plate with a finite thickness is modulated by a sinc function (equation (22)). This is illustrated in Figure 5.

The shaded FDC (Fourier double cone) region refers to the sampled region of an infinite number of projections for a tomosynthesis scan with angular range Θ. Note the pitched angle of the sine plate object is outside the sampled region in the above figure. Yet, because the Fourier transform of a pitched sine plate is modulated by a sinc function, the reconstruction is expected to retain some information about the object. We make a simple modification to illustrate the data sampling with a finite number of projections in Figure 5. This is equivalent to an orthogonal slice of Figure 2a (right).

As we decrease the number of projections, sampling within the shaded region becomes less dense. Therefore, the sinc-modulated signal may only be sampled at certain points (i.e., the intersection of blue lines and black lines upon which the red sinc functions are plotted in figure 5) and the information retained in the reconstruction for the function is reduced.

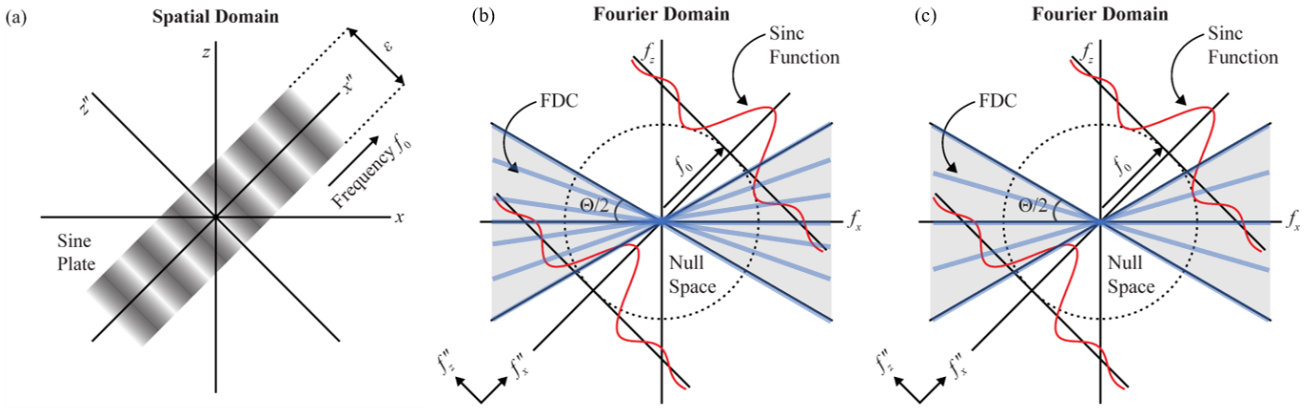

Figure 5. The angled sine plate (Figure 5a) is imaged with only seven (Figure 5b) and five (Figure 5c) projections. Each blue solid line in the figures represents the plane sampled by one x-ray projection. (Figure adapted from Acciavatti *et al*[17])

4.2 The null space and the nearest sampled plane

A close examination of the distributions of the histograms in Figure 2 reveals that the acquisition geometry that most comprehensively samples Fourier space will meet the following criteria:

1) The percentage of voxels sampled by zero projections (i.e., volume of the null space) is minimized.
2) The percentage of voxels sampled by one projection is maximized.
3) The percentage of voxels sampled by more than one projection decreases rapidly with increasing number of projections.

Furthermore, as seen in Figure 5, the amplitude of the sinc-modulated Fourier transforms decreases as we move away from the plane. Hence, the nearest sampled plane from a point (f_x, f_y, f_z) carries the greatest amount of information about that frequency. Note that while this assertion will generally hold true, it is possible that the sampled frequencies will occur at the zeros of the sinc; however, the likelihood of sampling such an object strictly at the zeros of its Fourier representation is small.

The distributions of the nearest projections (Figure 3) present distinct patterns for each acquisition geometry. In the conventional geometry, more than 90% of the space is adjacent to the two most angled projections. This indicates that the distances between the sampled planes are small. In other words, the imaged object would not be comprehensively sampled but would be densely sampled in certain regions in Fourier space; and sparsely sampled elsewhere. The T-shape and the bowtie trajectories add additional directionalities; as a result, the frequency space is more uniformly and comprehensively sampled than it would be with the conventional geometry. The histogram of the circular geometry is quite distinctive from others; voxels are evenly distributed between all 15 projections. Fourier space would be most comprehensively sampled compared to other geometries described above.

This observation adds two more criteria to the above list:

4) The nearest planes are distributed as uniformly as possible.
5) The distance from each voxel to its nearest plane is minimized.

According to these criteria, the acquisition geometry that most comprehensively samples the space is the circular geometry, whereas the acquisition geometry that least comprehensively samples the space is the conventional (linear) geometry.

4.3 Interpretation of comprehensiveness

The ultimate question for tomosynthesis system designers comes down to "how do we acquire the most information of the object within the dose and time constraints of the imaging task?". We will not discuss the scan time constraint in this paper as it may be managed with advanced hardware such as a multisource array[18]. Assuming taking any one projection contributes to $1/n^{th}$ of the total dose limit, the question becomes: "how do we efficiently select n projections for the best image quality?".

In Figure 5, two imaging modes are illustrated: Figure 5b with seven projections, and 5c with only five projections. Figure 5c effectively has more dose budget left than figure 5b in which it can use to fill the FDC more densely or fill outside the FDC. If one chooses to fill the FDC more densely, it will result in a less comprehensive sampling but input frequencies within the region will be better sampled. If one chooses to spend the budget to fill outside the FDC, it will result in a more comprehensive sampling but input frequencies within the FDC will not be as well-sampled.

Each geometry uses this budget differently. The conventional (linear) geometry fills the FDC more densely and input frequencies within or close to the FDC are well sampled. Some geometries, such as the T-shape and bowtie geometries, use a portion of the budget to fill the space in other directions. More complex geometries, such as the circular geometry, spend the budget for the most uniform and comprehensive sampling.

4.4 Theoretical strategies for choosing an acquisition geometry

The decision on an acquisition geometry must consider the fact that the geometry directly affects how the object will be sampled, and hence, the quality of its reconstruction. Although we proposed "sampling comprehensiveness" as a factor to assess system geometries, an acquisition geometry with high comprehensiveness is not necessarily superior to acquisition geometries with relatively low comprehensiveness. We propose that this decision should consider other factors including: (1) the task to be performed, (2) the thickness of the object being imaged, (3) system specification, and (4) reconstruction algorithm. We will briefly discuss the effect of each factor.

First, the decision on tomosynthesis acquisition geometry should be task dependent. As discussed in previous sections, unique geometries use the dose budget for filling the Fourier space differently. If the presence of a lesion is unknown and the probability is equal throughout the imaged object, a uniform distribution of dose might be more appropriate. One of the geometries that could be used for this purpose is the circular geometry. The circular geometry may remove out-of-plane artifacts more effectively with the complicated system motion and appropriate reconstruction filters[4,6]. Furthermore, it would allow super-resolution in both directions and oblique reconstructions over a broad range of pitches[5,10,11,12,13,17], all of which would be beneficial for a thorough inspection of the lesion. On the other hand, if the presence and more importantly the location and orientation of the lesion is known, a selective distribution of dose should be considered.

Moreover, specific requirements related to the performed task may help to determine which acquisition geometry would be used. For example, real-time tomosynthesis guided biopsy proposed by Singh *et al.* requires a repeated scan at the same source positions[15,16]. This is only feasible with an acquisition geometry which has a cyclical behavior. In his work, Singh simulates the scan with a circular geometry.

The thickness of the object being imaged should impact the decision as well. We refer back to the work of Acciavatti *et al.* where they prove that the Fourier transform of a pitched sine plate is modulated by a sinc function.[17] This sinc function, in fact, is dependent on the thickness of the pitched plate (eq. (22)). The amplitude of the sinc function that intersects the sampled planes increases and broadens as the thickness of the object decreases. If the object is sufficiently thin, dense sampling might be unnecessary for a certain range of input frequencies.

The specifications of the tomosynthesis system should also be considered to investigate various acquisition geometries thoroughly. We have noted that Figure 2 does not consider any parameters of the imaging system, such as the detector element size, shape and orientation. Therefore, the Nyquist frequency in any direction, including the depth (z) direction, is not illustrated in the figure. Incorporation of the effects of the Nyquist frequencies will essentially truncate the figure in all three directions as illustrated in Figure 6[19]. Sampling of the object outside the truncated region does not have to be considered when inspecting an acquisition geometry, as it would be null.

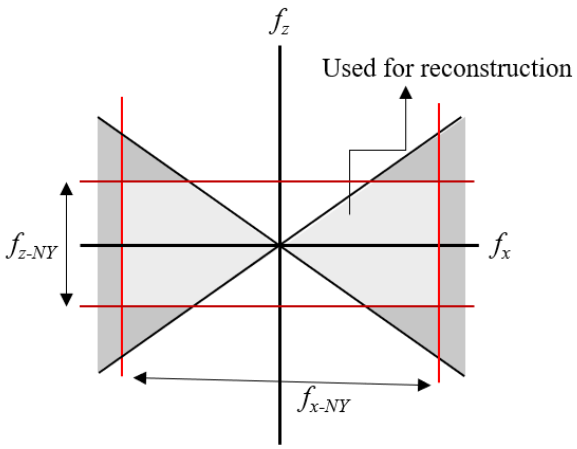

Figure 6. Incorporation of the effects of the Nyquist frequencies ($f_{x\text{-}NY}$, $f_{y\text{-}NY}$, $f_{z\text{-}NY}$) will essentially truncate the sampled region in all three directions, f_x, f_y, and f_z. Only f_x and f_z directions are shown in the figure for simplicity.

Although they are not examined in this paper, reconstruction algorithms are often specific to acquisition geometries. One advantage of acquisition-specific reconstruction filters is more effective removal of out-of-plane artifacts in tomosynthesis. Researchers have investigated to optimize filter design and assess filter performance for various geometries[4,6,17,18]. Availability of appropriate filters and of different reconstruction algorithms should be recognized.

5. CONCLUSION

This study introduces the concept of the sampling comprehensiveness and propose two measurements to assess it for each acquisition geometry. It further discusses tomosynthesis data sampling in the Fourier domain with a finite number of projections and how it relates to the proposed measurements. It further provides how to interpret sampling comprehensiveness in terms of the dose budget and image quality. Theoretical strategies for deciding an acquisition geometry suggested based on five factors: (1) sampling comprehensiveness, (2) task to be performed, (3) thickness of the imaged object, (4) system specifications, and (5) reconstruction algorithm.

6. ACKNOWLEDGEMENT

ADAM has received research support from Hologic Inc., Barco NV, and Analogic Corporation; is a spouse to an employee and stockholder of Real Time Tomography (RTT), LLC; is a member of the scientific advisory board of RTT; and is an owner of Daimroc Imaging, LLC.

Support was provided by the following grants: W81XWH-18-1-0082 from the Department of Defense Breast Cancer Research Program, IRSA 1016451 from the Burroughs Wellcome Fund, 1R01CA196528 from the National Institute of Health, and IIR13264610 from Susan G. Komen®. In addition, equipment support was provided by Analogic Inc., Barco NV, and RTT. The content is solely the responsibility of the authors and does not necessarily represent the official views of the funding agencies.

7. REFERENCES

[1] Dobbins III, J. T., “Tomosynthesis imaging: at a translational crossroads,” Med. Phys. 36 (6), 1956-1967 (2009).

[2] Dobbins III, J. T. and Godfrey, D. J., “Digital X-ray tomosynthesis: current state of the art and clinical potential,” Phys. Med. Biol. 48 (19), 65-106 (2003).

[3] Dance, D. R., Christofides, S., Maidment, A. D. A., McLean, I.D., and Ng, K.H., [Diagnostic Radiology Physics: A Handbook for Teachers and Students], IAEA, Austria, 231-232 (2014).

[4] Reiser, I. and Glick, S. Chapter 5: Cicular Tomosynthesis. [Tomosynthesis Imaging], Taylor & Francis, New York, 65-79 (2014).

[5] Acciavatti, R. J. and Maidment, A. D. A., “Observation of super-resolution in digital breast tomosynthesis”, Med. Phys., 39 (12), 7518-7539 (2012).

[6] Stevens, G. M., Fahrig, R., and Pelc, N. J., “Filtered backprojection for modifying the impulse response of circular tomosynthesis, Med. Phys. 28 (3), 372-380 (2001).

[7] Curry, T. S., Dowdey, J. E., and Murray Jr, R. C. [Christensen’s physics of diagnostic radiology], Wolter, 242-256 (1990).

[8] Levakhina, Y. M., Duschka, R. L., Vogt, F. M., Barkhausen, J., and Buzug, T. M., “A dual-axis tilt acquisition geometry for digital musculoskeletal tomosynthesis”, Phys. Med. Biol. 58, 4827-4848 (2013).

[9] Maidment, T. D., Vent, T. L., Ferris, W. S., Wurtele, D. E., Acciavatti, R. J. and Maidment, A. D. A., “Comparing the imaging performance of computed super resolution and magnification tomosynthesis,” Med. Imaging 2017 Phys. Med. Imaging 10132, 1013222 (2017).

[10] Vent, T. L., Lepore, B., and Maidment, A. D. A., “Evaluating the imaging performance of a next-generation digital breast tomosynthesis prototype”, Proc. SPIE 10948, Medical Imaging 2019: Physics of Medical Imaging, 109480K (1 March 2019)

[11] Vent, T. L., Barufaldi, B. and Maidment, A. D. A., "Simulation and experimental validation of high-resolution test objects for evaluating a next-generation digital breast tomosynthesis prototype", Proc. SPIE 10948, Medical Imaging 2019: Physics of Medical Imaging, 109480M (1 March 2019);

[12] Eben, J. E., Vent, T. L., Choi, C. J., Yarrabothula, S., Chai, L., Nolan, M., Kobe, E., Acciavatti, R. J. and Maidment, A. D. A., “Development of a Next Generation Tomosynthesis System,” Med. Imaging 2018 Phys. Med. Imaging, 10573 (2018).

[13] Acciavatti, R. J. and Maidment, A. D. A., “Proposing an Acquisition Geometry that Optimizes Super-Resolution in Digital Breast Tomosynthesis”, IWDM 2012: Breast Imaging, 386-396 (2012).

[14] Kak, A. C. and Slaney, M., [Principles of Computerized Tomographic Imaging], IEEE Press, 49-112 (1988).

[15] Singh, P., Choi, C. J., Vent, T. L., and Maidment, A. D. A, “Novel Reconstruction Algorithms that Facilitate Real Time 4D Tomosynthesis”, Med. Imaging 2021 Phys. Med. Imaging (2020).

[16] Singh, P., Choi, C., Vent, T. L., Maidment, A. D. A., “Real Time Image Reconstruction Technique for Digital Breast Tomosynthesis-Guided Needle Biopsy,” PO-GeP-I-185, Med. Phys. 2020: 47 (6). E551

[17] Acciavatti, R. J. and Maidment, A. D. A., “Oblique reconstructions in tomosynthesis. I. Linear systems theory”, Med. Phys. 40 (11), 111911-1-111911-21 (2013).

[18] Neculaes, V. B., Edic, P. M., Frontera, M., Caiafa, A., Wang, G. and Man, B. D., “Multisource X-Ray and CT: Lessons Learned and Future Outlook”, IEEE, 1568-1585 (2014).

[19] Zhao, B. and Zhao, W., “Three-dimensional linear system analysis for breast tomosynthesis”, Med. Phys. 35 (12), 5219-5232 (2008).

[20] Mertelmeier, T., Orman, J., Haerer, W. and Dudam, M. K., "Optimizing filtered backprojection reconstruction for a breast tomosynthesis prototype device," Proc. SPIE 6142, Medical Imaging 2006: Physics of Medical Imaging, 61420F (2006).

[21] Lauritsch, G. and Haerer, W. H., “A theoretical framework for filtered backrprojection in tomosynthesis”, Proc. SPIE 3338, 1127-1137 (1998).

[22] Vent, T. L., Barufaldi, B., Acciavatti, R. J., Krishnamoorthy, S., Surti, Suleman, and Maidment, A. D. A., “Next Generation Tomosynthesis Image Acquisition Optimization for Dedicated PET-DBT Attenuation Corrections”, Proc. SPIE 11595, Medical Imaging 2021 Phys. Med. Imaging (2021).

Signal-to-Noise Ratio and Contrast-to-Noise Ratio Measurements for Next Generation Tomosynthesis

David A. Martin, Trevor L. Vent, Chloe J. Choi, Bruno Barufaldi,
Raymond J. Acciavatti, Andrew D. A. Maidment
University of Pennsylvania, Department of Radiology, 3400 Spruce Street, Philadelphia PA 19104
Email: {Dave.Martin, Trevor.Vent, Bruno.Barufaldi, Jeongin.Choi,
Raymond.Acciavatti, Andrew.Maidment}@pennmedicine.upenn.edu

ABSTRACT

It is standard for the x-ray source in conventional digital breast tomosynthesis (DBT) acquisitions to move strictly along the chest wall of the patient. A prototype, next-generation tomosynthesis (NGT) system has been developed that is capable of acquiring customized geometries with source motion parallel and perpendicular to the chest wall. One well-known consequence of acquiring projections with the x-ray source anterior to the chest wall is that a small volume of tissue adjacent to the chest wall is missed. Here we evaluate strategies in DBT to avoid missing tissue while improving overall image quality. Acquisition geometries tested in this study include the conventional (control), "T-shape," and "bowtie" geometries. To evaluate the impact of moving the x-ray source away from the chest wall, the signal-to-noise ratio (SNR) and contrast-to-noise ratio (CNR) were measured as a function of location within the reconstructed volume. Using simulations and physical experiments, the SNR and CNR were compared with conventional DBT. Simulations of two different phantoms were performed: a "tube" phantom and a "lattice" phantom. Experiments with uniform and textured phantoms were also conducted. While the image quality was slightly reduced immediately adjacent to the chest wall, there was no missed tissue and both the T-shape and Bowtie geometries exhibited SNR and CNR improvement over the vast majority of the reconstruction volume; the overall result being an improvement in image quality with both the T-shape and bowtie geometries.

INTRODUCTION

Digital breast tomosynthesis (DBT) has been shown to improve cancer detection and reduce false positive recalls in screening when compared to traditional 2D mammography[1,2]. DBT acquires x-ray projections over a limited angular range to create a three-dimensional (3D) or volumetric image of the breast. Conventional DBT systems acquire x-ray projections strictly along the chest wall. Customized DBT acquisition geometries have been proposed as an alternative to improve the visualization of breast tissue[3–6]. It has been shown previously that acquisition geometries with a two-dimensional source trajectory can improve image quality by better estimating breast shape (i.e., outline and volume), reducing artifacts and out-of-plane blurring, and improving in-plane spatial resolution and super-resolution[4–9].

Designing a new acquisition geometry for breast imaging must consider certain criteria, including: (i) the acquisition geometry should be designed to avoid missing tissue at the chest wall[10,11], and (ii) overall image quality throughout the entire breast must be maximized. The conventional DBT geometry satisfies (i) by acquiring x-ray projections directly over the chest wall. With regard to criterion (ii), we will define the conventional geometry as the control case. In designing our NGT system, it has been our hypothesis that by varying the source location in both the lateral and posteroanterior (PA) directions, the image quality could be improved (ii) while ensuring that the breast is sampled by including a sufficient number of projections along the chest wall to avoid missed tissue (i).

In this work, we evaluate the overall image quality of DBT reconstructions resulting from two custom acquisition geometries, T-shape and bowtie. As shall be made clear in this work, we have intentionally located half of the source locations in the plane of the chest wall. This will ensure that all of the breast will be exposed to at least half of the full radiation dose budget; the remainder of the dose budget can be used to acquire projections outside of the chest wall plane. Note, here we are assuming an equal distribution of dose between projections.

We assess the image quality of the reconstructions for each geometry in terms of spatially-dependent signal-to-noise ratio (SNR) and contrast-to-noise ratio (CNR). Based on Poisson statistics, one can assert that when using half the dose, the reduction in SNR and CNR at the chest wall is proportional to $1/\sqrt{2}$, thus neither SNR or CNR should be reduced by more

Medical Imaging 2021: Physics of Medical Imaging, edited by Hilde Bosmans, Wei Zhao,
Lifeng Yu, Proceedings of SPIE Vol. 11595, 115951L · © 2021 SPIE
CCC code: 1605-7422/21/$21 · doi: 10.1117/12.2582279

than 30%. By contrast, one would expect that SNR and CNR will increase anteriorly if x-ray source locations are positioned anterior to the chest wall plane due to the inverse square law and the reduced obliquity of the incident rays.

We posit that acquisition geometries with PA source motion, such as the T-shape and bowtie geometries, may be designed to improve SNR and CNR over the bulk of the reconstructed volume, and thus improve lesion conspicuity, while minimizing the impact on lesions immediately adjacent to the chest wall. The ultimate goal of this study is to develop a method for optimizing customized DBT acquisitions using objective metrics commonly used for image quality, such as SNR and CNR.

MATERIALS

The NGT Prototype

The configuration of the NGT prototype was used to simulate image acquisition of three typical acquisition geometries (conventional, T-shape, and bowtie)[7,8,12] using the OpenVCT simulation framework[13] and physical experiments. The conventional acquisition geometry does not incorporate PA source motion, while the T-shape and bowtie geometries both incorporate PA source motion.

Virtual Phantoms

Two virtual phantoms were created to evaluate SNR and CNR for the three acquisition geometries. The tube phantom (Figure 1, left) is 306 mm x 240 mm x 40 mm (in x, y, and z, respectively) and comprises 29 equidistant tubes of glandular tissue placed in the center (z dimension) of a volume of adipose tissue. Tubes are spaced equidistantly in the mediolateral direction (ML, x). The lattice phantom (Figure 1, right) is the same shape and comprises the same materials as the tube phantom, with 23 additional tubes of glandular tissue spaced equidistantly in the PA direction.

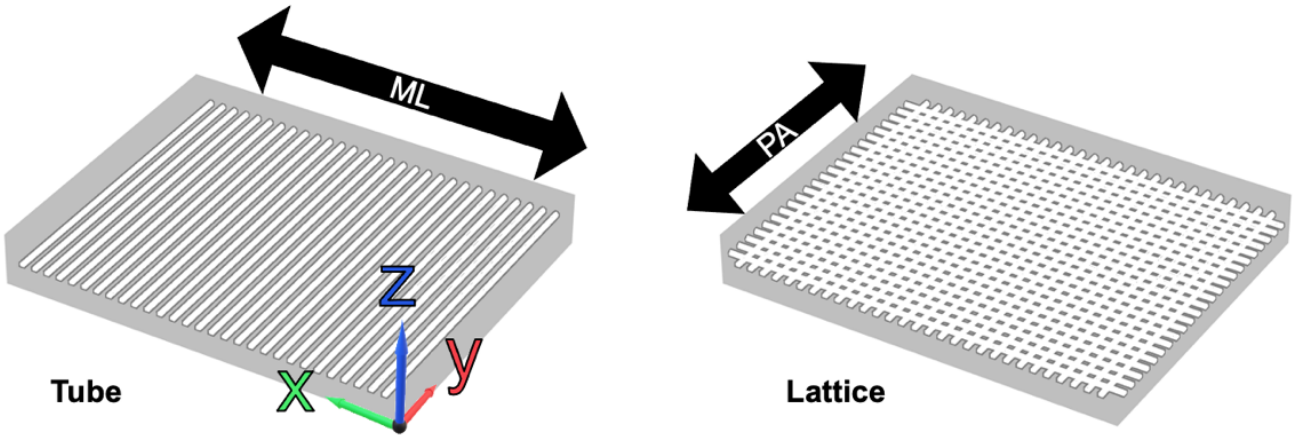

Figure 1: Volume renderings of the tube (left) and lattice (right) phantoms and the coordinate axis.

Physical Phantoms

A uniform Lucite phantom (FF) was used to measure SNR of the acquisition geometries with the NGT prototype. Similarly, a low-frequency contrast phantom (LFC) was used to measure CNR. The LFC was created by placing a 3.18 mm thick perforated polypropylene sheet with 3.18 mm diameter holes between the flat field phantom and the detector. The LFC and FF phantoms both cover the entire detector field of view (Figure 2).

Figure 2: Experimental design for the physical CNR measurements using the LFC phantom. SNR measurements were performed without the LFC in place.

METHODS

Simulated SNR and CNR Measurements

X-ray projection images of the lattice and tube phantoms were acquired using the OpenVCT simulation framework. Fifteen projection images were simulated for each geometry at 32kVp, 5mAs, and 0.5mm Al filtration per projection. Central slices of the phantoms were reconstructed using commercial reconstruction software (Briona version 7.12, Real Time Tomography, Villanova, PA). Acquisitions were repeated 10 times with random noise, and the central slices of each reconstruction were used to measure SNR and CNR.

For the tube phantom, 15x15 pixel regions of interest (ROIs) were centered on the tubes and background regions. Starting at y = 0 mm ROIs were incremented by one pixel to y = 238.7 mm (Figure 3, left). The lattice phantom has tubes intersecting in both directions. ROIs were defined to measure SNR and CNR in the PA direction only (Figure 3, right).

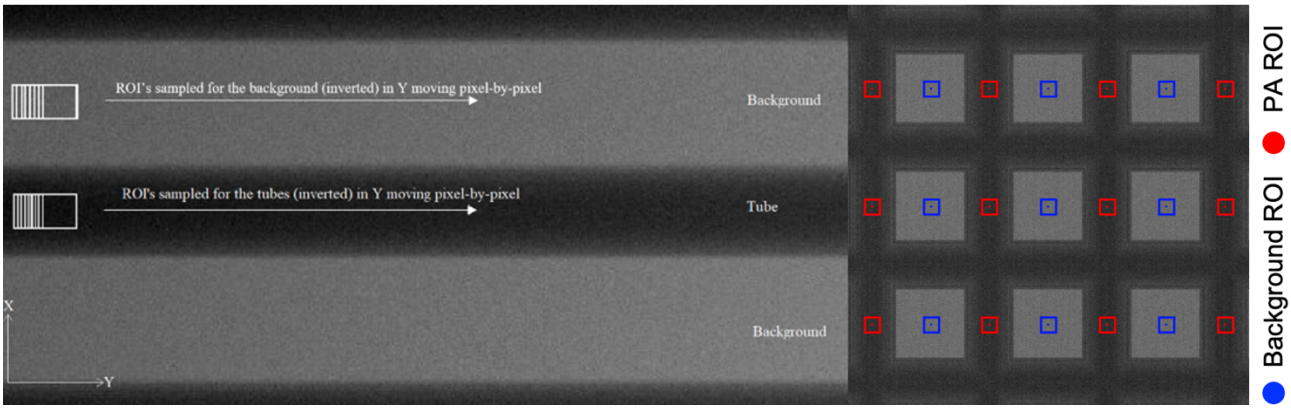

Figure 3: ROIs for the tube phantom (left). ROIs for the Lattice phantom (Right).

The SNR was measured for each ROI of the tube and lattice phantoms using eq. (1). σ[R(x, y)] is the standard deviation and $\overline{R}$(x,y) is the mean value of each ROI at each respective location (x, y). The CNR was measured for each ROI using eq. (2). Where $\overline{R}(x,y)_{tube}$ and $\overline{R}(x,y)_{bgd}$ are the mean values of each ROI for the glandular and adipose tissue regions, respectively. σ_{tube} and σ_{bgd} are the standard deviations. SNR and CNR was repeated for ten central reconstruction slices of each geometry.

$$SNR(x,y) = \frac{(|\overline{R}(x,y)|_{tube})}{\sigma[R(x,y)_{tube}]} \quad (1)$$

$$CNR(x,y) = \frac{\overline{R}(x,y)_{tube} - \overline{R}(x,y)_{bgd}}{\sqrt{\frac{(\sigma^2_{tube} + \sigma^2_{bgd})}{2}}} \quad (2)$$

Physical SNR and CNR Measurements

The NGT prototype was used to acquire experimental images of the physical FF and LFC phantoms. Acquisitions were acquired for each geometry at 31 kVp, 4.5 mAs, and 0.5 mm Al filtration per projection. Acquisitions were repeated ten times for FF and twice for LFC phantoms. Central slices were reconstructed using the method described above. Central slices of FF and LFC reconstructions were used to measure SNR and CNR across the detector, respectively.

For FF SNR measurements, 15x15 pixel ROIs were incremented by 4 pixels in x and y across the image. For the LFC CNR measurements, the contrast was measured using line profiles of LFC reconstructions. Noise was measured using noise only images created by subtracting one reconstruction slice from another. Five line profiles were created in the PA direction, at equidistant positions mediolaterally, from one edge of the image to the other for contrast and noise measurements (Figure 9, below). Contrast was measured by the difference between peaks and valleys of the profile. Differences in SNR and CNR for all measurements were evaluated using a two-sample T-test.

RESULTS

Areal Analysis of Mammograms

We analyzed the PA extent of 1091 craniocaudal (CC) and 1311 mediolateral-oblique (MLO) mammograms from a previous study.[14] The maximum PA extent of tissue was measured using the binary masks of the mammograms. The average values are 120.83 mm and 131.32 mm with standard deviations of 39.54 mm and 38.73 mm for CC and MLO views, respectively. The results are summarized as histograms for each laterality in Figure 4. In addition, 54 images had breasts which extended off the anterior edge of the detector. These images are excluded from the calculate of the mean and standard deviation.

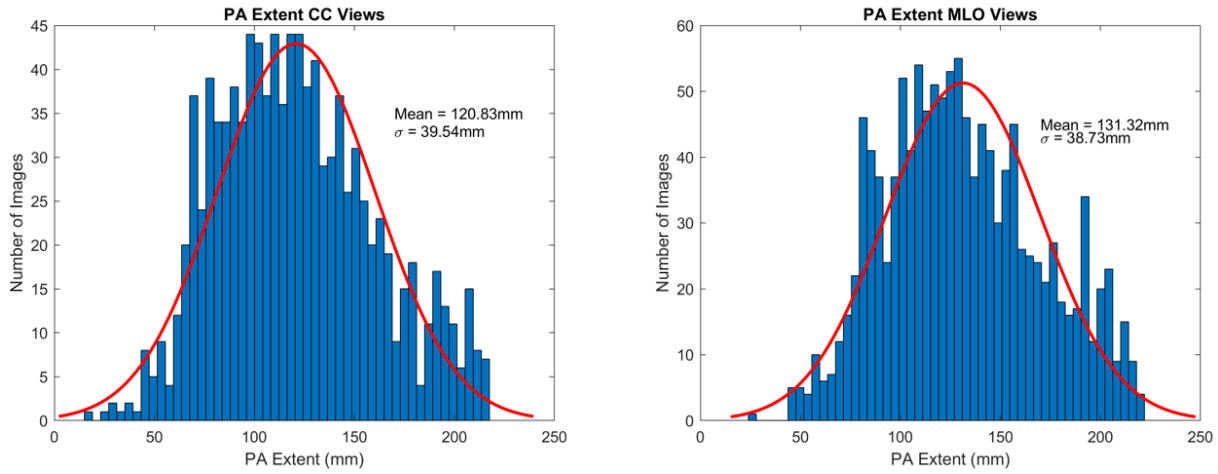

Figure 4: Areal analysis of the maximum PA extent for 1091 CC and 1311 MLO mammograms.

Simulated SNR and CNR Measurements

Figures 5 and 6 show central reconstruction slices, SNR, and CNR for the tube (ML evaluation) and lattice phantoms (PA evaluation), respectively. For ML tubes, the conventional geometry has higher SNR at the chest wall, whereas bowtie and T-shape have higher SNR away from the chest wall. The T-shape has higher SNR medially, and the bowtie has higher SNR laterally. SNR for conventional is lower overall (Figure 5). For PA tubes (Figure 6), the trends are very similar, and again the bowtie geometry had the highest SNR overall. The T-shape and bowtie geometries have higher overall SNR and CNR for the PA tube orientation. The CNR of PA tube measurements decreases with increasing PA distance.

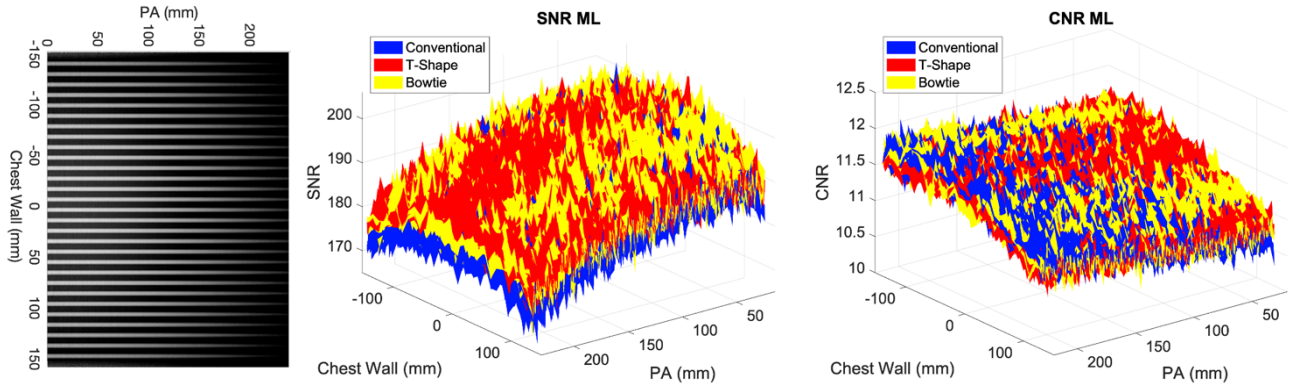

Figure 5: Central reconstruction slice, SNR, and CNR for ML measurements.

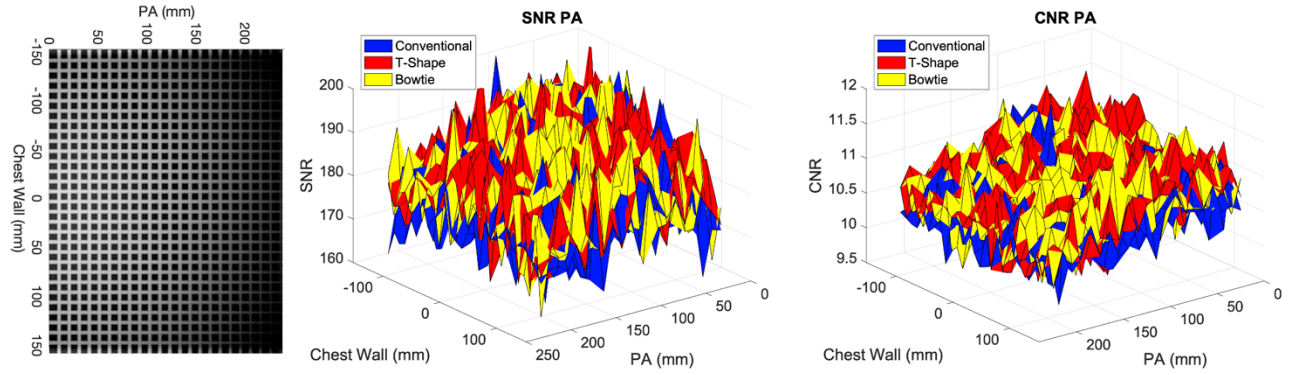

Figure 6: Central reconstruction slice, SNR, and CNR for PA measurements.

SNR and CNR Physical Phantoms

SNR FF measurements are higher for bowtie and T-shape geometries away from the chest wall. Only the central profile of the SNR is shown for FF (Figure 7). The zoomed window of the SNR shows the impact of missed tissue in the reconstruction for the T-shape geometry (Figure 7, right). Little difference is seen between the conventional and bowtie performance near the chest wall. The T-shape motion which has a larger motion in the PA (y) direction has a lower signal at the chestwall. This signal deficit extends for about 3 mm in the reconstructed plane. The CNR for the LFC is consistent with simulation results (Figure 8).

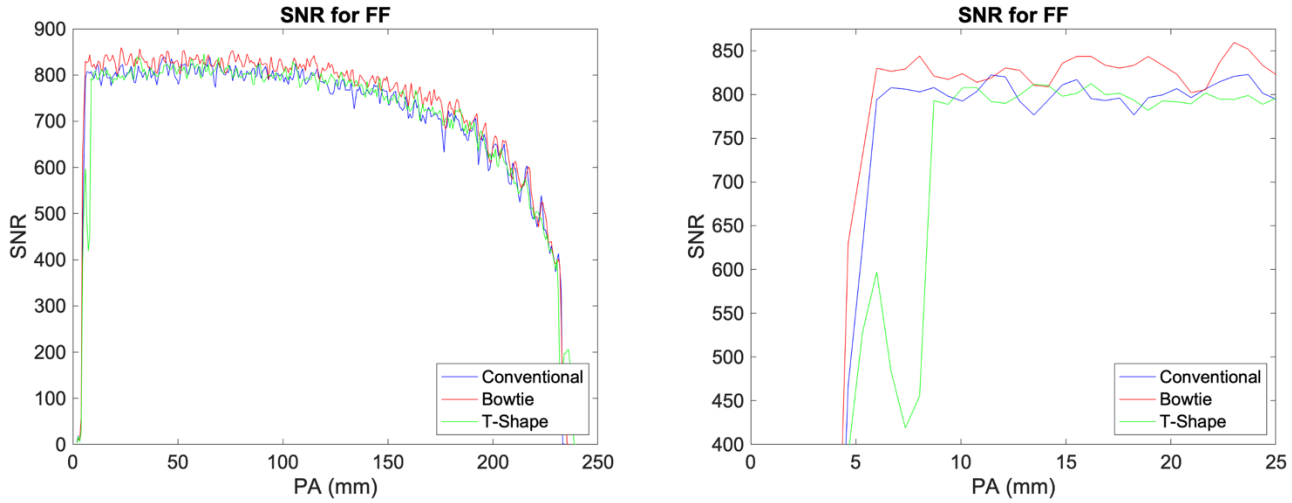

Figure 7: SNR of FF. Note the lag in SNR for T-Shape geometry before it reaches its maximum. This represents the lower exposure for the tissue near the chest wall compared with the other geometries.

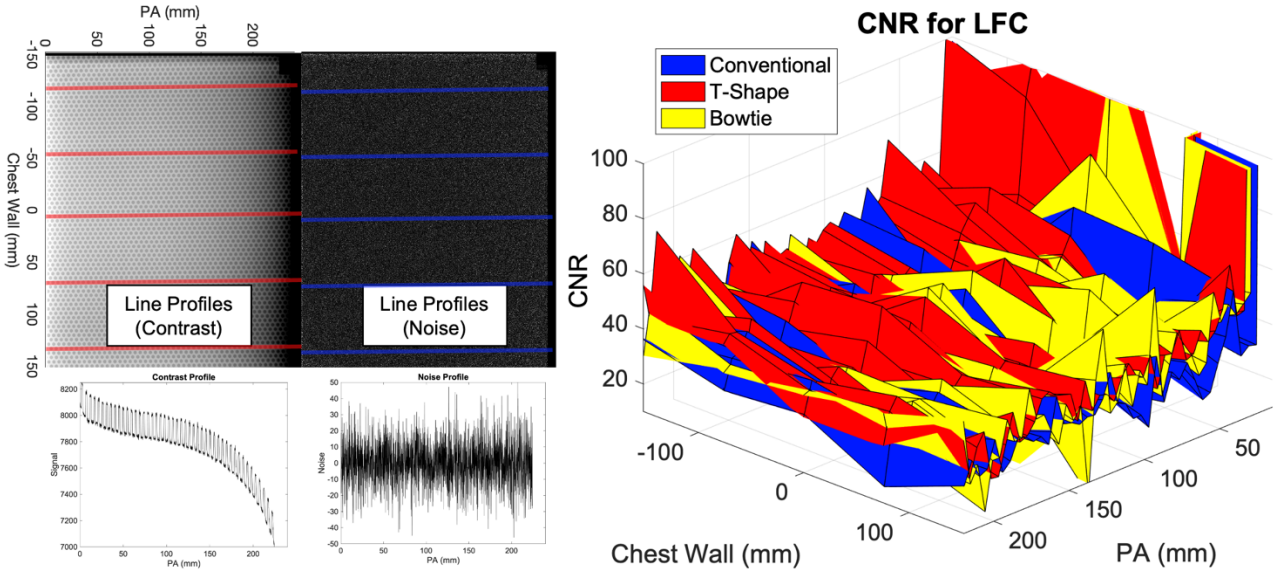

Figure 8: An example of line profiles across the LFC central reconstruction slice and noise image for CNR measurements and the LFC CNR results.

Table 1: Comparison of mean SNR and CNR for NGT acquisition geometries vs. conventional. All p-values are referenced to the conventional geometry. Note that even small differences in means were statistically significant due to the fact that the data were averaged over the entire reconstructed plane.

	SNR			CNR		
Phantom	**Conventional**	**T-Shape**	**Bowtie**	**Conventional**	**T-Shape**	**Bowtie**
Tube	187.5	190.1 p<<0.05	190.3 p<<0.05	11.30	11.30 p<<0.05	11.33 p<<0.05
Lattice (PA)	179.9	183.8 p<<0.05	182.8 p<<0.05	10.55	10.75 p<<0.05	10.72 p<<0.05
FF	650.2	645.5 p<<0.05	667.13 p<<0.05			

DISCUSSION

As shown in Figure 4, within the studied population, the majority of women had breasts that covered at least half of the PA dimension of the detector, and more than 50 had breasts that extended beyond the anterior limits of the detector. These results are specific to the population studied. The exact numbers will vary by geographic location and population; however, the fact remains that most breasts have substantial PA extent. As evidenced by Figures 5-8, there is a strong spatial dependence on the SNR and CNR of the reconstructed image. Thus, consideration of the breast size and spatial dependence of image quality are both important.

The simulations and measurements of SNR and CNR for the NGT acquisition geometries do show an overall higher performance compared with conventional DBT, both for ML and PA measurements. In fact, the vast majority of the reconstructed volume is benefited by x-ray projections made with motion in the PA direction. In addition, through careful allocation of source locations and projection dose, it is possible to have only minimal impact on the SNR and CNR adjacent to the chest wall with the NGT geometries. These results suggest that the benefit of the NGT geometries exceeds any possible detriment. As detailed by Caulkin *et al*[15], the vast majority of breast tumors are more proximal to the nipple than the chest wall, so that the vast majority of breast lesions would benefit in terms of SNR and CNR from the NGT geometries.

The results further suggest that individuals with larger breasts could benefit more from acquisition geometries that incorporate PA source motion. Approximately 2% of the reconstruction volume will be adversely affected by the experimental geometries in terms of SNR and CNR. The maximum SNR reduction is about 30%. By comparison, the other 98% of the reconstructed volume shows a benefit in terms of SNR and CNR. The average SNR improvement is about 3%. Thus, the larger the breast the more benefit derived.

These data also support the concept of customized scanning. We have previously shown[6] that acquisition geometries customized to the shape and size of a woman's breast are superior to generic acquisition geometries. In this study, customized scanning geometries scaled to the size of the breast would serve to minimize the impact of PA source motion immediately adjacent to the chest wall. Women with small breasts would require less PA motion and hence the region of reduced SNR would be minimized.

Given that we have already shown numerous benefits to the NGT system, one of the goals of this research was to address concerns expressed by some attendees at previous SPIE Medical Imaging conferences that the NGT system would "miss tissue". To be clear, from our first NGT design meeting, we were cognizant that PA source motion could miss tissue adjacent to the chest wall. For that reason, we have always ensured that the dose was appropriately budgeted between source locations within and without the plane of the chest wall.

In this work, we have shown that this strategy is sound. This work also provides support for the methods used. As such, we will continue in future work to explore additional strategies to improve image quality with the NGT system, including acquisition geometries customized to each breast, by assessing the spatial distribution of SNR and CNR. We also plan to incorporate anthropomorphic models that test for lesion detectability adjacent to the chest wall using virtual clinical trials. We also plan to evaluate different corrective image processing, image reconstruction, and noise stabilization[16] techniques to ameliorate the loss of radiation dose in the area immediately adjacent to the chest wall. Such techniques would also have value at the far lateral extent of the reconstructed volume where source locations opposite to the reconstructed location are collimated to avoid being projected off the detector.

CONCLUSION

In conclusion, we have shown that adding PA source motion does improve the image quality, as measured by SNR and CNR, for the vast majority of the reconstructed breast volume. We have also shown that these geometries do not result in "missed tissue". Future studies need to examine the impact on specific breast sizes, explore the option to customize acquisition geometry to specific breast sizes, and measure the impact on lesion detectability.

ACKNOWLEDGEMENT

ADAM has received research support from Hologic Inc., Barco NV, and Analogic Corporation; is a spouse to an employee and stockholder of Real Time Tomography (RTT), LLC; is a member of the scientific advisory board of RTT; and is an owner of Daimroc Imaging, LLC.

We thank Johnny Kuo, Susan Ng, and Peter Ringer of RTT for technical assistance with the reconstruction software. Support was provided by the following grants: W81XWH-18-1-0082 from the Department of Defense Breast Cancer Research Program, IRSA 1016451 from the Burroughs Welcome Fund, 1R01CA196528 from the National Institute of Health, IIR13264610 from Susan G. Komen®, and 2020 Research Seed Grant from American Association of Physicists in Medicine. In addition, equipment support was provided by Analogic Inc., Barco NV, and RTT. The content is solely the responsibility of the authors and does not necessarily represent the official views of the funding agencies.

REFERENCES

[1] Aujero, M. P., Gavenonis, S. C., Benjamin, R., Zhang, Z. and Holt, J. S., "Clinical performance of synthesized two-dimensional mammography combined with tomosynthesis in a large screening population," Radiology (2017).

[2] Michell, M. J., Iqbal, A., Wasan, R. K., Evans, D. R., Peacock, C., Lawinski, C. P., Douiri, A., Wilson, R. and Whelehan, P., "A comparison of the accuracy of film-screen mammography, full-field digital mammography, and digital breast tomosynthesis," Clin. Radiol. (2012).

[3] Acciavatti, R. J. and Maidment, A. D. A., "Proposing an acquisition geometry that optimizes super-resolution in digital breast tomosynthesis," Lect. Notes Comput. Sci. (including Subser. Lect. Notes Artif. Intell. Lect. Notes Bioinformatics) (2012).

[4] Acciavatti, R. J., Vent, T. L., Barufaldi, B., Wileyto, E. P., Noël, P. B. and Maidment, A. D., "Super-resolution in digital breast tomosynthesis: limitations of the conventional system design and strategies for optimization," 2020.

[5] Barufaldi, B., Vent, T. L., Acciavatti, R. J., Bakic, P. R., Noel, P. B., Conant, E. F. and Maidment, A. D. A., "Determining the optimal angular range of the X-ray source motion in tomosynthesis using virtual clinical trials," 18 (2020).

[6] Acciavatti, R. J., Barufaldi, B., Vent, T. L., Wileyto, E. P. and Maidment, A. D. A., "Personalization of x-ray tube motion in digital breast tomosynthesis using virtual Defrise phantoms," SPIE Med. Imaging(March), 10 (2019).

[7] Vent, T. L., Lepore, B. L. and Maidment, A. D. A., "Evaluating the imaging performance of a next-generation digital breast tomosynthesis prototype," SPIE Med. Imaging(March), 19 (2019).

[8] Vent, T. L., Barufaldi, B. and Maidment, A. D. A., "Simulation and experimental validation of high-resolution test objects for evaluating a next-generation digital breast tomosynthesis prototype," 21 (2019).

[9] Acciavatti, R. J., Rodriguez-Ruiz, A., Vent, T. L., Bakic, P. R., Reiser, I., Sechopoulos, I. and Maidment, A. D. A., "Analysis of volume overestimation artifacts in the breast outline segmentation in tomosynthesis," SPIE Med. Imaging, 10573 (2018).

[10] Bloomquist, A. K., Yaffe, M. J., Pisano, E. D., Hendrick, R. E., Mawdsley, G. E., Bright, S., Shen, S. Z., Mahesh, M., Nickoloff, E. L., Fleischman, R. C., Williams, M. B., Maidment, A. D. A., Beideck, D. J., Och, J. and Seibert, J. A., "Quality control for digital mammography in the ACRIN DMIST trial: Part I," Med. Phys. (2006).

[11] Yaffe, M. J., Bloomquist, A. K., Mawdsley, G. E., Pisano, E. D., Hendrick, R. E., Fajardo, L. L., Boone, J. M., Kanal, K., Mahesh, M., Fleischman, R. C., Och, J., Williams, M. B., Beideck, D. J. and Maidment, A. D. A., "Quality control for digital mammography: Part II recommendations from the ACRIN DMIST trial," Med. Phys. (2006).

[12] Eben, J. E., Vent, T. L., Choi, C. J., Yarrabothula, S., Chai, L., Nolan, M., Kobe, E., Acciavatti, R. J. and Maidment, A. D. A., "Development of a Next Generation Tomosynthesis System," Med. Imaging 2018 Phys. Med. Imaging, 10573 (2018).

[13] Barufaldi, B., Bakic, P. R., Higginbotham, D. and Maidment, A. D. A., "OpenVCT: a GPU-accelerated virtual clinical trial pipeline for mammography and digital breast tomosynthesis," Med. Imaging 2018 Phys. Med.

Imaging **1057358**(March), 194 (2018).

[14] Barufaldi, B., Borges, L. R., Bakic, P. R., Vieira, M. A. C., Schiabel, H. and Maidment, A. D. A., "Assessment of automatic exposure control performance in digital mammography using a no-reference anisotropic quality index," Med. Imaging 2017 Image Perception, Obs. Performance, Technol. Assess. **10136**, 101360U (2017).

[15] Caulkin, S., Astley, S., Asquith, J. and Boggis, C., "Sites of Occurrence of Malignancies in Mammograms" (1998).

[16] Brandão, R., Borges, L. R., Barufaldi, B., Vent, T. L., Caron, R. F., Oliveira, B. B., Maidment, A. D. A. and Vieira, M. A. C., "Iterative method to achieve noise variance stabilization in single raw digital breast tomosynthesis," Med. Imaging 2021 Phys. Med. Imaging **11595-93**.

Next generation tomosynthesis image acquisition optimization for dedicated PET-DBT attenuation corrections

Trevor L. Vent*, Bruno Barufaldi, Raymond J. Acciavatti, Srilalan Krishnamoorthy, Suleman Surti, Andrew D.A. Maidment
Department of Radiology, University of Pennsylvania, Philadelphia, United States.
*Trevor.Vent@pennmedicine.upenn.edu

ABSTRACT

A next generation tomosynthesis (NGT) prototype is under development to investigate alternative acquisition geometries for digital breast tomosynthesis (DBT). A positron emission tomography (PET) device will be integrated into the NGT prototype to facilitate DBT acquisition followed immediately by PET acquisition (PET-DBT). The aim of this study was to identify custom acquisition geometries that (1) improve dense/adipose tissue classification and (2) improve breast outline segmentation. Our lab's virtual clinical trial framework (OpenVCT) was used to simulate various NGT acquisitions of anthropomorphic breast phantoms. Five custom acquisition geometries of the NGT prototype, with posteroanterior (PA) x-ray source motion ranging from 40-200 mm in 40 mm steps, were simulated for five phantoms. These acquisition geometries were compared against the simulation of a conventional DBT acquisition geometry. Signal in the reconstruction was compared against the ground truth on a voxel-by-voxel basis. The segmentation of breast from air is performed during reconstruction. Within the breast, we use a threshold-based classification of glandular tissue. The threshold was varied to produce a receiver operating characteristic (ROC) curve, representing the proportion of true fibroglandular classification as a function of the proportion of false fibroglandular classification at each threshold. The area under the ROC curve (AUC) was the figure-of-merit used to quantify adipose-glandular classification performance. Reconstructed breast volume estimation and sensitivity index (*d'*) were calculated for all image reconstructions. Volume overestimation is highest for conventional DBT and decreases with increasing PA source motion. AUC and *d'* increase with increasing PA source motion. These results suggest that NGT can improve PET-DBT attenuation corrections over conventional DBT.

Keywords: multi-modality imaging, digital breast tomosynthesis, positron emission tomography, attenuation correction, virtual clinical trial; ray tracing, binary classification, sensitivity index

1. INTRODUCTION

Digital breast tomosynthesis (DBT) has been shown to improve breast cancer detection and reduce patient callbacks,[1] indicating an increase in sensitivity and specificity.[2] Despite these advantages over full-field digital mammography, conventional DBT does not favor the detection and characterization of calcifications; and lacks prognostic capability.[2] Next generation tomosynthesis (NGT) is under development to investigate potential advances in breast cancer diagnostics and prognostics.

The first stage of development for the NGT prototype was the incorporation of novel x-ray acquisition geometries, including two-dimensional (2D) x-ray source motion in the mediolateral (ML) and posteroanterior (PA) directions and craniocaudal (CC) detector motion. We have evaluated the imaging capabilities of the preliminary NGT prototype using tests of physics and image quality.[3] NGT has been shown to support isotropic and high-quality super resolution,[4,5] improved breast volume estimation,[6,7] and reduced image reconstruction artifacts.[6,8]

Two planar positron emission tomography (PET) detectors will be integrated with the NGT prototype to provide functional imaging as a dedicated PET-DBT device (Figure 1). As an emission imaging modality, the 511 keV annihilation photons that form a PET signal are susceptible to Compton scatter and photoelectric absorption within the breast prior to detection leading to image nonuniformities. In order to achieve quantitative PET images, accurate attenuation correction of the PET data is necessary. In commercial whole-body PET/CT, the CT image is routinely used for PET attenuation correction. In a similar fashion, we anticipate using the DBT images for accurate attenuation correction of the PET data.

Adipose and fibroglandular tissue are the primary breast tissues in the female breast.[9] The task of determining the 3D volumetric outline (breast segmentation and breast volume estimation) and the task of classifying the adipose and fibroglandular tissue using DBT image reconstructions are two of the primary concerns for attenuation correction of the PET-DBT device.[10] DBT is an under-sampled tomographic technique and is thus prone to cone-beam artifacts and out-of-

Medical Imaging 2021: Physics of Medical Imaging, edited by Hilde Bosmans, Wei Zhao, Lifeng Yu, Proceedings of SPIE Vol. 11595, 115954V · © 2021 SPIE
CCC code: 1605-7422/21/$21 · doi: 10.1117/12.2581097

plane reconstruction artifacts in the depth dimension due to overlapping structures. Cone-beam artifacts overestimate the breast volume and out-of-plane artifacts introduce difficulties for distinguishing fibroglandular tissue from adipose tissue. For these reasons, it is especially difficult to determine the true percent density of patient breasts without known ground truth.[11] The 2D x-ray source motion of the NGT prototype can be optimized using a virtual clinical trial (VCT) framework for these tasks with known ground truth. We hypothesize introducing PA source motion will improve breast volume segmentation and adipose-fibroglandular tissue classification.

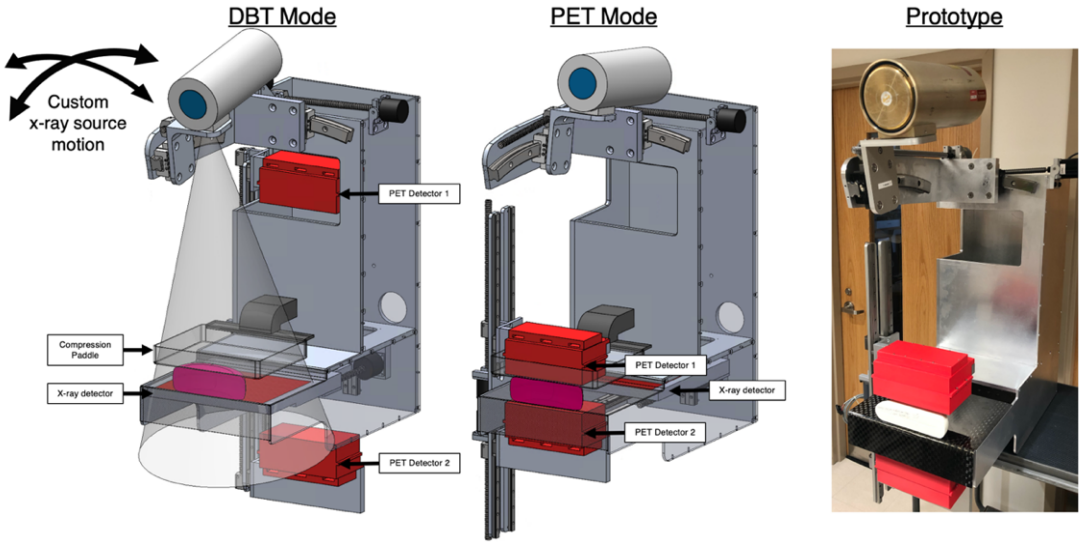

Figure 1: Design and photograph of the PET-DBT prototype. During **DBT Mode**, x-ray images are acquired while PET detectors are retracted into a homing position. Immediately following a tomosynthesis acquisition, PET detectors are positioned above and under the compressed breast and a PET scan is acquired (**PET mode**).

2. MATERIALS & METHOD

Image Acquisition

We used our open-source virtual clinical trial framework (OpenVCT)[12] to evaluate breast segmentation (breast volume estimation), and adipose-glandular classification for custom NGT acquisition geometries compared with conventional DBT. Five phantoms were generated and simulated using mediolateral (ML) compression (Figure 3). Each phantom consisted of a random distribution of adipose and glandular tissue compartments with skin surrounding these tissues. Phantoms were created using an isotropic voxel resolution of 0.1 mm. Each phantom has a volume of 700 mL and measures 7.8 cm × 6.3 cm × 20.5 cm after compression.

Five bowtie acquisition geometries that incorporate increasing distances of x-ray source motion in the PA direction, forming a V (Figure 2), were simulated for each phantom. In addition, a conventional acquisition geometry with the same number of projections and no PA source motion, was used to acquire projection images for all 5 phantoms. Each acquisition geometry consisted of 15 x-ray projections. The source to detector distance was constant at 652 mm. Images were acquired using 35 kVp, 70 mAs (4.67 mAs/projection), and aluminum filtration per projection.

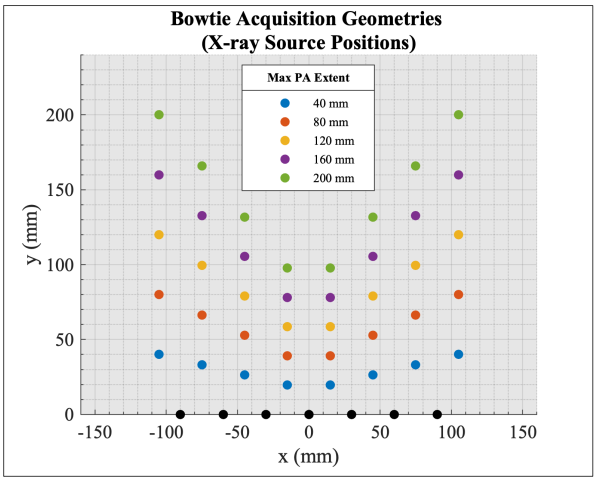

Figure 2: The bowtie acquisition geometries that were used for this study. The black dots represent the common projection locations amongst the 5 geometries. The maximum extent of PA-source motion (y) is indicated in the legend for each geometry. The coordinate (0,0) represents the origin of the NGT prototype at the center of the chest wall.

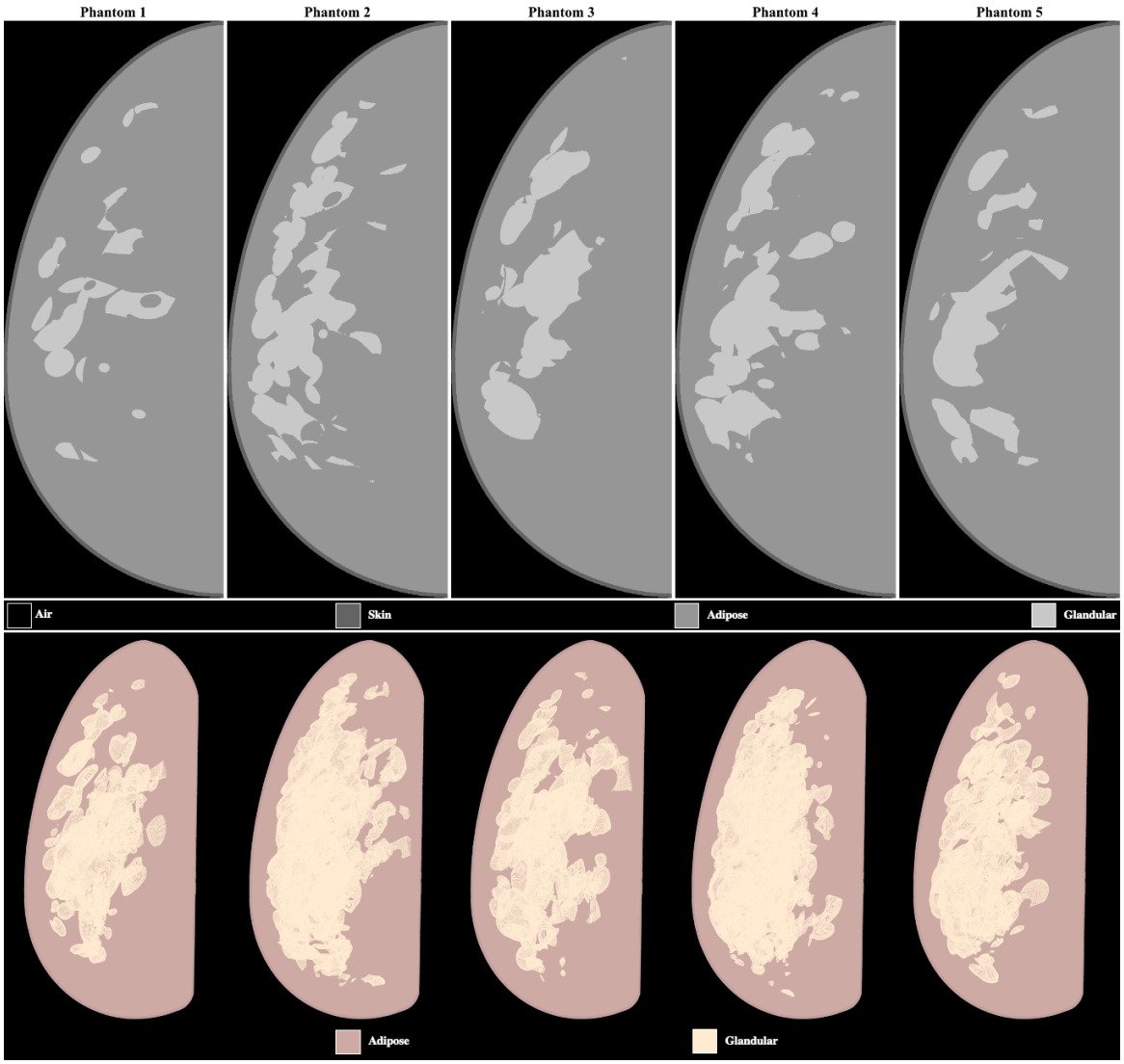

Figure 3: The central slice and maximum intensity projection render of each of the five phantoms are shown. Adipose, skin, and glandular breast tissue are the only materials that were simulated for the phantoms used in this study.

Simulated projection images were used to create image reconstructions of each acquisition using commercial reconstruction software. The outline of the breast was segmented from the background for each image reconstruction. Reconstructions were produced with a voxel resolution of $0.1 \times 0.1 \times 0.5$ mm^3 and processed with contrast enhancement filtering isotropically and bilaterally on each projection image (Piccolo version 4.0.5, Real Time Tomography, Villanova, PA).

Quantitative assessment

The reconstructed breast volume was estimated using the full-resolution image reconstructions. The reconstruction mask of each simulated acquisition was determined by the total volume of voxels with a signal greater than zero. Then, the reconstruction mask was normalized to the phantom mask of non-air voxels for each respective phantom (ground truth).

The reconstruction of the adipose-fibroglandular structures was assessed using a binary classification metric akin to ROC methods previously developed in our lab.[6] This analysis is computationally burdensome for full-resolution phantoms and reconstructions, so both the phantom and image reconstructions were down sampled to an isotropic resolution of 0.5 mm. The phantoms were down-sampled using nearest-neighbor interpolation (mode), and image reconstructions were down sampled using bilinear interpolation. The down-sampled image reconstructions were compared against the phantom ground truth.

ROC curves were produced by using the signal intensity of the image reconstruction as a threshold for a binary classification task. Signals above the threshold were classified as glandular tissue (including voxels containing skin) and signals below were classified as adipose. The true positive rate (TPR) was graphed against the false positive rate (FPR) for each image reconstruction as a function of the threshold value. Area under the curve (AUC) was calculated for each ROC. Colormap images, showing voxel-by-voxel representations of the binary classifications, were created to visualize the differences in image reconstructions of the various acquisition geometries.

In binary classification tasks, the sensitivity index (d') quantifies the effective signal-to-noise ratio of a two-alternative forced choice classification.[13] We use d' to determine differences between different geometries. d' is obtained using an inverse error function and AUC:

$$d' = 2 \cdot \mathrm{erf}^{-1}(2 \cdot \mathrm{AUC} - 1) \tag{1}$$

We then calculated the difference in d' ($\Delta_{d'}$) between bowtie acquisition geometries (b) and the conventional acquisition geometry (c) to quantify performance:

$$\Delta_{d'} = \frac{d'_b - d'_c}{d'_c} \tag{2}$$

3. RESULTS AND DISCUSSION

The central slice of the bowtie acquisition geometry with 80 mm of PA source motion is shown as an example for all five phantoms in Figure 4. Image reconstructions for the conventional and remaining bowtie acquisition geometries have a similar overall appearance. It is difficult to discern any differences qualitatively between the reconstructions of the various acquisition geometries in the conventionally reconstructed sagittal slices. Therefore, coronal and transverse reconstruction slices near respective midplanes of Phantom 2 are shown for the six geometries alongside the ground truth in Figure 5.

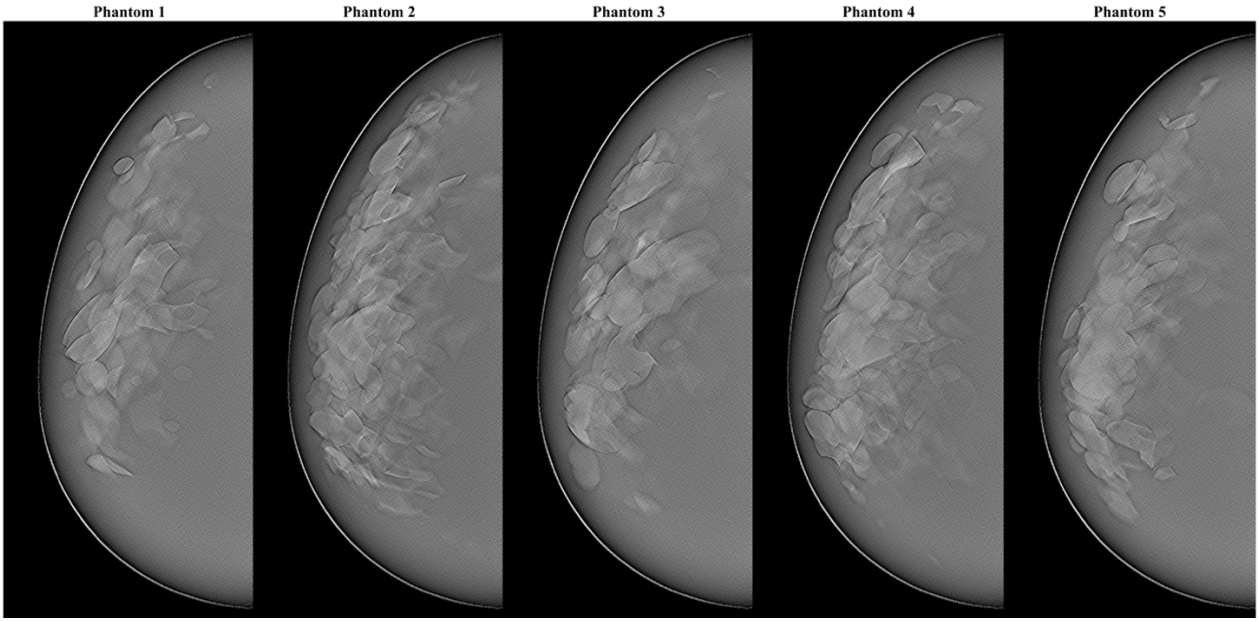

Figure 4: Examples of the central slice of image reconstructions for each of the five phantoms in the conventionally reconstructed sagittal slices (bowtie acquisition with 80 mm PA source motion).

Coronal and sagittal reconstruction slices show trends of improved breast outline delineation and signal contrast of overlapping tissue that scale with PA source motion. Coronal slices Additionally, the effect of cone-beam artifacts is observed in the transverse slices. The artifacts are most prominent in the conventional acquisition geometry (0 mm) and are reduced for acquisition geometries with PA source motion greater than 80 mm.

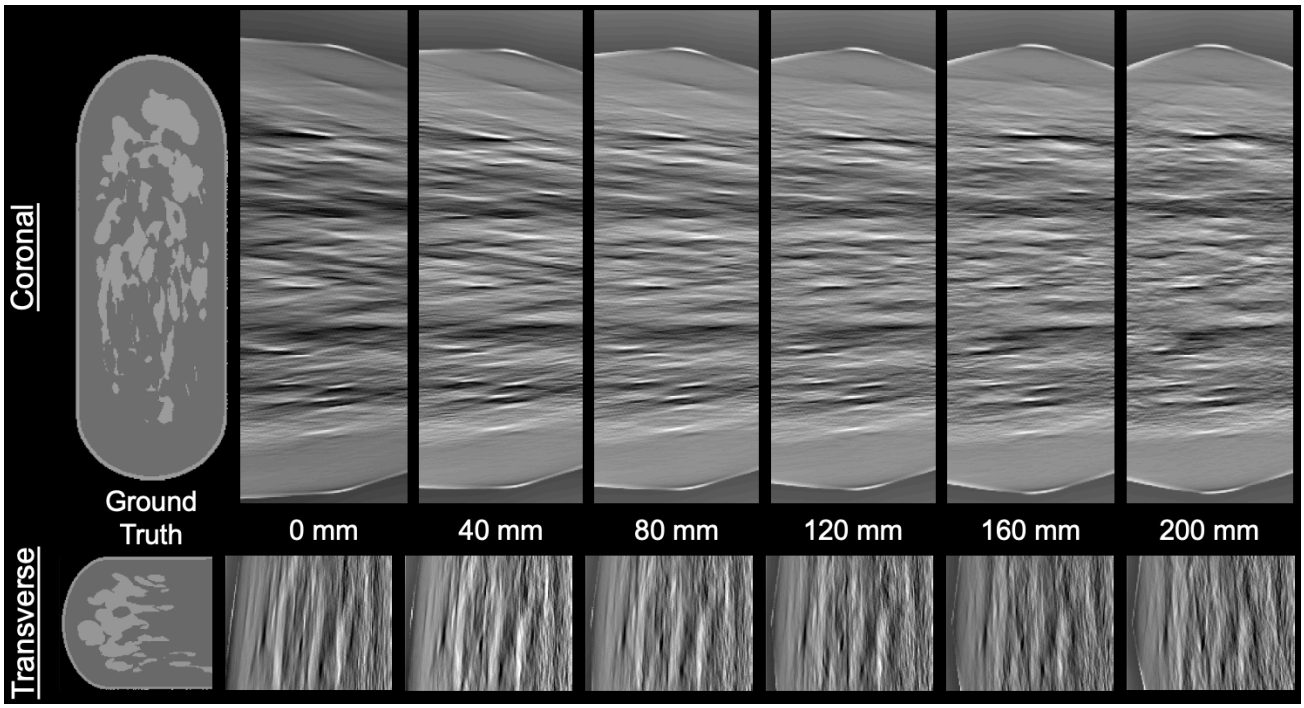

Figure 5: Coronal and transverse reconstruction slices of the conventional acquisition geometry (0 mm) and the five NGT acquisition geometries with increasing PA source motion (40 – 200 mm).

An example of the binary classification is shown for the central slice of a conventional acquisition geometry and an NGT acquisition geometry with 200 mm of PA source motion as a colormap in Figure 6 (sagittal plane) and Figure 7 (transverse plane). This example is shown with a signal threshold at the optimal operating cut-point and was determined by the minimum Euclidean distance from the top left corner (0,1) of the ROC curve. The colormap images of the NGT geometry show fewer out-of-plane reconstruction artifacts compared with the conventional geometry.

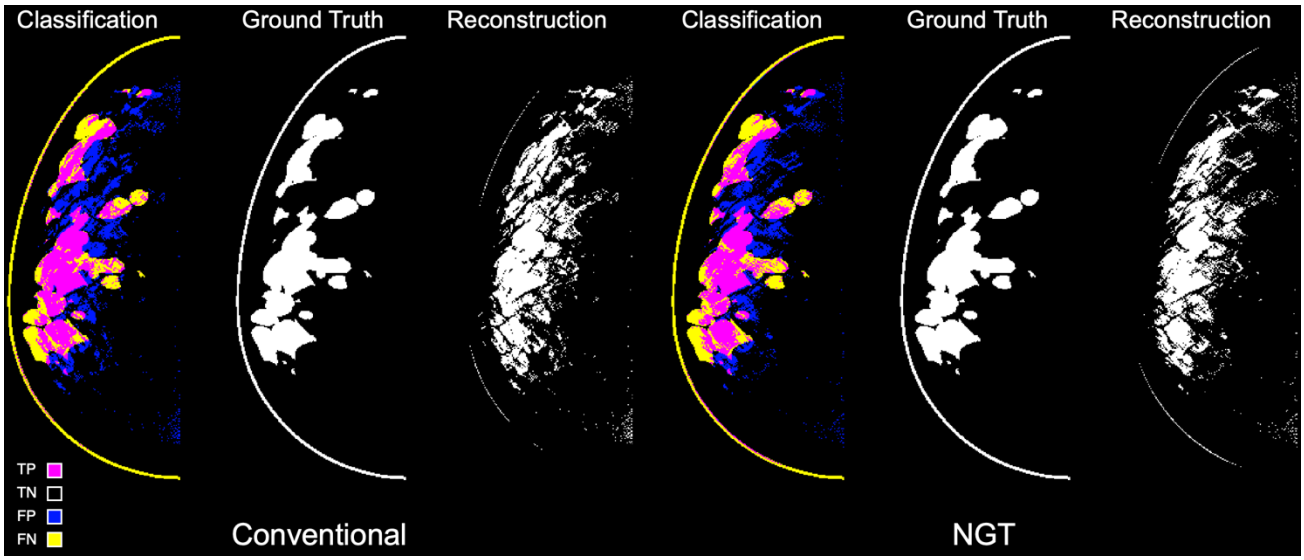

Figure 6: Binary classification colormap of a conventional reconstruction and NGT acquisition with 200 mm of PA source motion. The classification image shows true positives (TP), true negatives (TN), false positives (FP), and false negatives (FN). For the Ground Truth and Reconstruction images, white represents fibroglandular tissue.

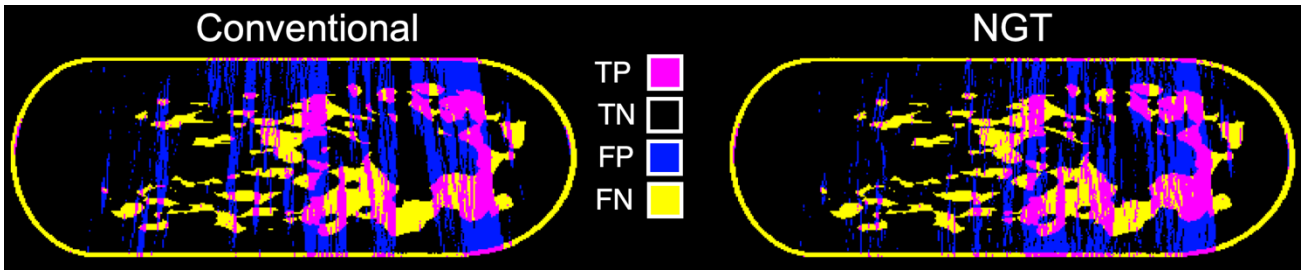

Figure 7: Coronal slice examples of the colormap images. The NGT acquisition geometry shows fewer out-of-plane artifacts (false positives) compared with the conventional geometry.

The mean volume overestimation of the five phantoms is graphed against PA source motion in Figure 8 (left). The conventional DBT acquisition geometry shows the highest overall volume estimation at 112.4% of the ground truth. Volume estimation decreases with increasing PA source motion to a low of 108.0% with 200 mm of PA source motion. This result is consistent with previous results[6,7] and indicates that PA source motion in DBT decreases artifacts in image reconstructions.

Average improvement in *d'* is graphed against PA source motion in Figure 8 (right). Positive values indicate that all bowtie acquisition geometries show improvement in *d'* over conventional DBT. The greatest overall improvement is 8% for two of the five phantoms. These results are preliminary and need to be evaluated further. Phantoms of different volumes and various percent density will be analyzed to evaluate additional factors that can affect volume overestimation and the sensitivity index. The impact of image processing has not been evaluated. For the sake of this study, image processing was the same across all acquisition geometries. Acquisition-geometry specific image processing could provide improved filtering of out-of-plane artifacts for novel geometries. We chose the simplest method of segmentation – threshold segmentation – to test the physics of the NGT system and optimize image acquisition geometries. This approach will improve input data for the ultimate segmentation task.

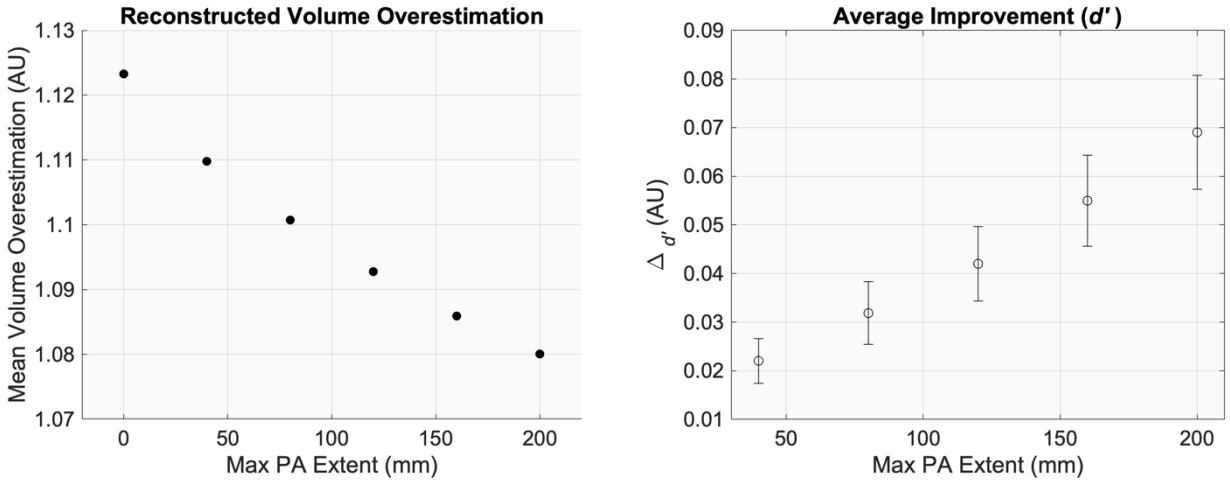

Figure 8: Mean volume overestimation as a function of PA source motion (left). Improvement in *d'* for bowtie acquisition geometries with PA-source motion ranging from 40 mm to 200 mm (right).

4. CONCLUSION

The PA source motion of the custom NGT acquisition geometries has been shown to improve volume estimation and adipose-glandular classification for DBT using a simple threshold-based method. Results suggest that the NGT acquisition geometries can improve the accuracy of PET-DBT attenuation corrections. This method will be used to evaluate additional phantom parameters and acquisition geometries. These results can also be used to help determine a superior classification or tissue segmentation method for DBT.

5. ACKNOWLEDGEMENTS

The authors would like to thank Johnny Kuo, Susan Ng, and Peter Ringer of Real Time Tomography for technical assistance with Piccolo. Andrew D. A. Maidment is a shareholder of Real Time Tomography and is a member of the scientific advisory board.

Support was provided by the following grants: W81XWH-18-1-0082 from the Department of Defense Breast Cancer Research Program, IRSA 1016451 from the Burroughs Welcome Fund, 1R01CA196528 from the National Institute of Health, IIR13264610 from Susan G. Komen, and 2020 Research Seed Grant from American Association of Physicists in Medicine. In addition, equipment support was provided by Analogic Inc., Barco NV, and Real Time Tomography. The content is solely the responsibility of the authors and does not necessarily represent the official views of the funding agencies.

REFERENCES

[1] Rafferty, E. a, Park, J. M., Philpotts, L. E., Poplack, S. P. and Sumkin, J. H., "Digital Mammography and Breast Tomosynthesis Compared with Digital Mammography Alone : Results of a Multicenter, multireader trial," Radiology **266**(1), 104–113 (2013).

[2] Conant, E. F., "Clinical Implementation of Digital Breast Tomosynthesis," Radiol. Clin. North Am. **52**(3), 499–518 (2014).

[3] Vent, T. L., Acciavatti, R. J. and Maidment, A. D. A., "Development and Evaluation of the Fourier Spectral Distortion Metric," IEEE Trans. Med. Imaging, 1 (2020).

[4] Vent, T. L., Barufaldi, B. and Maidment, A. D. A., "Simulation and experimental validation of high-resolution test objects for evaluating a next-generation digital breast tomosynthesis prototype," 21 (2019).

[5] Vent, T. L., Lepore, B. L. and Maidment, A. D. A., "Evaluating the imaging performance of a next-generation digital breast tomosynthesis prototype," SPIE Med. Imaging(March), 19 (2019).

[6] Acciavatti, R. J., Barufaldi, B., Vent, T. L., Wileyto, E. P. and Maidment, A. D. A., "Personalization of x-ray tube motion in digital breast tomosynthesis using virtual Defrise phantoms," SPIE Med. Imaging(March), 10 (2019).

[7] Acciavatti, R. J., Rodriguez-Ruiz, A., Vent, T. L., Bakic, P. R., Reiser, I., Sechopoulos, I. and Maidment, A. D. A., "Analysis of volume overestimation artifacts in the breast outline segmentation in tomosynthesis," SPIE Med. Imaging, 10573 (2018).

[8] Vent, T. L., Barufaldi, B., Acciavatti, R. J. and Maidment, A., "Simulation of high-resolution test objects using non-isocentric acquisition geometries in next-generation digital tomosynthesis," 15th Int. Work. Breast Imaging **11513**, C. Van Ongeval, N. Marshall, and H. Bosmans, Eds., 23, SPIE (2020).

[9] McCarthy, A. M., Kontos, D., Synnestvedt, M., Tan, K. S., Heitjan, D. F., Schnall, M. and Conant, E. F., "Screening outcomes following implementation of digital breast tomosynthesis in a general-population screening program," J. Natl. Cancer Inst. **106**(11) (2014).

[10] Krishnamoorthy, S., Vent, T., Barufaldi, B., Maidment, A. D. A., Karp, J. S. and Surti, S., "Evaluating attenuation correction strategies in a dedicated, single-gantry breast PET-tomosynthesis scanner," Phys. Med. Biol. (2020).

[11] Pertuz, S., McDonald, E. S., Weinstein, S. P., Conant, E. F. and Kontos, D., "Fully automated quantitative estimation of volumetric breast density from digital breast tomosynthesis images: Preliminary results and comparison with digital mammography and MR imaging," Radiology (2016).

[12] Barufaldi, B., Bakic, P. R., Higginbotham, D. and Maidment, A. D. A., "OpenVCT: a GPU-accelerated virtual clinical trial pipeline for mammography and digital breast tomosynthesis," Med. Imaging 2018 Phys. Med. Imaging **1057358**(March), 194 (2018).

Development and Evaluation of the Fourier Spectral Distortion Metric

Trevor Lewis Vent, *Graduate Student Member, IEEE*, Raymond Joseph Acciavatti, and Andrew D. A. Maidment, *Senior Member, IEEE*

***Abstract*— A spatial resolution metric is presented for tomosynthesis. The Fourier spectral distortion metric (FSD) was developed to evaluate specific resolution properties of different imaging techniques for digital tomosynthesis using a star pattern image to plot modulation in the frequency domain. The FSD samples the spatial resolution of a star-pattern image tangentially over an acute angle and for a range of spatial frequencies in a 2D image or 3D image reconstruction slice. The FSD graph portrays all frequencies present in a star pattern quadrant. In addition to the fundamental input frequency of the star pattern, the FSD graph shows spectral leakage, square wave harmonics, and residual noise. The contrast transfer function (CTF) is obtained using the FSD graph. The CTF is analogous to the modulation transfer function (MTF), but it is not normalized to unity at zero spatial frequency. Unlike the MTF, this metric separates the fundamental input-frequency from the other signals in the Fourier domain. This metric helps determine optimal image reconstruction parameters, the in-plane limit of spatial resolution with respect to aliased signals, and a threshold criterion for an image to support super resolution and reduce aliasing artifacts. Various sampling parameters were evaluated to optimize this metric and ascertain measurement accuracy. The FSD adequately compares resolution properties of 2D images and 3D image reconstruction slices for various x ray imaging modes without suppressing aliased signals.**

***Index Terms*— Aliasing, contrast transfer function, digital breast tomosynthesis, Fourier spectral distortion metric, modulation transfer function, spectral leakage, super resolution.**

I. Introduction

DIGITAL breast tomosynthesis (DBT) systems acquire multiple two-dimensional (2D) x-ray projections over a range of angles. The collected projections are used to reconstruct a three-dimensional (3D) image. Various DBT systems are available for screening mammography, and each system is constructed with different x-ray components and a distinct mechanical design and geometric configuration. These systems vary in terms of the number of projections and angular range. In-plane spatial-resolving capabilities of digital tomosynthesis systems are limited most commonly by the detector element spacing (d_{el}) or by the sampling aperture (λ) used for 3D image reconstruction. The variation in the mechanical design and acquisition techniques of these systems necessitates a spatial resolution metric that is specific to differences in tomosynthesis design and implementation.

The preferred method for evaluating spatial resolution of x-ray imaging devices is the pre-sampled modulation transfer function (MTF). The importance of measuring both the 3D MTF and the in-plane MTF for tomosynthesis was presented by Zhao *et al* [1]. IEC 62220-1 outlines a method to measure the MTF of x-ray systems using the slanted edge [2], and AAPM TG-245 proposes an alternative approach by using a tilted tungsten wire. Both of these methods suppress aliasing through super-sampling. We sought a resolution metric that would reveal evidence of aliasing.

The MTF has proven reliable for 2D imaging modalities such as conventional radiography and mammography, but the spatial resolution properties of tomosynthesis image reconstruction slices exhibit behavior atypical of 2D x-ray images. Spatial resolution is generally isotropic for 2D projection images and anisotropic for tomosynthesis reconstruction slices (Fig. 1). For tomosynthesis image reconstructions, the frequencies aligned parallel with x-ray source motion ($\sigma_{\parallel}$) are favored by super-resolution, whereas the frequencies aligned perpendicular to x-ray source motion ($\sigma_{\perp}$) are prone to aliasing (manifest as Moiré patterns in Fig. 1) [3]–[6]. The pre-sampled MTF will typically show modulation up to the sampling frequency and will be in close agreement for both frequency orientations (as shown in Fig. 14 of this work) [7]; ostensibly however, this behavior is not reflected in the tomosynthesis image reconstruction slice due to aliasing.

Although the spatial-resolving capabilities of digital x-ray detectors are limited by the aliasing frequency (ξ), the pre-sampled MTF measures modulation up to f_N for detectors that have an active area of 100%. ξ is given by one half of the first zero of the Fourier transform of the system's d_{el}. The Fourier transform of an aperture is a sinc function, where f_N is the first zero of the sinc function ($f_N = 1/d_{el}$) and the alias frequency relates to d_{el} by:

$$\xi(d_{el}) = \frac{0.5}{d_{el}} \tag{1}$$

Manuscript received October 30, 2020; revised December 10, 2020; accepted December 13, 2020. Date of publication December 16, 2020; date of current version March 2, 2021. This work was supported in part by the Department of Defense Breast Cancer Research Program under Grant W81XWH-18-1-0082, in part by the Burroughs Welcome Fund under Grant IRSA 1016451, in part by the National Institute of Health under Grant 1R01CA196528, and in part by Susan G. Komen under Grant IIR13264610. *(Corresponding author: Trevor L. Vent.)*

Trevor Lewis Vent is with the Department of Bioengineering, University of Pennsylvania, Philadelphia, PA 19104 USA (e-mail: tvent@seas.upenn.edu).

Raymond Joseph Acciavatti and Andrew D. A. Maidment are with the Department of Radiology, University of Pennsylvania, Philadelphia, PA 19104 USA (e-mail: racci@pennmedicine.upenn.edu; andrew.maidment@pennmedicine.upenn.edu).

Digital Object Identifier 10.1109/TMI.2020.3045325

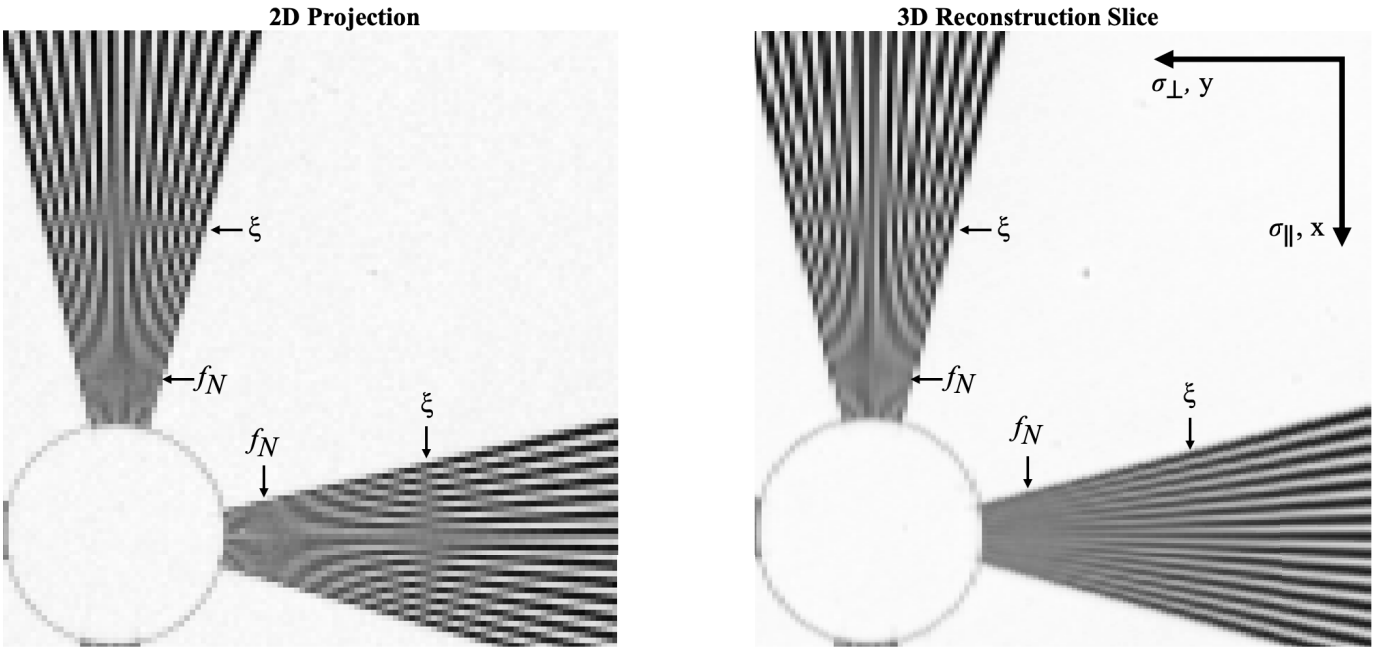

Fig. 1. The 2D projection image shows isotropic resolution and aliasing in both directions, whereas the 3D reconstruction slice shows anisotropic resolution with aliasing for $\sigma_\perp$ and super resolution for $\sigma_\parallel$.

Aliasing is predominant in 2D images for both frequency orientations, $\sigma_\parallel$ and $\sigma_\perp$, at any spatial frequency above ξ. It is important to consider the impact of aliasing on image quality to ensure that erroneous information for clinical readings is mitigated.

The prominence of aliasing in 3D image reconstructions is more nuanced, when compared with 2D images, and depends on sampling techniques, the orientation of the input object, and the acquisition geometry [8]. Two factors can give rise to aliasing in 3D image reconstructions; d_{el} and λ. The alias frequency of λ in 3D reconstruction slices can be determined by substituting λ for d_{el} in (1). In the Fourier domain, aliasing takes the form of *spectral leakage*, which is the misrepresentation of the input-frequency modulation at an incorrect, lower or higher response-frequency (the shaded regions in Fig. 2c). Aliasing dominates the input signal of these reconstructions because the magnitude of the spectral-leakage modulation is greater than the magnitude of the input-frequency modulation in the Fourier domain. A pre-sampled MTF calculation for any x-ray imaging device shows modulation for frequencies higher than ξ. This is evidence that super-resolution is achievable with proper sampling and reconstruction techniques [10]. However, the pre-sampled MTF will not show that the frequencies above ξ are dominated by aliasing.

In this work, we propose the Fourier spectral distortion metric (FSD) and the contrast transfer function (CTF) that evaluate spatial resolution for digital images without suppressing relevant information, such as aliasing. This metric can be applied to 2D digital images and 3D image reconstruction slices (for in-plane evaluation), where it is particularly useful for comparing differences in tomosynthesis acquisition. The FSD discerns aliasing by identifying signals of spectral leakage separate from fundamental input frequencies in the Fourier domain. Another goal of this study is to optimize the FSD for various sampling factors and imaging characteristics.

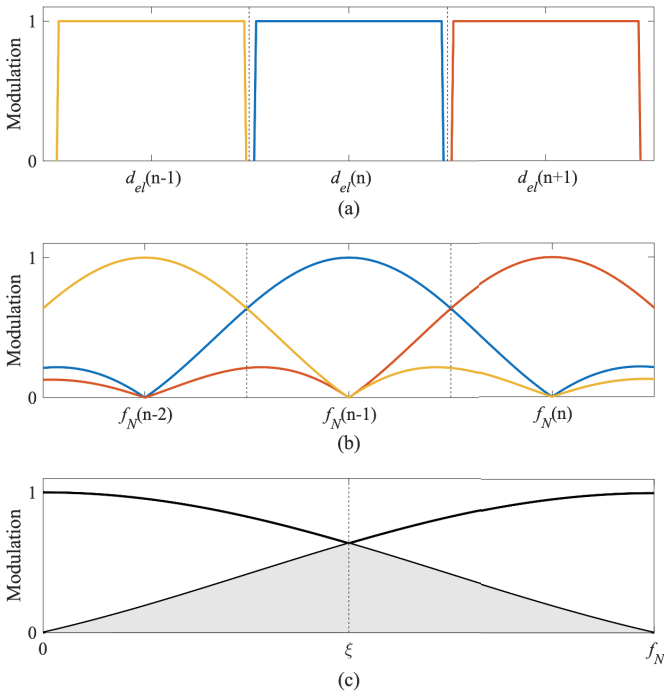

Fig. 2. A one-dimensional diagram of a digital detector aperture function for three detector aperture samples (a), the impulse responses of the three apertures (b), and an example of the aliased signals from d_{el}(n+1) reflected back into the impulse response function for half of one detector aperture, d_{el}(n) (c)

This metric is better suited to evaluating tomosynthesis image reconstructions by presenting data in a more useful format, capturing modulation contrast, and revealing aliased signals.

II. Materials & Method

A. Next Generation Tomosynthesis Prototype

The FSD was developed for characterizing our next generation tomosynthesis (NGT) prototype system. The NGT

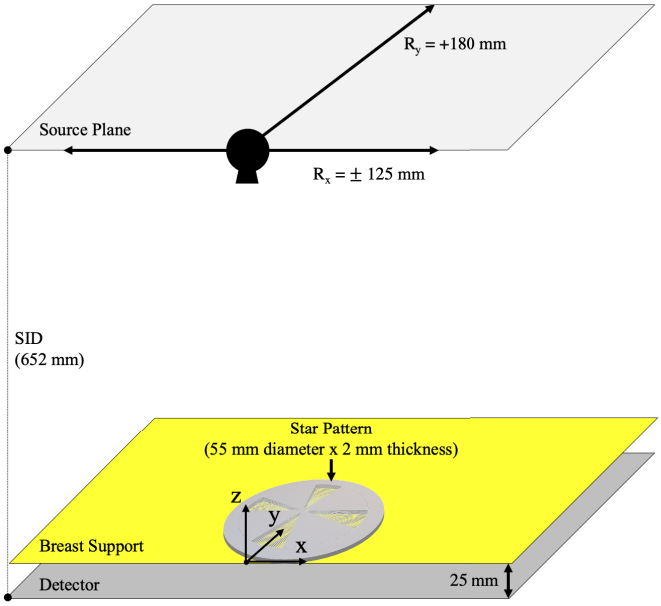

Fig. 3. The coordinate axes and the design geometry are defined for the NGT prototype. The Cartesian coordinate system defines the origin of the NGT system. It is located at the center of the of the detector along the chest-wall edge relative to the patient. The **x**-axis is parallel to the chest wall and is also parallel with $\sigma_{\|}$ for NGT-X.

system configuration is shown in Fig. 3. This prototype was developed to investigate novel acquisition geometries for DBT. Whereas a conventional DBT system scans linearly in one dimension, the NGT prototype positions the x-ray source at various locations within the source plane for a 3D acquisition, introducing x-ray source motion in the posteroanterior direction. This sampling technique enhances the sampled frequencies in the Fourier domain [8], [9]. The source-to-image distance (SID) for the NGT system is 652 mm. The range of motion for the x-ray tube is $\pm$125 mm in **x** (R_x) and $+$180 mm in **y** (R_y). Given these ranges, the NGT prototype is capable of investigating myriad acquisition geometries [10]. For this work, we use a DBT acquisition geometry with source motion in the x-direction only (NGT-X) to introduce this metric.

B. Star Pattern Test Object

To obtain the CTF, we use the frequencies contained in one quadrant of a star-pattern test object as the fundamental input frequency (ν). The star pattern consists of four quadrants of 29 alternating lead and acrylic sectors at 1° spacings. Thus, the angular range of each quadrant is 29° (model 07-542). The sharpness of the edge on the lead foil is a square-wave input similar to a bar-pattern test object. The Fourier transform of a square-wave of input frequency, ω, and period of the star pattern quadrant, L, is a series of sinusoidal waves:

$$\mathrm{F}(\omega) = \frac{4}{\pi}\sum_{m=1}^{\infty}\sin\left(\frac{2\pi(2m-1)\omega \mathrm{L}}{2m-1}\right) \tag{2}$$

The fundamental frequency ($m = 1$) is the dominant frequency in an image reconstruction without aliasing. The finite size of the focal spot and the detector blur the signal of the angle at which thehigh frequencies, producing a sinusoidal response function (Fig. 4). As predicted by Coltman [11],

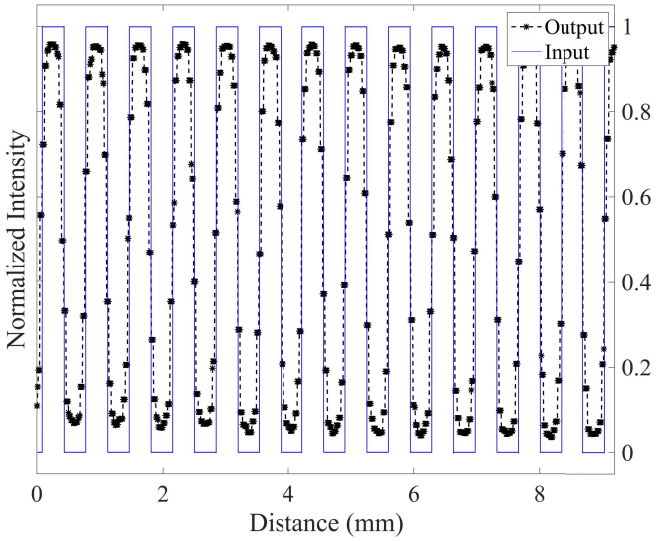

Fig. 4. The sine-wave response (Output) of the square wave (Input) at a resolution of 1.4 lp/mm in the image reconstruction of the star pattern [11].

square-wave harmonics are also present in image reconstructions at lower spatial frequencies of the star pattern.

C. Image Acquisition

Images of the star pattern were acquired on the NGT prototype using various techniques. We use the term, ϕ, to describe the angle of ν relative to the detector grid. The star pattern was positioned at the origin with a ϕ of 0° for all image acquisitions. NGT-X supports an angular range (15°) and projection-to-projection angular spacing (1°) that are similar to a commercial DBT system (Selenia Dimensions, Hologic, Marlborough, MA), but utilizes a step-and-shoot acquisition technique. Projection images from NGT-X were used in image reconstructions. NGT-X was repeated ten times by removing and repositioning the star pattern at the origin, with the same ϕ, between each acquisition. The central projection from each of the ten tomosynthesis acquisitions was used to obtain 2D data. Each projection image was acquired using 28 kV, 1.5 mAs, and 0.5 mm Aluminum filtration. The anode for this system is a tungsten alloy with a nominal focal spot size of 0.3 mm.

The projection images were reconstructed using commercial reconstruction software (Piccolo™; version 4.0.5; Real Time Tomography; Villanova, PA). This software can produce super-sampled reconstructed volumes with a λ of up to 10 times smaller than the detector aperture. The 3D images were reconstructed at 5 different λ values: 85.0 μm (1.0x), 56.7 μm (1.5x), 42.5 μm (2.0x), 37.0 μm (2.3x), and 28.3 μm (3.0x). The 3D images are reconstructed conventionally, with slices parallel to the **x**-**y** plane using simple back-projection. The exact depth of the reconstruction is arbitrary. Images were reconstructed with a slice spacing of 0.1 mm initially; but to achieve greater accuracy, we used 0.01 mm slice spacing compared with the 0.03 mm lead foil thickness of the star pattern. Either the slice of the in-focus star pattern (in-plane 3D) or individual projections (2D) are used as the 3D and 2D inputs to the FSD. A summary of the acquisitions and reconstruction techniques performed for this study is shown in Table I.

TABLE I
IMAGE ACQUISITION

Acquisition	Acquisition Geometry	Star Pattern Alignment (ϕ)	λ (μm)	Technique
a			85.0 (1.0x)	
b			56.7 (1.5x)	28 kV
c	NGT-X	0°	42.5 (2.0x)	1.5 mAs
d			37.0 (2.3x)	0.5 mm Al Filter
e			28.3 (3.0x)	

Images were obtained using the NGT prototype. The same technique was used for all acquisitions. The NGT-X acquisition geometry was repeated ten times and reconstructed at a λ of 42.5 μm for each acquisition to obtain average spectra. The ten 2D images were obtained from the central projection of each tomosynthesis acquisition.

D. Fourier Spectral Distortion Metric

The FSD is calculated using one quadrant of a star pattern image as an input to create a graph of modulation in the frequency domain. This graph is referred to as the Fourier spectral distortion (FSD) graph. The FSD graph is the normalized modulation of all frequencies contained within a quadrant of the star pattern.

The center of the star pattern is determined using an image of the star pattern. The center is calculated using the perpendicular bisectors of two secant lines created by choosing two intersections arbitrarily between the three points located along the profile of the outer circle of the star pattern image (Fig. 5), requiring user input. Then, starting at the radius (r) from the center of the star pattern to the inner ring ($r_{\min} \hat{=}$ 16 lp/mm), the plot profile, $\psi_r(\delta\omega)$, is extracted tangentially along an arc for the quadrant of interest. The quadrants are named by the angle in radians relative to the center (0, $\pi/2$, π, and $3\pi/2$).

The 1D fast Fourier transform (FFT) is computed for this profile. The 1D FFT of $\psi_r(\delta\omega)$ computes the modulation of each frequency – aliased or not – within the quadrant. The radius is then incremented by one pixel and the process is repeated to the outer ring of the star pattern ($r_{\max} \hat{=} 1.27$ lp/mm). An example of one FFT calculation at a radius of 8 lp/mm is shown in Fig. 6 for $\sigma_{\parallel}$ and $\sigma_{\perp}$.

The waveform of each quadrant is sampled using Fourier interpolation with four increments at each r: 512, 1024, 1536, and 2048. These four conditions and oversampling factors, $\Gamma(r)$, for the range of frequencies of the star pattern are summarized in Table II. The value of Γ is determined by the number of samples (N) over the number of pixels per $\psi_r(\delta\omega)$ at $r_{\min}$ and $r_{\max}$ and a 37 μm λ by (3).

$$\Gamma(r) = \frac{N}{\text{pixels}/\psi_r(\omega)} \tag{3}$$

The angle at which the star pattern input frequencies are oriented across the reconstruction grid varies from one edge of the quadrant to the other. When $\phi = 0$, the largest angle of orientation for the frequencies is approximately 15° relative to the reconstruction grid (Fig. 7). For comparison, the MTF should be computed using an edge that is aligned between 2-3° (relative to the detector grid) with an ROI of at least 10 cm to achieve sufficient sampling [12]–[14]. The tangential sampling of the star pattern samples various orientations across the detector grid. This is shown by the various different vertical positions of the star points in Fig. 4.

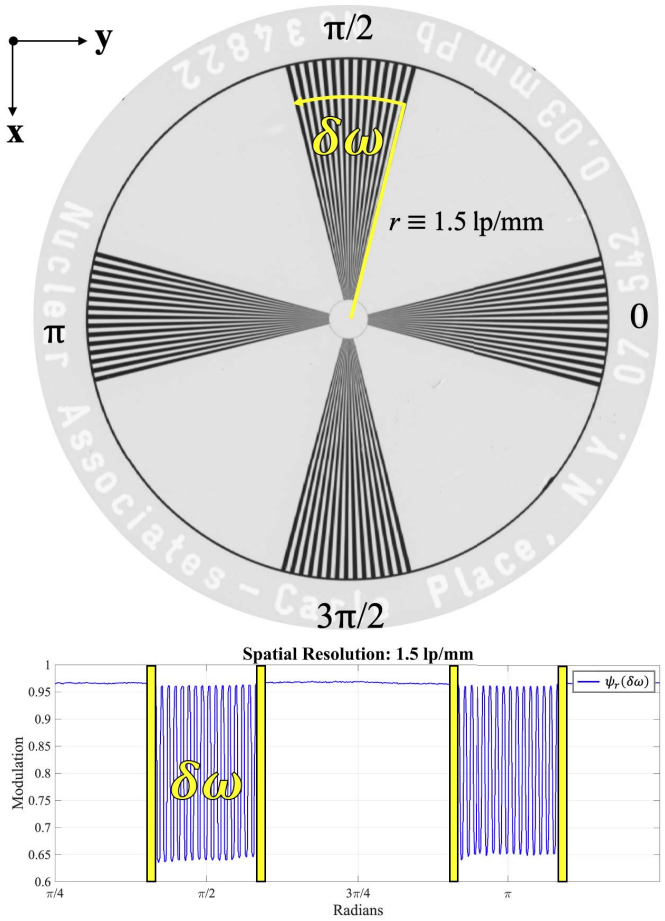

Fig. 5. The profile extraction of the 0-radian quadrant for f_y at a resolution of 1.5 lp/mm. $\delta\omega$ represents the range of the quadrant at all radii. The plot profile, $\psi_r(\delta\omega)$, is shown in blue and the quadrant is named by the angle of the unit circle in radians.

TABLE II
FSD SAMPLING FOR $\delta\omega$

Condition	SAMPLES (N)	Oversampling Factors, Γ(1.27 – 16 lp/mm)
A	512	1.6 – 22.3
B	1024	3.2 – 44.5
C	1536	4.8 – 89.0
D	2048	6.4 – 178.1

The four conditions of sampling used to determine optimal sampling rate for FSD calculations. The values of Γ correspond to a reconstructed pixel pitch of 37 μm. The oversampling factor increases with resolution, and the N is the same for each $\delta\omega$.

The maximum modulation of ν is normalized to the value of the pre-sampled MTF at 1.27 lp/mm. The 1D FFT profiles are plotted as a function of star pattern frequency (lp/mm) and normalized frequency response (cycles/$\delta\omega$) to create the FSD graph (Fig. 8). The most prominent spine in the graph is the signal of the input frequency, located at 15 cycles per quadrant (cycles/$\delta\omega$), corresponding to the period of the star

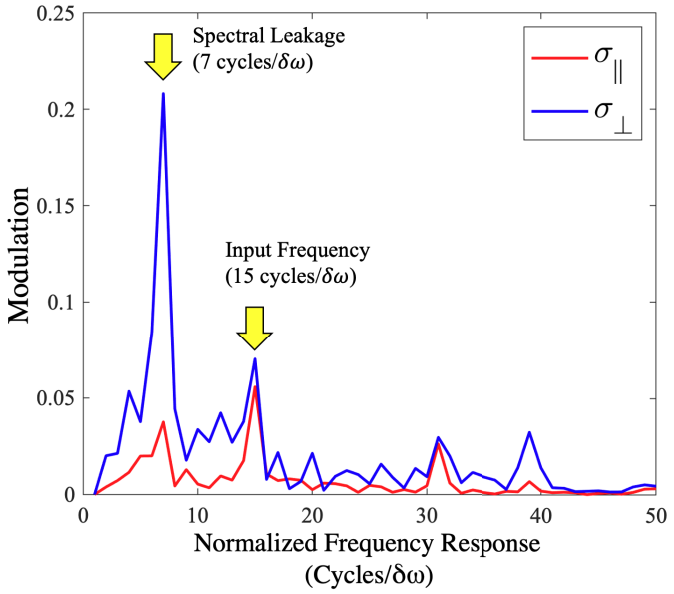

Fig. 6. Example of the 1D FFT at a radius which corresponds to a star pattern frequency of 8 lp/mm. The modulation of spectral leakage, occurring at a frequency response of 7 Cycles/$\delta\omega$, is well above that of the input frequency occurring at a frequency response of 15 Cycles/$\delta\omega$ for $\sigma_{\perp}$. This indicates aliasing at this star pattern frequency in the image. In contrast, the modulation of the input frequency for $\sigma_{\parallel}$ is greater than that of spectral leakage, demonstrating super resolution.

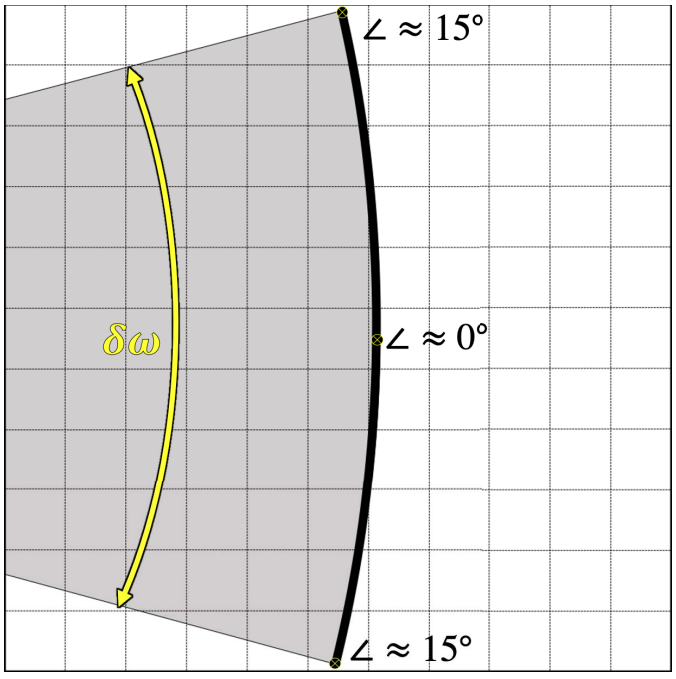

Fig. 7. Angular variation of the plot profile, with respect to the detector grid, over the range, $\delta\omega$.

pattern input (e.g. reference the plot profile in Fig. 5). This arises because the angular spacing is independent of radius, and, hence, input frequency. Spectral leakage that arises from the sampling aperture is also prominent at various other cycles, creating a spine of frequencies that intersects ν at ξ. Spectral leakage that arises from λ creates a spine that intersects ν at $1/\lambda$. When present with a greater magnitude than the input frequencies, aliased signals dominate the input signals

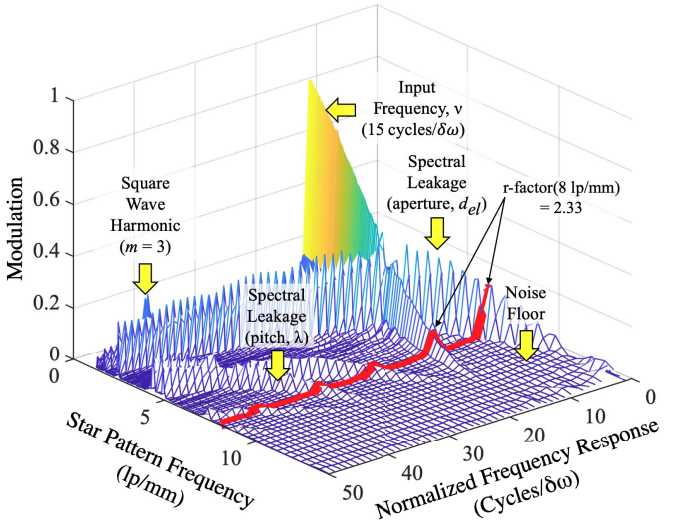

Fig. 8. An example of the FSD graph for $\sigma_{\perp}$ of a star pattern. The spine of ν occurs at a period of 15 Cycles/$\delta\omega$. This spine is the expected response signal from a single quadrant of the star pattern. The spine of spectral leakage intersects the fundamental frequency at a resolution of 5.88 lp/mm (ξ). The spine of the square wave harmonic for m = 3 occurs at 45 cycles/$\delta\omega$.

in image reconstructions. The least prominent spine in the plot occurs at 45 Cycles/$\delta\omega$ and represents the modulation for a square wave harmonic of the star pattern ($m = 3$). The input of the star pattern would produce an exact square wave response function if there were no intrinsic blurring of the system. The waveform is sinusoidal in the plot profile but maintains square-wave characteristics for resolutions lower than 2.5 lp/mm. This follows the findings of Coltman for the sine-wave response function given a square-wave input [11]. Image noise contributes to the rough texture observed in the other areas of the graph. The FSD graph produces a super-sampled Fourier transform of a quadrant in the star pattern. In contrast to the pre-sampled MTF, the FSD identifies aliasing as spectral leakage in digital x-ray images.

The r-factor described by Acciavatti [15] is used as the criterion for distinguishing super resolution from aliasing-dominated image reconstructions. It is important to note that the r-factor is typically computed for a sine-wave input. Although we start with a square-wave input, the FFT is performed, producing a sinewave decomposition of the frequencies in the image. This suggests that the r-factor can be determined using the frequency response computed by the FSD without performing the Coltman transform. If the peak of ν is greater than the value of the peak of spectral leakage at any resolution greater than ξ, the r-factor will be below a value of 1, indicating super resolution; otherwise, aliasing is predominant and super resolution is not achieved.

E. Contrast Transfer Function

The contrast transfer function (CTF) graph is the normalized modulation of ν, obtained from the FSD graph, as a function of resolution. The CTF corresponds to a square-wave response function calculated from the sine-wave response of the star pattern input [11]. The CTF can be used to discern the aliasing-dependent limit of spatial resolution (LSR) and is plotted against the pre-sampled MTF (Fig. 9).

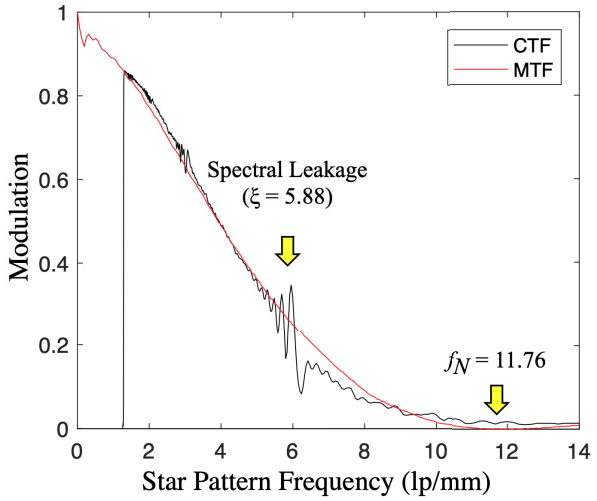

Fig. 9. The normalized modulation of the CTF and MTF are plotted as a function of spatial resolution. The distinction between the MTF and CTF is the characteristic oscillatory behavior of the CTF plot. These oscillations are a manifestation of spectral leakage.

The MTF calculation for this system was measured using the slanted edge method [8]. The slanted-edge method enforces a fixed phase shift of one line relative to another which suppresses spectral leakage through super-sampling and thus renders the MTF unable to discern aliasing. An example is the oscillatory behavior of the CTF graph in Fig. 9. The CTF is analogous to the MTF but is not normalized to unity at zero spatial frequency.

III. Results

A. Evaluation of Sampling Rate for FSD

The FSD is computed at the four different sampling rates using the $\pi/2$-radian quadrant (f_y) for one image reconstruction slice from acquisition **a**. The differences in the FSD graph are indiscernible via visual inspection; thus, only the two spectra that show the greatest absolute differences are used as examples ($N = 512$ and 2048) in Fig. 10a-b. Also presented in Fig. 10c is a graph that shows the differences between the two examples. The maximum absolute difference at any point of the conditions tested is 0.018 (shown in Fig. 10). The average absolute difference is 0.001 (for all conditions tested, not shown in Fig. 10) compared with the 0.0017 average measurement error (95% confidence, assuming normality) across the entire spectrogram.

B. 2D FSD for NGT System

The FSD was computed for the ten 2D projection images using the central projection obtained from acquisition **c**. The range of Γ at this pixel size (85 μm) is approximately 6.4-178.1. Fig. 11 shows a single sample of the FSD graph for the 0-radian quadrant (f_x) as an example. The average spectra of the ten 2D projection images is shown for f_x (Fig. 12a) and for f_y (Fig. 12b). The spectral leakage of d_{el} intersects ν at ξ, and λ intersects at the sampling rate of the detector.

C. Evaluation of Reconstruction Sampling Pitch for FSD

The FSD is computed using images that are obtained from the five λ values of NGT-X described in Table I using acquisitions **a**-**e**. The five FSD and CTF graphs are summarized

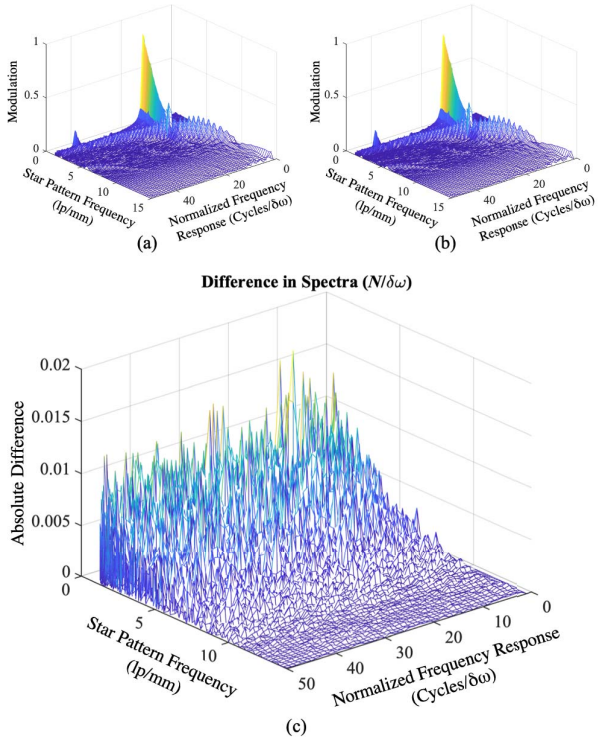

Fig. 10. Sampling rates: (a) 512, (b) 2048, and their difference (c) used to determine optimal sampling for the FSD.

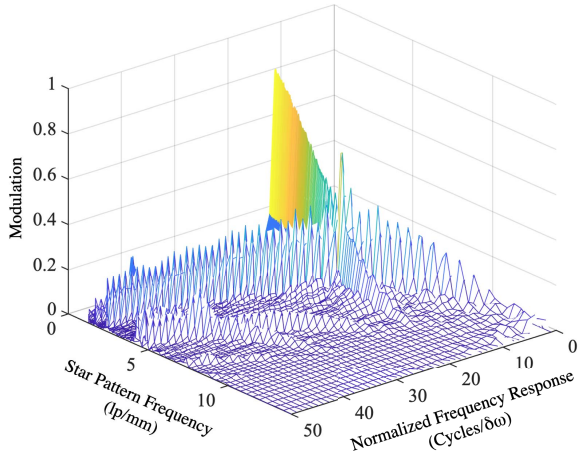

Fig. 11. FSD graph of a single 2D projection image.

in Fig. 13 for each respective λ. The spectral leakage due to λ intersects ν at the resolution corresponding to the $1/\lambda$ for each graph. Similarly, residual spectral leakage is seen at the resolution corresponding to d_{el}.

D. Comparing f_x With f_y for NGT-X

The results for NGT-X are represented in Fig. 14a and Fig. 14b for the 0- and $\pi/2$-radian quadrants of the star pattern, respectively. Images for NGT-X are obtained from acquisition **c**; these graphs represent the average of the ten spectra. The average spectra are less noisy than the individual spectra realizations above, and the details within the FSD and CTF graphs are accentuated. For Fig. 14 (a and b): top left is the FSD graph, top right is a plot of the CTF and corresponding pre-sampled MTF, and the bottom are cropped images of the

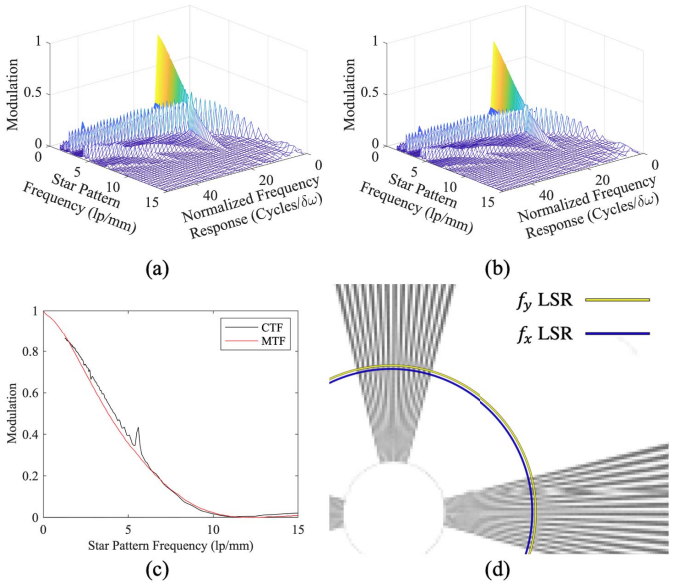

Fig. 12. The results for the average 2D spectra include the FSD graphs for f_y (a), f_x (b), the CTF graph for f_y (c), and the image indicating the LSR for f_y and f_x (d)

in-plane reconstructions for the quadrants being analyzed. The blue arcs in the images indicate the LSR, measured at 5% modulation in the presence of super resolution or near ξ if aliasing is predominant.

The 0-radian quadrant, f_x, of NGT-X shows evidence of super-resolution and residual aliasing artifacts. It is important to note that f_x is $\sigma_{\parallel}$ for NGT-X. The FSD graph (Fig. 14a, top left) shows the spine of ν, the spine of the square-wave harmonic, and spines of residual spectral leakage arising from ξ and d_{el}. The prominence of spectral leakage is diminished, and super-resolution is observed in the image reconstruction. The fundamental frequency is essentially the only frequency with significant modulation. As a result, the image reconstruction accurately portrays ν for modulation above ξ. The CTF (Fig. 14a, top right) is normalized at 1.27 lp/mm using the modulation of the MTF at the same star pattern frequency. Like the pre-sampled MTF, the CTF shows modulation up to the sampling frequency of the detector. The image in Fig. 14a shows the 0-radian quadrant of the reconstructed star pattern, and the blue line indicates the LSR measured at 5% modulation.

The $\pi/2$-radian quadrant contains f_y, which is $\sigma_{\perp}$ for NGT-X. The results for this orientation are represented in Fig. 14b. The FSD graph shows the same spines of ν and the square-wave harmonic as before; however, in contrast to f_x, spectral leakage is prominent for f_y. The spine of spectral leakage has higher modulation for frequencies above and below ξ (the intersection at ν). The CTF for f_y (Fig. 14b, top right) shows characteristic oscillatory behavior at the same location and is determined as the LSR, due to aliasing. The image for f_y shows Moiré patterns for frequencies above and below ξ. The oscillatory behavior in the CTF and the Moiré patterns in the image reconstructions repeat according to the detector's pixels (n), described by (4):

$$M(n) = \frac{\xi}{n} \tag{4}$$

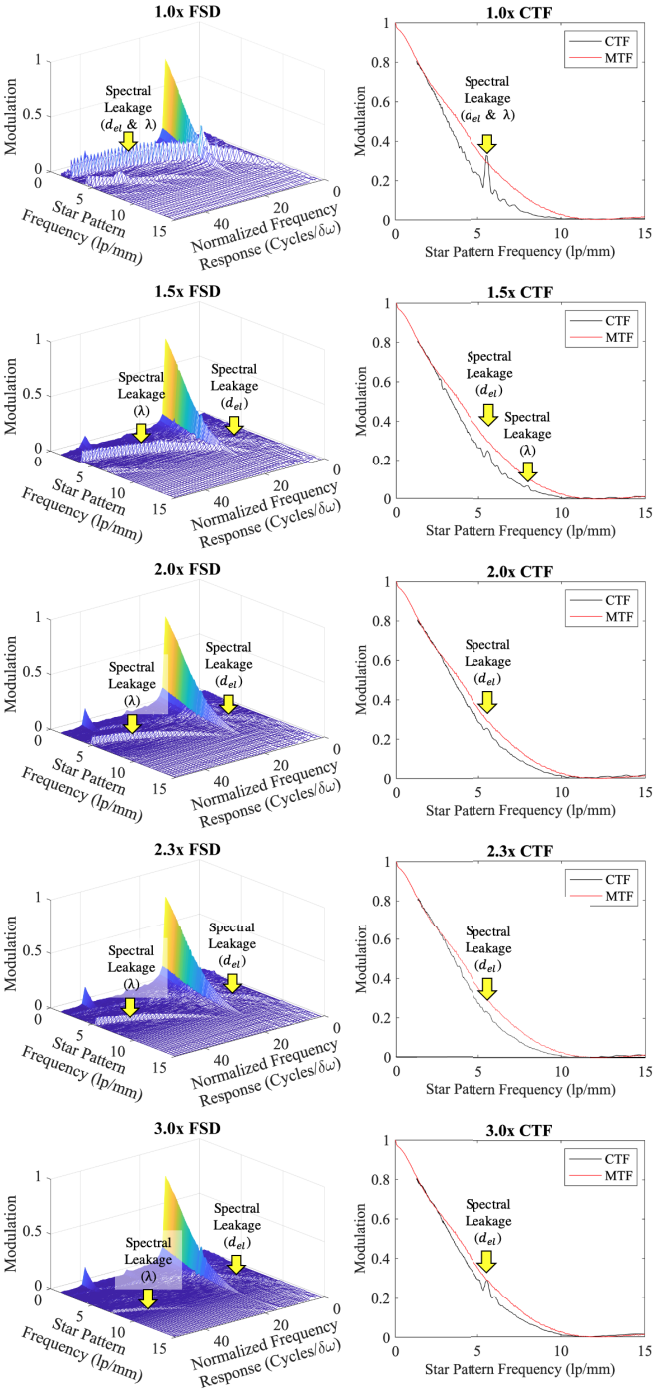

Fig. 13. Results for different reconstruction pitch values, λ. These graphs were created using f_x of NGT-X. The FSD (left column) and CTF vs. pre-sampled MTF (right column) graphs for the five λ values from Table I are shown. The two forms of spectral leakage, aperture (d_{el}) and pitch (λ) are indicated. Note that the aperture spectral leakage is only residual for f_x.

The repetition of the Moiré patterns and how they correspond to the FSD graph are depicted in Fig. 15 by viewing the FSD graph from an aerial perspective next to its corresponding quadrant in the image reconstruction. This figure portrays ν vertically from top to bottom. The spectral leakage appears as the diagonal ripples that intersect the fundamental frequency at three locations. This first occurs near 6 lp/mm, which is 1/2 cycles per pixel ($n = 1$). Residual peaks of spectral

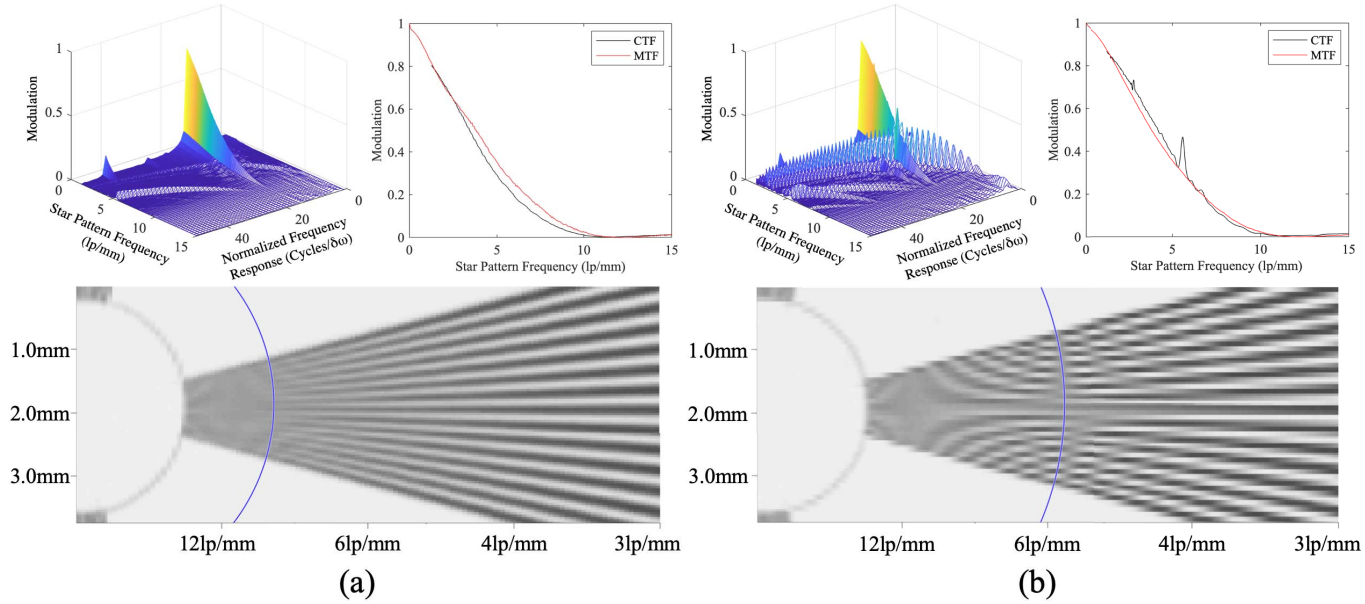

Fig. 14. Results for NGT-X f_x (a) and f_y (b) for the 0-radian and $\pi/2$-radian quadrants, respectively. The FSD graph (top left graph), CTF plot (top right graph), and image with the LSR (bottom image) are shown. The input frequency, ν, and square wave harmonic are the only dominant signals in (a). The LSR is evident in the CTF plot near 9 lp/mm where modulation is 5%. The FSD graph of (b) is similar to that of (a), but shows significant spectral leakage. The spectral leakage intersects ν at ξ in the FSD graph and the LSR is reduced to ξ.

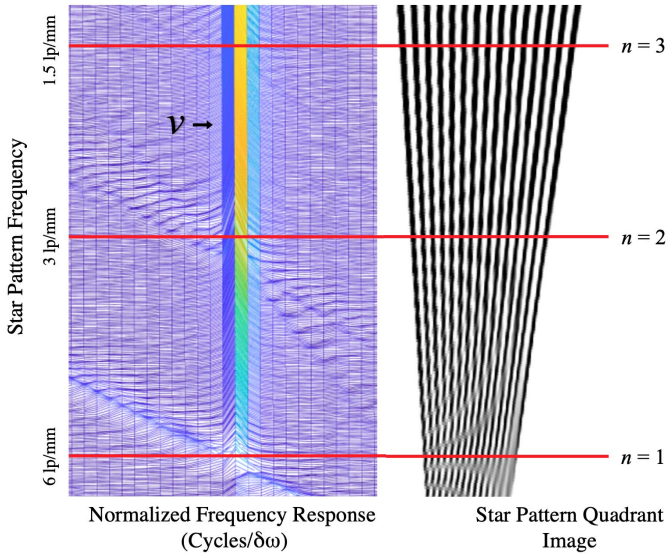

Fig. 15. Depiction of the FSD graph from an aerial perspective alongside the corresponding star pattern quadrant with repeating Moiré patterns. The integer value n corresponds to (4). The repeating oscillations are observed in Fig. 14b.

leakage then repeat at integer values of n: 3 lp/mm (1/4 cycles per pixel, $n = 2$) and at 1.5 lp/mm (1/6 cycles per pixel, $n = 3$).

IV. Discussion

By presenting the imaging system with spatially separated stimuli of various known spatial frequencies, the FSD is able to separate the frequency response into the fundamental frequency, harmonics, spectral leakage, and aliasing. By contrast, conventional measures of MTF confound these factors. For these reasons, it is particularly useful for tomosynthesis and other modalities supporting super resolution. Studies suggest that the FSD can also distinguish differences between tomosynthesis acquisition geometries [5], [6], [8], [16], which makes it a useful tool for evaluating the myriad acquisition geometries of the NGT prototype.

In this work, the FSD is demonstrated using one acquisition geometry of the NGT prototype. The FSD graphs show full visualization of the spectral leakage, which can change significantly with even minor changes in acquisition geometry. The CTF graphs do show evidence of spectral leakage, but not spectral leakage itself. The FSD graphs show *all* frequency responses (including spectral leakage) for every input frequency, whereas the CTF graphs show the response at the specific period of the fundamental input frequency only. Furthermore, the r-factor which is the criterion for determining super resolution, cannot be computed using the CTF alone. Optimization of tomosynthesis acquisition geometries and other factors requires a full account of all the response signals of the star pattern input, suggesting a preference for visualizing FSD graphs over CTF graphs.

The results suggest this method can motivate the design of novel test objects with different resolution properties to separate the response frequencies from fundamental input frequencies. The FSD evaluates the in-plane spatial resolution of a DBT image reconstruction in the conventional reconstruction plane successfully. Similar to the tilted tungsten wire for MTF calculations, the star pattern can be oriented arbitrarily to evaluate spatial resolution for any frequency orientation – including frequencies aligned in the z-axis – to evaluate multiplanar image reconstruction slices for f_z [4].

The sample size (N) used in the FSD calculation is sufficient for the images that we analyzed. If λ were to increase, it is possible that N would also need to increase to achieve sufficient oversampling. For example, in Fig. 10, the absolute difference between conditions A and D decreases

as the resolution increases. Condition A is below f_N at the lowest resolution of the star pattern. The absolute difference between any of the conditions with Γ values above 2.0 has no measurable error. This supports the notion that the FSD should not be computed at any Γ below f_N.

Averaging the spectra of individual 2D projections improves the visualization of the spectral features (spectral leakage, square-wave harmonics, etc.). Aliasing is evident in the form of spectral leakage that arises from the detector aperture, and the spectral leakage that arises from the sampling pitch intersects the fundamental input frequency at the sampling rate of the detector, as expected. The aperture spectral leakage is greater for f_y than for f_x. This difference may arise if the focal spot is non-isometric or when the measurement is not proximal to the central ray of the x-ray beam.

The various reconstruction sizes provide insight into proper sampling techniques for tomosynthesis image reconstructions. To achieve super-resolution, $1/\lambda$ needs to be equal to or greater than f_N. A λ of 37μm appears to have the least prominent residual spectral leakage in Fig. 13. This suggests it is advantageous to sample a tomosynthesis reconstruction at a λ that is not an integer multiple of d_{el}, such as 42.5 μm (2.0x) or 28.3μm (3.0x). While we have experimental evidence strictly for our planar-source system, we have seen similar results using a rotational-source system. We posit that the benefit of incorporating non-integer multiples of d_{el} for the reconstruction pitch has more to do with the detector aperture than differences in acquisition geometry (e.g. planar x-ray source sampling vs. rotational x-ray source sampling).

For an NGT-X reconstruction, aliasing is present and manifested as Moiré patterns for f_x and f_y in digital images if $1/\lambda$ is below f_N for the given d_{el}, regardless of the object orientation or acquisition geometry. However, if we consider a conventional DBT acquisition geometry where $1/\lambda$ is at or above f_N for an image reconstruction, aliasing is only present for $\sigma_\perp$.

These results represent a specific image reconstruction method that supports computed super resolution; however, the FSD is agnostic to reconstruction technique. This study focuses on a simple back projection technique to evaluate the underlying physics of conventional tomosynthesis without complicating the analysis with various parameters such as non-linear reconstruction methods or image processing. The FSD has the potential to provide a means of comparing different reconstruction and image processing methods, especially for analyzing spectral leakage and aliasing.

Although the initial application for developing this metric is tomosynthesis, the FSD can be extended to other x-ray imaging modalities and optical imaging devices that utilize digital detectors. Furthermore, it has the potential to be used to evaluate digital monitors. We have already applied the metric to evaluate spatial resolution in the presence of spectral leakage for various systems and a variety of star pattern images, including: virtual clinical trials of a simulated star pattern [16], [17], proton and electron radiation therapy beams on direct conversion detectors [18], and a specimen tomosynthesis system [19] (Mozart 3D, Kubtec, Milford, CT).

V. Conclusion

In this work, we demonstrate the FSD using two frequency orientations for a 2D image and a 3D image reconstruction slice. The FSD successfully compares resolution properties of all conditions. It separates the frequencies of spectral leakage (arising from d_{el} and λ) from fundamental input frequencies in 2D images and 3D image reconstructions. The FSD produces the CTF of an in-plane image reconstruction without suppressing spectral leakage through super-sampling. The FSD is a more detailed representation of in-plane resolution properties and imaging artifacts for tomosynthesis than the corresponding pre-sampled MTF. The conceptual change in viewpoint, from a single spectrogram in which the contributions of multiple input frequencies are superimposed, to a 2D spectrogram, in which the detailed response of each input frequency is separated provides additional details of imaging performance: aliasing, square-wave response, and limiting spatial resolution. We have already begun to use the FSD to evaluate resolution properties for all acquisition geometries of our NGT prototype. The tools and instructions for this metric were created using MATLAB and are available online at: https://github.com/trevorvent/FSD.

Acknowledgment

The authors would like to thank Johnny Kuo, Susan Ng, and Peter Ringer of Real Time Tomography for technical assistance with Piccolo. Andrew D. A. Maidment is a shareholder of Real Time Tomography and is a member of the scientific advisory board.

In addition, equipment support was provided by Analogic Inc., Barco NV, and Real Time Tomography. The content is solely the responsibility of the authors and does not necessarily represent the official views of the funding agencies.

References

[1] B. Zhao, J. Zhou, Y.-H. Hu, T. Mertelmeier, J. Ludwig, and W. Zhao, "Experimental validation of a three-dimensional linear system model for breast tomosynthesis," *Med. Phys.*, vol. 36, no. 1, pp. 240–251, 2009.

[2] *Medical Electrical Equipment—Characteristics of Digital X-ray Imaging Devices—Part 1–2: Determination of the Detective Quantum Efficiency—Detectors Used in Mammography*, Standard IEC 62220-1-2:2007, IEC. Accessed: Feb. 12, 2019. [Online]. Available: https://webstore.iec.ch/publication/6598

[3] R. J. Acciavatti and A. D. A. Maidment, "Observation of super-resolution in digital breast tomosynthesis," *Med. Phys.*, vol. 39, no. 12, pp. 7518–7539, Nov. 2012.

[4] T. L. Vent, R. J. Acciavatti, Y. J. Kwon, and A. D. A. Maidment, "Quantification of resolution in multiplanar reconstructions for digital breast tomosynthesis," *Proc. SPIE*, vol. 9783, Mar. 2016, Art. no. 978303.

[5] C. J. Choi, T. L. Vent, A. D. A. Maidment, and R. J. Acciavatti, "Geometric calibration for a next-generation digital breast tomosynthesis system using virtual line segments," *Proc. SPIE*, vol. 10573, Mar. 2018, Art. no. 105730D.

[6] T. D. Maidment, T. L. Vent, W. S. Ferris, D. E. Wurtele, R. J. Acciavatti, and A. D. A. Maidment, "Comparing the imaging performance of computed super resolution and magnification tomosynthesis," *Proc. SPIE*, vol. 10132, Mar. 2017, Art. no. 1013222.

[7] A. Kuhls-Gilcrist, A. Jain, D. R. Bednarek, K. R. Hoffmann, and S. Rudin, "Accurate MTF measurement in digital radiography using noise response," *Med. Phys.*, vol. 37, no. 2, pp. 724–735, Jan. 2010.

[8] R. J. Acciavatti and A. D. A. Maidment, "Oblique reconstructions in tomosynthesis. II. Super-resolution," *Med. Phys.*, vol. 40, no. 11, pp. 1–19, 2013.

[9] T. L. Vent, B. L. Lepore, and A. D. A. Maidment, "Evaluating the imaging performance of a next-generation digital breast tomosynthesis prototype," *Proc. SPIE*, vol. 10948, Mar. 2019, Art. no. 109480K.

[10] R. J. Acciavatti *et al.*, "Analysis of volume overestimation artifacts in the breast outline segmentation in tomosynthesis," *Proc. SPIE*, vol. 10573, Mar. 2018, Art. no. 1057359.

[11] R. J. Acciavatti, B. Barufaldi, T. L. Vent, E. P. Wileyto, and A. D. A. Maidment, "Personalization of X-ray tube motion in digital breast tomosynthesis using virtual defrise phantoms," *Proc. SPIE*, vol. 10948, Mar. 2019, Art. no. 109480B.

[12] J. W. Coltman, "The specification of imaging properties by response to a sine wave input," *J. Opt. Soc. Amer.*, vol. 44, no. 6, p. 468, Jun. 1954.

[13] E. Samei, M. J. Flynn, and D. A. Reimann, "A method for measuring the presampled MTF of digital radiographic systems using an edge test device," *Med. Phys.*, vol. 25, no. 1, pp. 102–113, Jan. 1998.

[14] H. Fujita, K. Ueda, J. Morishita, T. Fujikawa, A. Ohtsuka, and T. Sai, "Basic imaging properties of a computed radiographic system with photostimulable phosphors," *Med. Phys.*, vol. 16, no. 1, pp. 52–59, Jan. 1989.

[15] S. N. Friedman and I. A. Cunningham, "Normalization of the modulation transfer function: The open-field approach," *Med. Phys.*, vol. 35, no. 10, pp. 4443–4449, Sep. 2008.

[16] T. L. Vent, B. Barufaldi, R. J. Acciavatti, and A. Maidment, "Simulation of high-resolution test objects using non-isocentric acquisition geometries in next-generation digital tomosynthesis," *Proc. SPIE*, vol. 11513, May 2020, Art. no. 1151317.

[17] T. L. Vent, B. Barufaldi, and A. D. A. Maidment, "Simulation and experimental validation of high-resolution test objects for evaluating a next-generation digital breast tomosynthesis prototype," *Proc. SPIE*, vol. 10948, Mar. 2019, Art. no. 109480M.

[18] D. L. Lee *et al.*, "Novel direct conversion imaging detector without selenium or semiconductor conversion layer," *Proc. SPIE*, vol. 10948, Mar. 2019, Art. no. 1094818.

[19] N. Partain *et al.*, "Differences in re-excision rates for breast-conserving surgery using intraoperative 2D versus 3D tomosynthesis specimen radiograph," *Ann. Surgical Oncol.*, vol. 27, no. 12, pp. 4767–4776, Nov. 2020.

Radiation Protection Dosimetry (2021), Vol. 195, No. 3–4, pp. 363–371
Advance Access publication 18 June 2021
https://doi.org/10.1093/rpd/ncab080

VIRTUAL CLINICAL TRIALS IN MEDICAL IMAGING SYSTEM EVALUATION AND OPTIMISATION

Bruno Barufaldi[1], Andrew D. A. Maidment[1], Magnus Dustler[2], Rebecca Axelsson[2], Hanna Tomic[2], Sophia Zackrisson[2], Anders Tingberg[2] and Predrag R. Bakic[1,2,*]
[1]Department of Radiology, University of Pennsylvania, 3400 Spruce Str., Philadelphia, PA 19104, USA
[2]Department of Translational Medicine, Lund University, Skane University Hospital, Carl-Bertil Laurells gata 9, Malmö 20502, Sweden

*Corresponding author: predrag.bakic@pennmedicine.upenn.edu

Received 31 October 2020; revised 14 April 2021; editorial decision 21 April 2021; accepted 21 April 2021

Virtual clinical trials (VCTs) can be used to evaluate and optimise medical imaging systems. VCTs are based on computer simulations of human anatomy, imaging modalities and image interpretation. OpenVCT is an open-source framework for conducting VCTs of medical imaging, with a particular focus on breast imaging. The aim of this paper was to evaluate the OpenVCT framework in two tasks involving digital breast tomosynthesis (DBT). First, VCTs were used to perform a detailed comparison of virtual and clinical reading studies for the detection of lesions in digital mammography and DBT. Then, the framework was expanded to include mechanical imaging (MI) and was used to optimise the novel combination of simultaneous DBT and MI. The first experiments showed close agreement between the clinical and the virtual study, confirming that VCTs can predict changes in performance of DBT accurately. Work in simultaneous DBT and MI system has demonstrated that the system can be optimised in terms of the DBT image quality. We are currently working to expand the OpenVCT software to simulate MI acquisition more accurately and to include models of tumour growth. Based on our experience to date, we envision a future in which VCTs have an important role in medical imaging, including support for more imaging modalities, use with rare diseases and a role in training and testing artificial intelligence (AI) systems.

INTRODUCTION

Virtual Clinical Trials (VCTs) in medical imaging have been used to design, evaluate and optimise imaging systems, to prototype clinical trials and for regulatory approval. VCTs are used as a rapid and cost-effective alternative to conducting some clinical trials, allowing researchers to answer fundamental questions using *in silico* simulations.

Researchers at the University of Pennsylvania (UPenn) developed a VCT framework that encompasses the use of computer models of human anatomy, imaging modalities and image interpretation[1]. In 1998, an anthropomorphic breast model was developed to support simulations of breast imaging[2, 3], and by 2009, a software framework to design and optimise breast imaging systems using VCTs was completed[4–10]. Numerous academic laboratories[11, 12], industrial developers[13, 14] and governmental regulatory bodies[15] have since adopted VCTs. Several VCT use-cases have been published, including the evaluation and optimisation of digital breast tomosynthesis (DBT)[16–22], breast and lung computed tomography (CT)[23–25], denoising of breast X-ray images[26, 27] and dermatology imaging[28, 29].

Today, VCTs are accepted as an efficient pre-clinical optimisation tool. Based on our experience in designing and conducting VCTs, in this paper, we review VCT principles and major simulation components. The benefits and challenges of VCTs are illustrated through our new results in the assessment of lesion detection in breast imaging and the review of our recently published design and optimisation of simultaneous DBT and mechanical imaging (MI) of the breast. (The breast lesion detection results presented here have been significantly expanded from our preliminary published report[16]).

OPENVCT SIMULATION FRAMEWORK

The OpenVCT framework[30] has been used to generate anthropomorphic breast models and simulate breast positioning, mammographic compression, X-ray image acquisition and human interpretation. The breast anatomy is simulated using an octree-based recursive partitioning algorithm[5], where random seeds are used to direct the simulation of glandular and adipose compartments bounded by fibrous Cooper's ligaments. The mammographic compression uses finite element (FE) software, which deforms the breast models in accordance with clinical breast views[31]. The image acquisition is simulated by a ray-tracing algorithm[30].

Human readings are simulated using the MeVIC software[32] (Barco Healthcare), which is integrated into the OpenVCT framework. The MeVIC software

is designed to simulate a high-resolution medical display, then process and analyse the displayed images based upon a Channelized Hotelling Observer (CHO) model[33]. The display simulation includes details of the video card and monitor, including the greyscale lookup table and luminance characteristics, temporal characteristics, modulation transfer function, noise and angular dependence[34, 35]. The CHOs can be trained and tested repeatedly to simulate human readers and that can be used to estimate multiple-reader multiple-case (MRMC) ROC statistics[36].

The execution of every simulation step and the data synchronisation between the simulation steps and between the OpenVCT and MeVIC software occur via a configurable XML schema and are recorded as a multipart compressed file (VCTx). The VCTx files contain the prescribed XML files and the input and output binary documents. The format was designed to optimise data exchange and storage for VCTs[30].

STUDY I: VCTS FOR SYSTEM EVALUATION

Methodology

Together, the OpenVCT and MeVIC software were used to evaluate lesion detectability in DM and DBT. Our preliminary results were published in 2018[16]. This study compared simulation results with published clinical data from two 2013 studies by Rafferty *et al*.[37]. A commercial DM and DBT system was simulated. Masses were simulated with an ellipsoidal shape, diameter of 7 mm and thickness of 0.5–2 mm. Single microcalcifications were simulated as containing 1–4 voxels of size $(100\ \mu m)^3$. Detection of lesions was simulated using CHOs. Performance of the machine observers was assessed by the MRMC ROC analysis. The VCTs were calibrated by selecting a set of simulated lesions to match the clinical lesion detectability with DM images. The lesions were varied in terms of size and attenuation.

Our study presented here expanded the previous analysis by detailed selection of simulated lesions to achieve close matching of the VCT with clinical DM results. Performance of the machine observers was assessed in detail by the MRMC ROC analysis. For each of the two clinical studies[37], an admixture of simulated lesions was used to match the clinical performance to DM only in terms of the shape and area under the ROC curve (AUC). The same sets of simulated lesions were then used to generate synthetic DBT images, and the simulated detectability was compared with the clinical DBT data.

Results and discussion

Examples of synthetic breast images with simulated microcalcifications and masses are shown in Figures 1 and 2. In this study of lesion detectability, close agreement between the virtual and clinical estimates of detectability (Figure 3) is observed. The AUCs, estimated from the VCTs and the published reader study, are tabulated for the detection of microcalcifications (Table 1) and masses (Table 2). Tables 1 and 2 also include the AUC differences and their corresponding *p*-values and 95% confidence intervals (CIs). The difference between the AUC values from VCTs and the published work was less than 4%, demonstrating the ability of VCTs to predict human reader performance.

The use of VCTs in this task had specific advantages. Using the OpenVCT framework, the computational effort to replicate the reader study as a VCT took less than 4 d on a single GPU card (P5000, NVidia Corp, Santa Clara, CA). By comparison, the original study took significantly more time and was much costlier. However, as noted in Figure 3, differences still exist between the shape of the ROC curves of the VCT and clinical trials, demonstrating a challenge for VCTs. We are currently working to fine-tune the virtual population and virtual lesions to better match the shape of the ROC curves from the VCTs and the clinical data.

STUDY II: VCTS FOR SYSTEM OPTIMISATION

Methodology

Currently, we are investigating methods to extend the use of VCTs to multimodality imaging, specifically to design, evaluate and optimise the prototype of a simultaneous DBT and MI system (DBTMI)[38, 39]. Combining the radiographic DBT characterisation of anatomy with the functional measurement of local tissue stiffness using MI is expected to increase cancer detection and reduce the rate of false positives, improving the specificity of cancer detection[38, 39].

To explore the relationship between sensitivity and specificity of the two constituent modalities (DBT and MI), together with their combined performance, we expanded the OpenVCT framework to include simulations of the MI. MI acquisition is simulated with the FE models of the breast tissue and mammographic compression[40]. A preliminary study[40] used linear elastic material models of the breast tissue, a spherical tumour approximation and tumour stiffness of 15–50 times the stiffness of the simulated breast tissue. The open source software, FEBio[41], was used to calculate the stress on the surface of the compressed breast and to simulate the response of the MI sensor (BRE 5350-2, Tekscan, Boston, MA). The simulated response was compared with the clinical values[42, 43]. A detailed description of the MI simulation and preliminary evaluation was presented at the 2021 SPIE Medical Imaging conference paper by Axelsson *et al*.[40].

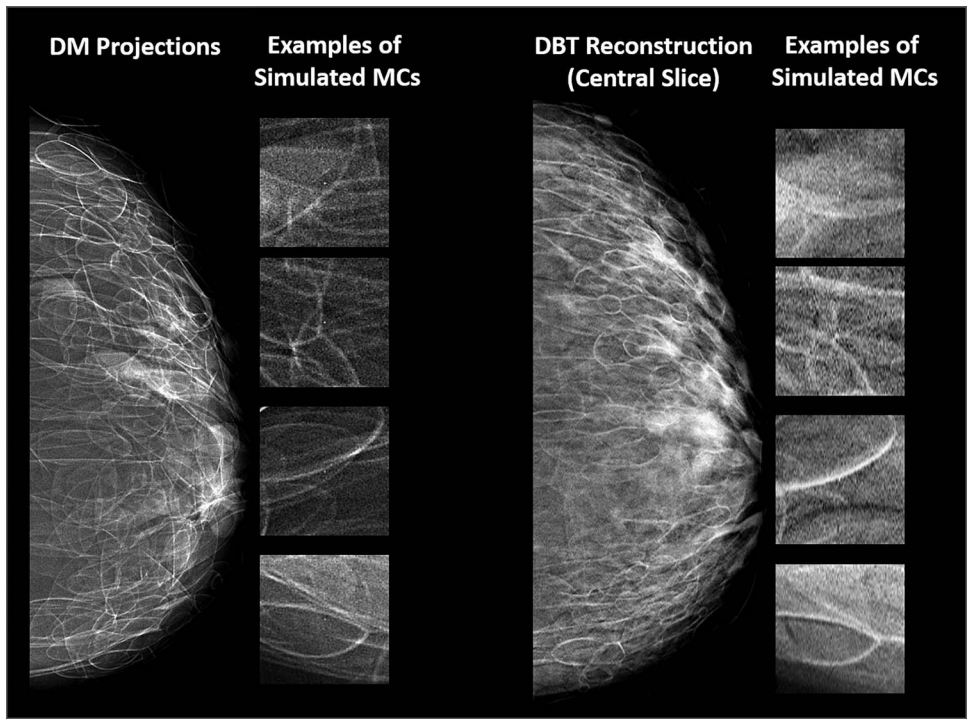

Figure 1. examples of synthetic breast images with simulated microcalcifications, generated using OpenVCT software.

A model of tumour growth is also under development to evaluate DBTMI. Modelling tumour growth can identify optimal screening intervals, aimed at reducing interval cancers. To model tumour growth, we simulated two screening exams of the same breast at the time of the cancer detection and at the prior screening round either 18 or 24 months earlier (following the protocol from the Swedish Screening Programme[44]).

The OpenVCT framework was used to simulate 30 breasts, with one spherical tumour in each breast[45]. Tumour growth was modelled by increasing the tumour volume exponentially over time according to the tumour volume doubling time (TVDT)[46, 47]. The woman's age, tumour diameter at the time of cancer detection and TVDT value were selected from the clinical data[46]. A radiologist manually indicated tumour diameters on the simulated mammograms. The diameters of the same lesions at the two time points were used to calculate the estimated TVDT. The growth model was evaluated by comparing TDVTs from the simulated mammograms with the clinical data. The growth model and its evaluation in an observer study were described by Tomic *et al*.[45].

Results and discussion

Figure 4 shows two stress surface maps obtained using the FE model for a virtual breast with spherical lesions of different sizes. The average stress over the virtual breast surface (6.2 ± 0.1 kPa) is in agreement with the average stress measured clinically[42] (5.6 ± 2.0 kPa). The average stress at the simulated tumour (10.8 ± 6.4 kPa) is higher than the clinically reported values[43] (6.8 ± 5.3 kPa). The simulation is affected by the tissue model. To improve the agreement, we are currently investigating the use of hyperelastic tissue models.

Figure 5 shows screening mammograms simulated 24 months apart, assuming a spherical lesion model with a TVDT of 374 d. The tumour sizes in the current and prior simulated mammograms were 11. and 7.2 mm, respectively. The sizes measured by the radiologist were 12.2 and 7.6 mm, respectively, corresponding to a TVDT of 356 d (18 d or 4.8% lower than the ground truth). Analysing all 30 simulated breasts, no significant difference was seen between the estimated and ground-truth TVDTs, with a median difference of 12 d (4%) ($p > 0.5$ using the Kolmogorov–Smirnov test)[45].

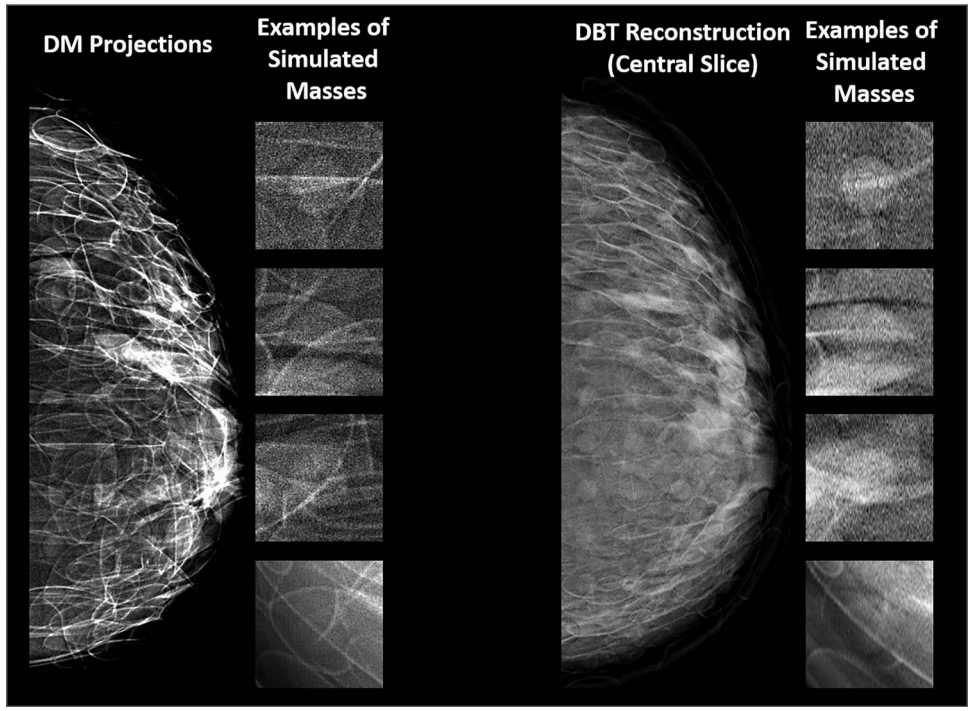

Figure 2. examples of synthetic breast images with simulated masses, generated using OpenVCT software.

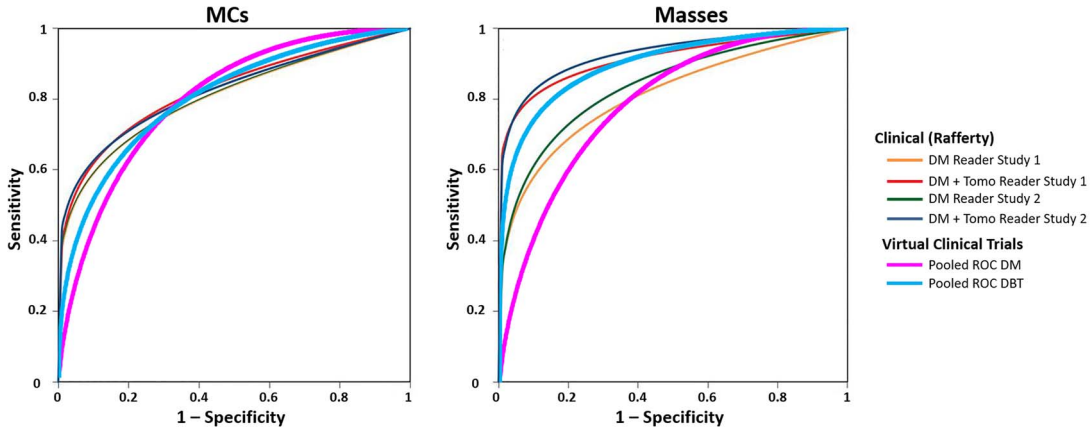

Figure 3. ROC curves of clinical and virtual lesion detectability in DM and DBT, fitted properly for the MRMC analysis using the ROC + KIT software (University of Chicago).

The limitations of the growth model include the spherical tumour shape and the lack of changes in the background breast tissue between the two simulated screening exams. To overcome these limitations, we are currently developing a model for irregularly shaped tumours. In addition, the temporal changes in the normal breast tissue will be simulated using an analysis of clinical images over multiple screening rounds.

CONCLUSIONS

Today, VCTs of medical imaging are sufficiently mature to play an important role in the design

Table 1. Result of the ROC analysis for detection of breast microcalcifications using DM and DBT, from virtual and clinical data. Listed are the AUC values estimated from synthetic breast images generated using OpenVCT, the AUC values from two clinical studies performed by Dr. Rafferty (denoted 1 and 2), the AUC differences and the corresponding *p*-values and 95% CIs.

Microcalcifications	AUC_{DM}	AUC_{DBT}	ΔAUC_{DBT-DM}	*p*	95% CI
VCT	0.802 ± 0.023	0.799 ± 0.026	−0.003	0.856	[−0.040, 0.034]
Clinical[37]					
1	0.804	0.840	0.036	0.073	[−0.004, 0.074]
2	0.817	0.831	0.014	0.082	[−0.002, 0.029]
AUC difference VCT versus clinical					
1	−0.002	−0.041			
2	−0.015	−0.032			

Table 2. Result of the ROC analysis for detection of breast masses using DM and DBT, from virtual and clinical data. Listed are the AUC values estimated from synthetic breast images generated using OpenVCT, the AUC values from two clinical studies performed by Dr. Rafferty's (denoted 1 and 2), the AUC differences and the corresponding *p*-values and 95% CIs.

Masses	AUC_{DM}	AUC_{DBT}	ΔAUC_{DBT-DM}	*p*	95% CI
VCT	0.794 ± 0.022	0.900 ± 0.017	0.106	<0.001	[0.089, 0.124]
Clinical[37]					
1	0.807	0.912	0.105	<0.001	[0.047, 0161]
2	0.842	0.930	0.088	<0.001	[0.051, 0.125]
AUC difference VCT versus clinical					
1	−0.013	−0.012			
2	−0.048	−0.03			

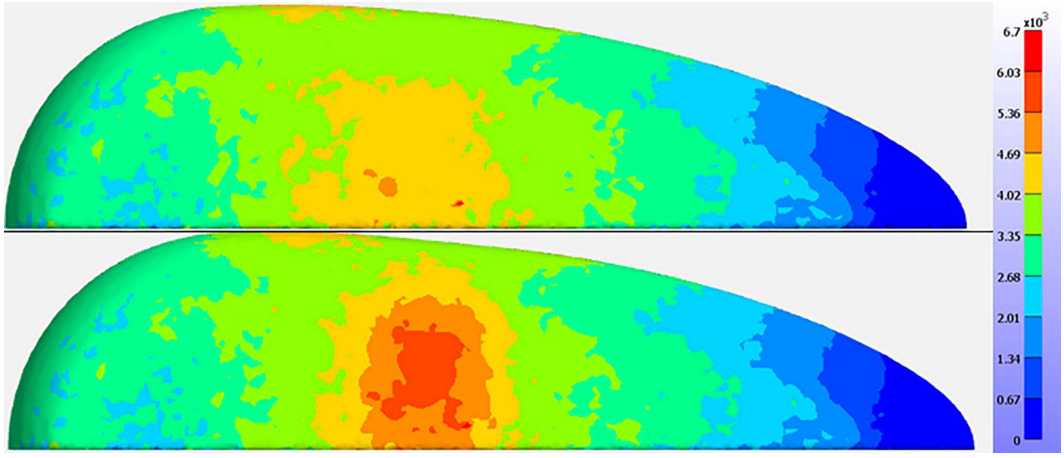

Figure 4. distribution of surface stress generated using FE software, FEBio, with simulated spherical tumours of two different sizes: 4 mm (top) and 7.5 mm (bottom).

of imaging systems and the validation of clinical trials, for use by engineers, physicians and regulatory authorities. The open-source OpenVCT framework software has been extensively validated as demonstrated and reviewed here. In a comparison of lesion detectability in DM and DBT, VCTs could accurately rank the imaging system performance and predict the level of performance improvement. In addition, VCTs played an important role in designing and optimising a novel combined imaging method, DBTMI.

Based upon our experience with VCTs, we continue to expand the OpenVCT framework. This includes work to calibrate the VCT observer studies to clinical studies by fine-tuning the virtual population

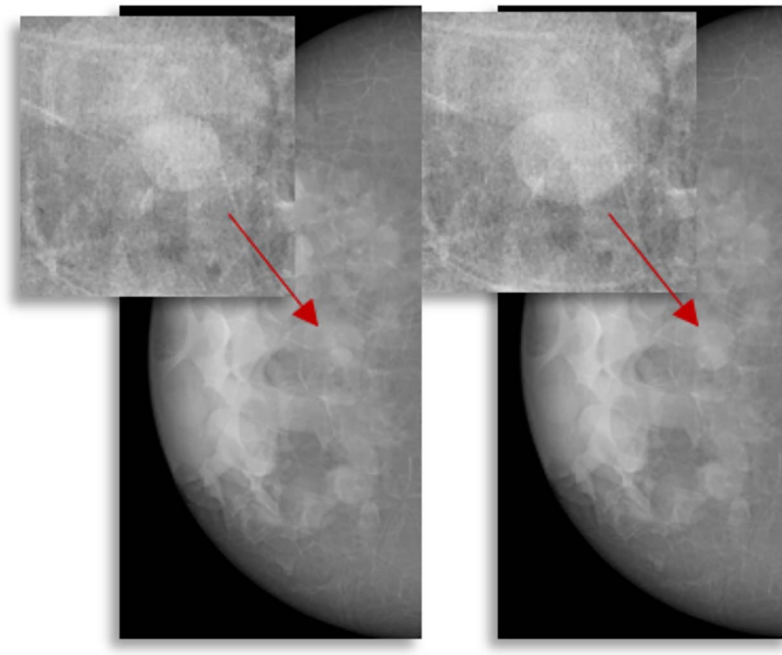

Figure 5. synthetic DM images of two consecutive screening episodes, containing a simulated tumour (arrows) with doubling time of 374 d.

and virtual lesions. We are also modelling tumour growth to relate equipment performance differences into the potential for screening benefits to women.

Looking at the future, there are several directions in which VCTs can benefit medical imaging. First, rare and paediatric diseases are characterised by a small number of patients and limited amount of available clinical images, which impedes the clinical research[48]. VCTs can play an important role once models of such diseases are available. Second, the demand for training and testing datasets for AI in medical imaging has increased. Synthetic images generated by VCTs may represent an efficient and cost-effective option to augment and expand clinical data. Given the rapid development of VCTs in medical imaging, we envision them to have a growing role in the future.

ACKNOWLEDGEMENTS

The authors are grateful to Ms. Susan Ng and Real Time Tomography for the use of Briona software to reconstruct and process synthetic DM and DBT images.

FUNDING

This work is supported by grants from the Horizon 2020 Marie Sklodowska Curie Action Fellowship (IF 846540); US National Institutes of Health (R01 CA154444); the Komen Foundation (IIR-13262248); the Burroughs-Wellcome Fund (IRSA 1016451); US Army Breast Cancer Research Program (W81XWH-18-1-0082); 2020 AAPM Research Seed Funding Grant and grants from Cancerfonden, the Swedish Breast Cancer Association and Stiftelsen för Cancerforskning vid Onklogiska kliniken vid Universitetssjukhuset MAS.

CONFLICT OF INTEREST

A.D.A.M. receives research support from Barco NV, and Analogic Inc.; he is spouse to an employee and stockholder of Real Time Tomography (RTT), LLC; and member of the RTT Scientific Advisory Board. S.Z. has received speaker's fees and travel support from Siemens Healthcare. Patent holder of US Patent (application no PCT/EP 2014/057372).

REFERENCES

1. Maidment, A. D. A. Virtual clinical trials for the assessment of novel breast screening modalities. In: International Workshop on Breast Imaging (IWDM), Vol.

8539. (LNCS). (Cham Heidelberg New York Dordrecht London: Springer) pp. 1–8 (2014).
2. Bakic, P. R., Brzakovic, D., Brzakovic, P. and Zhu, Z. An approach to using a generalized breast model to segment digital mammograms. In: 11th Symposium on Computer-Based Medical Systems, (Los Alamitos, CA: IEEE Computer Society) pp. 84–89 (1998).
3. Bakic, P. R. and Brzakovic, D. Simulation of digital mammogram acquisition. In: Proceedings of SPIE 3659, Medical Imaging: Physics of Medical Imaging, San Diego, CA, (Bellingham, WA: SPIE – The International Society of Optics and Photonics) pp. 866–877 (1999).
4. Bakic, P. R. Simulation of breast anatomy: anthropomorphic software phantoms. In: 2011 AAPM Annual Meeting and Exhibition (Alexandria, VA: American Association of Physicists in Medicine) (2011).
5. Pokrajac, D. D., Maidment, A. D. A. and Bakic, P. R. *Optimized generation of high resolution breast anthropomorphic software phantoms*. Med. Phys. **39**(4), 2290–2302 (2012).
6. Tischenko, O., Hoeschen, C., Dance, D. R., Hunt, R. A., Maidment, A. D. A. and Bakic, P. R. *Evaluation of a novel method of noise reduction using computer-simulated mammograms*. Radiat. Prot. Dosimetry **114**(1–3), 81–84 (2005).
7. Hunt, R. A., Dance, D. R., Bakic, P. R., Maidment, A. D. A., Sandborg, M., Ullman, G. and Carlsson, G. A. *Calculation of the properties of digital mammograms using a computer simulation*. Radiat. Prot. Dosimetry **114**(1–3), 395–398 (2005).
8. Dance, D. R., Hunt, R. A., Bakic, P. R., Maidment, A. D. A., Sandborg, M., Ullman, G. and Carlsson, G. A. *Breast dosimetry using high-resolution voxel phantoms*. Radiat. Prot. Dosimetry **114**(1–3), 359–363 (2005).
9. Richard, F. J. P., Bakic, P. R. and Maidment, A. D. A. *Mammogram registration: a phantom-based evaluation of compressed breast thickness variation effects*. IEEE Trans Med Imaging **25**(2), 188–197 (2006).
10. Ruiter, N. V., Zhang, C., Bakic, P. R., Carton, A.-K., Kuo, J. and Maidment, A. D. A. Simulation of tomosynthesis images based on an anthropomorphic software breast tissue phantom. In: Proceedings of SPIE 6918, Medical Imaging: Visualization, Image-guided Procedures, and Modeling, 69182I, San Diego, CA (Bellingham, WA: SPIE – The International Society of Optics and Photonics) (2008).
11. Bakic, P. R., Myers, K. J., Reiser, I., Kiarashi, N. and Zeng, R. *Virtual tools for validation of X-ray breast imaging systems*. Med. Phys. **40**(6), 390 (2013).
12. Bakic, P. R., Myers, K. J., Glick, S. J. and Maidment, A. D. Virtual tools for the evaluation of breast imaging: state-of-the science and future directions. In: International Workshop on Breast Imaging (IWDM), Vol. **9699**. (LNCS). pp. 478–485 (2016).
13. Healthineers, S. A Virtual Patient for your ARTIS Angiography System: Siemens Healthineers Vascular Patient Link. (Gothenburg, Sweden: Mentice) (2020) Available at https://www.mentice.com/vist-virtual-patient-siemens.
14. Li, Z., Desolneux, A., Muller, S., de Carvalho, P. M. and Carton, A.-K. Comparison of microcalcification detectability in FFDM and DBT using a virtual clinical trial. In: Proceedings of SPIE 10577, SPIE Medical Imaging: Image Perception, Observer Performance, and Technology Assessment, 105770D, Houston, TX (Bellingham, WA: SPIE – The International Society of Optics and Photonics) (2018).
15. FDA. VICTRE: Virtual Imaging Clinical Trials for Regulatory Evaluation. (Silver Spring, MD: U.S. Food and Drug Administration) (2018) Available at https://www.fda.gov/medical-devices/cdrh-research-programs/victre-virtual-imaging-clinical-trials-regulatory-evaluation.
16. Bakic, P. R., Barufaldi, B., Higginbotham, D., Weinstein, S. P., Avanaki, A. N., Espig, K. S., Xthona, A., Kimpe, T. R. L. and Maidment, A. D. A. Virtual clinical trial of lesion detection in digital mammography and digital breast tomosynthesis. In: Proceedings of SPIE 10573, Medical Imaging 2018: Physics of Medical Imaging, 1057306, Houston, TX (Bellingham, WA: SPIE – The International Society of Optics and Photonics) (2018).
17. Barufaldi, B., Bakic, P. and Maidment, A. Multiple-reader, multiple-case ROC analysis for determining the limit of calcification detection in tomosynthesis. In: Proceedings of SPIE 10948, Medical Imaging: Physics of Medical Imaging, 109480N, San Diego, CA (Bellingham, WA: SPIE – The International Society of Optics and Photonics) (2019).
18. Young, S., Bakic, P. R., Myers, K. J., Jennings, R. J. and Park, S. *A virtual trial framework for quantifying the detectability of masses in breast tomosynthesis projection data*. Med. Phys. **40**(5), 051914–1–15 (2013).
19. Zeng, R., Park, S., Bakic, P. and Myers, K. J. *Evaluating the sensitivity of the optimization of acquisition geometry to the choice of reconstruction algorithm in digital breast tomosynthesis through a simulation study*. Phys. Med. Biol. **60**(3), 1259 (2015).
20. Badano, A., Graff, C. G., Badal, A., Sharma, D., Zeng, R., Samuelson, F. W., Glick, S. J. and Myers, K. J. *Evaluation of digital breast tomosynthesis as replacement of full-field digital mammography using an in silico imaging trial*. JAMA Netw. Open **1**(7), e185474–1–12 (2018).
21. Mackenzie, A., Marshall, N. W., Hadjipanteli, A., Dance, D. R., Bosmans, H. and Young, K. C. *Characterisation of noise and sharpness of images from four digital breast tomosynthesis systems for simulation of images for virtual clinical trials*. Phys. Med. Biol. **62**(6), 2376–2397 (2017).
22. Vancoillie, L., Marshall, N., Cockmartin, L., Vignero, J., Zhang, G. and Bosmans, H. *Verification of the accuracy of a hybrid breast imaging simulation framework for virtual clinical trial applications*. J. Med. Medical Imaging **7**(4), 1–17 (2020).
23. Mettivier, G., Sarno, S., Boone, J. M., Bliznakova, K., di Franco, F. and Russo, P. Virtual clinical trials in 3D and 2D breast imaging with digital phantoms derived from clinical breast CT scans. In: Proceedings of SPIE 11312, SPIE Medical Imaging: Physics of Medical Imaging, 1131259, Houston, TX (Bellingham,

WA: SPIE – The International Society of Optics and Photonics) (2020).
24. Abadi, E., Segars, W. P., Chalian, H. and Samei, E. *Virtual imaging trials for coronavirus disease (COVID-19)*. Am. J. Roentgenol. **216**, 362–368 (2020).
25. Abadi, E., Segars, W. P., Harrawood, B., Sharma, S., Kapadia, A. J. and Samei, E. *Virtual clinical trial for quantifying the effects of beam collimation and pitch on image quality in computed tomography*. J. Med. Imaging **7**(4), 1–17 (2020).
26. Vimieiro, R. B., Borges, L. R., Caron, R. F., Barufaldi, B., Bakic, P. R., Maidment, A. D. and Vieira, M. A. Noise measurements from reconstructed digital breast tomosynthesis. In: Proceedings of SPIE 10948, Medical Imaging: Physics of Medical Imaging, 109480C, San Diego, CA (Bellingham, WA: SPIE – The International Society of Optics and Photonics) (2019).
27. Borges, L. R., Oliveira, H. C. d., Nunes, P. F., Bakic, P. R., Maidment, A. D. and Vieira, M. A. *Method for simulating dose reduction in digital mammography using the Anscombe transformation*. Med. Phys. **43**(6Part1), 2704–2714 (2016).
28. Vasudev, V., Piepers, B., Maidment, A. D., Kimpe, T., Platisa, L., Philips, W. and Bakic, P. R. Simulation pipeline for virtual clinical trials of dermatology images. In: Proceedings of SPIE 10948, Medical Imaging: Physics of Medical Imaging, 109482D, San Diego, CA (Bellingham, WA: SPIE – The International Society of Optics and Photonics) (2019).
29. Vasudev, V., De Paepe, L., Maidment, A., Kimpe, K., Platisa, L., Philips, W. and Bakic, P. Impact of chromophores on colour appearance in a computational skin model. In: Proceedings of SPIE 11312, Medical Imaging: Physics of Medical Imaging, 1131232, Houston, TX (Bellingham, WA: SPIE – The International Society of Optics and Photonics) (2020).
30. Barufaldi, B., Higginbotham, D., Bakic, P. R. and Maidment, A. D. OpenVCT: a GPU-accelerated virtual clinical trial pipeline for mammography and digital breast tomosynthesis. In: Proceedings of SPIE, Medical Imaging: Physics of Medical Imaging, 1057358, Houston, TX (Bellingham, WA: SPIE – The International Society of Optics and Photonics) (2018).
31. Lago, M. A., Maidment, A. D. A. and Bakic, P. R. *Modelling of mammographic compression of anthropomorphic software breast phantom using FEBio. Int'l Symposium on*. Comput. Methods Biomech. Biomed. Engin. 487–488 (2013).
32. Marchessoux, C., Kimpe, T. R. L. and Bert, T. *A virtual image chain for perceived and clinical image quality of medical display*. J. Display Technol. **4**, 356–368 (2008).
33. Barrett, H. H., Yao, J., Rolland, J. P. and Myers, K. J. *Model observers for assessment of image quality*. In: Proceedings of the National Academy of Sciences, USA, Vol. **90**, (Washington, D.C.: National Academy of Sciences) pp. 9758–9765 (1993).
34. Marchessoux, C., Avanaki, A., Bakic, P. R., Kimpe, T. R. L. and Maidment, A. D. A. Effects of medical display luminance, contrast and temporal compensation on CHO detection performance at various browsing speeds and on digital breast tomosynthesis images. In: International Workshop on Breast Imaging (IWDM), Vol. **7361**. (LNCS). (Berlin Heidelberg: Springer-Verlag) pp. 292–299 (2012).
35. Avanaki, A. N., Espig, K. S., Maidment, A. D. A., Marchessoux, C., Bakic, P. R. and Kimpe, T. R. L. Development and evaluation of a 3D model observer with nonlinear spatiotemporal contrast sensitivity. In: Proceedings of SPIE 9037, Medical Imaging 2014: Image Perception, Observer Performance, and Technology Assessment, 90370X, San Diego, CA (Bellingham, WA: SPIE – The International Society of Optics and Photonics) (2014).
36. Gallas, B. D. *One-shot estimate of MRMC variance: AUC*. Acad. Radiol. **13**(3), 353–362 (2006).
37. Rafferty, E. A., Park, J. M., Philpotts, L. E., Poplack, S. P., Sumkin, J. H., Halpern, E. F. and Niklason, L. T. *Assessing radiologist performance using combined digital mammography and breast tomosynthesis compared with digital mammography alone: results of a multicenter*. Multireader Trial. Radiology. **266**(1), 105–113 (2013).
38. Bakic, P. R., Dustler, M., Lau, K. C., Maidment, A. D. A., Zackrisson, S. and Tingberg, A. Evaluation of a flat fielding method for simultaneous DBT and MI acquisition. In: Proceedings of SPIE 11513, 15th International Workshop on Breast Imaging (IWBI2020), 11513OU, Houston, TX (Bellingham, WA: SPIE – The International Society of Optics and Photonics) (2020).
39. Bakic, P. R., Dustler, M., Ng, S., Maidment, A. D. A., Zachrisson, S. and Tingberg, A. Pre-processing for image quality improvement in simultaneous DBT and mechanical imaging. In: Proceedings of SPIE 11312, Medical Imaging: Physics of Medical Imaging, 1131257, Houston, TX (Bellingham, WA: SPIE – The International Society of Optics and Photonics) (2020).
40. Axelsson, R., Isaksson, H., Zachrisson, S., Tingberg, A., Bakic, P. R. and Dustler, M. Computer model of mechanical imaging acquisition for virtual clinical trials. In: Proceedings of SPIE 11595, Medical Imaging: Physics of Medical Imaging, 11595OQ (Bellingham, WA: SPIE – The International Society of Optics and Photonics) (2021).
41. Maas, S., Ellis, B., Ateshian, G. and Weiss, J. *FEBio: finite elements for biomechanics*. J. Biomech. Eng. **134**(1), 011005–1–10 (2012).
42. Dustler, M., Andersson, I., Brorson, H., Fröjd, P., Mattsson, S., Tingberg, A., Zackrisson, S. and Förnvik, D. *Breast compression in mammography: pressure distribution patterns*. Acta Radiol. **53**(9), 973–980 (2012).
43. Förnvik, D., Andersson, I., Dustler, M., Ehrnström, R., Ryden, L., Tingberg, A., Zackrisson, S. and Aaltonen, K. *No evidence for shedding of circulating tumor cells to the peripheral venous blood as a result of mammographic breast compression*. Breast Cancer Res. Treat. **141**, 187–195 (2013).
44. National Guidelines for Breast. Colorectal and Prostate Cancer Screening. (Stockholm, Sweden: The Swedish National Board of Health and Welfare) (2014).
45. Tomic, H., Bejnö, A., Hellgren, G., Johnson, K., Förnvik, D., Zackrisson, S., Tingberg, A., Dustler, M. and Bakic, P. R. Assessment of a tumour growth model for virtual clinical trials of breast cancer screening. In: Proceedings of SPIE 11595, Medical Imaging: Physics of Medical Imaging, 115954Q (Bellingham, WA: SPIE

– The International Society of Optics and Photonics) (2021).
46. Förnvik, D., Lång, K., Andersson, I., Dustler, M., Borgquist, S. and Timberg, P. *Estimates of breast cancer growth rate from mammograms and its relation to tumour characteristics*. Radiat. Prot. Dosimetry **139** (1–4), 151–157 (2016).
47. Ryu, E., Chang, J., Seo, M., Kim, S., Lim, J. and Moon, W. *Tumour volume doubling time of molecular breast cancer subtypes assessed by serial breast ultrasound*. Eur. Radiol. **24**, 2227–2235 (2014).
48. Mitani, A. A. and Haneuse, S. *Small data challenges of studying rare diseases*. JAMA Netw. Open **3**(3), e201965–1–3 (2020).

SU-F-TRACK 1-01
J. Fontenot, Mary Bird Perkins Cancer Center:
Professional Economics Updates
SU-F-TRACK 1-02
W. Fuss, Health Policy Solutions:
Professional Economics Updates
SU-F-TRACK 1-03
Audience Q&A

This presentation will describe reimbursement changes implemented in 2021 and proposed changes for 2022, including the radiation oncology alternative payment model, . A review of changes that impact radiation oncology and radiology will be provided. A discussion of the Hospital Outpatient Prospective Payment System (HOPPS), the Medicare Physician Fee Schedule (MPFS), and the ambulatory surgery settings will be discussed. Lastly, an overview of the resources available to membership and tips for interacting with the professional economics committee will be provided.

Learning Objectives:
1. Basic understanding of payment models impacting medical physics clinical services.
2. Basic understanding of the 2022 HOPPS and MPFS proposed rules, including the RO-APM.
3. Basic understanding of economics and policy resources that are available from the AAPM and how to interact with the professional economics committee.

Imaging Scientific Session
TRACK 3
Breast Imaging

SU-F-TRACK 3-01
Anisotropies in Super-Resolution in 3D Magnification Mammography Using a Next-Generation Tomosynthesis System
R Acciavatti*, T Vent, C Choi, P Noel, A Maidment, Hospital of University of Pennsylvania, Philadelphia, PA

Purpose: In breast imaging, microcalcifications detected in a screening exam can be characterized with better detail in magnification mammography. In this exam, the breast is elevated closer to the x-ray source, and a 2D image is acquired. Unlike clinical systems, the next-generation tomosynthesis (NGT) system built in our lab is capable of 3D magnification mammography. We are also designing the system to generate super-resolution (SR) reconstructions. In our earlier work modeling the tomosynthesis acquisition in screening mammography, we found that there are anisotropies in SR at various positions in the image. This study analyzes how the anisotropies in SR vary with the use of magnification**. Methods:** A high-frequency sinusoidal test object was analyzed with theoretical modeling. The input frequency was oriented in the direction of x-ray source motion. Image quality in the reconstruction was quantified using the Fourier transform. The amplitude of low-frequency information was measured relative to the input frequency; this ratio should be as small as possible to achieve SR. We used these calculations to identify anisotropies in SR at various magnifications. For experimental validation of the anisotropies, a bar pattern phantom was analyzed with the NGT system**. Results:** In screening mode, there are anisotropies in SR in the direction perpendicular to the breast support; i.e., in various slices of the reconstruction. With theoretical modeling, we demonstrated that the spacing between anisotropies is reduced with increasing magnification; however, the relative amplitude of low-frequency (aliasing) signal at the anisotropies is not as pronounced as in screening mode. The anisotropies were validated experimentally with the NGT system**. Conclusion:** SR can be achieved in tomosynthesis reconstructions. Using the conventional acquisition geometry, anisotropies in SR exist in both screening and magnification tomosynthesis. Our future work will use this model of SR to optimize the acquisition geometry for magnification tomosynthesis.

A.M. is the spouse of a shareholder of Real Time Tomography (RTT). P.N. receives support from Philips Healthcare and is consultant to Stryker. Support was provided by grants W81XWH-18-1-0082 (DoD), IRSA 1016451 (Burroughs Wellcome), R01CA196528 (NIH), and IIR13264610 (Komen). Equipment support was provided by Analogic Inc., Barco NV, and RTT.

SU-F-TRACK 3-02
Histological Validation of Anatomical Imaging for Breast Modeling
A Sen*, C Kingsley, A Kulp, M McCulloch, B Willis, K Brewer Savannah, A Contreras, M Bordes, T Huynh, N Fowlkes, G Reece, K Brock, UT MD Anderson Cancer Center, Houston, TX

Purpose: Develop a framework to register in vivo and ex vivo images with histology using a novel cryo-microtome for validation of anatomical structures to improve tissue modeling and imaging signals. **Methods:** Breast tissue obtained from a mastectomy patient and a formalin-fixed entire breast including chest wall from a cadaver were imaged using magnetic resonance (MR) imaging (3D T1 and 3D T2 Dixon, fat/water-saturated, in/out-of-phase). Specimens were frozen and embedded in optical cutting temperature (OCT) compound. The OCT block was placed in a cryo-microtome mounted with an overhead camera (Xerra, Emit Imaging). Slices of 33μm and 50μm were successively shaved off the block for the tissue and cadaver specimens, respectively. After each shaving, the blockface was photographed. At select tissue sites (connective/adipose, muscle, skin, fibroglandular), 20μm sections were transferred onto cryotape for manual H&E staining and histological analysis. A 3D blockface image was automatically reconstructed from the photographs by aligning fiducial markers embedded into the OCT block. The 3D MR, blockface images, and histology images were rigidly registered. Target registration errors (TRE) were computed based on corresponding points marked at fibroglandular intersections (5 for tissue, 10 for cadaver). The overall MR-histology registration was used to compare the MR intensities at tissue extraction sites with a one-way ANOVA. **Results:** The MRI-blockface TREs were 0.34±0.11mm and 0.73±25mm for the tissue and cadaver datasets, respectively (both less than respective MR slice thicknesses of 0.35 and 1.00mm). The blockface-histology registration showed alignment of anatomical structures and tissue boundaries. The MR intensities at the four tissue sites showed statistically significant differences ($P<0.01$). Each pair of tissues except skin-connective/adipose were also significantly different ($P<0.01$)**. Conclusion:** Fine sectioning in a highly controlled imaging/sectioning environment enabled accurate registration between the MR image and histology and differentiation of tissue types in the MR image.

Research reported was supported in part by resources of the Image Guided Cancer Therapy Research Program from The University of Texas MD Anderson Cancer Center and the Helen Black Image-Guided Fund.

SU-F-TRACK 3-03
Direct-Indirect Dual-Layer Detector for Contrast Enhanced Digital Breast Tomosynthesis: Feasibility Using Image Simulation
X Duan*, H Huang, A Howansky, J Stavro, A Lubinsky, A Goldan, W Zhao, Stony Brook Medicine, Stony Brook, NY

cancers

MDPI

Article

Incorporating Robustness to Imaging Physics into Radiomic Feature Selection for Breast Cancer Risk Estimation

Raymond J. Acciavatti [1,*], Eric A. Cohen [1], Omid Haji Maghsoudi [1,†], Aimilia Gastounioti [1,†], Lauren Pantalone [1], Meng-Kang Hsieh [1,†], Emily F. Conant [1], Christopher G. Scott [2], Stacey J. Winham [2], Karla Kerlikowske [3], Celine Vachon [2], Andrew D. A. Maidment [1] and Despina Kontos [1]

[1] Department of Radiology, Perelman School of Medicine, University of Pennsylvania, Philadelphia, PA 19104, USA; Eric.Cohen@pennmedicine.upenn.edu (E.A.C.); o.maghsoudi@gmail.com (O.H.M.); a.gastounioti@wustl.edu (A.G.); Lauren.Pantalone@pennmedicine.upenn.edu (L.P.); michaelhsieh42@gmail.com (M.-K.H.); Emily.Conant@pennmedicine.upenn.edu (E.F.C.); Andrew.Maidment@pennmedicine.upenn.edu (A.D.A.M.); Despina.Kontos@pennmedicine.upenn.edu (D.K.)

[2] Division of Epidemiology, Department of Health Sciences Research, Mayo Clinic, Rochester, MN 55905, USA; Scott.Christopher@mayo.edu (C.G.S.); Winham.Stacey@mayo.edu (S.J.W.); Vachon.Celine@mayo.edu (C.V.)

[3] Departments of Medicine and Epidemiology/Biostatistics, Women's Health Clinical Research Center, UCSF, San Francisco, CA 94143, USA; karla.kerlikowske@ucsf.edu

* Correspondence: racci@pennmedicine.upenn.edu

† These authors changed employment before the submission of this manuscript to Cancers, but made contributions to this manuscript solely while employed by the University of Pennsylvania.

Simple Summary: Mammographic density estimates can be combined with radiomic texture features to offer an even better assessment of breast cancer risk. However, some feature variations will be due to true parenchymal differences between women, but others will be due to imaging physics effects (contrast, noise, and image sharpness); features robust to imaging physics effects should better model risk. To investigate this, we imaged an anthropomorphic phantom at various x-ray technique settings, allowing us to directly measure the effects of imaging physics on feature values. We compared these variations, for each feature, with the inter-woman variation in a screening population (552 cancer-free women) and the intra-woman variation between each woman's left and right breasts, to assess which features were relatively robust to physics settings. We then tested more- versus less-robust features in modeling cancer risk on an independent case-control data set, and demonstrated that more-robust features were indeed better at risk prediction.

Abstract: Digital mammography has seen an explosion in the number of radiomic features used for risk-assessment modeling. However, having more features is not necessarily beneficial, as some features may be overly sensitive to imaging physics (contrast, noise, and image sharpness). To measure the effects of imaging physics, we analyzed the feature variation across imaging acquisition settings (kV, mAs) using an anthropomorphic phantom. We also analyzed the intra-woman variation (IWV), a measure of how much a feature varies between breasts with similar parenchymal patterns—a woman's left and right breasts. From 341 features, we identified "robust" features that minimized the effects of imaging physics and IWV. We also investigated whether robust features offered better case-control classification in an independent data set of 575 images, all with an overall BI-RADS® assessment of 1 (negative) or 2 (benign); 115 images (cases) were of women who developed cancer at least one year after that screening image, matched to 460 controls. We modeled cancer occurrence via logistic regression, using cross-validated area under the receiver-operating-characteristic curve (AUC) to measure model performance. Models using features from the most-robust quartile of features yielded an AUC = 0.59, versus 0.54 for the least-robust, with $p < 0.005$ for the difference among the quartiles.

Keywords: radiomics; digital mammography; robustness; feature selection; anthropomorphic phantom; case-control analysis; risk assessment; imaging acquisition physics; breast cancer

Citation: Acciavatti, R.J.; Cohen, E.A.; Maghsoudi, O.H.; Gastounioti, A.; Pantalone, L.; Hsieh, M.-K.; Conant, E.F.; Scott, C.G.; Winham, S.J.; Kerlikowske, K.; et al. Incorporating Robustness to Imaging Physics into Radiomic Feature Selection for Breast Cancer Risk Estimation. *Cancers* **2021**, *13*, 5497. https://doi.org/10.3390/cancers13215497

Academic Editor: Elif Hindie

Received: 21 July 2021
Accepted: 27 October 2021
Published: 1 November 2021

1. Introduction

Breast density has consistently been shown to be an independent predictor of breast cancer risk [1–3]. Recent studies have demonstrated that combining estimates of breast density with radiomic features obtained from digital mammography (DM) images results in an improved discrimination of breast cancer risk, and that these calculations have important applications in developing personalized screening and prevention strategies for breast cancer [4–6].

The number of potentially predictive radiomic features is constantly growing. However, risk-assessment models are not necessarily improved with the use of more features, since features can be highly-correlated with each other. Previous works have proposed dimensionality reduction techniques to filter out correlated features based on cluster analysis and principal component analysis [7–14].

As an independent (but complementary) filtering strategy, one can identify the features that are robust to variations in imaging physics. The goal is to identify features that are not overly sensitive to contrast, noise, and image sharpness, which may change due to variations in imaging acquisition settings, scanner make and model, image processing, or even software version. Instead, it is important to select features that capture underlying parenchymal and pathophysiological differences between women, which could be suggestive of breast cancer risk.

Previous works have analyzed women imaged under different conditions (for example, with different DM vendors) to identify robust features. Mendel et al. found that features measuring spatial patterns were insensitive to vendor (for example, fractal dimension, power law β, and correlation from the co-occurrence matrix) [15]. However, intensity- and directionality-based features were sensitive to vendor (for example, entropy, balance, and mean gradient). In a follow-up study, this analysis was applied in combination with hierarchical clustering to identify features that were robust across vendors and also non-redundant [14].

Although it is ideal to identify robust features based on data sets of women imaged under different conditions, these data sets are rare and become quickly obsolete with the changing imaging technologies. An alternative is to use an anthropomorphic phantom which has the advantage of being able to be imaged under an unlimited number of conditions, so that the effects of imaging physics can be measured directly. Keller et al. showed that a phantom (Gammex 169, "Rachel", Madison, WI, USA) can successfully be used to measure the robustness of features across different DM vendors [16,17]. In their work, each image was Z-score normalized, and feature distributions across vendors were analyzed with equivalence tests to identify robust features.

We extended this prior work to investigate the effect of varying the x-ray technique settings (kV and mAs) using the same phantom as in Keller's study, but with a larger number of features (341 features as opposed to 29). Additionally, unlike all the works described previously, we identified robust features using acquisitions from a single vendor. For each feature, a robustness metric called imaging acquisition variation (IAV) was calculated; it measures how much the variation due to x-ray technique settings (kV and mAs) in a phantom scales against the variation across women in a screening population. All images in this screening population had an overall assessment of 1 (negative) or 2 (benign) according to the Breast Imaging Reporting and Database System (BI-RADS®). The women were validated to be cancer-free with at least 12 months of follow-up in a subsequent screening exam with an overall BI-RADS® assessment of 1 or 2. This clinical data set was derived from only one vendor; our method for identifying robust features does not require women to have been imaged with different technique settings or different DM vendors, as was the case in the work of Mendel et al. [15]. In order for a feature to be considered robust, the variation across technique settings in a single phantom should be small compared against the variation across a population of women, where there are broadly differing parenchymal patterns.

In addition, we calculated intra-woman variation (IWV) for each feature using the same data set of clinical mammograms. IWV is a measure of how much the feature varies across the left and right breasts of the same woman. For a feature to provide clinically-meaningful information about breast cancer risk, it is assumed that the feature should not be highly sensitive to left–right breast differences in the same woman, but instead, be more sensitive to differences across a population of women. We identified features that are overly sensitive to bilateral differences in the same woman so that these features are excluded in risk-assessment analyses, just as features that are highly sensitive to the effects of imaging physics can be excluded. For this purpose, we developed a composite measure of variation (CMV) that combines both IAV and IWV, with the goal of using CMV to identify robust features.

Because CMV is calculated exclusively with mammograms from women who were validated to be cancer-free (overall BI-RADS® assessment of 1 or 2) in a subsequent screening exam, it was necessary to consider a separate clinical data set to investigate the relationship between CMV and case-control classification performance. For these calculations, there were four classes of features (quartiles), ranked in order of robustness scores (CMV). We built a logistic regression model for case-control classification with nine randomly-selected features in each class using cross-validated area under the receiver-operating-characteristic curve (AUC) to measure model performance. Since a relatively small number of features (nine) was utilized in this AUC calculation and since established risk factors for breast cancer (e.g., age, breast density, and body mass index) were not modeled, it should be emphasized that the purpose of these calculations was not to develop a model with the highest possible AUC. Rather, the aim was to demonstrate a statistically-significant improvement in AUC in models built with more robust features. Ultimately, we did indeed demonstrate that there is a trend of better discrimination in models built using more robust features, and therefore, we conclude that a robustness analysis is an essential step in selecting features for risk-assessment modeling.

2. Materials and Methods

2.1. Roadmap

This study consisted of two components. First, we developed a metric (CMV) which measures the robustness of each feature (Section 2.2). The metric captures two sources of undesirable feature variation: the variation due to differences in imaging physics settings; and intra-woman (left–right) variation that is unlikely to be related to meaningful breast differences. In developing this metric, we employed a dataset of women with negative or benign screening exams, for which there was a subsequent negative or benign follow-up exam at least one year later. Second, we validated the utility of the CMV metric in a case-control classification, testing whether more-robust features give superior classification performance (Section 2.3). This analysis employed an independent case-control data set. In this, all mammograms are negative or benign, but the population includes cases—women who developed cancer at least one year later.

2.2. Robust Feature Identification

2.2.1. Study Population

This study was HIPAA-compliant and approved by the University of Pennsylvania Institutional Review Board with a waiver of consent under expedited review category 5 (Review Board IRB #7, Protocol #825735). We retrospectively analyzed DM screening images from 997 women acquired at one facility, sequentially from 2 September through 31 October 2014; this represents a subset of a larger cohort described in a previous work [18]. All images had an overall BI-RADS® assessment of 1 or 2; each woman had a similar overall BI-RADS® assessment in a subsequent screening exam at least 12 months later. The women were imaged with Selenia Dimensions systems (Hologic Inc., Bedford, MA, USA). We analyzed only cranial–caudal (CC) view images of breasts with thickness in [40, 60] mm

to compare to breast properties to those of a phantom modeling a 50-mm thick breast in CC view.

2.2.2. Phantom Data Acquisitions

DM images of the phantom were acquired in a CC projection using a Selenia Dimensions system in "Manual" mode over a range of kV and mAs combinations (examples shown in Figure S1). Two target/filter combinations are supported by this system: W/Rh and W/Ag. According to Hologic data tables for automatic exposure control settings, breasts with thickness in [40, 60] mm are imaged with W/Rh, thus all phantom images were acquired with this target/filter combination. First, images were acquired between 27 and 35 kV in 1 kV increments, with mAs determined with auto timing (Table S1). Second, at the central kV (31), we varied the mAs between 13 and 180 mAs in increments varying by a factor of $2^{1/2}$ or 1.41 (at the closest mAs supported by the system). The phantom was imaged twice at each technique setting.

The Supplementary Materials illustrate the trends for two features across the full range of kV and mAs settings (Figures S2 and S3), but our goal was to develop a robustness metric that captured the effect of kV and mAs variations that might be seen clinically. To do this, we identified the (kV, mAs) settings represented in our clinical image dataset (images of breasts similar in thickness to the phantom), and kept only the phantom images acquired at settings in these bounds (Table S2). Six technique settings met this criterion: 28 kV (160 mAs), 29 kV (140 mAs), 30 kV (120 mAs), and 31 kV (120, 140, and 180 mAs). Since each acquisition was repeated, a total of 12 images were analyzed.

2.2.3. Feature Extraction

Texture features were calculated on raw ("FOR PROCESSING") images; automatic segmentation of the breast area was performed using the publically available LIBRA software package (version 1.0.4) [19]. Partitioning the breast into a lattice of 6.3 mm square windows, for a given feature, the feature value was calculated within every window, and then averaged over all the windows. This approach was motivated by previous work by Zheng et al., which showed that the use of a lattice results in better case-control classification than the use of a single region of interest [4]. Zheng et al. also studied the effect of varying the window size (between 6.3 and 25.5 mm), and found that the area under the receiver operating characteristic curve (AUC) was highest at the 6.3-mm window size.

A total of 341 features were analyzed: 12 grey-level histogram, 7 co-occurrence, 7 run length, 2 fractal dimension, 36 local binary pattern (LBP), 125 Laws, 120 co-occurrence Laws, and 32 Gabor wavelet features [20–24].

2.2.4. Imaging Acquisition Variation

To measure how much each feature was affected by imaging physics, the range of variation across 12 phantom acquisitions was calculated, and scaled against the spread of the clinical distribution (Figure 1). In a robust feature (Figure 1a), the phantom values are clustered over a narrow range of values relative to the variation in the population. By contrast, in a feature that is strongly affected by imaging physics (Figure 1b), the phantom data points are spread across a broad range.

This motivated our first feature quality metric, imaging acquisition variation (IAV). The range of phantom variation is scaled against the width of the middle 90% of the clinical distribution. (This width was chosen, as opposed to the full range of the distribution, as the tails could be sensitive to outliers.) Denoting p_{ik} as the value of the kth feature for the ith phantom acquisition, IAV was thus defined as:

$$\mathrm{IAV}_k = \frac{\max_i \{ p_{ik} \}_{i=1}^{m} - \min_i \{ p_{ik} \}_{i=1}^{m}}{c_{95,k} - c_{5,k}} \quad (1)$$

where i runs from 1 to the number of phantom acquisitions (m = 12), k runs from 1 to the number of features (341), and $c_{95,k}$ and $c_{5,k}$ (dashed vertical lines, Figure 1) denote the 95th

and 5th percentile of the clinical distribution for the kth feature. In a robust feature, IAV should effectively be zero, since variations due to imaging physics (the numerator) should represent a much smaller effect than variations between women (the denominator).

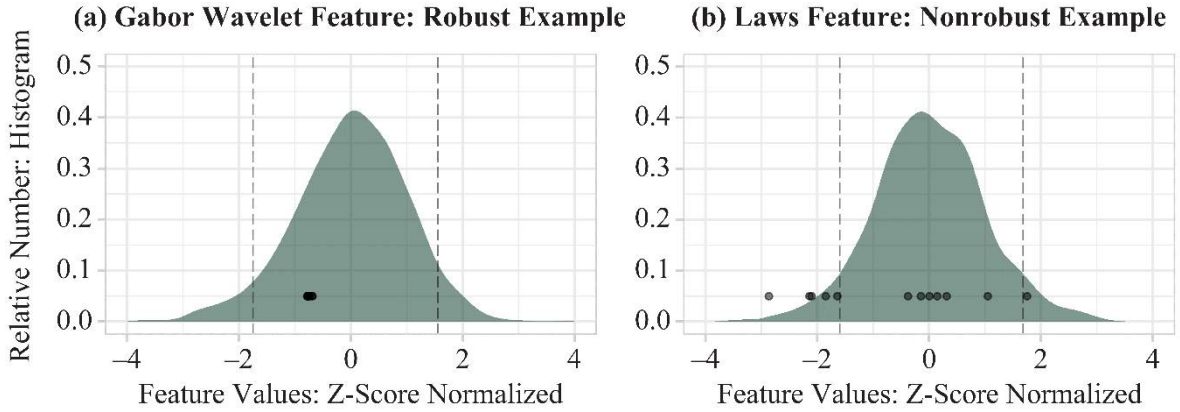

Figure 1. Histograms of the clinical distributions of two radiomic features. Superimposed points show the values obtained from imaging the phantom, with each data point corresponding to an x-ray acquisition (six unique kV/mAs combinations, repeated twice). (**a**) An example of a robust feature. The 12 phantom data points show very little variation relative to the clinical distribution; (**b**) An example of a nonrobust feature. The data derived from the phantom span a broader range.

2.2.5. Intra-Woman Variation

A second feature quality metric, the intra-woman variation (IWV), was calculated based on an analysis of bilateral (left–right) differences in each woman. Just as IAV should effectively be zero, one would expect IWV to be minimized in a robust feature, since parenchymal patterns are generally similar across a woman's two breasts. Denoting l_{jk} as the value of the kth feature in the left breast of the jth woman and r_{jk} as the corresponding value in her right breast, IWV was then defined as:

$$\mathrm{IWV}_k = \frac{\mathrm{median}_j\{|l_{jk} - r_{jk}|\}_{j=1}^{q}}{c_{95,k} - c_{5,k}} \tag{2}$$

where q is the number of women with at least one breast with thickness in [40, 60] mm in CC view. (We chose the median as the summary measure over all women as less sensitive to outliers than the mean.) The denominator is the same as that for IAV, scaling the value to the feature's variation over all breasts with thickness in [40, 60] mm in CC view.

2.2.6. Composite Measure of Variation

The two feature quality metrics were visualized for all 341 features with a scatter plot in IAV × IWV space. More robust features are closer to the origin (the point for which IAV = IWV = 0) in this space. For this reason, we calculated the Euclidean distance of each data point from the origin as a composite measure of variation (CMV), a metric that takes into account the combined influence of IAV and IWV:

$$\mathrm{CMV}_k = \sqrt{\mathrm{IAV}_k{}^2 + \mathrm{IWV}_k{}^2} \tag{3}$$

where $0 \leq \mathrm{CMV}_k < \infty$. The purpose of CMV was to capture, in a single metric, how much each feature is sensitive to imaging physics as well as left–right differences in the same woman, with the ultimate goal of using CMV to identify features that minimize both sources of variation.

2.3. Case-Control Analysis

If a feature is less sensitive to changes in imaging settings, this may make it less sensitive to the variations in facility, device manufacturer, and protocol that are found in

real-world imaging data; and this feature may then offer more information and less noise when used in modeling on a heterogeneous data set. We therefore also analyzed whether modeling cancer risk using lower-CMV features tended to perform better than the same modeling using higher-CMV features.

2.3.1. Study Population

For this purpose, we analyzed an independent case-control data set described by Gastounioti et al. [25]. It consisted of 575 images with an overall BI-RADS® assessment of 1 or 2, with a subset of 115 images (cases) known to have developed cancer at least one year later. As described in Gastounioti's work, the remaining 460 images were controls matched on the basis of age, ethnicity, and screening exam date (within one year), who were known to have an overall BI-RADS® assessment of 1 or 2 in a follow-up screening exam at least 12 months later. We analyzed the raw ("FOR PROCESSING") DM images, which were acquired with Selenia Dimensions systems. All images were mediolateral-oblique (MLO) views, with the exception of two CC views.

2.3.2. Dimensionality Reduction

First, recalling the data set of CC views of 997 women (the data set used to calculate robustness metrics IAV, IWV, and CMV), we analyzed the clinical distribution of each feature as the basis for an initial dimensionality reduction step. We Z-score normalized each distribution, and excluded features with highly-skewed (skewness >6) and highly asymmetric (kurtosis >50) distributions. All CC views independent of thickness were used in this analysis.

To remove highly-correlated features, we then identified pairs of features with >95% Pearson's correlation. For each pair, the feature with the lower inter quartile range (IQR) was excluded (similar to the approach used by Gastounioti et al.) [25].

2.3.3. Case-Control Classification

Next, the remaining features were ranked by CMV and partitioned, by quartiles, into four feature robustness classes, A (lowest CMV) through D (highest). Our aim then was to test whether models built on features from class A would, on average, predict case-control status better than models built on features from class D (with the other two classes falling in between). We divided the set of features into quartiles, rather than contrasting robust with nonrobust features via a numeric cutoff on CMV, as quartiles allowed a consistent evaluation, with the same number of features in each comparison group. Using more than two feature groups allowed for better discovery of any possible trend in performance versus robustness, and four quartiles permitted an adequate number of features in each group.

To do this, we employed the features in logistic regression models, with five-fold cross-validated AUC as the measure of model performance: for each model, four-folds (460 women—92 cases, 368 controls) were employed for modeling, and the remaining fold (115 women—23 cases, 92 controls) for calculating AUC. (Case-control matching was preserved in all partitions.) Since early investigation showed that the partitioning used for cross-validation had a substantial impact on AUC, we (a) tested each model on ten different random partitions of the data, to smooth this effect over multiple partitions; and (b) used the same ten partitions for all models, to provide an even playing field across models and feature classes. In all, we built ten models for each feature class, each model using nine features randomly selected from that class; tested each model ten times, each time using a different one of the ten data partitions; and recorded these 100 five-fold cross-validated AUCs as performance measures for each feature class (Figure 2). (Each logistic regression model employed nine features as, with 115 cases, and four of the five folds used to build each model, this was the maximum possible allowing a rule-of-thumb 10 cases for each coefficient in the model).

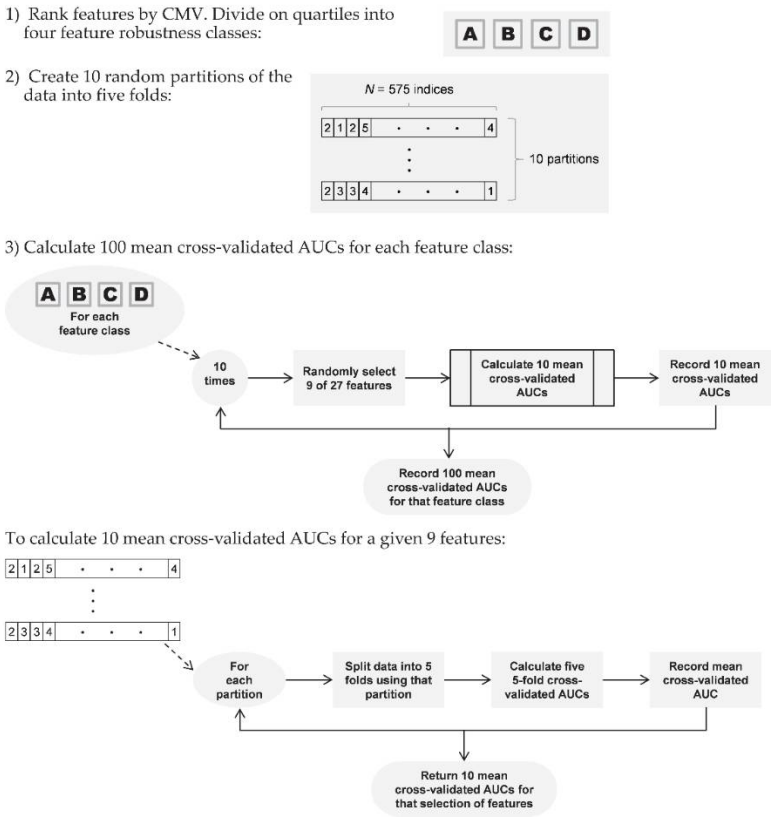

Figure 2. Flow diagram of AUC calculation on case-control data using logistic regression modeling.

Finally, those 400 values were used to build a linear mixed model testing against the null hypothesis that AUC was unrelated to class, with mean cross-validated AUC as the outcome, treating robustness class as a fixed effect (with reference level D) and partition as a random effect. Selecting a reference class permitted linear regression versus mean AUC, and employing class D as the reference allowed us to understand the gain in AUC versus the performance of the least-robust features. This analysis was done at the 0.05 level of significance. All statistical analysis was performed using the R language version 4.0.0 and Python version 3.6.0 with the following installed packages: Numpy 1.18.5, Scipy 1.4.1., Pandas 1.0.3, statsmodels 0.11.1, matplotlib 3.3.0, and sklearn 0.23.0 [26].

3. Results

3.1. Roadmap

Our two research aims yield two key results. First, we developed the CMV metric, deriving it from two underlying metrics, IAV and IWV, measuring imaging physics effects and intra-woman variation (Section 3.2). This allowed us to rank the features in their overall robustness. Second, we validated the utility of the CMV metric in a case-control classification on an independent data set (Section 3.3), finding a trend of better modeling performance in features with lower CMV.

3.2. Robust Feature Identification

3.2.1. Study Population

The data set of CC views of 997 women yielded 1984 raw CC mammograms that successfully underwent automated segmentation and texture feature extraction. Restricting these to only images of breasts in [40, 60] mm thickness resulted in 970 images representing 552 women (Table 1). Of these, 968 images were acquired with W/Rh target/filter combination and two images (from the same patient) were acquired with W/Ag target/filter

combination. Images derived from both target/filter combinations were used in all calculations and analyses.

Table 1. Characteristics of participants used to calculate radiomic feature robustness metrics; both the source population and the subpopulation used for calculation of robustness metrics, with compressed breast thickness in [40, 60] mm.

Characteristic	Source Population: 997 Women *	Neither Breast with Thickness in [40, 60] mm: 445 Women	At Least One Breast with Thickness in [40, 60] mm: 552 Women †	*p*-Value ‡
Age				
<40	29 (2.9%)	18 (4.0%)	11 (2.0%)	0.01
[40, 50)	270 (27.1%)	128 (28.8%)	142 (25.7%)	
[50, 60)	304 (30.5%)	144 (32.4%)	160 (29.0%)	
[60, 70)	268 (26.9%)	113 (25.4%)	155 (28.1%)	
≥70	126 (12.6%)	42 (9.4%)	84 (15.2%)	
Race				
Black	464 (46.5%)	206 (46.3%)	258 (46.7%)	0.96
White	457 (45.8%)	207 (46.5%)	250 (45.3%)	
Other	64 (6.4%)	28 (6.3%)	36 (6.5%)	
Missing	12 (1.2%)	4 (0.9%)	8 (1.4%)	
BI-RADS® Density				
A	113 (11.3%)	58 (13.0%)	55 (10.0%)	<0.005
B	552 (55.4%)	258 (58.0%)	294 (53.3%)	
C	310 (31.1%)	113 (25.4%)	197 (35.7%)	
D	22 (2.2%)	16 (3.6%)	6 (1.1%)	
BMI, Median (IQR)	28.1 (23.8–33.6)	26.7 (23.5–32.3)	29.9 (24.6–35.3)	<0.005

* Population used for radiomic feature dimensionality reduction steps described in Section 2.3.2. † Subpopulation used for calculation of radiomic feature robustness metrics: IAV, IWV, and CMV. ‡ *p*-Value by Fisher's exact test for categorical covariates, Mann–Whitney-Wilcoxon test for BMI.

3.2.2. Robustness Calculations

Most IAV scores were clustered around zero, with a long tail corresponding to features highly sensitive to imaging physics: range = 0–1.85, median = 0.12, mean = 0.20, IQR = 0.04–0.19 (Figure 3a). IWV scores, however, showed a peak above zero, indicating that some difference in texture between the two lateralities of the same woman is normal. IWV range = 0–0.4, median = 0.09, mean = 0.10, IQR = 0.08–0.11 (Figure 3b).

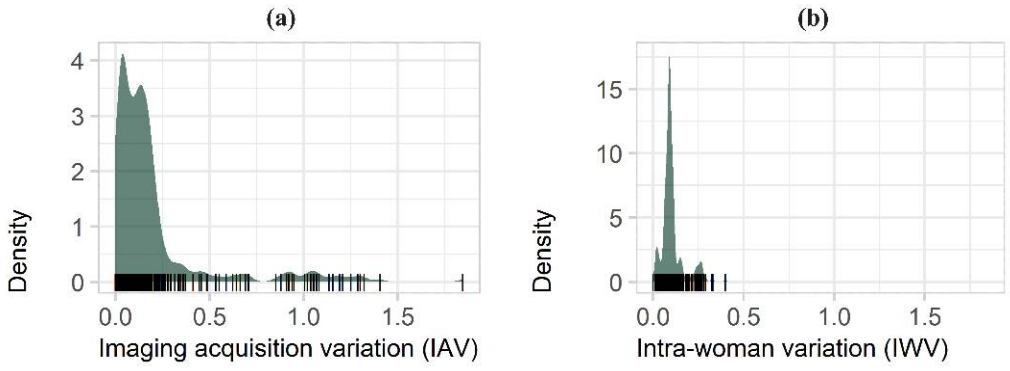

Figure 3. Summary of IAV and IWV results for all 341 features. (**a**) Histogram of IAV scores, with the long tail of features that are highly sensitive to imaging physics; (**b**) Histogram of IWV scores (this shows no such long tail).

In the IAV × IWV space (Figure 4), each feature corresponds to a data point from which we calculated CMV; i.e., Euclidean distance from the origin (the point for which IAV = IWV = 0). More robust features have lower CMV scores, approaching zero. In the Supplementary Materials, the distribution of CMV scores is analyzed explicitly in each of the eight feature families (Figure S4).

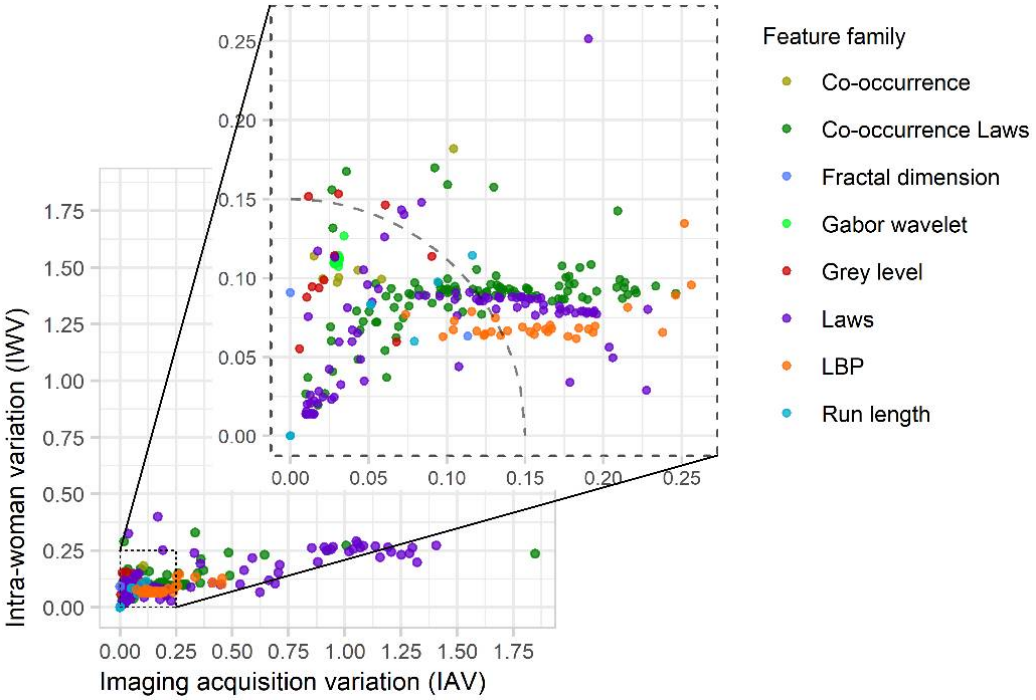

Figure 4. Summary of results obtained in IAV × IWV space for 341 features. The circular arc illustrates a threshold (CMV = 0.15) used to identify robust features (158 of 341 features, or 46%, are within this cutoff).

For this work, a strict cut-off dichotomizing features as either robust or nonrobust is not being proposed. However, if one were to accept 15% non-meaningful variation as the maximum for either clinical use or research, the circular arc in Figure 4 shows a CMV threshold of 0.15 as an example that might be chosen. There are 158 features of 341 (46%) that meet this threshold. Depending on the application, a more conservative or more liberal threshold might be chosen.

3.2.3. Examples of Robust and Non-Robust Features

Heatmaps of feature intensity within a breast can show the effects of imaging acquisition physics. Heatmaps of a feature in clinical images, corresponding to the 5th, 50th, and 95th percentiles of the histograms (Figure 1), show clear differences between those breasts (Figures 5a–c and 6a–c). Heatmaps of the phantom, at the extremes and middle value of physics settings (Figure 1), show almost no variation in a robust feature (CMV = 0.11) (Figure 5d–f). However, in a feature that is strongly affected by imaging physics (CMV = 1.43), differences are evident among heatmaps of that feature in the phantom under different imaging settings (Figure 6d–f).

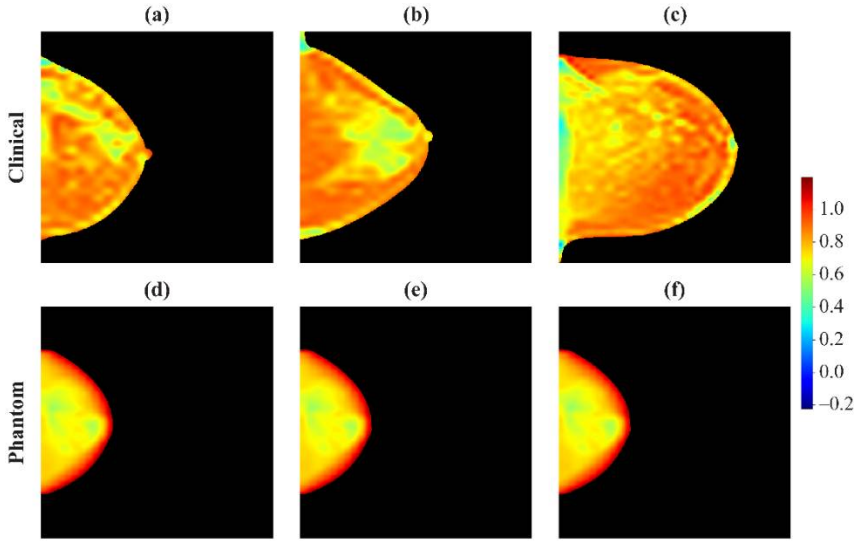

Figure 5. Heat maps for a robust feature (a Gabor Wavelet feature, CMV = 0.11) used as an example in Figure 1a. Top row: Clinical images at the (**a**) 5th, (**b**) 50th, and (**c**) 95th percentiles of the distribution in Figure 1a. Bottom row: Phantom images derived from various acquisition settings, corresponding to (**d**) left-most, (**e**) intermediate, and (**f**) right-most data points in Figure 1a. While there are clear differences between the three patients, the heat maps for the phantom are effectively identical. For the purposes of illustration, these figures are smoothed to avoid artifacts of pixelation.

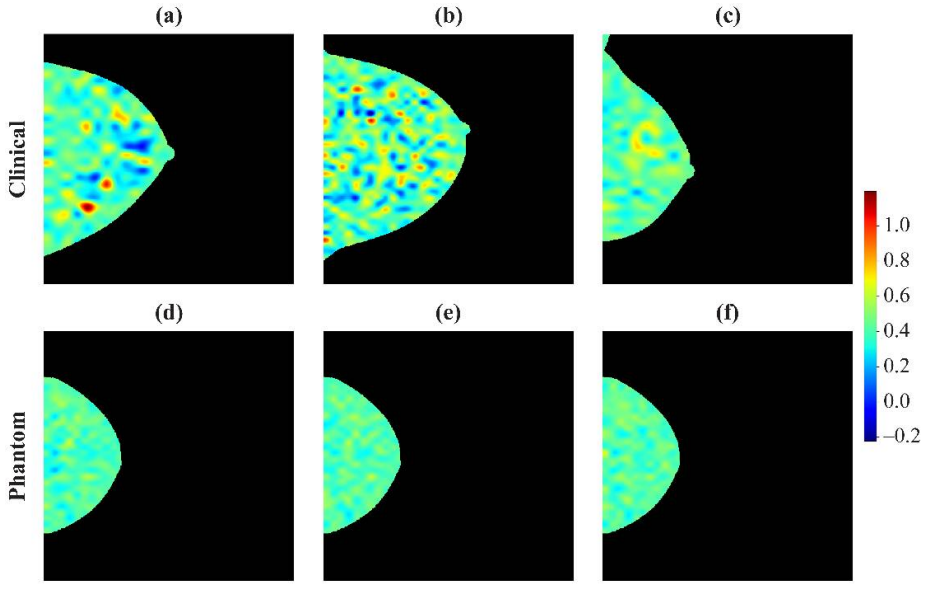

Figure 6. Heat maps for a non-robust feature (a Laws feature, CMV = 1.43) used as an example in Figure 1b. Top row: Heat maps derived from patients at the (**a**) 5th, (**b**) 50th, and (**c**) 95th percentiles of the distribution in Figure 1b. Bottom row: Heat maps illustrating how this feature is affected by variations in the imaging acquisition parameters, i.e., the (**d**) left-most, (**e**) intermediate, and (**f**) right-most data points in Figure 1b. Similar to Figure 5, these heat maps are smoothed to avoid artifacts of pixelation.

3.3. Case-Control Evaluation

3.3.1. Dimensionality Reduction

After eliminating the highly-skewed, highly-tailed, and highly-correlated features, we retained 109 features. It was necessary to exclude one feature to ensure equal sized feature robustness quartiles, thus we excluded the highest-CMV of the 109. In the Supplementary

Materials, we summarize (by feature family) which of the 341 features were retained (Table S3).

3.3.2. Performance Evaluation

In the independent case-control data set, there were 115 cases, including 86 invasive cancers (75%) and 29 in situ cancers (25%). The remaining 460 images were matched controls (Table 2). There was an overall trend to higher AUC (better case-control classification) in models built using more robust features, with mean (SD) AUC for classes D–A of 0.54 (0.029), 0.56 (0.023), 0.56 (0.029), and 0.59 (0.023) (Figure 7).

Table 2. Characteristics of participants in independent data set used to test the performance of radiomic features in case-control regression.

Characteristic	Total Population: 575 Women	Cases: 115 Women	Controls: 460 Women	*p*-Value *
Age				
<40	10 (1.7%)	2 (1.7%)	8 (1.7%)	1
[40, 50)	145 (25.2%)	29 (25.2%)	116 (25.2%)	
[50, 60)	135 (23.5%)	27 (23.5%)	108 (23.5%)	
[60, 70)	180 (31.3%)	36 (31.3%)	144 (31.3%)	
≥70	105 (18.3%)	21 (18.3%)	84 (18.3%)	
Race				
Black	305 (53.0%)	61 (53.0%)	244 (53.0%)	1
White	270 (47.0%)	54 (47.0%)	216 (47.0%)	
BI-RADS® Density				
A	63 (11.0%)	9 (7.8%)	54 (11.7%)	0.08
B	340 (59.1%)	61 (53.0%)	279 (60.7%)	
C	161 (28.0%)	38 (33.0%)	123 (26.7%)	
D	6 (1.0%)	3 (2.6%)	3 (0.7%)	
Missing	5 (0.9%)	4 (3.5%)	1 (0.2%)	
BMI, Median (IQR)	28.3 (23.7–34.6)	28.1 (23.6–34.7)	29 (24.2–34.5)	0.54

* *p*-value by Fisher's exact test for categorical covariates, Mann–Whitney–Wilcoxon test for BMI.

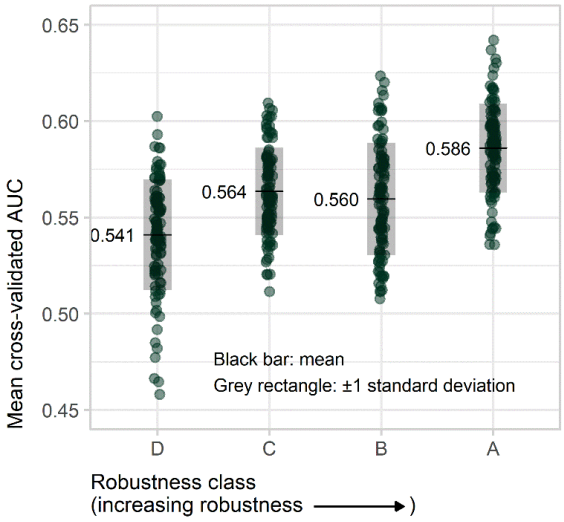

Figure 7. Mean five-fold cross-validated AUC results obtained with resampling techniques. There is an overall trend of higher AUC going from class D (least robust features) to A (most robust features). This demonstrates that more robust features offer superior case-control classification performance in risk-assessment calculations.

The linear mixed model regression of AUC on feature class, with class D (the least robust features) as the reference class, gave $p < 0.005$ for a difference between each of classes A through C and the reference class (Table 3).

Table 3. Statistical analysis of AUC results in four robustness classes using mixed model logistic regression. The reference class (D) consists of the least robust features. Classes with more robust features (A, B, and C) tend to offer statistically-higher AUCs in case-control classification.

Robustness Class	CMV Range (Mean)	AUC Mean (SD)	Coefficient (95% CI)	Standard Error	*p*-Value *
D	0.47–1.43 (0.97)	0.54 (0.029)	*Reference*		
C	0.19–0.46 (0.30)	0.56 (0.023)	0.022 (0.015–0.030)	0.004	<0.005
B	0.14–0.19 (0.16)	0.56 (0.029)	0.018 (0.011–0.026)	0.004	<0.005
A	0.020–0.14 (0.089)	0.59 (0.023)	0.045 (0.038–0.052)	0.004	<0.005

* Versus null hypothesis that coefficient is zero. SD of random effects: 0.004. Model *p*-value < 0.005 (versus null hypothesis that AUC is unrelated to robustness class).

4. Discussion

As the number of features used in radiomics studies continues to grow, it is essential to understand whether features capture information about parenchymal and pathophysiological differences between women, and/or measure variations in imaging acquisition physics (contrast, noise, and image sharpness). In this study, we investigated how much a feature varies across imaging acquisition settings (kV and mAs) in DM. It is not practical or ethical to image the same woman multiple times under various acquisition settings. An alternate approach is to perform these experiments with a phantom. We analyzed a phantom that was derived from an actual woman's mammogram [16]. The x-ray experiments in this study were equivalent to imaging that woman under various technique settings. These acquisitions included three different physics effects: (1) variation in kV (contrast); (2) variation in mAs (relative signal to noise); and (3) image replication (quantum noise).

Although a phantom is essential for understanding the effect of imaging acquisition physics, the phantom alone is insufficient for identifying robust features. Combining the phantom results with a large clinical data set allowed us to measure how much the variation across technique setting scales against the variation across women. In addition, the clinical data set allowed us to calculate IWV for each feature, so that we could identify features that are insensitive to both imaging physics effects and to left–right differences in the same woman.

Our previous work showed that radiomic features may vary with the compressed breast thickness [27]. This observation motivated us to define the robustness metrics (Equations (1)–(3)) in such a way as to capture information from only a subset of women (thickness of $\pm$10 mm relative to the phantom in CC view). The purpose of restricting the thickness range was to ensure that the denominator of IAV (Equation (1)) is not skewed in some features that may be more strongly sensitive to thickness (given that the numerator models only one thickness, 50 mm, in the phantom). We are cognizant that this approach is a potential limitation of this study and that future work also needs to explore how the metrics IAV and IWV would change if a different phantom or a different clinical data set were chosen for the analysis (differing, for example, in terms of ethnicity, age, breast density, and body mass index).

Prior works have proposed the idea of standardizing feature calculations across different acquisition settings. For example, Andrearczyk et al. used neural networks and domain adversarial training to standardize radiomic features across computed tomography scanners with different protocols using a texture phantom [28]. Our current study offers

a different perspective on understanding a feature's variation across imaging acquisition settings. The emphasis of our current study is not on developing a transformation to standardize the feature's values across different acquisition settings, but instead, on identifying which features are least sensitive to these settings, so that risk-assessment models in future studies could be built exclusively with robust features.

With an independent case-control data set, we demonstrated a statistically-significant increase in AUC in logistic regression models built with lower-CMV (more robust) features. Based on these results, we project that models built exclusively with robust features will offer superior estimates of breast cancer risk.

One potential criticism is that the AUCs observed in this study are lower than those in other published works [5,25]. However, the mean cross-validated AUC of 0.59 obtained here from the most robust class of features was not much lower than those in the work of Gastounioti et al. on the same dataset (cross-validated AUCs 0.59 to 0.67) [25]. Crucially, the risk-assessment models in Gastounioti's work, and elsewhere in the literature, incorporate established demographic and clinical risk factors for breast cancer. We project that the best modeling practices described elsewhere, combined with a preference for low-CMV radiomic features, will further improve predictive performance.

One limitation of our study is the nature of the case-control analysis. In comparing the performance of features from one CMV quartile with those from another, we are necessarily comparing different features; moreover, different radiomic features will have different associations with cancer incidence regardless of CMV. Some radiomic features and combinations of features capture more information reflective of cancer risk, some less. We mitigate this weakness through, first, measuring AUC over multiple subsets of features within each quartile—reducing the impact of any single feature or feature combination with particularly good or bad predictive power; and second, via the mixed-model regression, assessing both the between-quartile and within-quartile variation in performance. However, the underlying limitation remains inherent to the nature of the comparison.

A further limitation is that, as the phantom was designed to simulate a CC view, we considered only CC views of clinical data in calculating the robustness metrics (Equations (1)–(3)). However, the data set used in the case-control analysis consisted predominately of MLO views, and we do not yet know how IAV and IWV are affected by CC versus MLO image data [25]. Further work could explore the effect of imaging view on feature robustness metrics.

An additional limitation of this paper is that we did not specifically identify the features that show so little variability in the population that they offer no predictive value in breast cancer risk assessment. Future work should explore strategies to identify such features; this strategy could potentially complement the robust feature selection method proposed in this paper as a way to improve cancer risk assessment.

A very important future extension will be to replicate the robustness calculations described in this study with data obtained with digital breast tomosynthesis (DBT) or "3D mammography", a modality now increasingly replacing DM for breast cancer screening [29–32]. Future experiments with DBT would require a phantom suited for 3D imaging, as the Gammex-169 phantom was designed specifically for 2D x-ray imaging in the 1980s, well before the clinical implementation of DBT [16].

More generally, to ensure the broad applicability of the calculations described here, the work should be extended to more image types. For the many medical centers that do not retain copies of the raw ("FOR PROCESSING") DM images, these should include processed ("FOR PRESENTATION") DM images; other important types are individual projection images in a tomosynthesis acquisition (both raw and processed), a DBT reconstruction or reconstructed slice, and synthetic 2D images derived from a DBT scan [33]. Future work should also replicate the calculations described in this study with different software packages for texture feature extraction, for example, with an open-source software such as PyRadiomics or the Cancer Imaging Phenotypes Toolkit (CaPTk) [34–36]. It will also be important to validate the conclusions of this study on images from multiple facilities and multiple imaging device manufacturers.

5. Conclusions

The number of radiomic features being developed for risk-assessment modeling is constantly growing. However, having more features is not necessarily beneficial if the features are highly sensitive to imaging physics effects (contrast, noise, and image sharpness) and to non-meaningful feature differences, such as those between a woman's left and right breasts. This paper proposes a method to identify robust radiomic features in DM by combining clinical data with phantom data acquired over a range of imaging acquisition settings. As new features are developed, this offers a method for selecting the features most likely to offer improvements in risk modeling—those which are more robust based on our measure of CMV.

Supplementary Materials: The following are available online at https://www.mdpi.com/article/10.3390/cancers13215497/s1, Figure S1: Example DM acquisitions of Gammex 169 phantom at two technique settings, illustrated here with processed ("FOR PRESENTATION") images, though the radiomic feature calculations were performed with raw ("FOR PROCESSING") images, Table S1: Auto-time mAs setting at each kV for Gammex 169 phantom using W/Rh target/filter combination (data from Proc. SPIE 11314, Medical Imaging 2020: Computer-Aided Diagnosis, 113140W (16 March 2020); https://doi.org/10.1117/12.2549163, Figure S2: (a) Trends across kV for a robust feature (a Gabor Wavelet feature for which CMV = 0.11), with mAs at each kV given by Table S1 and each data point determined by the average of two acquisitions of the phantom, (b) Trends across mAs at a fixed kV (31 kV) for the same feature, with each data point determined by the average of two acquisitions of the phantom, (c) Distribution of feature values, used for Z-score normalization in all three subplots, derived from the subpopulation of women in Table 1 with thickness in [40, 60] mm, Figure S3: (a) Trends across kV for a nonrobust feature (a Laws feature for which CMV = 1.43), with mAs at each kV given by Table S1 and each data point determined by the average of two acquisitions of the phantom, (b) Trends across mAs at a fixed kV (31 kV) for the same feature, with each data point determined by the average of two acquisitions of the phantom, (c) Distribution of feature values, used for Z-score normalization in all three subplots, derived from the subpopulation of women in Table 1 with thickness in [40, 60] mm, Table S2: Range of mAs values seen clinically in women with compressed breast thickness in [40, 60] mm; i.e., $\pm$10 mm relative to the phantom thickness (adapted from Proc. SPIE 11314, Medical Imaging 2020: Computer-Aided Diagnosis, 113140W (16 March 2020); https://doi.org/10.1117/12.2549163), Figure S4: CMV results by feature family, with dots indicating individual features, shaded box the IQR, and crossbar the median value; there is no obvious association between family and feature robustness, with some families yielding very similar CMV for all features and some families spanning quite a range, Table S3: Feature robustness quartile versus feature family (only features retained for case-control regression).

Author Contributions: Conceptualization, R.J.A., A.D.A.M. and D.K.; Data curation, R.J.A., E.A.C., O.H.M., A.G., L.P., M.-K.H., E.F.C., A.D.A.M. and D.K.; Formal analysis, R.J.A., E.A.C., O.H.M., A.G., E.F.C., C.G.S., S.J.W., K.K., C.V., A.D.A.M. and D.K.; Funding acquisition, C.V. and D.K.; Investigation, R.J.A., E.A.C., O.H.M., A.G., E.F.C., C.G.S., S.J.W., C.V., A.D.A.M. and D.K.; Methodology, R.J.A., E.A.C., O.H.M., A.G., M.-K.H., A.D.A.M. and D.K.; Project administration, C.V. and D.K.; Resources, E.F.C., C.V., A.D.A.M. and D.K.; Software, E.A.C., O.H.M. and M.-K.H.; Supervision, C.V., A.D.A.M. and D.K.; Validation, R.J.A., E.A.C., O.H.M., A.G., A.D.A.M. and D.K.; Visualization, R.J.A., E.A.C., O.H.M. and A.G.; Writing—original draft, R.J.A. and E.A.C.; Writing—review & editing, O.H.M., A.G., L.P., M.-K.H., E.F.C., C.G.S., S.J.W., K.K., C.V., A.D.A.M. and D.K. All authors have read and agreed to the published version of the manuscript.

Funding: This research was funded by the National Institutes of Health, grant numbers R01CA207084, R01CA161749, and U54CA163313; the Department of Defense Breast Cancer Research Program, grant number W81XWH-18-1-0082; and the Susan G. Komen® Foundation, grant number PDF17479714. The APC was funded by the National Institutes of Health, grant number R01CA161749. The content is solely the responsibility of the authors and does not necessarily represent the official views of the funding agencies.

Institutional Review Board Statement: The study was conducted according to the guidelines of the Declaration of Helsinki, and approved by the Institutional Review Board (IRB) of the University of Pennsylvania under expedited review category 5 on 8/27/2018 authorized by 45 CFR 46.110 (Review Board IRB #7, Protocol #825735). All methods were performed in accordance with the guidelines and regulations related to the IRB approval and HIPAA.

Informed Consent Statement: Patient consent was waived under expedited review category 5 by the University of Pennsylvania IRB.

Data Availability Statement: The data generated during the current study are available from the corresponding author on reasonable request.

Conflicts of Interest: E.F.C. reports membership on the Hologic, Inc., Scientific Advisory Board and a research grant with the same vendor; E.F.C. also reports membership in the iCAD, Inc., Scientific Advisory Board and a research grant with the same vendor. A.D.A.M. reports research support from Hologic, Inc., Barco nv, and Analogic Corporation; is a spouse to an employee and stockholder of Real Time Tomography (RTT), LLC; is a member of the scientific advisory board of RTT; and is an owner of Daimroc Imaging, LLC. The other authors have no relevant conflicts of interest to disclose. These vendors had no role in the design of the study; the collection, analysis, or interpretation of the data; the writing of the manuscript; or the decision to submit the manuscript for publication. R.J.A., E.A.C., O.H.M., A.G., L.P., M.-K.H., C.G.S., S.J.W., K.K., C.V. and D.K. declare no competing interests.

References

1. Boyd, N.F.; Rommens, J.M.; Vogt, K.; Lee, V.; Hopper, J.L.; Yaffe, M.J.; Paterson, A. Mammographic breast density as an intermediate phenotype for breast cancer. *Lancet Oncol.* **2005**, *6*, 798–808. [CrossRef]
2. Boyd, N.F.; Guo, H.; Martin, L.J.; Sun, L.; Stone, J.; Fishell, E.; Jong, R.A.; Hislop, G.; Chiarelli, A.; Minkin, S.; et al. Mammographic Density and the Risk and Detection of Breast Cancer. *N. Engl. J. Med.* **2007**, *356*, 227–236. [CrossRef] [PubMed]
3. Wanders, J.O.P.; Holland, K.; Karssemeijer, N.; Peeters, P.H.M.; Veldhuis, W.B.; Mann, R.M.; van Gils, C.H. The effect of volumetric breast density on the risk of screen-detected and interval breast cancers: A cohort study. *Breast Cancer Res.* **2017**, *19*, 67. [CrossRef] [PubMed]
4. Zheng, Y.; Keller, B.M.; Ray, S.; Wang, Y.; Conant, E.F.; Gee, J.C.; Kontos, D. Parenchymal texture analysis in digital mammography: A fully automated pipeline for breast cancer risk assessment. *Med. Phys.* **2015**, *42*, 4149–4160. [CrossRef] [PubMed]
5. Gastounioti, A.; Conant, E.F.; Kontos, D. Beyond breast density: A review on the advancing role of parenchymal texture analysis in breast cancer risk assessment. *Breast Cancer Res.* **2016**, *18*, 1–12. [CrossRef]
6. Malkov, S.; Shepherd, J.A.; Scott, C.G.; Tamimi, R.M.; Ma, L.; Bertrand, K.A.; Couch, F.; Jensen, M.R.; Mahmoudzadeh, A.P.; Fan, B.; et al. Mammographic texture and risk of breast cancer by tumor type and estrogen receptor status. *Breast Cancer Res.* **2016**, *18*, 122, Erratum in **2017**, *19*, 1. [CrossRef]
7. Balagurunathan, Y.; Kumar, V.; Gu, Y.; Kim, J.; Wang, H.; Liu, Y.; Goldgof, D.B.; Hall, L.O.; Korn, R.; Zhao, B.; et al. Test–Retest Reproducibility Analysis of Lung CT Image Features. *J. Digit. Imaging* **2014**, *27*, 805–823. [CrossRef]
8. Zhang, Y.; Oikonomou, A.; Wong, A.; Haider, M.A.; Khalvati, F. Radiomics-based Prognosis Analysis for Non-Small Cell Lung Cancer. *Sci. Rep.* **2017**, *7*, srep46349. [CrossRef]
9. Parmar, C.; Grossmann, P.; Bussink, J.; Lambin, P.; Aerts, H.J.W.L. Machine Learning methods for Quantitative Radiomic Biomarkers. *Sci. Rep.* **2015**, *5*, 13087. [CrossRef]
10. Rizzo, S.; Botta, F.; Raimondi, S.; Origgi, D.; Buscarino, V.; Colarieti, A.; Tomao, F.; Aletti, G.; Zanagnolo, V.; Del Grande, M.; et al. Radiomics of high-grade serous ovarian cancer: Association between quantitative CT features, residual tumour and disease progression within 12 months. *Eur. Radiol.* **2018**, *28*, 4849–4859. [CrossRef] [PubMed]
11. Huynh, E.; Coroller, T.P.; Narayan, V.; Agrawal, V.; Romano, J.; Franco, I.; Parmar, C.; Hou, Y.; Mak, R.H.; Aerts, H.J.W.L. Associations of Radiomic Data Extracted from Static and Respiratory-Gated CT Scans with Disease Recurrence in Lung Cancer Patients Treated with SBRT. *PLoS ONE* **2017**, *12*, e0169172. [CrossRef]
12. Wilkinson, L.; Friendly, M. The History of the Cluster Heat Map. *Am. Stat.* **2009**, *63*, 179–184. [CrossRef]
13. Rizzo, S.; Botta, F.; Raimondi, S.; Origgi, D.; Fanciullo, C.; Morganti, A.G.; Bellomi, M. Radiomics: The facts and the challenges of image analysis. *Eur. Radiol. Exp.* **2018**, *2*, 1–8. [CrossRef]
14. Robinson, K.; Li, H.; Lan, L.; Schacht, D.; Giger, M. Radiomics robustness assessment and classification evaluation: A two-stage method demonstrated on multivendor FFDM. *Med. Phys.* **2019**, *46*, 2145–2156. [CrossRef]
15. Mendel, K.R.; Li, H.; Lan, L.; Cahill, C.M.; Rael, V.; Abe, H.; Giger, M.L. Quantitative texture analysis: Robustness of radiomics across two digital mammography manufacturers' systems. *J. Med. Imaging* **2017**, *5*, 011002. [CrossRef]
16. Yaffe, M.J.; Johns, P.C.; Nishikawa, R.M.; Mawdsley, G.E.; Caldwell, C.B. Anthropomorphic radiologic phantoms. *Radiology* **1986**, *158*, 550–552. [CrossRef]

17. Keller, B.M.; Oustimov, A.; Wang, Y.; Chen, J.; Acciavatti, R.J.; Zheng, Y.; Ray, S.; Gee, J.C.; Maidment, A.D.A.; Kontos, D. Parenchymal texture analysis in digital mammography: Robust texture feature identification and equivalence across devices. *J. Med. Imaging* **2015**, *2*, 24501. [CrossRef] [PubMed]
18. Conant, E.F.; Keller, B.M.; Pantalone, L.; Gastounioti, A.; McDonald, E.S.; Kontos, D. Agreement between Breast Percentage Density Estimations from Standard-Dose versus Synthetic Digital Mammograms: Results from a Large Screening Cohort Using Automated Measures. *Radiology* **2017**, *283*, 673–680. [CrossRef]
19. Keller, B.M.; Nathan, D.L.; Wang, Y.; Zheng, Y.; Gee, J.C.; Conant, E.F.; Kontos, D. Estimation of breast percent density in raw and processed full field digital mammography images via adaptive fuzzy c-means clustering and support vector machine segmentation. *Med. Phys.* **2012**, *39*, 4903–4917. [CrossRef] [PubMed]
20. Haralick, R.M.; Shanmugam, K.; Dinstein, I. Textural Features for Image Classification. *IEEE Trans. Syst. Man. Cybern.* **1973**, *3*, 610–621. [CrossRef]
21. Galloway, M.M. Texture analysis using gray level run lengths. *Comput. Graph. Image Process.* **1975**, *4*, 172–179. [CrossRef]
22. Chu, A.; Sehgal, C.; Greenleaf, J. Use of gray value distribution of run lengths for texture analysis. *Pattern Recognit. Lett.* **1990**, *11*, 415–419. [CrossRef]
23. Ojala, T.; Pietikainen, M.; Maenpaa, T. Multiresolution gray-scale and rotation invariant texture classification with local binary patterns. *IEEE Trans. Pattern Anal. Mach. Intell.* **2002**, *24*, 971–987. [CrossRef]
24. Manduca, A.; Carston, M.J.; Heine, J.J.; Scott, C.; Pankratz, V.S.; Brandt, K.R.; Sellers, T.A.; Vachon, C.M.; Cerhan, J.R. Texture Features from Mammographic Images and Risk of Breast Cancer. *Cancer Epidemiol. Biomarkers Prev.* **2009**, *18*, 837–845. [CrossRef]
25. Gastounioti, A.; Hsieh, M.-K.; Cohen, E.; Pantalone, L.; Conant, E.F.; Kontos, D. Incorporating Breast Anatomy in Computational Phenotyping of Mammographic Parenchymal Patterns for Breast Cancer Risk Estimation. *Sci. Rep.* **2018**, *8*, 1–10. [CrossRef]
26. Gandrud, C. *Reproducible Research with R and R Studio*; CRC Press: Boca Raton, FL, USA, 2013.
27. Acciavatti, R.J.; Gastounioti, A.; Hu, Y.; Maidment, A.D.; Kontos, D.; Chen, J.; Hsieh, M.-K. Validation of the textural realism of a 3D anthropomorphic phantom for digital breast tomosynthesis. In Proceedings of the 14th International Workshop on Breast Imaging (IWBI 2018), Atlanta, GA, USA, 8–11 July 2018; Volume 10718, p. 107180R. [CrossRef]
28. Andrearczyk, V.; Depeursinge, A.; Müller, H. Neural network training for cross-protocol radiomic feature standardization in computed tomography. *J. Med. Imaging* **2019**, *6*, 024008. [CrossRef]
29. Sechopoulos, I. A review of breast tomosynthesis. Part I. The image acquisition process. *Med. Phys.* **2013**, *40*, 014301. [CrossRef] [PubMed]
30. Sechopoulos, I. A review of breast tomosynthesis. Part II. Image reconstruction, processing and analysis, and advanced applications. *Med. Phys.* **2013**, *40*, 014302. [CrossRef] [PubMed]
31. Friedewald, S.M.; Rafferty, E.A.; Rose, S.L.; Durand, M.A.; Plecha, D.M.; Greenberg, J.S.; Hayes, M.K.; Copit, D.S.; Carlson, K.L.; Cink, T.M.; et al. Breast Cancer Screening Using Tomosynthesis in Combination With Digital Mammography. *JAMA* **2014**, *311*, 2499–2507. [CrossRef] [PubMed]
32. Conant, E.F.; Zuckerman, S.P.; McDonald, E.S.; Weinstein, S.P.; Korhonen, K.E.; Birnbaum, J.A.; Tobey, J.D.; Schnall, M.D.; Hubbard, R.A. Five Consecutive Years of Screening with Digital Breast Tomosynthesis: Outcomes by Screening Year and Round. *Radiology* **2020**, *295*, 285–293. [CrossRef]
33. Gastounioti, A.; Oustimov, A.; Keller, B.M.; Pantalone, L.; Hsieh, M.-K.; Conant, E.F.; Kontos, D. Breast parenchymal patterns in processed versus raw digital mammograms: A large population study toward assessing differences in quantitative measures across image representations. *Med. Phys.* **2016**, *43*, 5862–5877. [CrossRef] [PubMed]
34. Van Griethuysen, J.J.; Fedorov, A.; Parmar, C.; Hosny, A.; Aucoin, N.; Narayan, V.; Beets-Tan, R.G.; Fillion-Robin, J.-C.; Pieper, S.; Aerts, H.J. Computational Radiomics System to Decode the Radiographic Phenotype. *Cancer Res.* **2017**, *77*, e104–e107. [CrossRef] [PubMed]
35. Davatzikos, C.; Rathore, S.; Bakas, S.; Pati, S.; Bergman, M.; Kalarot, R.; Sridharan, P.; Ou, Y.; Jahani, N.; Cohen, E.; et al. Cancer imaging phenomics toolkit: Quantitative imaging analytics for precision diagnostics and predictive modeling of clinical outcome. *J. Med. Imaging* **2018**, *5*, 011018. [CrossRef]
36. Pati, S.; Singh, A.; Rathore, S.; Gastounioti, A.; Bergman, M.; Ngo, P.; Ha, S.M.; Bounias, D.; Minock, J.; Murphy, G.; et al. The Cancer Imaging Phenomics Toolkit (CaPTk): Technical Overview. In *Brainlesion: Glioma, Multiple Sclerosis, Stroke and Traumatic Brain Injuries*; Springer: Berlin, Germany, 2020; Volume 11993, pp. 380–394. [CrossRef]

Computational Breast Anatomy Simulation Using Multi-Scale Perlin Noise

Bruno Barufaldi, Craig K. Abbey, Miguel A. Lago, Trevor L. Vent, *Graduate Student Member, IEEE*, Raymond J. Acciavatti, Predrag R. Bakic, and Andrew D. A. Maidment, *Senior Member, IEEE*

***Abstract*— Virtual clinical trials (VCTs) of medical imaging require realistic models of human anatomy. For VCTs in breast imaging, a multi-scale Perlin noise method is proposed to simulate anatomical structures of breast tissue in the context of an ongoing breast phantom development effort. Four Perlin noise distributions were used to replace voxels representing the tissue compartments and Cooper's ligaments in the breast phantoms. Digital mammography and tomosynthesis projections were simulated using a clinical DBT system configuration. Power-spectrum analyses and higher-order statistics properties using Laplacian fractional entropy (LFE) of the parenchymal texture are presented. These objective measures were calculated in phantom and patient images using a sample of 140 clinical mammograms and 500 phantom images. Power-law exponents were calculated using the slope of the curve fitted in the low frequency [0.1, 1.0] mm^{-1} region of the power spectrum. The results show that the images simulated with our prior and proposed Perlin method have similar power-law spectra when compared with clinical mammograms. The power-law exponents calculated are −3.10, −3.55, and −3.46, for the log-power spectra of patient, prior phantom and proposed phantom images, respectively. The results also indicate an improved agreement between the mean LFE estimates of Perlin-noise based phantoms and patients than our prior phantoms and patients. Thus, the proposed method improved the simulation of anatomic noise substantially compared to our prior method, showing close agreement with breast parenchyma measures.**

***Index Terms*— Perlin noise, virtual clinical trial, anthropomorphic breast phantom, digital breast tomosynthesis.**

Manuscript received January 29, 2021; revised April 21, 2021 and June 3, 2021; accepted June 6, 2021. Date of publication June 9, 2021; date of current version November 30, 2021. This work was supported in part by the Department of Defense Breast Cancer Research Program under Grant W81XWH-18-1-0082; in part by the Burroughs Wellcome Fund (BWF) under Grant IRSA 1016451; in part by the 2020 AAPM Research Seed Funding Grant from American Association of Physicists in Medicine; in part by the National Institute of Health (NIH) under Grant NIH R01 CA154444, Grant NIH R01 EB018958, Grant NIH R01-EB025829; and in part by the Komen Foundation under Grant IIR-13262248. *(Corresponding author: Bruno Barufaldi.)*

Bruno Barufaldi, Trevor L. Vent, Raymond J. Acciavatti, Predrag R. Bakic, and Andrew D. A. Maidment are with the Department of Radiology, University of Pennsylvania, Philadelphia, PA 19104 USA (e-mail: bruno.barufaldi@pennmedicine.upenn.edu; trevor.vent@pennmedicine.upenn.edu; racci@pennmedicine.upenn.edu; predrag.bakic@pennmedicine.upenn.edu; andrew.maidment@pennmedicine.upenn.edu).

Craig K. Abbey and Miguel A. Lago are with the Department of Psychological and Brain Sciences, University of California at Santa Barbara, Santa Barbara, CA 93106 USA (e-mail: ckabbey@ucsb.edu; miguel.lago@ucsb.edu).

Digital Object Identifier 10.1109/TMI.2021.3087958

I. Introduction

VIRTUAL clinical trials (VCTs) for the evaluation, optimization, and validation of novel imaging systems require computational simulations of human anatomy (phantoms) [1]–[8] These phantoms have been used widely in breast imaging VCTs to support the pre-clinical assessment of mammography systems [9]–[11]. A VCT requires representative phantoms of a specific population with and without disease conditions and pathologies [1], especially when the VCT is targeted toward a particular clinical task [8]. For instance, breast imaging VCTs should simulate the anatomic noise seen in images of the mammary parenchyma, in particular for applications that require characterization of breast lesions or estimation of risk of masking cancers. Parenchymal texture is highly correlated to masking risk [12]–[14], affecting the ability of observers to detect and characterize breast abnormalities [15].

Digital mammography (DM), including digital breast tomosynthesis (DBT), has evolved rapidly over the last decade, resulting in improved visualization of the mammary parenchyma and increased sensitivity of cancer detection [16]–[19] VCTs offer a powerful *in-silico* alternative to accelerate the development of novel imaging technologies. VCTs should be able to replicate clinical trial studies by demonstrating the magnitude of improvement in imaging modalities. VCTs should also be sensitive to changes in diagnostic performance using new or modified imaging modalities. In x-ray breast imaging, many researchers have been using VCTs to predict improvements in DBT over DM [2], [6].

There is an ongoing effort by VCT researchers to improve the realism of human breast anatomy phantoms [15], [20]–[23]. We have been using anthropomorphic breast models developed at the University of Pennsylvania in several breast-imaging applications [2], [24]–[30]. These anthropomorphic phantoms simulate anatomic structures of the breast including: skin, adipose and fibroglandular tissue, and Cooper's ligaments [10], [31] However, depending upon the selection of simulation parameters, the resulting images may contain visible geometric structures [24], [32] that are considered unrealistic by human observers. It may also be possible to construct phantoms that are deemed to be realistic by humans but differ in higher-order statistics that would be perceived by machine observers.

Perlin noise has been used to simulate natural looking images, such as computer-rendered scenes in

computer-generated imagery (CGI) [33]–[37] (e.g., clouds, fog, and water), and texture or patterns in medical imaging [38]–[42] Perlin noise uses random gradient values that are smoothly connected by an interpolation function to simulate complex textures [43]. The simulation of Perlin textures depends on the combination of scaled noise functions that are implemented on a spatial frequency band with octave bandwidth [44], [45].

A fractal implementation of Perlin noise has been developed to simulate different amounts of breast density for anthropomorphic phantoms [38], [39]. The proposed method builds upon this work by dividing the breast tissue into regions with different noise characteristics to simulate glandular and adipose tissues more realistically. We routinely use human readers to tune and evaluate subjectively the realism of the simulated parenchyma. However, human reader studies must necessarily be limited in extent due to concerns of reader fatigue and time constraints. Thus, objective measures should be considered when one must optimize a large number of simulation parameters.

Power spectra measurements have been extensively explored to investigate, compare, and characterize breast images [30], [46]–[48]. However, these measurements do not fully characterize anatomical noise variability, since higher-order statistical structures are not necessarily captured in a second-order statistic [49], [50]. In a previous study, we proposed the use of the power spectra and Laplacian fractional entropy (LFE) measures to evaluate higher-order statistical properties of phantom images objectively [30]. The LFE measure is calculated from the relative entropy of the response histogram of an image compared to that of a Gaussian histogram matched for mean and variance [50]. These measures have shown to be an effective method to evaluate phantom realism and to select simulation parameters [30].

In this paper, we present a new method to simulate fine structures of breast tissue. The shape and gross anatomy are based on our existing breast phantom software [51], however the relatively uniform breast tissue compartments and Cooper's ligaments are replaced with mixtures of glandular and adipose voxels. The phantom is divided into four layers (masks) and a unique Perlin noise distribution is created for each layer. A multi-scale approach was used to define the Perlin noise between layers. The resulting Perlin noise was then used to introduce fine-scaled anatomical noise in the breast phantom. DM and DBT projections of the breast phantoms are synthesized using computer simulations of a clinical system. Finally, power-spectrum profiles and LFE measures are used to assess the breast phantom images through comparison with clinical mammograms.

II. Materials and Methods

A. Perlin Noise

Perlin's method involves the combination of multiple, scaled versions of a noise function [44], [45], [52]. The noise function is calculated from a discrete sequence of random gradient values g_u ($u \in \mathbb{Z}$); the gradients are uniformly distributed in the $[-1, 1]$ interval [43]. The values of the noise function (N) are obtained by piecewise interpolation using a local interpolating function F at arbitrary positions $x \in \mathbb{R}$ following the formalism:

$$N(x) = F(x, g_u, g_{u+1}), \quad \text{with } u = \lfloor x \rfloor; \tag{1}$$

The Perlin noise function (PN) is defined as the linear combination of multiple scaled version of the same noise function with K different frequencies and amplitudes: [43]

$$PN(x) = \sum_{i=0}^{K-1} a_i \cdot N(f_i \cdot x) \tag{2}$$

The frequencies are not arbitrary; i is an "octave" step. The frequencies are successively doubled in each octave step in the form $f_i = 2^i f_{min}$, for $i = 0, 1, \ldots, K-1$, where K represents the total number of frequencies [53], [54].

The amplitude values vary with the power of i in the form $a_i = \Phi^i$. The coefficient Φ is a constant that represents the "persistence" and it is typically set in a [0.25, 0.5] interval [43]. The properties of the Perlin noise depend essentially on the selection of the coefficients Φ, f_{min}, and the number of noise frequencies (K). A detailed formalism of the N-dimensional Perlin noise is found in Burger and Burge [43].

The noise functions are implemented in Java and distributed using a common library containing a collection of ImageJ plugins [55]. The common library was integrated into our open source Virtual Clinical Trial (VCT) framework [51], [56]. The VCT framework uses multithreaded processing on 3D phantoms through slice-wise 2D Perlin noise simulations. The slice-wise approach accelerates phantom creation and reduces computational burden from the 3D Perlin noise simulation. The Perlin noise library includes a hashing function [43], which ensures that there is textural continuity between slices. Thus, it is not necessary to use a 3D noise generator. Fig. 1 shows example regions of interest (ROIs), simulated using the implementation of 2D Perlin noise [43]. These examples are representative of the simulation parameters used in this work.

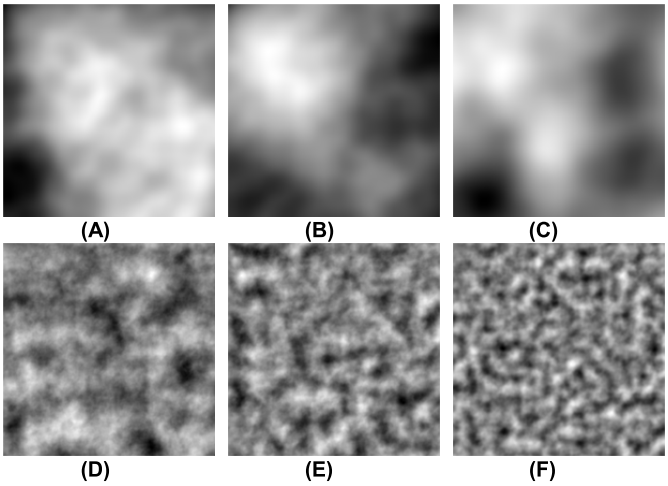

Fig. 1. Examples of Perlin noise frequencies (2D) simulated using respective coefficients f_{min}, K, and Φ: (A) 0.001, 4, 0.5; (B) 0.002, 3, 0.4; (C) 0.003, 2, 0.3; (D) 0.01, 4, 0.5; (E) 0.02, 3, 0.4; and (F) 0.03, 2, 0.3.

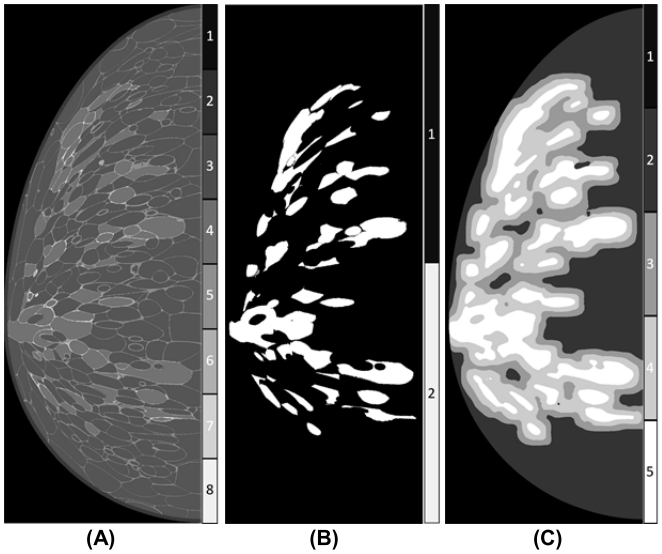

Fig. 2. (A) Central slice (sagittal plane) of one anthropomorphic breast phantom, which contains a complex combination of background (1) and breast tissue structures (2-8). (B) Glandular binary mask (2) used for morphological operations and (C) resulting adipose (2-3) and glandular (4-5) masks used for Perlin noise simulation.

B. Anthropomorphic Breast Phantoms

The VCT framework [51], [56] was used to generate voxelized breast phantoms [10], [31]. The phantoms are created using an octree-based recursive partitioning algorithm [10] that simulates anatomical structures of the breast. The algorithm sets compartment seeds randomly within a semi-ellipsoidal phantom model. Using the seed locations, ellipsoidal compartments split recursively, and fibrous Cooper's ligaments are set to connect the gap between compartments. Finally, a beta function is used to determine the composition of each breast compartment.

In total, 500 voxelized phantoms [$(0.1\ \text{mm})^3$ voxel size, 700 mL volume, and uncompressed breast thickness of 126.6 mm] were simulated. The phantom compartments consist of two fundamental voxel materials: adipose and glandular tissue. Each compartment is connected by Cooper's ligaments ([0.1, 0.18] mm thick) and filled with various tissue compositions ({0.1, 10, 20, 30, 50}% dense) [31]. Breast compression was simulated using GPU accelerated mesh software [1], [57] to a medio-lateral (ML) compression of 50% (63.3 mm thick).

A sample breast phantom is shown in Fig. 2A. Major modifications in the breast phantom generation software were implemented in this study to simulate more realistic breast compartments and Cooper's ligaments.

1) Breast Tissue Masks: The breast phantoms are composed of voxel material labels that represent the ground-truth for various tissue types and air (Fig. 2A). Glandular tissue labels were used to create glandular binary masks (Fig. 2B). Two morphological operations of dilation were applied on the binary masks using the methods implemented in the Imglib2 library developed in Java [58]. The dilation operations expand and create glandular tissue mask layers, which connect breast compartments and reduce the geometrical appearance of the dense compartments. We used dilations of 20 and 60 voxels with disk structuring elements. The output of each dilation mask and the original binary mask were combined, resulting in a three-layer dilation mask. Skin and background voxels were used to set the boundaries of the dilation mask. Dilated voxels located at the skin or in the background were cropped out from the dilation mask. Similarly, voxels that represent adipose compartments and adipose ligaments were identified to create a fourth binary mask for the adipose regions. This binary mask was combined with the dilated masks. The final resulting mask contains four layers; a different multi-scale Perlin noise distribution was calculated for each layer (Fig. 2C).

2) Perlin Noise Simulation: For each of the four mask layers, unique values of f_{min}, K, and Φ were selected based upon the work described by Burger and Burge [43] and values selected manually in a preliminary study we conducted with human observers. Thus, four independent distributions of Perlin noise were created to modify the voxels of the breast phantom.

For the most glandular layer, Perlin noise was simulated using f_{min}, K, and Φ in ranges [0.001, 0.007], [2, 4], and [0.2, 0.5], using steps of 0.001, 1, and 0.1, respectively. For the most adipose layer, Perlin noise was simulated using f_{min}, K, and Φ in ranges [0.01, 0.05], [2, 4], and [0.2, 0.5], using steps of 0.005, 1, and 0.1, respectively. For the two intervening layers, the parameter f_{min} was increased in equal steps from the glandular to the adipose layers, while Φ and K have the same values assigned to the most glandular layer.

The Perlin noise was normalized using a $[1, n]$ interval, where $n \in \mathbb{Z}^+$ and represents the number of voxel types assigned for the breast phantom. In this study, we considered $n = \{4, 8, 16, 32, 63\}$ to normalize the noise distributions. Thus, the voxels that represent the binary compartments in the prior breast phantoms (i.e., either adipose or glandular) were replaced to create multi-scaled voxels.

We varied each voxel based on the normalized Perlin noise distributions using a complementary mixture of adipose and glandular tissue (partial volume) [2], [27]. For voxels located at the most adipose layer (Fig. 2C.2), the adipose composition decreases from 99.9% to 50%; for the most glandular layer (Fig. 2C.5), the glandular composition increases from 50% to 99.9%. Similarly, for the partial volume of voxels located at the two intervening layers (Fig. 2C.3 and 2C.4), the percentage of glandular composition increases from 50% to 99.9%. A total of n partial volume combinations are simulated. The increase and decrease of the percent of tissue composition in the partial volume of each distribution follow two functions of n – linear $(an + b)$ and hyperbolic tangent $[\tanh(4n - 2)/2 + 0.5]$. Each value of n represents a particular voxel in the modified phantom (Perlin noise phantom) and it corresponds to a unique x-ray attenuation on the simulated images [59].

Finally, the voxels that represent Cooper's ligaments in the prior breast phantom were added back to the Perlin noise phantom. The x-ray attenuation of these voxels was also modified using partial volume of adipose and glandular tissue. We increased the portion of glandular composition by 20% to 50% and decreased the adipose composition accordingly in the Perlin noise phantoms.

TABLE I
SUMMARY OF IMAGING ACQUISITION GEOMETRIES SIMULATED

X-ray Modality	DBT	DM
Anode Material (a.u)	W	W
Filter Material (a.u)	Al	Rh/Ag
Filter Thickness (mm)	0.7	0.05
Angular Range (°)	[-7.5, +7.5]	-
Number of Projections (#)	15	1
Tube Motion (a.u)	Continuous	Stationary
Detector		
Detection Material (a.u.)	a-Se	a-Se
Detector Element Size (mm)	0.14×0.14	0.07×0.07
Number of Elements (#)	2048×1664	4096×3328
Detector Size (mm)	286.72×232.96	286.72×232.96
Source-to-Image Dist. (mm)	700.00	700.00
Reconstruction		
Pixel Size (mm)	0.10×0.10	-

C. Image Acquisition Simulation

DM and DBT projections of the breast phantoms were simulated using the OpenVCT Manager module [51], [56], which executes a fast GPU implementation of the Siddon algorithm for ray-tracing [60]. The Siddon algorithm traces a ray model from the source, through the phantom volume, onto each detector element. The radiological path length is determined by the sum of the length traveled by this ray in each voxel, multiplied by the density-ray attenuation of each voxel. This process is repeated for each ray trajectory, and the intensity of the rays in a detector element determine the pixel value for the projection image.

The DM and DBT projections were synthesized assuming the acquisition geometries shown in Table I. The acquisition exposure settings were simulated from automatic exposure control data of a clinical system [61]. We simulated polychromatic x-ray spectra. For DM images, the x-ray spectrum is simulated using W anode and Ag or Rh filtering materials. For DBT images, the x-ray spectrum is simulated using W anode with Al filtering materials. The attenuation coefficient data come from the ICRU Report 44 [62]. Reconstructed DBT slices were produced using simple backprojection with commercially available software library [63], [64].

D. Objective Assessment

A sample of clinical mammograms was used to collect objective measures of power spectrum and LFE. The clinical mammograms were acquired on Selenia Dimensions DBT systems (Hologic Inc., Bedford, MA). In total, 35 patients having 140 "for processing" screening mammograms (CC and MLO breast views). Similarly, DBT exams (CC and MLO breast views) were collected using a subset of these 35 patients (n=26). Nine patients were excluded because of incomplete data. In total, 104 DBT reconstructions were used for analysis [50]. Both DM and DBT clinical images were used as a reference for this study. The clinical data were collected retrospectively at UC Davis Medical Center and the Perlman Center for Advanced Medicine under IRB-approved human-subject protocols and HIPPA-compliant non-identifiable exams. All clinical data were published and validated in a previous study [50].

Binary masks of the breast outline were provided and used to calculate power spectra and LFE measurements in regions of interest (ROI). These masks were used to exclude background (air) and a 10 mm boundary (chest wall and skin) of the clinical images. This exclusion criterion was also used in phantom images. A summary of methods used to collect sample ROIs and calculate the power spectrum and LFE measures are shown in Fig. 3.

1) Power Spectrum: Anatomical structure can be captured using power spectra measures collected in breast images [48], [49]. Burgess *et al.* have shown that these structures are characterized by a power-law function in the form κ/f^{β}, where f is the radial spatial frequency of the noise power spectrum, κ is the magnitude, and β is the power-law exponent of the image spectrum [48], [49].

In this study, we calculated and compared β estimates using an ROI of size 512×512 pixels (35.84 mm^2), extracted from each DM phantom image and clinical mammogram. We used the center of mass calculated on the binary masks to select ROIs within the breast or phantom images (Fig. 3A). The center of mass is used as a reference point to automate the process of cropping ROIs, ensuring only valid values (nonzero) to estimate power-spectrum (PS). The PS is estimated using the fast Fourier transform (FFT) of each ROI sample:

$$PS(u,v) = \frac{1}{N}\sum_{i=0}^{N-1} |FFT[w(x,y) * (r_i(x,y) - \bar{r}(x,y))]|^2 \tag{3}$$

where $r_i(x,y)$ represents a ROI sample, $\bar{r}(x,y)$ is the average of samples, and $w(x,y)$ is a spatial window that is centered at the ROI. This spatial window remains constant out to a radius of 8.96 mm before decreasing to zero with a cosine profile at a radius of 17.92 mm. The spatial window is used to reduce spectral leakage in the power spectrum estimates. The spatial frequency indices (u,v) are both in the interval [0, N-1]. This method was validated and published in a previous study [50].

We calculated the logarithm (base 10) of PS over the radial spatial-frequency interval to plot the profile of the power spectrum. The radial frequencies were binned using a bin width of size 0.0274 cycles per mm [(1/(ROI size × pixel size)] [50]. The standard deviation across every sample was used to quantify the variability of the log-power spectrum [50]. We used a total of 140 and 500 ROIs of mammograms and phantoms, resulting in a standard error of 8.5% and 4.5%, respectively.

To compare the power spectra of phantom and patient images, β estimates of the power spectra were calculated using the slope of the linear regression of frequencies from 0.1 to 1 cycles per mm [30], [49].

2) Laplacian Fractional Entropy: LFE has been used to evaluate statistical-properties of phantoms [30] and clinical images acquired or simulated using various breast imaging modalities [50] (e.g., computed tomography, DM, and DBT). The LFE metric is based on Gabor-filter response histograms resulting from 2D convolutions of Gabor kernels with an

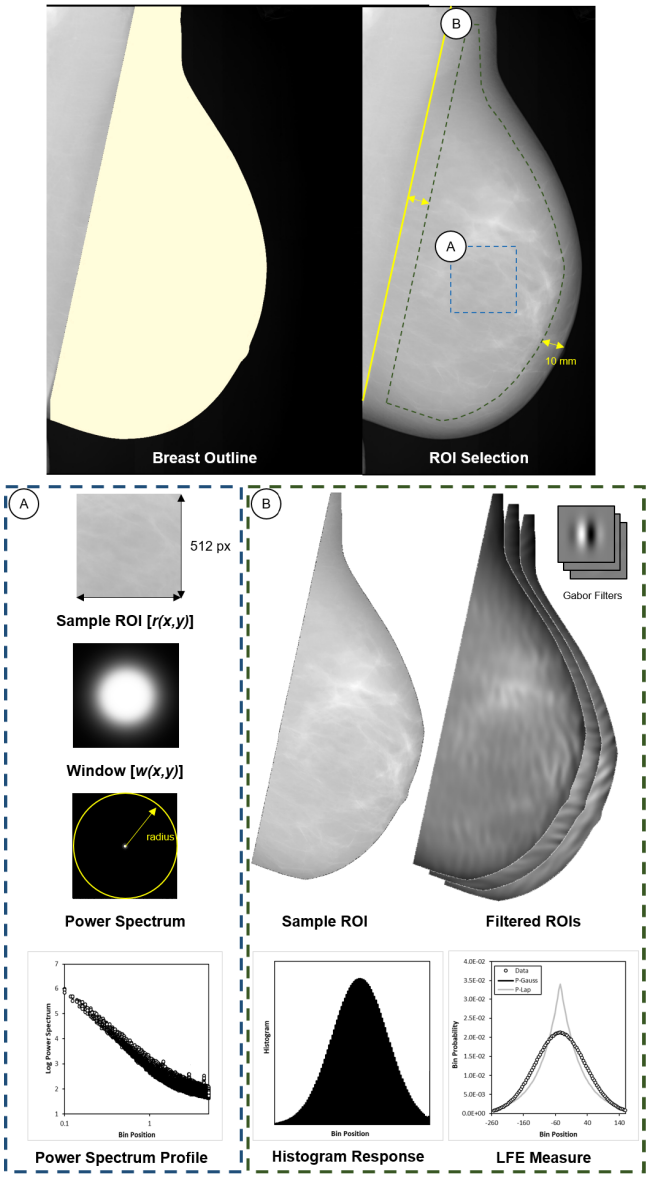

Fig. 3. Summary of method used to evaluate x-ray breast images objectively. (A) Assessment of the image power spectrum, and (B) Laplacian fractional entropy.

image in a region of interest (Fig. 3B). The measure is calculated from the relative entropy of the response histogram and that of a Gaussian histogram matched for mean and variance [30]. The result is normalized by the relative entropy of a matched Laplacian distribution, meaning that an LFE value of 100% is as different from a Gaussian distribution (in entropic terms) as a Laplacian distribution. This metric evaluates higher-order structural features in images, since it is invariant to the mean and variance of the histogram and only sensitive to higher-order statistical properties [50].

A set of Gabor filters was used and the kernel parameters were varied in accordance with previous publications [30], [50]. The center frequencies were varied from 0.125 to 4.0 cycles/mm and evaluated at six different orientations (from 0° to 150° in 30° increments). We used a bandwidth of 1.4 octaves, aspect ratio of 1, and shift phase of

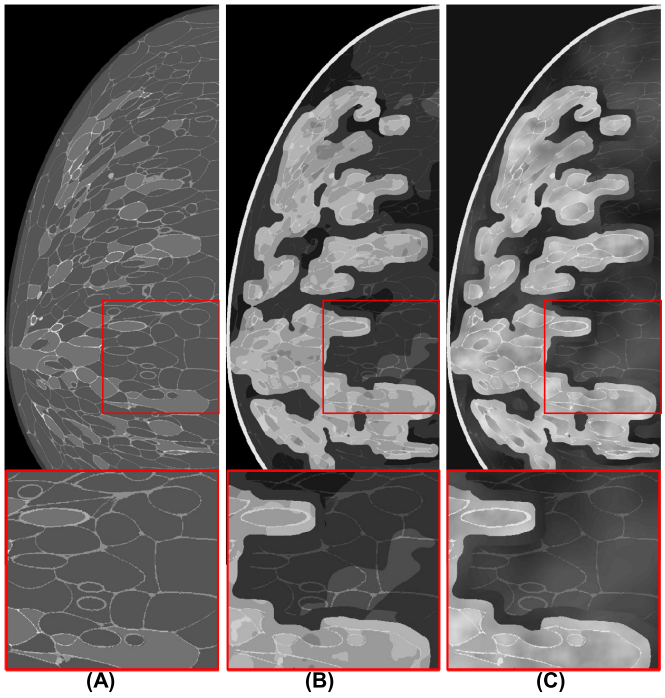

Fig. 4. Example of central slice (sagittal plane) of a breast phantom after processed using the normalized Perlin noise method. The distributions of Perlin noise were simulated using coefficients f_{min}, K, and Φ: 0.001, 3, 0.5 for the most adipose layer and 0.01, 3, 0.5 for the most glandular layer. (A) Prior phantom, Perlin phantom with (B) $n = 8$, and (C) $n = 63$.

$\pi/4$ radians. The histogram responses were obtained using 2D convolution through a selected ROI.

The response histograms were calculated in each filtered ROI and the LFE measures were calculated at different frequencies. The histograms were binned using 99% of responses, with an additional 1% bin for the remaining extremal values. The LFE was estimated using the methods specified in previous publications [30], [50].

Each DM projection was processed by log-converting the transmission values to density before LFE analysis [30], [50]. For DBT reconstructions, the LFE is calculated only in the central slice. No additional imaging processing was applied to the DM projections or DBT reconstructions.

The LFE results were averaged over the six Gabor filter orientations at each spatial frequency. For the clinical images, we averaged the LFE results over the 35 patients; separately, the result of the 500 phantoms were averaged. Based on previously reported results [30], [50], the standard error of the mean LFE (across breast views and patient exams) is relatively small (<4% of the mean on average). The LFE measures were compared using plot profiles, where mean and standard error are reported.

III. Results

A. Perlin Noise Phantom

The Perlin noise and breast tissue masks modify the prior phantom to incorporate novel texture into the simulated mammary parenchyma (Fig. 4). Each normalized distribution of Perlin noise is used to assign a range of n voxel-materials.

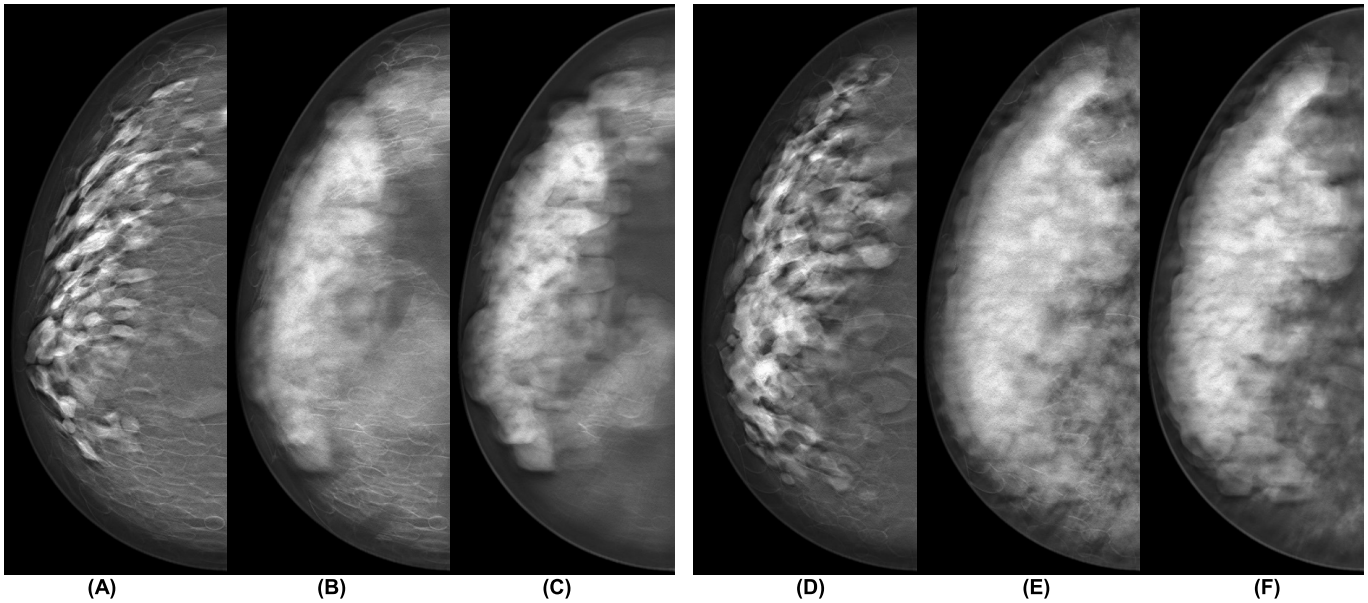

Fig. 5. Central slice (sagittal plane) of the DBT reconstruction of the two anthropomorphic breast phantoms used in this study. (A and D) prior reconstruction, and (B, C, E, and F) reconstruction using Perlin noise coefficients f_{min}, K, and Φ: {(0.001, 2, 0.4), (0.007, 4, 0.6)} for the most adipose layer and {(0.05, 4, 0.6), (0.03, 5, 0.6)} for the most glandular layer. The percent of breast tissue in the partial volume of each distribution follows the functions of $n = 63$: (B, and E) linear and (C, and F) hyperbolic tangent. For illustration, these particular images were processed using Briona (Real-Time Tomography, Villanova PA) imaging processing.

The n voxel-materials represent a different composition (i.e., partial volume combination) that vary in the fraction of glandular and adipose mixture. In this section, we report on $n = 63$ (Fig. 4C) to avoid unrealistic noise patterns in the simulated x-ray images.

Distinct x-ray attenuation properties are assigned for each voxel material. X-ray attenuation functions are used to control the attenuation and partial volume of adipose and glandular composition. Fig. 5 shows differences in the phantom images simulated using linear (Fig. 5B and E) and hyperbolic-tangent attenuation functions (Fig. 5C and F). These functions modify the overall breast density of the Perlin phantoms, and consequently, affect the contrast of the simulated x-ray images. In comparing images reconstructed using both functions, the hyperbolic-tangent function reduces the x-ray attenuation of the breast tissue substantially.

Note that our proposed method reduces the geometric features of the prior phantom compartments, resulting in Perlin texture that looks similar to anatomical noise structures found in the mammary parenchyma [30], [50]. Power spectrum and LFE measures were used to evaluate the phantom texture in simulated x-ray breast images.

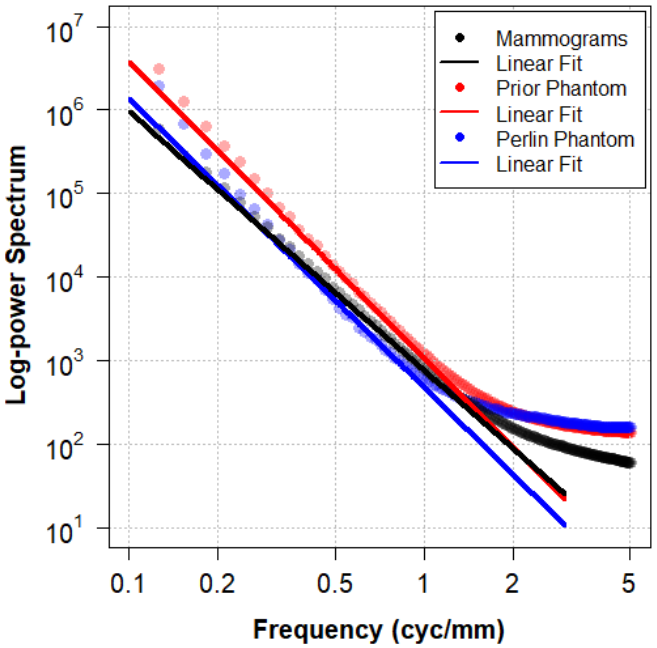

Fig. 6. Power spectrum profiles. These profiles are compared using simulated images and clinical mammograms. Linear regressions of the power spectrum are calculated across a frequency interval [0.1, 1] cycles per mm to determine values of the power-law exponent (β).

B. Power Spectrum

The power spectrum profiles are shown in Fig.6. The log-power spectrum was fitted using radial frequencies in the range 0.1 to 1 cycles per mm. The power-law exponents resulted in β values of -3.10, -3.55, and -3.46, for the profiles calculated using clinical mammograms, DM images simulated with our prior phantoms, and DM images simulated with the proposed Perlin phantoms, respectively. The relative errors in β are within 10% of the sample estimate, which is consistent with the previously reported results [30]. These results indicate that the power-law estimations of the proposed method are in agreement with the reference power spectrum calculated using clinical mammograms.

Note that these profiles suggest that both simulation methods are in a similar range of the power spectrum calculated

using clinical mammograms, even though the visual appearance of phantom and patient images are substantially different. These results illustrate the need for investigating additional objective metrics to evaluate statistical properties of Gaussian processes.

C. Laplacian Fractional Entropy

The LFE results for the various simulation conditions is graphed in Fig. 7. The general profile of the LFE measures is comparable to previous publications [30]. The simulated noise of the acquisition dominates the phantom signal at frequencies higher than 1 cycle/mm, driving the LFE results close to zero. The prior phantom shows substantial peaks in LFE measures across all frequencies that are not present in the clinical images. Note that the LFE computed using DM and DBT images simulated with Perlin phantoms have the closest agreement with the mammograms across the tested frequency range.

LFE shows substantial differences between the original phantom simulation procedure and the procedure that has been modified to include Perlin noise, and this comparison suggests that the proposed method produces more realistic textures in simulated images. Despite using parameters without separate optimization for Perlin noise (f_{min}, K, and Φ), the simulated DM and DBT images resulted in the closest agreement with the clinical data (Fig. 7A and Fig. 7B). These results support that the simulation procedure using Perlin noise more closely matches the LFE values from actual patient images.

The average LFE in the DBT images peaks slightly above the DM images in midrange frequencies from 0.25–0.5 cycles per mm and decays more rapidly to 0 above 1 cycle per mm [50]. In this study, the LFE distributions calculated using DBT images simulated with Perlin phantoms also peaks above the DM clinical images in the midrange frequencies and decays rapidly to 0 above 1 cycle per mm. However, more LFE analyses on clinical DBT images are recommended to support the use of the proposed methods. Ideally, LFE measures calculated in DBT images should consider the three-dimensionality of the reconstructions.

Examples of ROIs are shown in Fig. 8. ROIs cropped on clinical mammograms are used as reference (right column). Note that the DM images simulated with Perlin noise are comparable to the reference ROIs. The proposed method simulates noise texture for the phantom simulations (middle column), while the prior phantom shows overly distinct geometric compartments that are delimitated by highly attenuated ligaments (right column). Ligaments and geometric compartments are "smoothed out" in images simulated using the proposed methods, supporting better LFE agreement between the anatomical texture of clinical images and the Perlin phantoms.

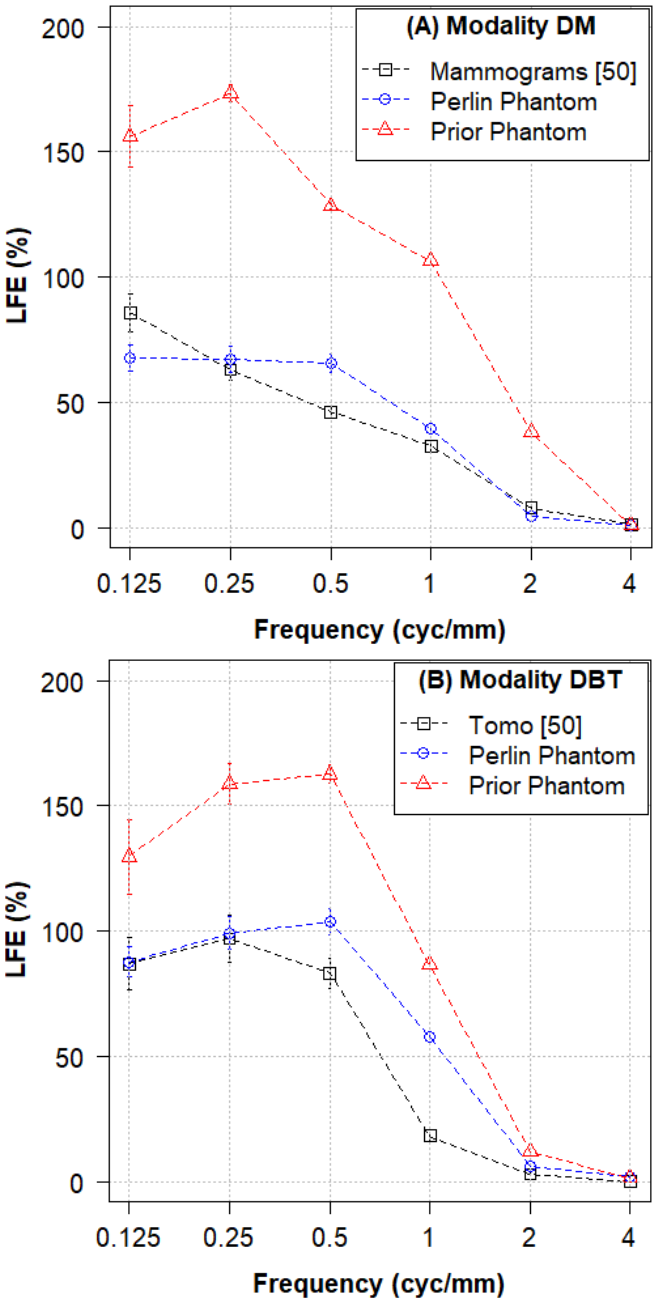

Fig. 7. Summary of LFE estimates (mean and standard error) collected using (A) DM and (B) DBT images. The LFE data for the clinical images (black box) is shown for reference [50]. The Perlin noise distribution (blue box) has the closest agreement with the reference clinical data across all frequencies.

IV. Discussion

We proposed a novel method to improve the simulation of anatomic noise and texture of anthropomorphic phantoms using multi-scale Perlin noise. The proposed method can be adapted, extended, and used in any phantom model if corresponding ground-truth of tissue labels is available. In this study, we used breast phantoms developed in our laboratory that have been consistently revised, improved, and validated over the last 22 years [10], [31], [51]. Our current breast models use a recursive partitioning algorithm [10], which simulates tissue compartments bounded by Cooper's ligaments. Depending upon the selection of simulation parameters, the Cooper's ligaments can enhance the geometric appearance of adipose and glandular compartments, resulting in simulated images that may not be considered realistic enough for specific VCT tasks (e.g., VCT applications that require realistic simulation

of cancer masking or assessment of breast cancer risk). The proposed Perlin method reduces the notable appearance of breast compartments in the simulated images, by introducing anatomic noise and connecting tissues.

Our results show that the images simulated with our prior and proposed methods have similar power-law spectra when compared with clinical mammograms. The greatest differences in the power spectra are in the lowest (< 0.2 cycles per mm) and highest (> 2 cycles per mm) frequencies. These differences indicate that we can still optimize the simulation and acquisition parameters to match more closely the power spectrum of phantom and patient images. However, the power-law exponents (β) calculated were -3.10, -3.55, and -3.46 for patient, prior and Perlin phantoms, respectively. The β values show only a 10% difference in relative errors between patient and Perlin-noise based phantoms. These results support the data published previously [30] and confirm the need for higher-order statistical analyses to evaluate realism of simulated images.

The LFE metric was used characterize non-Gaussian statistics in textures that was incorporated into our breast models. This metric has been suggested previously as a way to characterize non-Gaussian statistics in textures found in mammograms [30], [50]. That work demonstrated that LFE is relatively insensitive to the power spectrum of phantoms [51]. The LFE results in Fig.7 show that the simulation procedure using Perlin noise more closely matches the values from actual patient images. This suggests that the Perlin-noise simulation more effectively captures the higher-order statistical properties of breast tissue. Since LFE is based on Gabor filters that are similar to the receptive fields in the early visual system [65], [66], these statistical properties should in principle be perceivable to human observers as well.

Our results show substantial LFE variability between Perlin and prior phantoms, phantoms and clinical mammograms, and between images simulated with different modalities (DM and DBT). The mean LFE of images simulated with Perlin noise provide closer agreement to the patient images compared with simulated images of our prior phantom. The LFE measures calculated using DM and DBT images with Perlin noise show a better agreement with the LFE calculated using patient images, especially at lower spatial frequencies of 0.125 and 0.25 cycles per mm that are dominated by anatomical variability. Based on these results, LFE has been demonstrated to be an authoritative metric for evaluating phantom realism objectively. This will allow us to evaluate modifications to our software, as well as the parameters are used to control and modify the texture appearance in the phantom images.

The combination of various simulation parameters affects and modifies the texture, overall density, and the realism of breast phantoms. In this study, we emphasized the following simulation conditions and parameters: (i) number and size of Perlin binary masks, (ii) range of Perlin frequencies, and (iii) x-ray attenuation functions. The simulation parameters used in (i) control and merge dense compartments, avoiding sharper and more geometric compartment edges in the prior phantoms. The number and range of Perlin frequencies

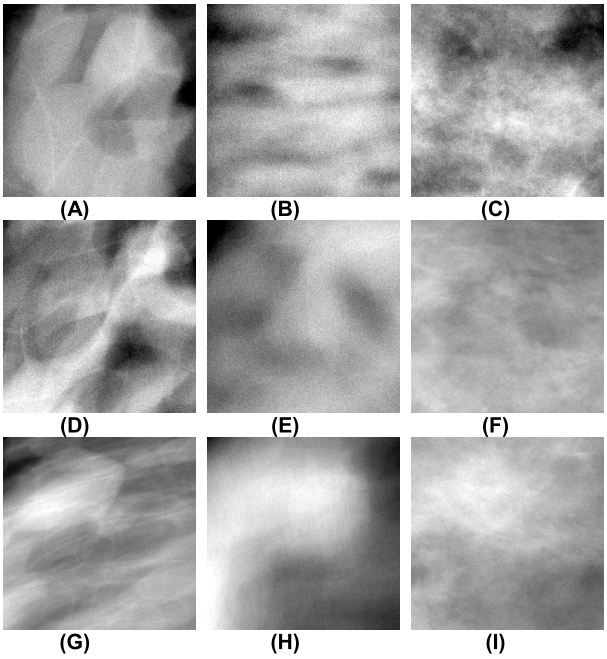

Fig. 8. Example of ROIs (256 × 256 pixels): (left) Prior phantom, (middle) Perlin phantom, and (right) clinical mammogram. The mean LFE ({0.125, 0.25, 0.5, and 1.0 cyc/mm }) results are: (A) {68.8, 76.8, 89.3, 79.11}, (B) {51.4, 40.0, 43.7, 31.9}, (C) {50.0, 39.9, 40.7, 30.6}, (D) {89.4, 88.8, 89.2, 82.7}, (E) {65.0, 36.5, 25.3, 19.3}, (F) {50.0, 36.5, 28.7, 19.8}, (G) {135.8, 146.1, 149.4, 118.8}, (H) {58.2, 57.2, 55.5, 28.2}, and (I) {65.4, 57.7, 44.1, 28.0}.

(ii) control the appearance of texture (Fig. 1) for each layer in the Perlin masks. Finally, the x-ray attenuation functions (iii) control the dense partial volume of each voxel-material. The hyperbolic attenuation function was selected to reduce the overall breast density and increase the density percent for the voxel-materials gradually. The simulation parameters should be carefully optimized and personalized for phantoms.

In this paper, the Perlin noise parameters (ii) were selected subjectively and applied to a diverse phantom population ($n = 500$). Although phantoms simulated with Perlin noise presented the closest LFE results to the sample of clinical images, the use of arbitrary parameters should be considered a limitation for this study. It will be beneficial to optimize the noise and phantom parameters using objective analyses, such as power spectrum and LFE. This optimization may further improve the phantom realism and match more closely the LFE and power spectrum of phantom images to the patient images. Thus, there is still some improvement to be made, both in terms of matching at higher and lower frequencies (below 0.2 and above 2 cycles per mm) and in terms of matching acquisition noise and breast density between patient and phantoms. Once the patient and phantoms are matched in terms of breast density, the LFE measures can be validated using visual interpretation of experts.

It is important to mention that the current study was not designed to match the most appropriate phantom image to a particular patient image. A more detailed phantom evaluation should consider a large clinical population of patients from which sample images are used. A larger sample of clinical DM

and DBT images is recommended to support the use of the proposed methods. Once the phantom and acquisition parameters are optimized and validated with larger clinical datasets, statistical significance tests should be performed to support the improvement in realism using Perlin noise phantoms.

Because DBT images reduce the superposition of breast tissue [16]–[19], we included samples of processed DBT reconstructions for the best visualization of differences in reconstructed slices simulated using both prior and Perlin phantoms. The examples provide some additional evidence that the proposed method improves the computer simulations, including anatomic noise in the simulated mammary parenchyma and reducing the effect of geometrical breast compartments in simulated images (Fig. 5A and D). The addition of more anatomical features will also help to reduce the geometric appearance of the phantom.

Our multi-scale Perlin method may eliminate the need of generating and combining phantoms (i.e., prior method [31]) to improve the phantom realism. In addition, our proposed method potentially can improve the algorithm performance for computer simulations. The software performance can be improved further by implementing the proposed methods using GPU-programming to accelerate the simulation of Perlin textures.

Finally, our VCT software inserts lesions using voxel replacement [31]. This method replaces phantom voxels with calcium (calcification clusters) or admixtures of glandular and adipose tissue (soft tissue masses). Voxel replacement for calcified lesions is very straightforward; calcium is highly attenuating. However, the simulation of masses is more difficult, especially in regions of uniform glandular tissue, because there may be no differentiating feature of the mass. Based on our observations, we believe that masses would be better differentiated from the parenchymal tissue based on differences in texture. We will investigate the simulation of masses with Perlin noise in a future publication.

V. Conclusion

This work describes a method to improve the realism of anthropomorphic phantoms. We propose the use of a VCT method that incorporates Perlin noise structures into anthropomorphic phantoms. Images simulated with Perlin-noise based phantoms have more similar power-law spectrum and power-law exponents than our previous phantoms when compared to mammograms; higher-order statistical properties of the Perlin-noise based phantoms, as measured by LFE, overlap the statistical properties measure in patient images.

The samples of simulated images presented in this study show that the proposed method improves the simulation of breast tissue, where Copper's ligaments and geometric compartment shapes are less evident in the simulated x-ray phantom images. These results suggest the use of Perlin-noise based phantoms for VCT applications that require the most realistic simulation of mammary parenchymal tissue.

Recruiting human readers to inspect images and score realism can be expensive, and time-consuming. The proposed validation method using power spectrum and LFE gives us a way to quantify improvements in realism objectively. Based on these results, we will use power spectrum and LFE as a primary tool for evaluating our future phantom design changes. We encourage the broader use of objective metrics, such as power spectrum and LFE, to evaluate phantom realism and to optimize simulation parameters in anthropomorphic x-ray simulations.

References

[1] P. R. Bakic, B. Barufaldi, D. Pokrajac, M. A. Lago, and A. D. Maidment, "Developing populations of software breast phantoms for virtual clinical trials," in *Proc. 14th Int. Workshop Breast Imag. (IWBI)*, Jul. 2018, p. 73.

[2] P. R. Bakic *et al.*, "Virtual clinical trial of lesion detection in digital mammography and digital breast tomosynthesis," *Proc. SPIE*, vol. 2018, Mar. 2018, Art. no. 1057306.

[3] T. Vent, R. Acciavatti, and A. Maidment, "Development and evaluation of a spatial resolution metric for tomosynthesis: We-g-601-02," *Med. Phys.*, vol. 44, no. 6, p. 3261, 2017.

[4] T. L. Vent, B. Barufaldi, and A. D. A. Maidment, "Simulation and experimental validation of high-resolution test objects for evaluating a next-generation digital breast tomosynthesis prototype," *Proc. SPIE*, vol. 2019, Mar. 2019, p. 21.

[5] T. M. Morrison, P. Pathmanathan, M. Adwan, and E. Margerrison, "Advancing regulatory science with computational modeling for medical devices at the FDA's office of science and engineering laboratories," *Frontiers Med.*, vol. 5, p. 241, Sep. 2018.

[6] A. Badano *et al.*, "In silico imaging clinical trials for regulatory evaluation: Initial considerations for VICTRE, a demonstration study," *Proc. SPIE*, vol. 10132, Mar. 2017, Art. no. 1013220.

[7] P. Elangovan *et al.*, "Design and validation of realistic breast models for use in multiple alternative forced choice virtual clinical trials," *Phys. Med. Biol.*, vol. 62, no. 7, pp. 2778–2794, Apr. 2017.

[8] E. Abadi *et al.*, "Virtual clinical trials in medical imaging: A review," *J. Med. Imag.*, vol. 7, no. 4, pp. 042805-1–042805-40, 2020.

[9] A. Badano *et al.*, "Evaluation of digital breast tomosynthesis as replacement of full-field digital mammography using an in silico imaging trial," *JAMA Netw. Open*, vol. 1, no. 7, pp. 1–12, 2018.

[10] D. D. Pokrajac, A. D. A. Maidment, and P. R. Bakic, "Optimized generation of high resolution breast anthropomorphic software phantoms," *Med. Phys.*, vol. 39, no. 4, p. 2290, 2012.

[11] B. Barufaldi, P. R. Bakic, and A. D. A. Maidment, "Multiple-reader, multiple-case ROC analysis for determining the limit of calcification detection in tomosynthesis," *Proc. SPIE*, vol. 10948, p. 22, Mar. 2019.

[12] R. J. Hooley, K. L. Greenberg, R. M. Stackhouse, J. L. Geisel, R. S. Butler, and L. E. Philpotts, "Screening US in patients with mammographically dense breasts: Initial experience with connecticut public act 09-41," *Radiology*, vol. 265, no. 1, pp. 59–69, Oct. 2012.

[13] E. Sala, R. Warren, J. McCann, S. Duffy, N. Day, and R. Luben, "Mammographic parenchymal patterns and mode of detection: Implications for the breast screening programme," *J. Med. Screening*, vol. 5, no. 4, pp. 207–212, Dec. 1998.

[14] K. Dembrower *et al.*, "Comparison of a deep learning risk score and standard mammographic density score for breast cancer risk prediction," *Radiology*, vol. 294, no. 2, pp. 265–272, Feb. 2020.

[15] R. J. Acciavatti *et al.*, "Validation of the textural realism of a 3D anthropomorphic phantom for digital breast tomosynthesis," *Proc. SPIE*, vol. 10718, Jul. 2018, Art. no. 107180R.

[16] R. A. Wahab, S.-J. Lee, B. Zhang, L. Sobel, and M. C. Mahoney, "A comparison of full-field digital mammograms versus 2D synthesized mammograms for detection of microcalcifications on screening," *Eur. J. Radiol.*, vol. 107, pp. 14–19, Oct. 2018.

[17] S. P. Zuckerman *et al.*, "Implementation of synthesized two-dimensional mammography in a population-based digital breast tomosynthesis screening," *Radiol. J.*, vol. 281, no. 3, pp. 1–7, 2016.

[18] P. Skaane *et al.*, "Two-view digital breast tomosynthesis screening with synthetically reconstructed projection images: Comparison with digital breast tomosynthesis with full-field digital mammographic images," *Radiol. J.*, vol. 271, no. 3, pp. 655–663, 2014.

[19] E. A. Rafferty, J. M. Park, L. E. Philpotts, S. P. Poplack, and J. H. Sumkin, "Digital mammography and breast tomosynthesis compared with digital mammography alone: Results of a multicenter, multireader trial," *Radiology*, vol. 266, no. 1, pp. 104–113, 2013.

[20] K. Bliznakova, S. Suryanarayanan, A. Karellas, and N. Pallikarakis, "Evaluation of an improved algorithm for producing realistic 3D breast software phantoms: Application for mammography," *Med. Phys.*, vol. 37, no. 11, pp. 5604–5617, Oct. 2010.

[21] P. R. Bakic, D. D. Pokrajac, R. De Caro, and A. D. A. Maidment, *Realistic Simulation of Breast Tissue Microstructure in Software Anthropomorphic Phantoms* (Lecture Notes in Computer Science: Lecture Notes in Artificial Intelligence and Lecture Notes in Bioinformatics). Cham, Switzerland: Springer, 2014.

[22] A.-A.-Z. Imran, P. R. Bakic, A. D. A. Maidment, and D. D. Pokrajac, "Optimization of the simulation parameters for improving realism in anthropomorphic breast phantoms," *Proc. SPIE*, vol. 10312, Mar. 2017, Art. no. 1013257.

[23] A.-A.-Z. Imran, D. D. Pokrajac, A. D. A. Maidment, and P. R. Bakic, "Estimation of adipose compartment volume in CT images of a mastectomy specimen," *Proc. SPIE*, vol. 9783, Mar. 2016, Art. no. 97832O.

[24] P. R. Bakic, D. D. Pokrajac, R. Caro, and A. D. A. Maidment, "Realistic simulation of breast tissue microstructure in software anthropomorphic phantoms," *Breast Imag.*, vol. 8539, pp. 348–355, Jun. 2014.

[25] A. Avanaki, K. Espig, and T. Kimpe, "Location- and lesion-dependent estimation of mammographic background tissue complexity," *J. Med. Imag.*, vol. 4, no. 1, p. 15501, 2017.

[26] L. R. Borges *et al.*, "Technical note: Noise models for virtual clinical trials of digital breast tomosynthesis," *Med. Phys.*, vol. 46, no. 6, pp. 2683–2689, Jun. 2019.

[27] B. Barufaldi, T. L. Vent, R. J. Acciavatti, P. R. Bakic, P. B. Noel, and A. D. Maidment, "MRMC ROC analysis of calcification detection in tomosynthesis using computed super resolution and virtual clinical trials," *Proc. SPIE*, vol. 1151313, p. 58, May 2020.

[28] A. Jonnalagadda *et al.*, "Evaluation of convolutional neural networks for search in $1/f^{2.8}$ filtered noise and digital breast tomosynthesis phantoms," *Proc. SPIE*, vol. 2020, Mar. 2020, Art. no. 1131617.

[29] M. A. Lago, B. B. Barufaldi, P. R. Bakic, C. K. Abbey, A. D. A. Maidment, and M. P. Eckstein, "Foveated model observer to predict human search performance on virtual digital breast tomosynthesis phantoms," *Proc. SPIE*, vol. 11316, Mar. 2020, Art. no. 113160V.

[30] C. K. Abbey, P. R. Bakic, D. D. Pokrajac, A. D. A. Maidment, M. P. Eckstein, and J. M. Boone, "Evaluation of non-Gaussian statistical properties in virtual breast phantoms," *J. Med. Imag.*, vol. 6, no. 2, p. 1, Jun. 2019.

[31] P. R. Bakic, B. Barufaldi, D. Pokrajac, S. Weinstein, and A. Maidment, "Optimized simulation of breast anatomy for virtual clinical trials," in *Proc. 14th Int. Workshop Breast Imag. (IWBI)*, Jul. 2018, p. 73.

[32] P. R. Bakic, D. Pokrajac, M. Feldman, and A. D. Maidment, "Simulation of sequential pathology images for the virtual clinical trials with rad-path correlation," in *Proc. 14th Int. Workshop Breast Imag. (IWBI)*, Jul. 2018, p. 74.

[33] W. J. Van Der Laan, S. Green, and M. Sainz, "Screen space fluid rendering with curvature flow," in *Proc. I3D ACM SIGGRAPH Symp. Interactive 3D Graph. Games*, 2009, pp. 91–98.

[34] F. Guo, J. Tang, and X. Xiao, "Foggy scene rendering based on transmission map estimation," *Int. J. Comput. Games Technol.*, vol. 2014, pp. 1–13, Jan. 2014.

[35] R. Bridson, J. Houriham, and M. Nordenstam, "Curl-noise for procedural fluid flow," *ACM Trans. Graph.*, vol. 26, no. 3, p. 46, Jul. 2007.

[36] W. Dong, X. Zhang, and C. Zhang, "Generation of cloud image based on Perlin noise," in *Proc. Int. Conf. Multimedia Commun.*, Aug. 2010, pp. 61–63.

[37] R. Barnard and S. Ural, "Rendering translucency with Perlin noise," in *Proc. 3rd Int. Conf. Comput. Graph. Interact. Techn. Australasia South East Asia (GRAPHITE)*, 2005, pp. 131–134.

[38] M. Dustler, P. Bakic, H. Petersson, P. Timberg, A. Tingberg, and S. Zackrisson, "Application of the fractal Perlin noise algorithm for the generation of simulated breast tissue," *Proc. SPIE*, vol. 2015, Mar. 2015, Art. no. 94123E.

[39] K. Lång, M. Dustler, and H. Petersson, "Binary implementation of fractal Perlin noise to simulate fibroglandular breast tissue," *Proc. SPIE*, vol. 1057357, Mar. 2018, p. 193.

[40] S. Worley, "A cellular texture basis function," in *Proc. 23rd Annu. Conf. Comput. Graph. Interact. Techn. (SIGGRAPH)*, 1996, pp. 291–294.

[41] M. Abdolhoseini, M. G. Kluge, F. R. Walker, and S. J. Johnson, "Neuron image synthesizer via Gaussian mixture model and perlin noise," in *Proc. IEEE 16th Int. Symp. Biomed. Imag. (ISBI)*, Apr. 2019, pp. 530–533.

[42] H.-J. Bae *et al.*, "A Perlin noise-based augmentation strategy for deep learning with small data samples of HRCT images," *Sci. Rep.*, vol. 8, no. 1, pp. 1–7, Dec. 2018.

[43] W. Burger and M. J. Burge, *Principles of Digital Image Processing: Advanced Methods (Supplemental Material)*, 3rd ed. London, U.K.: Springer, 2013.

[44] K. Perlin, "Image synthesizer," *Comput. Graph.*, vol. 19, no. 3, pp. 287–296, 1985.

[45] K. Perlin, "Improving noise," *ACM Trans. Graph.*, vol. 21, no. 3, pp. 681–682, 2002.

[46] K. G. Metheany, C. K. Abbey, N. Packard, and J. M. Boone, "Characterizing anatomical variability in breast CT images," *Med. Phys.*, vol. 35, no. 10, pp. 4685–4694, Sep. 2008.

[47] L. Chen, J. M. Boone, A. Nosratieh, and C. K. Abbey, "NPS comparison of anatomical noise characteristics in mammography, tomosynthesis, and breast CT images using power law metrics," *Proc. SPIE*, vol. 7961, Mar. 2011, Art. no. 79610F.

[48] L. Cockmartin, H. Bosmans, and N. W. Marshall, "Comparative power law analysis of structured breast phantom and patient images in digital mammography and breast tomosynthesis," *Med. Phys.*, vol. 40, no. 8, Jul. 2013, Art. no. 081920.

[49] A. E. Burgess, F. L. Jacobson, and P. F. Judy, "Human observer detection experiments with mammograms and power-law noise," *Med. Phys.*, vol. 28, no. 4, pp. 419–437, Apr. 2001.

[50] C. K. Abbey, A. Nosratieh, J. Sohl-Dickstein, K. Yang, and J. M. Boone, "Non-Gaussian statistical properties of breast images," *Med. Phys.*, vol. 39, no. 11, pp. 7121–7130, Nov. 2012.

[51] B. Barufaldi, P. R. Bakic, D. Higginbotham, and A. D. A. Maidment, "OpenVCT: A GPU-accelerated virtual clinical trial pipeline for mammography and digital breast tomosynthesis," *Proc. SPIE*, vol. 1057, Mar. 2018, Art. no. 1057358.

[52] K. Perlin and E. M. Hoffert, "Hypertexture," in *Proc. 16th Annu. Conf. Comput. Graph. Interact. Techn., SIGGRAPH*, 1989, pp. 253–262.

[53] A. Mertins, "Wavelet transform," in *Signal Analysis*. Chichester, NY, USA: Wiley, 2003, pp. 210–264.

[54] A. F. Laine and X. Zong, "A multiscale sub-octave wavelet transform for de-noising and enhacement," in *Wavelet Applications in Signal and Image Processing IV*. Denver, CO, USA: SPIE, 1996, pp. 238–249.

[55] W. Burger, "Imagingbook-common.jar: A compiled collection of Java files," Tech. Rep., 2013.

[56] B. Barufaldi, P. Bakic, and A. D. A. Maidment. (2020). Open Virtual Clinical Trials. *OpenVCT: A GPU-Accelerated Virtual Clinical Trial Pipeline for Mammography and Digital Breast Tomosynthesis*. Accessed: Mar. 10, 2019. [Online]. Available: https://sourceforge.net/projects/openvct/

[57] M. A. Lago, A. D. A. Maidment, and P. R. Bakic, "Modelling of mammographic compression of anthropomorphic software breast phantom using FEBio," in *Proc. Int. Symp. Comput. Methods Biomech. Biomed. Eng.* Salt Lake, UT, USA: European Society of Biomechanics, 2013, pp. 487–488.

[58] T. Pietzsch, S. Preibisch, P. Tomank, and S. Saalfeld, "IMG lib 2—Generic image processing in Java," *Bioinformatics*, vol. 28, no. 22, pp. 3009–3011, 2012.

[59] J. R. Rumble, D. M. Bickham, and C. J. Powell, "The NIST X-ray photoelectron spectroscopy database," Surf. Interface Anal., 1992.

[60] R. L. Siddon, "Fast calculation of the exact radiological path for a three-dimensional CT array," *Med. Phys.*, vol. 12, no. 2, pp. 252–255, Mar. 1985.

[61] S. S. J. Feng and I. Sechopoulos, "Clinical digital breast tomosynthesis system: Dosimetric characterization," *Radiology*, vol. 263, no. 1, pp. 35–42, Apr. 2012.

[62] *ICRU Report 44—Tissue Substitutes in Radiation Dosimetry and Measurement*, ICRU, Bethesda, MD, USA, 1988.

[63] J. Kuo, P. A. Ringer, S. G. Fallows, P. R. Bakic, A. D. A. Maidment, and S. Ng, "Dynamic reconstruction and rendering of 3D tomosynthesis images," *Proc. SPIE*, vol. 796116, Mar. 2011, pp. 796116-1–796116-11.

[64] J. H. Chui, D. D. Pokrajac, A. A. D. A. Maidment, and P. R. Bakic, "Roadmap for efficient parallelization of breast anatomy simulation," *Proc. SPIE*, vol. 8313, Mar. 2012, p. 83134T.

[65] J. G. Daugman, "Two-dimensional spectral analysis of cortical receptive field profiles," *Vis. Res.*, vol. 20, no. 10, pp. 847–856, Jan. 1980.

[66] J. P. Jones and L. A. Palmer, "An evaluation of the two-dimensional Gabor filter model of simple receptive fields in cat striate cortex," *J. Neurophysiol.*, vol. 58, no. 6, pp. 1233–1258, Dec. 1987.

Received: 19 July 2021 | Revised: 7 February 2022 | Accepted: 13 February 2022

DOI: 10.1002/mp.15553

RESEARCH ARTICLE

MEDICAL PHYSICS

Computer simulations of case difficulty in digital breast tomosynthesis using virtual clinical trials

Bruno Barufaldi[1] | **Trevor Lewis Vent**[1] | **Predrag Radomir Bakic**[1,2] | **Andrew Douglas Arnould Maidment**[1]

[1]Department of Radiology, University of Pennsylvania, Philadelphia, Pennsylvania, USA

[2]Department of Translational Medicine, Lund University, Malmö, Sweden

Correspondence
Bruno Barufaldi, Department of Radiology, University of Pennsylvania, 3620 Hamilton Walk, John Morgan Building, Room 155, Philadelphia, PA 19104, USA.
Email: Bruno.Barufaldi@pennmedicine.upenn.edu

Funding information
the 2020 AAPM Research Seed Grant, Grant/Award Numbers: NIH R01 CA154444, NIH R01 EB018958, Komen IIR13262248; EU Horizon 2020 Marie Skłodowska-Curie Action Fellowship IF 846540 Marie Sklodowska Curie Action Fellowship, Grant/Award Numbers: IF 846540, BWF IRSA 1016451, DoD W81XWH-18-1-0082

[Correction added on 12 Mar, 2022 after first online publication: the spelling was corrected for Trevor Lewis Vent.]

Abstract

Purpose: Virtual clinical trials (VCTs) require computer simulations of representative patients and images to evaluate and compare changes in performance of imaging technologies. The simulated images are usually interpreted by model observers whose performance depends upon the selection of imaging cases used in training evaluation models. This work proposes an efficient method to simulate and calibrate soft tissue lesions, which matches the detectability threshold of virtual and human readings.

Methods: Anthropomorphic breast phantoms were used to evaluate the simulation of four mass models (I–IV) that vary in shape and composition of soft tissue. Ellipsoidal (I) and spiculated (II–IV) masses were simulated using composite voxels with partial volumes. Digital breast tomosynthesis projections and reconstructions of a clinical system were simulated. Channelized Hotelling observers (CHOs) were evaluated using reconstructed slices of masses that varied in shape, composition, and density of surrounded tissue. The detectability threshold of each mass model was evaluated using receiver operating characteristic (ROC) curves calculated with the CHO's scores.

Results: The area under the curve (AUC) of each calibrated mass model were within the 95% confidence interval (mean AUC [95% CI]) reported in a previous reader study (0.93 [0.89, 0.97]). The mean AUC [95% CI] obtained were 0.94 [0.93, 0.96], 0.92 [0.90, 0.93], 0.92 [0.90, 0.94], 0.93 [0.92, 0.95] for models I to IV, respectively. The mean AUC results varied substantially as a function of shape, composition, and density of surrounded tissue.

Conclusions: For successful VCTs, lesions composed of soft tissue should be calibrated to simulate imaging cases that match the case difficulty predicted by human readers. Lesion composition, shape, and size are parameters that should be carefully selected to calibrate VCTs.

KEYWORDS
anthropomorphic breast phantom, digital breast tomosynthesis, virtual clinical trials

1 | INTRODUCTION

1.1 | Background

Virtual clinical trials (VCTs) have been widely used as a rapid and cost-effective alternative for evaluating and optimizing imaging technologies.[1–5] VCTs allow for the simulation of images with voxel-wise ground-truth, which is not available in clinical practice. The images and ground truth can be used to evaluate the performance of imaging systems, modalities, and techniques.[1,6,7] The ground truth yields information regarding the strengths and weaknesses of imaging systems, providing valuable knowledge that can be used for myriad purposes including to support the regulatory approval of novel imaging systems.[8]

Imaging VCTs are usually targeted to a specific clinical task,[1] which requires the correct and accurate

interpretation of a "case." Similar to traditional clinical trials, VCTs must be conducted using representative cases of patients and images from a particular patient population.[9] Each case is represented by an image (or a set of images) of the corresponding virtual patients with and without disease conditions or pathologies. In VCTs, these cases are analyzed by virtual readers,[10] whose performance aspires to match that of human experts.

Virtual readers are available across a variety of clinical tasks (e.g., search,[11,12] classification,[13] detection,[7,14] etc.). These readers, known as model observers (MOs),[15–17] are developed based on either a human or mathematical model, representing the response of the visual system trained for a particular clinical task.[18] They are usually trained with many images to estimate the performance of a clinical task with the objective of predicting human interpretation. The most common MO is trained using a set of images with signal-known-exactly (SKE) and location-known-exactly (LKE).[19] SKE and LKE MOs have previous knowledge of the size, shape, contrast, and location of the signal to be detected. VCTs provide a well-suited environment with essentially unlimited resources to train MOs for a specific clinical task.[1] However, training MOs can be challenging, since VCTs must emulate the realistic response of "case difficulty" as determined by human responses to similar stimuli.[14]

MOs require a large and representative sample of images where the true signal (lesion) is acquired at different signal levels or different dose levels to predict the performance of human experts. Today, machine learning algorithms can be used as MOs to predict the human performance in SKE tasks. Kopp et al. developed an intelligent MO to detect spherical lesions of multiple sizes on X-ray computed tomography images (n = 7,488) of uniform phantoms acquired at various dose levels.[20] As a result, the authors demonstrated that the performance of the proposed intelligent MO is comparable to both human readings and traditional channelized Hotelling observers (CHOs).[21] It is important to recognize, however, that while these experiments accurately replicate the *stimuli* for the model and human observer, the lesions or background often lack realism, whether in terms of the contrast, shape, or complexity.

By their very nature, VCTs are complex software simulations incorporating disparate simulation regimes (physics, anatomy, psychophysics, etc.). Each software component must be validated to ensure that simulation inaccuracies do not limit the generalizability of the results. To address clinically meaningful problems, VCTs also need to be trained and "calibrated" with a proper image set, considering realistic lesions that represent thresholds in detectability that match human performance accurately. The thresholds in detectability are usually expressed in terms of metrics used in clinical trials, such as receiver operating characteristics (ROC) and the area under the curve (AUC).[1,5,8,14] Rafferty et al. conducted a reader study to compare humans' diagnostic accuracy and recall rates using digital breast tomosynthesis (DBT) combined with digital mammography (DM) in comparison with DM alone.[22] The authors reported that DM combined with DBT improves the diagnostic accuracy, resulting in differences (Δ) in AUC of 0.088 (95% CI ΔAUC [0.051, 0.125], $P < 0.001$) for non-calcified lesions. To predict the diagnostic performance of this reader study using VCTs, virtual readers should be trained using sets of images with non-calcified lesions within the same threshold of detectability.[5,8,14]

In previous studies, we attempted to replicate a clinical trial of a pre-market approval system using an *in silico* trial.[5,14] We conducted an extensive VCT using simulated DM and DBT images of voxelized breast phantoms with various lesions. We observed that the difference in AUC (ΔAUC) was greater for masses (ΔAUC = 0.106) than for calcifications (ΔAUC = –0.003), which was consistent with the findings of the comparative trial. Badano et al. have also investigated the ability of VCTs to predict the performance of human readers in detectability of calcifications and masses in DM and DBT images.[8] The authors also observed differences in AUCs of masses (ΔAUC = 0.090) and calcifications (ΔAUC = 0.027) consistent with the findings of the comparative trial. In both VCT studies, the simulated results closely matched the ΔAUC reported in the reader studies; however, neither study predicted the response of ROC curves accurately in terms of case complexity; additionally, in the case of the latter study, the predicate AUC values were not matched for calcifications resulting in ΔAUC which were discordant in terms of perceived signal-to-noise (d') changes.[8]

1.2 | Rationale

Although there are many uses for VCTs, as a research group which develops imaging devices, we have primarily used VCTs to design and test novel devices and imaging algorithms.[5,23–26] In our research, we first calibrate the VCT in terms of patient population, lesion admixture, and case difficulty to an *existing study* of a *predicate device* such that the VCT matches the existing clinical trial in terms of the study design and observed AUC.[1,5,14] We can then use this calibrated VCT dataset to evaluate a novel *study device* with the goal of demonstrating either equivalency or superiority to the predicate technology. Determining equivalency or superiority is a statistical task.[1]

As stated above, VCTs use computer methods to generate phantoms which simulate a patient population with or without pathologies. If, as is our practice, the goal of the VCT is to measure performance in terms of ROC metrics such as AUC or d', the pathologies should encompass a multitude of lesions, varying in terms of the difficulty for detection to simulate clinically relevant tasks realistically. This is because the ROC curve

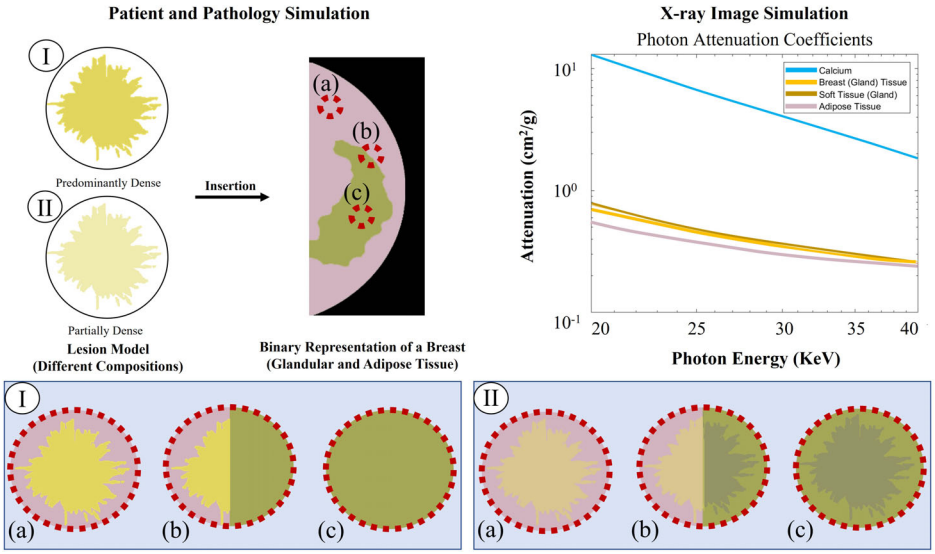

FIGURE 1 Schematic of voxel replacement method used to simulate lesions composed of soft tissue. (I, lesion model predominantly dense) and (II, lesion model partially dense) represent two hypothetical scenarios seen in imaging virtual clinical trial (VCTs), where (a) is an example of region predominantly dense, (b) predominantly adipose, and (c) partially dense

stratifies cases in terms of case difficulty—the lower left side of the ROC curve consists of lesions which were easy to identify with little to no risk of calling a false positive, while the upper right side of the curve consists of lesions which were extremely difficult to identify, where in fact the only strategy to identify them was to call all cases positive. Thus, the radiographic characteristics (lesion type, composition, and shape) significantly impact the performance of virtual readers trained for detection tasks, and the methods used to simulate lesions must be carefully investigated and controlled to simulate realistic cases of diseased conditions. This is particularly important for research into the effect of lesion masking in breast imaging, which is the current focus of this research.[27,28]

When a lesion is inserted into an existing phantom, the voxels in the region of the lesion must be modified to account for the presence of the lesion. We have explored a number of methods for modifying the voxels, but these largely devolve into two classes: voxel replacement and voxel blending. The voxel replacement method,[29] as the name suggests, replaces the contents of selected voxels that represent healthy tissue (e.g., adipose or glandular compartments, Cooper's ligaments, skin, etc.) with the corresponding material of the particular pathological finding (e.g., duct carcinoma, fibroadenoma, cyst, calcification, etc.). In the replacement method, each voxel that represents a pathological finding is assigned to a mass attenuation coefficient (μ/ρ) of the corresponding lesion material (strictly speaking, our phantoms consist of material labels, so the voxel labels are changed in the phantom and the new labels correspond to the new X-ray properties—or any other material property). In breast imaging, the voxel replacement method works efficiently for calcified lesions, since the X-ray mass attenuation of calcium is much greater than the healthy breast tissue[30] (Figure 1). There are many analogous situations which can be imagined; for example, lung nodules in which soft tissue supplants air, bone fractures in which a fluid-filled crack is created in bone, or caries in teeth.

In comparison, multiple spectral imaging analyses have shown that the attenuation coefficients of malignant lesions composed of soft tissue (e.g., masses) and breast (glandular) tissue are very close at mammography energies[30–32] (Figure 1, plot). Thus, the voxel replacement method cannot guarantee that the X-ray attenuation properties of masses will be simulated adequately. Consider the following simple thought experiment. The schematic shown in Figure 1 illustrates two scenarios (I and II) that we have commonly observed in our breast imaging VCTs.

In scenario I, masses which are composed of materials comparable (or slightly higher) in attenuation to glandular tissue will be (a) highly visible in a simulated breast parenchyma which is composed predominantly of adipose tissue, while it is likely that the mass is (b) partially masked or (c) totally obscured in dense parenchyma. Under these circumstances, the detection of lesions is essentially binary—they are always detected in adipose regions and never detected in glandular regions. As such, case difficulty is not well simulated as compared to clinical studies, and overall AUC is determined by the faction of lesions located in fat or gland. It is necessary, therefore, to decrease the attenuation of the tumor to make it harder to see in an adipose background. Thus, in scenario II, we can imagine imaging masses composed of a fixed admixture of a background tissue and tumor that potentially has a lower attenuation than scenario I. Using the pixel replacement method will therefore result in (a) less attenuating lesions in a

simulated breast parenchyma composed predominantly of adipose, as compared to scenario I, while (b) being partially visible with negative contrast or (c) being totally obscured. Such lesions simply lack realism because of the risk of negative contrast in certain regions of the phantom. We have repeatedly attempted more elaborate pixel replacement methods for masses without success; for example, stepped increases in attenuation (akin to a stepped pyramid) and other such tricks just lead to different negative contrast artifacts.

Thus, one must adopt a method which considers the underlying tissue when a lesion is added; that is, voxel blending rather than voxel replacement. For some time, our VCT pipeline has supported partial volumes, such that each voxel consists of an admixture of materials.[33] Voxels composed of partial volumes can be used to simulate complex structures in imaging VCTs.[33] In this paper, we explore the hypothesis that a method that uses partial volumes to enable the blending of materials from the phantom and lesion through weighted addition can eliminate the inverted X-ray attenuation of the signal in structures simulated in the breast parenchyma (Figure 1 II-bc). In this "voxel additive method," lesion voxels in the phantom are composed jointly of lesion (l) and breast tissue (b) to a variable extent:

$$\mu = w_l \rho_l \frac{\mu_l}{\rho_l} + w_b \rho_b \frac{\mu_b}{\rho_b}, \quad w_l + w_b = 1.0, \qquad (1)$$

where w is the fraction by weight (percent) of a particular material, ρ is the material density, and μ/ρ represents the mass attenuation coefficient. The X-ray attenuation of lesions can be controlled by varying w_l of the partial volume. One can then ensure that negative contrast lesions are avoided provided $\mu_l \geq \mu_b$, and a representative set of lesions of varying difficulty can be achieved by varying μ_l.

This study uses an implementation of the proposed "voxel additive" method to calibrate lesions composed of soft tissue. Anthropomorphic breast phantoms were used to evaluate the two lesion insertion methods: voxel replacement and voxel addition. DBT projections and reconstructions were simulated using the acquisition geometry of a clinical system. Spiculated and ellipsoidal lesion models were used. The virtual reader model was a previously-evaluated CHO.[14] The detectability threshold of each mass model was evaluated using ROC curves calculated with the CHO's scores. The simulated results were compared with the predicate data (95% CI AUC) reported previously by Raffety.[22] We would like to emphasize that this mass simulation is still based on published material properties of the tumor and breast tissue, however we now allow individual voxels, which are macroscopic and typically have linear dimensions of 0.1–0.5 mm, to contain an admixture of tissue types. This is analogous, at least at a high level, to the difference between low-magnification and high-magnification histology, where one can reasonably expect greater tissue heterogeneity as the magnification is decreased.

2 | MATERIALS AND METHODS

2.1 | Anatomical breast models

Voxelized anatomical models (phantoms) of the breast were simulated using a VCT framework[6] developed at the University of Pennsylvania (Figure 2). The breast phantoms represent a model of healthy breast anatomy created using an efficient recursive partitioning algorithm.[34] The algorithm sets compartment seeds randomly within a semi-ellipsoidal breast outline to simulate glandular and adipose tissue bounded by fibrous Cooper's ligaments. The amount of simulated tissue affects the volumetric breast density (VBD) estimates and lesion detectability. A summary of phantom parameters used in this study is given in Table 1.

The voxelized phantoms consist of labels (ground truth) representing tissue types and air (Figure 2c). The phantoms are compressed using reusable finite-element (FE) breast meshes (Simpleware, FE Module, Synopsys Inc., Mountain View, CA) generated based on the material properties of each label and the mechanical response of breast tissue to compression.[9] The actual breast compression is simulated using deformable FE breast meshes (FEBio, Univ. Utah, Salt Lake City, UT) and GPU accelerated 3D mapping software developed in-house,[9] assuming 50% thickness compression in the medio-lateral (ML) view.

The phantom population consists of five sets of phantoms for each VBD category, five phantoms in each set ($n = 25$). The phantoms were used to calibrate the composition of masses and characterize case difficulty by lesion composition (details described in Sections 2.3 and 2.4).

The spiculated mass models were segmented and scaled from contrast-enhanced magnetic resonance images in three orthogonal views (sagittal, coronal, and transversal).[35] The segmented models were resampled to have isotropic voxels and they were grouped by shape. An ellipsoidal mass model (Model I: Figure 3a) was designed to match with the "core" of the spiculated models. In addition, three other shapes[35] were used in this study, the so-called *hairy* (Model II: Figure 3b), *grouped* (Model III: Figure 3c), and *stellate* (Model IV: Figure 3d) lesions.

The bounding boxes of the four mass models have original dimensions of 35×35×35 mm.[3] The models were resized in all three dimensions to a range of 6–34 mm (median 14 mm) of non-calcified lesions reported in a previous reader study.[22] The fitting and measurements were obtained using the ImageJ package "3D Analysis."[36] Shape measurements (Table 2) were calculated using 3D ellipsoid fitting. Note that mass

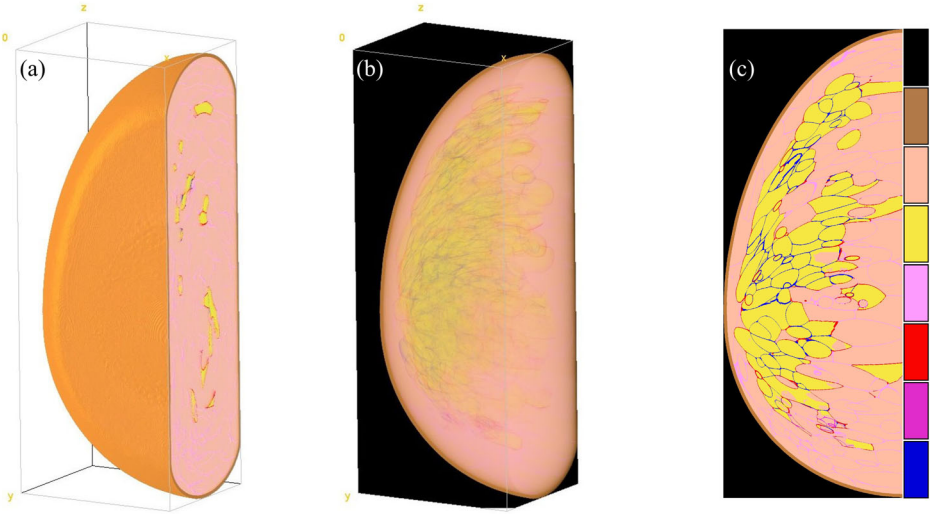

FIGURE 2 (a) Volumetric view of a voxelized breast phantom after 50% medio-lateral (ML) breast compression, (b) 3D projection view of breast tissue labels, and (c) central slice of breast phantom with colormap that represents the various tissue labels (top–bottom color bar: air, skin, adipose, glandular, and four types of ligaments)

TABLE 1 Summary of breast phantom parameters used in this study

Phantoms	
Number of simulations (#)	25
Fraction of dense compartments (%)	0, 10, 20, 30, and 50
Volume (ml)	700
Overall VBD {[4,10], [10,15], [15,21], [21,26], [26,32]} % (#, per bin)	{241, 307, 291, 169, 132}
Breast compression (50% compression in *z*)	Medio-lateral
Dimensions (*x*×*y*×*z*, mm)	78.4×205.3×63.3
Voxel size (mm)	0.10
Number of compartments (#)	425, 850, 1275, and 1700
Compartment shape (a.u.)	{(0.1;1;1;2), (0.01; 1; 1; 4)}
Number of ligament material (#)	4
Ligament thickness (mm)	[0.1, 0.3]
Skin thickness (mm)	0.15

models I and II have the same volume of interest (VOI) and the closest shape measurements in terms of compactness, sphericity, elongation, and flatness. These two models (I and II) were used to illustrate the lesion calibration process, described in Section 2.4.

2.2 | Lesion insertion and X-ray imaging

Two lesion insertion methods were evaluated in this study: voxel replacement[29] and voxel addition. For the additive method, the partial volume of lesions was simulated using glandular tissue (w_l), since the differences between the attenuation of soft tissue (e.g., malignant lesion) and normal glandular tissue are minimum at mammography energies.[30–32] The X-ray spectrum was simulated using a W anode with Al filtering. The X-ray attenuation coefficient data come from ICRU Report 44.[30] Polychromatic spectra were simulated using an X-ray tracing algorithm.[37] The algorithm traces a ray model from the source, through the phantom volume, onto each detector element. The radiological path length is determined by the sum of the length traveled by this ray in each voxel, multiplied by the attenuation of each voxel. This process is repeated for each ray, and the intensity of the rays in a detector element determines the pixel value for the projection image. The acquisition geometry and automatic exposure settings of a clinical DBT system (Table 3) were used to simulate the projection images.[38] Reconstructed DBT slices were produced using simple backprojection with a commercially available software library.[39]

To evaluate differences between the two insertion methods (replacement and addition), ellipsoidal lesions (Figure 3a) were inserted into a phantom selected randomly from the calibration group. Noiseless DBT projections and raw reconstructions (i.e., without additional imaging processing) of the phantom were simulated with and without lesions. Reconstructed slices of the phantom with and without lesions were subtracted and the resulting pixel values (lesion signal only) were compared.

2.3 | Calibration

A dense grid of 42 equally-spaced lesions (Figure 4b) was embedded into each voxelized phantom (Figure 4a). The grid was inserted in the mid-plane (z) of each phantom. This grid was used to maximize the number of

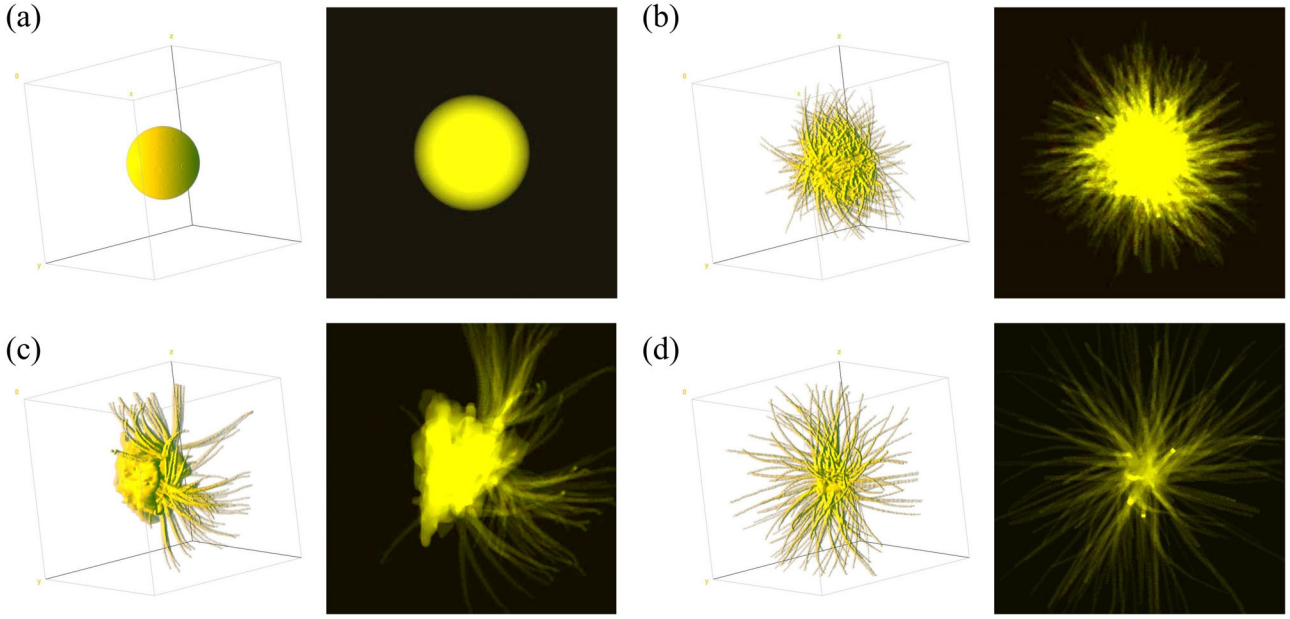

FIGURE 3 (Left) Volume view of breast lesion models and (right) average intensity of lesion slices: (a) ellipsoidal—model I, and (b–d) spiculated masses—models II–IV

TABLE 2 Summary of breast lesion measurements used in this study. Compactness, sphericity, elongation, and flatness were calculated using 3D ellipsoid fitting

Mass model	VOI size (mm^3)	Lesion voxels (#)	Compactness	Sphericity	Elongation	Flatness
(A) I	11×11×3.5	14,943	0.21	0.59	1.00	2.86
(B) II	11×11×3.5	30,760	0.16	0.54	1.04	3.76
(C) III	14×14×3.5	36,711	0.10	0.47	1.21	4.89
(D) IV	15×15×3.5	40,313	0.09	0.45	1.24	5.60

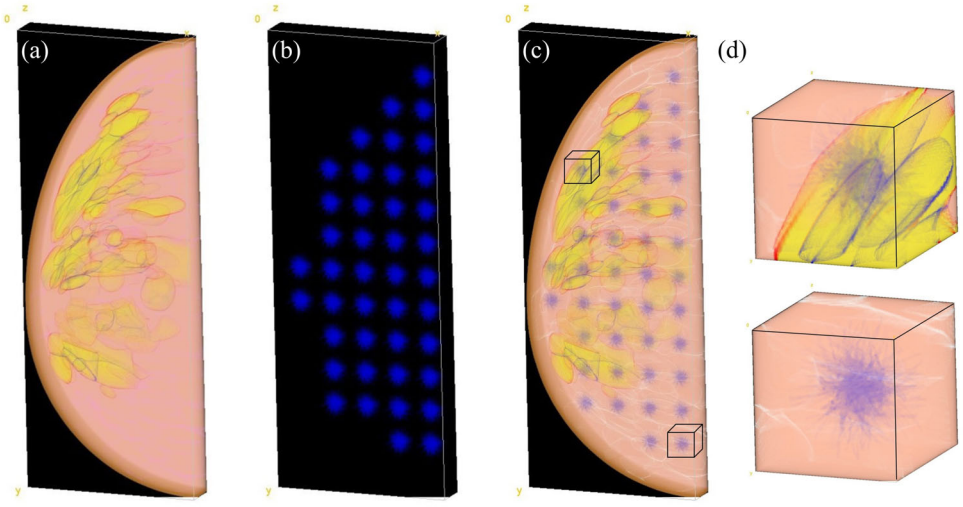

FIGURE 4 Example of (a) 3D projection view of a partial section of a breast phantom (ML view), (b) dense grid of lesions used to embed into breast phantoms, (c) partial section of a breast phantom after lesion insertion, and (d) two examples of volumes of interest (VOIs) containing lesions embedded into different breast phantom tissues

lesions in a phantom and accelerate the simulation process.

The calibration process requires the simulation of masses that consist of various partial volumes. The calibration determines the lesion (dimensions) and partial volumes (composition) that are in the actual range of detectability performed by humans. For ellipsoidal masses (Model I), w_l was varied from 1% to 10%, whereas for spiculated masses (Models II–IV) w_l was varied from 10% to 50%.

DBT projections and reconstructions of each phantom with and without lesions were simulated. For phantoms with lesions, projections and reconstructions were simulated for each lesion model and partial volume. Regions of interest (ROIs) were cropped using the acquisition geometry of the DBT system (Table 3), location of each lesion, and x–y dimensions of the VOIs (Table 2).

2.3.1 | Image interpretation

The database of ROIs with and without lesions was used to train and test the CHOs. For each CHO, the independent training and testing image sets included 500 ROIs with a mass model simulated using a particular partial volume, and 500 mass-free ROIs. The training and testing ROIs were selected randomly using the phantom dataset (Table 1). The VCTs were calibrated to match the threshold of mass detectability of virtual readers (CHOs) and human readers.

TABLE 3 Summary of digital breast tomosynthesis (DBT) acquisition parameters used in this study

X-ray source	
Anode material (a.u)	Tungsten
Filter material (a.u)	Aluminum
Filter thickness (mm)	0.7
Angular range (°)	[-7.5, +7.5]
Number of projections (#)	15
Tube motion (a.u)	Continuous
Focal spot size (mm)	0.3
Detector	
Detection material (a.u.)	a-Se
Detector element size (mm)	0.140 × 0.140
Number of elements (#)	2048 × 1664
Detector size (mm)	286.72 × 232.96
Source-to-image distance (mm)	700.0
Reconstruction	
Number of slices (# in z)	633
Voxel size (x×y, mm)	0.1×0.1×0.1
Bits stored (bits, [min, max] value)	14 [0, 16384]

The threshold of detectability is defined using ROC curves calculated from the CHO scores. The ROC curves, and the AUCs reported were calculated and compared with AUCs reported in a previous reader study (the predicate data).[22] Our aim is to achieve detectability thresholds of each mass model that is concordant and consistent with this predicate study. The 95% confidence interval (CI) of AUCs were reported. Lesion models and partial volumes that produce CHO's scores that match with human scores (i.e., AUCs in the 95% CI intervals) were considered to be "calibrated" and reproducible.

The Medical Virtual Image Chain software (MeVIC, Barco NV, Kortrijk, Belgium) was used to simulate video card features of a high-resolution medical display and collect the ROC statistics. The CHOs were trained using 15 Laguerre–Gauss (LG) channels. The LG channels represent the impulse response centered on the mass location.[17] The CHOs use the product of Laguerre polynomials and Gaussian functions defined by Equation (2):[17]

$$u_p\ (r) = \frac{\sqrt{2}}{a_u}\exp\left(\frac{-\pi r^2}{a_u^2}\right) L_p\left(\frac{2\pi r^2}{a_u^2}\right), \qquad (2)$$

where $r \in \mathbb{R}^2$, a_u is the spread parameter of the LG channel, and L_p represents the Laguerre polynomials (Equation (3)):[17]

$$L_p\ (x) = \sum_{k=0}^{p} (-1)^p \left(\frac{p}{k}\right) \frac{x^k}{k!}. \qquad (3)$$

The weight of the polynomials is concentrated within a Gaussian envelope with spread σ_u, where $a_u^2 = 2\pi{\sigma_u}^2$. In this study, we used a_u values of 15, 20, and 21, for each image reconstructed ROI sizes of 11 mm,^{2} 14 mm,^{2} and 15 mm^2 (10-bit depth). These parameters were selected based on values previously reported on the literature.[14]

2.3.2 | Statistical analyses

ROC curves and AUCs were calculated for each individual CHO using the readers' scores. The ROCs were categorized by lesion type and partial volume. AUC differences between two paired ROCs were reported using 2000 stratified bootstrap replicates computed based on the Delong method.[40] The 95% CI was also reported using 2000 stratified bootstrap replicates computed based on the Delong method. The standard error of the AUC scores was computed using the equivalence Wilcoxon test. The R packages "pROC" (version 1.17) and "auctestr" (version 1.0) were used to collect the ROC statistics.[40,41] The ROCs and AUCs were also categorized by lesion calibration.

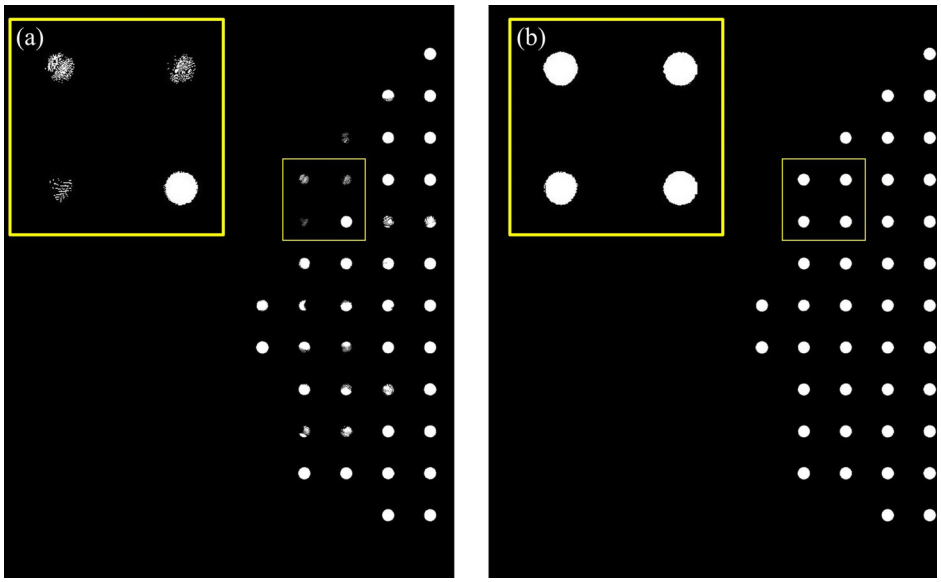

FIGURE 5 Resulted reconstruction slice (central) after subtraction of lesion signal and phantom background (binary image with threshold of positive pixel values). The yellow boxes show the zoom-in (300%) of four ellipsoidal lesions simulated using the (a) replacement and (b) additive insertion methods

3 | RESULTS

3.1 | Assessment of lesion insertion methods

Figure 5 shows the binary images resulted from the subtraction of noiseless reconstructed slices of a phantom with and without lesions. Note that the replacement method (Figure 5a) can result in negative pixel values (≤ 0) in these difference images for simulated with lesions composed of soft tissue, which corresponds to a negative lesion contrast in the source image. By comparison, the additive method with partial volumes (Figure 5b, additive method) only resulted in reconstructed images with positive values for the pixels that represent masses.

3.2 | Effect of partial volume and mass models in lesion detectability

Case difficulty on mass detection varied with the shape and partial volume of lesions (Figure 6). Mass models I (Figure 6a) and II (Figure 6b) were used to illustrate the effect of partial volume and shape on lesion detectability. For model I (ellipsoidal), $w_l = 0.1$ resulted in an AUC = 0.934 in the calibration process, while model II (spiculated) achieved AUC = 0.743. This large difference between AUCs (ΔAUC = 0.191) of ellipsoidal and spiculated lesions (models I and II) is because of the shape lesion and the impact of that shape on the manufacturers' image reconstruction and image post-processing (Figure 7). Note that the image reconstruction software used to reconstruct the DBT images enhances borders of circular lesions and creates a "shadowing artifact" (Figure 7a) that affects significantly the lesion detectability of CHOs.

Table 4 shows the statistical differences between paired ROCs illustrated in Figure 6a,b. The differences in AUCs are statistically significant for the evaluated partial volumes ($P < 0.001$), except for model I and paired ROCs that represent partial volumes with $w_l = 0.01$ and $w_l = 0.05$.

The calibration process using lesions with various partial volumes was repeated for every lesion model. ROC results from the CHO analyses of the calibrated lesion models are shown in Figure 8a. After calibration, the mean AUC [95% CI] results are in the interval reported in a previous reader study used as reference (0.93 [0.89, 0.97]). The calibrated lesions were simulated using $w_l = 0.1$ for ellipsoidal masses (model I) and $w_l = 0.5$ for spiculated masses (models II–IV), respectively.

Table 5 shows statistical differences between paired ROCs illustrated in Figure 8a. Note that the differences in AUCs are not statistically significant between spiculated lesions (II–III, II–IV, and III–IV). The differences in AUCs are statistically significant between ellipsoidal and spiculated lesions (I–II and I–III), except between lesion models I and IV ($P = 0.37$).

4 | DISCUSSION

In our research, we use VCTs to design and evaluate systems in terms of metrics that most closely match clinical metrics. We use predicate data of existing systems for comparison against our novel technologies, using a set of virtual patients with (and without) pathological findings that match clinical populations closely. In

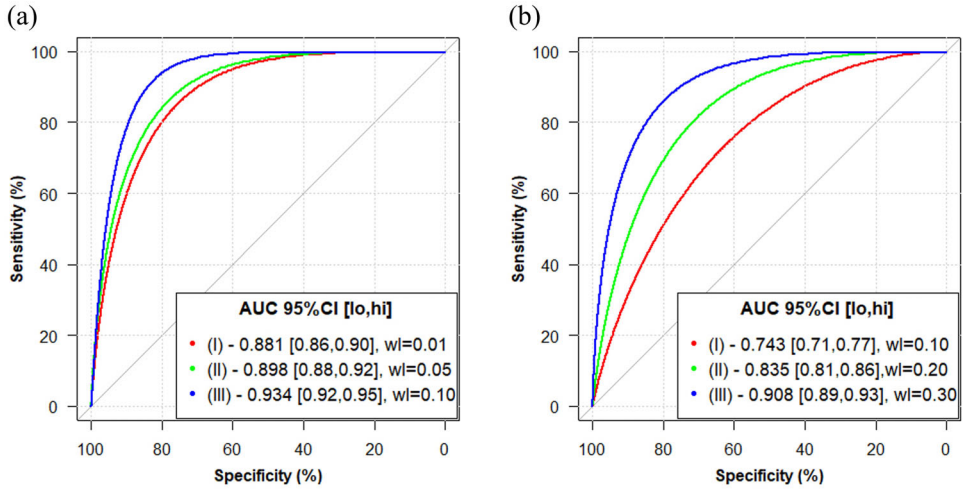

FIGURE 6 Receiver operating characteristic (ROCs) calculated using scores of channelized Hotelling observers (CHOs) to estimate detectability of lesions composed of soft tissue. The ROCs were categorized by partial volume (red, green, blue). (a) Model I and (b) model II

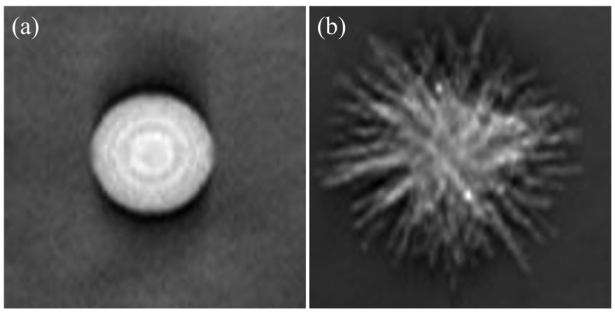

FIGURE 7 Average of 500 regions of interest (ROIs) of digital breast tomosynthesis (DBT) images reconstructed with masses on focus (central slice)

TABLE 4 AUC comparison of paired ROCs evaluated using different w_l. Statistical differences (*p*-value) and differences in AUC (ΔAUC) are shown for models (A) I and (B) II

	(A)		(B)	
Pairwise Comparison,w_l	**|ΔAUC|**	***P*-Value**	**|ΔAUC|**	***P*-Value**
(A) 0.01–0.05 and (B) 0.1–0.3	0.02	0.12	0.09	<0.001
(A) 0.01–0.10 and (B) 0.1–0.5	0.05	<0.001	0.16	<0.001
(A) 0.05–0.10 and (B) 0.3–0.5	0.03	<0.001	0.07	<0.001

so doing, VCTs can evaluate the performance of these novel imaging systems using the exact same cases and exposure conditions including the same breast compression as the predicate device, which is generally difficult to achieve in real clinical trials; we attribute any differences in performance observed to differences in the system and/or the interaction of the model observer with the system. In the current study, the methods previously used for simulating breast pathologies were revised to avoid non-clinical images. Alternative methods clearly exist, such as hybrid VCTs[42,43] in which lesions are added to clinical images, but this presupposes that the novel system already exists. Similarly, alterative phantoms which simulate breast anatomy exist.[44–47] In both of these cases, we believe that the methods presented here (voxel replacement and voxel addition) would still be beneficial.

We have previously shown that voxel-replacement for calcifications results in realistic images.[5,7,9,14] This arises because the attenuation of calcifications is markedly higher than any soft tissue. As a result, the calcifications will always show positive contrast again breast tissue, either adipose, glandular, or carcinoma. However, we have observed through various experiments that the voxel-replacement method can result in negative lesion contrast in the simulated X-ray image of masses (Figure 5a). In no instance does carcinoma appear with negative contrast in clinical images. This is not observed in voxel-addition (Figure 5b). The additive method is reasonable anatomically too. Cancer invades adjacent tissues; if one were to select a small cube of tissue (analogous to a voxel) and analyze it under a microscope, one would expect to see both normal and cancerous cells. Thus, an insertion method that uses partial volumes of cancer and breast tissue(s) should simulate X-ray images more realistically. As an aside, it is worth noting that even with calcifications, we use a weighting factor to simulate partial attenuation; however, in this case we do not use an admixture of tissue and calcium. Experiments with voxel addition for calcifications (not shown here) have not yielded benefit over voxel replacement.

In this study, the response of CHOs varied with (i) lesion shape and (ii) composition. (i) We have shown that ellipsoidal masses have a higher detectability threshold

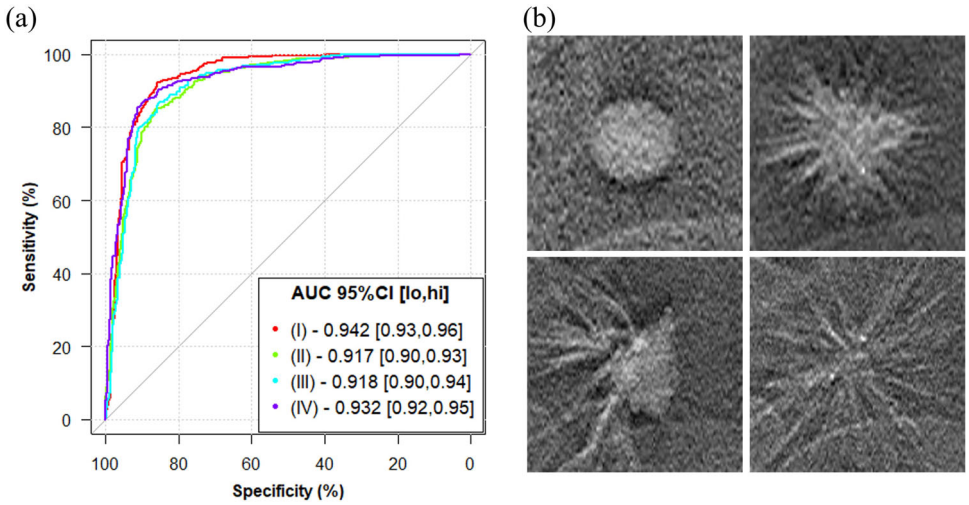

FIGURE 8 (a) Receiver operating characteristics (ROCs) categorized by calibrated lesion models and (b) example of regions of interest (ROIs) of digital breast tomosynthesis (DBT) images reconstructed with calibrated masses on focus (central slice)

TABLE 5 AUC comparison of paired ROCs evaluated using different calibrated lesion models. Statistical differences (*P*-value) and differences in AUC (ΔAUC) are shown for models (a) I and (b) II

Pairwise comparison, model	|ΔAUC|	*P*-value
I–II	0.025	0.03
I–III	0.024	0.04
I–IV	0.009	0.37
II–III	0.001	0.93
II–IV	0.015	0.22
III–IV	0.014	0.24

than spiculated lesions in VCTs (Figure 6). In addition, (ii) masses composed of denser tissue result in an increased detectability threshold. Both (i and ii) support the necessity of an efficient calibration method to match the detectability threshold of virtual and human readings; lesion detectability is not linear with increased w_l of glandular tissue. Computers tend to be more sensitive than humans in detection tasks[48,49]; the detectability threshold must be scaled and calibrated accordingly. MOs should be trained using a realistic dataset that results in the proper response of case difficulty predicted by human readers.[1]

The lesion size, shape, and composition were selected based on the ROC results calculated using CHOs and matched within the 95% CI AUC reported in a previous reader study.[22] While our VCT results are within the 95% CI AUC (Figure 8a), they do not predict the shape of the ROC curves reported by Rafferty et al. curves accurately, especially for lower values of sensitivity. We believe that CHOs must be trained using datasets of mixed cases that *vary in difficulty*, including images with lesions that are below, at, and above the thresholds of detectability. Future work is still needed to predict human performance more accurately and to match the shape of the ROC curves better. It is important to mention that our VCT framework[6] allows the fast simulation of patients and images, making the calibration process feasible for large-scale VCTs.

The shape of masses, in terms of core size and/or elongation of spicules, has a greater effect on lesion detectability than volume. Although mass model IV consists of the largest number of lesion voxels, this model represents masses with the smallest core and largest elongation of spicules (Table 2). Especially for this mass model, the signal-to-noise ratio (SNR) and CHO scores were affected substantially; the actual lesion signal is less intense and less clearly bounded (Figure 8b).

Imaging reconstruction and image processing can affect lesion detectability. Structures with ellipsoidal shapes or large cores demonstrate edge enhancement due to the sharp transition from tumor to the surrounding tissue, leading to artifacts that can be noted in the X-ray images, especially in the tube motion direction (Figure 7a). These artifacts also affect the SNR and CHOs' scores. Thus, ellipsoidal lesions result in increased AUC and *d'* values, which in turn require lower weighting factors in the admixture of tumor and breast tissue for calibration to the predicate experiments.

Some limitations exist in terms of the breast size, volume, and textural complexity of mammary parenchyma in the anatomical models. In addition, only four lesion models were evaluated for testing the proposed calibration method. However, the anatomical breast and lesion models were intentionally constrained to simplify the detection task and to evaluate the impact of the lesion parameters and simulation methods used to calibrate masses. Also, in this work we simulate a uniform admixture throughout the lesion; in future work, we can consider more realistic spatial heterogeneity within tumors.

Finally, it is worth discussing our choice of metrics for VCTs. There are many possibly ways in which VCTs can be conducted. For example, we have conducted VCTs in which no machine observer is used; rather, we have used quantitative tools such as breast density[50]; similarly, we have recently begun to use *physics VCTs*[24] in which quantitative measures such as phantom score[25] or spatial resolution[24] are evaluated. While physics VCTs were developed as a pass–fail step in moving a VCT-designed imaging system into real clinical trials, they have proven to be useful in their own right. There are myriad other methods that can be used for VCTs. For example, a number of papers[51–53] have used the threshold detectable diameter of specific lesion models to rank different imaging systems. Vancoillie et al. were able to demonstrate that DBT could resolve smaller lesions that DM.[51] While this can be compared to human performance in terms of the detectability of targets in phantom images, it is not possible to conduct a clinical study to investigate the minimum detectable size of findings in vitro, as no accurate and reproducible method of measuring lesion size exists, nor would it be possible to compare such a measure with the threshold of detectability achieved with VCTs. Thus, while providing a useful tool to design new imaging systems or compare existing systems, it does not have a direct clinical correlate.

Our repeated use of the joint evaluation of AUC and *d'* is also noteworthy. AUC is one of the most common and respected metrics for evaluating or comparing imaging systems clinically. AUC is relatively insensitive to cancer prevalence,[54] which allows it to be used to compare between different study populations (such as screening and diagnostic populations). But, AUC is sensitive to lesion conspicuity (the relative difficulty of detection); very different AUCs result from sets of images with different levels of difficulty. This was one of the reasons that CAD researchers moved to standardized test sets, because CAD performance is sensitive both to the algorithm and case difficulty.[55,56] It is important to remember, however, that AUC is also a nonlinear function of the perceived SNR of the images (*d'*).[57] Thus, for example, the change in SNR required to increase AUC by 0.01 is markedly different for an AUC of 0.80 as compared to 0.98. *d'* linearizes the performance changes; it is for this reason that (1) we calibrate our VCTs to a predicate AUC, and (2) we always report *d'*. In doing so, we can demonstrate that we do not run afoul of the nonlinearity of the AUC.

5 | CONCLUSION

In summary, the difficulty of virtual imaging cases varies with shape, composition, and breast density. VCTs require an efficient method to simulate pathologies and to calibrate lesions, matching the detectability threshold of virtual and human readings. We have shown in this study that lesion composition and shape are parameters that should be carefully modified to calibrate VCTs to match the human performance in terms of AUCs. In future work, the shape of the ROCs will be improved to match the curves reported by human readers accurately.

ACKNOWLEDGMENTS

We would like to thank Dr. Bosmans for providing the spiculated mass models used in this work, and to Real-Time Tomography (RTT) for providing the reconstruction software. Andrew D. A. Maidment is a scientific advisor to RTT, and his spouse is an employee and shareholder of RTT.

CONFLICT OF INTEREST

The authors declare that there is no conflict of interest that could be perceived as prejudicing the impartiality of the research reported.

REFERENCES

1. Abadi E, Segars WP, Tsui BMW, et al. Virtual clinical trials in medical imaging: A review. *J Med Imaging*. 2020;7(4):042805-1-40. http://doi.org/10.1117/1.JMI.7.4.042805.
2. Mackenzie A, Thomson EL, Mitchell M, et al. Virtual clinical trial to compare cancer detection using combinations of 2D mammography, digital breast tomosynthesis and synthetic 2D imaging. *Eur Radiol*. 2021;32(2):806-814. http://doi.org/10.1007/s00330-021-08197-x.
3. Vancoillie L, Marshall N, Cockmartin L, Vignero J, Zhang G, Bosmans H. Verification of the accuracy of a hybrid breast imaging simulation framework for virtual clinical trial applications. *J Med Imaging*. 2020;7(04): 042804. http://doi.org/10.1117/1.jmi.7.4.042804.
4. Cockmartin L, Marshall NW, Van Ongeval C, et al. Comparison of digital breast tomosynthesis and 2D digital mammography using a hybrid performance test. *Phys Med Biol*. 2015;60(10):3939. http://doi.org/10.1088/0031-9155/60/10/3939.
5. Barufaldi B, Maidment ADA, Dustler M, et al. Virtual clinical trials in medical imaging system evaluation and optimisation. *Radiat Prot Dosimetry*. 2021;195(3-4):363-371. http://doi.org/10.1093/rpd/ncab080.
6. Barufaldi B, Bakic PR, Higginbotham D, Maidment ADA. OpenVCT: A GPU-accelerated virtual clinical trial pipeline for mammography and digital breast tomosynthesis. *SPIE Med Imaging*. 2018;1057358:10573588. http://doi.org/10.1117/12.2294935.
7. Barufaldi B, Bakic PR, Maidment ADA. Multiple-reader, multiple-case ROC analysis for determining the limit of calcification detection in tomosynthesis. *SPIE Med Imaging*. 2019;10948. http://doi.org/10.1117/12.2512884.
8. Badano A, Badal A, Glick S, et al. In silico imaging clinical trials for regulatory evaluation: Initial considerations for VICTRE, a demonstration study. *SPIE Med Imaging 2017*. 2017;1013220:1013220. http://doi.org/10.1117/12.2255746.
9. Barufaldi B, Bakic PR, Pokrajac DD, Lago MA, Maidment ADA. Developing populations of software breast phantoms for virtual clinical trials. *14th International Workshop on Breast Imaging (IWBI 2018)*. SPIE Digital Library; 2018:73. http://doi.org/10.1117/12.2318473.
10. Park S, Zhang G, Myers KJ. Comparison of channel methods and observer models for the task-based assessment of multi-projection imaging in the presence of structured anatomical noise. *IEEE Trans Med Imaging*. 2016;35(6):1431-1442. http://doi.org/10.1109/TMI.2016.2515027.

11. Lago MA, Barufaldi BB, Bakic PR, Abbey CK, Maidment ADA, Eckstein MP. Foveated model observer to predict human search performance on virtual digital breast tomosynthesis phantoms. SPIE Medical Imaging *2020*. SPIE Digital Library; 2020:11316V7. http://doi.org/10.1117/12.2550485.
12. Lago MA, Jonnalagadda A, Abbey CK, et al. Under-exploration of three-dimensional images leads to search errors for small salient targets. *Curr Biol*. 2021;31(5):1099-1106. http://doi.org/10.1016/j.cub.2020.12.029.
13. Pourvaziri A, Parakh A, Mojtahed A, Kambadakone A, Sahani DV. Diagnostic performance of dual-energy CT and subtraction CT for renal lesion detection and characterization. *Eur Radiol*. 2019;29(12):6559-6570. http://doi.org/10.1007/s00330-019-06224-6.
14. Bakic PR, Barufaldi B, Higginbotham D, et al. Virtual clinical trial of lesion detection in digital mammography and digital breast tomosynthesis. *SPIE Med Imaging*. 2018;1057306:1-13. http://doi.org/10.1117/12.2294934.
15. Zeng R, Samuelson FW, Sharma D, et al. Computational reader design and statistical performance evaluation of an in-silico imaging clinical trial comparing digital breast tomosynthesis with full-field digital mammography. *J Med Imaging*. 2020;7(04):042802. http://doi.org/10.1117/1.jmi.7.4.042802.
16. Park S, Zhang GZ, Zeng R, Myers KJ. Comparing observer models and feature selection methods for a task-based statistical assessment of digital breast tomsynthesis in reconstruction space. *SPIE Med Imaging*. 2014;9037:90370M. http://doi.org/10.1117/12.2043598.
17. Platiša L, Goossens B, Vansteenkiste E, et al. Channelized Hotelling observers for the assessment of volumetric imaging data sets. *J Opt Soc Am A*. 2011;28(6):1145-1163. http://doi.org/10.1364/josaa.28.001145.
18. Barrett HH, Yao J, Rolland JP, Myers KJ. Model observers for assessment of image quality. *Natl Acad Sci USA*. 1993;90:9758-9765. http://doi.org/10.1073/pnas.90.21.9758.
19. Tanner WP, Swets JA. The human use of information: I. Signal detection for the case of the signal known exactly. *IRE Prof Gr Inf Theory*. 1954;4(4):213-221. http://doi.org/10.1109/TIT.1954.1057461.
20. Kopp FK, Catalano M, Pfeiffer D, Fingerle AA, Rummeny EJ, Noël PB. CNN as model observer in a liver lesion detection task for X-ray computed tomography: A phantom study. *Med Phys*. 2018;45(10):4439-4447. http://doi.org/10.1002/mp.13151.
21. Abbey CK, Barrett HH. Human- and model-observer performance in ramp-spectrum noise: Effects of regularization and object variability. *J Opt Soc Am A*. 2000;18:473-488. http://doi.org/10.1364/JOSAA.18.000473.
22. Rafferty EA, Park JM, Philpotts LE, Poplack SP, Sumkin JH. Digital mammography and breast tomosynthesis compared with digital mammography alone: Results of a multicenter, multireader trial. *Radiology*. 2013;266(1):104-113. http://doi.org/10.1148/radiol.12120674/-/DC1.
23. Barufaldi B, Vent TL, Acciavatti RJ, Bakic PR, Noel PB, Maidment AD. MRMC ROC analysis of calcification detection in tomosynthesis using computed super resolution and virtual clinical trials. *15th International Workshop on Breast Imaging (IWBI2020)*. SPIE Digital Library; 2020:1151313. http://doi.org/10.1117/12.2564118.
24. Vent TL, Barufaldi B, Maidment ADA. Simulation and experimental validation of high-resolution test objects for evaluating a next-generation digital breast tomosynthesis prototype. *SPIE Med Imaging*. 2019;109480M:1-21. http://doi.org/10.1117/12.2511304.
25. Acciavatti RJ, Barufaldi B, Vent TL, Wileyto EP, Maidment ADA. Personalization of X-ray tube motion in digital breast tomosynthesis using virtual Defrise phantoms. *SPIE Med Imaging*. 2019;10:1-9. http://doi.org/10.1117/12.2511780.
26. Vent TL, Barufaldi B, Acciavatti RJ, Maidment A. Simulation of high-resolution test objects using non-isocentric acquisition geometries in next-generation digital tomosynthesis. *SPIE Med Imaging*. 2020;1151317:23. http://doi.org/10.1117/12.2561098.
27. Hinton B, Ma L, Mahmoudzadeh AP, et al. Derived mammographic masking measures based on simulated lesions predict the risk of interval cancer after controlling for known risk factors: A case–case analysis. *Med Phys*. 2019;46(3):1309-1316. http://doi.org/10.1002/mp.13410.
28. Holland K, van Gils CH, Mann RM, Karssemeijer N. Quantification of masking risk in screening mammography with volumetric breast density maps. *Breast Cancer Res Treat*. 2017;162(3):541-548. http://doi.org/10.1007/s10549-017-4137-4.
29. Bakic PR, Barufaldi B, Pokrajac D, Weinstein SP, Maidment AD. Optimized simulation of breast anatomy for virtual clinical trials. *14th International Workshop on Breast Imaging (IWBI 2018)*. SPIE Digital Library; 2018. http://doi.org/10.1117/12.2318473.
30. ICRU. ICRU Report 44: Tissue substitutes in radiation dosimetry and measurement. 1988.
31. Johns PC, Yaffe MJ. X-ray characterisation of normal and neoplastic breast tissues. *Phys Med Biol*. 1987;32(6):675. http://doi.org/10.1088/0031-9155/32/6/002.
32. Fredenberg E, Willsher P, Moa E, Dance DR, Young KC, Wallis MG. Measurement of breast-tissue X-ray attenuation by spectral imaging: Fresh and fixed normal and malignant tissue. *Phys Med Biol*. 2018;63(23):235003. http://doi.org/10.1088/1361-6560/aaea83.
33. Chen F, Bakic PR, Maidment ADA, Jensen ST, Shi X, Pokrajac DD. Description and characterization of a novel method for partial volume simulation in software breast phantoms. *IEEE Trans Med Imaging*. 2015;34(10):2146-2161. http://doi.org/10.1109/TMI.2015.2424854.
34. Pokrajac DD, Maidment ADA, Bakic PR. Optimized generation of high resolution breast anthropomorphic software phantoms. *Med Phys*. 2012;39(4):2290. http://doi.org/10.1118/1.3697523.
35. Shaheen E, De Keyzer F, Bosmans H, Dance DR, Young KC, Van Ongeval C. The simulation of 3D mass models in 2D digital mammography and breast tomosynthesis. *Med Phys*. 2014;41(8):10-12. http://doi.org/10.1118/1.4890590.
36. Ollion J, Cochennec J, Loll F, Escudé C, Boudier T. TANGO: A generic tool for high-throughput 3D image analysis for studying nuclear organization. *Bioinformatics*. 2013;29(14):1840-1841. http://doi.org/10.1093/bioinformatics/btt276.
37. Siddon RL. Fast calculation of the exact radiological path for a three-dimensional CT array. *Med Phys*. 1985;12(2):252-255. http://doi.org/10.1118/1.595715.
38. Feng SSJ, Sechopoulos I. Clinical digital breast tomosynthesis system: Dosimetric characterization. *Radiology*. 2012;263(1):35-42.
39. Chui JH, Pokrajac DD, Maidment ADA, Bakic PR. Roadmap for efficient parallelization of breast anatomy simulation. *SPIE Med Imaging*. 2012;8313:83134T. http://doi.org/10.1117/12.912125. SPIE Digital Library.
40. Robin X, Turck N, Hainard A, et al. pROC: An open-source package for R and S+ to analyze and compare ROC curves. *BMC Bioinform*. 2011;12(77):1-8. http://doi.org/10.1186/1471-2105-12-77.
41. Fogarty J, Baker RS, Hudson SE, Case studies in the use of ROC curve analysis for sensor-based estimates in human computer interaction. In: *ProceedingsGraphics Interface*. 2005:1-8.
42. Schebesch F, Herbst M, Ritschl L, Mertelmeier T, Maier A. A hybrid approach for virtual clinical trials for mammographic imaging. *14th International Workshop on Breast Imaging (IWBI 2018)*. SPIE Digital Library; 2018:1-12. http://doi.org/10.1117/12.2318452.
43. Mackenzie A, Kaur S, Thomson EL, et al. Effect of glandularity on the detection of simulated cancers in planar, tomosynthesis, and synthetic 2D imaging of the breast using a hybrid virtual clinical trial. *Med Phys*. 2021;48(11):6859-6868. http://doi.org/10.1002/mp.15216.

44. Carton AK, Bakic P, Ullberg C, Derand H, Maidment ADA. Development of a physical 3D anthropomorphic breast phantom. *Med Phys*. 2011;38(2):891-896. http://doi.org/10.1118/1.3533896.
45. Glick SJ, Ikejimba LC. Advances in digital and physical anthropomorphic breast phantoms for X-ray imaging. *Med Phys*. 2018;45(10):e870-e875. http://doi.org/10.1002/mp.13110.
46. Caballo M, Mann R, Sechopoulos I. Patient-based 4D digital breast phantom for perfusion contrast-enhanced breast CT imaging. *Med Phys*. 2018;45(10):4448-4460. http://doi.org/10.1002/mp.13156.
47. He Y, Liu Y, Dyer BA, et al. 3D-printed breast phantom for multi-purpose and multi-modality imaging. *Quant Imaging Med Surg*. 2019;9(1):63-74. https://doi.org/10.21037/qims.2019.01.05.
48. Sang KY, Woo KM, Cho N, et al. Screening mammography-detected cancers: sensitivity of a computer-aided detection system applied to full-field digital mammograms. *Radiology*. 2007;244(1):104-11. http://doi.org/10.1148/radiol.2441060756.
49. Silva M, Schaefer-Prokop CM, Jacobs C, et al. Detection of subsolid nodules in lung cancer screening: Complementary sensitivity of visual reading and computer-aided diagnosis. *Invest Radiol*. 2018;53(8):441-449. http://doi.org/10.1097/RLI.0000000000000464.
50. Peregrino LR, Gomes JV, do Rêgo TG, et al. Automatic segmentation of mammary tissue using computer simulations of breast phantoms and deep-learning techniques. In: *14th International Joint Conference on Biomedical Engineering Systems and Technologies*. SCITEPRESS; 2021. p. 252-259. http://doi.org.10.5220/0010310402520259
51. Vancoillie L, Cockmartin L, Tri Wigati K, et al. Performance evaluation of a 3D structured phantom with simulated lesions on breast imaging systems. *14th International Workshop on Breast Imaging (IWBI 2018)*. SPIE Digital Library; 2018:10718. http://doi.org/10.1117/12.2318472.
52. Mackenzie A, Eales TD, Dunn HL, Yip Braidley M, Dance DR, Young KC. Simulation of images of CDMAM phantom and the estimation of measurement uncertainties of threshold gold thickness. *Phys Med*. 2017;39:137-146. http://doi.org/10.1016/j.ejmp.2017.06.019.
53. Strudley CJ, Young KC. Evaluation of a new design of contrast-detail phantom for mammography: cDMAM model 4.0. *Lecture Notes in Computer Science*. 2014;8539. http://doi.org/10.1007/978-3-319-07887-8_31.
54. Carrington AM, Fieguth PW, Qazi H, et al. A new concordant partial AUC and partial C statistic for imbalanced data in the evaluation of machine learning algorithms. *BMC Med Inform Decis Mak*. 2020;20(1):4. http://doi.org/10.1186/s12911-019-1014-6.
55. Lehman CD, Wellman RD, Buist DSM, Kerlikowske K, Tosteson ANA, Miglioretti DL. Diagnostic accuracy of digital screening mammography with and without computer-aided detection. *JAMA Intern Med*. 2015;175(11)1828-37. http://doi.org/10.1001/jamainternmed.2015.5231.
56. Nishikawa RM, Gur D. CADe for early detection of breast cancer-current status and why we need to continue to explore new approaches. *Acad Radiol*. 2014;21(10):1320-1. http://doi.org/10.1016/j.acra.2014.05.018.
57. Swets JA, Pickett RM. *Evaluation of Diagnostic Systems: Methods from Signal Detection Theory*. Academic Press; 1982.

How to cite this article: Barufaldi B, Vent TL, Bakic PR, Maidment ADA. Computer simulations of case difficulty in digital breast tomosynthesis using virtual clinical trials. *Med Phys.* 2022;49:2220–2232. https://doi.org/10.1002/mp.15553

Achieving Isotropic Super-Resolution with a Non-Isocentric Acquisition Geometry in a Next-Generation Tomosynthesis System

Raymond J. Acciavatti, Chloe J. Choi, Trevor L. Vent, Bruno Barufaldi, Andrew D. A. Maidment
University of Pennsylvania, Department of Radiology, 3400 Spruce Street, Philadelphia PA 19104
E-mail: {Raymond.Acciavatti | Jeongin.Choi | Trevor.Vent | Bruno.Barufaldi | Andrew.Maidment}@pennmedicine.upenn.edu

ABSTRACT

We have constructed a prototype next-generation tomosynthesis (NGT) system that supports a non-isocentric acquisition geometry for digital breast tomosynthesis (DBT). In this geometry, the detector gradually descends in the superior-to-inferior direction. The aim of this work is to demonstrate that this geometry offers isotropic super-resolution (SR), unlike clinical DBT systems which are characterized by anisotropies in SR. To this end, a theoretical model of a sinusoidal test object was developed with frequency exceeding the alias frequency of the detector. We simulated two geometries: (1) a conventional geometry with a stationary detector, and (2) a non-isocentric geometry. The input frequency was varied over the full 360° range of angles in the plane of the object. To investigate whether SR was achieved, we calculated the Fourier transform of the reconstruction. The amplitude of the tallest peak below the alias frequency was measured relative to the peak at the input frequency. This ratio (termed the *r*-factor) should approach zero to achieve high-quality SR. In the conventional geometry, the *r*-factor was minimized (approaching zero) if the orientation of the frequency was parallel with the source motion, yet exceeded unity (prohibiting SR) in the orientation perpendicular to the source motion. However, in the non-isocentric geometry, the *r*-factor was minimized (approaching zero) for all orientations of the frequency, meaning SR was achieved isotropically. In summary, isotropic SR in DBT can be achieved using the non-isocentric acquisition geometry supported by the NGT system.

Keywords: Digital breast tomosynthesis, super-resolution, aliasing, Fourier transform, digital imaging, image quality, image reconstruction.

1. INTRODUCTION

Digital breast tomosynthesis (DBT) or "3D mammography" offers superior sensitivity and specificity for breast cancer screening relative to 2D-alone mammography.[1-3] DBT mitigates tissue superposition effects, benefiting *z*-axis resolution (Figure 1). Various works have demonstrated that increasing the angular range of the scan is beneficial for mass imaging, by improving *z*-axis resolution[4,5], but not for calcification imaging.[6-8] We previously found that super-resolution (SR) is a mechanism to improve calcification imaging in DBT.[9,10] A necessary condition for SR is that the reconstruction is prepared with finer pixelation than the detector.

In our previous works, we simulated high-frequency test patterns, and found that DBT suffers from anisotropies in SR at regularly-spaced increments in the *z* direction.[11,12] The anisotropies are suppressed by a non-isocentric geometry; that is, a geometry with detector motion in the superior-to-inferior ($-z$) direction. Our previous works focused on the spatial dependency of SR; we now focus on the orientation dependency. The purpose of this paper is to demonstrate that the non-isocentric geometry allows for SR over all orientations of a high-frequency test pattern from 0° to 360°.

We have built a next-generation tomosynthesis (NGT) system with a non-isocentric geometry.[13,14] The advantage of this geometry can be understood from the projection images of a point-like object [Figure 1(a)]. The x-ray source is translated in the *x* direction (laterally). Therefore, in the projection images, there are subpixel shifts in the *x* direction (achieving SR in this direction). The net shift in the posteroanterior (PA) direction is minimal, since there is no x-ray source motion in this direction, and thus SR is not achievable in this direction. In a non-isocentric geometry the net shift in the PA direction is more pronounced, allowing for subpixel sampling gain and hence SR in the PA direction.

Medical Imaging 2022: Physics of Medical Imaging, edited by Wei Zhao, Lifeng Yu, Proc. of SPIE
Vol. 12031, 120314B · © 2022 SPIE · 1605-7422 · doi: 10.1117/12.2612451

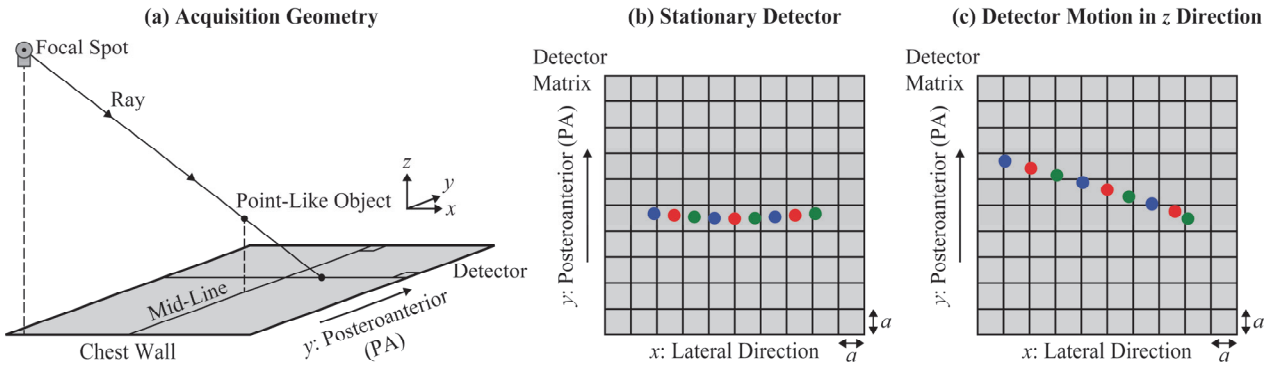

Figure 1. (a) Projection images of a point-like object are illustrated in a DBT system with lateral source motion. (b) In a conventional geometry, SR is achieved in the x direction due to shifts in this direction; shifts are minimal in the PA direction. (c) In a non-isocentric geometry, the detector descends in the $-z$ direction during the scan, resulting in more pronounced shifts in the PA direction and thus SR in the PA direction.

2. METHODS

2.1 Acquisition Geometry

A DBT system with N projections is modeled with source motion in the xz plane with angular range Θ. The center-of-rotation (COR) is treated as the midpoint of the breast support in this plane, and modeled as the origin, O (Figure 2). The radius of the source motion is z_M. The detector coordinate b_z (with midpoint O′ in this plane) is taken to be –10.0 mm at the start of the scan for the purpose of simulations. The coordinate b_z is constant in a conventional geometry but varies during the scan in a non-isocentric geometry. This paper presumes that the detector motion is superior-to-inferior ($-z$ direction).

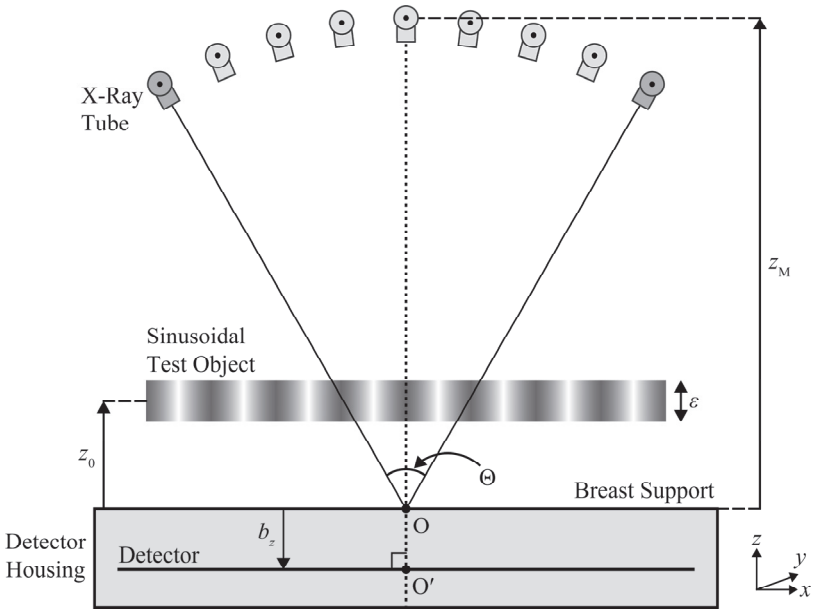

Figure 2. X-ray source motion follows a circular arc in the chest-wall plane with angular range Θ. The COR at the origin (point O) is taken to be the midpoint of the breast support in this plane. The sinusoidal test object (thickness ε) is simulated in both conventional and non-isocentric geometries.

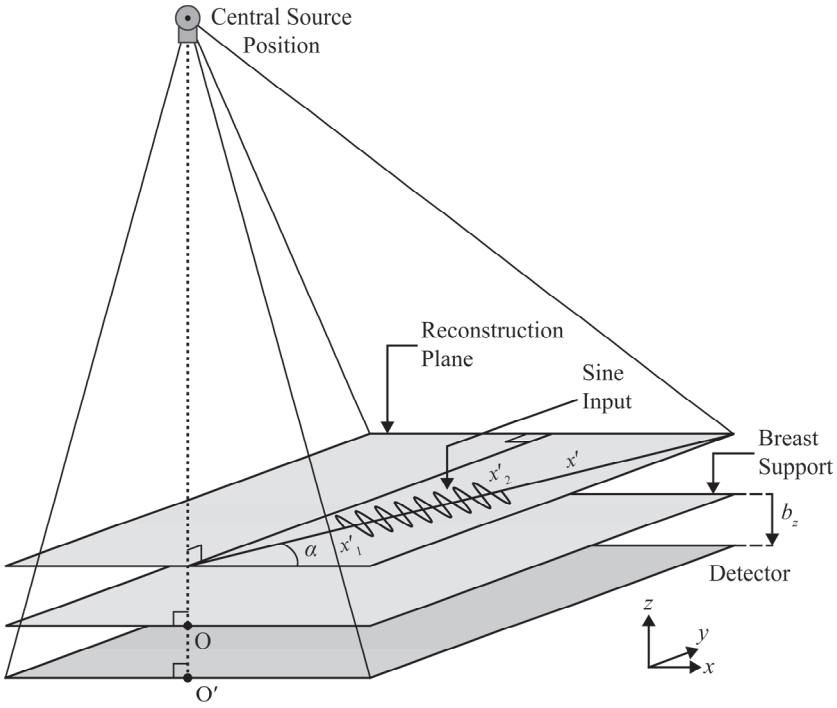

Figure 3. The frequency angle (α) is varied from 0° to 360° to investigate the orientation dependency of SR. The Fourier transform of the reconstruction is calculated along the x' direction between endpoints x'_1 and x'_2.

2.2 Simulated Test Object for Super-Resolution

We derived a theoretical model of the simple backprojection (SBP) reconstruction of a sinusoidal test object with frequency f_0 (9.5 mm^{-1}) and thickness ε in our previous work.[11] This model is used to investigate the orientation dependency of SR by varying the polar angle α in Figure 3 from 0° to 360°. The Fourier transform of the SBP reconstruction, μ_R, is calculated with the midpoint integration formula similar to our previous work[11]

$$\mathcal{F}\mu_R \approx \left(\frac{x'_2 - x'_1}{K}\right)\sum_{k=1}^{K} \mu_R e^{-2\pi i f x'}\Big|_{x'=x'_1+(x'_2-x'_1)\left(\frac{k-1/2}{K}\right)}, \quad (1)$$

where K is the number of samples, x' is position measured along the angle α, and x'_1 and x'_2 are the endpoints of the interval over which the Fourier transform is calculated. Our previous works used the Fourier transform to calculate the r-factor, a metric of image quality.[9,11] We now illustrate how the r-factor is calculated at a single point in space, specifically the coordinate (0, 40.0, 49.0) (in mm) in a conventional geometry, under two orientations for the input frequency considered as examples: α = 30° and α = 80° (Figure 4).

Table 1. The parameters for the acquisition geometry and sinusoidal test object are summarized below.

Parameter	Value
Θ: Angular range of x-ray source motion	14.3°
z_M: Distance from breast support to central source position	738.01 mm
N: Number of projections	15
a: Detector element (del) size	0.085 mm
ε: Thickness of sinusoidal test object	0.030 mm
f_0: Frequency of sinusoidal test object	9.5 mm^{-1}
K: Number of samples in Fourier transform summation	1,000
x'_1: Lower endpoint of Fourier transform	–2.63 mm
x'_2: Upper endpoint of Fourier transform	2.63 mm

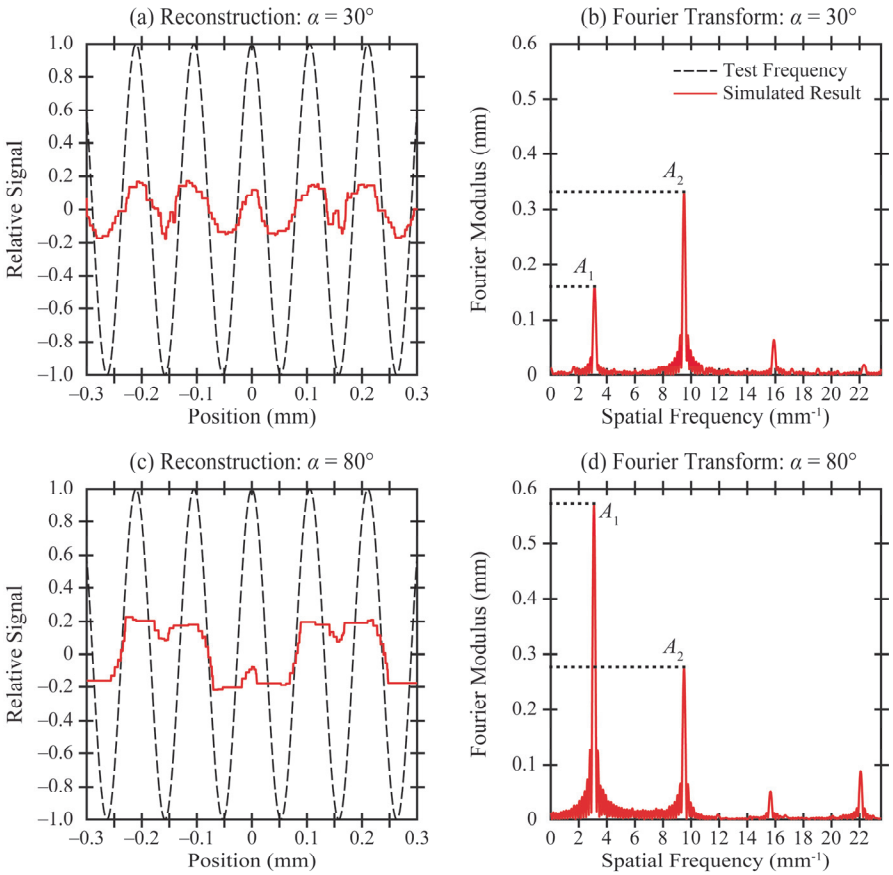

Figure 4. (a) With frequency oriented along a 30° angle, the peaks and troughs of the reconstruction match the sinusoidal test object with frequency 9.5 mm^{-1}. (b) In this orientation, the major peak in Fourier space matches the input frequency, 9.5 mm^{-1}, and thus the object is resolved. (c) By contrast, with frequency oriented along an 80° angle, each peak and trough are not resolved properly. (d) In this orientation, the major peak (amplitude A_1) is at the frequency 3.1 mm^{-1} and thus the input waveform is aliased.

Along the 30° angle, shown as an example of an orientation in which SR is achieved, the input object is clearly resolved [Figure 4(a)] and the major peak in Fourier space matches the input frequency, 9.5 mm^{-1} [Figure 4(b)]. The *r*-factor is defined to be the ratio of the amplitude of the low-frequency peak (A_1) to the amplitude at the input frequency (A_2).

$$r\text{-Factor} = \frac{A_1}{A_2} \tag{2}$$

SR is achieved if *r*-factor < 1.0. The *r*-factor should be as close to zero as possible to achieve SR with high quality. In Figure 4(b), $A_1 = 0.16$ and $A_2 = 0.33$, giving *r*-factor = 0.48. By contrast, along the 80° angle shown as an example of an orientation in which SR is not achieved [Figure 4(c)], the low-frequency peak is dominant and hence *r*-factor = 2.1 [Figure 4(d)].

2.3 Statistical Calculations

Next, the *r*-factor is analyzed throughout a volume-of-interest (VOI); namely, a rectangular prism with dimensions 200.0 × 100.0 × 50.0 (in mm) and 0.020 mm spacing between points in each direction. The *r*-factor is calculated at 1,000 randomly sampled points in the VOI. The VOI is displaced 4.0 mm anterior to the chest wall (in the +*y* direction); this ensures that the interval $[x'_1, x'_2]$ is included fully within the field-of-view of the detector for all possible orientations (α) of the input frequency.

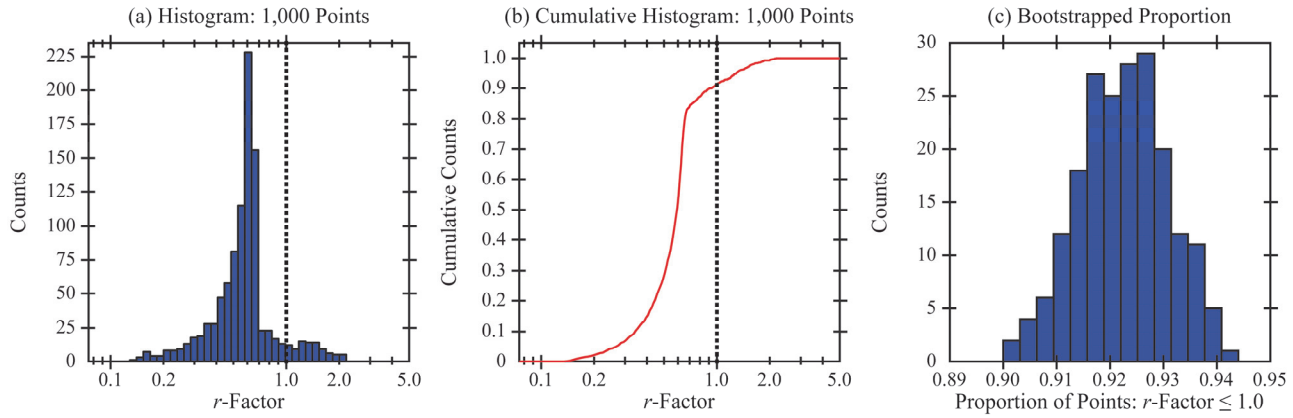

Figure 5. In the conventional geometry, the *r*-factor is calculated at 1,000 randomly-sampled points in a VOI, using a 30° frequency angle as an example. (a) This histogram illustrates the anisotropy of image quality. (b) This cumulative histogram shows the proportion of points at which *r*-factor meets a given threshold. (c) With 200 bootstrapped resamplings of the proportion of points for which *r*-factor ≤ 1.0, it is possible to generate a 95% confidence interval from the middle 95% of this histogram.

The distribution of *r*-factor values in the VOI can be visualized with a histogram [Figure 5(a)] or cumulative histogram [Figure 5(b)], as can be illustrated in a conventional geometry with a frequency angle (α) of 30° considered as an example. The cumulative histogram can be analyzed further with bootstrapped resampling.[11] For example, the proportion of points meeting the threshold of 1.0 is illustrated in Figure 5(c) with 200 bootstrapped resamplings. The middle 95% of the distribution in Figure 5(c) yields a 95% confidence interval of [0.91, 0.94]. By repeating these calculations for all thresholds for the *r*-factor, cumulative histograms can be generated with shaded areas denoting 95% confidence intervals.

2.4 Experimental Validation

For experimental validation of SR, a 360°-star pattern (Type 9/10/360-003, Supertech®, Elkhart, IN) was positioned on the breast support of the NGT system and imaged. This system has a PMX x-ray generator, (Spellman, Hauppauge, NY), an XM1016T x-ray tube (IAE, Milan, Italy), and an AXS-2430 detector (Analogic Canada Corporation, Montreal, Quebec) with an amorphous selenium (*a*-Se) x-ray converter and 0.085 mm pixelation. Images were acquired with a W/Al target/filter combination at 30 kV with a 30 ms exposure time per projection and 50 mA tube current per projection. In the conventional geometry, the detector was stationary during the scan (24.46 mm below the breast support). In the non-isocentric geometry, the starting detector position was 24.46 mm below the breast support, and the range of descending detector motion was 44.8 mm. The angular range (Θ), source-to-support distance (z_M), and number of projections (N) were consistent with Table 1. A phantom with BBs described in our previous work was used for geometric calibration of source and detector positions.[13] Reconstructions were generated with Piccolo™ software[15] (Real Time Tomography LLC, Villanova, PA) with 0.0386 mm pixelation, and subsequently analyzed with the Fourier spectral distortion (FSD) metric.[16] The FSD metric was proposed in our previous work to analyze the Fourier transform of a 30° sector of a star pattern.

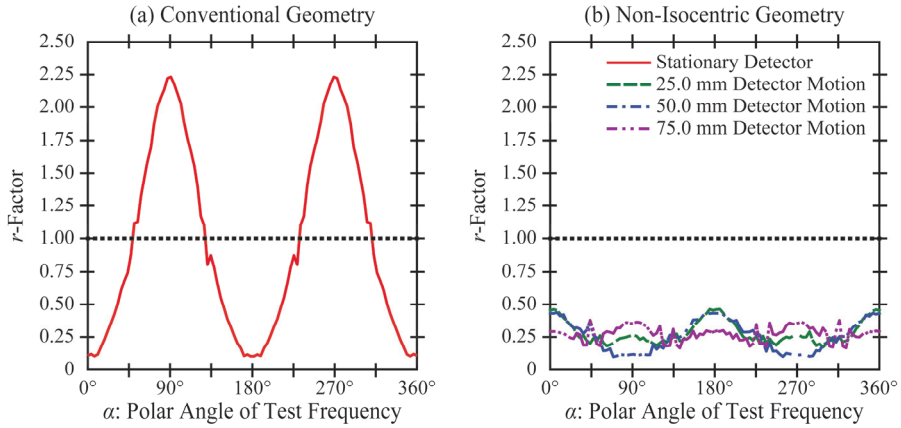

Figure 6. (a) In the conventional geometry, the *r*-factor varies broadly over the 360° range of frequency angles. (b) By contrast, in the non-isocentric geometry, the *r*-factor is minimized (approaching zero) at all angles, yielding isotropic SR.

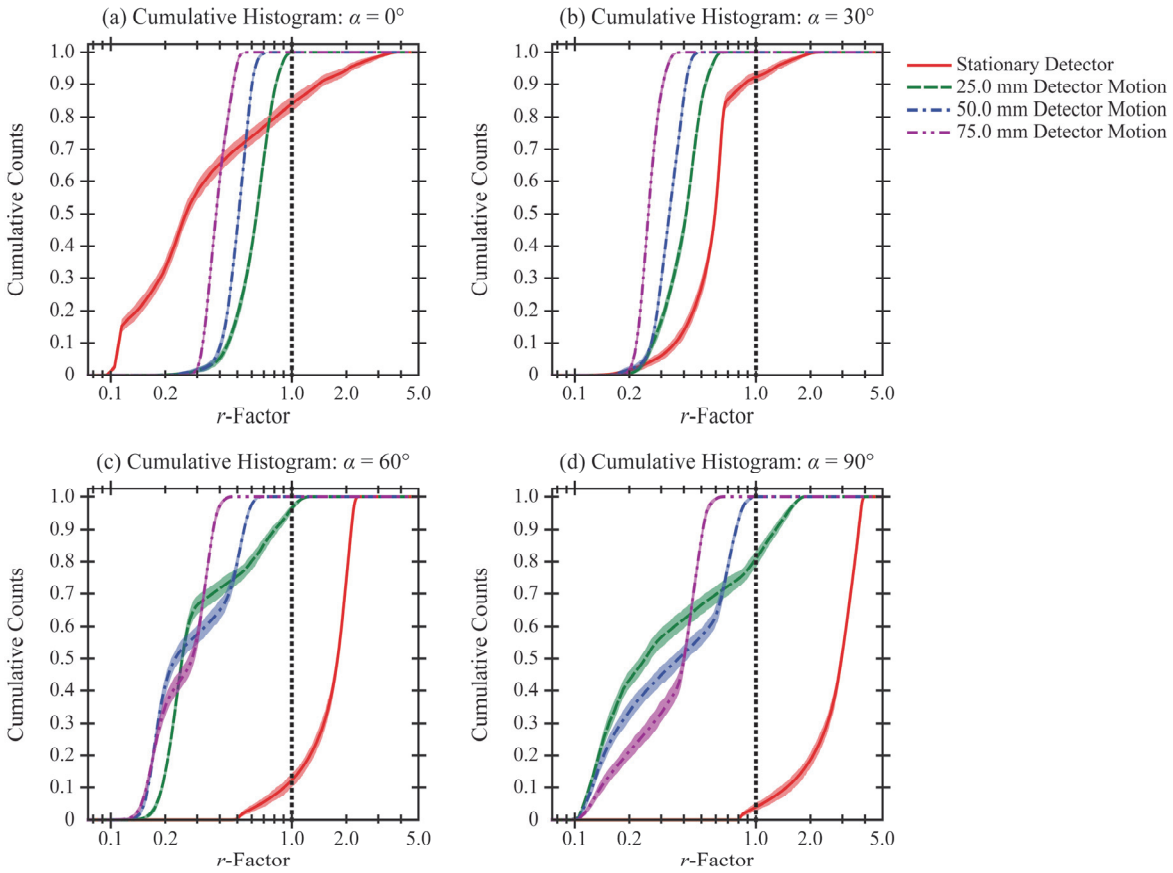

Figure 7. The anisotropy of the *r*-factor throughout the VOI is analyzed with cumulative histograms. Shaded areas denote 95% confidence intervals. To ensure isotropic SR, the *r*-factor should be below 1.0 for all frequency angles; this can be achieved by increasing the detector motion range.

3. RESULTS

3.1 Dependency of Super-Resolution on Frequency Angle

The *r*-factor was analyzed over the range of angles, α, from 0° to 360° (Figure 6). For the purpose of illustrating the effect of orientation, the *r*-factor was calculated at a single point in space with coordinate (0, 40.0, 49.0) in mm. In the conventional geometry, the *r*-factor is 1.0 or greater (prohibiting SR) for angles ranging between 47° and 133°, as well as between 227° and 313° [Figure 6(a)]. This result illustrates the anisotropy of SR; there is a strong dependency on angle. By contrast, in the non-isocentric geometry, the *r*-factor is well below 1.0 at all angles, as can be illustrated with detector motion ranges of 25.0, 50.0, and 75.0 mm [Figure 6(b)].

3.2 Statistical Calculations

To analyze the *r*-factor throughout a VOI as opposed to a single point in space, cumulative histograms were subsequently calculated (Figure 7). Shaded areas denote 95% confidence intervals. In the subplot corresponding to the polar angle $\alpha = 0°$ [Figure 7(a)], the cumulative histogram for the conventional geometry spans a broader range of *r*-factor values than the corresponding curves for non-isocentric geometries. The advantage of a non-isocentric geometry is that it yields more uniform image quality, as evidenced by the sharper rise to a plateau. Also, by increasing the range of detector motion, it is demonstrated that the *r*-factor is below 1.0 everywhere in the VOI; this result holds for all frequency angles ($\alpha = 0°$, 30°, 60°, and 90°) considered as examples in Figure 7. In summary, SR is achieved isotropically with a non-isocentric geometry.

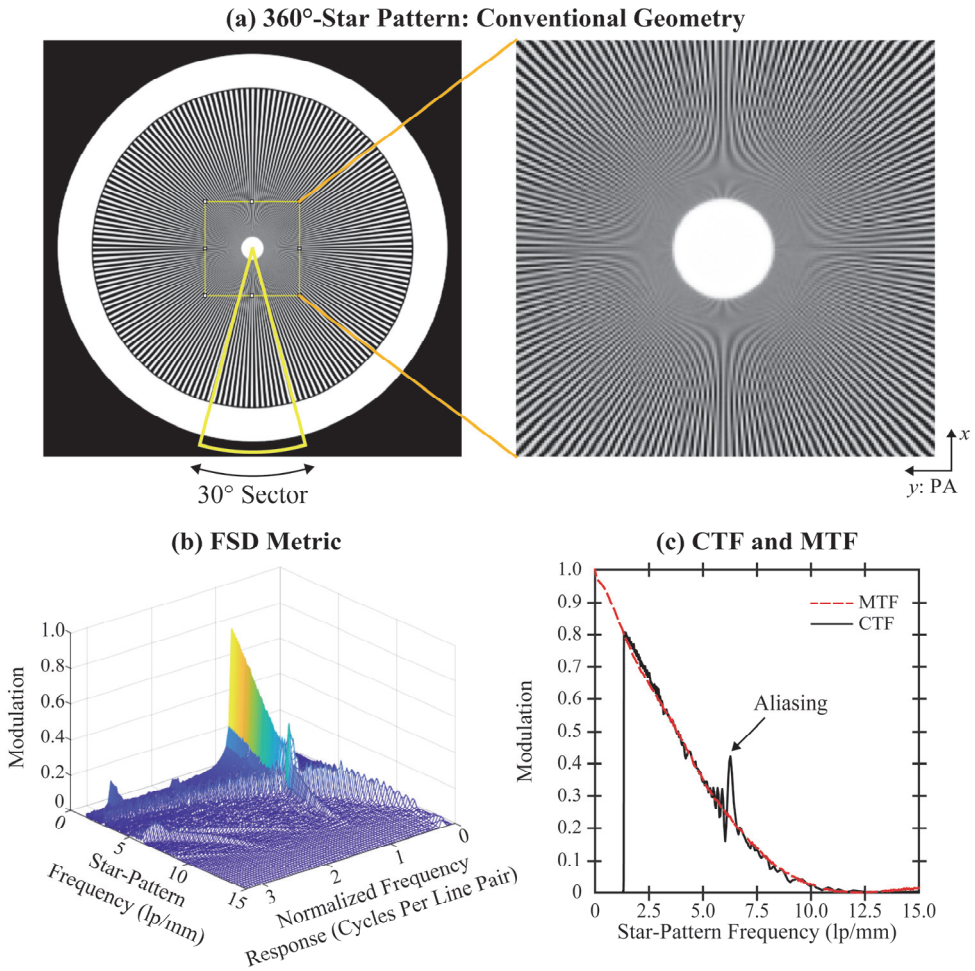

Figure 8. (a) In the reconstruction of a 360°-star pattern in the conventional geometry, there are anisotropies in the PA direction, as evidenced by Moiré artifacts. (b) The FSD metric was calculated in a 30° sector of the phantom to quantify aliasing in the PA direction. (c) Unlike the MTF which does not capture aliasing artifacts, the CTF captures these artifacts at frequencies exceeding the detector alias frequency (5.9 mm^{-1}).

3.3 Experimental Validation

In the conventional geometry [Figure 8(a)], the reconstruction of the 360°-star pattern phantom suffers from anisotropies; namely, Moiré artifacts, most noticeably in frequencies oriented in the PA direction (y). These artifacts are suppressed in the non-isocentric geometry [Figure 9(a)], which supports SR over the full 360° range of angles.

The reconstructions were analyzed further with FSD[16], a measure of the Fourier transform of a 30° sector of the phantom, corresponding to frequencies oriented in the PA direction [Figures 8(a) an 9(a)]. At each input frequency in the phantom, we calculated the Fourier transform as a function of the normalized frequency response (cycles per line pair). The FSD metric should ideally peak at a normalized frequency response of 1.0, corresponding to the input frequency (the spine with the highest modulation); all other signal reflects the presence of spectral leakage. The conventional geometry clearly suffers from spectral leakage [Figure 8(b)]. These aliasing signals are suppressed in the non-isocentric geometry [Figure 9(b)].

A limitation of the modulation transfer function (MTF) is that it does not capture whether aliasing artifacts are present at each frequency. Our previous work used the FSD to define the contrast transfer function (CTF) as an alternate metric to MTF.[16] The CTF is derived from the spine of the FSD corresponding to a normalized frequency response of 1.0. In the conventional geometry, there are aliasing artifacts in the CTF at frequencies exceeding the detector alias frequency, 5.9 mm^{-1} [Figure 8(c)]. However, these artifacts are suppressed in the CTF of the non-isocentric geometry [Figure 9(c)].

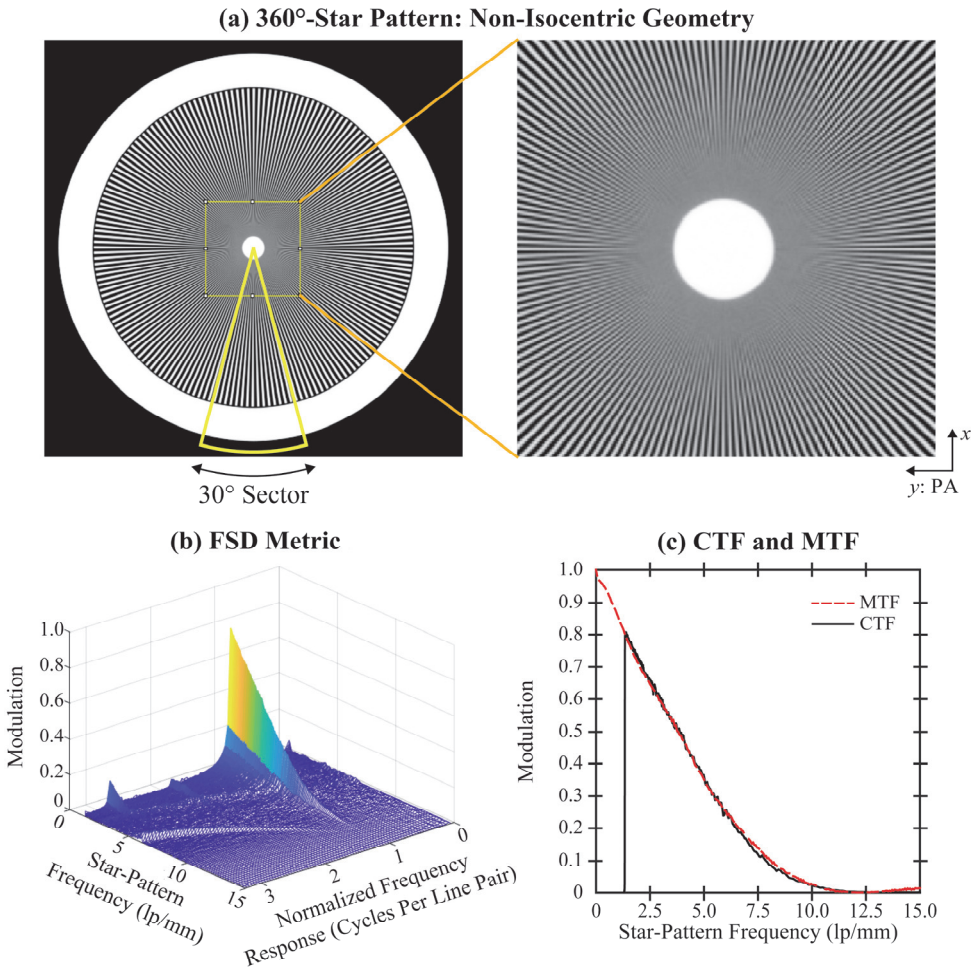

Figure 9. (a) With the use of a non-isocentric geometry, there are no longer Moiré artifacts in the PA direction in the 360°-star pattern. (b) Spectral leakage in the FSD metric is minimized relative to the conventional geometry in Figure 8. (c) The CTF illustrates how aliasing artifacts at frequencies exceeding the detector alias frequency (5.9 mm^{-1}) are suppressed relative to Figure 8.

4. DISCUSSION AND CONCLUSION

In our previous work, we explored theoretical modeling and simulations of the non-isocentric geometry with high-frequency test patterns.[11,12] However, this paper is set apart from our previous work in that we consider all possible polar angles (α) for the orientation of the test pattern, unlike prior modeling which was limited to 0° and 90°. With theoretical modeling, we show that with the use of a non-isocentric geometry, isotropic SR can indeed be achieved at all polar angles from 0° to 360°.

The NGT system was built to support a non-isocentric geometry.[13] In the reconstruction of the 360°-star pattern in this geometry (Figure 9), high frequencies exceeding the alias frequency of the detector (5.9 mm^{-1}) were resolved at all polar angles. There is increased geometric magnification as the detector descends during the scan. The MTF of the focal spot is reduced with increased magnification.[17] To minimize focal spot blurring, it is beneficial to minimize the gap between the detector and breast support. In the NGT system, the gap between the breast support and detector is 24.46 mm at the start of the scan. Implementing a gap as low as 10 mm at the start of the scan (as was considered with theoretical modeling) would minimize focal spot blurring even further, benefiting high-frequency MTF.

Since the focal spot was treated as point-like, the theoretical model does not capture the effect of focal spot blurring. Additionally, the theoretical model implicitly assumes that the point-spread function of the *a*-Se x-ray converter is a delta function, since detector blurring effects were not modeled. Previous work quantified the MTF degradation due to oblique

x-ray incidence in *a*-Se detectors[18-21]; this effect should be incorporated into future modeling and simulations of SR. The theoretical model presumes a SBP reconstruction with no filtering; future work should explore strategies for optimizing the reconstruction filter.

5. ACKNOWLEDGEMENT

ADAM has received research support from Hologic Inc., Barco NV, and Analogic Corporation; is a spouse to an employee and stockholder of Real Time Tomography (RTT), LLC; is a member of the scientific advisory board of RTT; and is an owner of Daimroc Imaging, LLC.

Support was provided by the following grants: W81XWH-18-1-0082 from the Department of Defense Breast Cancer Research Program, IRSA 1016451 from the Burroughs Wellcome Fund, IIR13264610 and PDF14302589 from Susan G. Komen®, 1R01CA196528 and NCI P30 CA016520 from the National Institute of Health, and a 2020 AAPM Research Seed Funding Grant from the American Association of Physicists in Medicine. In addition, equipment support was provided by Analogic Inc., Barco NV, and RTT. The content is solely the responsibility of the authors and does not necessarily represent the official views of the funding agencies.

6. REFERENCES

1. Friedewald SM, Rafferty EA, Rose SL, et al. Breast Cancer Screening Using Tomosynthesis in Combination With Digital Mammography. *JAMA.* 2014;311(24):2499-2507.
2. Conant EF, Zuckerman SP, McDonald ES, et al. Five Consecutive Years of Screening with Digital Breast Tomosynthesis: Outcomes by Screening Year and Round. *Radiology.* 2020;295(2):285-293.
3. Conant EF, Barlow WE, Herschorn SD, et al. Association of Digital Breast Tomosynthesis vs Digital Mammography With Cancer Detection and Recall Rates by Age and Breast Density. *JAMA Oncology.* 2019;5(5):635-642.
4. Mertelmeier T, Ludwig J, Zhao B, Zhao W. Optimization of Tomosynthesis Acquisition Parameters: Angular Range and Number of Projections. *Lecture Notes in Computer Science.* 2008;5116:220-227.
5. Zhao B, Zhao W. Three-dimensional linear system analysis for breast tomosynthesis. *Medical Physics.* 2008;35(12):5219-5232.
6. Barufaldi B, Vent TL, Acciavatti RJ, et al. Determining the Optimal Angular Range of the X-Ray Source Motion in Tomosynthesis Using Virtual Clinical Trials. Paper presented at: SPIE Medical Imaging2020; Houston, TX.
7. Fajardo LL, Yang L, Park JM. Comparison of 15° and 30° Angle Acquisition Digital Breast Tomosynthesis for Visualization and Characterization of Breast Abnormalities. *Lecture Notes in Computer Science.* 2012;7361:369-376.
8. Chan H-P, Goodsitt MM, Helvie MA, et al. Digital Breast Tomosynthesis: Observer Performance of Clustered Microcalcification Detection on Breast Phantom Images Acquired with an Experimental System Using Variable Scan Angles, Angular Increments, and Number of Projections Views. *Radiology.* 2014;273(3):675-685.
9. Acciavatti RJ, Maidment ADA. Observation of super-resolution in digital breast tomosynthesis. *Medical Physics.* 2012;39(12):7518-7539.
10. Barufaldi B, Vent TL, Acciavatti RJ, Bakic PR, Noel PB, Maidment ADA. MRMC ROC Analysis of Calcification Detection in Tomosynthesis Using Computed Super Resolution and Virtual Clinical Trials. Paper presented at: 15th International Workshop on Breast Imaging2020.
11. Acciavatti RJ, Wileyto EP, Maidment ADA. Modeling Acquisition Geometries with Improved Super-Resolution in Digital Breast Tomosynthesis. Paper presented at: SPIE Medical Imaging2016; San Diego, CA.
12. Vent TL, Barufaldi B, Acciavatti RJ, Maidment ADA. Simulation of high-resolution test objects using non-isocentric acquisition geometries in next-generation digital tomosynthesis. Paper presented at: 15th International Workshop on Breast Imaging2020.
13. Choi CJ, Vent TL, Acciavatti RJ, Maidment ADA. Geometric Calibration for a Next-Generation Digital Breast Tomosynthesis System Using Virtual Line Segments. Paper presented at: SPIE Medical Imaging2018; Houston, TX.
14. Eben JE, Vent TL, Choi CJ, et al. Development of a Next Generation Tomosynthesis System. Paper presented at: SPIE Medical Imaging2018; Houston, TX.
15. Kuo J, Ringer PA, Fallows SG, Bakic PR, Maidment ADA, Ng S. Dynamic Reconstruction and Rendering of 3D Tomosynthesis Images. Paper presented at: SPIE Medical Imaging2011; Lake Buena Vista, FL.

16. Vent TL, Acciavatti RJ, Maidment ADA. Development and Evaluation of the Fourier Spectral Distortion Metric. *IEEE Transactions on Medical Imaging.* 2021;40(3):1055-1064.
17. Johns HE, Cunningham JR. Chapter 16: Diagnostic Radiology. *The Physics of Radiology*. 4th ed. Springfield, IL: Charles C Thomas; 1983:557-669.
18. Acciavatti RJ, Maidment ADA. Non-stationary model of oblique x-ray incidence in amorphous selenium detectors: I. Point spread function. *Medical Physics.* 2019;46(2):494-504.
19. Acciavatti RJ, Maidment ADA. Nonstationary model of oblique x-ray incidence in amorphous selenium detectors: II. Transfer functions. *Medical Physics.* 2019;46(2):505-516.
20. Hajdok G, Cunningham IA. Penalty on the detective quantum efficiency from off-axis incident x rays. Paper presented at: Medical Imaging 2004: Physics of Medical Imaging2004; San Diego, CA.
21. Que W, Rowlands JA. X-ray imaging using amorphous selenium: Inherent spatial resolution. *Medical Physics.* 1995;22(4):365-374.

Investigation of optimal angular range and projection density for next generation tomosynthesis

*Chloe J. Choi, Trevor L. Vent, Michael J. Geagan, Peter B. Noël, and Andrew D. A. Maidment

Department of Radiology, University of Pennsylvania, Philadelphia, PA 19104 USA
E-mail: {Jeongin.Choi* | Trevor.Vent | Peter.Noel | Andrew.Maidment}@pennmedicine.upenn.edu

Abstract: Conventional digital breast tomosynthesis (DBT) acquires x-ray projections over a limited angular range strictly along the chest wall. The impact of the angular range is a trade-off in image quality; increasing the angular range improves in-depth resolution and isotropic sampling across the detector, but at the cost of in-plane resolution. A next-generation tomosynthesis (NGT) system developed at the University of Pennsylvania is capable of two-dimensional source trajectories and thus can incorporates narrow- and wide-angle acquisition in orthogonal directions in a single tomosynthesis scan. In this work, we evaluate the performance of NGT geometries for high- and low-frequency objects across the detector via computer simulations. Two virtual test objects, a high-frequency star pattern and a low-frequency octagon phantom, were used to simulate tomosynthesis image acquisition; various angular ranges were evaluated. The two test objects were placed throughout the detector field-of-view at nine different locations to analyze the anisotropic nature of tomosynthesis. In addition to acquisitions exploring angular range, acquisitions were simulated to test the impact of the number of projections on image quality for a fixed angular range. The performance of the NGT geometries was analyzed for each experimental geometry. Reconstructions of the star pattern were analyzed both qualitatively and quantitatively using the Fourier Distortion Metrics (FSD). Reconstructions of the octagon phantom were analyzed with visually and with modulation analysis. Selected results were confirmed with physical experiments. This work has shown that NGT acquisition geometries present high in-plane resolution and highly isotropic sampling and thus combine the benefits of narrow-angle and wide-angle tomosynthesis.

Keyword: digital breast tomosynthesis, narrow angle tomosynthesis, wide angle tomosynthesis, next generation tomosynthesis

1. INTRODUCTION

Digital breast tomosynthesis (DBT) is a tomographic technique which provides a high-resolution three-dimensional (3D) reconstruction of the breast. In conventional DBT, multiple x-ray projections are acquired over a limited angular range along the chest wall. The acquisition angular range (θ) creates unavoidable trade-offs in overall image quality, especially between in-plane (x-y) and in-depth (z) resolution. In general, increasing the angular range of acquisition, θ, results in improved in-depth resolution at the expense of in-plane resolution.[2] More germane to the current work, increasing θ generally also results in better isotropy across the reconstructed volume.

In our previous work, we analyzed DBT sampling in Fourier space and stated that each acquisition geometry uses its "dose budget" differently. Given the same total dose and number of projections, an acquisition geometry with a wider source range samples a larger volume in Fourier space more sparsely, while an acquisition geometry with a narrower source range samples a smaller volume in Fourier space more densely.[4] Although our discussion assumed that the imaged object is always located at the center of the chest wall, the concept of Fourier sampling extends further and is applicable when discussing spatial anisotropy.

The rationale for the spatial anisotropy observed in tomosynthesis can be most easily gleaned from Fourier analysis. In Figure 1A (left) we consider an object located at the chest wall center of the detector (located normal to the central projection) imaged with two angular ranges θ_1 and θ_2 ($\theta_2 > \theta_1$). A double-napped cone of the Fourier domain is sampled symmetrically about the f_x and f_y axes. For the same number of projections per acquisition, narrow angle tomosynthesis (θ_1, Figure 1A, middle) samples a smaller volume in Fourier space more densely, whilst wide angle tomosynthesis (θ_2, Figure 1A, right) samples a greater volume in Fourier space more sparsely.

When the imaged object is displaced left laterally from the center of the chest wall, the sampled volume in Fourier space rotates accordingly (Figure 1B). This rotation results in different Fourier components of the object being sampled (i.e., the null space differs between various locations in the reconstructed volume), and hence the

Medical Imaging 2022: Physics of Medical Imaging, edited by Wei Zhao, Lifeng Yu, Proc. of SPIE
Vol. 12031, 120314C · © 2022 SPIE · 1605-7422 · doi: 10.1117/12.2612419

reconstructed image will exhibit spatial anisotropy in image quality; in other words, the tomosynthesis reconstruction of the same object will look different depending upon where the object is located relative to the system origin.

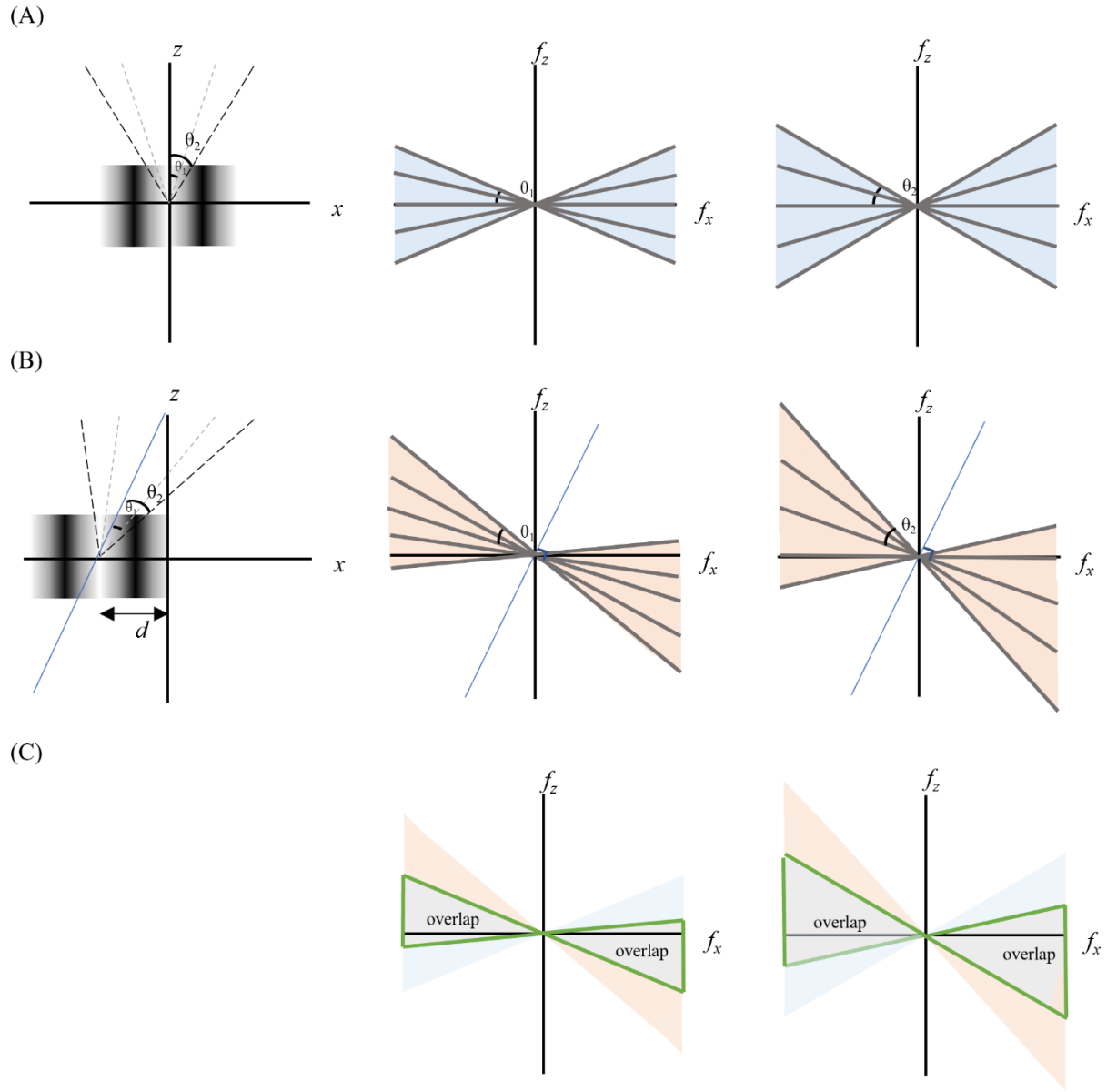

Figure 1. Tomosynthesis sampling in narrow angle tomosynthesis and wide angle tomosynthesis for an object located in the center (Figure 1A) and displaced from the center (Figure 1B). The overlap between the two volumes in Fourier domain (Figure 1C) represents the common data in two scans.

The region of overlap between the sampled volumes (Figure 1C) represents the common data available for the object when placed at the two locations. The greater the distance between the locations, the less overlap of the Fourier components. By the same argument, narrow angle scans will exhibit less overlap than wide angle scans, when the object is displaced. Thus, as illustrated in Figure 1C, wide angle tomosynthesis will exhibit higher spatial isotropy and can tolerate wider object displacements better than narrow angle tomosynthesis. Although Figure 1 is only concerned with object displacement in one direction (mediolaterally, ML), this argument can be generalized easily to the perpendicular (posteroanterior, PA) direction. Since conventional breast tomosynthesis lacks source motion in the PA

direction, conventional images will exhibit greater anisotropy in the PA direction than laterally[5]. Introducing source motion in the PA direction should increase spatial isotropy; this is the focus of this paper.

It should be noted that the region of overlap is smaller in the lower frequency region than in the higher frequency region. Therefore, we hypothesize that thick low-frequency objects are more susceptible to spatial anisotropy than thin high-frequency objects.

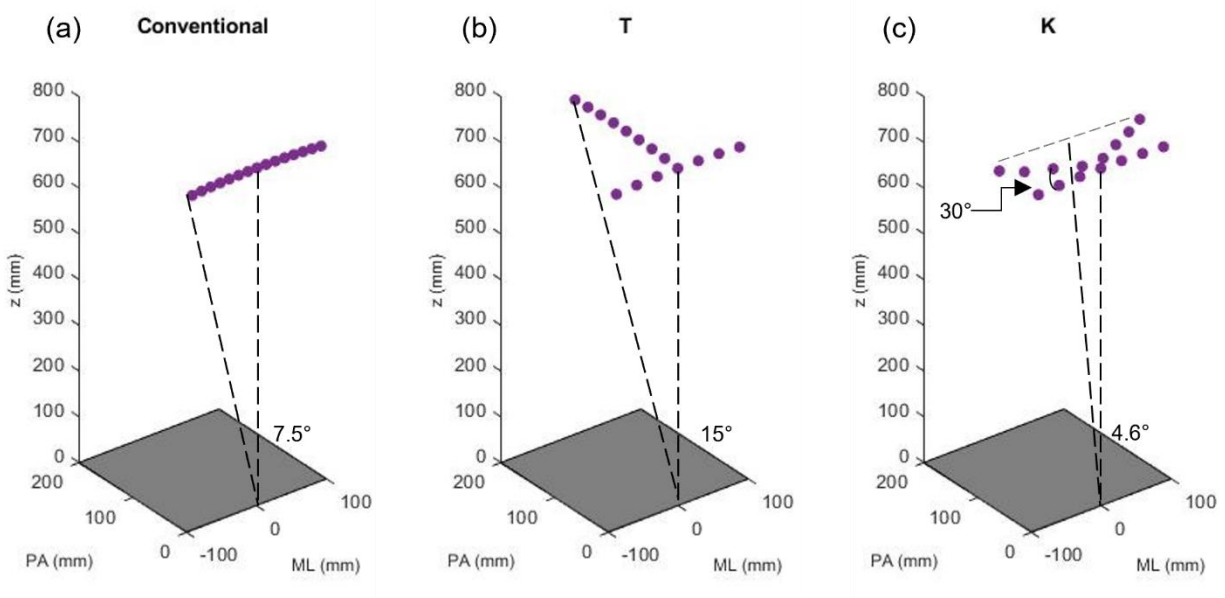

Figure 2. (a) Conventional DBT geometry, (b) T NGT geometry, (c) K NGT geometry. NGT acquisition geometries incorporate 2D source trajectories both parallel (x) and perpendicular to the chest wall (y).

The next generation tomosynthesis (NGT) system developed at the University of Pennsylvania is capable of two-dimensional x-ray source trajectories, namely lateral (ML) and PA motions.[1] Thus, the NGT system supports acquisitions which incorporate narrow angle and wide angle motions orthogonal to each other, as shown in Figure 2 with two custom acquisition geometries.

In the examples presented in Figure 2, the total number of projections was 15 and the source-to-image distance (SID) was 738 mm for all geometries. The angular range of the conventional geometry is ±7.5°. The NGT geometries use seven projections along the chest wall, making a narrow angle of ±7.5° in one direction. The T geometry adds eight projections PA that span a wider angle of +15° (maximum PA extent of 190 mm). K geometry makes a PA angle of 4.6° in two directions, 30° relative to the chest wall with a maximum PA extent of 60 mm.

In this work, we show that NGT geometries can be designed to combine the benefits of narrow-angle and wide-angle tomosynthesis, while minimizing the compromise in image quality, by analyzing the effects of object displacement on image quality via computer simulations. The simulated results are compared to experimental results from the NGT system for validation.

2. MATERIALS AND METHODS

2.1 Physics Virtual Clinical Trial Framework and virtual test objects

The Physics Virtual Clinical Trial Framework (PhysicsVCT) is a simplified version of the OpenVCT simulation framework[6] and allows users to simulate x-ray projections of known test objects and evaluate the performance of imaging systems. PhysicsVCT was used to simulate image acquisitions of two virtual phantoms with various acquisition geometries.

The virtual star pattern was presented in previous work[7] as a voxelized version of the physical star pattern (Model 07-542-1000, Supertech, Elkhart, IN). It was designed using isovolumetric voxels with 5μm resolution, 45mm diameter, and 30μm thickness. The range of spatial frequencies is 1.27 line-pairs per millimeter (lp/mm) to 16 lp/mm. The star pattern contains four quadrants, each named according to its angle relative to an imaginary horizontal line through the phantom: 0°, 90°, 180°, and 270° quadrants.

The virtual octagon phantom was also created using Matlab (MathWorks, Natick, Massachusetts, version 2020a) as a low-frequency test object in various orientations. It was designed using isovolumetric voxels of 125μm with the side length of 28mm and the thickness of 20mm. The frequency of 0.5 lp/mm was created by alternating acrylic and air materials and placed at each side of the octagon.

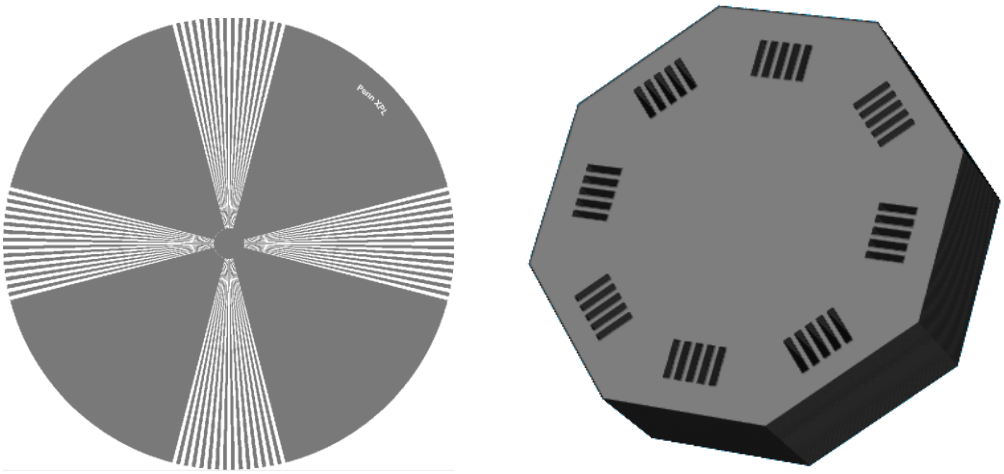

Figure 3. The virtual star pattern phantom (a)[7], and the octagon phantom (b).

2.2 Acquisition parameters

The x-ray techniques and detector configurations used for all acquisitions, either experimental or virtual, are summarized in Table 1.

Table 1. Summary of acquisition parameters and detector configurations.

X-ray Techniques	
Anode Material	Tungsten
Filter Material	Aluminum
Filter Thickness (mm)	0.7
Tube Motion	Step and Shoot
kV	35
mAs (per projection)	1.5
Detector	
Detector Element Size (mm)	0.085
Detector Element count	3584 x 2816
Detector Size (mm)	304.64 x 239.36

In this work, tomosynthesis acquisitions of various angular ranges were simulated. The virtual star pattern phantom was placed at the center of the chest wall (origin) and simulated with angular ranges of 10 to 35° (±5° to ±17.5°) to

compare the effects of angular range on high-frequency in-plane resolution. For the angular range of 15 degrees (±7.5°), the total number of projections was varied from 3 to 15. The virtual octagon phantom was also simulated with angular ranges of 10 to 35° with a total of 15 projections for all acquisitions. The low-frequency octagon phantom was placed at nine different locations to evaluate the effects of angular range on isotropic image quality.

Table 2. Summary of conventional acquisition geometries for simulating star pattern and octagon test objects.

Test object	Angular range (degrees)	Number of projections	Phantom displacement (ML)	Phantom displacement (PA)
Star pattern	10, 20, 25, 30, 35	15	-100, 0, 100 mm	0, 60, 120 mm
	15	3 to 15	-100, 0, 100 mm	0, 60, 120 mm
Octagon	10, 15, 20, 25, 30, 35	15	-100, 0, 100 mm	0, 60, 120 mm

Selected experiments were repeated, both experimentally and virtually, with the NGT acquisition geometries as summarized in Table 3.

Table 3. Summary of NGT acquisition geometries for imaging and simulating octagon test object.

Test object	NGT Geometry	Number of projections	Phantom displacement (ML)	Phantom displacement (PA)
Octagon	X, T and K	15	-100, 0, 100 mm	0, 60, 120 mm

2.3 Image Reconstruction and analysis

The simulated x-ray projections were reconstructed using commercial software with simple back projection (Piccolo version 5.0.2 and Briona version 9.0.4, Real Time Tomography, Villanova, PA). The central slice of the octagon phantom was used for low-frequency resolution analysis. The line pairs in the octagon phantom will be referred to their clock position as oriented in Figure 4. The central slice of the star pattern phantom was reconstructed at 4.5x magnification and was analyzed using the Fourier Spectral Distortion metric (FSD)[8].

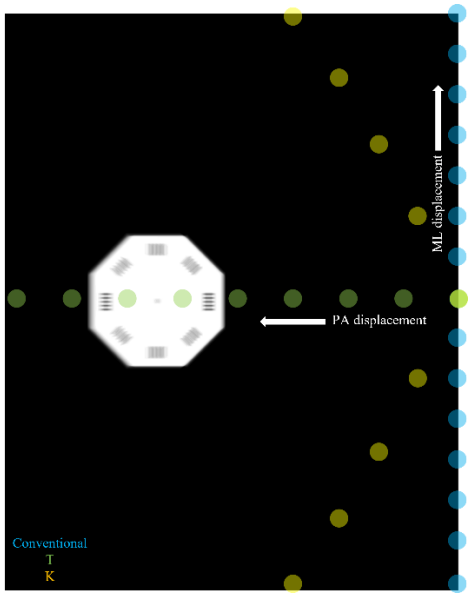

Figure 4. Example of a displaced octagon phantom reconstruction is shown (ML displacement = 0 mm, PA displacement = 120 mm). Approximate source trajectories for NGT geometries are shown on the reconstruction plane. For T and K geometries, source

positions along the chest wall are not shown for simplicity. In this paper, the line pairs in the octagon phantom will be referred to their clock position as oriented in this figure.

2.3.1 Fourier Spectral Distortion Metrics

The FSD graph is the normalized modulation of all frequencies present in one quadrant of the star pattern and reveals evidence of aliasing along with other relevant information as shown in Figure 5. The modulation of input frequency occurs at 15 cycles/δω, where δω represents the range of the quadrant at all radii. This is the expected signal as each quadrant of the star pattern consists of 15 pairs of alternating acrylic and lead. The aliasing takes a form of spectral leakage, caused by the detector element spacing (d_{el}) or by the sampling aperture (λ). The intensity of spectral leakage decreases as super-resolution is achieved. Specifically, super-resolution is indicated when the input frequency response is higher than the spectral leakage at any resolution greater than the alias frequency.

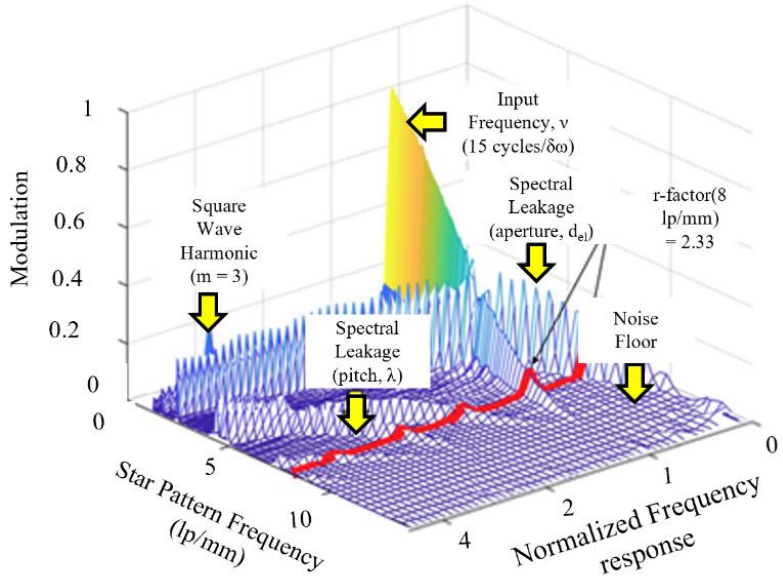

Figure 5. An example of the FSD graph is shown (Figure adapted from Vent *et al*[8]). The r-factor, described in the work by Acciavatti[9,10], relates frequency response to super-resolution.

3. RESULTS

3.1 Impact of the angular range on visualization of high-frequency objects

The high frequency star pattern phantom was placed at different locations and imaged with various angular ranges. The most extreme angular ranges were selected for comparison in Figure 6. When the object was placed at the center of the chest wall (Figure 6, top), narrow angle tomosynthesis with 10° of sweep angle (Figure 6, left) showed super-resolution in the direction of the tube motion. No spectral leakage is observed in the corresponding FSD graph, which indicates that super-resolution is achieved, and aliasing is minimized. At 35° (Figure 6, right), high frequency line pairs are distorted, and spectral leakage is observed in the corresponding FSD graph. The angular range generally showed an inverse relationship with spatial resolution parallel to the scan direction.

Object displacements were generally insignificant for the visualization of high frequency objects (Figure 6, bottom). The angular range of 10° still achieved super-resolution and did not exhibit any spectral leakage in its FSD graph, whereas the angular range of 35° presented a small amount of aliasing.

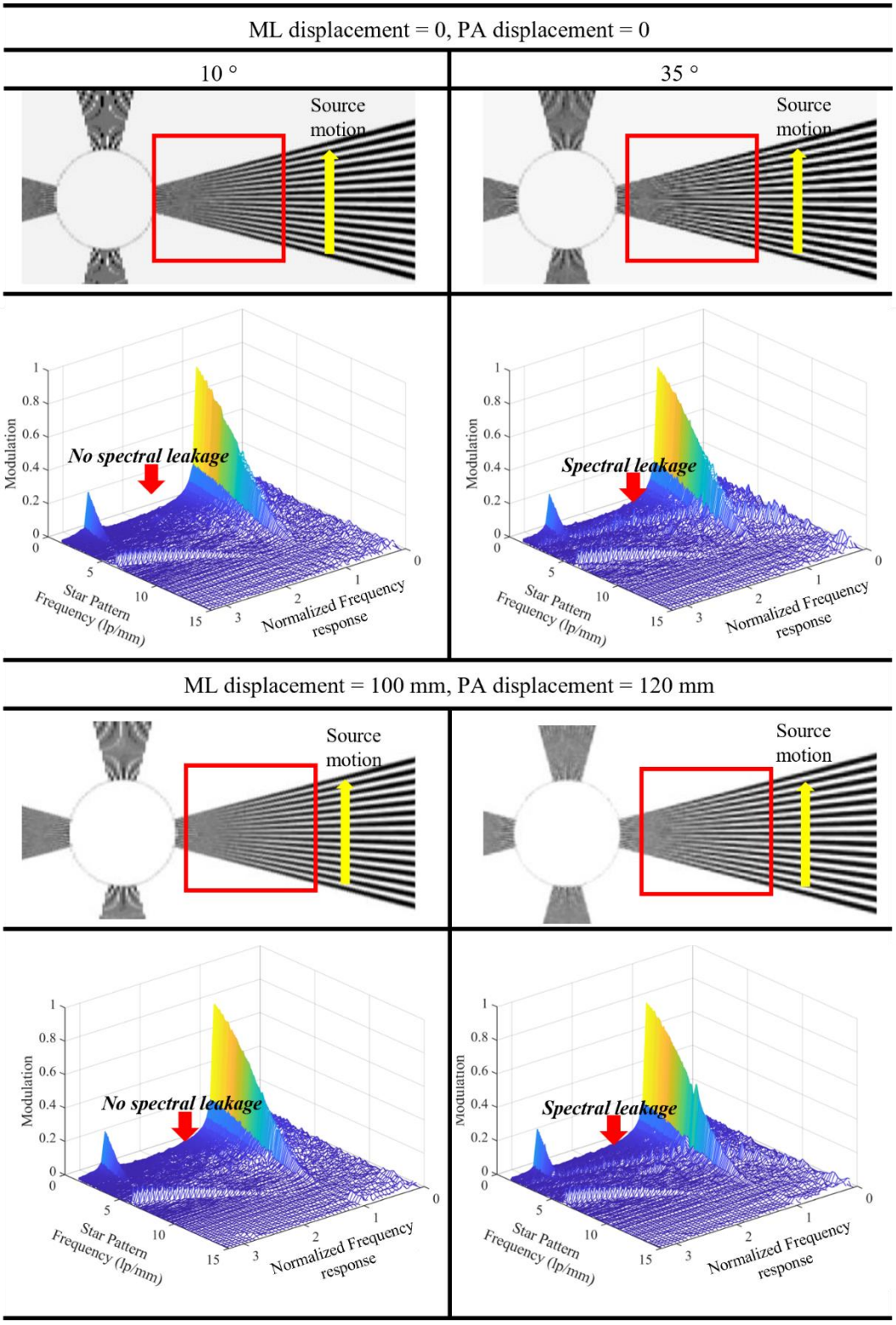

Figure 6. Reconstructed star pattern imaged with 10 degrees (left) and 35 degrees (right) of angular range. Acquisitions were performed with the test object at two different locations and with 15 projections. The FSD graphs for the angular range of 35° show slight aliasing in the form of spectral leakage.

3.2 Impact of the number of projections on visualization of high-frequency objects

The virtual star pattern phantom was imaged with the angular range of 15° with various number of projections, ranging from 3 projections to 15 projections. As a greater number of projections is used, high frequencies in the star pattern were more accurately preserved as shown in Figure 7. With the total dose increasing, the noise floor gradually reduces as shown in Figure 8, where FSD plots for 360° quadrants of reconstructed star patterns are presented. The greatest reduction in aliasing occurred between five and seven projections as seen in Figure 8. With seven projections along the chest wall, spectral leakage was greatly reduced and comparable to that with 15 projections.

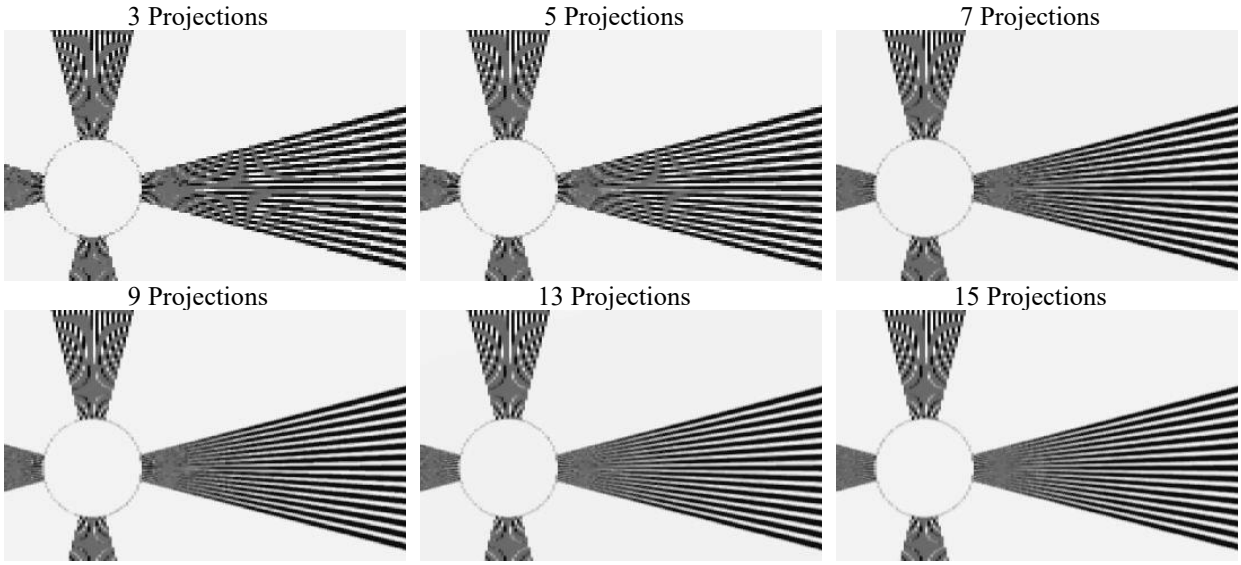

Figure 7. Reconstructed star pattern at the center of the chest wall.

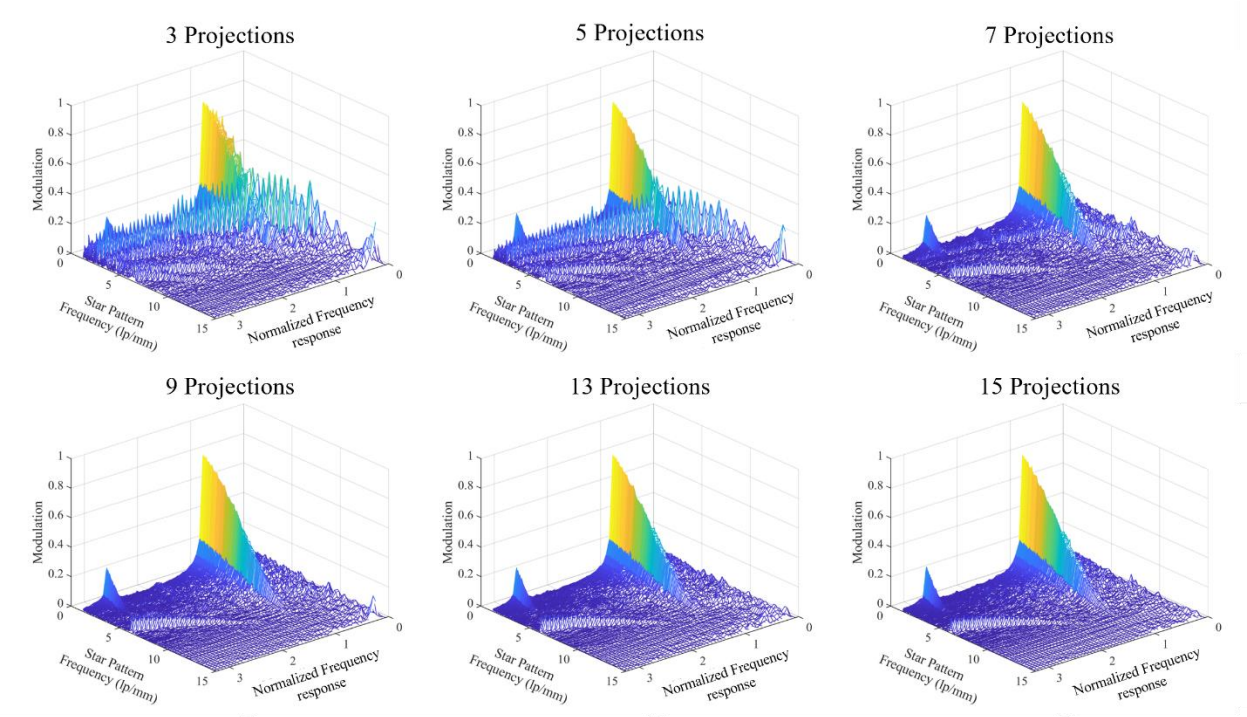

Figure 8. FSD plots for 360° quadrants of reconstructed star pattern test object (Figure 7).

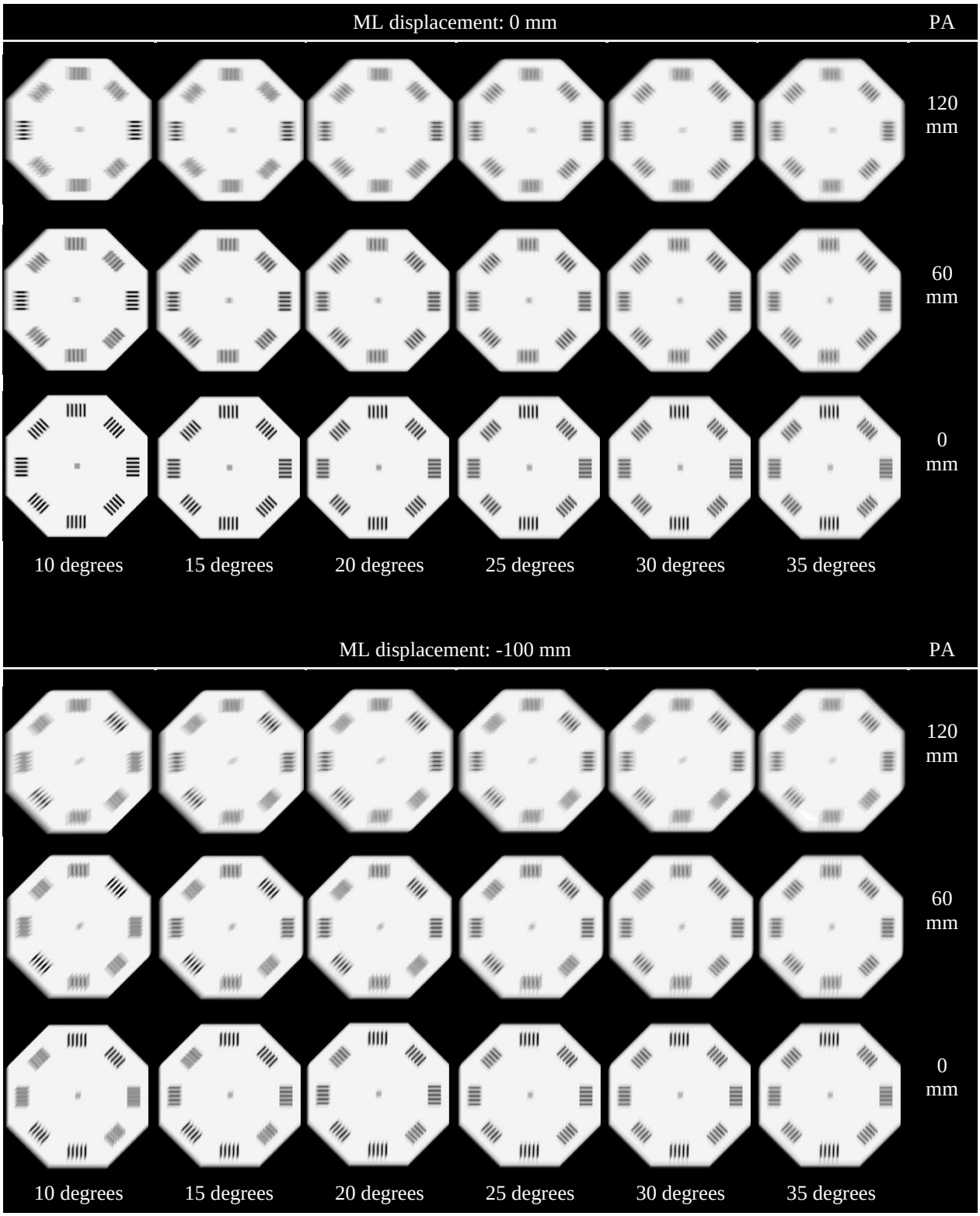

Figure 9. Reconstructed octagon phantom with various angular range at different ML and PA displacements from the center of the chest wall.

3.4 Impact of the angular range on visualization of low-frequency objects

The impact of the angular range on visualization of low-frequency objects was evaluated by simulating an octagon phantom (Figure 9). It was shown that wider angle tomosynthesis presents more isotropic resolution across the detector, whereas narrow angle tomosynthesis shows extensive blurring artifacts at positions distal to the origin center of the chest wall.

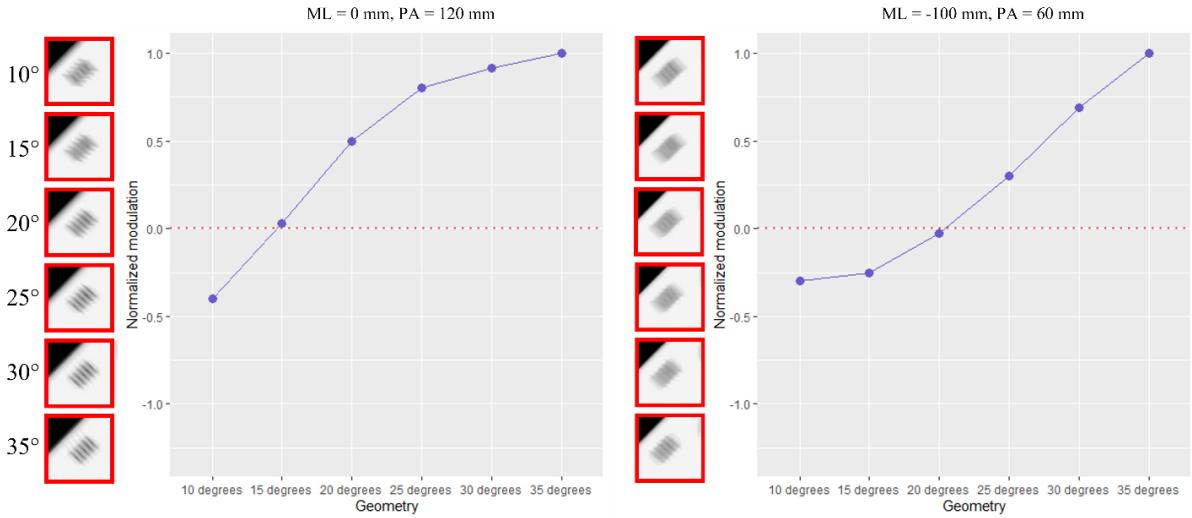

Figure 10. Normalized modulation of line pairs located at 11 o'clock position is summarized for two types of phantom displacement.

Close examination of the line pairs reveals this trend more clearly. The line pairs located at the 11 o'clock position at two different displacements were selected for modulation analysis, as summarized in Figure 10. The modulation normalized to that of the widest angle (35°) decreases with decreasing angular range and eventually inverts due to aliasing. The points of inversion and plateau occur at different angular range, depending upon where the line pairs were located.

3.5 Simulation of NGT acquisition geometries

The performance of NGT geometries on visualization of low-frequency objects was evaluated (Figure 11). NGT geometries support more isotropic sampling of the object than narrow angle tomosynthesis. The quality of reconstruction was comparable or even superior to that of wide angle tomosynthesis for certain line pair orientations and displacements.

T geometry was highly tolerant to PA displacement compared to all other geometries, given no ML displacement from the center. K geometry was moderately tolerant to both ML and PA displacements and presented rather uniform image quality over the detector plane.

For the 12 o'clock line pairs with a PA displacement of 60 mm (Figure 12, top left), conventional tomosynthesis showed inverted line pairs due to aliasing, regardless of its angular range. The NGT designs offer higher image quality by incorporating x-ray positions away from the chest wall. Conventional tomosynthesis was better able to resolve the 1 o'clock line pairs with a PA displacement of 120 mm (Figure 12, top right), although narrow angle tomosynthesis (10° and 15°) showed blurred and inverted modulation. K geometry showed 26.7% amplitude compared to T, which stands between the 15° (1.1% modulation) and 20° (39.8%) acquisitions.

The line pairs at the 3 o'clock position with a PA displacement of 120 mm and ML displacement of 100 mm revealed different patterns. The amplitude increased rapidly until 20°, and slowly decreased afterwards with conventional tomosynthesis. There was no inversion of modulation. K geometry showed 80.6% amplitude compared to 20°, which stands between 25° (88.7%) and 30° (74.2%). T geometry showed low tolerance against the displacement in the ML

direction; the 3 o'clock line pairs were inverted regardless of the PA displacement. At 120 mm of PA displacement, the modulation was inverted with -14.5% compared to 20°.

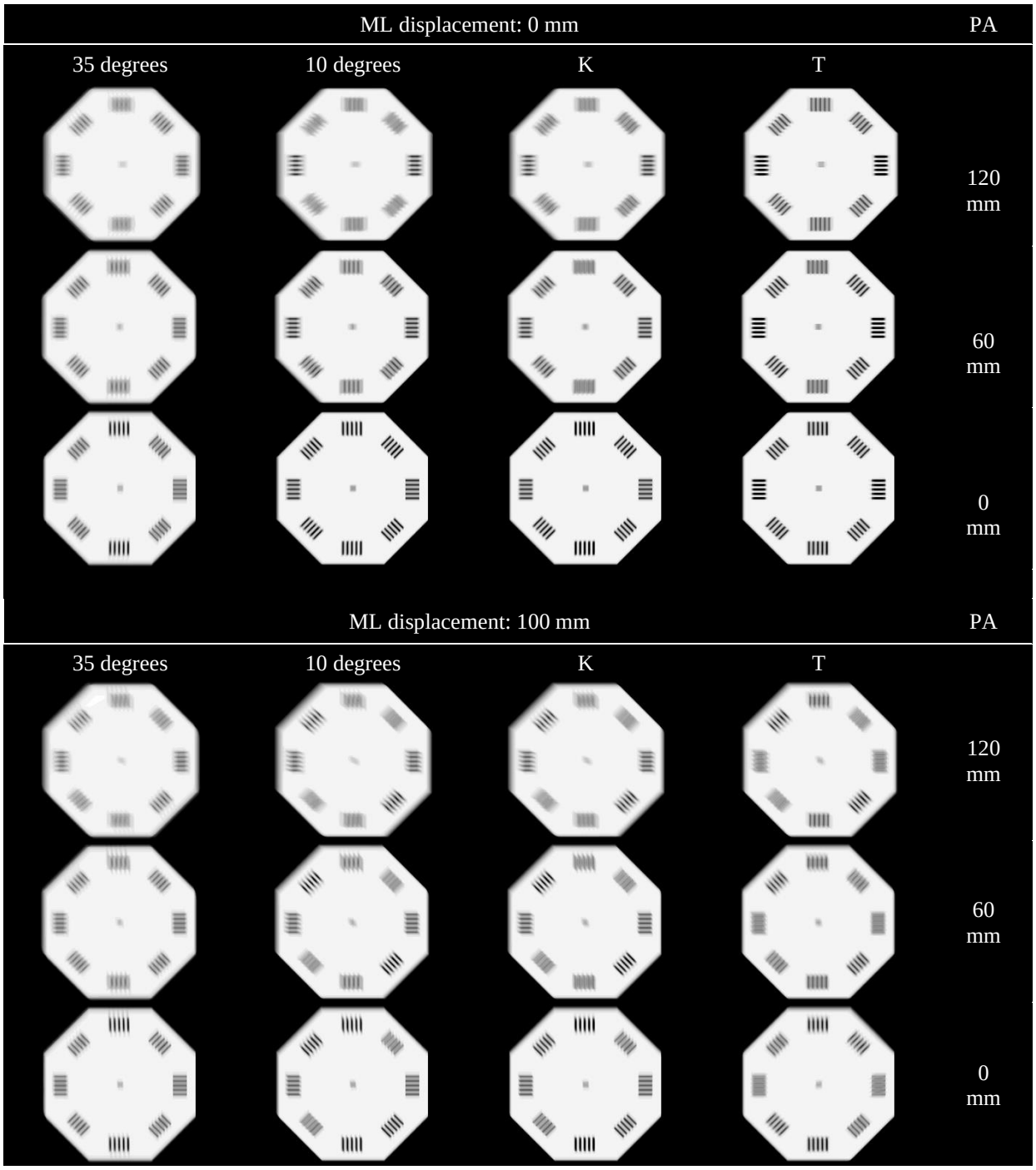

Figure 11. Reconstructed octagon phantom with NGT geometries is shown at different ML and PA displacements from the center of the chest wall. The reconstructed phantoms with the angular range of 15 and 35 degrees are shown for comparison.

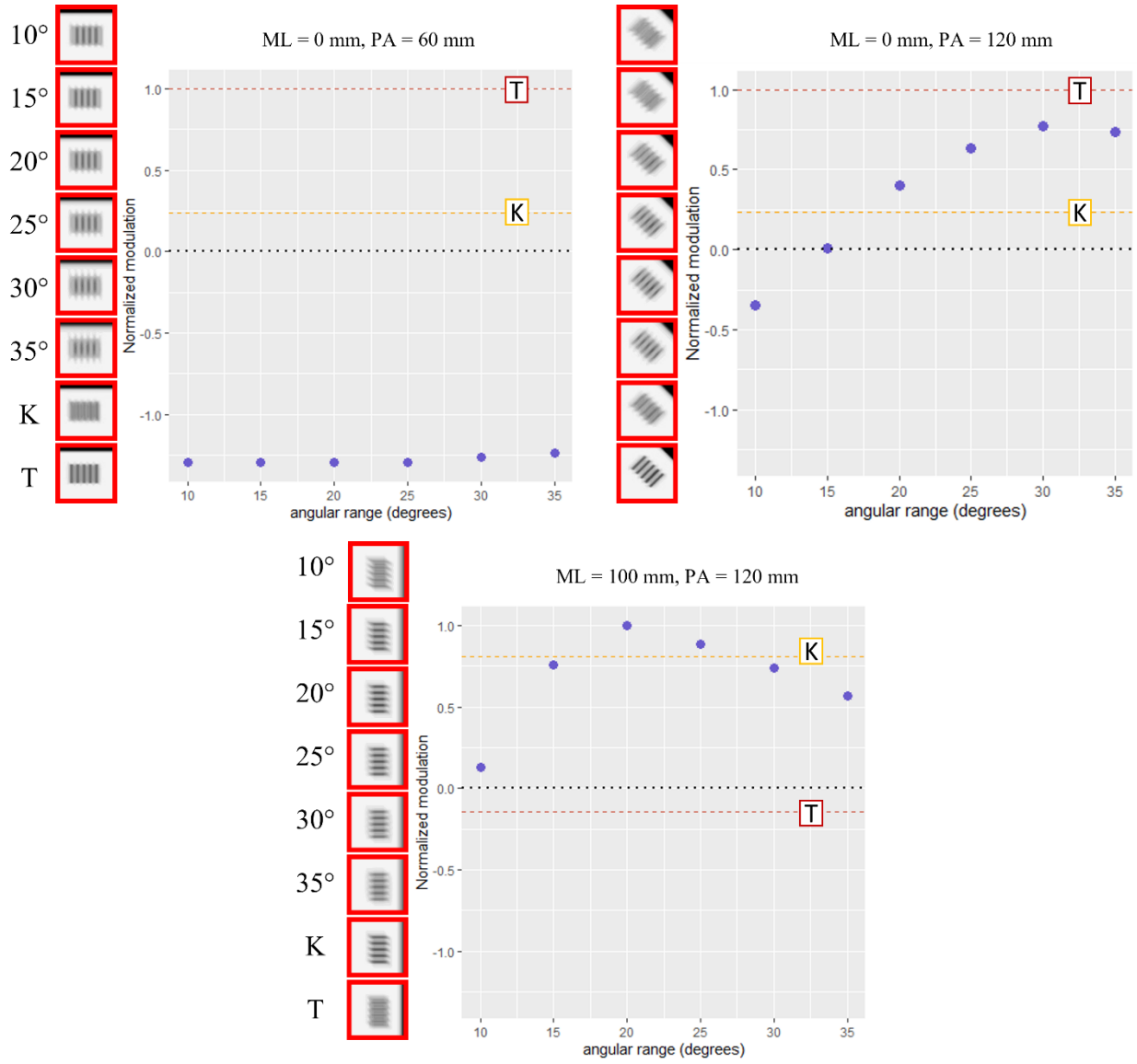

Figure 12. Normalized modulations of line pairs located at the 12 o'clock (top left), 1 o'clock (top right), and 3 o'clock (bottom) are presented.

3.6 Experiments of NGT geometries

The 3D printed octagon phantom was imaged with the NGT system to validate the simulation results (Figure 13). Close agreement between the experimental and simulated results is noted.

4. DISCUSSION AND CONCLUSION

In this work, we showed distinct, but different, benefits of narrow and wide angle tomosynthesis using a high-frequency test object (star pattern phantom) and a low-frequency test object (octagon phantom). We further showed that next generation tomosynthesis, by incorporating two-dimensional source trajectories, can capture the benefits of both narrow and wide angle tomosynthesis while minimizing any compromise in image quality.

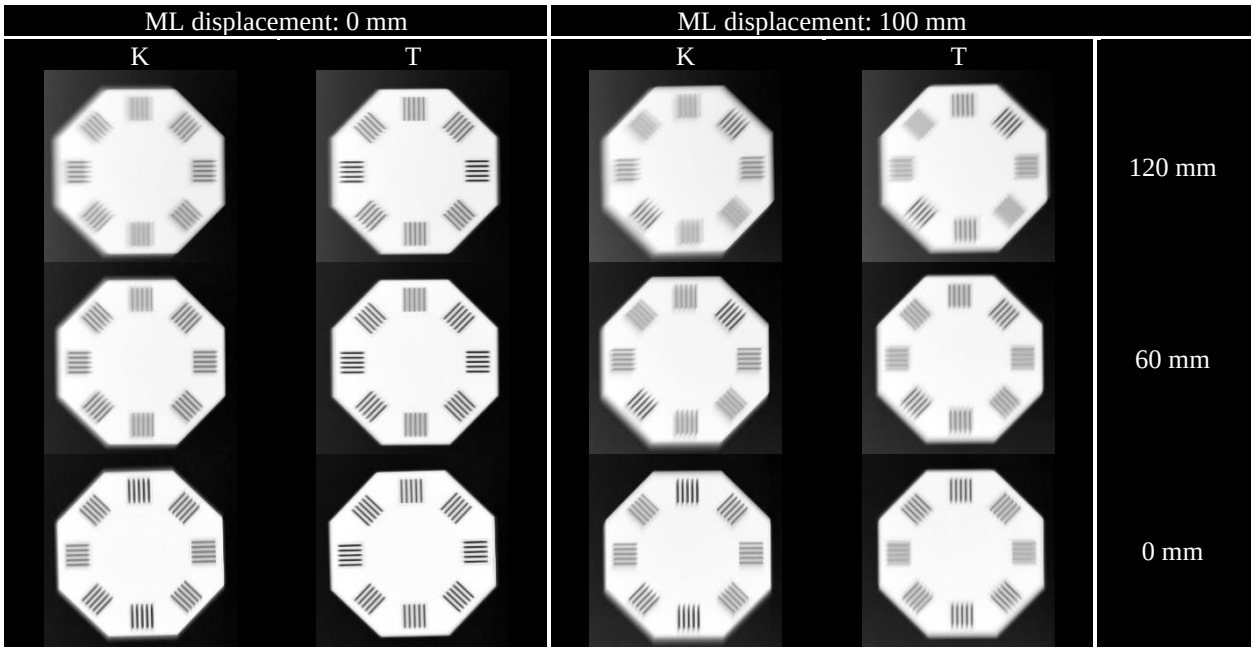

Figure 13. 3D printed octagon phantom was imaged with the NGT system.

4.1. Narrow angle tomosynthesis and super-resolution

Narrow angle tomosynthesis generally reduced aliasing in the scanning direction and offered higher in-plane resolution compared to wide angle tomosynthesis. Increasing the total number of projections generally increased in-plane resolution while reducing overall image nonuniformity, when the angular range is kept constant. For an angular range of 15°, the greatest improvement occurred between 5 projections and 7 projections. With 7 projections, super-resolution is easily achieved in our system. NGT geometries are designed with 7 projections along the chest wall to ensure super-resolution in both directions.[5]

It should be noted that super-resolution can be achieved with a careful selection of source positions which ensures sub-pixel detector element shifts. The improvement that occurred between 5 and 7 projections in this experiment may be achieved with a fewer number of projections and/or with a wider angular range. By the same logic, super-resolution might not always be achieved with a higher number of projections and/or with a narrower angular range.

4.2. Wide angle tomosynthesis and spatial isotropy

In this work, we expand the concept of sampling comprehensiveness[4] to spatial isotropy and hypothesized that the spatial isotropy in DBT generally increases with increasing sampled Fourier volume. We also hypothesized that low-frequency objects are more susceptible to spatial anisotropy as the volume of overlap is smaller in the low-frequency region in Fourier space (Figure 1). We support these hypotheses with a series of experiments imaging low-frequency and high-frequency test objects.

With the octagon phantom, we have shown that both location and orientation of the input frequencies relative to the source positions determine the image quality, especially the extent of blurring artifacts and inversion of modulation. The angular range and spatial isotropy are generally proportional to each other as hypothesized. For certain line pairs, especially away from the center of the chest wall, quality of modulation and angular range are directly proportional as shown in Figure 10. Points of inversion and plateau depended on the location of the phantom, which suggests that optimal angular range depends on the location and orientation.

By contrast, the thin, high-frequency star pattern phantom is less susceptible anisotropy based on its location above the detector (Figure 6), and therefore presents higher spatial isotropy, as hypothesized.

4.3. Next generation tomosynthesis as a combination of narrow and wide angle tomosynthesis

In a previous work by Vent *et al*[11], it was concluded that NGT geometries are capable of improved super-resolution in both ML and PA directions over the conventional DBT acquisition geometries. In this work, we justified the use of seven projections along the chest wall for visualization of high-frequency objects and demonstrated higher spatial isotropy for low-frequency objects with NGT geometries.

NGT geometries were better at resolving low frequencies away from the chest wall, as expected. The T geometry was most tolerant to PA displacement, given no ML displacement from the center. K geometry was moderately tolerant to both ML and PA displacements and presented rather uniform image quality.

The line pairs at the 12 o'clock position were distinctively better resolved with NGT geometries. Conventional tomosynthesis showed inverted and blurred line pairs due to aliasing regardless of the angular range (Figure 12). This is expected based on the work by Acciavatti *et al*[5], which concluded that input frequencies perpendicular to the source motion exhibit blurring and inversions and NGT designs offer higher image quality by including 2D source positions. In the present work, we analyzed the results for input frequencies of different orientations and locations and supported the superior image quality in NGT geometries.

In conclusion, we have successfully shown that NGT acquisition geometries present high in-plane resolution and highly isotropic sampling and thus combine the benefits of narrow-angle and wide-angle tomosynthesis.

5. ACKNOWLEDGEMENT

ADAM is a member of the scientific advisory board of Real Time Tomography (RTT) and is a spouse to an employee and stockholder of RTT. Support was provided by the following grants: W81XWH-18-1-0082 from the Department of Defense Breast Cancer Research Program, IRSA 1016451 from the Burroughs Welcome Fund, 1R01CA196528 from the National Institute of Health, and IIR13264610 from Susan G. Komen. In addition, equipment support was provided by Analogic Inc. and Barco NV. The content is solely the responsibility of the authors and does not necessarily represent the official views of the funding agencies.

REFERENCES

[1] J. E. Eben, T. L. Vent, C. J. Choi, S. Yarrabothula, L. Chai, M. Nolan, E. Kobe, R. J. Acciavatti, and A. D. A. Maidment, "Development of a next generation tomosynthesis system", Proc. SPIE 10573, Medical Imaging 2018: Physics of Medical Imaging, 105735Q (9 March 2018).

[2] I. Sechopoulos and C. Ghetti, "Optimization of the acquisition geometry in digital breast tomosynthesis of the breast", Med. Phys., 36: pp. 1199-1207, 2009.

[3] D. A. Martin, T. L. Vent, C. J. Choi, B. Barufaldi, R. J. Acciavatti, and A. D. A. Maidment, "Signal-to-noise ratio and contrast-to-noise ratio measurements for next generation tomosynthesis", Proc. SPIE 11595, Medical Imaging 2021: Physics of Medical Imaging, 115951L (2021).

[4] C. J. Choi, T. L. Vent, R. J. Acciavatti, and A. D. A. Maidment, "Analysis of digital breast tomosynthesis acquisition geometries in sampling Fourier space", Proc SPIE 115995, Medical Imaging 2021: Physics of Medical Imaging, 115954W (15 February, 2021).

[5] R. J. Acciavatti, A. Chang, L. Woodbridge, and A. D. A. Maidment, "Optimizing the acquisition geometry for digital breast tomosynthesis using the Defrise phantom", Proc. SPIE 9033, Medical Imaging 2014: Physics of medical Imaging, 903315 (19 March 2014).

[6] B. Barufaldi, D. Higginbotham, P. R. Bakic, and A. D. A. Maidment, "OpenVCT: a GPU-accelerated virtual clinical trial pipeline for mammography and digital breast tomosynthesis", Proc. SPIE 10573, Medical Imaging 2018: Physics of Medical Imaging, 1057358 (9 March 2018).

[7] T. L. Vent, B. Barufaldi, and A. D. A. Maidment, “Simulation and experimental validation of high-resolution test objects for evaluating a next-generation digital breast tomosynthesis prototype”, Proc. SPIE 10948, Medical Imaging 2019: Physics of Medical Imaging, 109480M (1 March 2019)

[8] T. L. Vent, R. J. Acciavatti, and A. D. A. Maidment, “Development and Evaluation of the Fourier Spectral Distortion Metric,” IEEE Trans. Med. Imaging, vol. 40, no. 3, pp. 1055–1064, 2021

[9] R. J. Acciavatti, and A. D. A. Maidment, “Observation of super-resolution in digital breast tomosynthesis”, Medical Physics. 2112;39(12):7518-7539.

[10] R. J. Acciavatti and A. D. A. Maidment, “Proposing an acquisition geometry that optimizes super-resolution in digital breast tomosynthesis, Lecture Notes in Computer Science. 2912; 7361:386-393.

[11] T. L. Vent, B. Barufaldi, and A. D. A. Maidment, “Simulation and experimental validation of high-resolution test objects for evaluating a next-generation digital breast tomosynthesis prototype,” Proc. SPIE 10948, Medical Imaging 2019: Physics of Medical Imaging, 109480M (1 March 2019)

Assessment of patch-based mammogram denoising methods using virtual clinical trials and deep learning: trade-off between denoising strength and preservation of structural details

Vincent Dong[a, b], Tristan D. Maidment[a], Lucas R. Borges[a], Bruno Barufaldi[b], Susan Ng[a], and Andrew D.A. Maidment[b]

[a]Real Time Tomography LLC, Villanova, PA, United States
[b]Department of Radiology, University of Pennsylvania, Philadelphia, PA, United States

ABSTRACT

Digital mammography (DM) is widely used for early breast cancer detection, where high quality, low-noise images are essential for screening. To provide radiologists with the highest quality images for diagnosis, denoising techniques including deep learning (DL) have been proposed in an attempt to suppress noise while preserving structural detail. DL model training depends on access to large training datasets with ground truth data to capture features relevant to the task. Ground truth, in the form of x-ray quantum-noise free DM images, is not available, so the use of computer simulations provides a viable method for this to be addressed. This study proposes a patch-based DL convolutional neural network (CNN) model for mammography denoising, trained on data obtained through our lab's virtual clinical trial (VCT) framework (OpenVCT). We extracted patches from VCT samples and trained a deep residual CNN to distinguish the patterns of noise from the underlying structure of the DM. Different denoising model configurations and combinations of denoising loss functions were explored to learn the simulated noise mappings and fine-tune the denoising performance to identify the trade-offs between denoising strength and fine structure preservation. We evaluated the denoising performance of these models by comparing the change in several image quality metrics, including peak signal-to-noise ratio (PSNR) and power spectra (PS). Our results indicate that our trained DL denoising model can detect and remove noise while preserving the original structure, resulting in a denoised reconstruction of simulated mammograms.

Keywords: Digital mammography, deep learning, denoising, residual convolutional neural network, virtual clinical trial

1. INTRODUCTION

Early stage breast cancer detection is commonly performed with digital mammography (DM), an imaging modality that is obtained through low-dose x-rays of the breast. Breast cancer screening involves detecting masses, architectural distortion, and small microcalcifications, which are hallmarks of cancers.[1] Thus, it is essential for DM images to exhibit high quality and low-noise for radiologists to make accurate clinical diagnoses. One approach to maximize the quality of DM images is through image denoising. Image denoising has been extensively researched in the general computer vision space; however, the application of these approaches has not been fully explored with DM images.[2,3]

Within the healthcare domain, the use of clinical trial data for training deep learning (DL) models has its limitations and is not always feasible for the initial development of new technologies. This is due to clinical trials requiring large financial investments for prototype design and patient recruiting, as well as limitations in clinical trial duration depending on patient and clinician availability. As a result, virtual clinical trials (VCTs) have emerged as an attractive alternative to validating new technologies before committing to a full-fledged clinical trial.[4–6]

Further author information:
Vincent Dong.: E-mail: vincent.dong@realtimetomography.com

Medical Imaging 2022: Physics of Medical Imaging, edited by Wei Zhao, Lifeng Yu, Proc. of SPIE
Vol. 12031, 120311W · © 2022 SPIE · 1605-7422 · doi: 10.1117/12.2612900

The use of VCT data allows for truly noiseless data to be simulated and used as ground truth data. VCT data also enables a fine level of control for the amount of noise that is added to the samples and can be changed to mirror different clinical environments better. However, there are limitations in the realism of simulated VCT mammograms in terms of breast shape and structure. In the context of denoising, the use of VCT data is highly promising.

Other works have demonstrated mammogram denoising results on full-field digital mammograms (FFDMs) with simulated dose reduction through noise generation.[7] In this study, we explore residual convolutional neural networks (CNNs) for denoising the aforementioned VCT data to understand the capabilities and trade-offs of denoising DM images for clinical analysis. Through investigations of different model configurations, hyperparameter selection, and loss functions, we propose a set of exploratory DL models that demonstrate accurate levels of denoising with varied visual outcome characteristics.

2. MATERIALS AND METHODS

2.1 Data Generation

A set of 25 DM samples was generated through the OpenVCT framework with clinically relevant simulated noise and dose levels. The OpenVCT framework is an open-source tool developed at the University of Pennsylvania dedicated to optimizing and validating breast imaging modalities.[8] This framework allows the fast simulation of the breast anatomy (phantoms) using a GPU implementation of an octree partitioning algorithm.[9] The breast compression is simulated using a 3D mapping technique with pre-calculated compression meshes.[10] In this study, the compressed phantoms were created using 0.1 mm^3 of voxel size, 700 mL of volume, and dimensions 78.4 x 205.3 x 63.3 mm^3. DM projections of the phantoms were simulated using ray-tracing software.[8] The radiographic technique factors were selected to match a clinical DM examination, with phototiming; thus the radiation dose and image quality were correctly matched to the thickness of the breast. A total of five image (and hence noise) realizations were generated for each phantom and averaged together to create the ground truth DM inputs for training our denoising models. In this manner, the simulated ground truth VCT samples maintained a similar level of underlying noise found in clinical trial data. Attempts to use strictly noise-free ground truth data were attempted initially but found to exhibit artifacts arising from limitations in the phantom realism, especially related to the voxel size. By averaging multiple image realizations, we could control the noise in the ground truth without artifacts.

2.2 Network Architecture

We explore two residual CNN model architectures. The first model, ResNet-DN is trained to learn the combination of signal and noise and predict the denoised output image. Our second proposed model, ResNet-RDN, is trained to learn the underlying noise and predict the difference between noiseless and noisy. The overall model architecture for both models is heavily influenced by the ResNet model architecture, a well-founded deep learning framework for the image recognition task.[11] Both ResNet-DN and ResNet-RDN follow the same fundamental design, where the only difference is in the activation functions used.

The first layer of our model is a convolution layer paired with a ReLU activation function. Following the same structure as the ResNet model, we then stack a series of residual blocks. Each residual block consists of convolution and batch normalization layers. The ResNet-DN model uses the ReLU activation function as the last layer within the block, while the ResNet-RDN model uses a hyperbolic tangent activation function. We chose to use fifteen residual blocks to create a model that finds the middle ground between being deep enough to effectively denoise our images while also avoiding being prone to overfitting. In total, both of our model architectures result in 107 total layers and 1,665,792 trainable parameters for the denoising task. An overview of the model architecture is shown in Fig. 1.

2.3 Model Training

We utilize a sliding-window, patch-based approach for training and evaluation of our models. Non-overlapping 64 x 64 pixel patches are extracted from the DM samples to form the training and validation sets. One sample provides a total of 3,584 patches. Thresholding was used to segment the breast from air, and only patches

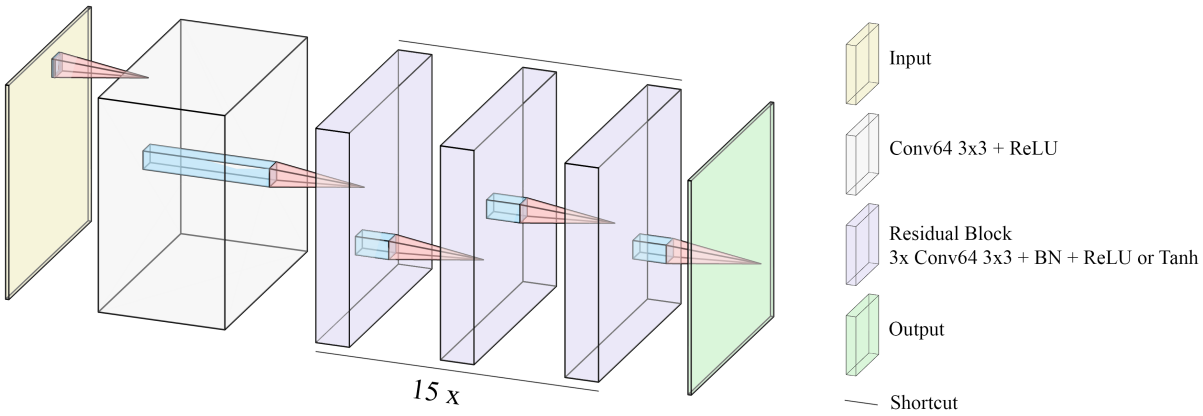

Figure 1. Diagram of residual model architectures. ResNet-DN uses ReLU activation functions in the residual block, while ResNet-RDN uses Tanh activation functions. The model expects a 64x64 pixel single-channel image and outputs in the same dimensions.

that exclusively contained breast tissue were used. We use 80 percent of the DM samples as our training set, resulting in 13,700 total patches used for training and 3,425 total patches held-out for validation. Both ResNet-DN and ResNet-RDN models are trained with the Adam optimizer. After a comprehensive hyperparameter search, the ResNet-DN model was trained with a batch size of 8 and a learning rate of 0.0001 for 25 epochs. The ResNet-RDN model was trained with a batch size of 4 and a learning rate of 0.02 for 70 epochs.

2.4 Loss Functions

Different loss functions have been explored in the context of denoising. The standard for deep learning denoising is Mean Squared Error (MSE) which is defined as

$$MSE(x, y) = \frac{1}{n}\sum_{i=1}^{n}(x_i - y_i)^2\,, \tag{1}$$

where x is the ground truth, noiseless image, and y is the predicted denoised image. However, other related works have argued the limitations of MSE as a denoising loss function, because MSE does not consider the structure of the image.[12] Thus, we investigate a variation of MSE, normalized mean square error (NMSE), to account for relative error within the image. The aforementioned MSE calculation is normalized by the square of the ground-truth estimation and is described as

$$NMSE(x, y) = \frac{1}{n}\sum_{i=1}^{n}\frac{(x_i - y_i)^2}{(y_i)^2}\,, \tag{2}$$

with x again being the ground truth, noiseless image, and y, the predicted denoised image. The weighting factor allows for more control of the trade-off between signal blur and noise suppression, which addresses the lack of structural consideration by the MSE loss function.

Another metric used for comparing the quality of two images is structural similarity index measure (SSIM), a full reference metric (relying on the noiseless image as a reference). SSIM is an equation that quantifies the

perceived quality and similarity between two images. It is a weighted combination of three comparative measures

$$SSIM(x,y) = l(x,y)^{\alpha} \cdot c(x,y)^{\beta} \cdot s(x,y)^{\gamma}\,, \tag{3}$$

where luminance (l), contrast (c), and structure (s) are weighed by α, β, and γ to make up the total SSIM value between two images x and y.

We can utilize a combination of these two loss functions by simply adding the two metrics together. To minimize SSIM, we use 1 - SSIM, as the SSIM between two images approaches 1 as they become equal. For our DM patches, however, the calculated values of NMSE and SSIM are different in scale. We note that the calculated SSIM is consistently 1 x 10^4 times smaller than the calculated NMSE. Thus, we performed experiments by weighing the SSIM value to have an equal influence on the training of the DL model, as well as conducting experiments in which the weight factor of SSIM is perturbed to investigate the effects of each loss metric during training. Our loss function can thus be expressed as

$$Loss(x,y) = w \cdot NMSE(x,y) + v \cdot (1 - SSIM(x,y))\,, \tag{4}$$

where w is the weight of the NMSE term that is varied, and v is the weight of the SSIM term that is varied. By weighing the components of the loss function in relation to SSIM, we balanced the trade-off between the noise suppression characteristic of NMSE and the structural detail preservation qualities of SSIM.

2.5 Patch Assembly

Due to the nature of patch-based denoising, the resulting patches were found to contain edge and border artifacts. In the evaluation phase of the denoising models, patches were sampled from the whole DM image in an overlapping manner with a stride smaller than the patch size. This modification allowed for the resulting artifacts to be removed from the denoised patches and allowed seamless restitching of the cropped sampled patches in the denoised DM reconstruction.

2.6 Evaluation Metrics

To evaluate the performance of our denoising models, we again extract non-overlapping patches from our test set. However, we do not apply thresholding and instead use all patches of the sample to feed into our trained network. The outputted denoised patches are then reconstructed into a fully assembled DM image, using the methods described in Section 2.5. This reconstruction of the DM is then evaluated with a variety of image quality metrics. Related works have used SSIM as an evaluation metric; however, due to its inclusion in our loss function, we excluded SSIM from our analysis.[7] Thus, we introduce two metrics for evaluating the denoising capabilities of our DL models - peak signal-to-noise ratio (PSNR) and power spectrum (PS). We calculate the PSNR between the noiseless ground truth image and the outputted denoised image. The PSNR expresses the ratio between the power of a signal and the power of distorting noise found in the image. It can be defined as

$$PSNR(I) = 20 \cdot log_{10}(\frac{MAX(I)}{\sqrt{MSE}})\,, \tag{5}$$

where $MAX(I)$ indicates the maximum possible pixel value in image I and MSE is the mean squared error between the noiseless phantom DM and the noisy realization. We quantify PSNR by calculating the difference between predicted denoised image PSNR and noisy image PSNR, using the original noiseless image as a reference. In this manner, a positive difference indicates improvement in PSNR value or successful denoising. We acknowledge that PSNR also includes a component of our loss function, MSE, but we include PSNR as an evaluation metric because the formulation of PSNR does differ from the NMSE used in the loss function.

Power spectra (PS) analysis is another image quality metric that quantifies the amount and frequency of signal and noise within an image. The characteristics of noise frequency in DM images are well studied, so the resulting PS of the denoised DM samples can be analyzed to evaluate denoising performance.[13] Mammographic anatomy dominates at lower spatial frequencies with roughly $1/f^3$ dependence, while noise tends to dominate at higher spatial frequencies with little frequency dependence.[14,15] By using the calculated two-dimensional Fast Fourier Transform (FFT) of the DM, multiple regions can be sampled and the average power spectrum of the denoised image can be obtained. The one-dimensional PS can then be plotted and analyzed to compare the trends of PS in different spatial frequencies.

3. RESULTS AND DISCUSSION

Using models trained to completion with tuned hyperparameters, results were generated for patch-based DL denoising on the held-out phantom DM test set. Using our defined PSNR evaluation metric, we observe an average PSNR difference of + 3.167 ± 0.020 dB for DM samples denoised by ResNet-DN, and an average PSNR difference of + 2.474 ± 0.011 dB for ResNet-RDN. The denoising outputs of the two models are shown in Fig. 2.

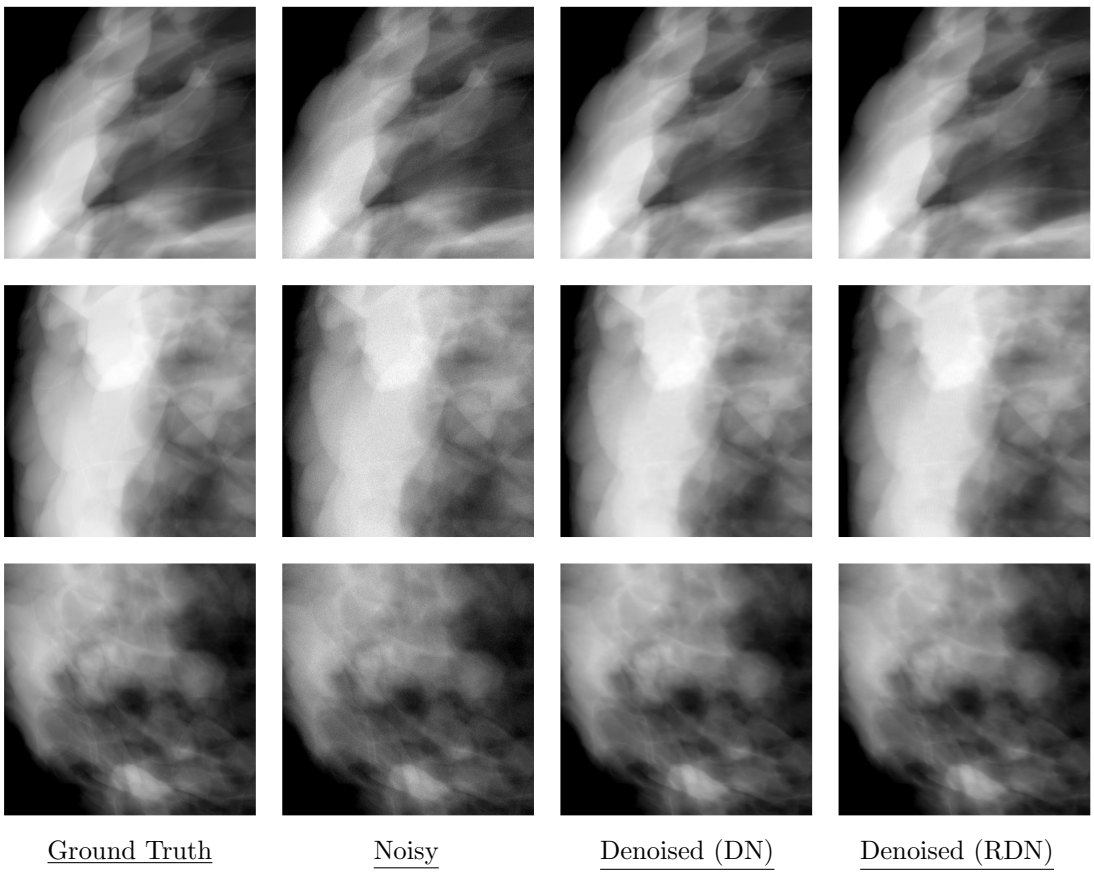

Figure 2. Magnified regions of interest (ROI) view of ground truth, noisy, and denoised results from ResNet-DN and ResNet-RDN. ROIs are taken from various samples to showcase different tissue densities and structural details. Results show promising levels of denoising for both models, with variance in levels of denoising as well as preservation of fine structures (e.g. Cooper's ligaments) within the DM image between the two model architectures.

Qualitatively, interesting results were observed between the two model architectures. Both models accomplished denoising of the DM samples, with a noticeable reduction in noise observable. For the ResNet-DN model, the denoised samples showcase less noise removal, but better preservation of the sharpness of fine anatomic structures like breast ducts, blood vessels and Cooper's ligaments. On the contrary, the ResNet-RDN model had a higher level of denoising but was more prone to removing detail in fine structures. In fact, certain ligaments are completely removed by ResNet-RDN. This trend is very noticeable in the less dense regions of the images. These visual trends are corroborated by the PS plots in Fig. 3.

Our reported results in Fig. 3 follow the discovered trends of power spectra in mammography.[14,15] Interestingly, both denoised outputs from the two model architectures removed very relatively little noise from the lower spatial frequencies, with most of the denoising occurring in high spatial frequencies. Furthermore, both denoising models tended to over-correct the noise at higher spatial frequencies. In fact, the blurring effect that was observed in the residual (ResNet-RDN) model is reflected in the PS plots, as ResNet-RDN reduced the PS

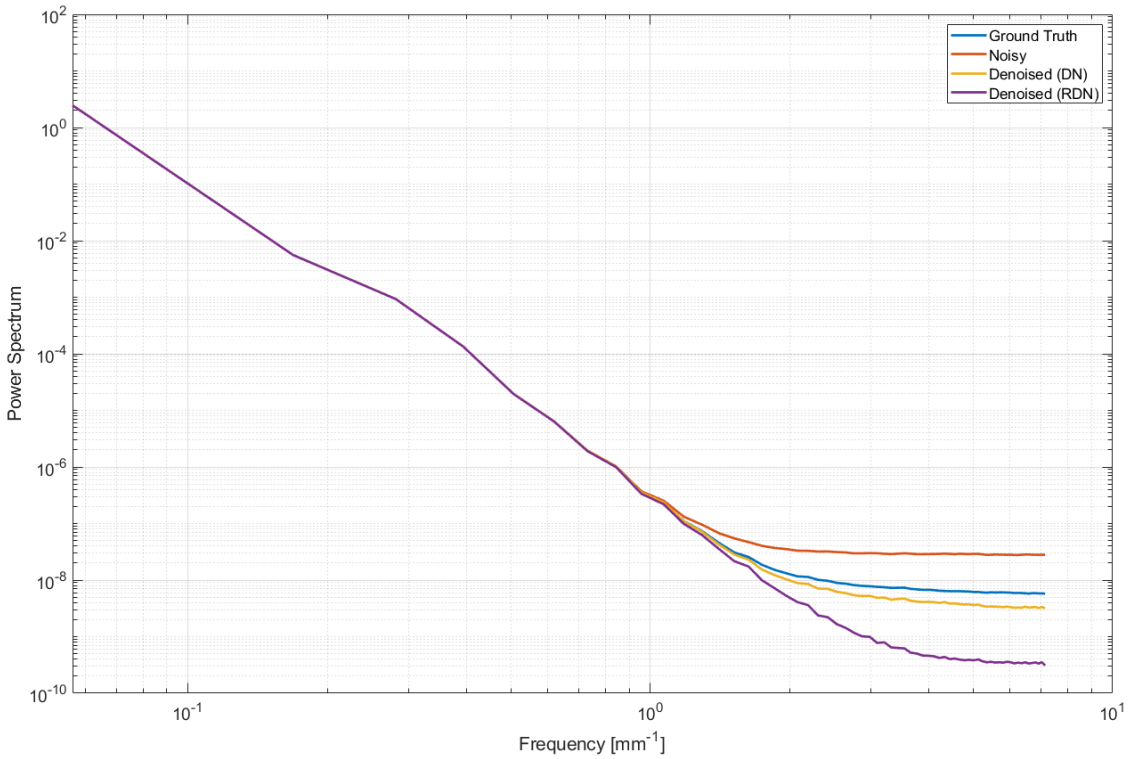

Figure 3. Power spectra (PS) plots of ground truth, noisy, and denoised outputs of ResNet-DN and ResNet-RDN models in log-log scale. These plots highlight noise removal in the high spatial frequencies of the DM images.

substantially below the ground truth for high spatial frequencies. Overall, PS difference plots show minimal difference between ground truth and denoised output in the lower frequencies, which indicate suitable preservation of anatomic structures.

In addition to comparing the two model architectures, we also investigated variations of weightings of NMSE and SSIM. We consistently observed positive PSNR differences with our best-found weights between NMSE and SSIM, indicating a quantified improvement in image quality regardless of model architectures. However, we recognized that our model denoising performance was highly sensitive to the weights between loss function components. We discovered that the PSNR difference between the denoised output and noisy DM varies greatly depending on the weighted loss function. To illustrate this phenomenon, we visualized the spectrum of PSNR difference values across many weights of NMSE and SSIM, as shown in Fig. 4

As expected, the tradeoff between denoising strength and preservation of structural detail was highly sensitive to the weighting of NMSE and SSIM. The PSNR difference steadily decreases as the weight of SSIM to NMSE increases, until it eventually reaches a point of instability and begins to oscillate heavily. The ResNet-RDN model demonstrates greater instability than ResNet-DN. These results are consistent with the visual appearance of the denoised images, where a smaller weight of SSIM yielded denoised outputs that were more appealing than those with a higher ratio of SSIM. When utilizing the combined loss function, a higher weight of NMSE resulted in stronger denoising at the cost of excessive blurring. A higher weight of SSIM resulted in better preservation of image pixel intensities and the structure of the mammogram but would have lower levels of noise removal.

We identified multiple important factors that influence a DL model's ability to denoise phantom mammograms while preserving structural detail. When comparing the visual qualities of the two proposed model architectures, ResNet-DN and ResNet-RDN, the trade-off between denoising strength and structure preservation is showcased.

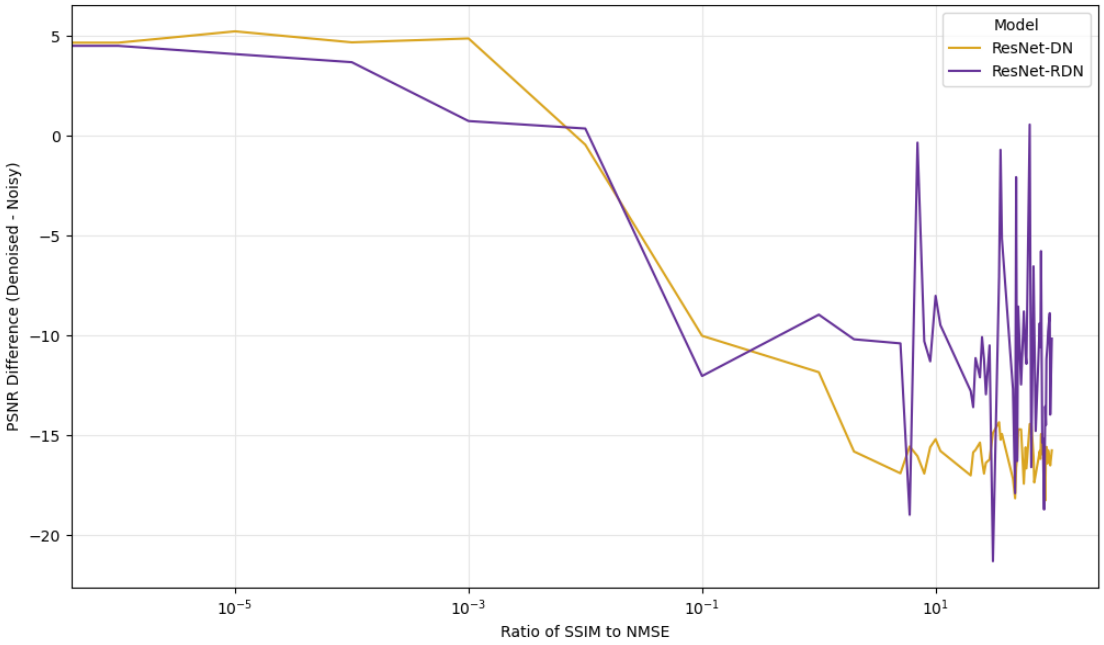

Figure 4. PSNR difference after denoising with a varied ratio of SSIM weight to NMSE weight. As the weight of SSIM increases, the resulting PSNR difference of the model outputs decreases. Eventually, the resulting denoised DMs become worse in PSNR than the original noisy input.

The ResNet-DN model visually appeared less denoised but retained most ligament structures within the breast tissue. For the ResNet-RDN model, however, our findings showed that there was still a degree of fine structural detail that was mistakenly interpreted as noise and consequently removed. We also observed that the denoised images of ResNet-RDN err on the side of being more blurred than the ResNet-DN outputs. There are also instances of residual noise patterns being left untouched by the model as well. We illustrated this trend by plotting the difference image between ground truth and denoised, as it identifies the regions where the noise realization was detected by the DL model and subsequently removed. The resulting difference plots for the two proposed DL models are shown in Fig. 5.

The difference between the denoised DM and the ground truth DM and the difference between the denoised DM and the noisy DM highlights the information removed by the denoising models. As a result, the underlying noise detected by the model can be seen in the two difference images. Furthermore, any structure that was subsequently removed by the denoising model will also appear in these difference images. Our prior observations of structural detail preservation between ResNet-DN and ResNet-RDN are further supported by these difference images, as they showcase ligaments that were mistakenly removed by the denoising model. Both model architectures remove structural detail, but it is more pronounced in ResNet-RDN. Note that the noise texture also differs.

These trends showcase the complexity of this denoising task. While both ResNet-DN and ResNet-RDN models achieve an acceptable level of denoising as shown by the PSNR metrics, there were noticeable visual differences between the resulting denoised mammograms. Furthermore, the high sensitivity of the model's denoising performance to the weights of the combined loss function suggests that an alternate loss function should be explored in order for a more robust and generalizable denoising model to be trained and used.

The resulting PS plots also identified an important finding in all variations of our denoising model. Within higher frequencies of the mammogram, the denoising outputs had lower power spectra than the "noiseless" ground

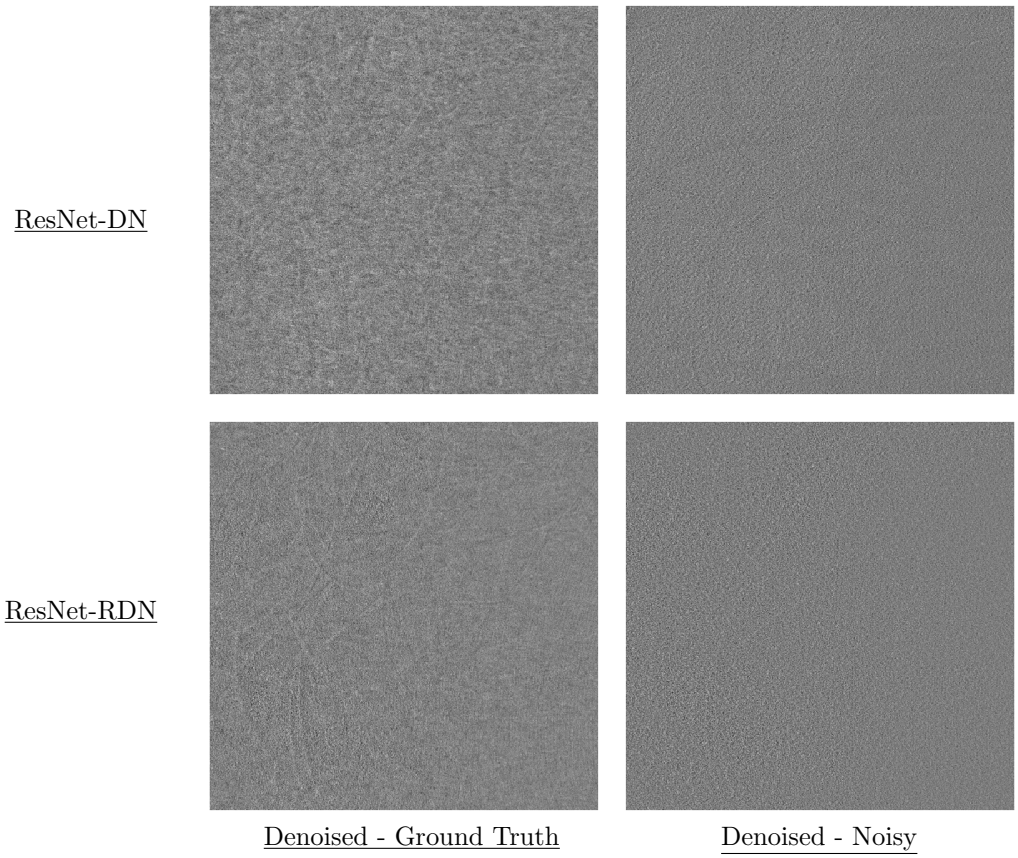

Figure 5. Difference images between denoised image and ground truth or noisy image of the ResNet-DN and ResNet-RDN models. Structural detail that is removed during the denoising process is showcased in these difference images, as well as the underlying noise realizations that are detected.

truth phantom mammograms, indicating that the model is indeed removing noise within this frequency range that has been attributed to acquisition noise in mammography.[14,15] However, the denoised outputs consistently overshoot the removal of high frequency noise, which suggests that more information is being removed in the denoising process than necessary.

This study contained obvious limitations for exploring denoising. Due to the inability to have completely noiseless DM images in clinical trial data, the usage of VCT data introduces its own limitations. First, the preservation of breast structure and shape can not be a consideration in our study due to the nature of our VCT data. Our denoising models are only exposed to one singular breast shape and may react unpredictably to variations in breast shape or size. Second, the results of the PS analysis may suggest that there are limitations in the VCT phantom noise realizations, as the resulting denoised images show that the VCT data may not be completely noiseless in the higher frequencies of the noise power spectrum. To date, we have not added microcalcifications to the phantom DM images which prevents analysis of the effects of denoising on these important visual markers of breast cancer, and thus prevents evaluating the denoising of our approach in its main clinical application setting. Finally, there were limitations in comparing our denoising performance with other studies, as our choice of loss function limited the evaluation metrics we could subsequently use.

4. CONCLUSION

The CNNs explored were shown to denoise simulated DM images successfully, at least to an extent. These results suggest that deep learning models can be trained to denoise images through two different methodologies, either by learning to output the final denoised image or by learning to output the difference between the noisy

and noiseless images. Regardless of the training task, these DL models can produce denoised predictions that preserve most of the original structure in the mammogram. Differences in model architecture create a tradeoff between denoising amount and the amount of structural detail preservation. However, the sensitivity of the two explored loss functions when weighted and combined indicates that our proposed loss function may not be well suited for training a robust and generalizable denoising model that can consistently remove noise while preserving structural information in clinical data. In conclusion, both ResNet-DN and ResNet-RDN models demonstrated a positive improvement in visual quality after denoising, where changes in model architecture and weighting of our loss function would introduce tradeoffs between denoising strength and preservation of structural detail.

ACKNOWLEDGMENTS

Vincent Dong, Tristan Maidment, Lucas Borges, and Susan Ng are members of RTT. Susan Ng is a shareholder of RTT. Andrew Maidment is a member of the scientific advisory board of RTT. The VCT data used in this research was provided by the University of Pennsylvania. That work was supported by the following grants: BWF IRSA 1016451, 2020 AAPM Research Seed Grant, DoD W81XWH-18-1-0082, and NCI P30 CA016520. The content is solely the responsibility of the authors and does not necessarily represent the official views of the funding agencies.

REFERENCES

[1] Morgan, M. P., Cooke, M. M., and McCarthy, G. M., "Microcalcifications associated with breast cancer: an epiphenomenon or biologically significant feature of selected tumors?," *J Mammary Gland Biol Neoplasia* **10**, 181–187 (Apr 2005).

[2] Abdelhafiz, D., Yang, C., Ammar, R., and Nabavi, S., "Deep convolutional neural networks for mammography: advances, challenges and applications," *BMC Bioinformatics* **20**, 281 (Jun 2019).

[3] Joseph, A. M., John, M. G., and Dhas, A. S., "Mammogram image denoising filters: A comparative study," in [*2017 Conference on Emerging Devices and Smart Systems (ICEDSS)*], 184–189 (2017).

[4] Zhao, B., Zhou, J., Hu, Y. H., Mertelmeier, T., Ludwig, J., and Zhao, W., "Experimental validation of a three-dimensional linear system model for breast tomosynthesis," *Med Phys* **36**, 240–251 (Jan 2009).

[5] Sechopoulos, I. and Ghetti, C., "Optimization of the acquisition geometry in digital tomosynthesis of the breast," *Med Phys* **36**, 1199–1207 (Apr 2009).

[6] Young, S., Bakic, P. R., Myers, K. J., Jennings, R. J., and Park, S., "A virtual trial framework for quantifying the detectability of masses in breast tomosynthesis projection data," *Med Phys* **40**, 051914 (May 2013).

[7] Eckert, D., Vesal, S., Ritschl, L., Kappler, S., and Maier, A., "Deep learning-based denoising of mammographic images using physics-driven data augmentation," (2019).

[8] Barufaldi, B., Higginbotham, D., Bakic, P. R., and Maidment, A. D. A., "OpenVCT: a GPU-accelerated virtual clinical trial pipeline for mammography and digital breast tomosynthesis," in [*Medical Imaging 2018: Physics of Medical Imaging*], Lo, J. Y., Schmidt, T. G., and Chen, G.-H., eds., **10573**, 1333 – 1340, International Society for Optics and Photonics, SPIE (2018).

[9] Pokrajac, D. D., Maidment, A. D. A., and Bakic, P. R., "Optimized generation of high resolution breast anthropomorphic software phantoms," *Medical Physics* **39**(4), 2290–2302 (2012).

[10] Barufaldi, B., Bakic, P. R., Pokrajac, D. D., Lago, M. A., and Maidment, A. D. A., "Developing populations of software breast phantoms for virtual clinical trials," in [*14th International Workshop on Breast Imaging (IWBI 2018)*], Krupinski, E. A., ed., **10718**, 481 – 489, International Society for Optics and Photonics, SPIE (2018).

[11] He, K., Zhang, X., Ren, S., and Sun, J., "Deep residual learning for image recognition," *CoRR* **abs/1512.03385** (2015).

[12] Zhao, H., Gallo, O., Frosio, I., and Kautz, J., "Loss functions for image restoration with neural networks," *IEEE Transactions on Computational Imaging* **3**(1), 47–57 (2017).

[13] Cunningham, I., "Applied linear-system theory," in [*Handbook of Medical Imaging: Physics and Psychophysics*], Van Metter, R., Beutel, J., and Kundel, H., eds., 79–155, SPIE (2000).

[14] Burgess, A. E., "Mammographic structure: data preparation and spatial statistics analysis," in [*Medical Imaging 1999: Image Processing*], Hanson, K. M., ed., **3661**, 642 – 653, International Society for Optics and Photonics, SPIE (1999).

[15] Barufaldi, B., Abbey, C. K., Lago, M. A., Vent, T. L., Acciavatti, R. J., Bakic, P. R., and Maidment, A. D. A., "Computational breast anatomy simulation using multi-scale perlin noise," *IEEE Transactions on Medical Imaging* **40**(12), 3436–3445 (2021).

Novel Perlin-based Phantoms Using 3D Models of Compressed Breast Shape and Fractal Noise

João P. V. Teixeira[1], Telmo M. Silva Filho[1], Thaís G. do Rêgo[1], Yuri B. Malheiros[1], Magnus Dustler[2], Predrag R. Bakic[2,3], Trevor L. Vent[3], Raymond J. Acciavatti[3], Srilalan Krishnamoorthy[3], Suleman Surti[3], Andrew D. A. Maidment[3] and Bruno Barufaldi[3*]
[1]Department of Computer Science, Federal University of Paraiba, João Pessoa, Brazil
[2]Department of Translational Medicine, Lund University, Malmö, Sweden
[3]Department of Radiology, University of Pennsylvania, Philadelphia, United States
[*]Bruno.Barufaldi@pennmedicine.upenn.edu

ABSTRACT

Virtual clinical trials (VCTs) have been used widely to evaluate digital breast tomosynthesis (DBT) systems. VCTs require realistic simulations of the breast anatomy (phantoms) to characterize lesions and to estimate risk of masking cancers. This study introduces the use of Perlin-based phantoms to optimize the acquisition geometry of a novel DBT prototype. These phantoms were developed using a GPU implementation of a novel library called Perlin-CuPy. The breast anatomy is simulated using 3D models under mammography cranio-caudal compression. In total, 240 phantoms were created using compressed breast thickness, chest-wall to nipple distance, and skin thickness that varied in a {[35, 75], [59, 130), [1.0, 2.0]} mm interval, respectively. DBT projections and reconstructions of the phantoms were simulated using two acquisition geometries of our DBT prototype. The performance of both acquisition geometries was compared using breast volume segmentations of the Perlin phantoms. Results show that breast volume estimates are improved with the introduction of posterior-anterior motion of the x-ray source in DBT acquisitions. The breast volume is overestimated in DBT, varying substantially with the acquisition geometry; segmentation errors are more evident for thicker and larger breasts. These results provide additional evidence and suggest that custom acquisition geometries can improve the performance and accuracy in DBT. Perlin phantoms help to identify limitations in acquisition geometries and to optimize the performance of the DBT prototypes.

Keywords: virtual clinical trial; Perlin noise; digital breast tomosynthesis, ray-tracing.

1. INTRODUCTION

Virtual clinical trials (VCTs) have been used to evaluate, optimize, and validate novel imaging systems.[1–3] Imaging VCTs are usually targeted toward specific clinical tasks, requiring computational simulations of human anatomy (phantoms).[1] In breast imaging VCTs, virtual phantoms should simulate the anatomic noise seen in images of the mammary parenchyma, especially for clinical tasks that require characterization of lesions or estimation of risk of masking cancers.[4]

We have shown in a previous VCT study that computer simulations of Perlin noise can improve substantially the realism of mammary parenchyma of virtual breast phantoms.[4] Perlin noise[5] uses gradient values that are smoothly connected by an interpolation function that is used to generate complex textures and patterns in medical imaging.[4,6] Dustler *et al*. have proposed the use of a variation of Perlin noise called fractal noise (or fractional Brownian motion) to simulate realistic small-scale breast structures that improve the realism of phantom images.[7,8] Fractal noise requires the combination of Perlin parameters with different frequencies to generate coherent noise textures. However, the combination of "Perlin textures" using 3D Perlin functions is cumbersome for CPU-processing applications, limiting the simulation of Perlin phantoms with high voxel resolution and/or with large volumes.[7,8] GPU-based applications are required to improve and accelerate simulations of Perlin-noise based phantoms for breast imaging.

Custom phantoms have been used to design and validate a proposed PET-DBT prototype.[9,10] This prototype integrates positron emission tomography (PET) and digital breast tomosynthesis (DBT) modalities to provide functional breast imaging. Our previous VCT work has shown that the dedicated PET-DBT device can facilitate attenuation corrections for functional breast imaging; potentially improving the reconstruction of coincident gamma rays.[9] Our results indicate that custom acquisition geometries of the PET-DBT device can improve significantly the adipose-glandular tissue

Medical Imaging 2022: Physics of Medical Imaging, edited by Wei Zhao, Lifeng Yu, Proc. of SPIE
Vol. 12031, 120313S · © 2022 SPIE · 1605-7422 · doi: 10.1117/12.2612565

classification for DBT.[9] Changes in performance of custom DBT acquisitions should be investigated using breast phantoms with realistic 3D curvature of compressed breasts, since the volumetric segmentation of breast outlines is one of the primary concerns for attenuation correction of our PET-DBT prototype.[11]

DBT acquisitions should be personalized on an individual basis, avoiding inherent limitations of the system for estimating breast volumes.[11] Rodríguez-Ruiz *et al.* have developed a software based on principal component analysis (PCA) method that creates 3D breast outlines under mammography compression.[12,13] This software provides a detailed characterization and modeling of the compressed breast tissue curvature between the support table and the compression paddle.[12,13] Breast volume estimates should be calculated using realistic breast outlines to evaluate the performance of DBT acquisitions.

This study presents a novel method to simulate the breast anatomy using 3D Perlin noise. These phantoms were used to evaluate changes in performance of acquisition geometries of our PET-DBT prototype. The PCA-based software was used to create realistic breast outlines. The breast outlines were varied in the range [35, 75] mm, [59, 130) mm, and [1.0, 2.0] mm, for breast thickness, breast extent (chest-wall to nipple distance), and skin thickness, respectively. Fractal noise was embedded into the breast outlines using an open-source library called Perlin-CuPy,[14] resulting in a total of 240 Perlin-phantoms.[4] DBT projections were simulated using two DBT acquisition geometries. The performance of the DBT acquisitions were evaluated using breast volume estimates of reconstructed images and respective ground truth.

2. MATERIALS & METHODS

2.1. Voxelized Breast Phantom

Voxelized breast outlines were simulated using a software that models breasts under mammography compression using the principal component analysis (PCA) method.[12,13] The PCA method provides a detailed characterization and modeling of the 3D compressed breast tissue curvature between the support table and the compression paddle (Figure 1A). In total, 20 breast outlines of 0.2 mm^3 voxel size were modeled under cranio-caudal (CC) compression. The outlines were categorized by compressed breast thickness (CBT) that varied in a [35, 75] mm interval in 10 mm steps. The chest-wall to nipple distance (CND) varied from 50 to 180 mm. The PCA software generates breast outlines with CND values that increase with thicker breasts.

The skin of each breast outline was simulated using a 3D erosion operation applied to the binary volumes. The breast skin thickness was determined by varying a ball structuring element of erosion operations.[15] The volume of each structural element varied randomly in a [1.0, 2.0] mm interval using 0.2 mm steps. The values of skin thickness were based on measures accurately calculated by Sutradhar and Miller.[16] The original and eroded breast volumes were combined, resulting in a mask that contains three indices: air, breast, and skin (Figure 1B).

A recursive partitioning software[2,17] was used to simulate adipose (70%) and glandular (30%) compartments, and Cooper's ligaments. The number of compartments was varied based on parameters previously validated.[18] The ligaments were simulated using [0-0.2] mm thickness. The compartments and ligaments were embedded into the breast outline, resulting in a multi-label breast phantom (Figure 1CD). These phantoms were used as baseline for a multi-scale Perlin simulation.[4]

2.2. Perlin-phantom Simulation

Perlin phantoms were created using a GPU-enabled environment and the Perlin-CuPy library.[4,14] Perlin-CuPy is an open-source library developed for GPU-accelerated Perlin noise generation.[14] The Perlin-CuPy library contains the implementation of Perlin-NumPy functions, compiled with the CuPy and CUDA Toolkit libraries.

The 3D functions of the Perlin-CuPy library were used to simulate fractal noise within the internal region of each breast tissue (Figure 1CD). The fractal noise parameters were validated in the work reported by Dustler *et al*.[19] In this study, we varied the persistence parameter from [0.25, 1] in 0.25 steps, while the number of octaves and lacunarity were set to 6 and 2, respectively. The volume of each Perlin-noise distribution was normalized to unsigned short values (2-bytes) and stored using a Lempel–Ziv–Markov algorithm (LZMA) for compression.

Perlin-CuPy library offers three implementations of 3D fractal noise to simulate phantoms: CPU-only (multi-threading), GPU-only, and hybrid (CPU+GPU). A data science workstation (mod. Precision 5820, Dell Inc.) was used to evaluate

the performance of fractal noise simulation using the three modes. This workstation is equipped with a core i9-10900X CPU @ 3.70GHz, 256 GB of RAM memory, and a 2×NVIDIA RTX A6000 card (48 GB VRAM).

Two independent Perlin-noise distribution were used for each phantom: glandular (Figure 1C, yellow) and adipose tissue (Figure 1C, light pink) distributions. The noise frequencies were normalized in the [0.0001, 1] interval to avoid negative values in the voxel distribution. We applied the log_e in the voxel distribution to reduce the range of frequencies, resulting in a narrow histogram. Note that the voxels following the logarithm are proportional to the linear x-ray attenuation of the materials[20] and the function log_e preserves noise structures in the log scale. For voxels that represent adipose, the Perlin-noise distribution was inverted. This inversion results in a Perlin noise distribution with predominant lower frequencies. Finally, the voxel values for both Perlin noise distributions (glandular and adipose) were normalized to the [1, 62] interval to convert the breast phantoms to Perlin phantoms with 6-bit noise resolution (n = 64, where materials 0 and 63 represent air and skin, respectively).

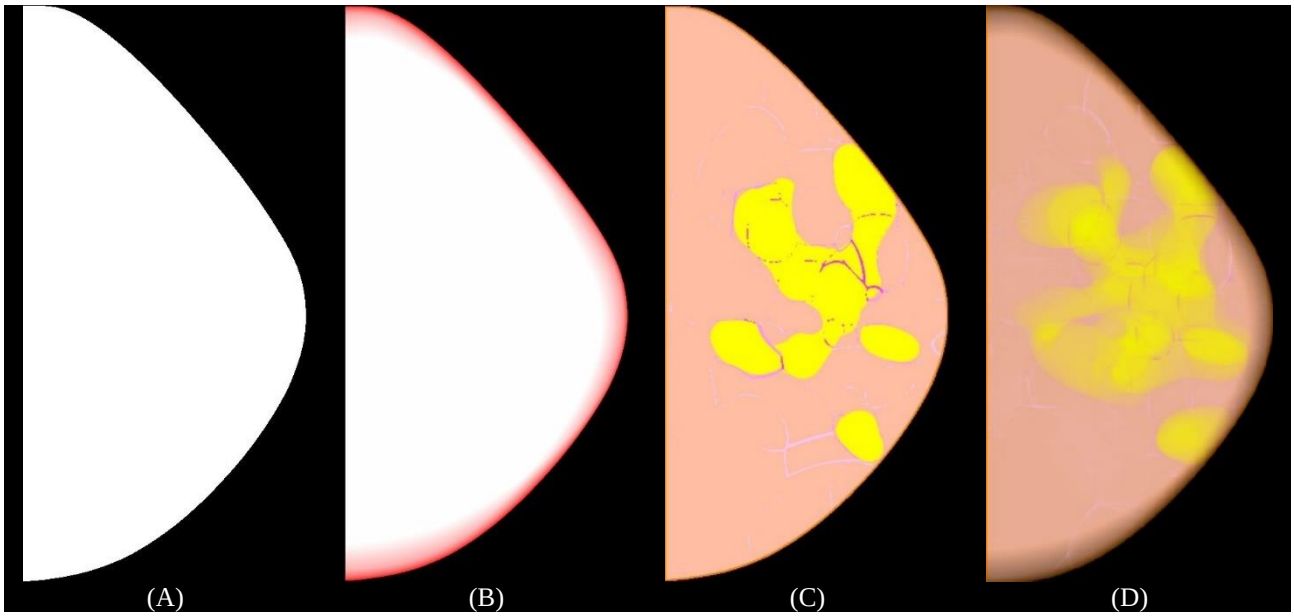

Figure 1. (A) Example of PCA-based breast outline, (B) sum of outline slices (in z: thickness), representing the skin line (red) with curvature (shades of red), (C) multi-label phantom outline – fat tissue (light pink) clusters of density (yellow), 4-type ligaments (dark pink to magenta), and skin (orange) –, and (D) volume visualization (z-projection) of phantom excluding skin line.

Each voxel from the normalized Perlin phantoms represents a composite material that consists of a complementary mixture of adipose and glandular tissue (partial volume, %).[4] For the 61 materials used to simulate Perlin noise, the composition of partial volume of voxels decreases linearly from 99% to 1% of adipose tissue and increases linearly from 1% to 99% of glandular tissue.[4] These composite materials (partial volume) vary the x-ray attenuation of the images.[4]

Finally, the log distribution of voxels consisting of composite materials are shifted to modify the volumetric breast density of each phantom. Since the partial volume of glandular tissue increases with higher indices of voxel materials ([1, 62]), a positive shift in the histogram results in phantoms with increased VBD%. In addition, since the logarithmic values of the histogram are narrow, the mode (i.e., peak of the histogram) indicates approximately the VBD% of each breast phantom. In this study, the voxels were shifted based on the mode of the histogram to control the VBD%. The mode of adipose and glandular distributions was set to 15 (90-10% adipose-glandular) and 26 (72-28% adipose-glandular), respectively. For the 4-type ligaments, we used the values 18, 30, 20, and 32, which correspond to a partial volume of 13-87%, 61-39%, 84-16%, and 55-45% adipose-glandular tissue composition. The values assigned for mode of Perlin distributions and 4-type ligaments were selected empirically using visual inspection of four medical physicists.

2.3. DBT Acquisition Simulation

DBT projections of the breast phantoms were simulated using the OpenVCT framework,[21] which executes a fast GPU implementation of the Siddon algorithm for ray-tracing.[22] The DBT projections were synthesized assuming the

conventional and "T-shape" acquisition geometries of the PET-DBT system (Table 1). The acquisition exposure settings were simulated using the automatic exposure control data of the NGT system.[9] The attenuation coefficient data of the materials used to simulate the phantoms come from the ICRU Report 44.[23] Reconstructed DBT slices were produced using simple backprojection with commercially available software library (Briona, version 7.12, Real-Time Tomography, Villanova, PA).[24]

The breast outlines were segmented from the background for each image reconstruction using Briona.[9] The reconstructed breast volume was estimated using the full-resolution image reconstructions. Each volume estimation was normalized to the ground truth of the respective phantom. The volume of each reconstruction was determined by the total volume of voxels that have a signal greater than zero normalized to the total volume of non-air voxels for each respective phantom (ground truth).

Table 1. Summary of DBT acquisition parameters. (A) Conventional and (B) T-shape acquisition geometries.

Acquisition Geometry	(A)	(B)
X-Ray Imaging		
Number of Projections	15	
Medio-lateral (ML) Distance of Projections (max, mm)	180	180
Posterior-anterior (PA) Distance of Projections (max, mm)	0	180
Anode and Filter Materials	Tungsten and aluminum	
Filter Thickness (mm)	0.7	
Angular Range ML (°)	±7.5	±7.5
Angular Range PA (°)	0	+15.0
Tube Motion	Step-and-Shoot	
Detector		
Detection Material	a-Se	
Detector Element Size (mm)	0.085 × 0.085	
Number of Elements	3584 × 2816	
Detector Size (mm)	304.64 × 239.36	
Source-to-Image Distance (mm)	722.0	
Reconstruction		
Voxel Size (mm^3)	0.085×0.085×0.2	

3. RESULTS & DISCUSSION

The processing time required to simulate Perlin phantoms is 88±56s (mean±SD, Figure 2). The processing time varies with phantom volume, and functions (CPU, GPU, and hybrid) used to simulate fractal noise. Note that the GPU implementation is much faster than the CPU or Hybrid implementations for the simulation, especially for the thickest breasts (CBT>65 mm). The order of complexity for GPU implementation is linear with phantom volume [$O(x)$], while CPU multi-threading processing is approximately exponential [$O(e^x)$]. Comparing CPU-only and hybrid implementations, we did not observe any improvement with the hybrid implementation. Transferring large amount of data from RAM to VRAM (and vice versa) is cumbersome, affecting the performance for simulating Perlin phantoms using the hybrid implementation.

The central slice of DBT reconstructions and respective ground-truth images are shown in Figure 3. In these examples, the CBT and CND values are {35, 55, 75} mm, and {59, 79, 125} mm, respectively. The selection of Perlin parameters significantly affects the texture of breast parenchyma. For future work, we will optimize the selection of noise parameters for simulating mammary parenchyma using human observers. In addition, we will power-law[25] and Laplacian fractional entropy[26] measures will be calculated using patient images to compare and evaluate the realism of the database of Perlin-based phantoms.

Differences in the breast outlines can be observed in DBT reconstructions simulated using the conventional and T acquisition geometries (Figure 4). The conventional geometry (Figure 4AD) overestimates the volume of the breast when compared to the custom acquisition geometry (Figure 4BE). In addition, the differences in the overestimated volume are more evident in breast skin regions of the reconstructed images (Figure 4CF), especially for outlines simulated with higher values of CBT and CND.

Volume estimates were calculated using the breast segmentation of DBT reconstructions and the respective ground-truth images. The ratio of volumes (reconstructed and ground-truth images) represents the percent of volume over or underestimated in the DBT reconstructions. The volume estimates were calculated (n=240, Figure 5). Note that the volume estimates are always greater for images reconstructed using the conventional acquisition geometry for every CBT (Figure 5A) and CND (Figure 5B).

The PA source motion in the DBT acquisitions minimizes blurring artifacts in the breast volume estimates. The errors in the breast segmentation are more evident on breasts with increased CBD and CND. The source motion in PA direction can be optimized to achieve the most accurate breast outline segmentation. Additional source paths will be evaluated in future work to improve the breast volume estimates.

Some limitations exist in terms of the voxel resolution used to simulate the breast anatomy. We will consider increasing the phantom resolution to minimize skin artifacts in the simulated breast skin. We will also consider including additional finer structures in the breast parenchyma using fractal noise. The noise and breast density parameters were not fully optimized to simulate realistic breast parenchyma. For future work, we will optimize the selection of noise and VBD% parameters, and also validate the realism of simulated breast parenchyma using statistical measures.[4]

4. CONCLUSION

This work proposes the use of a novel implementation of Perlin-based phantoms. These phantoms were created using a GPU implementation of the Perlin-noise library (Perlin-CuPy) that allows us to accelerate the breast anatomy simulation. The simulation of Perlin noise using PCA-based models improves the realism in the 3D curvature of the breast phantoms.

We demonstrated that the overall breast volume is overestimated in DBT reconstructions. For conventional DBT acquisitions, the errors in the volume estimate are always greater than the T-shape acquisition. We have shown that Perlin-phantoms with realistic breast outlines can help to identify limitations in DBT acquisition geometries and to optimize the performance of the PET-DBT prototype. Results presented in this paper suggest that custom acquisition geometries can potentially improve the accuracy of PET-DBT attenuation corrections.

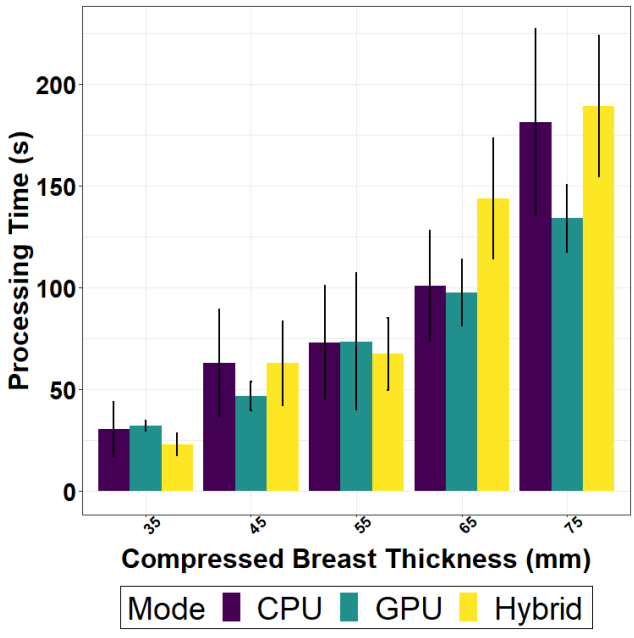

Figure 2. Processing time required to simualte phantoms using fractal noise.

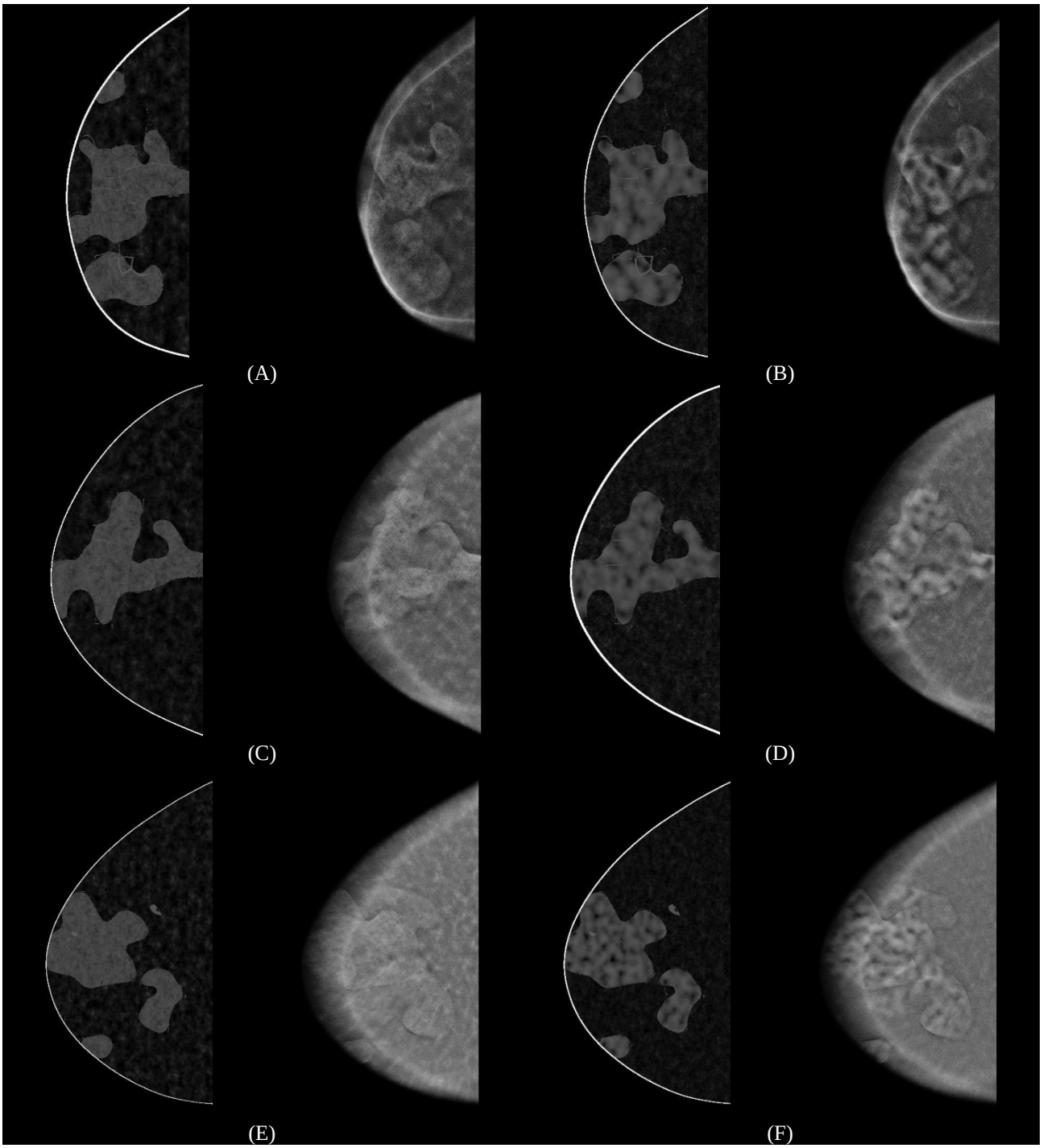

Figure 3. Central slices of (left) ground truth and (right) DBT reconstruction. CND, and CBT values of (A, B) 59 mm, and 35 mm, (C, D) 79 mm, and 55 mm, (E, F) 125 mm, and 75 mm, respectively. The pairs lacunarity and persistency values for adipose and glandular distribution are [(2, 0.75), (2,1)] and [(2, 1), (2, 0.25)], respectively for (A, C, E) left and (B, D, F) right columns.

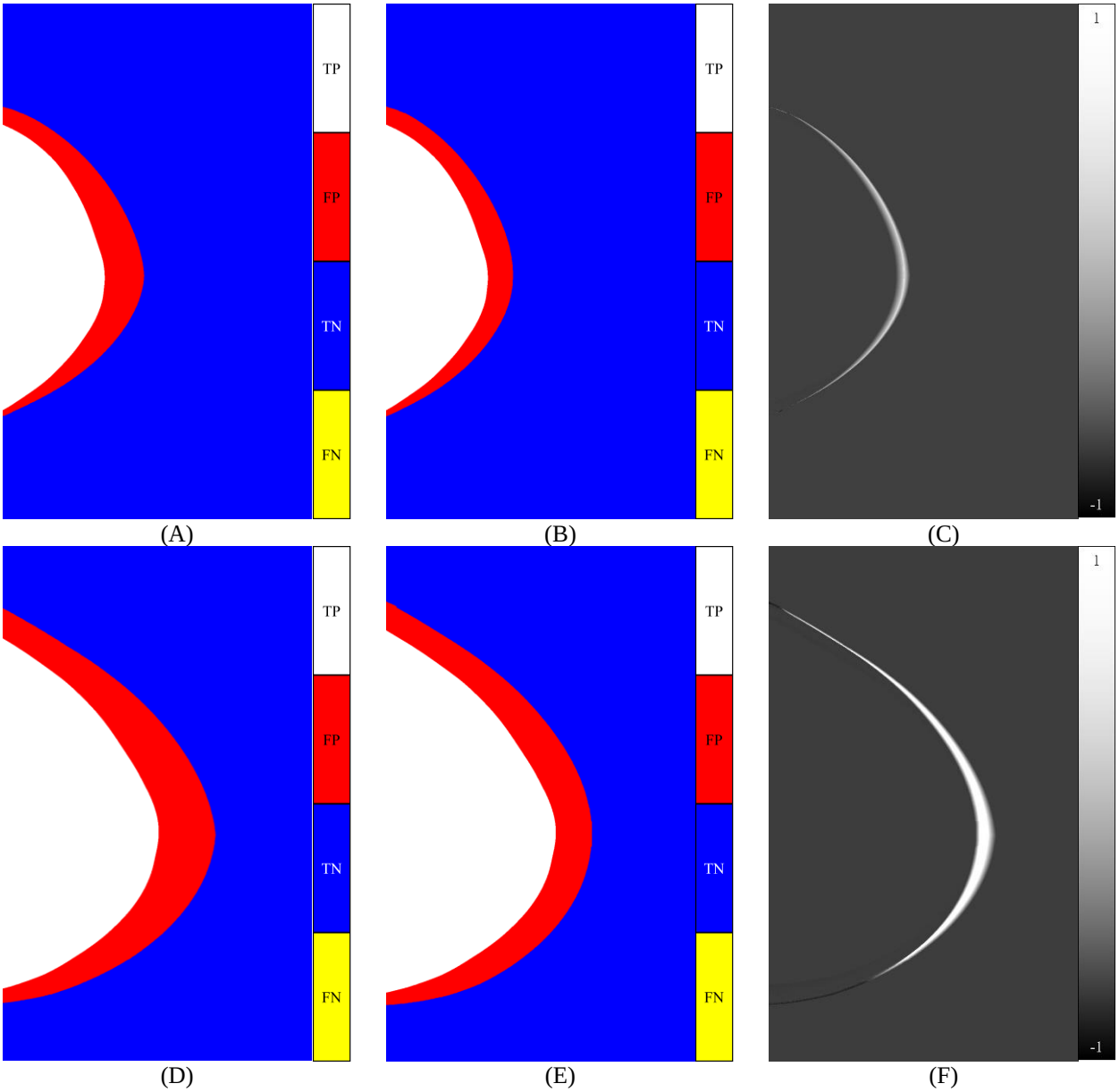

Figure 4. Segmented breast of DBT reconstructions (uppermost slice) of a Perlin phantom with magnified regions of breast skin (accuracy map). The accuracy map of (A, D) conventional and (B, E) t-shape acquisition geometries are shown. (C, F) Sum of differences between reconstructed slices using the conventional and t-shape acquisition geometries are also shown.

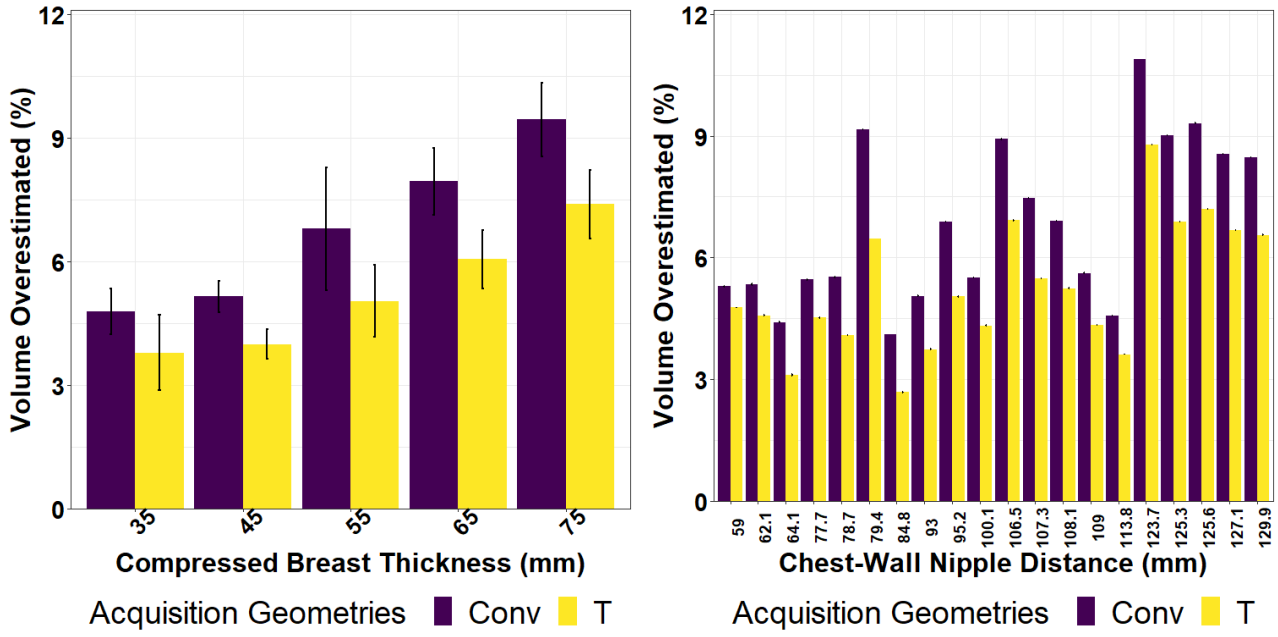

(A) (B)

Figure 5. Summary of volume overestimated categorized by (A) compressed breast thickness and (B) chest-wall to nipple distance.

ACKNOWLEDGEMENTS

The authors want to thank Dr. Koen Michielsen for helping with the use of the software that generates breast outlines under mammography compression. Funding for the research is supported primarily by the 2020 AAPM Research Seed Funding Grant. The following grants also support this research: NIH R01 (CA154444 and EB018958), Swedish Breast Cancer Association, H2020 MSCA-IF 846540, Komen IIR-13262248, BWF IRSA 1016451, DoD W81XWH-18-1-0082, NCI P30 CA016520, and EU Horizon 2020 Marie Skłodowska-Curie Action Fellowship IF 846540.

REFERENCES

[1] Abadi, E., Segars, W. P., Tsui, B. M. W., Kinahan, P. E., Bottenus, N., Frangi, A. F., Maidment, A., Lo, J. and Samei, E., "Virtual clinical trials in medical imaging: a review," Journal of Medical Imaging **7**(4), 042805-1–40 (2020).

[2] Barufaldi, B., Bakic, P. R., Higginbotham, D. and Maidment, A. D. A., "OpenVCT: a GPU-accelerated virtual clinical trial pipeline for mammography and digital breast tomosynthesis," SPIE Medical Imaging 2018 **1057358**(March), 1–8, SPIE Digital Library, Houston, TX (2018).

[3] Vent, T. L., Barufaldi, B., Acciavatti, R. J. and Maidment, A., "Simulation of high-resolution test objects using non-isocentric acquisition geometries in next-generation digital tomosynthesis," SPIE Medical Imaging 2020 **1151317**(May), 23, SPIE Digital Library (2020).

[4] Barufaldi, B., Abbey, C. K., Lago, M. A., Vent, T. L., Acciavatti, R. J., Bakic, P. R. and Maidment, A. D. A., "Computational Breast Anatomy Simulation Using Multi-scale Perlin Noise," IEEE Transactions on Medical Imaging **xx**(X), 1–11 (2021).

[5] Perlin, K., “Improving Noise,” ACM Transactions on Graphics (2002).

[6] Worley, S., “A cellular texture basis function,” Proceedings of the 23rd Annual Conference on Computer Graphics and Interactive Techniques, SIGGRAPH 1996 (1996).

[7] Dustler, M., Bakic, P., Petersson, H., Timberg, P., Tingberg, A. and Zackrisson, S., “Application of the fractal Perlin noise algorithm for the generation of simulated breast tissue,” Medical Imaging 2015: Physics of Medical Imaging (2015).

[8] Dustler, M., Lång, K. and Petersson, H., “Binary implementation of fractal Perlin noise to simulate fibroglandular breast tissue,” 193 (2018).

[9] Vent, T. L., Barufaldi, B., Acciavatti, R. J., Krishnamoorthy, S., Surti, S. and Maidment, A. D. A., “Next generation tomosynthesis image acquisition optimization for dedicated PET-DBT attenuation corrections,” 2021.

[10] Krishnamoorthy, S., Vent, T. L., Barufaldi, B., Maidment, A. D. A., Karp, J. S. and Surti, S., “Evaluating attenuation correction strategies in a dedicated, single-gantry breast PET-tomosynthesis scanner,” Physics in Medicine & Biology **65**(23), 5035–5040 (2020).

[11] Acciavatti, R. J., Reiser, I., Sechopoulos, I., Maidment, A. D. A., Bakic, P. R., Rodriguez-Ruiz, A. and Vent, T. L., “Analysis of volume overestimation artifacts in the breast outline segmentation in tomosynthesis,” SPIE Medical Imaging 2018 **1057359**(March 2018), 195 (2018).

[12] Rodríguez-Ruiz, A., Agasthya, G. A. and Sechopoulos, I., “The compressed breast during mammography and breast tomosynthesis: *in vivo* shape characterization and modeling,” Physics in Medicine & Biology **62**(17), 6920–6937 (2017).

[13] Rodriguez-Ruiz, A., Feng, S. S. J., Van Zelst, J., Vreemann, S., Mann, J. R., D’Orsi, C. J. and Sechopoulos, I., “Improvements of an objective model of compressed breasts undergoing mammography: Generation and characterization of breast shapes,” Medical Physics **44**(6), 2161–2172 (2017).

[14] Teixeira, J. P. V. and Barufaldi, B., “Perlin-CuPy: Perlin-NumPy for GPU,” Github, 2021, <https://github.com/jpvt/perlin-cupy>.

[15] Pietzsch, T., Preibisch, S., Tomančák, P. and Saalfeld, S., “Img lib 2-generic image processing in Java,” Bioinformatics (2012).

[16] Sutradhar, A. and Miller, M. J., “In vivo measurement of breast skin elasticity and breast skin thickness,” Skin Research and Technology **19**(1), 191–199 (2013).

[17] Pokrajac, D. D., Maidment, A. D. A. and Bakic, P. R., “Optimized generation of high resolution breast anthropomorphic software phantoms,” Medical Physics **39**(4), 2290 (2012).

[18] Bakic, P. R., Pokrajac, D. D. and Maidment, A. D. A., “Computer simulation of the breast subcutaneous and retromammary tissue for use in virtual clinical trials,” Medical Imaging 2017: Physics of Medical Imaging (2017).

[19] Dustler, M., Bakic, P., Petersson, H., Timberg, P., Tingberg, A. and Zackrisson, S., “Application of the fractal Perlin noise algorithm for the generation of simulated breast tissue,” Medical Imaging 2015: Physics of Medical Imaging (2015).

[20] Rumble, J. R., Bickham, D. M. and Powell, C. J., “The NIST x-ray photoelectron spectroscopy database,” Surface and Interface Analysis (1992).

[21] Barufaldi, B., Bakic, P. and Maidment, A. D. A., “Open Virtual Clinical Trials,” OpenVCT: a GPU-accelerated virtual clinical trial pipeline for mammography and digital breast tomosynthesis, 2020, <https://sourceforge.net/projects/openvct/> (10 March 2019).

[22] Siddon, R. L., “Fast calculation of the exact radiological path for a three dimensional CT array,” Medical Physics **12**(2), 252–255 (1985).

[23] ICRU., “ICRU Report 44 - Tissue Substitutes in Radiation Dosimetry and Measurement” (1988).

[24] Kuo, J., Ringer, P. A., Fallows, S. G., Bakic, P. R., Maidment, A. D. A. and Ng, S., “Dynamic reconstruction and rendering of 3D tomosynthesis images,” SPIE Medical Imaging **796116**(March 2011), 796116-796116–11, Orlando, FL (2011).

[25] Burgess, A. E., Jacobson, F. L. and Judy, P. F., “Human observer detection experiments with mammograms and power-law noise,” Medical Physics (2001).

[26] Abbey, C. K., Nosrateih, A., Sohl-Dickstein, J., Yang, K. and Boone, J. M., “Non-Gaussian statistical properties of breast images,” Medical Physics **39**(11), 7121–7130 (2012).

Pre-clinical evaluation and optimization of image quality for a Next Generation Tomosynthesis prototype

Trevor L. Vent[1,*], Raymond J. Acciavatti[1], Chloe Choi[1],
Bruno Barufaldi[1], Srilalan Krishnamoorthy[1], Lucas Borges[2], Johnny Kuo[2],
Peter A. Ringer[2], Susan Ng[2], Suleman Surti[1], Andrew D.A. Maidment[1]
[1]Department of Radiology, University of Pennsylvania, Philadelphia, United States.
[2]Real-Time Tomography LLC, Villanova, PA
[*]{Trevor.Vent|Andrew.Maidment}@pennmedicine.upenn.edu

ABSTRACT

A next generation tomosynthesis (NGT) prototype has been developed to investigate alternative scanning geometries for digital breast tomosynthesis (DBT). The NGT system uses a 2D plane as an address space for the x-ray source to define an acquisition geometry. In previous work, tests of physics have been used as objective metrics to evaluate image quality for NGT. In this work, the performance of custom NGT acquisition geometries is evaluated for mastectomy specimens to validate previous phantom experiments. Two custom acquisition geometries – incorporating T- and K-shaped source motion paths in the posteroanterior direction – were compared with a conventional DBT acquisition geometry. Noise power spectra (NPS) are calculated using 3D image reconstructions of the three acquisition geometries to evaluate the degradation of image quality due to noise and to visualize NGT sampling properties in the Fourier domain. NPS are used to describe features of the specimen image reconstructions and compare acquisition geometries. NGT acquisition geometries were found to improve high-frequency performance with isotropic super resolution, reduce out-of-plane reconstruction artifacts, and improve overall image reconstruction quality. The T-geometry combines the benefits of narrow- and wide-angle tomosynthesis in a single scan improving high-frequency spatial resolution and out-of-plane blurring, respectively.

Keywords: digital breast tomosynthesis, noise power spectra, acquisition geometry, super resolution, cone beam artifact, mastectomy specimen, out-of-plane blurring

1. INTRODUCTION

Early detection is one of the best predictors for successful breast cancer treatment[1]. Malignancies are detected by routine breast cancer screening exams. Digital breast tomosynthesis (DBT) is the primary screening modality in the US used for cancer detection. DBT acquires multiple two-dimensional (2D) projections of a patient's breast to reconstruct a three-dimensional (3D) volumetric image, separating signals of overlapping structures within the breast tissue. Compared with screening completed using full-field digital mammography (FFDM), early DBT studies showed improved sensitivity and specificity for mass detection and commensurate sensitivity and specificity for microcalcification detection[2]. In a clinical review of DBT, Conant *et al.* identified the detection of microcalcifications as one of the modality's greatest challenge[3]. Another challenge for DBT is the detection of malignancies in patients with dense breasts. We posit the limitations of current DBT are inherent to the conventional system design, in particular, the acquisition geometry.

Conventional DBT acquires multiple x-ray projections along a linear source trajectory over a limited angular range (e.g., less than 180°) with the x-ray source positioned within the patient chest-wall plane.[4,5] Previous studies have explored the impact of angular range and number of projections for optimizing DBT acquisition geometry[6], but have not explored alternative acquisition methods. Whereas conventional DBT is capable of 3D image reconstruction, the information extracted from internal structures is limited and prone to artifacts. Specific limitations include spatial anisotropies[7–13], cone-beam artifacts[9,14–17], limited out-of-plane blurring[16,18], and reconstructed volume overestimation[14–16]. In addition, restricting the source positions to the patient chest wall plane does not benefit all patient anatomies. In previous studies, the average anterior extent of the breast – excluding breasts that extended off the detector – was measured to be 12.1 cm and 13.1 cm for craniocaudal and mediolateral-oblique mammograms, respectively.[19,20] Most clinical digital detectors for DBT measure 18 to 24 cm in the posteroanterior (PA) direction.[5] This is especially important given that Cauklin *et al.*[21] concluded that malignancies are detected more anteriorly (nipple) than posteriorly (chest wall).

Medical Imaging 2022: Physics of Medical Imaging, edited by Wei Zhao, Lifeng Yu, Proc. of SPIE
Vol. 12031, 1203142 · © 2022 SPIE · 1605-7422 · doi: 10.1117/12.2608811

The first stage of development for our NGT prototype was the incorporation of novel x-ray acquisition geometries, including two-dimensional (2D) x-ray source motion in the mediolateral (ML)- and posteroanterior (PA)-directions and craniocaudal (CC) detector motion. We have evaluated the imaging capabilities of the preliminary NGT prototype using tests of physics and image quality. The NGT has been shown to support isotropic and high-quality super resolution[9,22], improved breast volume estimation[14,15], and reduced image reconstruction artifacts[12,15]. In this work we compare physics results with clinical mastectomy specimens to validate phantom experiments.

2. MATERIALS & METHOD

We evaluated image quality of the NGT system (Table 1) using three acquisition geometries (Figure 1): a "conventional" geometry with the source spaced equidistantly in the chest-wall plane, ranging from -7.5° to +7.5°; a "T" geometry with 7 projections in the chest wall plane (same angular range as conventional) and 8 centered mediolaterally extending in the PA direction from 0° to +15°; and a "K" geometry with the same chest-wall plane projections as the T geometry with two linear sets of projections in the PA direction.

Table 1: NGT system properties.

NGT System Properties			
Detector	d_{el}		85 µm
	Frame Rate		908 ms
	Field of View		305 × 240 mm
X-Ray Tube	Focal Spot Size (nominal)	Small	0.1 mm
		Large	0.3 mm
Reconstruction Engine	BrionaStadard 9.0 (Real Time Tomography, Villanova, PA)		
Acquisition Geometries			
Number of Projections			15
Angular Range (°)			
Conventional		**ML (x)**	±7.5
		PA (y)	0.0
T		**ML (x)**	±7.5
		PA (y)	0.0 − 15.0
K		**ML (x)**	±7.5
		PA (y)	0.0 − 5.0

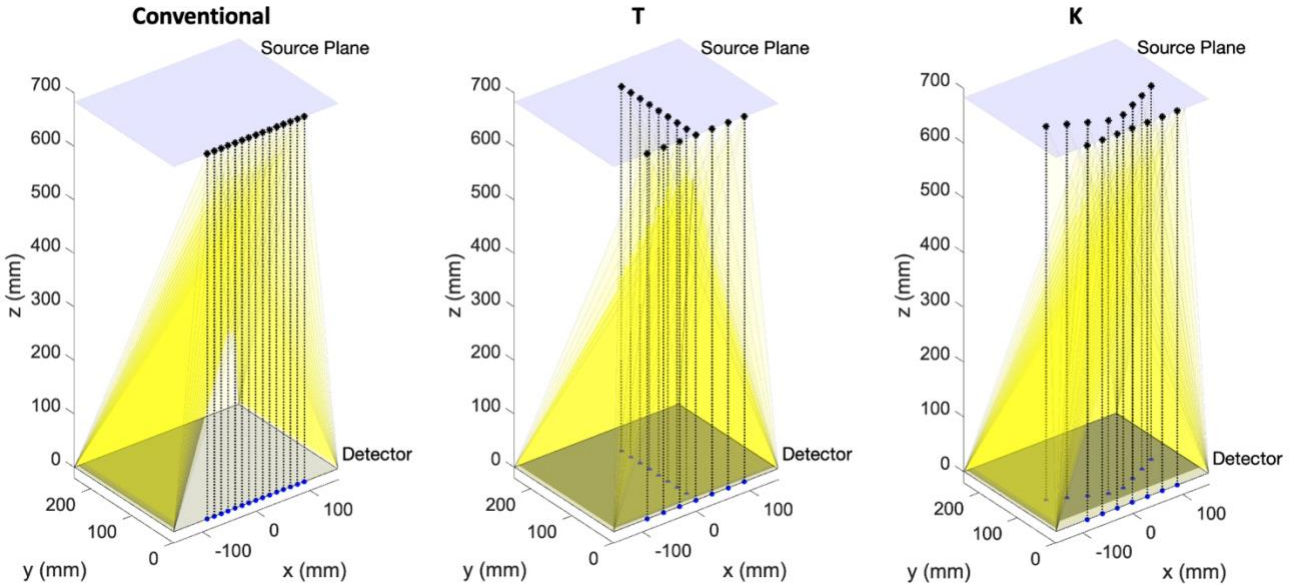

Figure 1: Acquisition geometries of the NGT prototype.

A 2.5 cm uniform block of poly(methyl methacrylate) (PMMA) was used to calculate noise power spectra (NPS) for the three NGT acquisition geometries. The PMMA block was positioned at a 1.5 magnification, and tomosynthesis scans were acquired for 3D NPS calculations. Ten tomosynthesis acquisitions were performed for each acquisition geometry. Projection images were acquired using 30 kV, 4.0 mAs, an aluminum filter, and the x-ray tube's large focal spot (0.3 mm, nominal). The projection images were reconstructed using BrionaStandard 9.0 (Real Time Tomography [RTT], Villanova, PA) to create a 3D volumetric image. Volumes were reconstructed with 42.5 µm in-plane resolution for 256 slices and a slice spacing of 85 µm.

A prophylactic mastectomy specimen with no known lesion present was provided by the Pathology Department at the University of Pennsylvania. This research was HIPAA compliant and approved by the University of Pennsylvania Institutional Review Board (protocol #825719, Review Board IRB #7) on August 26th, 2016 to meet the criteria for exemption authorized by 45 CFR 46.101, category 4. All methods were performed in accordance with the guidelines and regulations related to the IRB approval and HIPAA. The specimen was placed in a plastic container without compression and had an uncompressed thickness of 11 cm. Image reconstructions of the mastectomy specimen were acquired for each geometry. An x-ray technique of 44kV, 4.4 mAs, large focal spot, and aluminum filtration per projection was used. Images were reconstructed by RTT with custom image processing techniques tailored to each acquisition geometry.

3. RESULTS

Noise power spectra (NPS) of the three acquisition geometries are represented as iso-volumes in Figure 2. The conventional geometry shows a double napped cone, typical of DBT, with no f_z sampling at $f_x = 0$ and $f_y > 0$. T and K geometries show sampling of f_z for all frequencies. Overall, f_z sampling is greatest in magnitude for the T geometry.

Figure 3 shows iso-volumes with planes (top) describing different slices (bottom) used to visualize the NPS for each geometry. Slices are represented up to the Nyquist frequency, f_N, for f_x and f_y. The $f_x - f_z$ plane shows similar behavior for each geometry. This is an expected result because the x-ray source motion is the same in **x** for each geometry. In contrast, the $f_y - f_z$ plane shows distinctions between geometries. f_z is not sampled for the conventional geometry but is sampled significantly for the T geometry and sampled moderately for the K geometry. Note that noise aliasing is present for the T and K geometries. The conventional geometry shows minimal differences in $f_x - f_z$ at $f_y = 2/3 \bullet f_N$ from $f_y = 0$, whereas the T and K geometries show significant sampling. NPS for each geometry provide insight about expected image quality in 3D image reconstructions.

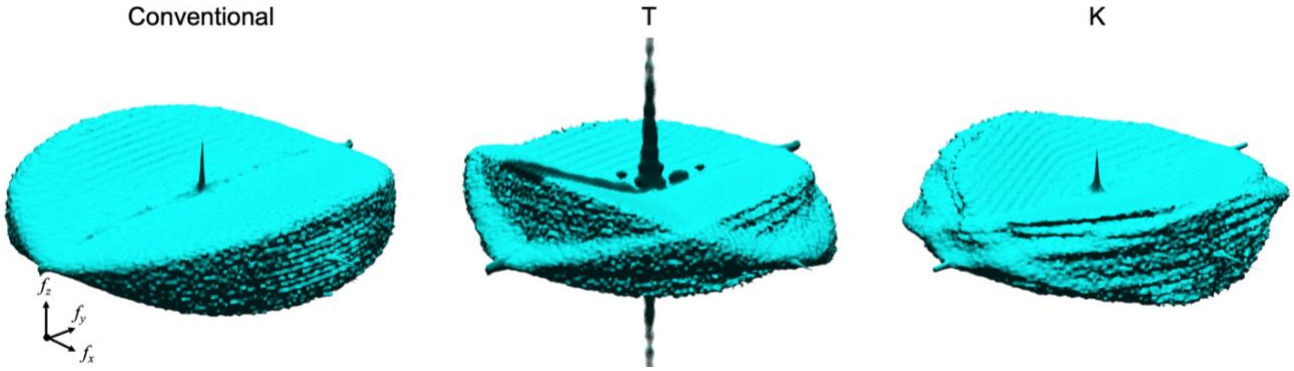

Figure 2: NPS of the three NGT acquisition geometries.

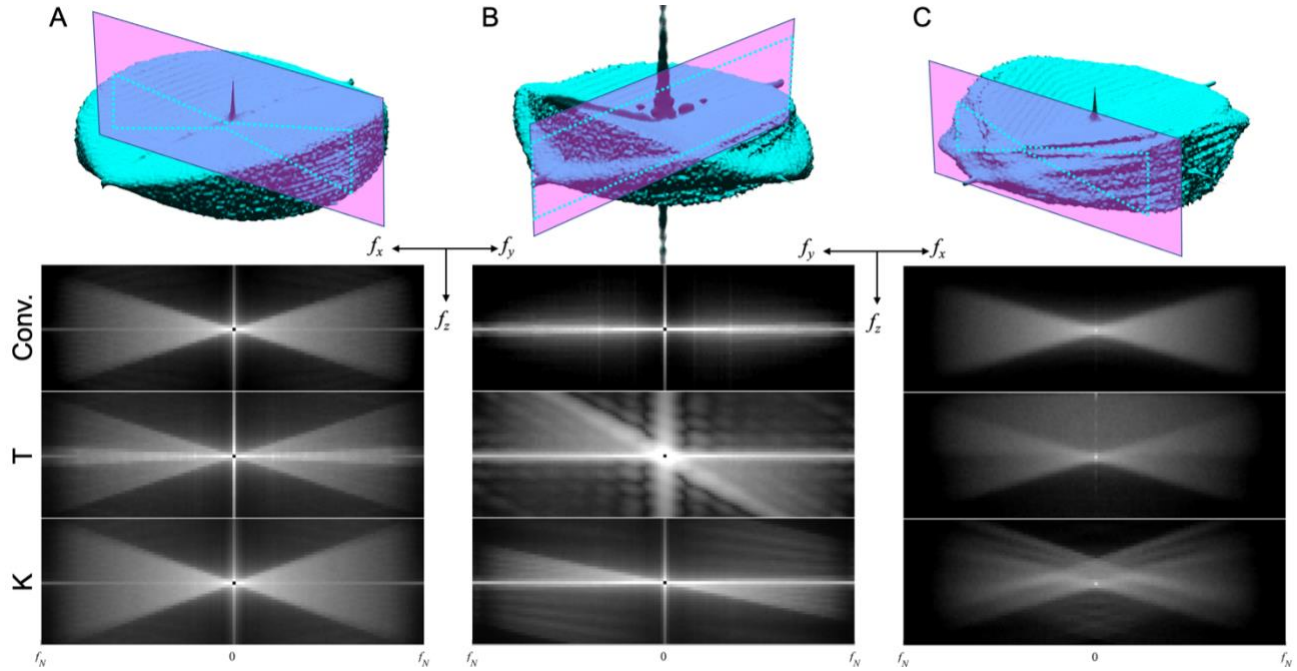

Figure 3: Examples of different slices through the NPS volumes for each geometry. Zero-frequency NPS slice of the $f_x - f_z$ plane (left). NPS slice of the $f_y - f_z$ plane at $f_x = 0$ (middle). High-frequency NPS slice in the $f_x - f_z$ plane at $f_y = 2/3 \bullet f_N$ (right).

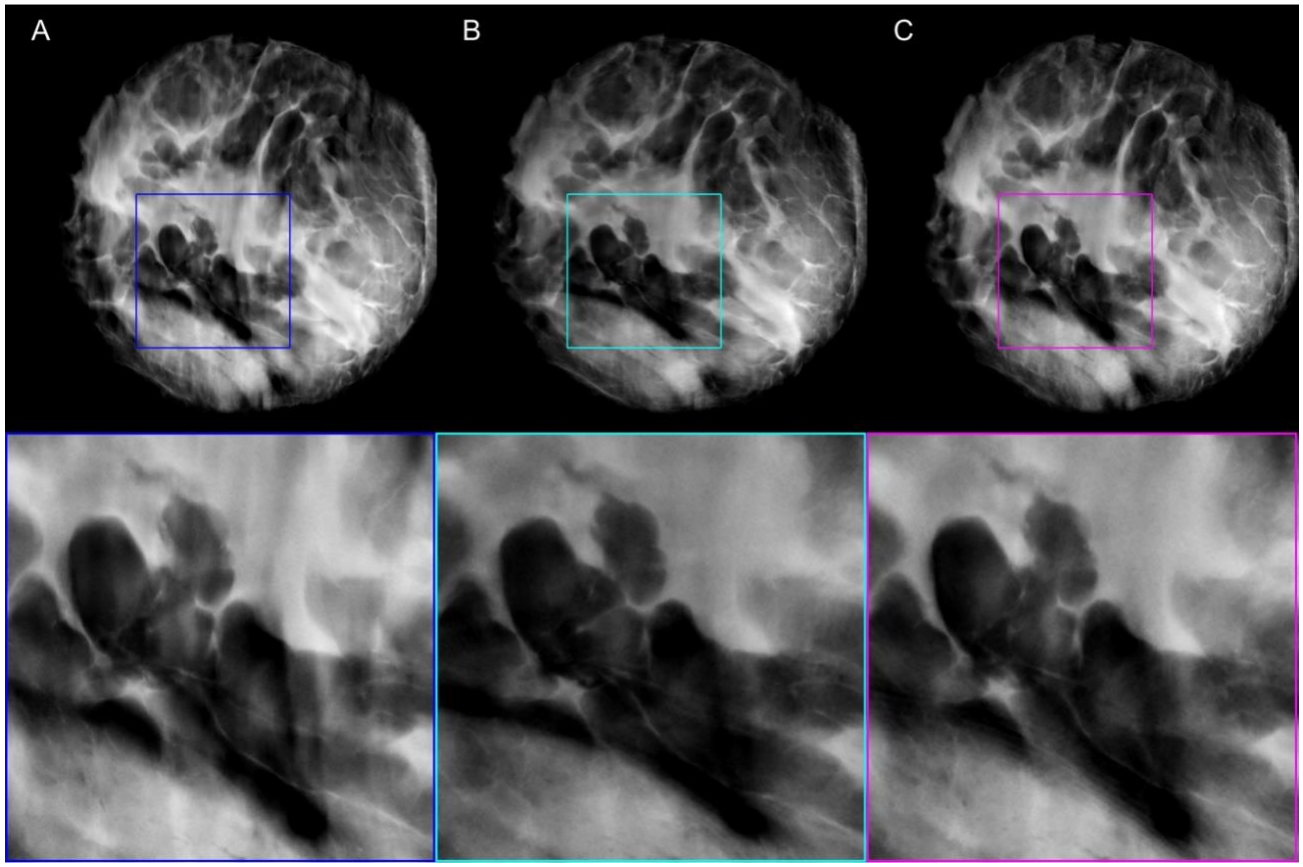

Figure 4: Example of the entire specimen and ROI for the conventional (A), T (B), and K (C) acquisition geometries. Image contrast settings are equivalent for all images.

Figure 4 shows a single slice of the mastectomy specimen with a magnified ROI for all three acquisition geometries. Images are displayed with the same contrast settings for comparison. Full-view reconstructions of the conventional geometry (Figure 4, A) show vertical streaking arising from out-of-plane reconstruction artifacts. Compared with the conventional reconstruction, NGT reconstructions show fewer out-of-plane reconstruction artifacts and improved demarcation of finer structures (e.g. Cooper's ligaments and calcifications). NGT also improves contrast of internal structures within the glandular signal noted in the top right corners of the magnified ROIs (Figure 4, B and C). Figure 5 highlights specific differences in another region of the reconstruction between the conventional and T geometry.

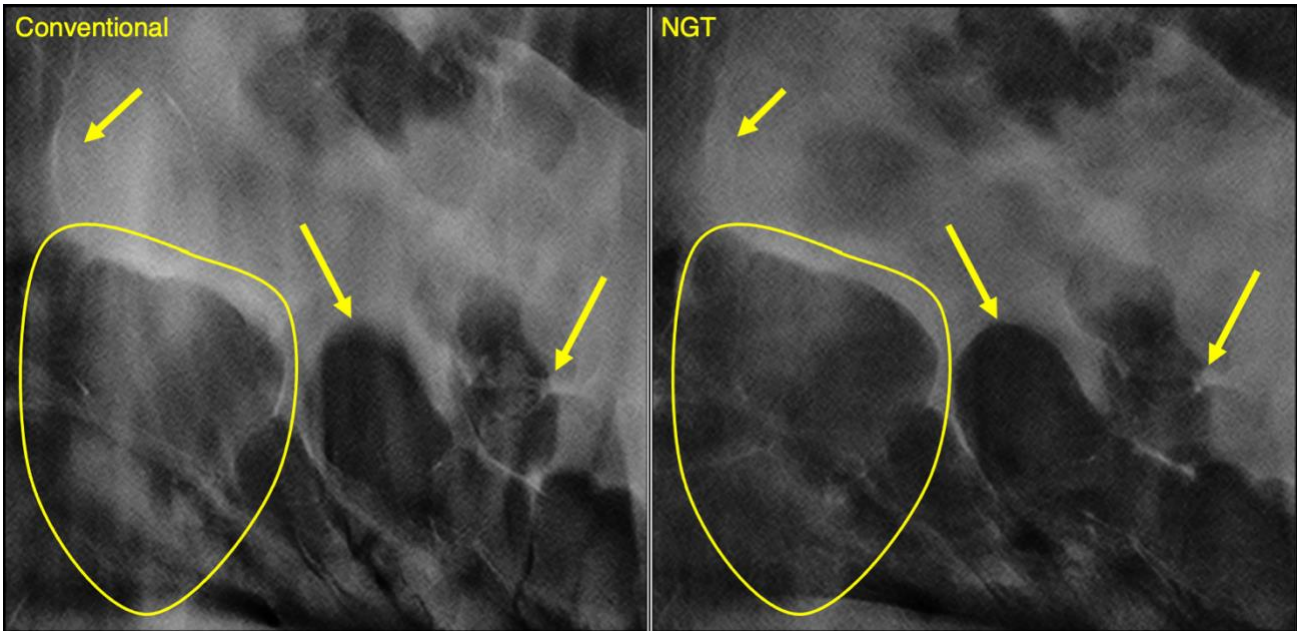

Figure 5: Clinical mastectomy reconstruction slices comparing conventional and NGT (T geometry). Specific features are highlighted in each image. NGT reconstructions show fewer out-of-plane reconstruction artifacts and improved demarcation of finer structures (e.g. Cooper's ligaments and calcifications). NGT also improves contrast of structures within the glandular signal (top left arrow).

4. DISCUSSION AND FUTURE WORK

The 3D NPS measurement was shown to be a valid method to evaluate and compare image quality for the various acquisition geometries. In our observation, the 3D NPS also serves as an indicator for geometric calibration accuracy. From the mastectomy specimen image reconstructions, out-of-plane artifacts appear to be commensurate with the f_z sampling in Figure 3C for each geometry. This result suggests that PA source motion of NGT geometries can separate the signal of overlapping breast tissue better than conventional DBT. Furthermore, the T acquisition geometry samples from $\pm 7.5°$ and from 0° to 15° in f_x and f_y, combining the benefits of narrow- and wide-angle tomosynthesis scans, respectively; namely, better demarcation of masses without loss of quality for microcalcifications.

In this study, phantom image reconstructions were created using simple back projection without image post- or pre-processing. Examining phantom results with simple back projection compares the physics performance adequately and ensures that other factors do not complicate results. Results from custom-tailored reconstructions of the mastectomy specimen images suggest that advanced reconstruction techniques can improve phantom experimental results. We posit that custom processing can further reduce spectral leakage and cone-beam-artifacts (CBA) for physics phantom reconstructions, respectively.

Conventional DBT has been treated as a one-size-fits-all approach to breast cancer screening, benefitting some patients but leaving others at risk of false positive or false negative diagnoses. Projection images of conventional DBT are constrained to the patient chest-wall plane; however, patient breasts extend anteriorly into the detector field of view[21] with some extending beyond the anterior edge of the detector. Patients with dense breasts are at risk of missed or delayed diagnoses due to overlapping fibroglandular tissue[23], often requiring supplemental screening. Clinical results confirm the benefit of PA source motion for tomosynthesis image reconstruction. Novel NGT acquisition geometries show promise

for individuals not helped by conventional DBT. NGT challenges the conventional DBT paradigm by introducing novel x-ray source motion paths for tomosynthesis acquisitions to benefit more patient anatomies while preserving at least half of the dose budget in the chest-wall plane[20,24]. Our future work will explore more advanced scanning motions with mastectomy specimens, including task-driven motions, to investigate further improvements in image quality.

5. CONCLUSION

Compared with the anisotropic spatial resolution properties of conventional DBT, NGT acquisition geometries produce image reconstructions with isotropic super resolution[9,12,26] and fewer reconstruction artifacts[15,22,25]. Projection images in the PA direction sample a greater extent of the Fourier space[9,27], improving cone beam artifacts, out-of-plane blurring[16], and reconstructed breast volume estimations[14,16]. NGT acquisition geometries improve the overall appearance of clinical image reconstructions compared with conventional DBT. Novel NGT acquisition geometries have specific advantages over conventional DBT:

- Isotropic super-resolution for improved visibility of finer structures
- Reduced cone beam artifacts, producing superior breast outline demarcation[15,22,25]
- Reduced out-of-plane artifacts, improving fibroglandular-adipose tissue contrast[16]
- Narrow- and wide-angle sampling in a single scan (T acquisition geometry samples from $\pm 7.5°$ and from 0° to 15° in f_x and f_y, respectively)

6. ACKNOWLEDGEMENTS

Johnny Kuo, Lucas Borges, Peter Ringer and Susan Ng are members of Real Time Tomography (RTT). Peter Ringer and Susan Ng are shareholders of RTT. Andrew Maidment is a member of the scientific advisory board of RTT. Support was provided by the following grants: W81XWH-18-1-0082 from the Department of Defense Breast Cancer Research Program, IRSA 1016451 from the Burroughs Welcome Fund, 1R01CA196528 from the National Institute of Health, and IIR13264610 from Susan G. Komen. In addition, equipment support was provided by Analogic Inc. and Barco NV. The content is solely the responsibility of the authors and does not necessarily represent the official views of the funding agencies.

REFERENCES

[1] Paci E. Nass SJ, Henderson IC, L. J. (eds)., [Mammography and Beyond: Developing Technologies for Early Detection of Breast Cancer.Washington, DC: National Academy Press, 2001. 316 pp] (2002).

[2] Rafferty, E. a, Park, J. M., Philpotts, L. E., Poplack, S. P. and Sumkin, J. H., "Digital Mammography and Breast Tomosynthesis Compared with Digital Mammography Alone : Results of a Multicenter, multireader trial," Radiology **266**(1), 104–113 (2013).

[3] Conant, E. F., "Clinical Implementation of Digital Breast Tomosynthesis," Radiol. Clin. North Am. **52**(3), 499–518 (2014).

[4] Dobbins, J. T. and Godfrey, D. J., "Digital x-ray tomosynthesis: Current state of the art and clinical potential," Phys. Med. Biol. **48**(19) (2003).

[5] Sechopoulos, I., "A review of breast tomosynthesis. Part I. The image acquisition process," Med. Phys. **40**(1), 1–12 (2013).

[6] Sechopoulos, I. and Ghetti, C., "Optimization of the acquisition geometry in digital tomosynthesis of the breast," Med. Phys. **36**(4), 1199–1207 (2009).

[7] Acciavatti, R. J. and Maidment, A. D. A., "Observation of super-resolution in digital breast tomosynthesis," Med. Phys. **39**(12), 7518–7539 (2012).

[8] Vent, T. L., Acciavatti, R. J., Kwon, Y. J. and Maidment, A. D. A., "Quantification of resolution in multiplanar reconstructions for digital breast tomosynthesis," SPIE Med. Imaging **9783**(March 2016), 978303 (2016).

[9] Vent, T. L., Lepore, B. L. and Maidment, A. D. A., "Evaluating the imaging performance of a next-generation digital breast tomosynthesis prototype," SPIE Med. Imaging(March 2019), 19 (2019).

[10] Acciavatti, R. J. and Maidment, A. D. A., "Oblique reconstructions in tomosynthesis. I. Linear systems theory,"

Med. Phys. **40**(11), 1–21 (2013).
[11] Acciavatti, R. J. and Maidment, A. D. A., "Oblique reconstructions in tomosynthesis. II. Super-resolution," Med. Phys. **40**(11), 1–19 (2013).
[12] Vent, T. L., Barufaldi, B., Acciavatti, R. J. and Maidment, A., "Simulation of high-resolution test objects using non-isocentric acquisition geometries in next-generation digital tomosynthesis," 15th Int. Work. Breast Imaging **11513**, C. Van Ongeval, N. Marshall, and H. Bosmans, Eds., 23, SPIE (2020).
[13] Vent, T. L., Acciavatti, R. J. and Maidment, A. D. A., "Development and Evaluation of the Fourier Spectral Distortion Metric," IEEE Trans. Med. Imaging **40**(3), 1055–1064 (2021).
[14] Acciavatti, R. J., Reiser, I., Sechopoulos, I., Maidment, A. D. A., Bakic, P. R., Rodriguez-Ruiz, A. and Vent, T. L., "Analysis of volume overestimation artifacts in the breast outline segmentation in tomosynthesis," SPIE Med. Imaging, 195 (2018).
[15] Acciavatti, R. J., Barufaldi, B., Vent, T. L., Wileyto, E. P. and Maidment, A. D. A., "Personalization of x-ray tube motion in digital breast tomosynthesis using virtual Defrise phantoms," SPIE Med. Imaging(March), 10 (2019).
[16] Vent, T. L., Barufaldi, B., Acciavatti, R. J., Krishnamoorthy, S., Surti, S. and Maidment, A. D. A., "Next generation tomosynthesis image acquisition optimization for dedicated PET-DBT attenuation corrections," Med. Imaging 2021 Phys. Med. Imaging **11595**, H. Bosmans, W. Zhao, and L. Yu, Eds., 1286–1292, SPIE (2021).
[17] Maidment, A. D. A. ., Acciavatti, R. J. ., Vent, T. L. ., Conant, E. F. ., Kwon, Y. J., NG, S., Kuo, J., Ringer, P. A. ., Maidment, T., Wurtele, D., Licata, J., Narayan, T., Zhang, D. and Higginbotham, D., "Construction of a Prototype Digital Breast Tomosynthesis System with Superior Spatial Resolution," RSNA Phys. Basic Sci., RSNA (2016).
[18] Hu, Y.-H., Zhao, B. and Zhao, W., "Image artifacts in digital breast tomosynthesis: Investigation of the effects of system geometry and reconstruction parameters using a linear system approach," Med. Phys. **35**(12), 5242–5252 (2008).
[19] Barufaldi, B., Borges, L. R., Bakic, P. R., Vieira, M. A. C., Schiabel, H. and Maidment, A. D. A., "Assessment of automatic exposure control performance in digital mammography using a no-reference anisotropic quality index," Med. Imaging 2017 Image Perception, Obs. Performance, Technol. Assess. **10136**(March 2017), 101360U (2017).
[20] Martin, D. A., Vent, T. L., Choi, C. J., Barufaldi, B., Acciavatti, R. J. and Maidment, A. D. A., "Signal-to-noise ratio and contrast-to-noise ratio measurements for next generation tomosynthesis," Med. Imaging 2021 Phys. Med. Imaging **11595**, H. Bosmans, W. Zhao, and L. Yu, Eds., 426–434, SPIE (2021).
[21] Caulkin, S., Astley, S., Asquith, J. and Boggis, C., "Sites of Occurrence of Malignancies in Mammograms," [Computational Imaging and Vision, Vol. 13], N. Karssemeijer, M. Thijssen, J. Hendriks, and L. van Erning, Eds., Springer, Derdrecht, 279–282 (1998).
[22] Vent, T. L., Barufaldi, B. and Maidment, A. D. A., "Simulation and experimental validation of high-resolution test objects for evaluating a next-generation digital breast tomosynthesis prototype," SPIE Med. Imaging(March 2019), 21 (2019).
[23] Chiu, S. Y. H., Duffy, S., Yen, A. M. F., Tabár, L., Smith, R. A. and Chen, H. H., "Effect of baseline breast density on breast cancer incidence, stage, mortality, and screening parameters: 25-Year follow-up of a Swedish mammographic screening," Cancer Epidemiol. Biomarkers Prev. **19**(5), 1219–1228 (2010).
[24] Eben, J. E., Vent, T. L., Choi, C. J., Yarrabothula, S., Chai, L., Nolan, M., Kobe, E., Acciavatti, R. J. and Maidment, A. D. A., "Development of a next generation tomosynthesis system," SPIE Med. Imaging **10573** (2018).
[25] Acciavatti, R. J., Chang, A., Woodbridge, L. and Maidment, A. D. A., "Optimizing the acquisition geometry for digital breast tomosynthesis using the Defrise phantom," Med. Imaging 2014 Phys. Med. Imaging **9033**(March 2014), 903315 (2014).
[26] Maidment, T. D., Vent, T. L., Ferris, W. S., Wurtele, D. E., Acciavatti, R. J. and Maidment, A. D. A., "Comparing the imaging performance of computed super resolution and magnification tomosynthesis," SPIE Med. Imaging **10132**, 1013222 (2017).
[27] Choi, C. J., Vent, T. L., Acciavatti, R. J. and Maidment, A. D. A., "Analysis of digital breast tomosynthesis acquisition geometries in sampling Fourier space," SPIE Med. Imaging **115954W**(February), 98 (2021).

Spatial dependency of lesion detectability in digital breast tomosynthesis

Chloe J. Choi[1*], Bruno Barufaldi[1], João P. V. Teixeira[2],
Raymond J. Acciavatti[1], and Andrew D. A. Maidment[1]
[1]Department of Radiology, University of Pennsylvania, Philadelphia, USA
[2]Federal University of Paraiba, João Pessoa, Brazil
*jeonginc@seas.upenn.edu

ABSTRACT

X-ray imaging results in inhomogeneous irradiation of the detector and distortion of structures in the periphery of the image; yet the spatial dependency of tomosynthesis image-quality metrics has not been extensively investigated. In this study, we use virtual clinical trials to quantify the spatial dependency of lesion detectability in our lab's next-generation tomosynthesis (NGT) system. Two geometries were analyzed: a conventional geometry with mediolateral source motion, and a NGT geometry with T-shaped motion. Breast parenchymal texture was simulated using an open-source library with Perlin noise using 400 random seeds and three breast densities. Spherical mass lesions were inserted in the central slice of the phantoms using the voxel additive method. Image acquisition was simulated using in-house ray-tracing software and simple backprojection was performed using commercial reconstruction software. Lesion detectability with Channelized Hotelling Observers (CHOs) was analyzed using receiver operating characteristic curves to measure the detectability index (d') at 154 unique locations for the lesions. We also divided images into three non-overlapping regions (differing in terms of distance from the chest wall). At the 0.05 level of significance, there was a statistically significant difference between the geometries in terms of d' in one of the three regions, with the T geometry offering superior detectability. Examining all 154 lesion locations, the T geometry was found to offer lower spread (standard deviation) in d' values throughout the image area, and superior d' at 83 of 154 locations (53.9%). In summary, the T geometry enables superior lesion detection and mitigates anisotropies.

Keywords: Virtual Clinical Trial (VCT), Digital Breast Tomosynthesis (DBT), Image Quality, Breast Cancer, Sensitivity, Specificity.

1. INTRODUCTION

X-rays originate from an angled point-like source and diverge as they travel. Due to its divergence, x-ray imaging often results in inhomogeneous illumination of the detector, while structures in the periphery of the image are distorted due to the divergency. This differential signal may be significant in tomosynthesis, where only a few x-ray projections are acquired over a limited range. A previous study by Martin *et al* has in fact shown that signal-to-noise ratio (SNR) and contrast-to-noise ratio (CNR) are functions of location within the reconstructed volume and that incorporation of anterior source locations may result in an improvement in overall image quality[1].

A next generation tomosynthesis (NGT) system developed at the University of Pennsylvania is capable of source motion in two directions: mediolateral (ML) and posteroanterior (PA), forming the shape of a "T" (Figure 1)[2]. Unlike the conventional scanning motion directed mediolaterally, the T geometry has been shown to improve super-resolution, modulation transfer function, noise power spectra, reconstructed breast volume estimation, and more[3-6]. The impact on the image quality due to changes in projection density in NGT was analyzed for both low- and high-frequency objects and discussed via Fourier analysis by Choi *et al*[7].

Virtual clinical trials (VCTs) are a cost-effective method to evaluate medical imaging systems on a specific task such as lesion detection. Previous studies by Bakic *et al* and Barufaldi *et al* have evaluated lesion detectability in digital breast tomosynthesis (DBT) using VCTs via Channelized Hotelling Observers (CHOs) and multi-reader, multi-case (MRMC) receiver operating characteristic (ROC) curves[8-10]. However, the spatial dependency of lesion detectability is yet to be investigated. The purpose of this study is to analyze spatial anisotropies in lesion detectability in DBT, and investigate how two acquisition geometries differ in terms of lesion detectability; namely, the conventional geometry [Figure 1(a)]

16th International Workshop on Breast Imaging (IWBI2022), edited by Hilde Bosmans, Nicholas Marshall, Chantal Van Ongeval, Proc. of SPIE Vol. 12286, 1228618
© 2022 SPIE · 0277-786X · doi: 10.1117/12.2626272

and the T geometry [Figure 1(b)]. This work has applications in designing the next generation of DBT systems with superior and more isotropic image quality.

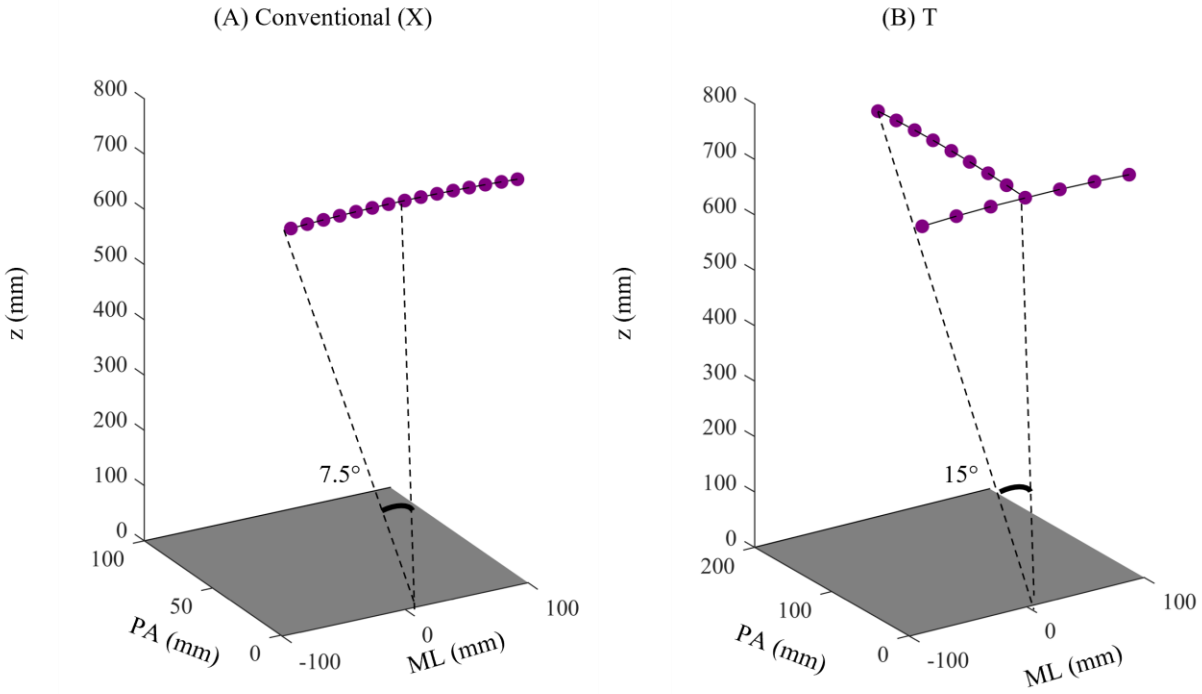

Figure 1. (a) Conventional or X geometry and (b) T geometry. In the T scan, there is source motion both parallel (ML) and perpendicular to the chest wall (PA). (Figure excerpt from Choi *et al*[7])

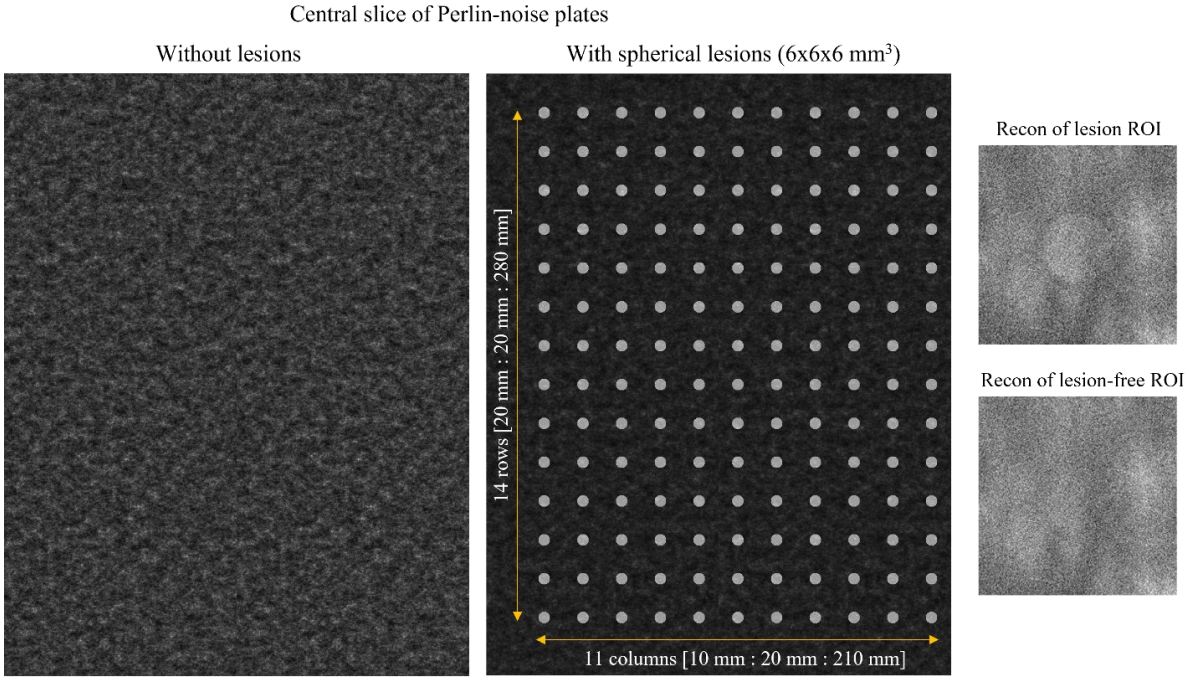

Figure 2. Perlin-noise plates were created with Perlin-CuPy[11]. Spherical lesions were inserted evenly in the central slice of the phantom (i.e., the mid-thickness of the phantom). The phantoms are indexed, and the figure above does not represent the true attenuation value of each voxel. Examples of reconstructed ROIs are shown on the right. The contrast of the lesion was modified for better illustration.

Table 1. Summary of the simulated acquisition parameters

X-ray Techniques	
Target / Filter Combination	Tungsten / Aluminum
Filter Thickness (mm)	0.7
Tube Motion	Step and Shoot
kVp	30
mAs (per projection)	4.6
Acquisition Geometry	
Angular range in ML direction (X and T geometries)	±7.5°
Angular range in PA direction (T geometry only)	+15°
Source-to-image distance in central projection (mm)	738
Distance between detector and breast support (mm)	24.46
Detector Configurations	
Detector Material	a-Se
Detector Element Size (mm)	0.085 × 0.085
Detector Element count	3584 × 2816
Detector Size (mm)	304.64 × 239.36
Reconstruction	
Pixel Size (mm)	0.085 × 0.085

2. MATERIALS AND METHODS

2.1 Data Simulation

2.1.1 Perlin-noise plate phantoms

Breast parenchymal texture was simulated using an open-source library with Perlin noise (Perlin-CuPy)[11]. A total of 1200 plate-shaped phantoms with dimensions of 310 mm × 240 mm × 45 mm was generated with 400 levels of Perlin-noise random seed [2:401] and three levels of breast density [9.3%, 16.3%, 26.5%] (Figure 2, left).

2.1.2 Lesions

The three-dimensional spherical breast mass model (6 × 6 × 6 mm^3) was generated with isotropic resolution. A total of 154 (14 × 11) lesions were evenly inserted in the central slice (i.e., mid-thickness) of each Perlin-noise plate phantom (Figure 2), using the voxel additive method described by Barufaldi *et al*[12]. The voxel additive method blends the added lesion with the underlying tissue rather than replacing it, for more realistic images. As such, the attenuation coefficient is represented by a weighted summation of the attenuation coefficients contributed by both the lesion (l) and the underlying breast tissue. In this work, the weighting factor for the lesion (w_l)[12] was defined to be 1.0%.

2.1.3 Image acquisition simulation and reconstruction

The PhysicsVCT was developed in-house as a simplified version of an open-source VCT framework (OpenVCT)[4] to simulate x-ray projections of test objects and evaluate imaging systems with a ray-tracing algorithm. PhysicsVCT was used to simulate image acquisitions of the generated phantoms with the two geometries described in Figure 1. The image acquisition parameters (Table 1) were simulated to resemble the NGT system, which was built with an AXS-2430 detector (Analogic Canada Corporation, Montreal, Quebec). The central slice of the reconstruction was generated using commercial software (Briona 9.0.4, Real Time Tomography, Villanova, PA) with simple backprojection.

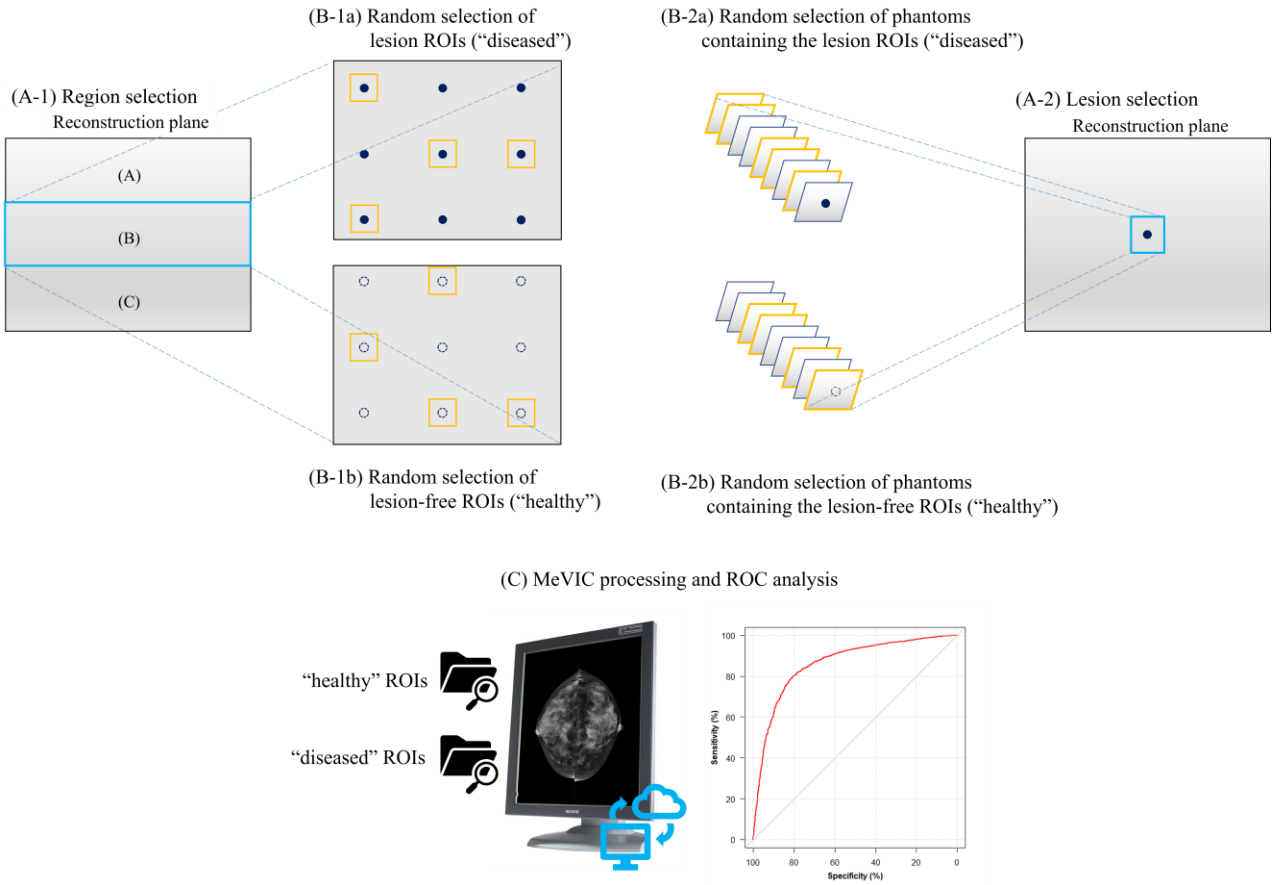

Figure 3. Lesion detectability CHO ROC analysis was performed independently per region (Figure 3A-1) and per geometry, in the central slice of the reconstruction (i.e., the mid-thickness of the phantom). Same analysis was performed independently per lesion (Figure 3A-2 and 3B-2) and per geometry, in the central slice of the reconstruction. A total of 1200 "diseased" and "healthy" ROIs was used for training and testing. The d′ value was calculated at each individual lesion location (154 locations per geometry) and compared between the geometries.

2.1.4 Virtual reader studies

The PhysicsVCT framework was integrated with the open-source Medical Virtual Image Chain (MeVIC)[10,13] software, which simulates image displays on a high-resolution monitor and lesion detection studies based on a mathematical virtual reader model. A CHO model with 15 Laguerre-Gauss channels and spread 21 was trained and tested.

2.2 Data analysis

To assess spatial anisotropy in lesion detectability, reconstructed images were divided into three non-overlapping rectangular regions (A, B, and C) corresponding to three different locations relative to the chest wall (Figure 3A-1). For each region, the CHO model was trained and tested with independent sets of randomly-chosen regions of interest (ROIs) of 201 × 201 pixels (Figure 3B-1). The image sets included 2000 lesion ("diseased") and 2000 lesion-free ("healthy") ROIs for each region. Lesion detection performance was quantified with regional ROC analysis (Figure 3C) using open-source R packages, including *pROC, auctestr,* and *psycho*[14-17], which facilitate measurements of area under the ROC curve (AUC) and detectability index (d′). The ROC curves were compared amongst themselves using the DeLong method[18]. The two geometries were analyzed in terms of the AUC difference, ΔAUC [T-X], at the 0.05 level of significance, with a positive sign indicating superior performance in the T geometry.

As a separate analysis, we also quantified d′ on a per-lesion basis, with 600 randomly chosen lesion ("diseased") and lesion-free ("healthy") 201 × 201 ROIs for training and testing using the same method (Figure 3-A2 and 3-B2). The d′ value was calculated for all performed studies, and the two geometries were compared pair-wise for each of the 154 lesions with a right-tailed exact binomial test (i.e., sign test) in terms of the difference in d′ values.

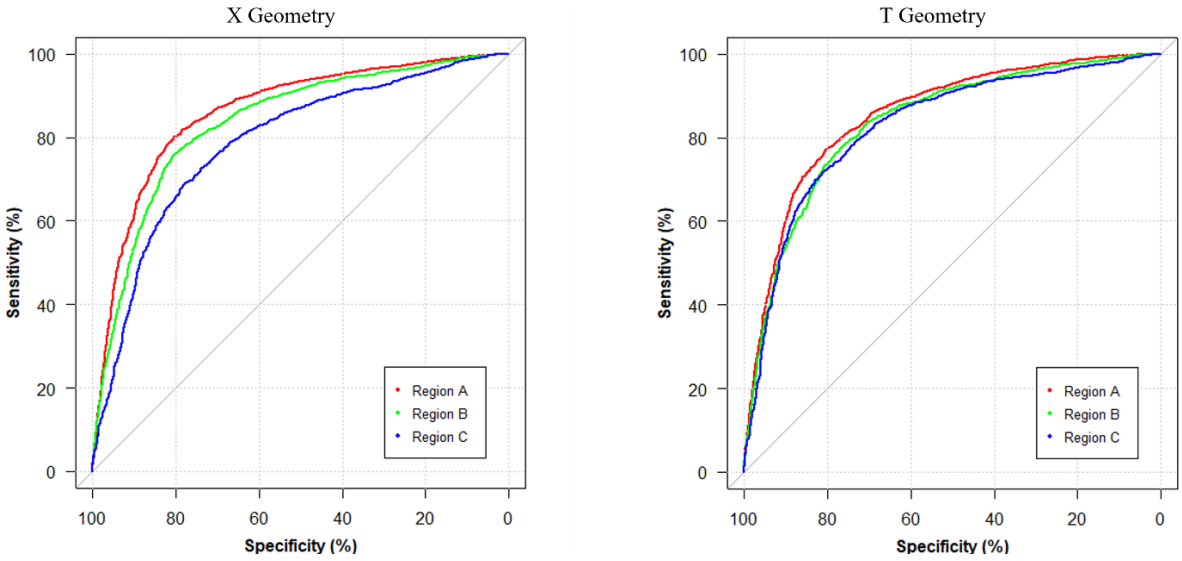

Figure 4. ROC curves for X geometry (left) and T geometry (right) are shown, with each curve corresponding to a different region. The gap between curves is narrower in the T geometry, indicating that image quality is more isotropic.

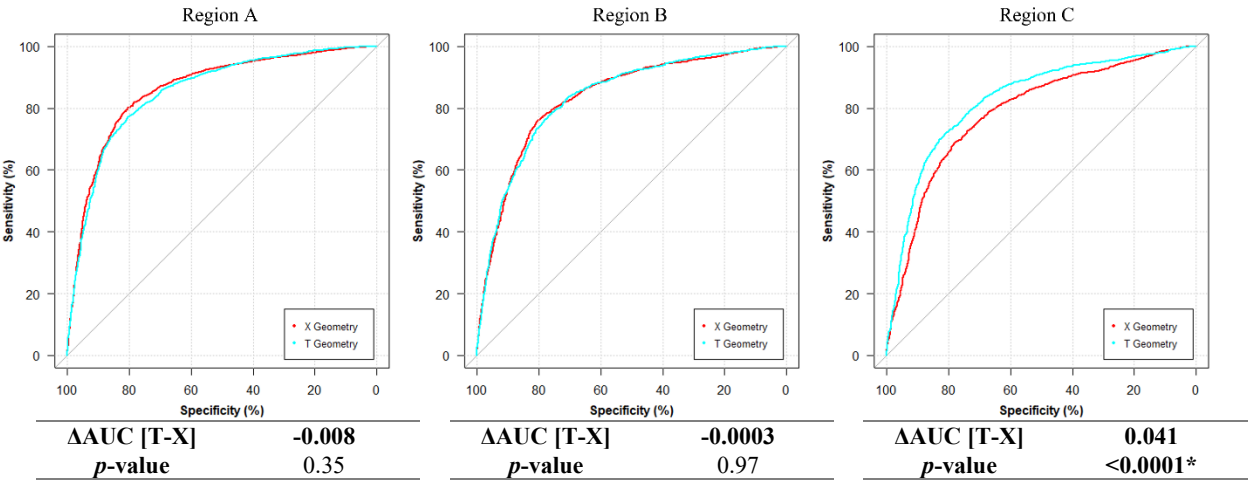

Figure 5. Regional ROCs are compared between the X and T geometries. A statistically significant comparison at the 0.05 level is marked with *. The T geometry offers superior image quality in Region C.

Table 2. Summary of regional ROC results for X and T geometries (statistically significant comparisons are marked with *).

Geo X	Region A	Region B	Region C
d′	1.70	1.55	1.24
AUC	0.862	0.836	0.787

Geo T	Region A	Region B	Region C
d′	1.60	1.50	1.45
AUC	0.854	0.835	0.827

ROC Comparison [ΔAUC, *p*-value]

	Region A	Region B
Region B	[-0.03, **0.003**]*	-
Region C	[-0.07, **<0.0001**]*	[-0.05, **<0.0001**]*

ROC Comparison [ΔAUC, *p*-value]

	Region A	Region B
Region B	[-0.018, **0.037**]*	-
Region C	[-0.026, **0.0034**]*	[-0.008, 0.38]

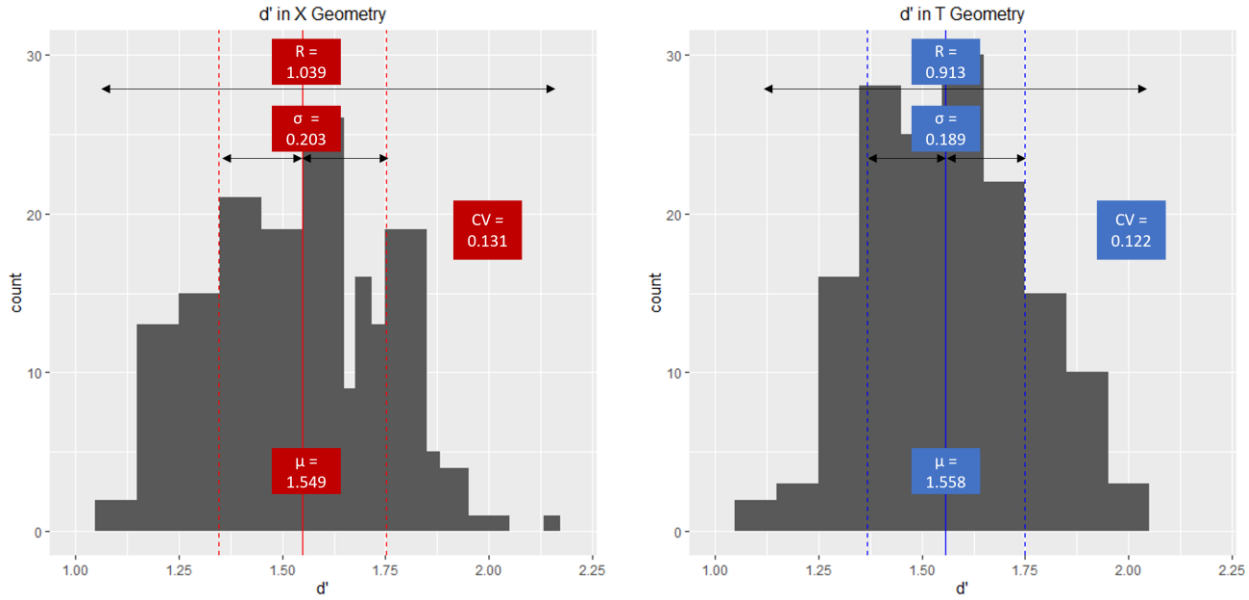

Figure 6. A histogram of d′ values for X geometry (left) and T geometry (right) is shown, along with the mean (μ), standard deviation (σ), range I and the coefficient of variation (CV). The total count is equal to the number of lesions in a phantom, which is 154.

3. RESULTS

3.1 Regional CHO ROC Analysis

First, the geometries were analyzed separately by region (Figure 4). In the conventional (X) geometry, there was a pronounced gap between the three ROC curves, with each curve corresponding to a different region; the AUC difference between any combination of two ROC curves was statistically significant at the 0.05 level (Table 2). By contrast, the AUC difference between any two combinations of ROC curves in the T geometry was less pronounced, meaning that there was more isotropic image quality. The differences in AUC were reduced by 40% and 63% compared to the X geometry, between regions A and B (-0.03 vs -0.018) and regions A and C (-0.07 vs -0.026), respectively (Table 2). The AUC difference between regions B and C was not statistically significant at the 0.05 level.

Although the T geometry showed smaller AUCs for regions A and B relative to the X geometry (Table 2), the AUC difference between each geometry was not statistically significant in either region (Figure 5). However, there was a statistically significant difference between T and X geometries in region C, with higher AUC achieved in the T geometry ($p < 0.0001$).

3.2 Per-Lesion d′ Analysis

Next, each geometry was analyzed in terms of the histogram of d′ values throughout the image (Figure 6). Each histogram represents the distribution of d′ values across 154 unique locations for the lesions. The T geometry presents a narrower histogram with a higher mean (1.558 vs 1.549), a lower range (0.913 vs 1.039), a lower standard deviation (0.189 vs 0.203), and thus a lower coefficient of variation (0.122 vs 0.131), indicating that image quality is generally superior and more isotropic in the T geometry. A right-tailed exact binomial test (i.e., sign test) applied to these two distributions yields a similar conclusion; the T geometry offers superior d' at 83 of 154 locations (53.9%) with a *p*-value of 0.188 (Table 3).

Table 3. A right-tailed binomial test (sign test) comparing d′ values from X and T geometries pairwise per lesion location.

	sign	N	**sign test**	
d′(T) – d′(X)	+	83	H_0 : proportion = 0.5	
	-	71	H_a : proportion > 0.5	
			***p*-value**	**0.188**
	total	154	Probability of success	0.539

4. DISCUSSION AND CONCLUSION

In this work, we explore the spatial dependency of mass detection in two geometries used in the NGT system; namely, the conventional and T geometries. The T geometry, by incorporating anterior source positions, was able to increase lesion detectability at a higher proportion of locations throughout the image (Figure 4, 5, Table 3) while minimizing the compromise in other regions (Table 2). The T geometry also provided more uniform image quality than the conventional geometry, in terms of lesion detectability.

Future work includes replacing the CHO with a MRMC variance method, confirming the experiments with Monte Carlo simulations for more accurate physics models, applying acquisition-specific reconstruction filters, and extending the experiments to consider different types of masses and calcifications of various densities, various thicknesses of the phantom, and lesion insertion at other heights (i.e., non-central slice insertion). Furthermore, we aim to understand how varying the number and spacing of x-ray sources in each geometry could potentially impact lesion detectability.

5. ACKNOWLEDGEMENT

ADAM has received research support from Hologic Inc., Barco NV, and Analogic Corporation; is the spouse to an employee and stockholder of Real Time Tomography (RTT), LLC; is a member of the scientific advisory board of RTT; and is an owner of Daimroc Imaging, LLC.

Support was provided by the following grants: W81XWH-18-1-0082 from the Department of Defense Breast Cancer Research Program; IRSA 1016451 from the Burroughs Wellcome Fund; IIR13264610 and PDF14302589 from Susan G. Komen®; T32-EB009384, 1R01CA196528, and NCI P30 CA016520 from the National Institute of Health; a 2020 AAPM Research Seed Funding Grant from the American Association of Physicists in Medicine; and a 2022 Young Investigator Grant through Breast Cancer Alliance, Inc. In addition, equipment support was provided by Analogic Inc., Barco NV, and RTT. The content is solely the responsibility of the authors and does not necessarily represent the official views of the funding agencies.

6. REFERENCES

[1] D. A. Martin, T. L. Vent, C. J. Choi, B. Barufaldi, R. J. Acciavatti, and A. D. A. Maidment, “Signal-to-noise ratio and contrast-to-noise ratio measurements for next generation tomosynthesis”, Proc. SPIE 11595, Medical Imaging 2021.
[2] Eben, J. E., Vent, T. L., Choi, C. J., Yarrabothula, S., Chai, L., Nolan, M., Kobe, E., Acciavatti, R. J. and Maidment, A. D. A., “Development of a Next Generation Tomosynthesis System,” Med. Imaging 2018 Phys. Med. Imaging, 10573 (2018).
[3] Vent, T. L., Lepore, B., and Maidment, A. D. A., “Evaluating the imaging performance of a next-generation digital breast tomosynthesis prototype”, Proc. SPIE 10948, Medical Imaging 2019: Physics of Medical Imaging, 109480K (1 March 2019)
[4] Vent, T. L., Barufaldi, B. and Maidment, A. D. A., "Simulation and experimental validation of high-resolution test objects for evaluating a next-generation digital breast tomosynthesis prototype", Proc. SPIE 10948, Medical Imaging 2019: Physics of Medical Imaging, 109480M (1 March 2019);
[5] Singh, P., Choi, C. J., Vent, T. L., and Maidment, A. D. A, “Novel Reconstruction Algorithms that Facilitate Real Time 4D Tomosynthesis”, Med. Imaging 2021 Phys. Med. Imaging (2020)
[6] Vent, T. L., Barufaldi, B., Acciavatti, R. J., Krishnamoorthy, S., Surti, Suleman, and Maidment, A. D. A., “Next Generation Tomosynthesis Image Acquisition Optimization for Dedicated PET-DBT Attenuation Corrections”, Proc. SPIE 11595, Medical Imaging 2021 Phys. Med. Imaging (2021)
[7] Choi, J. C., Vent, T. L., Geagan, M. J., Noël, P. B. and Maidment, A. D. A., “Investigation of optimal angular range and projection density for next generation tomosynthesis”, Proc. SPIE
[8] P. R. Bakic, B. Barufaldi, D. Higginbotham, S. Weinstein, A. Avanaki, K. S. Espig, A. Xthona, T. R. L. Kimpe, and A. D. A. Maidment, “Virtual clinical trial of lesion detection in digital mammoraphy and digital breast tomosynthesis”, Proc. SPIE 10573, Medical Imaging 2018.
[9] B. Barufaldi, P. R. Bakic, and A. D. A. Maidment, “Multi-reader, multi-case ROC analysis for determining the limit of calcification detection in tomosynthesis”, Proc. SPIE 10948, Medical Imaging 2019.

[10] B. Barufaldi, D. Higginbotham, P. R. Bakic, and A. D. A. Maidment, “OpenVCT: a GPU-accelerated virtual clinical trial pipeline for mammography and digital breast tomosynthesis”, Proc. SPIE 10573, Medical Imaging 2018: Physics of Medical Imaging, 1057358 (9 March 2018).
[11] B. Barufaldi, C. K. Abbey, M. A. Lago, T. L. Vent, R. J. Acciavatti, P. R. Bakic, and A. D. A. Maidment, “Computational breast anatomy simulation using multi-scale Perlin noise”, IEEE Transactions on Medical Imaging (2021).
[12] B. Barufaldi, T. L. Vent, P. R. Bakic, and A. D. A. Maidment, “Computer simulations of case difficulty in digital breast tomosynthesis using virtual clinical trials,” Medical Physics (2022).
[13] C. Marchessoux, T. Kimpe, and T. Bert, “A virtual image chain for perceived and clinical image quality of medical display”, Journal of Display Technology 4.4 (2008): 356-368.
[14] Robin, X., Turch, N., Hainard, A. *et al*. “pROC: an open-source package for R and S+ to analyze and compare ROC curves”, BMC Bioinformatics 12, 77 (2011).
[15] R Core Team (2021). R: A language and environment for statistical computing. R Fsoundation for Statistical Computing, Vienna, Austria.
[16] Makowski, D. (2018). The Psycho Package: An Efficient and Publishing-Oriented Workflow for Psychological Science. Journal of Open Source Software, 3(22), 470.
[17] Josh Gardner (2017). Dates and Times Made Easy with lubridate. Model Evaluation with auctestr. URL https://github.com/jpgard/auctestr.
[18] DeLong, E. R., DeLong, D. M., Clarke-Pearson, D. L. “Comparing the areas under two or more correlated receiver operating characteristic curves: a nonparametric approach. Biometrics. 1988 Sep;44(3):837-45. PMID: 3203132.

Multiclass Segmentation of Suspicious Findings in Simulated Breast Tomosynthesis Images Using a U-Net

Yann N. G. da Nobrega[¥,1], Giulia Carvalhal[¥,2], João P. V. Teixeira[1], Barbara P. de Camargo[1], Thais G. do Rego[1], Yuri Malheiros[1], Telmo de M. E Silva Filho[1,3], Trevor L. Vent[4], Raymond J. Acciavatti[4], Andrew D. A. Maidment[4], and Bruno Barufaldi[4,*]

[1]Federal University of Paraíba, João Pessoa, Brazil
[2]Federal University of Campina Grande, Campina Grande, Brazil
[3]University of Bristol, Bristol, United Kingdom
[4]University of Pennsylvania, Philadelphia, United States
[*]Corresponding author: Bruno.Barufaldi@pennmedicine.upenn.edu
[¥]Joint first authorship

ABSTRACT

Our lab has built a next-generation tomosynthesis (NGT) system utilizing scanning motions with more degrees of freedom than clinical digital breast tomosynthesis systems. We are working toward designing scanning motions that are customized around the locations of suspicious findings. The first step in this direction is to demonstrate that these findings can be detected with a single projection image, which can guide the remainder of the scan. This paper develops an automated method to identify findings that are prone to be masked. Perlin-noise phantoms and synthetic lesions were used to simulate masked cancers. NGT projections of phantoms were simulated using ray-tracing software. The risk of masking cancers was mapped using the ground-truth labels of phantoms. The phantom labels were used to denote regions of low and high risk of masking suspicious findings. A U-Net model was trained for multiclass segmentation of phantom images. Model performance was quantified with a receiver operating characteristic (ROC) curve using area under the curve (AUC). The ROC operating point was defined to be the point closest to the upper left corner of ROC space. The output predictions showed an accurate segmentation of tissue predominantly adipose (mean AUC of 0.93). The predictions also indicate regions of suspicious findings; for the highest risk class, mean AUC was 0.89, with a true positive rate of 0.80 and a true negative rate of 0.83 at the operating point. In summary, this paper demonstrates with virtual phantoms that a single projection can indeed be used to identify suspicious findings.

Keywords: Digital Breast Tomosynthesis (DBT), Virtual Clinical Trial (VCT); Anthropomorphic Phantom; Cancer Masking; Artificial Intelligence (AI); Risk-Stratified Breast Cancer Screening; Sensitivity; Specificity.

1. INTRODUCTION

Women with radiographically dense parenchyma are usually associated with having an increased risk of cancer.[1,2] Breast density can limit the sensitivity of screening exams and potentially result in missed detections (known as masked cancers) or mischaracterizations of lesions.[3] Personalized screening programs recommend additional or supplemental imaging for women with dense or complex mammary parenchyma to detect more cancers at early stages.[3–8] However, for those who receive supplemental imaging, the current imaging methods lack specificity.[9–12] Currently, no direct quantitative criterion exists to identify women for supplemental or triaged imaging, resulting in a greater number of false-positive (FP) findings.

A prototype next-generation tomosynthesis (NGT) system was built at the University of Pennsylvania (Penn) to improve the detection and characterization of breast lesions and the discrimination of glandular (dense) from adipose tissue.[13] The NGT design incorporates in the x-ray source scanning an additional component of motion in the posteroanterior direction, reducing out-of-focus structures when compared with conventional imaging systems.[13,14] Our ultimate goal is to integrate fast and intelligent methods into the NGT engine (and future designs) to identify suspicious areas and to improve the image quality in regions that are prone to mask cancers. In this paper, we investigate how a single 2D projection image can be used to identify regions that are prone to masking. Our long-term goal is to design more complex scanning motions that are directed specifically around these regions. This paper represents the first step in that direction by demonstrating the feasibility of real-time image analysis using a single 2D projection image, which could be used to guide the choice of x-ray source locations in the remainder of the scan.

16th International Workshop on Breast Imaging (IWBI2022), edited by Hilde Bosmans, Nicholas Marshall, Chantal Van Ongeval, Proc. of SPIE Vol. 12286, 122860L
 · 0277-786X · doi: 10.1117/12.2626225

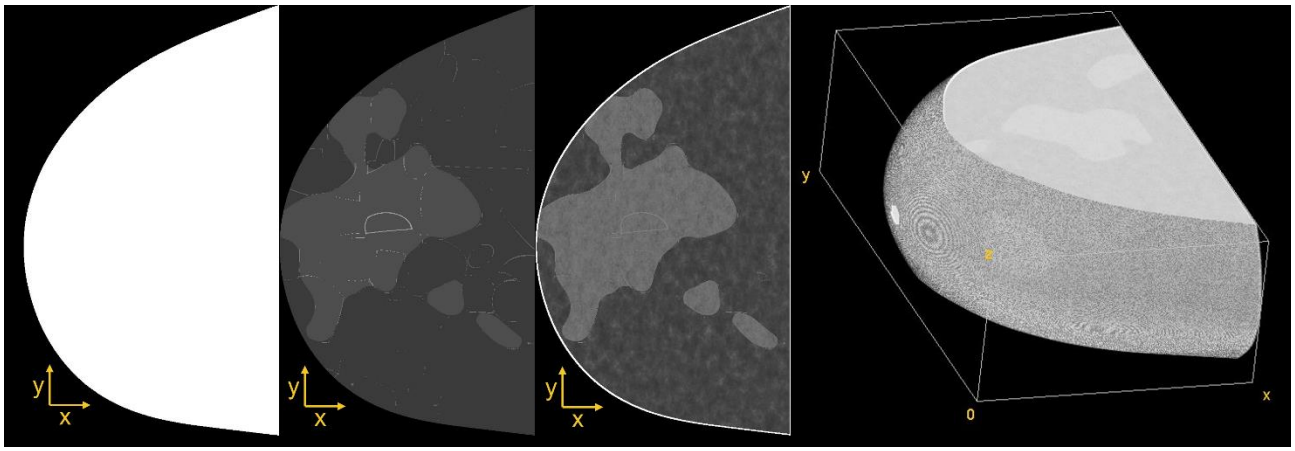

(A) (B) (C) (D)

Figure 1. (A) Example of PCA-based breast outline, (B) simulation of coarse tissue, (C) parenchyma simulation, and (D) volume view resulting from Perlin noise-based breast phantom (CC compression).

Virtual clinical trial (VCT) methods have been used to evaluate, optimize, and validate the acquisitions of the NGT design.[15–17] VCTs are usually targeted toward specific clinical tasks, requiring computational simulations of human anatomy (anthropomorphic phantoms).[15] To simulate clinical tasks that require a risk assessment of masked cancers or characterization of breast lesions, anthropomorphic phantoms should realistically simulate the anatomic noise seen in images of the mammary parenchyma.[18] Just a few studies have been reported in the literature about VCT methods for assessing and estimating the risk of masking cancers.[19,20] Mainprize *et al*. developed a masking index that locally assesses the signal-to-noise ratio of synthetic images using noise spectrum, modulation transfer function, and a task function that represents the psycho-visual model for lesion detectability.[19] However, nonlinear imaging modalities, such as digital breast tomosynthesis (DBT), complicate the use of these traditional metrics of image quality.[21] In addition, the simulation of complex mammary parenchyma is required to validate the use of objective metrics proposed for estimating the risk of masking cancers.[18]

Computer simulations of Perlin noise can improve substantially the realism of mammary parenchyma of virtual breast phantoms.[18] Perlin noise[22] uses gradient values that are smoothly connected by an interpolation function that is used to generate complex textures and patterns in medical imaging.[18,23] Dustler *et al*. have proposed the use of a variation of Perlin noise called fractal noise (or fractional Brownian motion) to simulate realistic small-scale breast structures that improve the complexity of simulated mammary parenchyma of phantoms.[24,25]

In this study, we used a Graphics Processing Unit (GPU) based library to accelerate simulations of Perlin-noise phantoms.[18] We developed an automated method to identify suspicious regions that are prone to mask cancers in Perlin-noise phantoms. These suspicious regions are considered "hotspots" for masking cancers. A U-Net architecture[26] was trained for multiclass segmentation of hotspot areas in breast images simulated using the NGT acquisition geometry. The central aim of this study is to demonstrate that hotspots can be detected in a single projection image, as this is motivated by our long-term goal of designing scanning motions that are customized around the locations of these findings.

2. MATERIALS & METHODS

2.1 Data Simulation

2.1.1 Breast Outline and Mammary Parenchyma

Breast outlines were simulated using software that models breasts under mammography compression using the principal component analysis (PCA) method.[27,28] The PCA software characterizes and models realistically the compressed breast curvature between the support table and the compression paddle. In total, 20 outlines of 0.2 mm^3 voxel size were modeled under craniocaudal (CC) compression (Figure 1A). The outlines were created using 30, 40, and 50 mm of compressed breast thickness (CBT). The chest-wall to nipple distance (CND) varied from 50 to 110 mm.

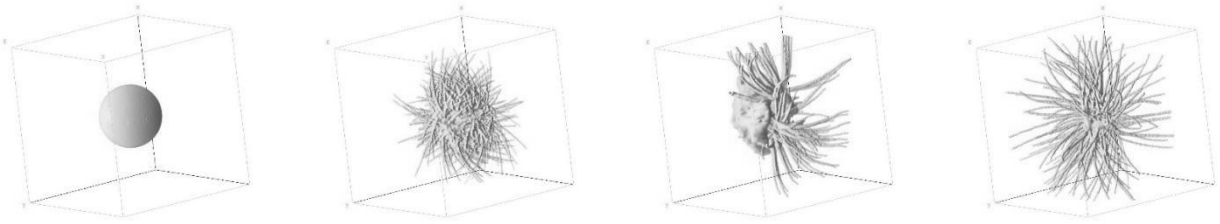

(A) (B) (C) (D)

Figure 2. Volume view of breast lesion models: (A) ellipsoidal, and (B-D) spiculated masses.[35]

Recursive partitioning software[29] was used to simulate coarse tissue within the binary outline (adipose, glandular, and Cooper's ligaments shown in Figure 1B). The coarse phantoms were simulated using 25-45% overall volumetric breast density. Note that only *dense phantoms* were simulated to represent breast anatomies with an *increased likelihood of masked lesions*. An erosion morphology operation was applied to the binary volumes to simulate the breast skin. The skin thickness was varied randomly in a [0.2, 2.4] mm interval using ball structuring elements.[30,31]

Finally, 3D fractal noise (also known as Perlin noise)[22] was simulated within the internal region of each outline to represent the anatomy of breast parenchyma (Figure 1C).[18,32] The fractal noise parameters known as lacunarity, persistence, and octaves were varied using the values {2, 3}, {0.75, 1.00}, and 6, respectively. These parameters were previously reported by Dustler *et al*.[24,25] The noise frequencies were normalized between [0.0001, 1] interval, and the log_e was applied to the voxel distribution, resulting in frequencies that are proportional to the linear x-ray attenuation of the materials in the log scale.[33] The voxel values were normalized within a 6-bit (unsigned) resolution (where materials 0 and 63 represent air and skin, respectively). The output of this normalization is known as the "Perlin phantom" (Figure 1D).[18,32] The Perlin phantoms were simulated using the open-source Perlin-CuPy methods (developed in-site).[18,32]

2.1.2 Lesions

Soft-tissue lesions (ellipsoidal and spiculated) were simulated and embedded in the Perlin-noise phantoms (Figure 2). Two lesions were embedded in each phantom using a random position in the posteroanterior (x) and chest-wall (y) direction but always in the center of the phantom in the craniocaudal direction (z). The spiculated models were segmented and scaled from contrast-enhanced magnetic resonance images in three orthogonal views (sagittal, coronal, and transverse).[34] A voxel additive method[35] was used to insert the lesion models in the phantoms. The attenuation of lesions is controlled by varying a weighting factor[35] (w_l) of the partial volume of voxels. In this study, w_l was set to 0.20 and 0.35 for lesions simulated using the ellipsoidal and spiculated models, respectively. The lesion dimensions were 7×7×7 mm^3 for both models.

Table 1. Summary of DBT acquisition parameters.

X-Ray Imaging	
Number of Projections	15
Medio-lateral (ML) Distance of Projections (max, mm)	180
Posterior-anterior (PA) Distance of Projections (max, mm)	0
Anode and Filter Materials	Tungsten and Aluminum
Filter Thickness (mm)	0.7
Angular Range ML (°)	±7.5
Tube Motion	Step-and-Shoot
Detector	
X-Ray Converter Material	Amorphous Selenium (*a*-Se)
Detector Element Size (width × height, mm)	0.085 × 0.085
Number of Elements (width × height, #)	3584 × 2816
Detector Size (width × height, mm)	304.64 × 239.36
Source-to-Image Distance in central projection (mm)	722.0

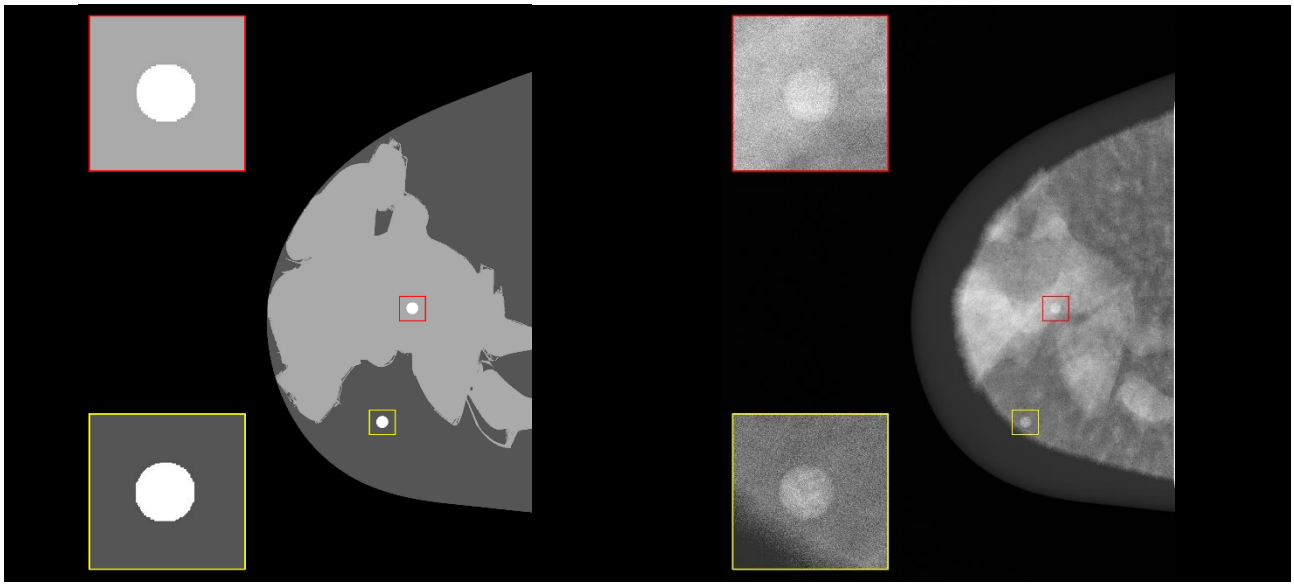

(A) (B)

Figure 3. Central slice (craniocaudal) of (A) mask using 4-class masks (background, predominantly adipose, predominantly dense, and diseased tissue) and (B) central DBT projection (for processing - contrast levels modified with window level settings) with highlighted breast curvature (dark gray). Spherical masses embedded in simulated tissue predominantly dense (red) and predominantly adipose (yellow) are shown.

2.1.3 X-ray Images and Risk Maps

Each voxel from the simulated breasts represents a composite material that consists of a complementary mixture of adipose and glandular tissue (partial volume).[18] For the 61 materials used to simulate Perlin noise (breast tissue and lesions), the composition of the partial volume of voxels decreases linearly from 99% to 1% of adipose tissue and increases linearly from 1% to 99% of glandular tissue.[18] These composite materials vary the x-ray attenuation of the images.[18]

The OpenVCT framework[36] was used to simulate DBT projections of the breast phantoms. The projection algorithm uses a fast GPU implementation of the Siddon method for ray-tracing.[37] The DBT projections were simulated assuming the conventional acquisition geometry of the NGT system, following a left-to-right scanning motion along the chest wall (Table 1). For the purpose of this study, *only the central projection image* was used to train the U-Net model (more details in the next section). We want to demonstrate the feasibility of modifying the subsequent x-ray source locations from the NGT default scan. The acquisition exposure settings were simulated using the automatic exposure control data.[14] The attenuation coefficient data of the materials used to simulate phantoms come from the International Commission on Radiation Units & Measurements (ICRU) Report 44.[38]

The maximum intensity projection (MIP) of the coarse phantoms (Figure 1B) was used to create "risk maps" (Figure 3A). MIP projects the coarse voxels from the phantoms with the maximum intensity (i.e., maximum risk) that falls in the way of parallel rays traced from the source to the plane projected at the x-ray detector. The maps were categorized into different classes: background+skin (risk 0), breast tissue predominantly adipose (risk 1), predominantly dense (risk 2), and lesion (risk 3). The maps were used to train a U-Net model along with the corresponding central DBT projection (Figure 3B). The purpose of training the U-Net model in this manner is to demonstrate the feasibility of using a single projection image to identify hotspots, as this could ultimately be applied to designing a system capable of real-time image analysis for task-directed scanning motions.

2.2 Multiclass Segmentation

The U-Net architecture[26] was used to predict risk maps from DBT projections ([0,1] normalization). The images were cropped to reduce the excessive background and the burden of processing. The cropped region corresponds to the max of CND size of the thickest phantom. The U-Net consists of 4-encoder layers that down-sample the reconstructed images and 4-decoder layers that up-sample the segmented regions of the risk maps (Figure 4). Two convolutions (3×3 kernel)

and one max-pooling (2×2 kernel) with leaky rectified linear unit (ReLU) activation are performed in each encoder layer. Padded kernels were used to maintain the aspect ratio of the input images. Batch normalization (BN) was used after each convolution. The final convolution (conv 1×1) maps a feature vector (feature maps) to the number of classes.

A U-Net model was trained for multi-class segmentation using four classes (Figure 3). The model was trained on two NVIDIA Quadro P5000 GPUs with 32 GB of RAM. We used a batch size of 22, 12 workers (sub-processes used for loading images), learning rate of 1×10^{-5}, and Adam optimizer. Early stopping was used to optimize the number of epochs of each training model (max of 250 epochs) and to avoid poor generalization performance. Weighted cross-entropy was used as the loss function (weights 1, 1, 2, 2). The hyperparameters multiplicator (weights) and learning rate were optimized using weights and bias sweeps (wandb, version 0.12). The model was built using PyTorch 1.10 and Python 3.9.9.

In total, 168, 48, and 24 input images (360×600 pixels) were used for training, validation, and testing, respectively (ratio 70:20:10%, respectively). For each set, the input images were randomly selected but equally distributed by volumetric breast density, lesion type, Perlin parameters, and breast thickness to avoid bias in the training models. The predictions of the test set were obtained, and the predictions for each class (softmax) were used to create hotspot maps (Figure 4).

The performance of the models was evaluated using the area under the pooled receiver operating characteristic (ROC) curve (AUC). The *R* libraries "pROC" (version 1.17) and "auctestr" (version 1.0) were used to collect the ROC statistics. The operating point of the ROC curve was defined to be the point that minimizes Euclidean distance relative to the upper left corner of ROC space; at this operating point, we calculated the true positive rate (TPR), true negative rate (TNR), positive predictive value (PPV), and negative predictive value (NPV). Finally, the segmentation metrics Jaccard (Jac) and Dice coefficients were calculated using the 4-class predictions.

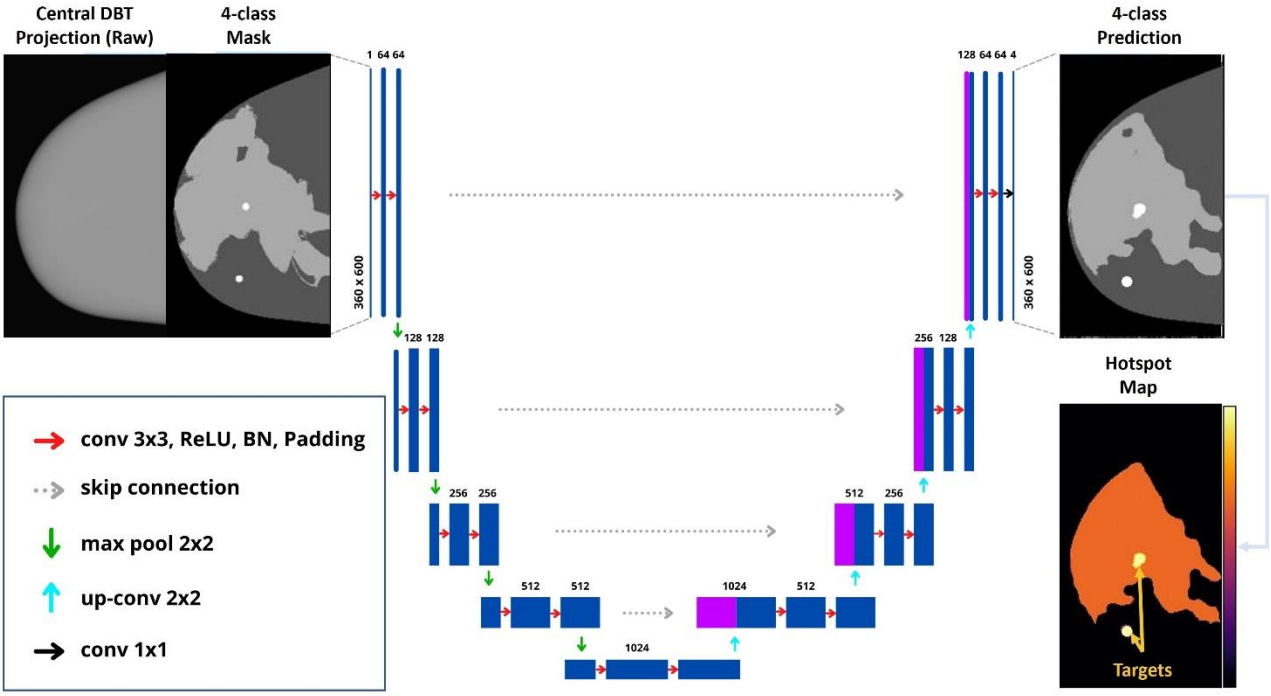

Figure 4. U-Net architecture implemented for multiclass segmentation of risk maps.

3. RESULTS

Our preliminary results have shown that the developed software is capable of precisely segmenting regions with the lowest risk of lesions (risk class 0, Figure 5B) in the central projection (Figure 5A). The software predictions (Figure 5C) indicate efficient differentiation between tissue predominantly adipose (risk class 1) and predominantly dense (risk class 2). In addition, regions with lesions are segmented by the U-Net models and classified with the highest risk (risk class 3). Note that the "hottest spots" (i.e., peaks of confidence) show the highest peaks of regions with lesions in the confidence images (Figure 5D). For future work, we will use the hotspot images to reduce the number of false positives from the predictions.

The multiclass model shows an ideal segmentation for risk class 0 (Figure 6B). Thus, the classification metrics were calculated without considering the predicted values for this class. For risk class 1, the ROC (Figure 6A) resulted in an AUC value of 0.93, demonstrating an effective segmentation of predominantly adipose tissue. Risk class 3 resulted in the lowest values of Dice (0.11) and Jaccard (0.06) due to a large number of false positives. However, this class shows a high TPR (0.80), which is comparable to risk class 2 (0.81). This result is consistent with the hotspots (i.e., peaks of confidence) found in the confidence images (Figure 5B).

The weighted cross-entropy loss maximizes the accuracy of the learning model, avoiding overfitting due to imbalanced data between the four classes. Based on these results, the sweeping of hyperparameters penalizes the segmentation of predominantly dense tissue to improve the segmentation of lesions, improving the accuracy of locating hotspot regions.

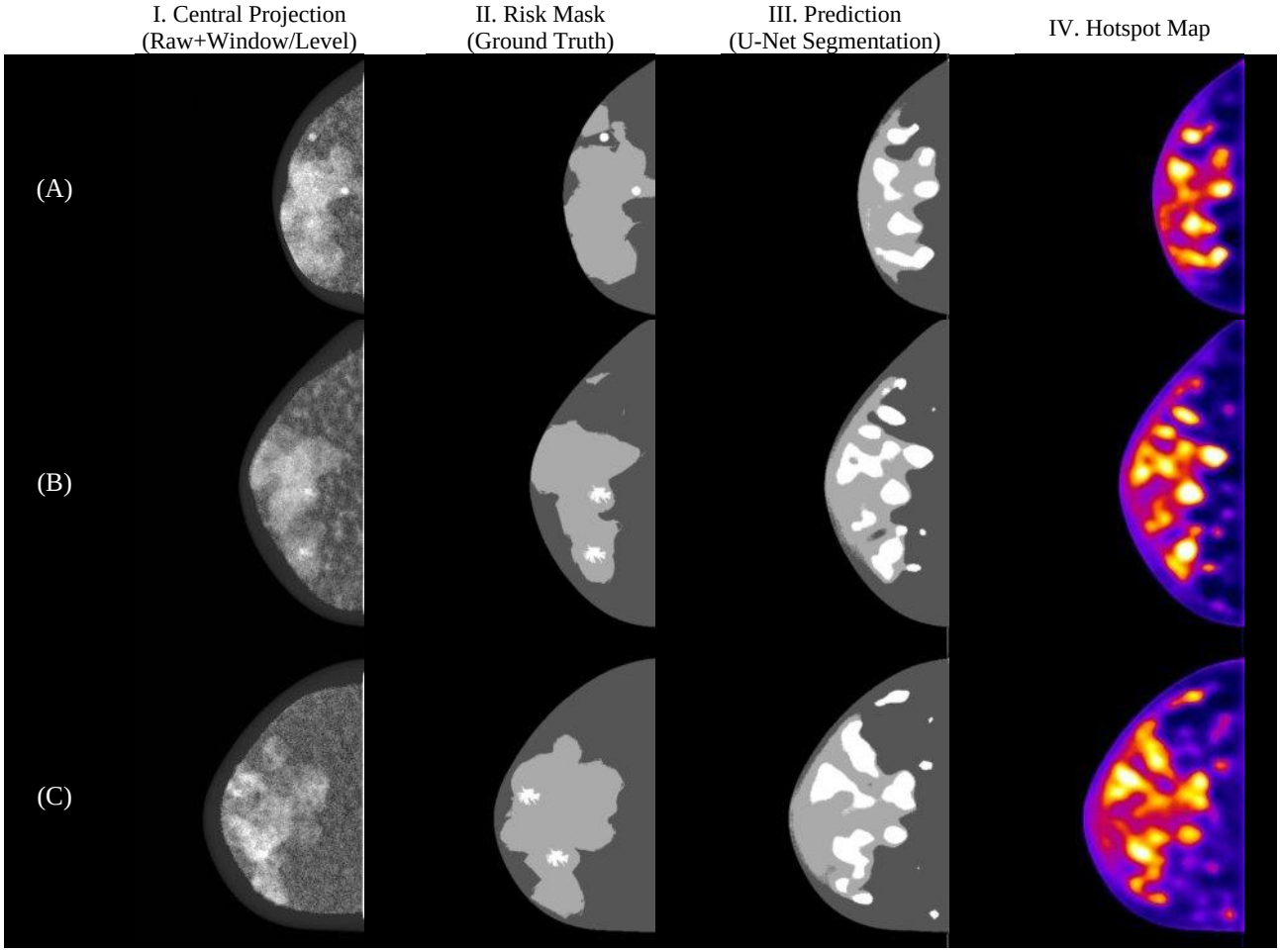

Figure 5. Examples of multi-class segmentation using U-Net model: (I) central projection, (II) risk masks, (III) predictions and (IV) hotspot map. (cont.)

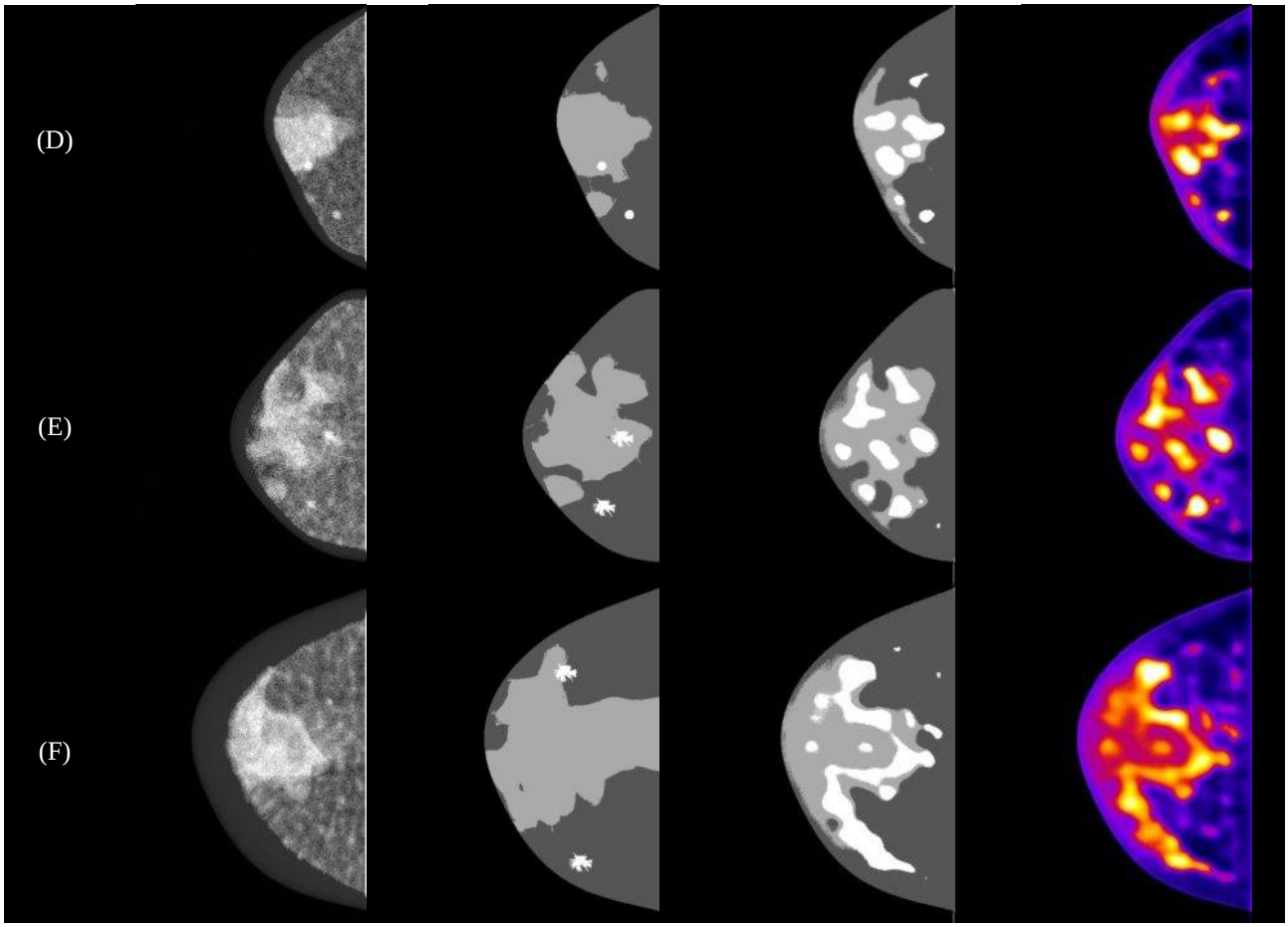

Figure 5. Examples of multi-class segmentation using U-Net model: (I) central projection, (II) risk masks, (III) predictions, and (IV) hotspot map.

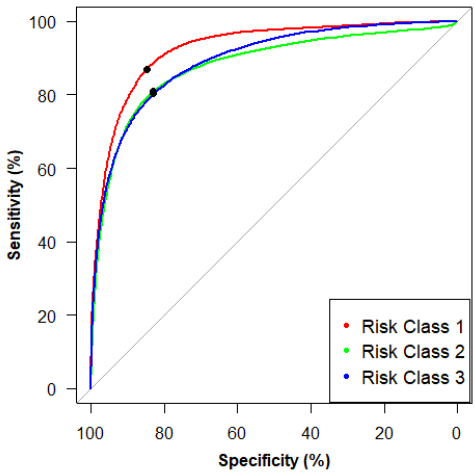

(A)

Risk Class	Dice	Jac	AUC	TPR	TNR	PPV	NPV
0	1.00	0.99	-	-	-	-	-
1	0.88	0.79	0.93	0.87	0.85	0.88	0.83
2	0.67	0.51	0.88	0.81	0.83	0.78	0.86
3	0.11	0.06	0.89	0.80	0.83	0.05	0.99

(B)

Figure 6. (A) Receiver operating characteristic curves (operating point in black) and (B) summary of segmentation and classification metrics.

4. DISCUSSION AND CONCLUSION

The sensitivity of cancer detection by screening mammography is reduced in women with dense breasts, resulting in masked cancers and mischaracterizations of lesions. In this work, we have developed an automated method to identify suspicious areas in breast phantoms with a single 2D projection image. Our future work will apply this method to designing a DBT system capable of identifying suspicious areas in real time and dynamically calculating the scanning motion that optimizes visualization of these areas, potentially improving the sensitivity of cancer detection and the characterization of suspicious findings. It is important to mention that the ultimate goal of the software is *not* to be used as a computer-aided diagnosis (CAD) system. Instead, the software should be used to indicate regions with a higher likelihood of cancer.

This study has some limitations. Spiculated lesions have sharp ramifications on the tumor that can vary greatly in density and length, from a few millimeters to several centimeters (Figure 2). These ramifications complicate the segmentation, reducing the performance of the model shown in the segmentation metrics (Figure 5B). In addition, the linear attenuation coefficient of the lesions composed of soft tissue is very close to the dense tissue, which compromises the differentiation between risk class 2 and 3. However, the ultimate goal of this study is *not* the perfect segmentation of lesions (or dense tissue). Instead, we will use this software to indicate the locations of suspicious findings to improve the NGT acquisitions.

Another limitation of this study is that the U-Net model for identifying hotspots was developed with virtual breast phantoms as opposed to clinical images. Future work will explore alternate strategies for training the U-Net model using clinical images with known findings. In addition, we will increase the number of images for the test and validation set, use cross-validation during the training process, and investigate the use of alternative focal loss functions to improve the segmentation of the U-Net.

ACKNOWLEDGEMENTS

The authors want to thank Dr. Hilde Bosmans for providing the models of spiculated masses used in this work. Funding for the research is supported primarily by the 2020 AAPM Research Seed Funding Grant. The following grants also support this research: BWF IRSA 1016451, DoD W81XWH-18-1-0082, NCI P30 CA016520, and a 2022 Young Investigator Grant through Breast Cancer Alliance, Inc.

REFERENCES

[1] Bird, R. E., Wallace, T. W. and Yankaskas, B. C., "Analysis of cancers missed at screening mammography.," Radiology (2014).

[2] Nelson, H. D., O'Meara, E. S., Kerlikowske, K., Balch, S. and Miglioretti, D., "Factors associated with rates of false-positive and false-negative results from digital mammography screening: An analysis of registry data," Annals of Internal Medicine (2016).

[3] Buchberger, W., Niehoff, A., Obrist, P., DeKoekkoek-Doll, P. and Dünser, M., "Clinically and mammographically occult breast lesions: Detection and classification with high-resolution sonography," Seminars in Ultrasound CT and MRI (2000).

[4] Crystal, P., Strano, S. D., Shcharynski, S. and Koretz, M. J., "Using sonography to screen women with mammographically dense breasts," American Journal of Roentgenology (2003).

[5] Gordon, P. B. and Goldenberg, S. L., "Malignant breast masses detected only by ultrasound. A retrospective review," Cancer (1995).

[6] Kaplan, S. S., "Clinical Utility of Bilateral Whole-Breast US in the Evaluation of Women with Dense Breast Tissue," Radiology (2001).

[7] Kolb, T. M., Lichy, J. and Newhouse, J. H., "Comparison of the Performance of Screening Mammography, Physical Examination, and Breast US and Evaluation of Factors that Influence Them: An Analysis of 27,825 Patient Evaluations," Radiology (2002).

[8] Leconte, I., Feger, C., Galant, C., Berlière, M., Vande Berg, B., D'Hoore, W. and Maldague, B., "Mammography and subsequent whole-breast sonography of nonpalpable breast cancers: The importance of radiologic breast density," American Journal of Roentgenology (2003).

[9] Vourtsis, A. and Berg, W. A., "Breast density implications and supplemental screening," European Radiology (2018).

[10] Berg, W. A., "Tailored supplemental screening for breast cancer: What now and what next?," American Journal of Roentgenology (2009).
[11] Kuhl, C. K., Schrading, S., Leutner, C. C., Morakkabati-Spitz, N., Wardelmann, E., Fimmers, R., Kuhn, W. and Schild, H. H., "Mammography, breast ultrasound, and magnetic resonance imaging for surveillance of women at high familial risk for breast cancer," Journal of Clinical Oncology (2005).
[12] Phi, X. A., Houssami, N., Hooning, M. J., Riedl, C. C., Leach, M. O., Sardanelli, F., Warner, E., Trop, I., Saadatmand, S., Tilanus-Linthorst, M. M. A., Helbich, T. H., van den Heuvel, E. R., de Koning, H. J., Obdeijn, I. M. and de Bock, G. H., "Accuracy of screening women at familial risk of breast cancer without a known gene mutation: Individual patient data meta-analysis," European Journal of Cancer (2017).
[13] Acciavatti, R. J., Barufaldi, B., Vent, T. L., Wileyto, E. P. and Maidment, A. D. A., "Personalization of x-ray tube motion in digital breast tomosynthesis using virtual Defrise phantoms," Progress in Biomedical Optics and Imaging - Proceedings of SPIE **10948** (2019).
[14] Vent, T. L., Barufaldi, B., Acciavatti, R. J., Krishnamoorthy, S., Surti, S. and Maidment, A. D. A., "Next generation tomosynthesis image acquisition optimization for dedicated PET-DBT attenuation corrections," 2021.
[15] Abadi, E., Segars, W. P., Tsui, B. M. W., Kinahan, P. E., Bottenus, N., Frangi, A. F., Maidment, A., Lo, J. and Samei, E., "Virtual clinical trials in medical imaging: a review," Journal of Medical Imaging **7**(4), 042805-1–40 (2020).
[16] Vent, T. L., Barufaldi, B., Acciavatti, R. J. and Maidment, A., "Simulation of high-resolution test objects using non-isocentric acquisition geometries in next-generation digital tomosynthesis," 2020.
[17] Barufaldi, B., Bakic, P. R., Higginbotham, D. and Maidment, A. D. A., "OpenVCT: a GPU-accelerated virtual clinical trial pipeline for mammography and digital breast tomosynthesis," SPIE Medical Imaging 2018 **1057358**(March), 1–8, SPIE Digital Library, Houston, TX (2018).
[18] Barufaldi, B., Abbey, C. K., Lago, M. A., Vent, T. L., Acciavatti, R. J., Bakic, P. R. and Maidment, A. D. A., "Computational Breast Anatomy Simulation Using Multi-scale Perlin Noise," IEEE Transactions on Medical Imaging **xx**(X), 1–11 (2021).
[19] Mainprize, J. G., Alonzo-Proulx, O., Jong, R. A. and Yaffe, M. J., "Quantifying masking in clinical mammograms via local detectability of simulated lesions," Medical Physics **43**(3), 1249–1258 (2016).
[20] Alonzo-Proulx, O., Mainprize, J. G., Harvey, J. A. and Yaffe, M. J., "Investigating the feasibility of stratified breast cancer screening using a masking risk predictor," Breast Cancer Research **21**(1), 1–9 (2019).
[21] Zhao, B., Zhou, J., Hu, Y. H., Mertelmeier, T., Ludwig, J. and Zhao, W., "Experimental validation of a three-dimensional linear system model for breast tomosynthesis," Medical Physics (2009).
[22] Perlin, K., "Improving Noise," ACM Transactions on Graphics (2002).
[23] Worley, S., "A cellular texture basis function," Proceedings of the 23rd Annual Conference on Computer Graphics and Interactive Techniques, SIGGRAPH 1996 (1996).
[24] Dustler, M., Bakic, P., Petersson, H., Timberg, P., Tingberg, A. and Zackrisson, S., "Application of the fractal Perlin noise algorithm for the generation of simulated breast tissue," Medical Imaging 2015: Physics of Medical Imaging (2015).
[25] Dustler, M., Lång, K. and Petersson, H., "Binary implementation of fractal Perlin noise to simulate fibroglandular breast tissue," 193 (2018).
[26] Ronneberger, O., Fischer, P. and Brox, T., "U-net: Convolutional networks for biomedical image segmentation," Lecture Notes in Computer Science (including subseries Lecture Notes in Artificial Intelligence and Lecture Notes in Bioinformatics) (2015).
[27] Rodríguez-Ruiz, A., Agasthya, G. A. and Sechopoulos, I., "The compressed breast during mammography and breast tomosynthesis: *in vivo* shape characterization and modeling," Physics in Medicine & Biology **62**(17), 6920–6937 (2017).
[28] Rodriguez-Ruiz, A., Feng, S. S. J., Van Zelst, J., Vreemann, S., Mann, J. R., D'Orsi, C. J. and Sechopoulos, I., "Improvements of an objective model of compressed breasts undergoing mammography: Generation and characterization of breast shapes," Medical Physics **44**(6), 2161–2172 (2017).
[29] Pokrajac, D. D., Maidment, A. D. A. and Bakic, P. R., "Optimized generation of high resolution breast anthropomorphic software phantoms," Medical Physics **39**(4), 2290 (2012).
[30] Pietzsch, T., Preibisch, S., Tomančák, P. and Saalfeld, S., "Img lib 2-generic image processing in Java," Bioinformatics (2012).

[31] Sutradhar, A. and Miller, M. J., “In vivo measurement of breast skin elasticity and breast skin thickness,” Skin Research and Technology **19**(1), 191–199 (2013).
[32] Teixeira, J. P. V. and Barufaldi, B., “Perlin-CuPy: Perlin-NumPy for GPU,” Github, 2021, <https://github.com/jpvt/perlin-cupy>.
[33] Rumble, J. R., Bickham, D. M. and Powell, C. J., “The NIST x-ray photoelectron spectroscopy database,” Surface and Interface Analysis (1992).
[34] Shaheen, E., De Keyzer, F., Bosmans, H., Dance, D. R., Young, K. C. and Ongeval, C. Van., “The simulation of 3D mass models in 2D digital mammography and breast tomosynthesis,” Medical Physics **41**(8), 10–12 (2014).
[35] Barufaldi, B., Vent, T. L., Bakic, P. R. and Maidment, A. D. A., “Computer simulations of case difficulty in digital breast tomosynthesis using virtual clinical trials,” Med. Phys. - Early View, 1–13 (2022).
[36] Barufaldi, B., Bakic, P. and Maidment, A. D. A., “Open Virtual Clinical Trials,” OpenVCT: a GPU-accelerated virtual clinical trial pipeline for mammography and digital breast tomosynthesis, 2020, <https://sourceforge.net/projects/openvct/> (10 March 2019).
[37] Siddon, R. L., “Fast calculation of the exact radiological path for a three dimensional CT array,” Medical Physics **12**(2), 252–255 (1985).
[38] ICRU., “ICRU Report 44 - Tissue Substitutes in Radiation Dosimetry and Measurement” (1988).
[39] Barufaldi, B., Bakic, P. R. and Maidment, A. D. A., “Multiple-reader, multiple-case ROC analysis for determining the limit of calcification detection in tomosynthesis,” SPIE Medical Imaging 2019: Physics of Medical Imaging **10948**(March), 22 (2019).

COMPLETE PERSONNEL LIST

Below is a list of all personnel who worked on this grant, as well as their job title / role at the University of Pennsylvania at the time of the project (DoD Grant W81XWH-18-1-0082).

1. Raymond J. Acciavatti, Ph.D. (PI)
   Research Assistant Professor of Radiology

2. Bruno Barufaldi, Ph.D.
   Research Associate in the Department of Radiology

3. Emily Conant, M.D.
   Professor of Radiology

4. David Higginbotham
   Software Developer in the Department of Radiology

5. Despina Kontos, Ph.D.
   Matthew J. Wilson Associate Professor of Research Radiology II

6. Andrew Maidment, Ph.D.
   Associate Professor of Radiology

7. E. Paul Wileyto, Ph.D.
   Senior Research Investigator, Department of Biostatistics and Epidemiology

8. Matthew Willardson
   Student in Master's Degree Program at the University of Pennsylvania

Transition Plan Questionnaire

Directions: Please answer all questions that apply for each product under development. Please fill out one document per product.
This is not an application for funding; however, answers will help us understand the outcomes and products from your award.

1. After the award closes, would you be willing to periodically provide voluntary information (via email) regarding the project status (i.e. where the research is headed)? **Yes** ☑ or **No** ☐
These responses will help CDMRP demonstrate the return on its investments and will help demonstrate that the CDMRP is a responsible and successful steward of federal research funding.

2. What **conclusion(s)** does your final data support?

Digital breast tomosynthesis (DBT) is the latest 3D advancement in breast cancer screening. In clinical DBT systems, the x-ray tube scans in just one direction (laterally). In this grant, virtual clinical trials (VCTs) with breast phantoms were performed to simulate the next generation of DBT systems with x-ray tube motion in two directions: laterally and posteroanteriorly (PA). We concluded that this new scanning geometry benefits the visualization of dense tissue (which is susceptible to cancer masking). More specifically, signal-intensity differences between dense and adipose tissue were improved in receiver operating characteristic (ROC) analyses. Also, model-observer performance in mass detection was more isotropic (less sensitive to position). We concluded that the range of PA motion should be customized around the breast size. Additionally, we concluded that super-resolution (SR) benefits calcification detection, as model-observer ROC performance was improved with SR. To optimize SR (both in terms of quality and suppression of anisotropies), the x-ray source positions should be re-arranged in clusters with submillimeter spacing, as could be achieved by rapidly pulsing the x-ray source. Finally, we concluded that magnification mammography, a diagnostic exam for suspicious calcifications, can indeed be re-designed to incorporate tomosynthesis (3D imaging), unlike clinical systems which acquire a single 2D image. We optimized the design of magnification tomosynthesis for SR, with the goal of achieving the highest image quality for calcifications.

3. Will you/have you applied for/obtained follow-on-funding for this project? **If yes**, please list (a) funding organization, (b) total budget requested/obtained, and (c) title of the funded proposal. *This information will be recorded as an outcome to this award*.

1. Penn internal grant "Feasibility of Self-Steering 3D Mammography" ($50,000) funded by Abramson Cancer Center's support grant NCI P30 CA016520 (7/1/21-6/30/22); 2. Penn internal grant "Self-Steering Tomosynthesis Using Mastectomy Specimens" ($50,000) supported by Institute for Translational Medicine & Therapeutics of Penn and NIH UL1TR001878 (3/1/22-2/28/23); 3. Breast Cancer Alliance Young Investigator Grant "Self-Steering 3D Mammography" ($125,000) from 3/1/22-2/28/24; 4. NIH R37CA273959 "Next-Generation Tomosynthesis Pilot Study" (FY Total Cost by IC $371,719 Year 2022) from 8/17/22-6/30/26.

4. What will be **the next step(s)** for this project?

This DoD grant (W81XWH-18-1-0082) focused on VCTs and simulations of the next-generation tomosynthesis (NGT) system; two separate grants funded the construction of the physical NGT system: NIH R01CA196528 (PI: Surti) and Komen IIR13264610 (PI: Maidment). Our next step is to recruit human subject volunteers to be imaged with the NGT system. The PI (Acciavatti) received funding from the NIH (R37CA273959: start date 8/17/22) to evaluate a next-generation scanning motion in comparison with a conventional scanning motion. A separate NIH grant (R01CA196528, PI: Surti) will be investigating how the tomosynthesis acquisition can be used in combination with positron emission tomography (PET) to co-register anatomical information with functional information derived from radiotracer uptake in human subject volunteers using the NGT system.

5. How would you classify your **lead candidate product**? e

(a) Therapeutic (Small Molecule, Biologic, Cell/Gene Therapy): Please choose, if applicable
(b) Diagnostic
(c) Device
(d) Research Tool to Address a Research Bottleneck
(e) Knowledge Product (Non-material product such as a compound library, database, something that improves clinical practice, education, etc.)
(f) Other - Please Specify:

6. How does your candidate product aid the Warfighter, Veteran, Beneficiary, and/or General Population?

Our long-term goal is to re-design the scanning geometries used in 3D mammography systems, thereby improving visualization of breast density and suspicious lesions. If 3D mammography systems are ultimately re-designed in clinical practice based on the results of this grant, it will benefit women in the Warfighter, Veteran, Beneficiary, and General Population based on the use of 3D mammography for breast cancer screening in women. It will also benefit some men in the Warfighter, Veteran, Beneficiary, and General Population, as some men do develop breast cancer (though the incidence is lower than in women).

7. Therapy / Product Development, Transition Strategies, and Intellectual Property

Describe the steps and relevant strategies required to move the candidate product (knowledge or tangible) to the next phase of development and/or commercialization. Please address any issues with intellectual property.

PIs are encouraged to explore the technical requirements and the current regulatory strategies involved in product development as well as to work with their organization's Technology Transfer Office (or equivalent regulatory/legal office), federal/international regulatory experts, to develop the transition plan and to explore developing relationships with industry, DoD advanced developers (e.g. USAMMDA), and/or other funding agencies to facilitate moving the product into the next phase.

This DoD grant performed computational modeling and simulations that led to the design of new scanning geometries for 3D mammography. As we implement these geometries in the NGT system, we will be pursuing three strategies to ensure that the new geometries are ultimately translated into clinical practice. First, we are aiming to recruit human subject volunteers to develop an understanding of how the new scanning geometry improves visualization of breast density and lesions (masses, calcifications, and architectural distortions) compared against the conventional scanning geometry (R37CA273959, PI: Acciavatti - start date 8/17/22). Second, we will continue communicating with manufacturers and presenting results at conferences to promote broader implementation of the new scanning geometries. Finally, to achieve the highest possible image quality, we will continue refining the scanning geometries to include the latest advancements in real-time image analysis that we are developing through the "self-steering" tomosynthesis grants described in Section 3.

W81XWH-18-1-0082 (BC170226): Design of a 3D Mammography System in the Age of Personalized Medicine

PI: Raymond J. Acciavatti, University of Pennsylvania

Budget: $603,749.00 **Topic Area:** Breast Cancer Research Program **Mechanism:** Breakthrough Award-Level 1

Research Area: X-Ray Imaging (708) Digital Imaging (704) **Award Status: Open** March 15, 2018 to March 14, 2022 (NCE)

Study Goals: Even with the latest "3D" digital breast tomosynthesis systems, most women that are recalled for follow-up testing after a suspicious mammogram are ultimately found to be cancer-free. To improve the sensitivity and specificity of breast imaging for cancer detection, we are proposing to re-design mammography systems around the principle of "personalized medicine", so that the orbits of the detector and x-ray tube are customized to the size, shape, and composition of each breast. The new designs for both screening and diagnostic mammography will be validated with a virtual clinical trial (VCT) using realistic simulations of breast anatomy and a highly-validated observer model.

Specific Aims: SA1: Design a personalized image acquisition technique for screening mammography. SA2: Design a 3D magnification mammography call-back exam. SA3: Evaluate the new designs for screening and call-back imaging with a virtual clinical trial.

Key Accomplishments:

Publications:

1. Acciavatti et al. Non-stationary model of oblique x-ray incidence in amorphous selenium detectors: I. Point spread function. Med. Phys. 2019; 46(2):494-504. 10.1002/mp.13313.
2. Acciavatti et al. Nonstationary model of oblique x-ray incidence in amorphous selenium detectors: II. Transfer Functions. Med. Phys. 2019; 46(2); 505-16. 10.1002/mp.13312.
3. Acciavatti et al. Personalization of x-ray tube motion in digital breast tomosynthesis using virtual Defrise phantoms. Proc. SPIE 2019, 109480B. 10.1117/12.2511780.
4. Acciavatti et al. Robust Radiomic Feature Selection in Digital Mammography: Understanding the Effect of Imaging Acquisition Physics Using Phantom and Clinical Data Analysis. Proc. SPIE 2020, 113140W. 10.1117/12.2549163.
5. Acciavatti et al. Proposing Rapid Source Pulsing for Improved Super-Resolution in Digital Breast Tomosynthesis. Proc. SPIE 2020, 113125G. 10.1117/12.2542551.
6. Barufaldi et al. Determining the Optimal Angular Range of the X-Ray Source Motion in Tomosynthesis Using Virtual Clinical Trials. Proc. SPIE 2020, 113120I. 10.1117/12.2549600.
7. Acciavatti et al. Calculation of Radiomic Features to Validate the Textural Realism of Physical Anthropomorphic Phantoms for Digital Mammography. Proc. SPIE 2020, 1151309. 10.1117/12.2564363.
8. Acciavatti et al. Super-Resolution in Digital Breast Tomosynthesis: Limitations of the Conventional System Design and Strategies for Optimization. Proc. SPIE 2020, 115130V. 10.1117/12.2563839.
9. Barufaldi et al. MRMC ROC Analysis of Calcification Detection in Tomosynthesis Using Computed Super Resolution and Virtual Clinical Trials. Proc. SPIE 2020, 1151313. 10.1117/12.2564118.
10. Vent et al. Simulation of high-resolution test objects using non isocentric acquisition geometries in next-generation digital tomosynthesis. Proc. SPIE 2020, 1151317. 10.1117/12.2561098.
11. Peregrino et al. Automatic Segmentation of Mammary Tissue using Computer Simulations of Breast Phantoms and Deep-Learning Techniques. Proceedings of the 14th International Joint Conference on Biomedical Engineering Systems and Technologies (BIOSTEC 2021) - Vol. 4: BIOSIGNALS, p. 252-259. 10.5220/0010310402520259.
12. Acciavatti et al. Development of Magnification Tomosynthesis for Superior Resolution in Diagnostic Mammography. Proc. SPIE 2021, 115951J. 10.1117/12.2580280.
13. Choi et al. Analysis of Digital Breast Tomosynthesis Acquisition Geometries in Sampling Fourier Space. Proc. SPIE 2021, 115954W. 10.1117/12.2582229.
14. Martin et al. Signal-to-Noise Ratio and Contrast-to-Noise Ratio Measurements for Next Generation Tomosynthesis. Proc. SPIE 2021, 115951L. 10.1117/12.2582279.
15. Vent et al. Next generation tomosynthesis image acquisition optimization for dedicated PET-DBT attenuation corrections. Proc. SPIE 2021, 115954V. 10.1117/12.2581097.
16. Vent et al. Development and Evaluation of the Fourier Spectral Distortion Metric. IEEE Transactions on Medical Imaging 2021; 40(3):1055-64. 10.1109/TMI.2020.3045325.
17. Barufaldi et al. Virtual Clinical Trials in Medical Imaging System Evaluation and Optimisation. Radiation Protection Dosimetry 2021; 195(3-4):363-371. 10.1093/rpd/ncab080.
18. Acciavatti et al. Anisotropies in Super-Resolution in 3D Magnification Mammography Using a Next-Generation Tomosynthesis System. Med. Phys. 2021; 48(6): 51. 10.1002/mp.15041.
19. Acciavatti et al. Incorporating Robustness to Imaging Physics into Radiomic Feature Selection for Breast Cancer Risk Estimation. Cancers 2021; 13(21):5497. 10.3390/cancers13215497..
20. Barufaldi et al. Computational Breast Anatomy Simulation Using Multi-Scale Perlin Noise. IEEE Transactions on Medical Imaging 2021; 40(12):3436-45. 10.1109/TMI.2021.3087958.
21. Barufaldi et al. Computer simulations of case difficulty in digital breast tomosynthesis using virtual clinical trials. Medical Physics 2022; 49:2220-2232. 10.1002/mp.15553.
22. Acciavatti et al. Achieving Isotropic Super-Resolution with a Non-Isocentric Acquisition Geometry in a Next-Generation Tomosynthesis System. Proc. SPIE 2022, 120314B. 10.1117/12.2612451.
23. Choi et al. Investigation of optimal angular range and projection density for next generation tomosynthesis. Proc. SPIE 2022, 120314C. 10.1117/12.2612419.
24. Dong et al. Assessment of patch-based mammogram denoising methods using virtual clinical trials and deep learning: trade-off between denoising strength and preservation of structural details. Proc. SPIE 2022, 120311W. 10.1117/12.2612900.
25. Teixeira et al. Novel Perlin-based Phantoms Using 3D Models of Compressed Breast Shape and Fractal Noise. Proc. SPIE 2022, 120313S. 10.1117/12.2612565.
26. Vent et al. Pre-clinical evaluation and optimization of image quality for a Next Generation Tomosynthesis prototype. Proc. SPIE 2022, 1203142. 10.1117/12.2608811.
27. Choi et al. Spatial dependency of lesion detectability in digital breast tomosynthesis. Proc. SPIE 2022. 10.1117/12.2626272.
28. Nobrega et al. Multiclass Segmentation of Suspicious Findings in Simulated Breast Tomosynthesis Images Using a U-Net. Proc. SPIE 2022. 10.1117/12.2626225.

Patents: None.

Funding Obtained: (1) R. Acciavatti was a mentor for the 2019 summer undergraduate fellowship program through the American Association of Physicists in Medicine (AAPM). (2) R. Acciavatti is PI of the grant "Feasibility of Self-Steering 3D Mammography" (Co-PI: Andrew Maidment). This Penn Pilot grant from 7/1/21 to 6/30/22 is funded by the Abramson Cancer Center's support grant NCI P30 CA016520. (3) R. Acciavatti is PI of the grant "Self-Steering Tomosynthesis Using Mastectomy Specimens" (Co-PI: Emily Conant / Michael Feldman). This Penn Pilot grant from 3/1/22 to 2/28/23 is supported in part by the Institute for Translational Medicine and Therapeutics at Penn and also by NIH UL1TR001878. (4) R. Acciavatti is PI of Young Investigator Grant "Self-Steering 3D Mammography" through Breast Cancer Alliance from 3/1/22 to 2/28/24. (5) R. Acciavatti is PI of NIH R37CA273959 ("Next-Generation Tomosynthesis Pilot Study") from 8/17/22 to 6/30/26.